EMERGING TECHNOLOGIES AND TECHNIQUES FOR REMOTE SENSING OF COASTAL AND INLAND WATERS

EDITED BY: Wesley Moses, Sherry L. Palacios and Andrea J. Vander Woude
PUBLISHED IN: Frontiers in Environmental Science

frontiers Research Topics

frontiers

Frontiers eBook Copyright Statement

The copyright in the text of individual articles in this eBook is the property of their respective authors or their respective institutions or funders. The copyright in graphics and images within each article may be subject to copyright of other parties. In both cases this is subject to a license granted to Frontiers.

The compilation of articles constituting this eBook is the property of Frontiers.

Each article within this eBook, and the eBook itself, are published under the most recent version of the Creative Commons CC-BY licence. The version current at the date of publication of this eBook is CC-BY 4.0. If the CC-BY licence is updated, the licence granted by Frontiers is automatically updated to the new version.

When exercising any right under the CC-BY licence, Frontiers must be attributed as the original publisher of the article or eBook, as applicable.

Authors have the responsibility of ensuring that any graphics or other materials which are the property of others may be included in the CC-BY licence, but this should be checked before relying on the CC-BY licence to reproduce those materials. Any copyright notices relating to those materials must be complied with.

Copyright and source acknowledgement notices may not be removed and must be displayed in any copy, derivative work or partial copy which includes the elements in question.

All copyright, and all rights therein, are protected by national and international copyright laws. The above represents a summary only. For further information please read Frontiers' Conditions for Website Use and Copyright Statement, and the applicable CC-BY licence.

ISSN 1664-8714
ISBN 978-2-83250-409-3
DOI 10.3389/978-2-83250-409-3

About Frontiers

Frontiers is more than just an open-access publisher of scholarly articles: it is a pioneering approach to the world of academia, radically improving the way scholarly research is managed. The grand vision of Frontiers is a world where all people have an equal opportunity to seek, share and generate knowledge. Frontiers provides immediate and permanent online open access to all its publications, but this alone is not enough to realize our grand goals.

Frontiers Journal Series

The Frontiers Journal Series is a multi-tier and interdisciplinary set of open-access, online journals, promising a paradigm shift from the current review, selection and dissemination processes in academic publishing. All Frontiers journals are driven by researchers for researchers; therefore, they constitute a service to the scholarly community. At the same time, the Frontiers Journal Series operates on a revolutionary invention, the tiered publishing system, initially addressing specific communities of scholars, and gradually climbing up to broader public understanding, thus serving the interests of the lay society, too.

Dedication to Quality

Each Frontiers article is a landmark of the highest quality, thanks to genuinely collaborative interactions between authors and review editors, who include some of the world's best academicians. Research must be certified by peers before entering a stream of knowledge that may eventually reach the public - and shape society; therefore, Frontiers only applies the most rigorous and unbiased reviews.
Frontiers revolutionizes research publishing by freely delivering the most outstanding research, evaluated with no bias from both the academic and social point of view. By applying the most advanced information technologies, Frontiers is catapulting scholarly publishing into a new generation.

What are Frontiers Research Topics?

Frontiers Research Topics are very popular trademarks of the Frontiers Journals Series: they are collections of at least ten articles, all centered on a particular subject. With their unique mix of varied contributions from Original Research to Review Articles, Frontiers Research Topics unify the most influential researchers, the latest key findings and historical advances in a hot research area! Find out more on how to host your own Frontiers Research Topic or contribute to one as an author by contacting the Frontiers Editorial Office: frontiersin.org/about/contact

EMERGING TECHNOLOGIES AND TECHNIQUES FOR REMOTE SENSING OF COASTAL AND INLAND WATERS

Topic Editors:
Wesley Moses, United States Naval Research Laboratory, United States
Sherry L. Palacios, California State University, United States
Andrea J. Vander Woude, NOAA-Great Lakes Environmental Research Laboratory, United States

Citation: Moses, W., Palacios, S. L., Woude, A. J. V., eds. (2022). Emerging Technologies and Techniques for Remote Sensing of Coastal and Inland Waters. Lausanne: Frontiers Media SA. doi: 10.3389/978-2-83250-409-3

Table of Contents

frontiers | Frontiers in Environmental Science

TYPE Editorial
PUBLISHED 21 September 2022
DOI 10.3389/fenvs.2022.1028307

Check for updates

OPEN ACCESS

EDITED AND REVIEWED BY
Alexander Kokhanovsky,
Max Planck Institute for Chemistry, Germany

*CORRESPONDENCE
Wesley J. Moses,
wesley.moses@nrl.navy.mil

SPECIALTY SECTION
This article was submitted to Environmental Informatics and Remote Sensing, a section of the journal Frontiers in Environmental Science

RECEIVED 25 August 2022
ACCEPTED 29 August 2022
PUBLISHED 21 September 2022

CITATION
Moses WJ, Vander Woude AJ and Palacios SL (2022), Editorial: Emerging technologies and techniques for remote sensing of coastal and inland waters. *Front. Environ. Sci.* 10:1028307. doi: 10.3389/fenvs.2022.1028307

COPYRIGHT
© 2022 Moses, Vander Woude and Palacios. This is an open-access article distributed under the terms of the Creative Commons Attribution License (CC BY). The use, distribution or reproduction in other forums is permitted, provided the original author(s) and the copyright owner(s) are credited and that the original publication in this journal is cited, in accordance with accepted academic practice. No use, distribution or reproduction is permitted which does not comply with these terms.

Editorial: Emerging technologies and techniques for remote sensing of coastal and inland waters

Wesley J. Moses[1]*, Andrea J. Vander Woude[2] and Sherry L. Palacios[3]

[1]U.S. Naval Research Laboratory, Washington, DC, United States, [2]National Oceanic and Atmospheric Administration, Great Lakes Environmental Research Laboratory, Ann Arbor, MI, United States, [3]California State University Monterey Bay, Seaside, CA, United States

KEYWORDS

hyperspectral, multispectral, unmanned aerial vehicles (UAVs), CubeSats, machine learning, coastal and inland waters, wetlands

Editorial on the Research Topic
Emerging Technologies and Techniques for Remote Sensing of Coastal and Inland Waters

Coastal and inland waters are critical resources of immense economic and environmental value (e.g., Ledoux and Turner, 2002; Revenga and Kura, 2003). However, due to natural and anthropogenic factors, coastal and inland waters around the globe are under increasing stress. The health and biophysical status of these ecosystems need to be regularly monitored in order to ensure that they maintain their ecological functionality and services. This includes estimating concentrations of organic and inorganic constituents in water (Hernes and Benner 2003; Spencer et al., 2012), monitoring the health and distribution of submerged aquatic vegetation (Maxwell et al., 2017) and corals (Hedley et al., 2016a, and references therein), characterizing the biodiversity of phytoplankton (Mouw et al., 2017), and tracking spatio-temporal dynamics of complex biophysical and biogeochemical processes occurring in the water and adjoining wetlands (Howarth et al., 2011).

Remote sensing has become an indispensable tool for monitoring coastal and inland waters (Turpie et al., 2021, and references therein), and hyperspectral remote sensing has gained increased use in the last decade (Dierssen et al., 2015). The optical complexity typically encountered in coastal and inland waters necessitates hyperspectral sensors with a fine spectral resolution. Hyperspectral capability enables species discrimination of aquatic vegetation (Dierssen et al., 2015; Hedley J. et al., 2016) and detection of fine reflectance features of biogenic and inorganic substances in water (Mouw et al., 2016) and accessory pigments such as phycocyanin and phycoerythrin that occur in significant amounts during bloom conditions (Kudela et al., 2015). In addition to hyperspectral capability, a fine spatial resolution is needed to capture spatial heterogeneity of bio-optical

Photo credit: Anna Windle, Horn Point Laboratory, University of Maryland Center for Environmental Science

FIGURE 1
Data acquisition using a UAV over the Choptank River, a tributary of the Chesapeake Bay, Maryland. The multispectral imagery acquired were used to estimate water quality parameters such as the concentrations of chlorophyll-a and suspended particulate matter.

features in waters where spatial variability may occur in scales as fine as a few meters (Moses et al., 2016). Sensors with hyperspectral capability and/or high spatial resolution are being used for coastal and inland water applications from a variety of platforms such as moorings, shipboard platforms, unmanned aerial vehicles (UAVs); Figure 1, and airborne and spaceborne systems.

Several spaceborne sensors, including CubeSats, with high resolution in the spatial and/or spectral domains that are suitable for coastal and inland water remote sensing have been launched recently or are scheduled to be launched in the near future (e.g., the Plankton, Aerosol, Cloud, ocean Ecosystem (PACE) mission; HawkEye). Current spaceborne assets have either the required spectral resolution (e.g., Hyperion; the Italian mission PRISMA - PRecursore IperSpettrale della Missione Applicativa) or spatial resolution (e.g., WorldView-3, Planet SkySat) but not both, thereby limiting their use for monitoring coastal and inland waters. This limitation is addressed through a number of software and hardware options. Advanced image processing algorithms can combine data from coarse-spatial-resolution hyperspectral data with fine-spatial-resolution multispectral data (e.g., Yokoya et al., 2017). Advanced algorithms based on radiative transfer modeling and machine learning concepts are being developed to retrieve multiple water quality parameters from airborne and spaceborne multispectral and hyperspectral data (Pahlevan et al., 2022). Hyperspectral sensors on UAVs are used to collect data at fine spatial and spectral resolutions (Joyce et al., 2018).

A special Research Topic has been dedicated to address achievements and challenges in the research, development, and application of innovative measurement technologies and water quality parameter retrieval algorithms for remote sensing of coastal and inland waters and wetlands. The following is a summary of the articles published in this Research Topic.

Submerged aquatic vegetation play a crucial ecological role primary producers and food source for marine life. Detecting their presence and estimating their biomass abundance are crucial for monitoring global biodiversity. McPherson et al. (2022) developed a rapid survey system based on UAV and diver imagery to estimate kelp canopy biomass. They successfully estimated canopy biomass in a third of their survey sites but encountered challenges due to differences in kelp patch-specific spatial characteristics across the survey sites and limitations of the survey design. They recommend optimal survey design strategies for successful retrieval of kelp canopy biomass from a UAV platform. Cavanaugh et al. (2021) developed an automated method to map kelp canopy using data from a five-channel multispectral sensor on a UAV. They reported 93% accuracy and noted that canopy cover estimates are affected by tides and currents. Wilson et al. (2020) used a combination of spectral indices and supervised image classifiers to map the presence of submerged seagrass and surface-canopy forming seaweed habitats in various water types in Atlantic Canada using data from the Multispectral Imager (MSI) onboard the Sentinel-2 satellite. The benthic habitat map had an overall accuracy of 79%.

Harmful algal blooms (HABs) in coastal and inland waters are a major environmental and health concern (e.g., Carmichael, 1997). Detecting the presence of HABs and monitoring their spread, especially in recreational areas and near drinking water intakes are critically important. Myer et al. (2020) developed a spatio-temporal model based on a hierarchical Bayesian approach to forecast the occurrence of cyanobacterial HABs in lakes across Florida. The model used data from the Ocean and Land Colour Instrument (OLCI) onboard the satellite Sentinel-3 and a number of environmental parameters. Sharp et al. (2021) investigated spatial scales of variability of the distribution of cyanobacteria in Clear Lake, California using data collected through a range of modalities including field spectrometers, autonomous underwater vehicles, UAVs, and spaceborne sensors, and discovered that the critical scale of variability is in the range of 75–175 m, consistent with previous studies.

The National Aeronautics and Space Administration (NASA) routinely conducts technology concept demonstrations to test technologies for future spaceborne missions. Guild et al. (2020) summarized results from a number of NASA-sponsored airborne experiments conducted over Monterey Bay, California and nearby inland waters, involving radiometers, sun photometers, and imaging spectrometers. The experiments demonstrated the utility and enhanced benefit from the combined use of various measurement modalities and provided valuable data for calibrating and validating algorithms for retrieving water quality parameters. Harringmeyer et al. (2021) used a partial least squares regression approach involving reflectance in the ultraviolet, blue, and near-infrared regions to detect the presence of colored dissolved organic matter (CDOM) and differentiate it from phytoplankton in water. The study was carried out in Santa Monica Bay using data from the airborne Portable Remote Imaging SpectroMeter (PRISM). The study illustrated the value of reflectance in the ultraviolet region for detecting CDOM.

Coastal wetlands are a critical part of the global ecosystem and provide valuable environmental and ecological services including storm surge protection, coastal erosion control, carbon sequestration, and habitat for a number of endangered species. Haskins et al. (2021) demonstrated the use of UAV-based techniques for monitoring restoration of a tidal marsh site in Elkhorn Slough, California by calculating the volume of soil moved, tracking whether elevation targets were achieved or not, quantifying and examining the patterns of vegetation development, and monitoring topographic change including subsidence, erosion, and creek development. Elmahdy et al. (2020) used three machine learning algorithms, namely, Random Forest, kernel logistic regression, and Naïve Bayes algorithm, to map mangrove forests in the eastern and western coastal areas of the United Arab Emirates using Landsat data over the period from 1990 to 2019. They found that the Random Forest method performed the best, and noted that there was a significant change in mangrove extent during the 2010–2019 decade compared to 1990–2000.

Ayad et al. (2020) used data from multiple spaceborne sensors, namely RapidEye, MSI, and the Operational Land Imager (OLI) onboard Landsat-8 to detect discharges of stormwater and wastewater into the coastal ocean in Southern California and differentiate between stormwater and wastewater plumes based on optical characteristics. Kravitz et al. (2021) developed a tool based on synthetic data and machine learning techniques to retrieve multiple water quality parameters from satellite data. The tool was used to successfully retrieve concentrations of chlorophyll-*a* and phycocyanin and absorption coefficient of phytoplankton from MSI and OLI data acquired over Hartbeespoort Dam, South Africa.

Windle et al. (2021) investigated methods to remove the effects of surface-reflected radiance (including sun glint) on UAV-measured data. They recommend a pixel-based approach that uses absorption characteristics of water in the near-infrared region to estimate and remove surface reflectance. Dierssen et al. (2021) provide a comprehensive review and commentary on the past, present, and future state of hyperspectral aquatic remote sensing, addressing advances in sensor design, modes of deployment, algorithm development, image analysis techniques, and open-source software, which make data and techniques available and easily accessible to the public.

These articles demonstrate that aquatic remote sensing is a fast-evolving field with rapid advances in sensor technologies, measurement modalities, and innovative algorithms. These advances enable us to address critical environmental and ecological questions related to coastal and inland water ecosystems.

Author contributions

This Research Topic was conceived and developed by WM, AV, and SP. All three editors equally participated in editing manuscripts submitted to this Research Topic and made decisions on the manuscripts in consultation with each other and with unanimity.

Acknowledgments

The editors' contributions to writing the editorial and editing the articles published in this Research Topic were supported by internal funds from their respective host institutes, namely, the U.S. Naval Research Laboratory, the National Oceanic and Atmospheric Administration Great Lakes Environmental

Research Laboratory, and the California State University Monterey Bay.

Conflict of interest

The authors declare that the research was conducted in the absence of any commercial or financial relationships that could be construed as a potential conflict of interest.

Publisher's note

All claims expressed in this article are solely those of the authors and do not necessarily represent those of their affiliated organizations, or those of the publisher, the editors and the reviewers. Any product that may be evaluated in this article, or claim that may be made by its manufacturer, is not guaranteed or endorsed by the publisher.

References

Carmichael, W. W. (1997). The cyanotoxins. *Adv. Botanical Res.* 2727, 211–256. doi:10.1016/s0065-2296(08)60282-7

Dierssen, H. M., Chlus, A., and Russell, B. (2015). Hyperspectral discrimination of floating mats of seagrass wrack and the macroalgae Sargassum in coastal waters of Greater Florida Bay using airborne remote sensing. *Remote Sens. Environ.* 167, 247–258. doi:10.1016/j.rse.2015.01.027

Hedley, J. D., Roelfsema, C. M., Chollett, I., Harborne, A. R., Heron, S. F., Weeks, J., et al. (2016a). Remote sensing of coral reefs for monitoring and management: A review. *Remote Sens.* 8 (2), 118. doi:10.3390/rs8020118

Hedley, J., Russell, B., Randolph, K., and Dierssen, H. (2016b). A physics-based method for the remote sensing of seagrasses. *Remote Sens. Environ.* 174, 134–147. doi:10.1016/j.rse.2015.12.001

Hernes, P., and Benner, R. (2003). Photochemical and microbial degradation of dissolved lignin phenols: Implications for the fate of terrigenous dissolved organic matter in marine environments. *J. Geophys. Res.* 108 (C9), 3291. doi:10.1029/2002JC001421

Howarth, R., Chan, F., Conley, D. J., Garnier, J., Doney, S. C., Marino, R., et al. (2011). Coupled biogeochemical cycles: Eutrophication and hypoxia in temperate estuaries and coastal marine ecosystems. *Front. Ecol. Environ.* 9 (1), 18–26. doi:10.1890/100008

Joyce, K. E., Duce, S., Leahy, S. M., Leon, J., and Maier, S. W. (2018). Principles and practice of acquiring drone-based image data in marine environments. *Mar. Freshw. Res.* 70 (7), 952–963. doi:10.1071/MF17380

Kudela, R. M., Palacios, S. L., Austerberry, D. C., Accorsi, E. K., Guild, L. S., and Torres-Perez, J. (2015). Application of hyperspectral remote sensing to cyanobacterial blooms in inland waters. *Remote Sens. Environ.* 167, 196–205. doi:10.1016/j.rse.2015.01.025

Ledoux, L., and Turner, R. K. (2002). Valuing Ocean and coastal resources: A review of practical examples and issues for further action. *Ocean Coast. Manag.* 45 (9-10), 583–616. doi:10.1016/s0964-5691(02)00088-1

Maxwell, P. S., Eklöf, J. S., van Katwijk, M. M., O'Brien, K. R., de la Torre-Castro, M., Boström, C., et al. (2017). The fundamental role of ecological feedback mechanisms for the adaptive management of seagrass ecosystems–a review. *Biol. Rev.* 92 (3), 1521–1538. doi:10.1111/brv.12294

Moses, W. J., Ackleson, S. G., Hair, J. W., Hostetler, C. A., and Miller, W. D. (2016). Spatial scales of optical variability in the coastal ocean: Implications for remote sensing and in situ sampling. *J. Geophys. Res. Oceans* 121, 4194–4208. doi:10.1002/2016jc011767

Mouw, C. B., Greb, S., Aurin, D., DiGiacomo, P. M., Lee, Z., Twardowski, M., et al. (2016). Aquatic color radiometry remote sensing of coastal and inland waters: Challenges and recommendations for future satellite missions. *Remote Sens. Environ.* 160, 15–30. doi:10.1016/j.rse.2015.02.001

Mouw, C. B., Hardman-Mountford, N. J., Alvain, S., Bracher, A., Brewin, R. J., Bricaud, A., et al. (2017). A consumer's guide to satellite remote sensing of multiple phytoplankton groups in the global ocean. *Front. Mar. Sci.* 4, 41. doi:10.3389/fmars.2017.00041

Pahlevan, N., Smith, B., Alikas, K., Anstee, J., Barbosa, C., Binding, C., et al. (2022). Simultaneous retrieval of selected optical water quality indicators from Landsat-8, Sentinel-2, and Sentinel-3. *Remote Sens. Environ.* 270, 112860. doi:10.1016/j.rse.2021.112860

Revenga, C., and Kura, Y. (2003). *Status and trends of biodiversity of inland water ecosystems*. Montreal: Secretariat of the Convention on Biological Diversity.

Spencer, R. G., Aiken, G. R., Dornblaser, M. M., Butler, K. D., Holmes, R. M., Fiske, G., et al. (2012). Chromophoric dissolved organic matter export from U.S. rivers. *Geophys. Res. Lett.* 40, 1575–1579. doi:10.1002/grl.50357

Turpie, K. R., Ackleson, S. G., Byrd, K. B., and Moisan, T. A. (2021). Editorial: Science and applications of coastal remote sensing. *Front. Mar. Sci.* 8, 641029. doi:10.3389/fmars.2021.641029

Yokoya, N., Grohnfeldt, C., and Chanussot, J. (2017). Hyperspectral and multispectral data fusion: A comparative review of the recent literature. *IEEE Geosci. Remote Sens. Mag.* 5 (2), 29–56. doi:10.1109/MGRS.2016.2637824

frontiers in Environmental Science

ORIGINAL RESEARCH
published: 16 July 2020
doi: 10.3389/fenvs.2020.00102

Spatiotemporal Mapping and Monitoring of Mangrove Forests Changes From 1990 to 2019 in the Northern Emirates, UAE Using Random Forest, Kernel Logistic Regression and Naive Bayes Tree Models

Samy I. Elmahdy[1], Tarig A. Ali[1,2], Mohamed M. Mohamed[3,4]*, Fares M. Howari[5], Mohamed Abouleish[6] and Daniel Simonet[7]*

[1] GIS and Mapping Lab, College of Engineering, American University of Sharjah, Sharjah, United Arab Emirates, [2] College of Engineering, American University of Sharjah, Sharjah, United Arab Emirates, [3] Department of Civil Engineering, College of Engineering, United Arab Emirates University, Al Ain, United Arab Emirates, [4] National Water Center, United Arab Emirates University, Al Ain, United Arab Emirates, [5] College of Natural and Health Sciences, Zayed University, Abu Dhabi, United Arab Emirates, [6] Department of Biology, Chemistry and Environmental Sciences, College of Arts and Sciences, American University of Sharjah, Sharjah, United Arab Emirates, [7] Department of Management, School of Business Administration, American University of Sharjah, Sharjah, United Arab Emirates

Mangrove forests are acting as a green lung for the coastal cities of the United Arab Emirates, providing a habitat for wildlife, storing blue carbon in sediment and protecting shoreline. Thus, the first step toward conservation and a better understanding of the ecological setting of mangroves is mapping and monitoring mangrove extent over multiple spatial scales. This study aims to develop a novel low-cost remote sensing approach for spatiotemporal mapping and monitoring mangrove forest extent in the northern part of the United Arab Emirates. The approach was developed based on random forest (RF), Kernel logistic regression (KLR), and Naive Bayes Tree machine learning algorithms which use multitemporal Landsat images. Our results of accuracy metrics include accuracy, precision, and recall, F1 score revealed that RF outperformed the KLR and NB with an F1 score of more than 0.90. Each pair of produced mangrove maps (1990–2000, 2000–2010, 2010–2019, and 1990–2019) was used to image difference algorithm to monitor mangrove extent by applying a threshold ranges from +1 to −1. Our results are of great importance to the ecological and research community. The new maps presented in this study will be a good reference and a useful source for the coastal management organization.

Keywords: NUAE, mangrove, FMNF, remote sensing, change detection, Landsat

OPEN ACCESS

Edited by:
Wesley Moses, United States Naval Research Laboratory, United States

Reviewed by:
Tien Dat Pham, Florida International University, United States
Kyle Cavanaugh, University of California, Los Angeles, United States

****Correspondence:***
Samy I. Elmahdy
selmahdy@aus.edu; samy903@yahoo.com
Mohamed M. Mohamed
mmohamed@uaeu.ac.ae

Specialty section:
This article was submitted to Environmental Informatics and Remote Sensing, a section of the journal Frontiers in Environmental Science

Received: *28 March 2020*
Accepted: *11 June 2020*
Published: *16 July 2020*

Citation:
Elmahdy SI, Ali TA, Mohamed MM, Howari FM, Abouleish M and Simonet D (2020) Spatiotemporal Mapping and Monitoring of Mangrove Forests Changes From 1990 to 2019 in the Northern Emirates, UAE Using Random Forest, Kernel Logistic Regression and Naive Bayes Tree Models. Front. Environ. Sci. 8:102. doi: 10.3389/fenvs.2020.00102

INTRODUCTION

Mangroves are woody plants that are extensively distributed in intertidal and estuary zones and their forests cover thousands of hectares along the shorelines (Sherrod and McMillan, 1985; Field et al., 1998). Mangroves are able to store 1200 Mg of carbon per hectare (Donato et al., 2011; Pham et al., 2019a,b). They form an essential component of the coastal ecosystem consisting of salt-tolerant plants with aerial breathing roots that supply a microenvironment to several marine species (Snedaker, 1982; Upadhyay and Mishra, 2008).

Mangroves provide a wide range of benefits to the economy and the environment as they play a vital role in ecology. Some ways they do this for example, are by supplying a safe breeding ground and suitable environment for fish species and birds nesting, as well as and stabilization and protection for shorelines from hurricanes (Fry and Cormier, 2011; Giri et al., 2011; Inoue et al., 2011; Barua et al., 2014).

Although mangroves have declined globally by 2% per annum, the mangroves of the United Arab Emirates appear to have rapidly increased. This is due to localized plantation activities and increased public awareness and conservation efforts during the last decade (Food and Agriculture Organization of the United Nations, 2007; Loughland et al., 2007; Howari et al., 2009). The most common mangrove species in the United Arab Emirates is *Avicennia marina* or gray mangrove and its protection is consequently an urgent conservation priority (**Figure 1**).

Our knowledge on the spatial variation, causes of degradation of the mangroves are still poor due to; (i) the northern part of the United Arab Emirates (NUAE) mangrove database suffering from significant errors and it is sometimes unavailable and has usage restricted, (ii) inaccessibility of the tidal fluctuation mangrove forests in isolated islands, and (iii) the majority of previous studies have been conducted based on field surveys and measurements over a local scale with manual screen digitizing (Moore et al., 2013; Alsumaiti, 2014). Understanding the spatiotemporal changes of the NUAE mangrove over a regional scale could provide valuable information for the ecologists and natural resources specialists in the United Arab Emirates and this requires a potential method.

Remote sensing data has proven to be a good tool for mapping and monitoring mangrove changes over a regional scale as it has low-cost and is not time-consuming (Boardman and Kruse, 1994; Guild et al., 2004; Ghanavati et al., 2008; Mondal et al., 2018, 2019; Elmahdy et al., 2019, 2020a,b; Spruce et al., 2020). The multi-temporal Landsat images have been widely used for mapping and monitoring mangrove changes due to their suitable of spatial and temporal resolutions, as well as their easy availability and accessibility (Birth and McVey, 1968; Edwards et al., 2007; Klemas, 2009; Vo et al., 2013; Nguyen et al., 2013; Kanniah et al., 2015; Chen et al., 2017; Elmahdy and Mohamed, 2018; Buitre et al., 2019).

The most common method for mapping vegetation are the vegetation indices such as the Simple Ratio Index (SRI) of Birth and McVey (1968), Normalized Difference Vegetation Index (NDVI) of Edwards and Richardson (2004), and the Normalized Difference Moisture Index (NDMI) is the oldest and most well known and most frequently used by several researchers (Fang and Liang, 2003; Huete et al., 2010). These indices were designed to enhance the sensitivity of the spectral reflectance contribution of vegetation while minimizing the soil background reflectance or atmospheric effects (Fang and Liang, 2008; Huete et al., 2010) and widely used in the literature (Díaz and Blackburn, 2003; Ishil and Tateda, 2004; Jean-Baptiste and Jensen, 2006; Kovacs et al., 2009; Rodríguez-Romero et al., 2011; Laongmanee et al., 2013; Nascimento et al., 2013; Pereira et al., 2018; Otero et al., 2019; Liu et al., 2020). These indices sometimes cannot discriminate between mangrove and non-mangroves areas such as grass and algae (Howari et al., 2009; Elmahdy and Mostafa Mohamed, 2013a,b). Generally, the classification methods can be divided into five types: (i) unsupervised learning; (ii) supervised; (iii) advanced learning; (iv) object-based image analysis (OBIA); and (v) sub-pixel. Recently, several machine learning algorithms have been designed for mapping and classifying land use land cover (LULC). Ensemble machine learning algorithms such as Random forest (RF) is widely used in LULC classification and mangrove mapping from Landsat images (Erftemeijer and Hamerlynck, 2005; Pal, 2005; Sesnie et al., 2008; Mountrakis et al., 2011), mangrove and sea grass mapping (Heumann, 2011; Hossain et al., 2015; Buitre et al., 2019; Diniz et al., 2019; Small and Sousa, 2019; Toosi et al., 2019), prediction in water resources (Zhao et al., 2012; McGinnis and Kerans, 2013; Naghibi et al., 2016; Naghibi and Dashtpagerdi, 2017), and prediction of land subsidence (Elmahdy et al., 2020a). Further studies combined image transformation and supervised classification to map and classify mangrove forests (Yokoya and Iwasaki, 2010; Ouerghemmi et al., 2018). Locally, only limited numbers of studies have been carried out using remote sensing data (Embabi, 1993; Moore et al., 2013; Almahasheer, 2018). However, these studies were based only on traditional techniques of traditional classifiers and visual interpretation of Landsat and spot images, sometimes coupled with manual digitization techniques for mapping mangrove forests. These techniques introduced a level of human bias and can be subjective and time-consuming owing to the rapid changes in the United Arab Emirates mangroves (Crouvi et al., 2006; Adam and Hutchings, 2010). Therefore, to construct and maintain a flexible regional database for the NUAE mangroves, it is urgent to modify an integrated powerful machine learning classifier.

Integration of RF, Kernel logistic regression (KLR), Naive Bayes Tree (NBT), and Image difference (ID) have shown the ability to achieve classification over a regional scale and precise monitoring extent of the mangrove (Colkesen and Kavzoglu, 2017). These techniques can reduce the variance and overfitting of the classification maps and assess many variables separately compared to traditional classifiers, such as maximum likelihood (Ha et al., 2020). Thus, integration of RF and KLR and ID was adopted to extract spatiotemporal information about the NUAE mangrove forests. The use of machine learning algorithms decreases the overfitting and variance in the classified maps (Belgiu and Dăguţ, 2016; Feng et al., 2018; Mondal et al., 2019; Elmahdy et al., 2020b; Ha et al., 2020). Thus, the main goals of this study were to present a novel ensemble machine learning approach which integrates RF with KLR and NBID

FIGURE 1 | Photos of the NUAE mangrove forests showing their spatial patterns and environment.

algorithms and uses Landsat images for spatiotemporal mapping of the NAEU mangroves, comparing the performance of these algorithms, and implementing a novel image to image change detection technique for monitoring mangrove changes over multiple scales.

STUDY AREA

The study area is in the eastern and western coastal areas of the United Arab Emirates. In particular, it extends between the longitudes E 53°56′ 23″ and E 60°15′ 22″ and latitudes 24° 21′ 2″ and 26° 12′ 20″ N (**Figures 2**, **3**). The area consists of two mangrove ecosystems; the Khor Fakkan mangrove is located in the Gulf of Oman (5.5 km length) and the Dubai's Greek, Ajman's Creek, Hammraih's Creek, Umm Al Quwain and Ras Al Khaimah (RAK) Estuaries (**Figures 2**, **3**). They are facing the Gulf of Oman in the east and the Arabian Gulf in the west and dominated by gray mangroves (*A. marina*) and locally referred to as Al Qurm, which is one of the most habitat-tolerant mangroves (Boer and Aspinall, 2005; Howari et al., 2009; Alsaaideh et al., 2013). The United Arab Emirates mangroves are able to grow in saline soil that exceeds the seawater salinity of the Arabian Gulf and Gulf of Oman (Alsumaiti, 2014). An Assessment of *A. marina* Forest Structure and Aboveground Biomass in Eastern Mangrove Lagoon National Park, Abu Dhabi

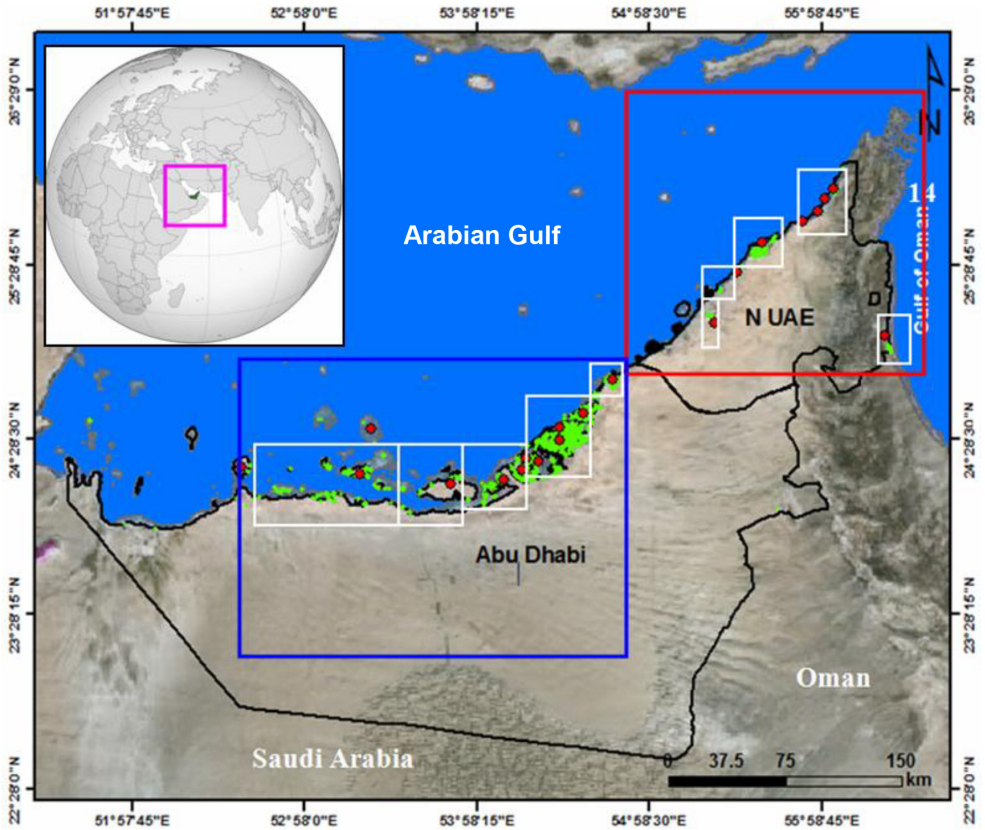

FIGURE 2 | RGB 541 band combination of Landsat image of the UAE showing the spatial distribution of the UAE mangroves and in the study area (red polygons).

(Alsumaiti, 2014). The height of the United Arab Emirates mangrove trees ranges from a few centimeters to 3–8 m (Moore et al., 2013; Alsumaiti, 2014). The mangrove soil texture is loamy clay and silt and characterized by high porosity and low permeability, which allows keeping the seawater in the soil porosity for a long time, especially during tidal times (Cintron et al., 1978; Bashitialshaaer et al., 2011).

DATASETS AND METHODS

Datasets and Preprocessing

Two remotely sensed data were used in this study. The first dataset was the Landsat Thematic Mapper (TM) acquired on August 23, 1990, the Landsat Enhanced Thematic Mapper (ETM+) acquired on August 23, 2000 and August 19, 2010 and the Operational Landsat Imager (OLI) Landsat 8 acquired on August 15, 2019 (Path 160, rows 42 and 43).The data were obtained via the USGS Earth Resources Observations and Science (EROS) Center through the Global Visualization Viewer[1]. The mangrove forests in Landsat images (coastal areas) were then clipped into five subsets to reduce the image processing time by avoiding unnecessary calculations (Amarsaikhan et al., 2009; Diniz et al., 2019; Ma et al., 2019). We used the Landsat images due to their suitability spectral and spatiotemporal resolutions, free of charge, easy accessibility, and time-series availability (Chander, 2009; Irons et al., 2012; Elmahdy and Mohamed, 2018; Milani, 2018; Toosi et al., 2019). Additionally, Landsat images are provided in orthorectification format at a lower level of cloud cover (Darvishsefat, 1995). The second dataset includes the QuickBird images with a spatial resolution of 0.6 m acquired on August 22, 2019, the Advanced Spaceborne Thermal Emission and Reflection Radiometer (ASTER), and Earth Observing-1 (EO-1) images with a spatial resolution of 30 m acquired on August 13, 2019 and July 29, 2019, respectively.

The spectral coverage of ASTER sensor consists of four visible and near-infrared bands (0.52–0.86 μm) with a spatial resolution of 15 m, six shortwave infrared (SWIR) bands (1.6–2.43 μm) with a spatial resolution of 30 m and five thermal bands (8.125–1165 μm) with a spatial resolution of 90 m. The EO-1 Advanced Land Imager (ALI) provides Landsat type panchromatic and multispectral bands. These bands have been designed to mimic six Landsat bands with three additional bands covering 0.433–0.453, 0.845–0.890, and 1.20–1.30 μm. The ALI also contains wide-angle optics designed to provide a continuous 15° × 1.625° field of view for a fully populated focal plane with a 30-m resolution

[1]www.glovis.usgs.gov

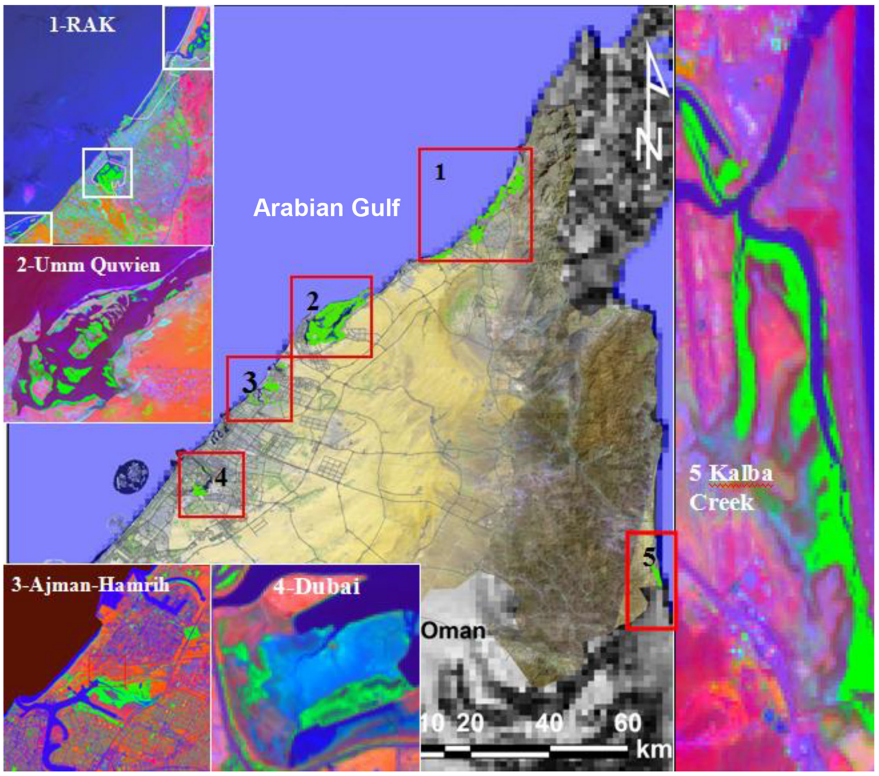

FIGURE 3 | RGB 541 band combination of Landsat image of the NUAE and zooms of the mangrove locations distributed along the eastern and western coastal areas in the NUAE.

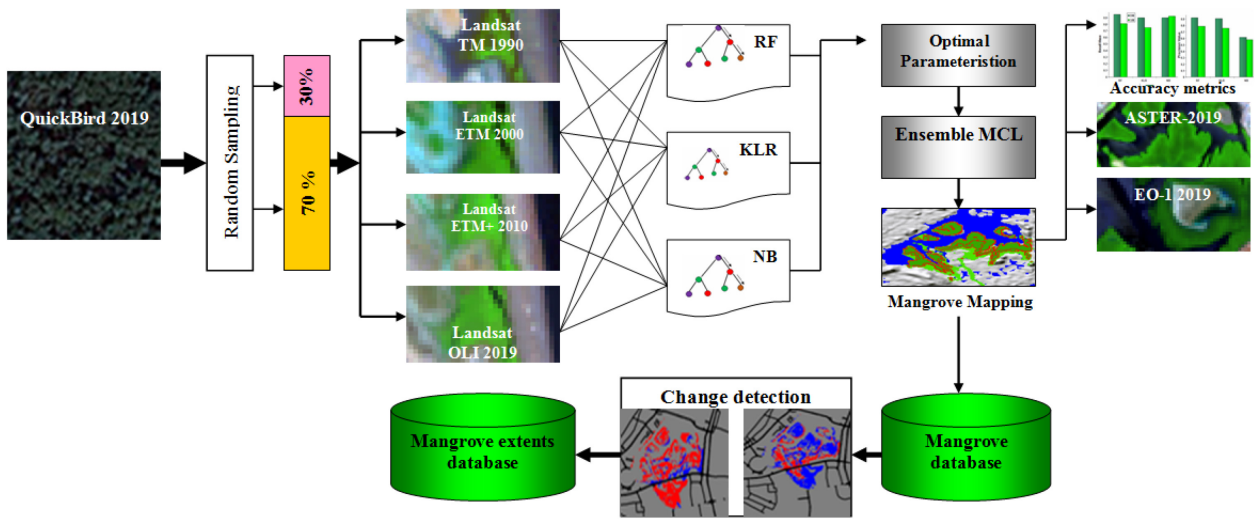

FIGURE 4 | Flowchart of the methodology applied in this study.

for the multispectral pixels and 10-m resolution for the panchromatic pixels.

These datasets were downloaded via the USGS EROS Center through the Global Visualization Viewer (see footnote 1). We used these various datasets to collect training datasets as input to the classifiers and visual verification of the obtained mangrove maps and compare the textural features (mangroves and non-mangrove areas), mapped from Landsat images against those mapped from the ASTER and EO-1 images using RF, KLR, and NB algorithms.

After collecting the remote sensing data, the datasets were all re-sampled to UTM WGS 84 projection, at a spatial resolution

of 30 m with mean root square error values of less than 0.40 pixels. All the United Arab Emirates images were assigned to a UTM zone 40 N and datum WGS 48 (Jensen, 1996; Foody, 2002) followed by an atmospheric correction. The atmospheric correction was performed by Fast Line-of-sight Atmospheric Analysis of Hypercubes (FLAASH) implemented in Envi v. 4.6 software. Fast Line-of-sight Atmospheric Analysis of Hypercubes process consists of radiometric calibration and dark subtraction. In radiometric calibration, beta nought calibration, all digital number (DN) values were converted into Top Of Atmosphere (TOA), reflectance. Top Of Atmosphere was performed using four parameters, namely, calibration type (reflectance), output interleave (BSQ), output data type (float), and scale factor value of 1. In dark objects subtraction, TOA was converted into surface reflectance (SR) using band minimum (Green et al., 1988; Foody, 2002; Todd and Chris, 2010).

Training Data Collections

The training data collection is a very important step in producing a higher quality of classification, especially when the classifiers trained with training datasets with higher spatial resolutions (Elmahdy and Mohamed, 2018). The training datasets were collected from QuickBird images with a spatial resolution of 0.6 m using a straight random sampling or proportional method, which reduces error and bias. This method divides the population into homogenous groups and produces training sample sizes that are directly related to the size of the classes. We used this method due to its ability to reduce bias and errors (Van Niel et al., 2005; Elmahdy and Mohamed, 2018).

Random sampling collection was performed using Envi v. 4.5 software. In total, 536 training datasets were collected and divided into 375 (70%) for training and mangrove mapping and 161 (30%) for validation of this study. The collected training datasets were checked using visual interpretation and knowledge and background of the authors and where they live (**Figure 4**).

Machine Learning for Image Classification

Random Forest

To classify and map mangrove forests in an accurate and low-cost way, it is important to employ machine learning algorithms, then learn these algorithms with training datasets with a higher spatial resolution as well as algorithm optimal parameterization (Huang et al., 2009; Elmahdy and Mohamed, 2018).

The RF algorithm can provide a higher quality of classification than linear classifiers and has been employed previously to map and classify mangroves in Iran based on Landsat images (Kamal and Phinn, 2011; Kamal et al., 2015). The algorithm performs well for mangroves mapping over a regional scale and its ability to handle data with unclassified pixels (Prasad et al., 2006; Taalab et al., 2018; Thomas et al., 2018). Random forest algorithm is a non-parametric ensemble machine learning and one of the most popular algorithms that provide high-quality of mangroves classification and environmental modeling (Strobl et al., 2008; Vyas et al., 2011; Bachmair and Weiler, 2012; Torres and Qiu, 2014; Fu et al., 2017). It is a combination of classification and regression tree (CART).

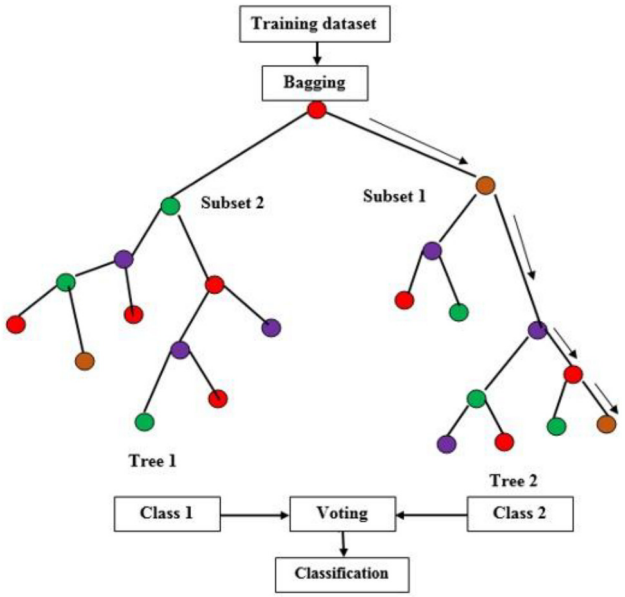

FIGURE 5 | Flow chart of classification using machine learning algorithms.

A regression tree is a hierarchy and comprises of a root node, node separator (decision rules) and end of a leaf node (desired classes). The algorithm involves an ensemble of tree- structure classifiers and each tree starts by choosing a set of random model units selected separately. Then, it creates a forest using the vote on all decision "tree" in the "forest." Then, two-thirds of the set was employed to make the decision tree and the remaining data are then used to estimate the model performance based on a bootstrapping procedure (Breiman, 2001; Schapire, 2003). Finally, the best model was chosen based on the majority vote approach (Yu et al., 2011). The model is flexible and can be used to solve problems related to classification and exploit the information provided by several condition variables (Catani et al., 2013; Ha et al., 2020). The model uses a random selection of predictor variables to divide each node of the trees. After that, each tree was developed in such a way as to reduce errors in the classification process. However, this type of random selection influences the results, hence creating a very unsuitable single-tree classification (**Figure 5**).

The algorithm is widely employed in environmental modeling (Strobl et al., 2008; Bachmair and Weiler, 2012), although only rarely in land subsidence and sinkholes susceptibility mapping (Vorpahl et al., 2012).

For b = 1 to B:

(b) Grow a random-forest tree Tb from the bootstrapped data, by recursively repeating the following steps for each terminal node of the tree, until the minimum node size nmin is reached.

1. Select m variables at random from the *p* variables.

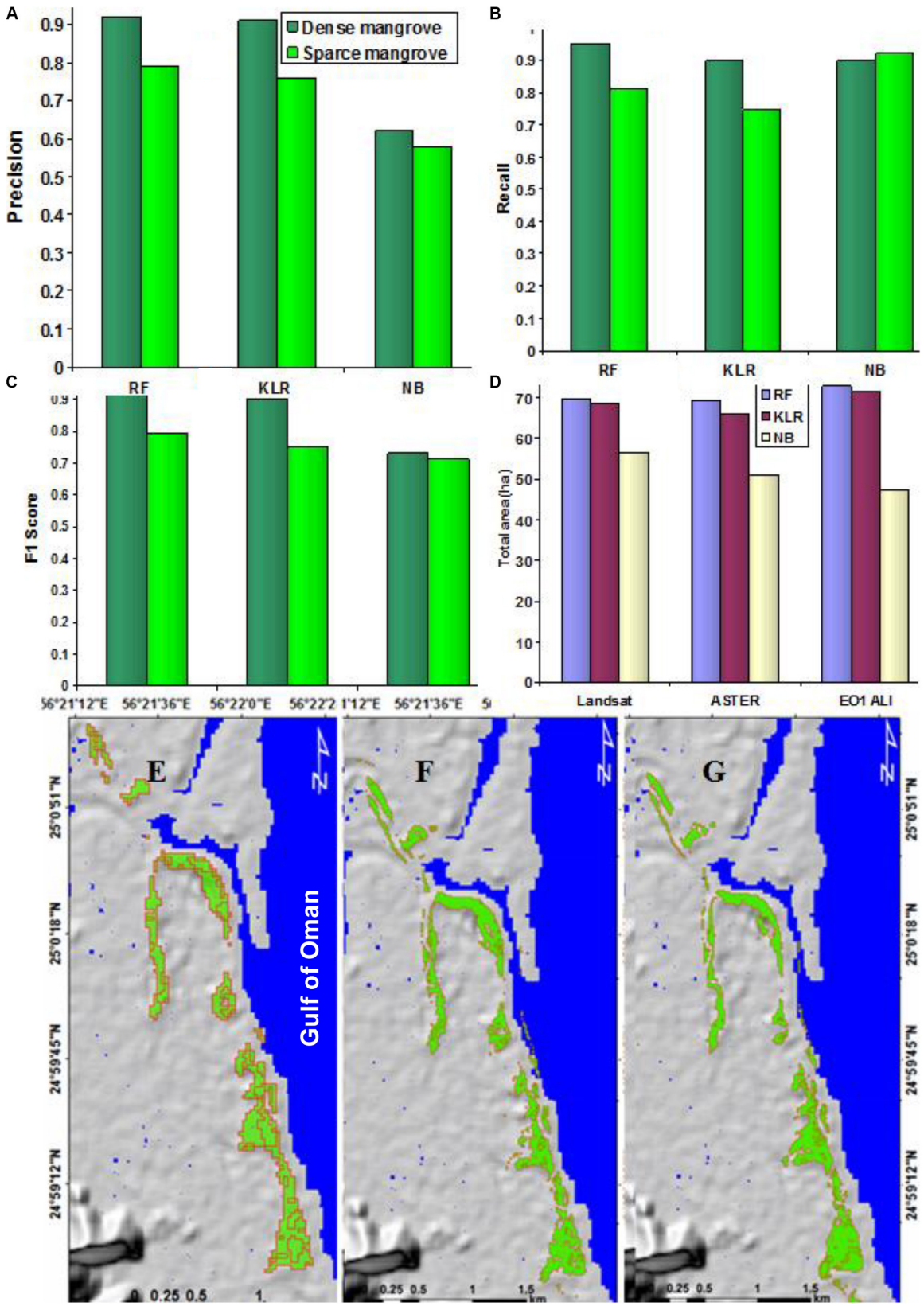

FIGURE 6 | A comparison of the precision **(A)**, recall **(B)**, and F1 scores **(C)** for the Landsat image (August 15, 2019) using RF, KLR, and NB classifiers and total area in ha mapped using RF, KLR, and NB **(D)** and feature extracted from the Landsat images **(E)**, ASTER images **(F)**, and EO-1 **(G)** for the year 2010.

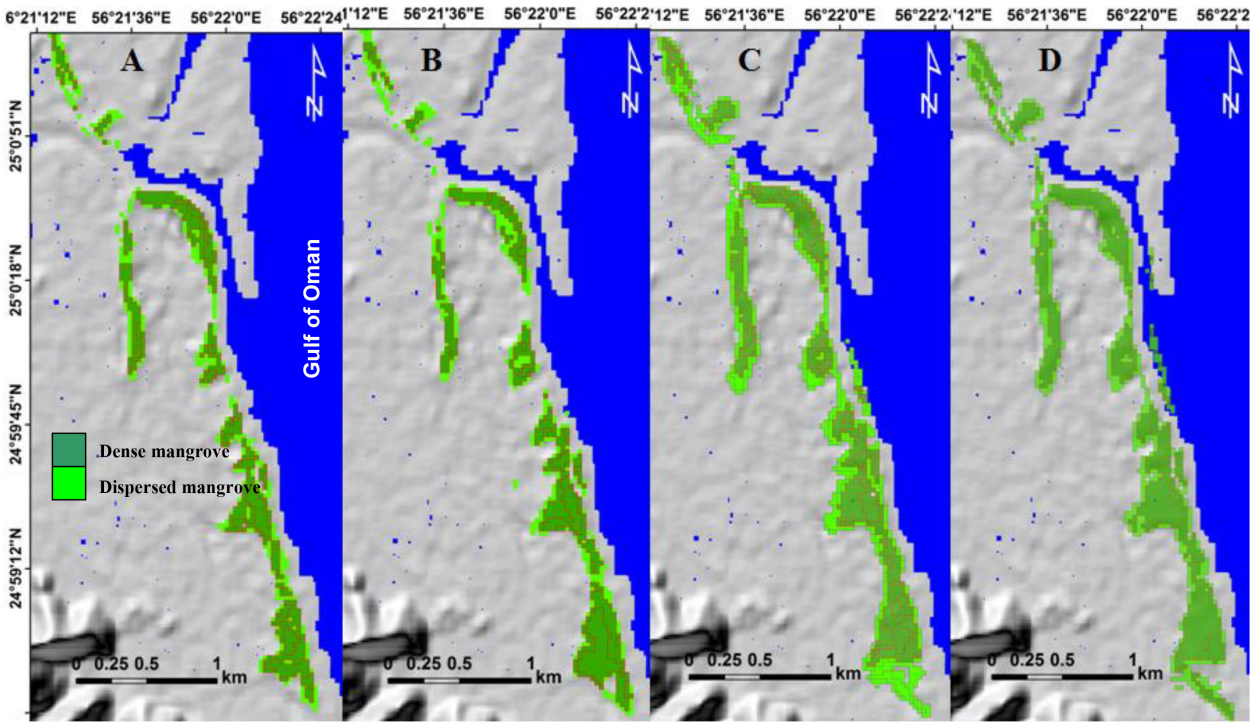

FIGURE 7 | Spatiotemporal variation of mangrove forests in Khor Kalba of the Emirate of Sharjah for the years 1990 **(A)**, 2000 **(B)**, 2010 **(C)**, and 2019 **(D)**.

2. Pick the best variable/split-point among the m variables.
3. Split the node into two daughter nodes.

Kernel Logistic Regression

Kernel logistic regression is a discriminative machine learning classifier that differentiate the mangrove and non-mangrove classes perfectly where probabilistic output are evaluated based on minimizing the negative log-likelihood function using the Broyden–Fletcher–Goldfarb–Shanno (BFGS) optimization (Yokoya and Iwasaki, 2010). It is described as the kernel version of logistic regression capable of converting into a high-dimensionality feature space of the original input feature space kernel functions (Tanaka et al., 2011).

The kernel function can be defined as the basic function in which ϕ is supposed to be unidentified:

$$K\left(x, x'\right) = \varphi\left(x\right)^T\left(x'\right) \quad (1)$$

where T is the inner product in the Z space.

Suppose a set of training dataset $\left\{x_i, y_i\right\}^{N_{i=1}}$ with $x_i \in R^n$ as input parameters with n variables and N data samples. Here, the input parameters are dense mangrove, dispersed mangrove and non mangrove.

$y_k \in \{1,0\}$ is the related label that indicates mangrove and non-mangrove classes. The KLR was applied to built a non-linear decision boundary that may divide the two classes in the feature space based on the following equation:

$$p\left(x\right) = e^{y(x)} / \left(1 + e^{y(x)}\right) = \sum^{N_{I=1}} \bar{\alpha}_i K\left(x_i, x_j\right) + b \quad (2)$$

where $y\ (x)$ is the logistic function with values in [0,1]; α_i is a vector of dual model parameters, whereas b is the intercept; $K(x_i, x_j)$ is the kernel function.

For our study, radial basis function (RBF), which is used widely in the literature, was chosen due its flexibility and reliability (Bui, 2015; Hong et al., 2015).

Naive Bayes Tree

Naive Bayes (NB) is a machine learning classifier that creates a probability-based model. It works based on Bayes Theorem, which is known as Naive Bayes. The NB uses a decision tree (DT) for its structure and organizes the NB model on every leaf node of the constructed DT. The NBT exhibits a significant classification performance and accuracy (Liang et al., 2006; Wang et al., 2015).

During the NB process, the impact of an attribute value on a specific class is an independent value of another attribute and known as class conditional independence. This conditional independence of NB makes the datasets to train quicker and it considers all the vectors as independent and applies the Bayes rule (Farid et al., 2014).

The theorem of the Bayes can be explained as follows:

$$P\left(A|B\right) = P\left(B|A\right) P\left(A\right) / P\left(B\right)$$

where:

P(A|B) = conditional probability of A given B;
P(B|A) = conditional probability of A given B;
P(A) = probability of event A;
P(B) = probability of event B.

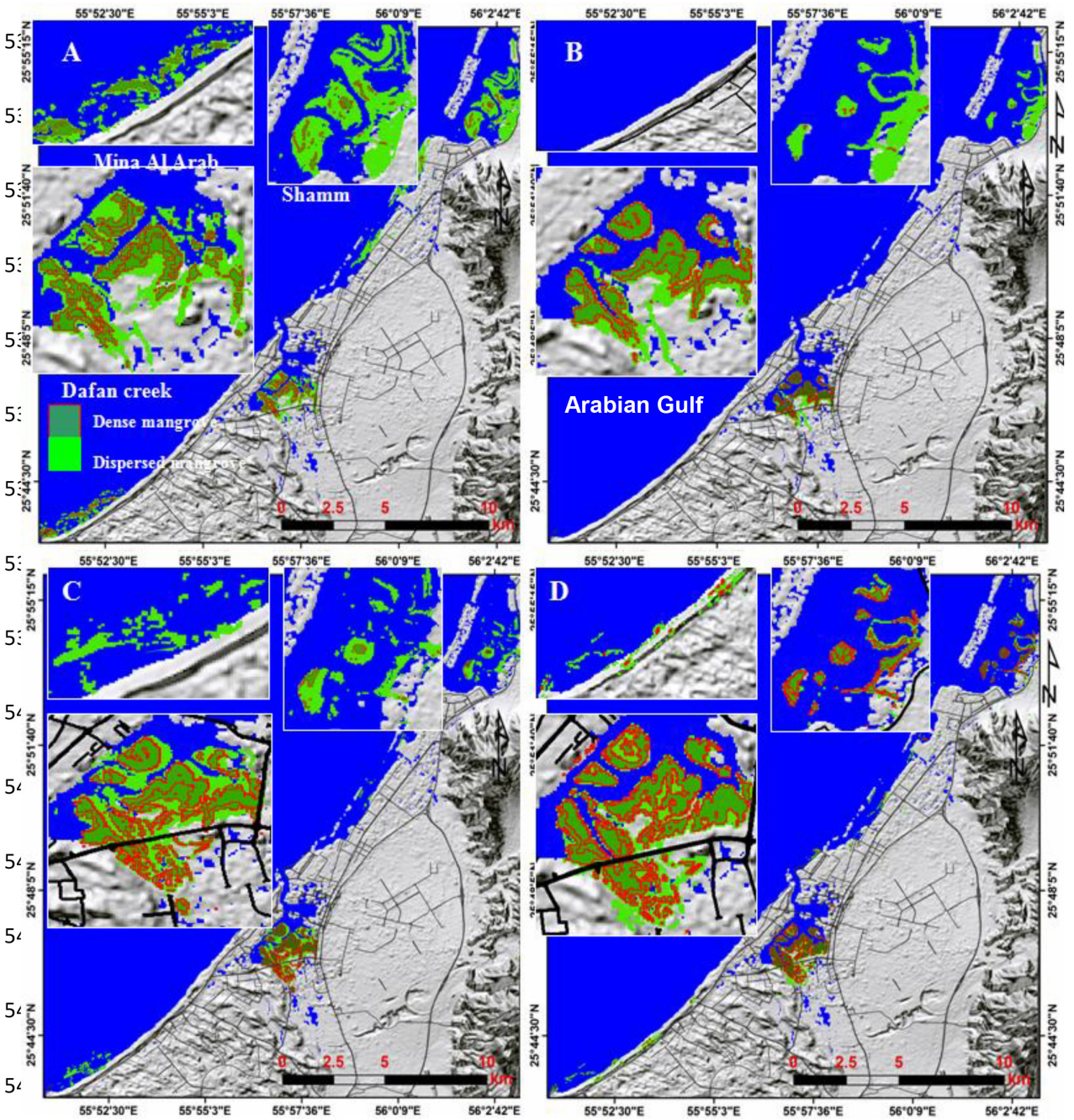

FIGURE 8 | Spatiotemporal variation of mangrove forests on the coastal area of RAK for the years 1990 **(A)**, 2000 **(B)**, 2010 **(C)**, and 2019 **(D)** and zooms of Mina Al Arab (southwest), Dafan creek (middle), and Shamm (northeast). Red polygons and dark green highlight dense mangroves.

This classifier was chosen due to its: (i) quick training and classification, (ii) powerful to irrelevant features, (iii) easy to use and understand, and (v) ability to work with few numbers of training datasets (Ho, 1998).

The model starts by estimating the probability of each class in the model, calculating covariance and variance matrix, and building the discrimination function for each class (Pham and Yoshino, 2015; Wang et al., 2015).

For the KLR and NB, mapping and monitoring of mangroves were performed using SATISTICA v. 7 (Fleiss et al., 2003; Hill and Lewicki, 2006) and Salford system (Friedman, 2001; Friedman, 2002). These tools have a stochastic gradient boosting tree which is used widely for regression problems related to predict and map a continues dependent variables (Hill and Lewicki, 2006). After that, the setting and optimizing of all parameters were performed. These parameters namely; learning rate, the number of additive

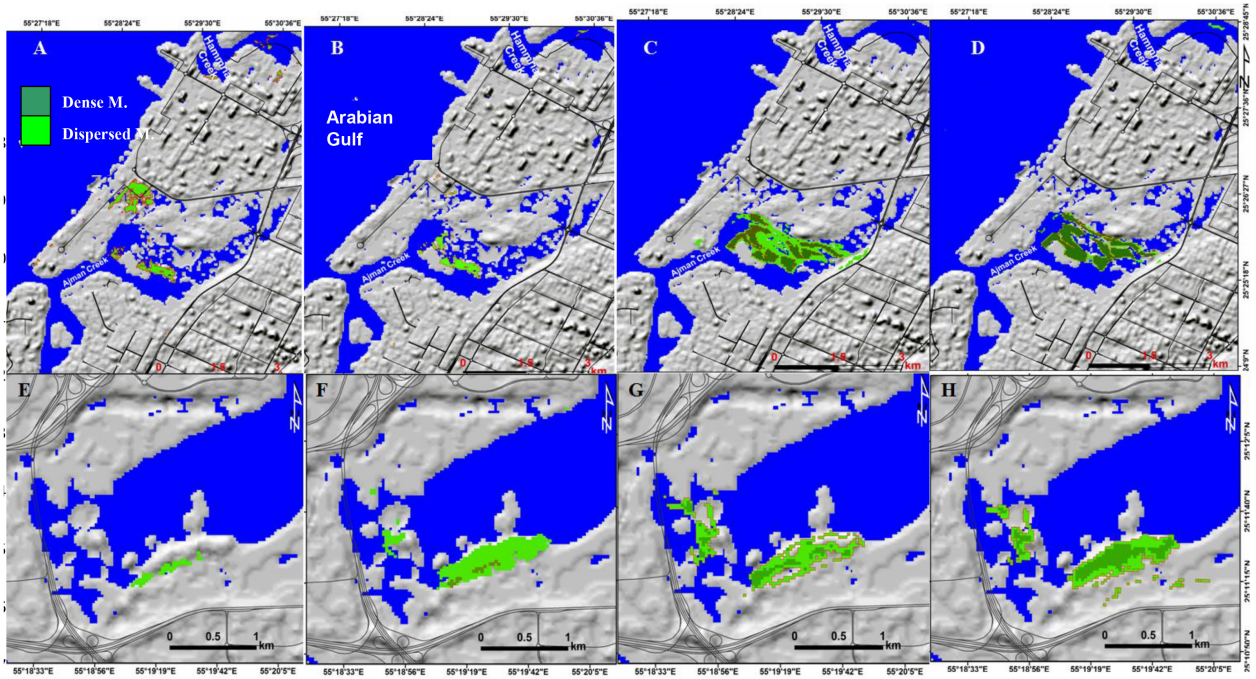

FIGURE 9 | Spatiotemporal variations of mangrove forests for the years in Ajman-Hammriah **(A–D)**, and Ras Al Khor **(E–H)** natural reserves for the years 1990, 2000, 2010, and 2019. Red polygons and dark green highlight dense mangroves.

trees, the proportion of subsampling, and so forth. Here, the optimal value for the learning rate was set as 0.1, additive trees were 185 and the maximum size of the tree was 5. These values may lead to precise result accuracy (Friedman, 2001).

To get the optimum RF parameter values, we tested several RF parameter values. These parameters include the maximum total of tree depth, the minimum numbers of samples per node (sample), and maximum tree number (tree number). The tested values of tree depth and minimum sample per node were 0,1,5, 10, 20, 50, 100, 500, and 1000, while the maximum tree number values were 50, 100, 200,400,800, and 1000. After that, the best band combination of RF parameters and the highest overall accuracy was chosen and applied. RF was applied to each Landsat image separately using 536 training data sets collected from QuickBird images with a spatial resolution of 0.6 m. The classification process was performed using the R package (Catani et al., 2013).

Ensemble of RF, KLR and NB

Among several ensemble methods, the stacking algorithm was employed to build the ensemble model with a threshold of 0.9 used to detect mangrove pixels. The algorithm builds a model on of the RF, KLR, and NB machine learning algorithms based on the selected training datasets R package via the "glmet".

Evaluation of the Performance of the Classifiers

To evaluate the performance of the classifiers, maps of mangroves were standardized and compared based on a pixel by pixel producing numerical values for mangrove commission, mangrove omission, total incorrect pixels, percentage of incorrect pixels, precession, recall, and F1 score (Congalton et al., 1983; Raschka, 2018; Raschka and Mirjalili, 2019). Once the classification process was achieved, it is important to evaluate classifiers' performance. Confusion metrics include accuracy, precision, recall, F1 score was found to the best technique and used widely in this literature (Ha et al., 2020). The calculation of accuracy, precision, recall, and F1 score is based on four parameters namely; true positive (TP), true- negative (TN), false-positive (FP), and false-negative (FN). Accuracy, precision, recall and F1 score can be calculated via the following equations:

$$Accuracy = TP + (TN/TP) + FP + FN + TN \tag{3}$$

or

$$Accuracy\left(y,\ y_{predi}\right) = 1/n_{samples} \sum_{i=0}^{n_{samples}-1} 1\left(y_{predi} = y_i\right)$$

where y_{predi} is the predicted value and y is the corresponding true value

$$\text{Kappa} = p_o - \ p_e/1 - p_e \tag{4}$$

where p_o is the observed agreement ratio and p_e is the expected agreement

$$Precision = TP/TP + FP \tag{5}$$

$$Recall = TP/TP + FN \tag{6}$$

$$F1 = 2 \times precision \times recall/precision + recall \tag{7}$$

where TP is the true positive; FP is the false positive; and FN is the false negative.

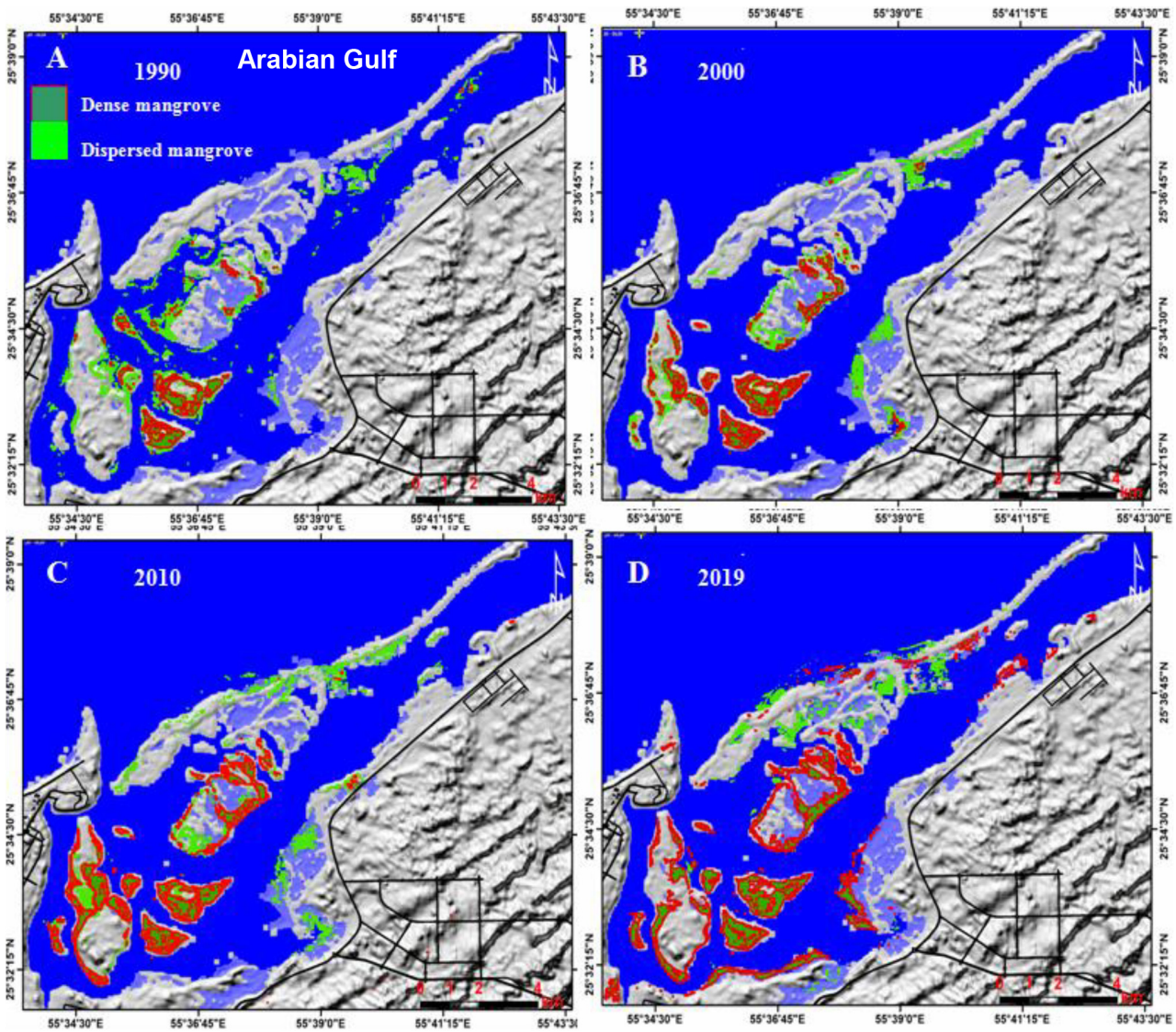

FIGURE 10 | Spatiotemporal variations of mangrove forests in Umm Al Quwain natural reserve for the years 1990 **(A)**, 2000 **(B)**, 2010 **(C)**, and 2019 **(D)**. Red polygons highlight dense mangroves.

The performance of machine learning algorithms were evaluated using the open source R 4.0.0 software.

Further evaluation of the performance of the RF, KLR, and NS algorithms were performed by applying them on the ASTER and EO-1 with a spatial resolution of 30 m and calculate the total area of mangrove (Mondal et al., 2019) and the textural features (mangroves and non-mangrove areas) evident from Landsat images were compared against those from the ASTER and EO-1 images with a spatial resolution of 30m using RF, KLR, and NB algorithms. This method was applied to the Kalba mangrove natural reserve on the eastern side of the study area. These two methods can be considered as an alternative way of field observation, especially when the mangrove forests are located in remote and inaccessible areas (Elmahdy and Mostafa Mohamed, 2013a,b; Elmahdy and Mohamed, 2018; Estoque et al., 2018).

Change Detection

Among several change detection techniques, ID algorithm was chosen to monitor mangrove changes. The ID algorithm was chosen due to its ability to locate the changes in mangroves within each class (dense and sparse) (Mishra et al., 2017; Elmahdy and Mohamed, 2018). The ID algorithm determines the difference in the DN values in each pair of mangrove images (1990–2000, 2000–2010, 2010–2019, and 1990–2019). This can serve as an indicator of mangrove change which has occurred over the NUAE. Monitoring changes start with proper input parameters such as the number of classes, threshold value and change detection type. Threshold value locates the changes in mangroves within each class, epending on the type of remote sensing data (Singh, 1986).

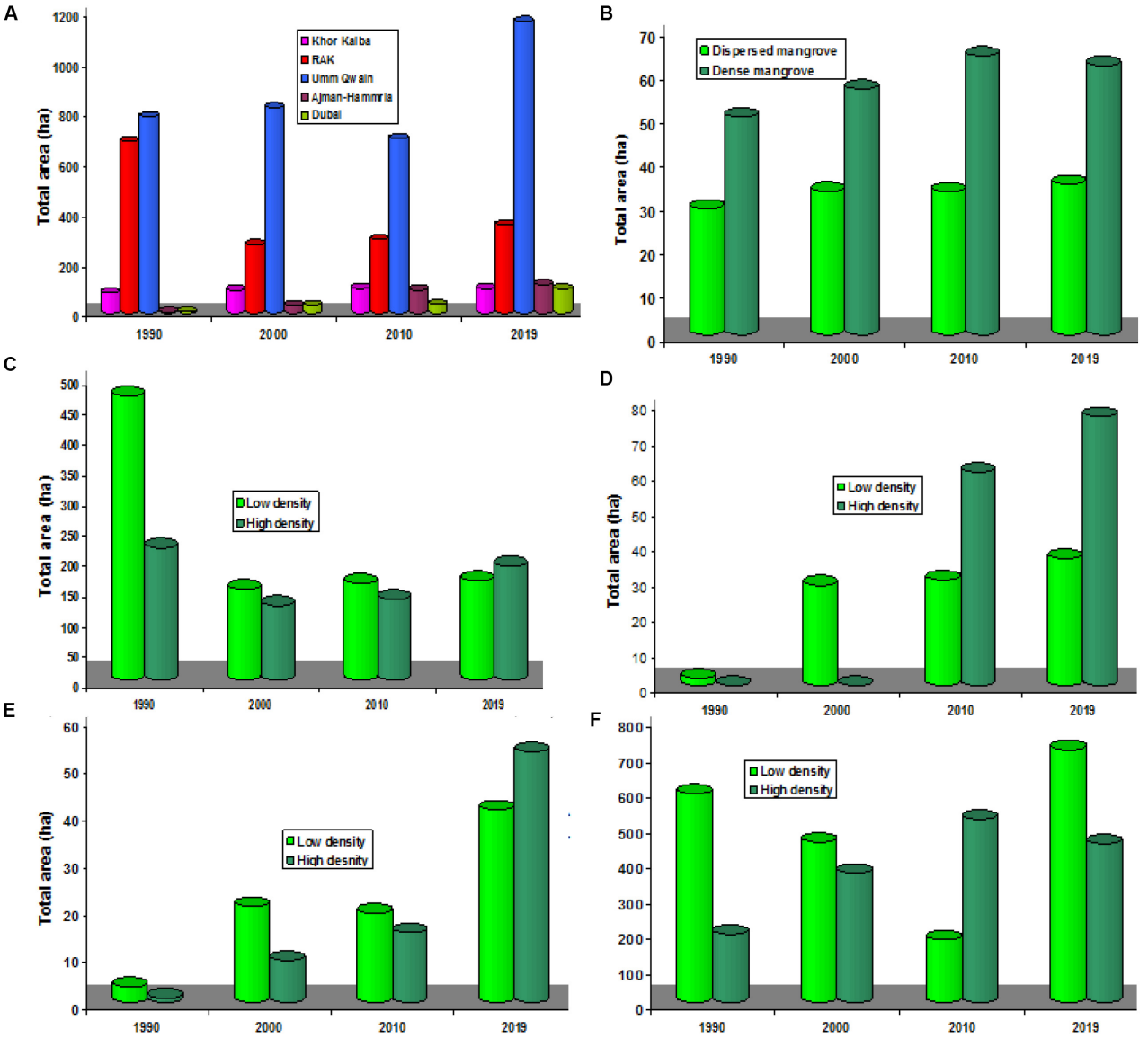

FIGURE 11 | The annual rate of the NUAE mangroves growth **(A)**, and mangrove types for Khor Kalba **(B)**, RAK **(C)**, Ajman-Hammriah **(D)**, Ras Al Khor **(E)**, and Umm Al Quwain **(F)**.

The threshold values are evenly spaced between (-1) and $(+1)$ for simple difference (the initial state image is subtracted from the final state image). The positive changes (positive value) represent the first $(n/2)$ classes, while the negative changes represent the last $(n/2)$ classes. The no-change class $[(n/2) + 1]$ represents the middle class (**Figure 4**), and normalizing the images (raster maps) by subtracting the image minimum. On the final change detection maps, a positive change was identified when pixels took on a red color code (final state image), while a negative change was identified when pixels took on a blue color code (initial state image). Monitoring the NUAE mangrove changes were performed using a change detection tool implemented in the Envi v.4.5 software.

RESULTS

Optimal Parameterization and Evaluation of Machine Learning Performance

Figures 6A–C show different precision, recall, and F1 values for RF, KLR, and NB. Random forest and KLR yielded the highest values (0.95) for F1 score, while NB presented the lowest value (0.75) for F1. Slight differences in F1 score between RF and KLR algorithms were observed. This difference appears to be due to the difference in precision and recall scores and this difference to be due to the difference in overall incorrect pixels between RF, KLR, and NB. Both RF and KLR showed a strong ability in discriminating between dense mangrove compared with NB. However, all models showed less ability

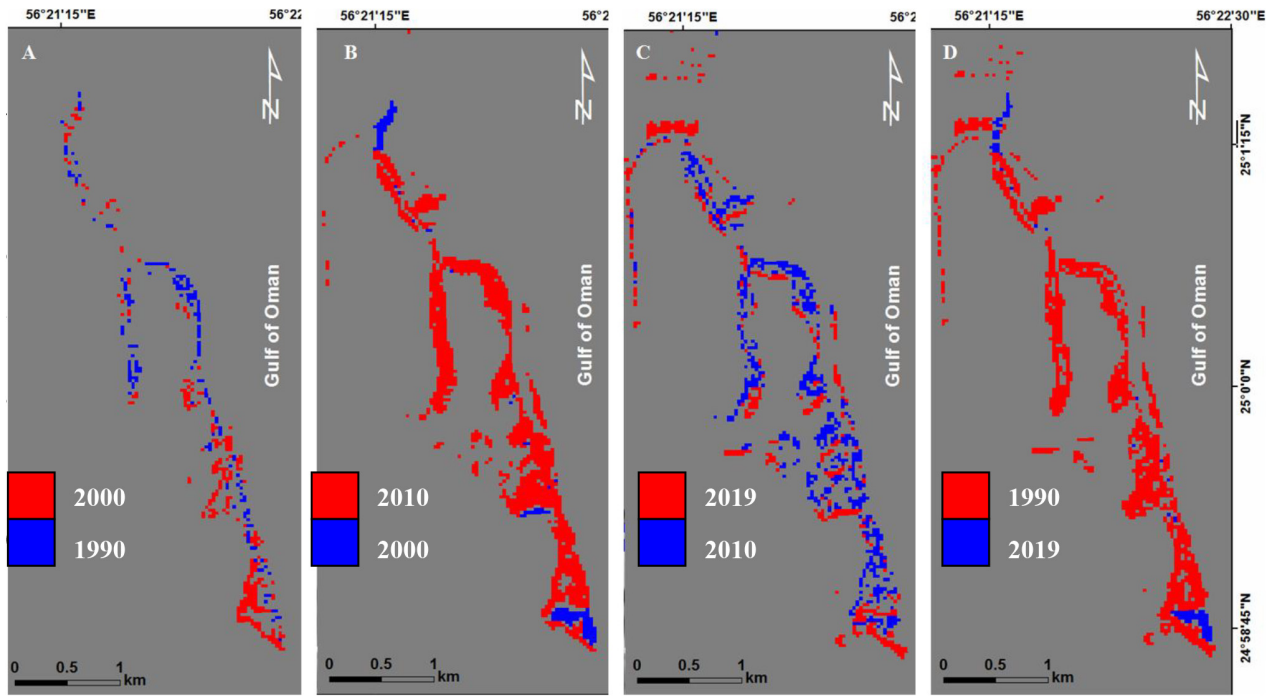

FIGURE 12 | Mangrove pattern change between 1990 and 2000 **(A)**, 2000 **(B)**, 2010–2019 **(C)**, and 1990–2019 **(D)** for Khor Kalba natural reserve. Red color highlights changes in mangroves.

to distinguish dispersed mangroves as indicated from F1 score (<0.8), and thus, lower ability to detect mangrove forests. This lower accuracy due to lower ability in discriminating between mangrove and non-mangrove areas and the lower ability in discriminating owing to the lower reflects. Results of cross-validation showed that the RF and KLR classifiers predicted and classified mangrove from the EO1 ALI better than NB classifier. The extent predicted mangrove areas by the RF and KLR have a wider range compared to those predicted by NB (**Figure 6D**).

Both RF and KLR predicted an area of 72.86 and 71.7 ha, respectively. However, the mangrove extent predicted by the NB has a lower range of mangroves from the Landsat, ASTER and EO-1 images. Although these images have the same spatial resolution, the ASTER and EO-1 miss the regular time span and geographical coverage of the NUAE mangrove. Further validation of the proposed approach was performed by comparing textural features from Landsat images against those extracted from the ASTER and EO-1 images using RF, KLR, and NB algorithms (**Figures 6E–G**).

Mangrove Mapping and Classification

Maps of mangrove forests produced from the Landsat images using RF classifier with a population minimum of 100 and 8 neighbors are shown in **Figures 7–10**. The figures comprise of two color codes to facilitate visual interpretation. The first color code is dark green corresponding to dense mangroves (healthy mangroves). These dense mangroves are located on the gentle slopes of tidal flats, easily discriminated and concentrated in the middle parts of the mangrove patches. The second color code is light green, corresponding to disperse mangroves and are difficult to discriminate and map and are clustered around the dense mangroves and submerged in the water. The figures show that the mangrove forests are mainly spatially distributed in creeks (Khors in local language) of Kalba (**Figures 7**, **11B**), Ras Al Khaimah (**Figures 8**, **11C**), Ajman-Hammria and Dubai (**Figure 9**), and Umm Al Quwain (**Figure 10**), which represent about 35% of the total area of the United Arab Emirates mangrove (Elmahdy and Mostafa Mohamed, 2013a,b).

In Khor Kalba (the Emirate of Sharjah), mangrove areas are spatially distributed as linear and curvilinear strips with a length of 5 km and a width of 300 m. Their common trends were found to be in the NNW-SSE and NNW-SSE directions (**Figures 7**, **11A**). From 1990 to 2019, sparse mangroves have slightly increased from 28.89 ha (1.53%) in 1990 to 34.56 ha (2.037%) in 2019, while dense mangroves increased from 49.95 ha (2.7%) in 1990 to 61.74 ha (4.11%) in 2010 and 63.9 ha (4.80%) in 2019. Most of the mangrove areas are mainly distributed in creeks and estuaries (that now are natural reserves) along the coastal area of the Arabian Gulf.

The highest spatial distribution of mangroves was observed to be in the estuarine area of Umm Al Quwain, covering an area ranging from 700 to 1200 ha, while the lowest spatial distribution of mangrove was observed to be in Ras Al Khor of Dubai covering an area ranging from 4 to 9 ha, where the saline tidal flats distributed in an area is currently dominated by intensive

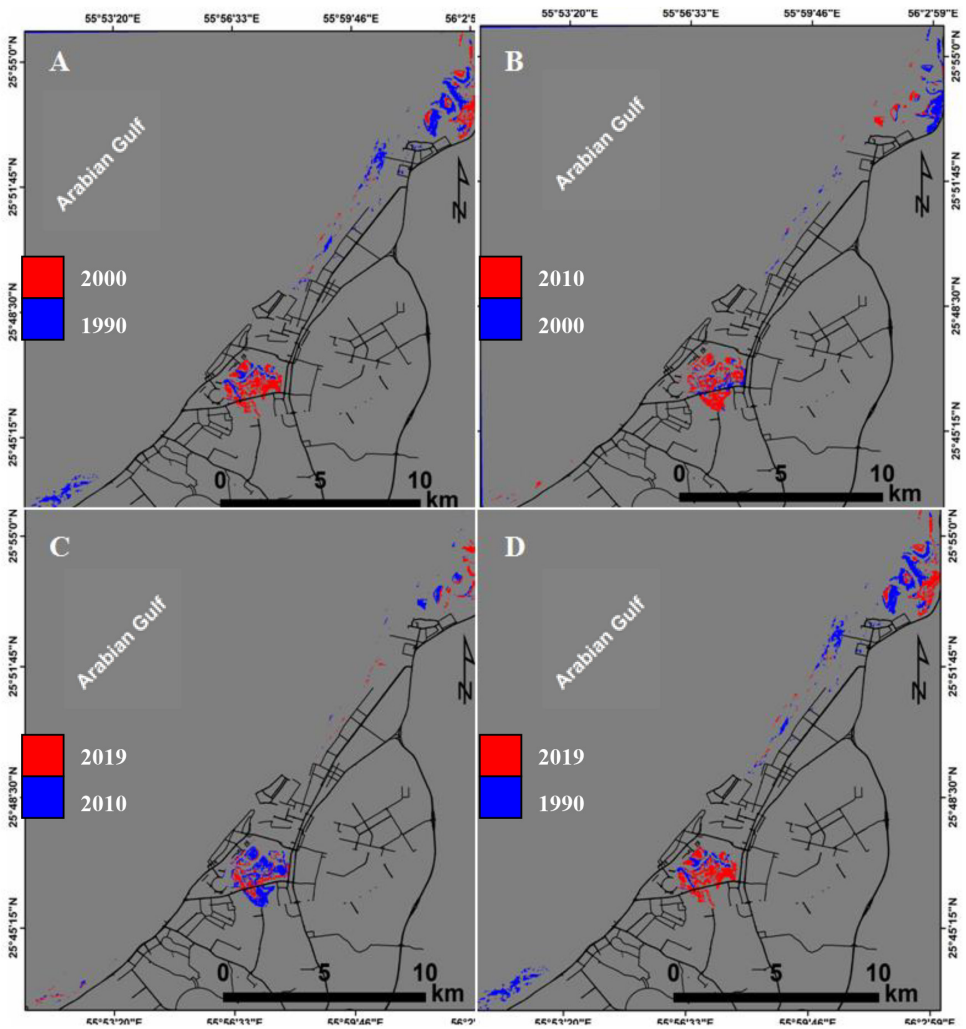

FIGURE 13 | Mangrove pattern changes between 1990 and 2000 **(A)**, 2000–2010 **(B)**, 2010–2019 **(C)**, and 1990–2019 **(D)** for the RAK natural reserves.

urbanization. Moving to the west, in Ras Al Khaima, mangroves are mainly distributed in Mina Al Arab (south), Dafan Creek (middle) and Shaam estuarine areas (north) (**Figures 8**, **11C**).

In Ajman and Hammria Creeks, dispersed mangroves occupied an area of 2.1 ha (0.0021%) in 1990, 28.42 ha (0.39%) in 2000 and 36 ha (0.41%) in 2019. Between 1990 and 2000, the mangroves were dispersed and occupied an area of 28.42 ha (0.39%) (**Figures 9A–D**, **11D**). In 2010, both types of mangroves were clearly observed. Dense and dispersed mangroves occupied an area of 29.88 (0.41%) and 60.39 ha (0.83%), respectively. Like the Ajman-Hammria area, small patches of dispersed and dense mangroves were observed in the 1990 map. Moving to Dubai, mangrove forests were observed to be the smallest mangrove area (**Figures 9E–H**).

The total area of dispersed mangroves in these three locations was 468 ha (1.38%) in 1990, 149.22 ha (0.305%) in 2000 and 163.53 ha (0.33%) in 2019 (**Figure 11D**). Similarly, dense mangrove occupied an area of 217.71 ha (0.44%) in 1990 to 187.65 ha (0.832%). These small patches of mangroves were observed in the western edges of Ras Al Khor and occupied an area of about 18.99 ha in 2010 and 40.95 ha in 2019, respectively. Dense mangroves were observed to be clustered in the southern edge of the Ras Al Khor and easily definable in remote sensing data than the dispersed mangrove distributed in the western edge of the Ras Al Khor. Since 1990, dense and dispersed mangroves have gradually increased from 4.3 ha in 1990 to 94.23 ha in 2019 (**Figure 11E**) and spatially distributed in the Ras Al Khor area. The dispersed mangroves were observed to be distributed in the western part of the Ras Al Khor, while dense mangroves were observed to be distributed in the southwestern edge of Ras Al Khor (**Figures 9**, **11E**). They occupied an area of about 3.22 ha (0.51%) and 0.97 ha (0.071%), respectively.

In Umm Al Quwain estuarine, dispersed mangrove occupied an area of 590.22 ha (2.29%) in 1990, 453.24 ha (1.764%) in 2000 and 715.32 (2.784%) in 2019 (**Figures 10**, **11F**). Similarly, the dense mangrove occupied an area of 194.13 ha (0. 75%) increased to 366.57 ha (0.42%) in 2000 and 518.58 ha (2%), then slightly

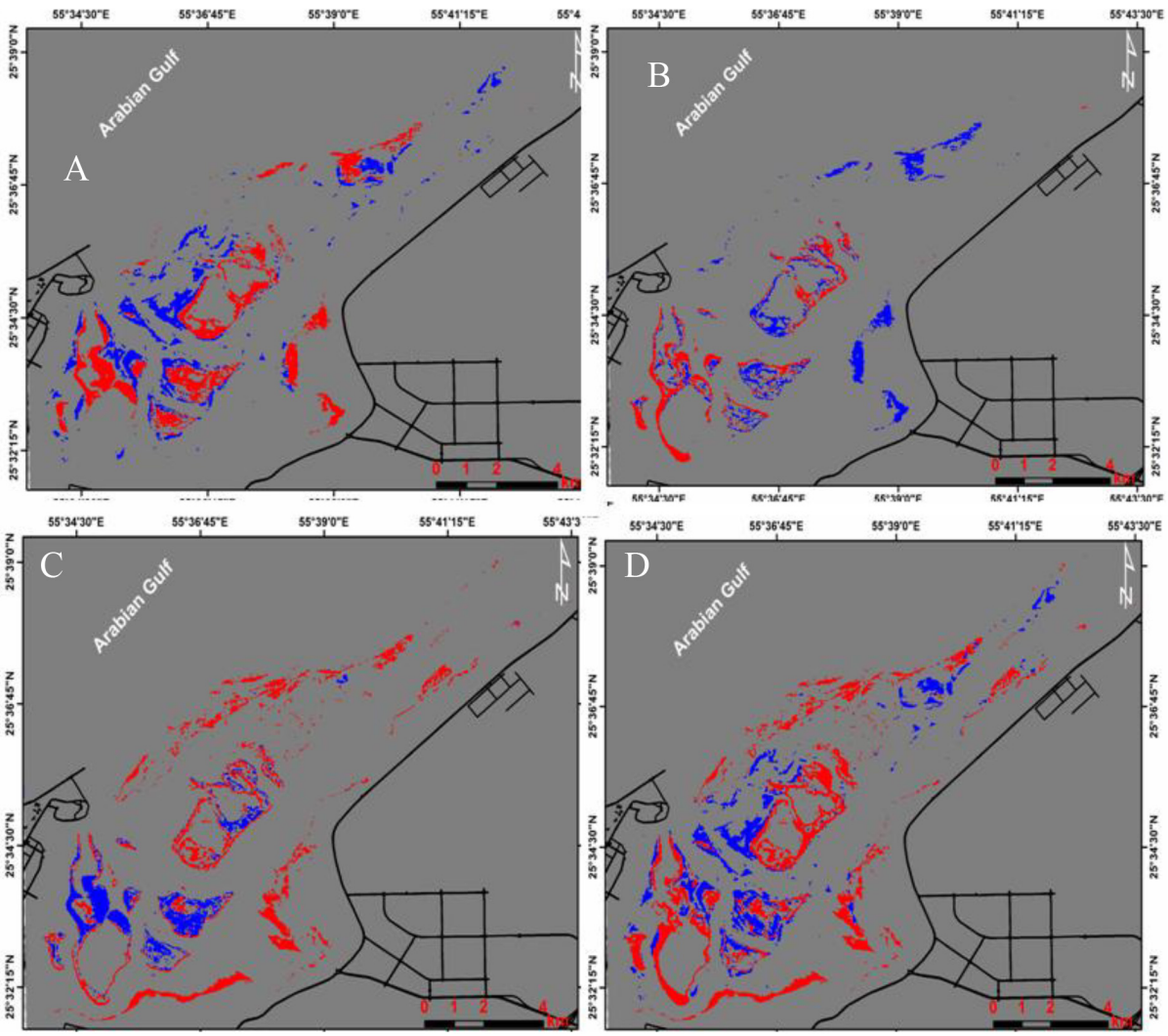

FIGURE 14 | Mangrove pattern changes between 1990 and 2000 **(A)**, 2000–2010 **(B)**, 2010–2019 **(C)**, and 1990–2019 **(D)** for Umm Al Quwain.

declined to 449.55 (1.74%) in 2019. In 2019, dispersed and dense mangroves increased, occupying an area of 36 ha (0.46%) and 76.14 ha (0.91%), respectively.

Change Detection of the NUAE Mangrove Forests

The results of monitoring mangrove changes in four periods: 1990–2000, 2000–2010, 2010–2019, and 1990–2019 with a time-span of 10 years are shown in **Figures 12–16** and their statistics are shown in **Figure 17**. In Khor Kalba (**Figure 12**), the total area of mangroves increased by about 10.35 ha from 1990 to 2000 and 7.47 ha (0.26%) between 2000 and 2010, and then decreased slightly by about 0.36 ha between 2010 and 2019. It can be noticed that although the Khor Kalba mangroves expansion is small. The rate of growth of the Khor Kalba mangrove remains relatively stable during the last 29 years (**Figures 12**, **17**).

In RAK areas, there is a negative change (mangrove loss) of -414.27 and -334.53 ha during the periods from 1990 to 2000 and from 1990 to 2019, respectively (**Figures 13A–D**). From 2000 to 2010, the mangrove increased slightly by 20.79 ha and more than double (58.95 ha) during the period from 2010 to 2019.

In Umm Al Quwain estuarine, similar changes (mangrove loss) were observed during the period from 2000 to 2010 (**Figures 14E–H**). The estimated lost area was about -122.76 ha. Conversely, the mangrove forests increased sharply by approximately 467.82 ha from 2010 to 2019. Between 1990 and 2019, the mangrove forests increased by about 380.52 ha (**Figure 17**).

Further south, the mangrove area in Ajman and Hammria creeks increased by about 26.32 ha from 1990 to 2000, then increased sharply by about 61.85 ha between 2000 and 2010 (**Figures 15A–D**). From 2010 to 2019, the mangroves increased slightly by about 28.87 ha. Since 1990, the total area of the mangroves increased by about 110.04 ha (1.88%).

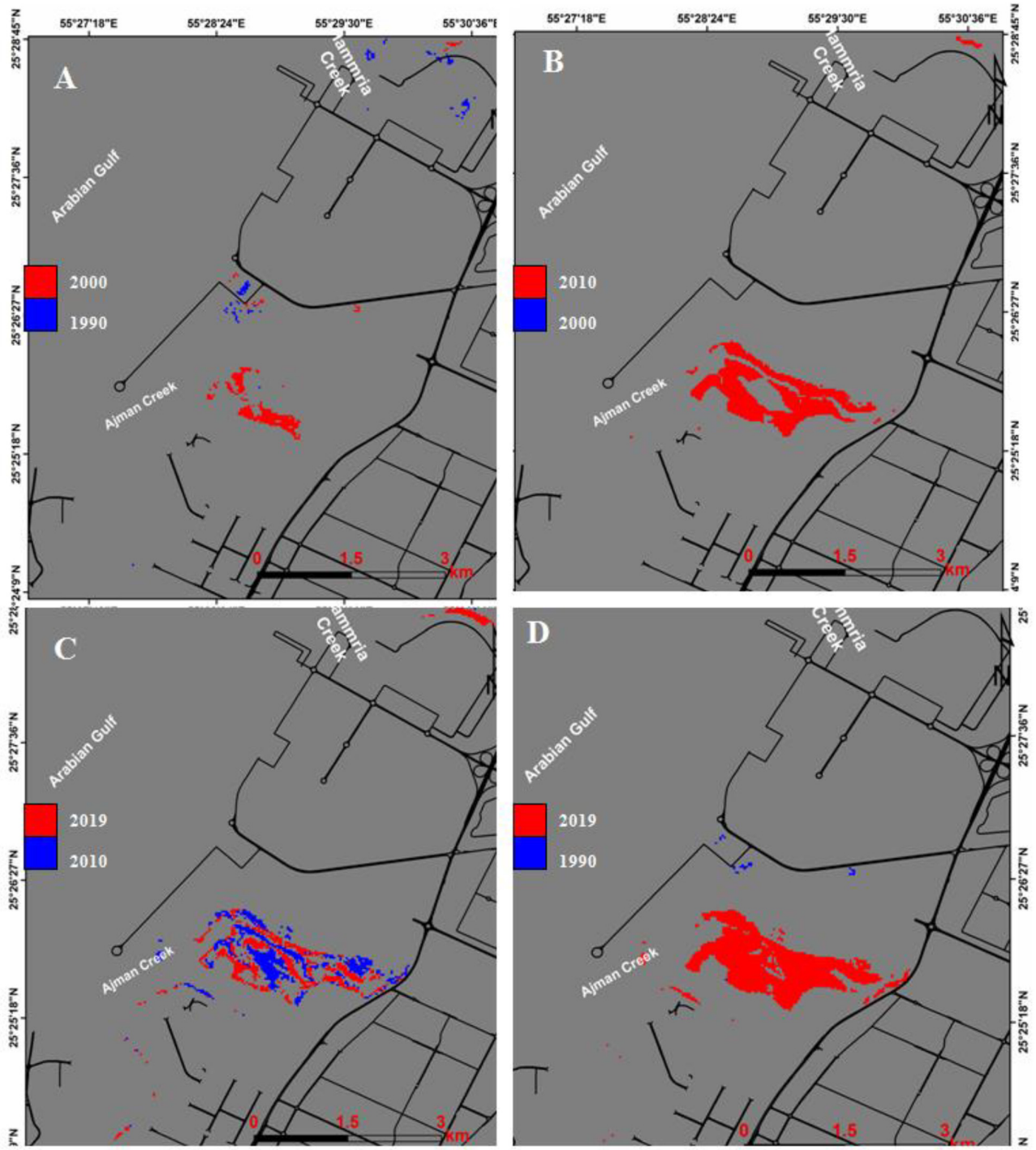

FIGURE 15 | Mangrove pattern changes between 1990 and 2000 **(A)**, 2000–2010 **(B)**, 2010–2019 **(C)**, and 1990–2019 **(D)** for Ajman-Hammriah.

In Ras Al Khor of Dubai, the lowest positive changes were observed to be during the periods from 1990 to 2000 (25.18 ha) and from 2000 to 2010 (4.36 ha), respectively. The largest changes were observed from 2010 to 2019 of about 60.39 ha (**Figures 16**, **17**). Since 1990, an increase (positive change) in the mangrove area was reported. The estimated area of mangrove was 89.93 ha which represents the third after Umm Al Quwain and Ajman and Hammria Creeks. Generally, the mangrove areas showed an increase in all locations except the RAK and Umm Al Quwain areas. Comparing between the two mangrove ecosystems there appears to be stability in the mangrove area faced to the Gulf of Oman than those facing the Arabian Gulf.

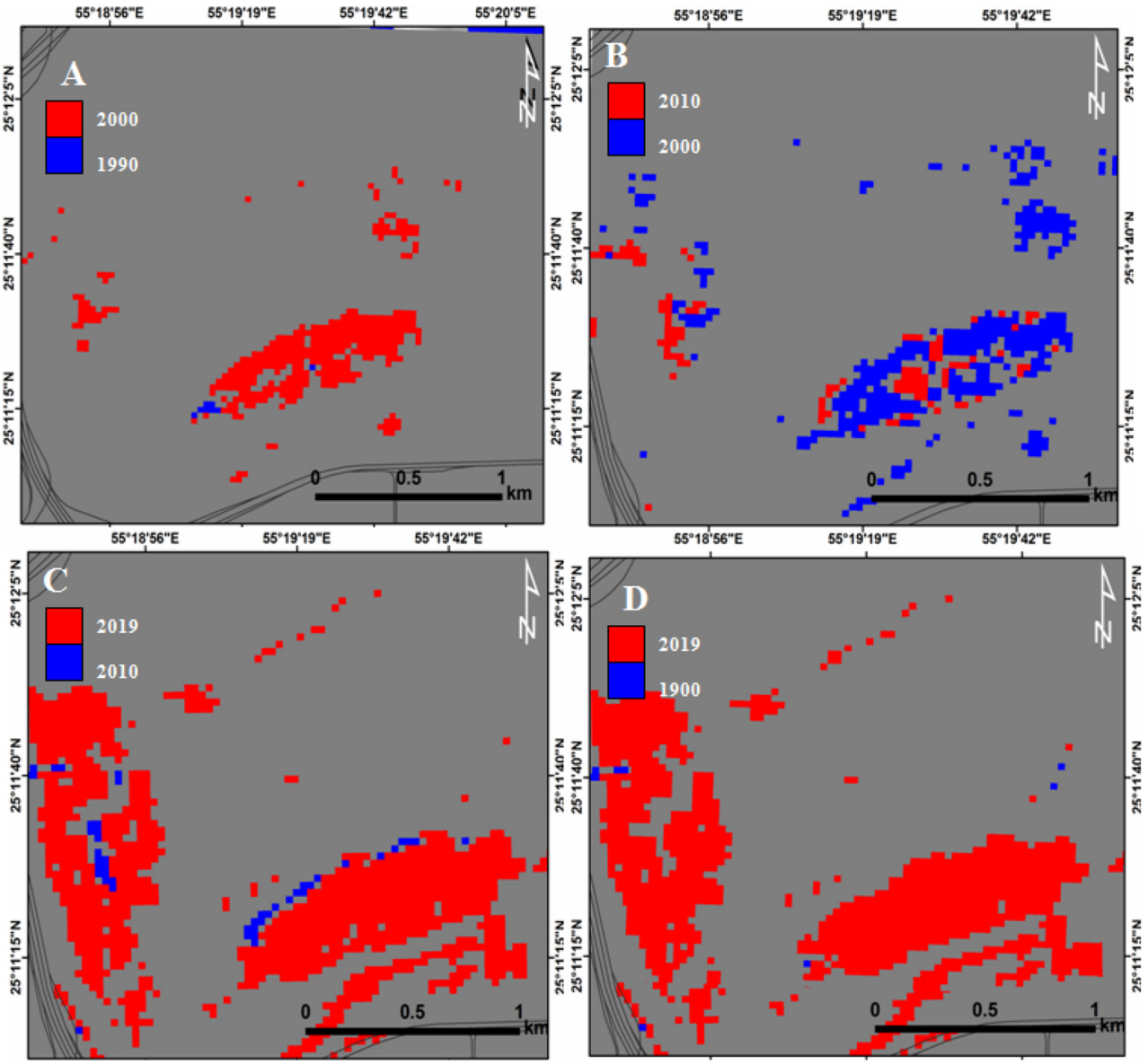

FIGURE 16 | Mangrove pattern changes between 1990 and 2000 **(A)**, 2000–2010 **(B)**, 2010–2019 **(C)**, and 1990–2019 **(D)** Ras Al Khor, Dubai.

DISCUSSION

Evaluation of the Performance of the Classifiers

The use and comparison of the performance of RF, KLR, NB, and ID algorithms permitted precisely mapping, classifying, and monitoring mangrove changes over 29 years in different ecological systems. Among the machine learning, RF yielded high precision, high recall and F1 score. This means that the RF has a powerful ability to map the mangrove forests in different ecosystems. These results also indicated that the RF and KLR are able to detect patches of dense mangrove that represent the majority of mangrove forests. On the other hand, NB yielded the lowest value for the F1 score (<0.8), and thus, lower ability to detect mangrove forests (**Figure 6**).

Random forest iterations predicted a slightly wider range of mangrove forest extent compared to those by KLR with F1 scores of 0.93 and 0.90, respectively. These findings were in good agreement with several studies that have indicated that RF algorithm has higher accuracy compared to CART (Mondal et al., 2019), support vector machine (SVM; Chen et al., 2020), and maximum likelihood (Ha et al., 2020) who compared machine learning methods against traditional classifiers and assist potentiality of groundwater.

These findings are also in accordance with Toosi et al. (2019) who compared different classifiers for monitoring mangrove changes and concluded that the RF which uses freely available

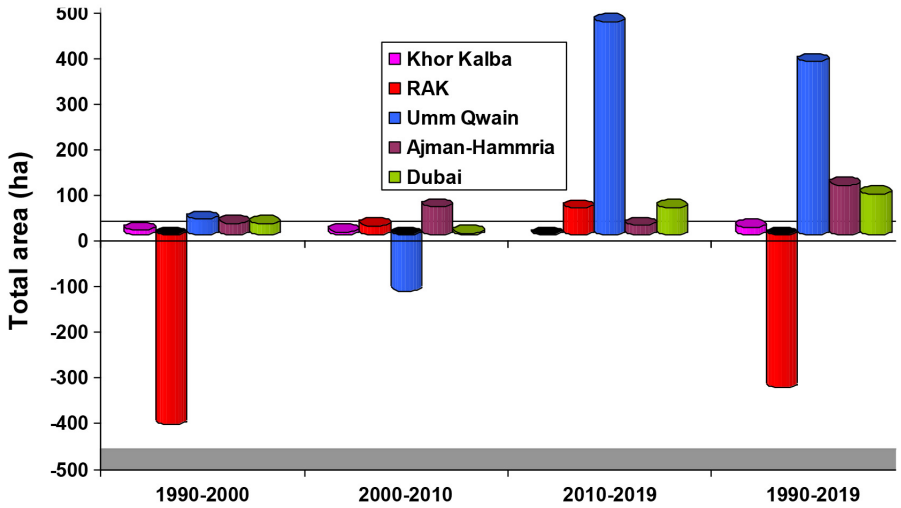

FIGURE 17 | The graphical representation of the NUAE mangrove forests extent from 1990 to 2019 (in hectare). The graph shows a significant decrease in RAK Mangroves from 1990 to 2000 (in hectare) and a slight decrease in Umm Al Quwain Mangroves from 2000 to 2010.

Landsat images, had performed best. Feng et al. (2018) implemented a novel change detection approach based on visual saliency and RF from multi-temporal high-resolution remote-sensing images. However, the opposite occurred for mapping mangrove using traditional classifiers.

The use of freely available Landsat images offered the ability to detect mangroves with overall accuracy comparable to the machine learning classifiers that involved the commercially remote sensing data such as LiDAR and WorldView-3 (Elmahdy and Mohamed, 2018; Toosi et al., 2019). Although the LiDAR, WorldView, and RapidEye images have high spatial resolution, the overall accuracy of RF only reached 82% (Ha et al., 2020). Other studies confirmed that the rotation forest (RoF) algorithm had a higher accuracy than the canonical correlation forest (CCF) in LULC classification, which has less sensitivity compared to the RF algorithm (Colkesen and Kavzoglu, 2017; Ha et al., 2020).

The proposed approach represents a significant modification in mangroves and LULC, as well as an enhancement of the performance of linear and non-linear classifiers. The machine learning algorithms, especially, when optimized, have their robust and a higher efficiency and quality of classification (Coppin and Bauer, 1996; Banfield et al., 2006; Wang et al., 2015; Gong et al., 2019).

The wide availability and ease of implementation of machine learning and free availability of Landsat images permitted an exceptional simplicity in processing vast amounts of remote sensing data promptly and at low costs (Elmahdy et al., 2019; Mondal et al., 2019).

Mangrove Classification

The use of machine learning algorithms and Landsat images provides up-to-date mangrove maps over multiple scales and able to discriminate between mangrove and non-mangrove areas and dense mangrove and dispersed mangrove patches than currently available. Between 1990 and 2019, the largest increase in mangrove forest extent occurred in the Umm Al Quwain Estuarine (1200 ha), while the largest decrease occurred in Dubai Natural Reserve (9 ha). Locally, these results are consistent with Su et al. (2009), Martins et al. (2016), Elmahdy and Mohamed (2018), and Gong et al. (2019) who optimized SVM, SAM, and RF classifiers and much more precisely than those mapped by Moore et al. (2013) using manual screen digitizing and field observations. This result is not consistent with our results, which indicated the mangrove of Khor Kalba was over 800 ha. The maps produced by Moore et al. (2013) had a lot of errors and bias and cannot be used as a reference. However, our results permitted better understanding of the NUAE mangrove's extent and can be updated in any future study, as well as building a new framework of the change detection. The proposed approach provides a better accuracy by reducing the level of noise associated with remote sensing data and helping in discriminating between mangrove and non-mangrove areas.

Mangrove Change Detection

During change detection, we observed that the ID algorithm using pair of bi-temporal mangrove classification of images with a threshed value between -1 and +1, is better than other algorithms such as an image to map and map to map (Elmahdy and Mohamed, 2018; Ma et al., 2019). The ID minimizes the errors created in one or two of the classification maps detecting greater presence pixels (+) and absence pixels (-) than those detected by image to map and map to map approaches. These approaches suffer from error propagation and differences in image calibration between Landsat sensors.

The rapid changes in mangrove forests during the period from 2010 to 2019 are much more than those during the period from 1990 to 2000. These changes are due to localized plantation activities and increased public and the local authorities

awareness and conservation efforts during the last decade (Food and Agriculture Organization of the United Nations, 2007; Loughland et al., 2007; Howari et al., 2009). Additionally, most of the mangrove forests are natural reserve and inaccessible areas. The mangrove forests play a vital role in ecosystems, supporting biodiversity and protecting coastal areas from erosion and storms. Mangrove forests have an incredible ability to store blue carbon in soil and subsoil and removing carbon from the atmosphere and the Arabian Gulf (Food and Agriculture Organization of the United Nations, 2007; Loughland et al., 2007; Howari et al., 2009). The soil of the United Arab Emirates stocks about 25% quantile of other sites globally (Schile et al., 2017).

The results of mangroves change detection show a significant change in mangrove forests facing the Arabian Gulf, while a slight increase in mangrove forests facing the Gulf of Oman, possibly due to lower human activities and urbanization, lower sea surface temperature (SST), lower sea surface salinity (SSS; Freeman et al., 2008; Elmahdy and Mohamed, 2018; Noori et al., 2019), and the coarser soil texture (Ooi et al., 2011; Rodriguez et al., 2016). These factors strongly influence the spatial distribution and density of mangrove forests and thus the carbon pools (Schile et al., 2017).

A low-cost remote sensing approach that integrates machine learning and ID algorithms have not been employed for mapping and monitoring mangroves extent over different ecological systems for the first time. The proposed approach is of great benefit for monitoring mangrove changes in remote and inaccessible areas where ecological and environmental information are unavailable, and the need for shoreline protection and fish breeding is critical. It performs very well in coastal and inland areas as well as the dense and dispersed mangroves. The main limitation of the proposed approach and Landsat images is that it cannot identify mangrove species, heights and small patches of mangroves in a submerged form. In future research, it might be interesting to estimate mangrove height using dual HH/VV SAR data and coastal survey using Lidar data, and compare the results from that study with those from the current study. Future studies will assess and investigate the impact of the climate and environment on landscape change.

CONCLUSION

This study presented an integration approach based on learning RF with training data with a higher spatial resolution, RF optimal parameterization and applying a post-classification enhancement to the produced mangrove maps. The best parameters were 7 for sample node, 0 for tree depth and 75 for a tree in a forest. The results indicated that the integration approach, which uses Landsat images, is able to discriminate mangrove and non-mangrove areas and had an overall accuracy of more than 90% with an increase of 6.7% compared with supervised classifications. The results also demonstrated that the NUAE mangroves increased in all locations over the last 29 years. The majority of the NUAE mangroves are spatially distributed in the western coastal area than those in the eastern coastal area and the dense mangrove is much more than dispersed mangrove and much easier to discriminate and map. The mangrove forests of Khor Kalba facing the Gulf of Oman are more stable than those facing the Arabian Gulf. The highest distribution of mangroves was observed to be in the Umm Al Quwain estuarine, occupying an area of 1200 ha, while the lowest distribution of mangrove was reported to be in Ras Al Khor of Dubai covering an area of about 9 ha. Although there is a rapid change in the built-up area along with the eastern and western coastal areas of the NUAE, the mangroves had increased in sites of the NUAE and predicted to increase further over the next decade. The proposed approach can be applied to any area in arid and semi-arid regions and the results can be used as reference maps and updated by future studies as well as to provide useful ecological and environmental information.

DATA AVAILABILITY STATEMENT

The original contributions presented in the study are included in the article/supplementary material, further inquiries can be directed to the corresponding author/s.

AUTHOR CONTRIBUTIONS

SE processed the data and developed the RF. TA supervised the project and provided data. MM provided data and reviewed the methods. FH coded the RF algorithm. MA contributed to the scientific review. DS reviewed the manuscript. All authors contributed to the article and approved the submitted version.

FUNDING

The research has received funding under financial grant SCRI 18 Grant EN0-284 and the grant of UAE Space Agency z01-2016-001.

ACKNOWLEDGMENTS

We would like to thank the American University of Sharjah, United Arab Emirates and UAE Space Agency for supporting this research.

REFERENCES

Adam, P., and Hutchings, P. (2010). The saltmarshes and mangroves of Jervis Bay. *Wetlands (Aust.)* 6,

Almahasheer, H. (2018). Spatial coverage of mangrove communities in the Arabian Gulf. *Environ. Monit. Assess.* 190:85.

Alsumaiti, T. S. (2014). An assessment of *Avicennia marina* forest structure and aboveground biomass in Eastern Mangrove Lagoon National Park, Abu Dhabi. *Arab. World Geogr.* 17, 166–185.

Alsaaideh, B., Al-Hanbali, A., Tateishi, R., Kobayashi, T., and Hoan, N. T. (2013). Mangrove forests mapping in the southern part of Japan using Landsat ETM+ with DEM. *J. Geogr. Inform. Syst.* 5, 369–377. doi: 10.4236/jgis.2013.54035

Amarsaikhan, D., Blotevogel, H. H., Ganzorig, M., and Moon, T. H. (2009). Applications of remote sensing and geographic information systems for urban land-cover change studies in Mongolia. *Geocarto Int.* 24, 257–271. doi: 10.1080/10106040802556173

Bachmair, S., and Weiler, M. (2012). Hillslope characteristics as controls of subsurface flow variability. *Hydrol. Earth Syst. Sci.* 16:3699. doi: 10.5194/hess-16-3699-2012

Banfield, R. E., Hall, L. O., Bowyer, K. W., and Kegelmeyer, W. P. (2006). A comparison of decision tree ensemble creation techniques. *IEEE Trans. Pattern Anal. Machine Intell.* 29, 173–180. doi: 10.1109/tpami.2007.250609

Barua, S., Karim, E., and Humayun, N. M. (2014). Present status and species composition of commercially important finfish in landed trawl catch from Bangladesh marine waters. *Int. J. Pure Appl. Zool.* 2, 150–159.

Bashitialshaaer, R. A., Persson, K. M., and Aljaradin, M. (2011). Estimated future salinity in the Arabian Gulf, the Mediterranean Sea and the Red Sea consequences of brine discharge from desalination. *Int. J. Acad. Res.* 3, 133–140.

Belgiu, M., and Dăguţ, L. (2016). Random forest in remote sensing: a review of applications and future directions. *ISPRS J. Photogram. Rem. Sens.* 114, 24–31. doi: 10.1016/j.isprsjprs.2016.01.011

Birth, G. S., and McVey, G. R. (1968). Measuring the color of growing turf with a reflectance spectrophotometer 1. *Agron. J.* 60, 640–643. doi: 10.2134/agronj1968.00021962006000060016x

Boardman, J. W., and Kruse, F. A. (1994). "Automated spectral analysis: a geological example using AVIRIS data, north Grapevine Mountains, Nevada," in *Proceedings of the ERIM Tenth Thematic Conference on Geologic Remote Sensing. Environmental Research*, ed. ERIM (Ann Arbor, MI: Institute of Michigan), 407–418.

Boer, B., and Aspinall, S. J. (2005). "Life in the Mangroves," in *The Emirates: a Natural History*, eds P. Hellyer and S. Aspinall (Cape Town: Trident Press).

Breiman, L. (2001). Random forests. *Machine Learn.* 45, 5–32.

Bui, T. (2015). Analysis of docker security. *arXiv* [Preprint]. arXiv:1501.02967.

Buitre, M. J. C., Zhang, H., and Lin, H. (2019). The mangrove forests change and impacts from tropical cyclones in the philippines using time series satellite imagery. *Rem. Sens.* 11:688. doi: 10.3390/rs11060688

Chander, J. (2009). A text book of Medical Mycology 3rd ed. Chapter 28. Oxford University Press.

Catani, F., Lagomarsino, D., Segoni, S., and Tofani, V. (2013). Landslide susceptibility estimation by random forests technique: sensitivity and scaling issues. *Nat. Hazards Earth Syst. Sci.* 13:2815. doi: 10.5194/nhess-13-2815-2013

Chen, B., Xiao, X., Li, X., Pan, L., Doughty, R., Ma, J., et al. (2017). A mangrove forest map of China in 2015: analysis of time series Landsat 7/8 and Sentinel-1A imagery in Google Earth Engine cloud computing platform. *ISPRS J. Photogram. Rem. Sens.* 131, 104–120. doi: 10.1016/j.isprsjprs.2017.07.011

Chen, J., Wang, P., Wang, C., and Gao, H. (2020). "Effects of six types of straw derived biochar on anaerobic biodegradation of polybrominated diphenyl ethers in mangrove sediments: a microcosm experiment," in *Proceedings of the IOP Conference Series: Earth and Environmental Science*, Vol. 435 (Bristol: IOP Publishing), 012003.

Cintron, G., Lugo, A. E., Pool, D. J., and Morris, G. (1978). Mangroves of arid environments in Puerto Rico and adjacent islands. *Biotropica* 10, 110–121.

Colkesen, I., and Kavzoglu, T. (2017). Ensemble-based canonical correlation forest (CCF) for land use and land cover classification using sentinel-2 and Landsat OLI imagery. *Rem. Sens. Lett.* 8, 1082–1091. doi: 10.1080/2150704x.2017.1354262

Congalton, R. G., Oderwald, R. G., and Mead, R. A. (1983). Assessing Landsat classification accuracy using discrete multivariate analysis statistical techniques. *Photogram. Eng. Rem. Sens.* 49, 1671–1678.

Coppin, P. R., and Bauer, M. E. (1996). Digital change detection in forest ecosystems with remote sensing imagery. *Rem. Sens. Rev.* 13, 207–234. doi: 10.1080/02757259609532305

Crouvi, O., Ben-Dor, E., Beyth, M., Avigad, D., and Amit, R. (2006). Quantitative mapping of arid alluvial fan surfaces using field spectrometer and hyperspectral remote sensing. *Rem. Sens. Environ.* 104, 103–117. doi: 10.1016/j.rse.2006.05.004

Darvishsefat, A. A. (1995). Einsatz und Fusion von Multisensoralen Satellitendaten zur Erfassung von Waldinventuren. *Rem. Sens. Ser.* 24:1995.

Díaz, B. M., and Blackburn, G. A. (2003). Remote sensing of mangrove biophysical properties: evidence from a laboratory simulation of the possible effects of background variation on spectral vegetation indices. *Int. J. Rem. Sens.* 24, 53–73. doi: 10.1080/01431160305012

Diniz, C., Cortinhas, L., Nerino, G., Rodrigues, J., Sadeck, L., Adami, M., et al. (2019). Brazilian mangrove status: three decades of satellite data analysis. *Rem. Sens.* 11:808. doi: 10.3390/rs11070808

Donato, D. C., Kauffman, J. B., Murdiyarso, D., Kurnianto, S., Stidham, M., and Kanninen, M. (2011). Mangroves among the most carbon-rich forests in the tropics. *Nat. Geosci.* 4, 293–297. doi: 10.1038/ngeo1123

Edwards, M., and Richardson, A. J. (2004). Impact of climate change on marine pelagic phenology and trophic mismatch. *Nature*. 430, 881–884. doi: 10.1038/nature02808

Edwards, J., Gustafsson, M., and Näslund-Landenmark, B. (2007). *Handbook for Vulnerability Mapping, EU Asia Pro Eco Project: Disaster Reduction Through Awareness, Preparedness and Prevention Mechanisms in Coastal Settlements in Asia. Demonstration in Tourism Destinations. Demonstration in Tourism Destinations*. Stockholm: Swedish Rescue Services Agency & EU and International Affairs Department.

Elmahdy, S. I., and Mostafa Mohamed, M. (2013a). Remote sensing and GIS applications of surface and near-surface hydromorphological features in Darfur region, Sudan. *Int. J. Rem. Sens.* 34, 4715–4735. doi: 10.1080/01431161.2013.781287

Elmahdy, S. I., and Mostafa Mohamed, M. (2013b). Change detection and mapping of mangrove using multi-temporal remote sensing data: a case study of Abu Dhabi, UAE. *J. Geomat.* 7, 41–46.

Elmahdy, S. I., and Mohamed, M. M. (2018). Monitoring and analysing the Emirate of Dubai's land use/land cover changes: an integrated, low-cost remote sensing approach. *Int. J. Digital Earth* 11, 1132–1150. doi: 10.1080/17538947.2017.1379563

Elmahdy, S. I., Mohamed, M. M., and Ali, T. A. (2019). Automated detection of lineaments express geological linear features of a tropical region using topographic fabric grain algorithm and the SRTM DEM. *Geocarto Int.* 1–20. doi: 10.1080/10106049.2019.1594393

Elmahdy, S. I., Mohamed, M. M., Ali, T. A., Abdalla, J. E. D., and Abouleish, M. (2020a). Land subsidence and sinkholes susceptibility mapping and analysis using random forest and frequency ratio models in Al Ain, UAE. *Geocarto Int.* 1–17. doi: 10.1080/10106049.2020.1716398

Elmahdy, S., Mohamed, M., and Ali, T. (2020b). Land use/land cover changes impact on groundwater level and quality in the Northern Part of the United Arab Emirates. *Rem. Sens.* 12:1715. doi: 10.3390/rs12111715

Embabi, N. S. (1993). "Environmental aspects of geographical distribution of mangrove in the United Arab Emirates," in *Towards the Rational Use of High Salinity Tolerant Plants*, eds H. Lieth and A. A. Al Masoom (Dordrecht: Springer), 45–58. doi: 10.1007/978-94-011-1858-3_5

Erftemeijer, P. L., and Hamerlynck, O. (2005). Die-back of the mangrove Heritiera littoralis dryand, in the Rufiji Delta (Tanzania) following El Nino floods. *J. Coast. Res.* 48, 228–235.

Estoque, R. C., Pontius, R. G. Jr., Murayama, Y., Hou, H., Thapa, R. B., Lasco, R. D., et al. (2018). Simultaneous comparison and assessment of eight remotely sensed maps of Philippine forests. *Int. J. Appl. Earth Observ. Geoinform.* 67, 123–134. doi: 10.1016/j.jag.2017.10.008

Farid, D. M., Zhang, L., Rahman, C. M., Hossain, M. A., and Strachan, R. (2014). Hybrid decision tree and naïve Bayes classifiers for multi-class classification tasks. *Expert Syst. Appl.* 41, 1937–1946. doi: 10.1016/j.eswa.2013.08.089

Fang, H., and Liang, S. (2008). "Leaf area index models," in *Reference Module in Earth Systems and Environmental Sciences*, ed. S. A. Elias (Amsterdam: Elsevier).

Fang, H. L., and Liang, S. L. (2003). Retrieving leaf area index with a neural network method: Simulation and validation. *IEEE Trans. Geosci. Rem. Sens.* 41, 2052–2062. doi: 10.1109/tgrs.2003.813493

Feng, W., Sui, H., Tu, J., Huang, W., and Sun, K. (2018). A novel change detection approach based on visual saliency and random forest from multi-temporal high-resolution remote-sensing images. *Int. J. Rem. Sens.* 39, 7998–8021. doi: 10.1080/01431161.2018.1479794

Field, C., Osborn, J., Hoffman, L., Polsenberg, J., Ackerly, D., Berry, J., et al. (1998). Mangrove biodiversity and ecosystem function. *Glob. Ecol. Biogeogr. Lett.* 7, 3–14.

Fleiss, J. L., Levin, B., and Paik, M. C. (2003). "Statistical inference for a single proportion," in *Anonymous Statistical Methods for Ratesand Proportions, Thirded*, (Hoboken, NJ: John Wiley & Sons,Inc), 17–49. doi: 10.1002/0471445428.ch2

Food and Agriculture Organization of the United Nations (2007). *The world's Mangroves 1980–2005. A Thematic Study Prepared in the Framework of the Global Forest Resources Assessment 2005*. Rome: Food and Agriculture Organization of the United Nations.

Foody, G. M. (2002). Status of land cover classification accuracy assessment. *Rem. Sens. Environ.* 80, 185–201. doi: 10.1016/s0034-4257(01)00295-4

Freeman, A. S., Short, F. T., Isnain, I., Razak, F. A., and Coles, R. G. (2008). Seagrass on the edge: Land-use practices threaten coastal seagrass communities in Sabah, Malaysia. *Biol.Conserv.* 141, 2993–3005. doi: 10.1016/j.biocon.2008.09.018

Friedman, J. H. (2001). Greedy function approximation: a gradient boosting machine. *Ann. Stat.* 29, 1189–1232.

Friedman, J. H. (2002). Stochastic gradient boosting. *Comput. Stat. Data Anal.* 38, 367–378. doi: 10.1016/s0167-9473(01)00065-2

Fry, B., and Cormier, N. (2011). Chemical ecology of red mangroves, *Rhizophora mangle*, in the Hawaiian Islands1. *Pac. Sci.* 65, 219–234. doi: 10.2984/65.2.219

Fu, B., Wang, Y., Campbell, A., Li, Y., Zhang, B., Yin, S., et al. (2017). Comparison of object-based and pixel-based Random Forest algorithm for wetland vegetation mapping using high spatial resolution GF-1 and SAR data. *Ecol. Indic.* 73, 105–117. doi: 10.1016/j.ecolind.2016.09.029

Ghanavati, E., Firouzabadi, P. Z., Jangi, A. A., and Khosravi, S. (2008). Monitoring geomorphologic changes using Landsat TM and ETM+ data in the Hendijan River delta, southwest Iran. *Int. J. Rem. Sens.* 29, 945–959. doi: 10.1080/01431160701294679

Giri, C., Ochieng, E., Tieszen, L. L., Zhu, Z., Singh, A., Loveland, T., et al. (2011). Status and distribution of mangrove forests of the world using earth observation satellite data. *Glob. Ecol. Biogeogr.* 20, 154–159. doi: 10.1111/j.1466-8238.2010.00584.x

Gong, P., Liu, H., Zhang, M., Li, C., Wang, J., Huang, H., et al. (2019). Stable classification with limited sample: transferring a 30-m resolution sample set collected in 2015 to mapping 10-m resolution global land cover in 2017. *Sci. Bull.* 64, 370–373. doi: 10.1016/j.scib.2019.03.002

Green, A. A., Berman, M., Switzer, P., and Craig, M. D. (1988). A transformation for ordering multispectral data in terms of image quality with implications for noise removal. *IEEE Trans. Geosci. Rem. Sens.* 26, 65–74. doi: 10.1109/36.3001

Guild, L. S., Cohen, W. B., and Kauffman, J. B. (2004). Detection of deforestation and land conversion in Rondonia, Brazil using change detection techniques. *Int. J. Rem. Sens.* 25, 731–750. doi: 10.1080/0143116031000159893 5

Ha, N. T., Manley-Harris, M., Pham, T. D., and Hawes, I. (2020). A comparative assessment of ensemble-based machine learning and maximum likelihood methods for mapping seagrass using sentinel-2 imagery in Tauranga Harbor, New Zealand. *Rem. Sens.* 12:355. doi: 10.3390/rs12030355

Heumann, B. W. (2011). An object-based classification of mangroves using a hybrid decision tree—Support vector machine approach. *Rem. Sens.* 3, 2440–2460. doi: 10.3390/rs3112440

Hill, T., and Lewicki, P. (2006). *Statistics: Methods and Applications: A Comprehensive Reference for Science, Industry, and Data Mining*. Tulsa, OK: StatSoft, Inc.

Ho, T. K. (1998). The random subspace method for constructing decision forests. *IEEE Trans. Pattern Anal. Mach. Intell.* 20, 832–844. doi: 10.1109/34.709601

Hong, H., Xu, C., Revhaug, I., and Bui, D. T. (2015). "Spatial prediction of landslide hazard at the Yihuang area (China): a comparative study on the predictive ability of backpropagation multi-layer perceptron neural networks and radial basic function neural networks," in *Cartography-Maps Connecting the World*, eds C. R. Sluter, C. M. Cruz, and P. L. de Menezes (Cham: Springer), 175–188. doi: 10.1007/978-3-319-17738-0_13

Hossain, M. S., Bujang, J. S., Zakaria, M. H., and Hashim, M. (2015). Application of Landsat images to seagrass areal cover change analysis for Lawas, Terengganu and Kelantan of Malaysia. *Cont. Shelf Res.* 110, 124–148. doi: 10.1016/j.csr.2015.10.009

Howari, F. M., Jordan, B. R., Bouhouche, N., and Wyllie-Echeverria, S. (2009). Field and remote-sensing assessment of mangrove forests and seagrass beds in the northwestern part of the United Arab Emirates. *J. Coast. Res.* 25, 48–56. doi: 10.2112/07-0867.1

Huang, X., Zhang, L., and Wang, L. (2009). Evaluation of morphological texture features for mangrove forest mapping and species discrimination using multispectral IKONOS imagery. *IEEE Geosci. Rem. Sens. Lett.* 6, 393–397. doi: 10.1109/lgrs.2009.2014398

Huete, A., Didan, K., van Leeuwen, W., Miura, T., and Glenn, E. (2010). "MODIS vegetation indices," in *Land Remote Sensing and Global Environmental Change*, eds B. Ramachandran, M. J. Abrams, and C. O. Justice (New York, NY: Springer), 579–602.

Inoue, T., Nohara, S., Matsumoto, K., and Anzai, Y. (2011). What happens to soil chemical properties after mangrove plants colonize? *Plant Soil* 346, 259. doi: 10.1007/s11104-011-0816-9

Irons, J. R., Dwyer, J. L., and Barsi, J. A. (2012). The next Landsat satellite: the landsat data continuity mission. *Rem. Sens. Environ.* 122, 11–21. doi: 10.1016/j.rse.2011.08.026

Ishil, T., and Tateda, Y. (2004). "Leaf area index and biomass estimation for mangrove plantation in Thailand," in *Proceedings of the IGARSS 2004. 2004 IEEE International Geoscience and Remote Sensing Symposium*, Vol. 4, (Anchorage, AK: IEEE), 2323–2326.

Jean-Baptiste, N., and Jensen, J. R. (2006). Measurement of mangrove biophysical characteristics in the Bocozelle ecosystem in Haiti using ASTER multispectral data. *Geocarto Int.* 21, 3–8. doi: 10.1080/10106040608542397

Jensen, J. R. (1996). *Introductory Digital Image Processing: A Remote Sensing Perspective* (No. Ed. 2). Upper Saddle River, NJ: Prentice-Hall Inc.

Kamal, M., and Phinn, S. (2011). Hyperspectral data for mangrove species mapping: a comparison of pixel-based and object-based approach. *Rem. Sens.* 3, 2222–2242. doi: 10.3390/rs3102222

Kamal, M., Phinn, S., and Johansen, K. (2015). Object-based approach for multi-scale mangrove composition mapping using multi-resolution image datasets. *Rem. Sens.* 7, 4753–4783. doi: 10.3390/rs70404753

Kanniah, K. D., Sheikhi, A., Cracknell, A. P., Goh, H. C., Tan, K. P., Ho, C. S., et al. (2015). Satellite images for monitoring mangrove cover changes in a fast growing economic region in southern Peninsular Malaysia. *Rem. Sens.* 7, 14360–14385. doi: 10.3390/rs71114360

Klemas, V. V. (2009). The role of remote sensing in predicting and determining coastal storm impacts. *J. Coast. Res.* 25, 1264–1275. doi: 10.2112/08-1146.1

Kovacs, J. M., King, J. M. L., De Santiago, F. F., and Flores-Verdugo, F. (2009). Evaluating the condition of a mangrove forest of the Mexican Pacific based on an estimated leaf area index mapping approach. *Environ. Monit. Assess.* 157, 137–149. doi: 10.1007/s10661-008-0523-z

Laongmanee, W., Vaiphasa, C., and Laongmanee, P. (2013). Assessment of spatial resolution in estimating leaf area index from satellite images: a case study with avicennia marina plantations in Thailand. *Int. J. Geoinform.* 9, 69–77.

Liang, N. Y., Saratchandran, P., Huang, G. B., and Sundararajan, N. (2006). Classification of mental tasks from EEG signals using extreme learning machine. *Int. J. Neural Syst.* 16, 29–38. doi: 10.1142/s0129065706000482

Liu, Y. L., Shen, Z. J., Simon, M., Li, H., Ma, D. N., Zhu, X. Y., et al. (2020). Comparative proteomic analysis reveals the regulatory effects of H_2S on salt tolerance of mangrove plant Kandelia obovata. *Int. J. Mol. Sci.* 21:118. doi: 10.3390/ijms21010118

Loughland, R. A., Saenger, P., Luker, G., Siddiqui, K., Saji, B., Belt, M., et al. (2007). Changes in the coastal zone of Abu Dhabi determined using satellite imagery (1972–2003). *Aquat. Ecosyst. Health Manag.* 10, 301–308. doi: 10.1080/14634980701512988

Ma, W., Xiong, Y., Wu, Y., Yang, H., Zhang, X., and Jiao, L. (2019). Change detection in remote sensing images based on image mapping and a deep capsule network. *Rem. Sens.* 11:626. doi: 10.3390/rs11060626

Martins, S., Bernardo, N., Ogashawara, I., and Alcantara, E. (2016). Support vector machine algorithm optimal parameterization for change detection mapping in funil hydroelectric reservoir (Rio de Janeiro State, Brazil). *Model. Earth Syst. Environ.* 2:138. doi: 10.1007/s40808-016-0190-y

McGinnis, S., and Kerans, B. L. (2013). Land use and host community characteristics as predictors of disease risk. *Landsc. Ecol.* 28, 29–44. doi: 10.1007/s10980-012-9810-8

Milani, A. S. (2018). "Mangrove Forests of the Persian Gulf and the Gulf of Oman," in *Threats to Mangrove Forests*, eds C. Makowski and C. Finkl (Cham: Springer), 53–75. doi: 10.1007/978-3-319-73016-5_3

Mishra, S., Shrivastava, P., and Dhurvey, P. (2017). Change detection techniques in remote sensing: a review. *Int. J. Wireless Mobile Commun. Ind. Syst.* 4, 1–8.

Mondal, P., Trzaska, S., and De Sherbinin, A. (2018). Landsat-derived estimates of mangrove extents in the Sierra Leone coastal landscape complex during 1990–2016. *Sensors* 18:12. doi: 10.3390/s18010012

Mondal, P., Liu, X., Fatoyinbo, T. E., and Lagomasino, D. (2019). Evaluating combinations of sentinel-2 data and machine-learning algorithms for mangrove mapping in West Africa. *Rem. Sens.* 11:2928. doi: 10.3390/rs11242928

Moore, G. E., Grizzle, R. E., and Ward, K. M. (2013). "Mangrove resources of the United Arab Emirates: mapping and site survey 2011–2013," in *Final Report to the United Arab Emirates Ministry of Environment and Water, University of New Hampshire*, (Durham, NC: Jackson Estuarine Laboratory).

Mountrakis, G., Im, J., and Ogole, C. (2011). Support vector machines in remote sensing: a review. *ISPRS J. Photogram. Rem. Sens.* 66, 247–259. doi: 10.1016/j.isprsjprs.2010.11.001

Naghibi, S. A., and Dashtpagerdi, M. M. (2017). Evaluation of four supervised learning methods for groundwater spring potential mapping in Khalkhal region (Iran) using GIS-based features. *Hydrogeol. J.* 25, 169–189. doi: 10.1007/s10040-016-1466-z

Naghibi, S. A., Pourghasemi, H. R., and Dixon, B. (2016). GIS-based groundwater potential mapping using boosted regression tree, classification and regression tree, and random forest machine learning models in Iran. *Environ. Monit. Assess.* 188:44.

Nascimento, W. R. Jr., Souza-Filho, P. W. M., Proisy, C., Lucas, R. M., and Rosenqvist, A. (2013). Mapping changes in the largest continuous Amazonian mangrove belt using object-based classification of multisensor satellite imagery. *Estuar. Coast. Shelf Sci.* 117, 83–93. doi: 10.1016/j.ecss.2012.10.005

Nguyen, H. H., McAlpine, C., Pullar, D., Johansen, K., and Duke, N. C. (2013). The relationship of spatial–temporal changes in fringe mangrove extent and adjacent land-use: case study of Kien Giang coast, Vietnam. *Ocean Coast. Manag.* 76, 12–22. doi: 10.1016/j.ocecoaman.2013.01.003

Noori, R., Tian, F., Berndtsson, R., Abbasi, M. R., Naseh, M. V., Modabberi, A., et al. (2019). Recent and future trends in sea surface temperature across the Persian Gulf and Gulf of Oman. *PLoS One* 14:e0212790. doi: 10.1371/journal.pone.0212790

Ooi, J. L. S., Kendrick, G. A., and VanNiel, K. P. (2011). Effects of sediment burial on tropical ruderal seagrasses are moderated by clonal integration.Cont. *Shelf Res.* 31, 1945–1954. doi: 10.1016/j.csr.2011.09.005

Otero, V., Van De Kerchove, R., Satyanarayana, B., Mohd-Lokman, H., Lucas, R., and Dahdouh-Guebas, F. (2019). An analysis of the early regeneration of mangrove forests using Landsat time series in the matang mangrove forest reserve, Peninsular Malaysia. *Rem. Sens.* 11:774. doi: 10.3390/rs11070774

Ouerghemmi, W., Gadal, S., Mozgeris, G., and Jonikavicius, D. (2018). "Urban vegetation mapping by airborne hyperspetral imagery; feasibility and limitations," in *Proceedings of the 2018 9th Workshop on Hyperspectral Image and Signal Processing: Evolution in Remote Sensing (WHISPERS)*, (Amsterdam: IEEE), 1–5.

Pal, M. (2005). Random forest classifier for remote sensing classification. *Int. J. Rem. Sens.* 26, 217–222. doi: 10.1080/01431160412331269698

Pereira, L. C. C., da Costa, ÁK. R., da Costa, R. M., Magalhães, A., de Jesus Flores-Montes, M., and Jiménez, J. A. (2018). Influence of a drought event on hydrological characteristics of a small estuary on the Amazon mangrove coast. *Estuar. Coasts* 41, 676–689. doi: 10.1007/s12237-017-0310-6

Pham, T. D., Xia, J., Ha, N. T., Bui, D. T., Le, N. N., and Tekeuchi, W. (2019b). A review of remote sensing approaches for monitoring blue carbon ecosystems: mangroves, seagrassesand salt marshes during 2010–2018. *Sensors* 19:1933. doi: 10.3390/s19081933

Pham, T. D., Yokoya, N., Bui, D. T., Yoshino, K., and Friess, D. A. (2019a). Remote sensing approaches for monitoring mangrove species, structure, and biomass: opportunities and challenges. *Rem. Sens.* 11:230. doi: 10.3390/rs11030230

Pham, T. D., and Yoshino, K. (2015). "Mangrove mapping and change detection using multi-temporal Landsat imagery in Hai Phong city, Vietnam," in *Proceedings of the International Symposium on Cartography in Internet and Ubiquitous Environments*, (Tokyo: The University of Tokyo), 17–19.

Prasad, P. V. V., Boote, K. J., Allen, L. H. Jr., and Sheehy, J. E. (2006). Species, ecotype and cultivar differences in spikelet fertility and harvest index of rice in response to high temperature stress. *Field Crops Res.* 95, 398–411. doi: 10.1016/j.fcr.2005.04.008

Raschka, S. (2018). Model evaluation, model selection, and algorithm selection in machine learning. *arXiv* [Preprint], 2.

Raschka, S., and Mirjalili, V. (2019). *Python Machine Learning: Machine Learning and Deep Learning with Python, scikit-learn, and TensorFlow 2*. Birmingham: Packt Publishing Ltd.

Rodríguez-Romero, J., del Carmen López-González, L., Galván-Magaña, F., Sánchez-Gutiérrez, F. J., Inohuye-Rivera, R. B., and Pérez-Urbiola, J. C. (2011). Seasonal changes in a fish assemblage associated with mangroves in a coastal lagoon of Baja California Sur, Mexico. *Latin Am. J. Aquat. Res.* 39, 250–260. doi: 10.3856/vol39-issue2-fulltext-6

Rodriguez, W., Feller, I. C., and Cavanaugh, K. C. (2016). Spatio-temporal changes of a mangrove–saltmarsh ecotone in the northeastern coast of Florida, USA. *Glob. Ecol. Conserv.* 7, 245–261. doi: 10.1016/j.gecco.2016.07.005

Schapire, R. E. (2003). The boosting approach to machine learning: an overview. *Nonl. Estim. Classif.* 171, 149–171. doi: 10.1007/978-0-387-21579-2_9

Schile, L. M., Kauffman, J. B., Crooks, S., Fourqurean, J. W., Glavan, J., and Megonigal, J. P. (2017). Limits on carbon sequestration in arid blue carbon ecosystems. *Ecol. Appl.* 27, 859–874. doi: 10.1002/eap.1489

Small, C., and Sousa, D. (2019). Spatiotemporal characterization of mangrove phenology and disturbance response: the Bangladesh Sundarban. *Rem. Sens.* 11:2063. doi: 10.3390/rs11172063

Sesnie, S. E., Hagell, S. E., Otterstrom, S. M., Chambers, C. L., and Dickson, B. G. (2008). SRTM-DEM and landsat ETM+ data for mapping tropical dry forest cover and biodiversity assessment in Nicaragua. *Revist. Geogr. Acad.* 2, 53–65.

Sherrod, C. L., and McMillan, C. (1985). The distributional history and ecology of mangrove vegetation along the northern Gulf of Mexico coastal region. *Contrib. Mar. Sci.* 28, 129–140.

Singh, A. (1986). "Change detection in the tropical forest environment of northeastern India using Landsat," in *Remote Sensing and Tropical Land Management*, eds M. J. Eden and J. T. Parry (London: John Wiley & Sons) 44, 273–254.

Snedaker, S. C. (1982). "Mangrove species zonation: why?," in *Contributions to the Ecology of Halophytes*, eds D. N. Sen and K. S. Rajpurohit (Dordrecht: Springer), 111–125. doi: 10.1007/978-94-009-8037-2_8

Spruce, J. P., Bolten, J., Mohammed, I. N., Srinivasan, R., and Lakshmi, V. (2020). Mapping land use land cover change in the lower mekong Basin from 1997 to 2010. *Front. Environ. Sci.* 8:21. doi: 10.3389/fenvs.2020.00021

Strobl, C., Boulesteix, A. L., Kneib, T., Augustin, T., and Zeileis, A. (2008). Conditional variable importance for random forests. *BMC Bioinform.* 9:307. doi: 10.1186/1471-2105-9-307

Su, G. S., Song, Y. C., and Yan, L. B. (2009). Application of Gaussian process machine learning to slope stability evaluation. *Rock Soil Mech.* 30, 675–687.

Taalab, K., Cheng, T., and Zhang, Y. (2018). Mapping landslide susceptibility and types using Random Forest. *Big Earth Data* 2, 159–178. doi: 10.1080/20964471.2018.1472392

Tanaka, K., Hanamura, Y., Chong, V. C., Watanabe, S., Man, A., Kassim, F. M., et al. (2011). Stable isotope analysis reveals ontogenetic migration and the importance of a large mangrove estuary as a feeding ground for juvenile John's snapper Lutjanus johnii. *Fish. Sci.* 77:809. doi: 10.1007/s12562-011-0396-x

Thomas, N., Bunting, P., Lucas, R., Hardy, A., Rosenqvist, A., and Fatoyinbo, T. (2018). Mapping mangrove extent and change: a globally applicable approach. *Rem. Sens.* 10:1466. doi: 10.3390/rs10091466

Todd, U., and Chris, C. (2010). *Radiometric use of WorldView-2 Imagery Technical note 1 WorldView-2 Instrument description*. Available online at: https://dg-cms-uploads-production.s3.amazonaws.com/uploads/document/file/104/Radiometric_Use_of_WorldView-2_Imagery.pdf

Torres, M., and Qiu, G. (2014). Automatic habitat classification using image analysis and random forest. *Ecol. Inform.* 23, 126–136. doi: 10.1016/j.ecoinf.2013.08.002

Toosi, N. B., Soffianian, A. R., Fakheran, S., Pourmanafi, S., Ginzler, C., and Waser, L. T. (2019). Comparing different classification algorithms for monitoring mangrove cover changes in southern Iran. *Glob. Ecol. Conserv.* 19:e00662. doi: 10.1016/j.gecco.2019.e00662

Wang, J., Zhao, Y., Li, C., Yu, L., Liu, D., and Gong, P. (2015). Mapping global land cover in 2001 and 2010 with spatial-temporal consistency at 250 m resolution. *ISPRS J. Photogram. Rem. Sens.* 103, 38–47. doi: 10.1016/j.isprsjprs.2014.03.007

Upadhyay, V. P., and Mishra, P. K. (2008). Population status of mangrove species in estuarine regions of Orissa coast, India. *Trop. Ecol.* 49, 183.

Van Niel, T. G., McVicar, T. R., and Datt, B. (2005). On the relationship between training sample size and data dimensionality: monte carlo analysis of broadband multi-temporal classification. *Rem. Sens. Environ.* 98, 468–480. doi: 10.1016/j.rse.2005.08.011

Vo, Q. T., Oppelt, N., Leinenkugel, P., and Kuenzer, C. (2013). Remote sensing in mapping mangrove ecosystems—An object-based approach. *Rem. Sens.* 5, 183–201. doi: 10.3390/rs5010183

Vorpahl, P., Elsenbeer, H., Märker, M., and Schröder, B. (2012). How can statistical models help to determine driving factors of landslides? *Ecol. Model.* 239, 27–39. doi: 10.1016/j.ecolmodel.2011.12.007

Vyas, D., Krishnayya, N. S. R., Manjunath, K. R., Ray, S. S., and Panigrahy, S. (2011). Evaluation of classifiers for processing Hyperion (EO-1) data of tropical vegetation. *Int. J. Appl. Earth Obs. Geoinf.* 13, 228–235. doi: 10.1016/j.jag.2010.11.007

Yokoya, N., and Iwasaki, A. (2010). "A maximum noise fraction transform based on a sensor noise model for hyperspectral data," in *Proceedings of the 31st Asian Conference on Remote Sensing (ACRS)*, (Tokyo: The University of Tokyo).

Yu, X., Hyyppä, J., Vastaranta, M., Holopainen, M., and Viitala, R. (2011). Predicting individual tree attributes from airborne laser point clouds based on the random forests technique. *ISPRS J. Photogram. Rem. Sens.* 66, 28–37. doi: 10.1016/j.isprsjprs.2010.08.003

Zhao, C., Gao, Z., Qin, Q., and Ruan, L. (2012). *Mangroviflexus xiamenensis* gen. nov., sp. nov., a member of the family Marinilabiliaceae isolated from mangrove sediment. *Int. J. Syst. Evol. Microbiol.* 62, 1819–1824. doi: 10.1099/ijs.0.036137-0

Conflict of Interest: The authors declare that the research was conducted in the absence of any commercial or financial relationships that could be construed as a potential conflict of interest.

Copyright © 2020 Elmahdy, Ali, Mohamed, Howari, Abouleish and Simonet. This is an open-access article distributed under the terms of the Creative Commons Attribution License (CC BY). The use, distribution or reproduction in other forums is permitted, provided the original author(s) and the copyright owner(s) are credited and that the original publication in this journal is cited, in accordance with accepted academic practice. No use, distribution or reproduction is permitted which does not comply with these terms.

frontiers in Environmental Science

ORIGINAL RESEARCH
published: 02 November 2020
doi: 10.3389/fenvs.2020.581091

Spatio-Temporal Modeling for Forecasting High-Risk Freshwater Cyanobacterial Harmful Algal Blooms in Florida

*Mark H. Myer[1], Erin Urquhart[2], Blake A. Schaeffer[3] and John M. Johnston[4]**

[1] US Environmental Protection Agency, Oak Ridge Institute for Science and Education (ORISE), Athens, GA, United States, [2] US Environmental Protection Agency, Oak Ridge Institute for Science and Education (ORISE), Research Triangle Park, NC, United States, [3] US Environmental Protection Agency, Center for Exposure Measurement and Modeling, Research Triangle Park, NC, United States, [4] US Environmental Protection Agency, Center for Exposure Measurement and Modeling, Athens, GA, United States

Due to the occurrence of more frequent and widespread toxic cyanobacteria events, the ability to predict freshwater cyanobacteria harmful algal blooms (cyanoHAB) is of critical importance for the management of drinking and recreational waters. Lake system specific geographic variation of cyanoHABs has been reported, but regional and state level variation is infrequently examined. A spatio-temporal modeling approach can be applied, via the computationally efficient Integrated Nested Laplace Approximation (INLA), to high-risk cyanoHAB exceedance rates to explore spatio-temporal variations across statewide geographic scales. We explore the potential for using satellite-derived data and environmental determinants to develop a short-term forecasting tool for cyanobacteria presence at varying space-time domains for the state of Florida. Weekly cyanobacteria abundance data were obtained using Sentinel-3 Ocean Land Color Imagery (OLCI), for a period of May 2016–June 2019. Time and space varying covariates include surface water temperature, ambient temperature, precipitation, and lake geomorphology. The hierarchical Bayesian spatio-temporal modeling approach in R-INLA represents a potential forecasting tool useful for water managers and associated public health applications for predicting near future high-risk cyanoHAB occurrence given the spatio-temporal characteristics of these events in the recent past. This method is robust to missing data and unbalanced sampling between waterbodies, both common issues in water quality datasets.

Keywords: harmful algal blooms, cyanobacteria, hierarchical Bayes, integrated nested Laplace approximation, remote sensing, predictive modeling

OPEN ACCESS

Edited by:
Sherry L. Palacios, California State University, Monterey Bay, United States

Reviewed by:
Eriita Jones, University of South Australia, Australia
Ana B. Ruescas, University of Valencia, Spain

***Correspondence:**
John M. Johnston
johnston.johnm@epa.gov

Specialty section:
This article was submitted to Environmental Informatics and Remote Sensing, a section of the journal Frontiers in Environmental Science

Received: *07 July 2020*
Accepted: *30 September 2020*
Published: *02 November 2020*

Citation:
Myer MH, Urquhart E, Schaeffer BA and Johnston JM (2020) Spatio-Temporal Modeling for Forecasting High-Risk Freshwater Cyanobacterial Harmful Algal Blooms in Florida. Front. Environ. Sci. 8:581091. doi: 10.3389/fenvs.2020.581091

INTRODUCTION

Harmful algal blooms are environmental events that occur when algal populations achieve sufficiently high density resulting in possible adverse ecological and public health effects (Smayda, 1997). Harmful cyanobacteria blooms (cyanoHABs) are made up of naturally occurring photosynthetic prokaryotes found in various aquatic systems and can produce toxins (cyanotoxins). Toxic cyanoHABs are common components of Florida's surface waters and have

been identified since the late 1980s (Carmichael, 1992; Chapman and Schelske, 1997; Burns, 2008) in Florida's freshwater and brackish environments, including those used for recreation, source waters used for drinking water supply, and finished drinking waters (Williams et al., 2001, 2007; Florida Fish Wildlife Conservation Commission, 2017). Florida freshwater cyanoHABs have consisted primarily of the genera *Microcystis*, *Anabaena,* and *Cylindrospermopsis* and their associated toxins: microcystins, anatoxin-a, and cylindrospermopsin, respectively (Burns et al., 2002; Phlips et al., 2002). Upon numerous sampling occasions, microcystin levels in Florida's recreational waters have exceeded the existing World Health Organization (WHO) (Chorus and Bartram, 1999; World Health Organization, 2003) and EPA (US EPA, 2019) guidelines for cyanobacterial toxins, underscoring the potential impact of cyanoHABs on public health (Williams et al., 2007).

Several of Florida's largest aquatic systems including Lake Okeechobee (Havens et al., 1998; Havens and Steinman, 2015); the Harris Chain of Lakes (Williams et al., 2001, 2007); and the St. Johns, St. Lucie and Caloosahatchee (Glibert et al., 2006; Boyer and FitzPatrick, 2016; United States Army Corps of Engineers, 2016) rivers have experienced the increasing adverse impacts of cyanoHABs. In 2005, the St. Johns County Department of Health released Florida's first official health alert for a toxigenic harmful algal bloom. In response, the St. Johns River Water Management District began routine daily sampling and issued weekly releases informing the public of high microcystin concentrations and risk (Williams et al., 2007). In July 2016, concentrations (4.5 mg L^{-1}) of microcystin were detected in the river-dominated Caloosahatchee and St. Lucie estuaries following very heavy rainstorms in Florida (Oehrle et al., 2017). Strong storms resulted in reservoir operators increasing the outflow from Lake Okeechobee causing the incursion of a toxic *M. aeruginosa* bloom into the St. Lucie Estuary (Boyer and FitzPatrick, 2016; United States Army Corps of Engineers, 2016).

Identification and quantification of the environmental factors that contribute to the proliferation of cyanoHABs in freshwater systems continues to be a topic of scientific research. It is generally understood that dense concentrations of cyanoHABs result from a combination of excess total anthropogenic nutrient loads, particularly phosphorus (Michalak et al., 2013). Other factors that can be important drivers of cyanoHAB abundance are positive associations with lake depth, water column stability, and water temperature (Paerl and Huisman, 2008; Taranu et al., 2012; Beaulieu et al., 2013) and a negative association with wind speed (Millie et al., 2014). Landscape alterations such as urbanization or agricultural practice can change sediment loading and further alter nutrient availability in watersheds (Lunetta et al., 2015).

Modeling efforts to identify and predict harmful algal blooms have used several approaches, including classical multivariate analysis with LOWESS smoothing (Downing et al., 2001), continuous artificial neural networks (Millie et al., 2014), linear, non-linear, and mixed-effect models (Beaulieu et al., 2014), and Bayesian modeling (Obenour et al., 2014).

These data-driven modeling efforts do not address spatial and temporal correlation in bloom occurrence. Failure to account for spatial and temporal autocorrelation violates the assumption of independent and identically distributed data and may lead to biased model estimates. Further, incorporating Bayesian inference into predictive models allows inclusion of prior knowledge, either through literature review and expert opinion or by using mathematical techniques to generate informative priors. We therefore aim to improve upon cyanoHAB models by addressing spatio-temporal correlations using Bayesian hierarchical models, leading to estimates of explanatory variable effects that are more reliable for scientific inference.

The integrated nested Laplace approximations (INLA) method (Rue et al., 2009) offers a simple way to compute complicated hierarchical models that include spatial and temporal structure. Large computational times remain a major drawback of modeling spatial correlation. However, a recent solution has been developed using stochastic partial differential equations (SPDE) to provide a faster and computationally cheaper solution to these modeling problems (Lindgren et al., 2011). R-INLA is a modeling framework developed and implemented for the statistical software R (R Core Team, 2015) that allows complex Bayesian spatial modeling with far fewer computational resources than previous approaches (Rue et al., 2017). One benefit of R-INLA is that it is applicable at any spatial and/or temporal scale. The SPDE approach allows the user to model spatial correlation and constructs flexible fields that are better able to handle complex spatial structures than alternative spatial correlation models such as kriging (Cameletti et al., 2013), making this approach appropriate for inland waterbody modeling because we see both regional clustering of blooms and vast areas of water and land with no cyanobacteria observations. See **Supplemental Material 2**, Statistical Appendix for definitions and discussion of these statistical terms.

In this study, we apply Bayesian spatio-temporal models using R-INLA for the purposes of mapping and predicting exceedance probabilities of World Health Organization (WHO) high-risk for recreational exposure blooms (>100,000 cells/mL) in lakes across Florida. Mapping state level cyanoHAB exceedance probabilities identifies areas where estimates are higher or lower than the state average and provides insight through visualization of patterns in both space and time in addition to inferences drawn from the effects of predictor variables.

METHODS

Study Area

This study was conducted for 103 lakes in the state of Florida, United States. Lakes and waterbodies within three Water Management Districts: St. Johns River, Southwest Florida, and South Florida, were included in the analysis (**Figure 1**). Lake water pixels were extracted using the USGS/EPA Hydrography Dataset Plus (NHDPlus) version 2 (http://www.horizon-systems.com/nhdplus/NHDplusV2_home.php). All NHDPlus features classified as lakes and reservoirs were selected using U.S. Environmental Protection Agency's 2012 National Lakes Assessment (NLA) site evaluation guidelines. Lakes in the NHDPlus shapefile with a minimum of three 300 m water pixels remaining after a land adjacency QA flag was applied were considered resolvable waterbodies. The number of pixels

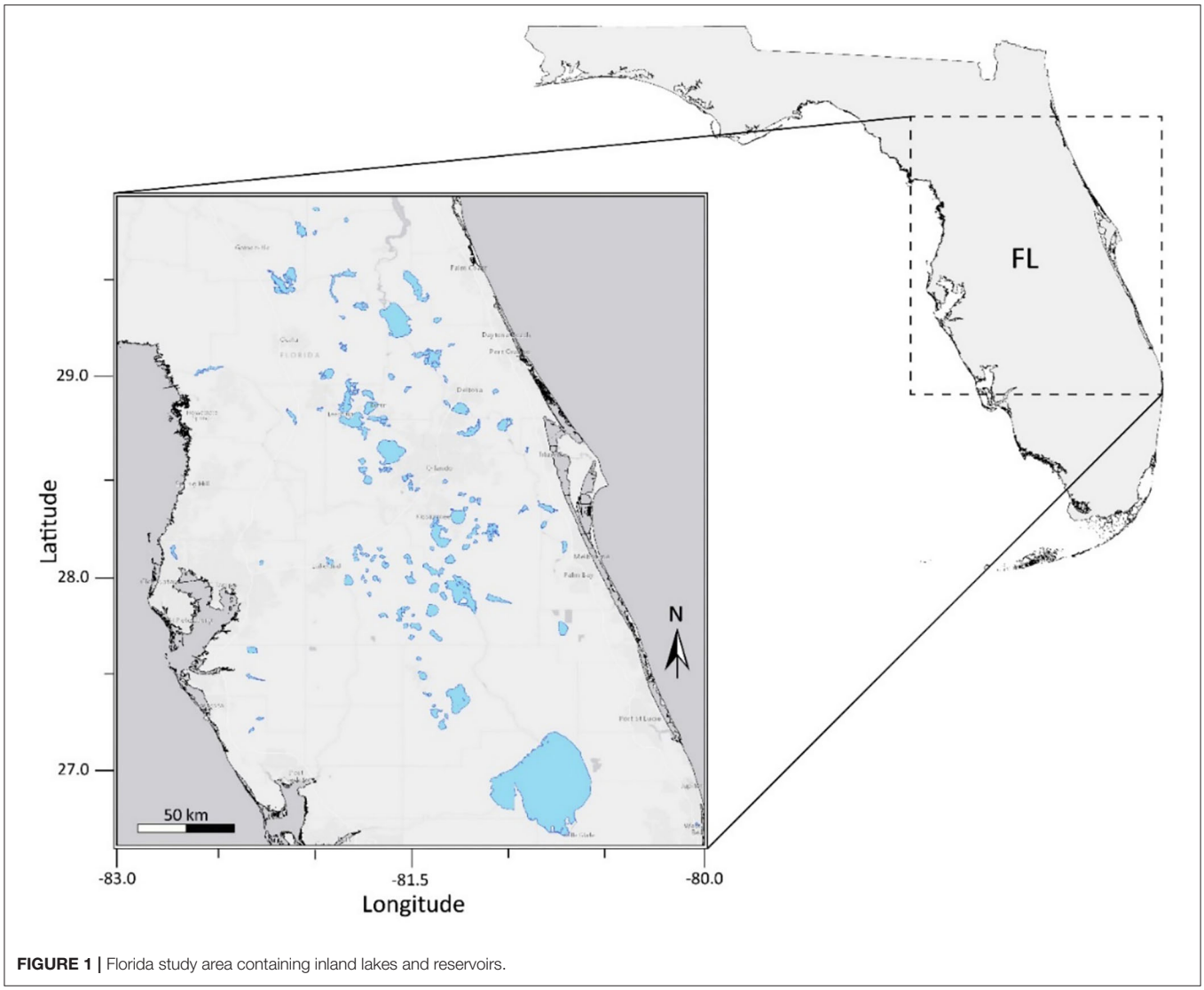

FIGURE 1 | Florida study area containing inland lakes and reservoirs.

included in each water body ranged from 3 to 14,499. The mean and median number of pixels in each water body were 228 and 23, respectively. The number of pixels in each water body considered in the analysis are provided in **Supplemental Material 2**. Waterbodies classified as intermittent, estuarine, rivers, streams, or waterbodies with a surface area <27 hectares are considered "unresolvable water" and thus QA flagged based on NLA criteria. Waterbodies with missing data were excluded from statistical analysis. The OLCI satellite scene extent for our study area is located within the NLA Coastal Plain (CPL) ecoregion. According to findings from the 2012 NLA report, 23% of lakes within the CPL ecoregion pose a high risk to exposure of cyanobacteria and cyanotoxins (US EPA, 2009).

Satellite-Derived Cyanobacteria Data Acquisition and Preparation

Satellite-derived cyanobacteria abundance data was obtained from Sentinel-3 imagery from May 2016 through May 2019 (n = 217 weeks). Standard OLCI Level-1B data were obtained from the NASA Ocean Biology Processing Group (https://oceandata.sci.gsfc.nasa.gov). Sentinel-3 OLCI Florida granules were in the time window of 15:20–16:00 with a frame along track coordinate of 2,520. The cyanobacteria index (CI) was calculated using a spectral shape curvature method, as originally described in Wynne et al. (2008), updated in Lunetta et al. (2015), and algorithm progression fully detailed in Coffer et al. (2020). The CI-Multi value is then converted to cyanobacteria abundance (cells/mL) as described in Wynne et al. (2010). This algorithm was previously validated across Florida watersheds (Lunetta et al., 2015; Tomlinson et al., 2016). Composite images of the maximum cyanobacteria abundance at each resolvable satellite pixel were obtained from the individual scenes within sequential 7-day (1 week) periods. Weekly maximum cyanobacteria abundance was used to minimize the effect of clouds or wind that might otherwise reduce detection of the bloom. Many cyanoHAB genera such as *Microcystis*, *Aphanizomenon*, and *Dolichospermum* have buoyancy control and will typically float to the surface in the day in the absence

of strong winds (Visser et al., 2015). Wind can mix the blooms into the water column, diluting the surface concentration seen by the satellite (Wynne et al., 2010). Mishra et al. (2005) found satellite measures in the red region, similar to the CI-multi, typically only penetrate to a depth of 2 m or less. The OLCI sensor was selected because of public availability of data, spectral range to support deriving cyanobacteria concentrations, and 2–3 day repeat cycle (Urquhart and Schaeffer, 2020). For each water body, the satellite-derived cyanobacterial counts were averaged spatially each week to obtain one summary observation. This 1-week averaging and spatial aggregation was necessary due to cloud cover and satellite repeat cycles, though it results in a loss of information relative to using all available cyanobacterial abundance measurements without averaging and may cause short-term blooms to be missed.

Covariates

We limited covariates that were relevant to cyanobacterial growth and were readily available at the state and U.S. national scale on a weekly basis for operational forecasting. Land use and nutrients are not readily available on a weekly time frame for the continental US. In addition, nutrient transport and availability is complex and system specific, with data lacking for most systems. Wind speed and direction were not included as it was not available for the entire OLCI time period during our analysis.

We retrieved and processed raster and GIS datasets into a set of covariates for the state of Florida at 300 m × 300 m resolution. These data were identified in our review of the cyanobacterial modeling literature as environmental determinants likely to be associated with cyanobacteria bloom occurrence including ambient temperature, surface water temperature, precipitation, and static geomorphic lake conditions (**Table 1**). All data were obtained from public sources. We scaled all covariates to the same resolution as our satellite imagery in order to exclude measures along the land and water interface, because we masked our lake imagery with a 300 m buffer to exclude mixed pixel contamination. Landsat surface water temperature (WTEMP) was upscaled from 30 to 300 m, while PRISM precipitation (PRECIP) and ambient air temperature (ATEMP) were downscaled from 4 km to 300 m. Upscaling is a process that transfers information from local scale to large scale. Downscaling, conversely, transfers from large scale to local scale. Processes that are heterogenous at small scales become homogenous at larger scales. All covariate data were temporally binned into weekly means by taking the arithmetic mean of 7 days within the numerical week (1 through 53) that bound each observation. Due to cloud cover and non-uniform scene acquisition, the monthly climatology of the Landsat Analysis Ready Data (ARD) surface water temperature product (Cook et al., 2014; Schaeffer et al., 2018) was used when the corresponding weekly data were not available. Spatial geographic coordinates were represented in kilometers using the Albers equal-area conic projection. Parameter-elevation Regressions on Independent Slopes Model (PRISM) mean, maximum, and minimum air temperatures and precipitation for North America was downloaded from the Oregon State PRISM Climate Group (PRISM Climate Group, 2004) through June 2019. Landsat ARD surface temperature was downloaded through USGS Earth Explorer through May 2019 in horizontal tiles 25, 26, and 27 and vertical tiles 16, 17, and 18.

All variables were averaged over all resolvable pixels within each water body each week, resulting in one summary observation per week for each water body. To aid in interpretation of relative variable influences on the response, predictor variables were centered and scaled by subtracting the mean and dividing by the standard deviation, transforming them into *Z*-scores. On this scale, a value of zero represents the mean, the units are standard deviations from the mean, and the value of the variable's coefficient in the model represents the effect in log-odds of a one standard deviation increase.

To identify the set of predictor variables most appropriate for modeling inland cyanobacterial bloom presence in Florida, we used non-spatial generalized linear models (**Supplementary Formula 4**), implemented in the R *glmulti* package (Calcagno and de Mazancourt, 2010), confirming the choice using stepwise-selection implemented in the R *stepAIC* package (Ripley, 2002). In this way, we constructed all possible non-redundant models with every combination of covariates. The best model was determined using Akaike's information criterion (AIC, **Supplementary Formula 6**), which is an estimator of out-of-sample prediction error and is used for model comparison (Akaike, 1998). See **Supplementary Material** for a discussion of the use of AIC. This step eliminated two variables, Maximum Lake Depth and Estimated Lake Volume. The best model, with the resulting fixed effect variables, was then used in the Bayesian spatio-temporal model.

TABLE 1 | Summary information for environmental datasets used for covariate selection.

Source	Variable name	Abbreviation	Units	Resolution
PRISM (Daly et al., 1997)	Air temperature	ATEMP	Degrees celsius (°C)	4 km; daily
	Precipitation	PRECIP	Millimeters rainfall (mm)	13.8 km; hourly
Landsat Analysis Ready Data (ARD) (Cook et al., 2014)	Surface water temperature	WTEMP	Degrees celsius (°C)	30 m; 16 and 8-day
lakeMorpho R-package (Hollister and Stachelek, 2017)	Surface area	Area	Square meters (m^2)	Static
	Mean lake depth	dMean	Meters (m)	Static

Hierarchical Bayesian Model Specification and Accuracy

We employed a hierarchical Bayesian spatio-temporal model to estimate exceedance probability over the WHO high-risk threshold with respect to environmental predictors. The response variable was the presence or absence of a high-risk cyanobacteria bloom, defined as a waterbody-wide average cell count above 100,000 cells/mL. Bayesian parameter estimates and prediction in the form of marginal posterior probability distributions were obtained via the R-INLA approach. For this study, weakly informative penalized-complexity priors were generated for all regression coefficients (fixed-effect parameters) and hyperparameters, allowing our large number of observations ($n = 11{,}096$) to inform the posterior distributions (Simpson et al., 2017). For the temporal component, we used a first order temporal autoregressive process (AR1, **Supplementary Formula 5**), which models the effect of time on bloom probability in each location as a function of the concentration in the previous week at that location plus an error term (Potzelberger, 1990). Spatial covariance was addressed using the INLA SPDE approach (Lindgren et al., 2011). The spatial effect represents residual error that can be attributed to location and may reflect the influence of an unmeasured or unmeasurable predictor that varies in space. We used a binomial logistic spatiotemporal model to predict harmful algal blooms (Formula 1).

$$logit\left(y_{st}\right) = \beta_1 X_1 + \ldots + \beta_n X_n + u_s + \mu_t$$

Formula 1. Generalized model structure for a binomial logistic model with spatial and temporal components.

y_{st} is the odds in favor of harmful bloom exceedance at location s and week t, β_1, ..., β_n are the n regression coefficients, X_1, ..., X_n are the n fixed independent variables, u_s is the value of the spatial random effect at location s, and μ_t is the value of the AR1 temporal random effect at time t. The *logit* is the logarithm of the odds in favor of an event and is also referred to as *log odds*. The β_n coefficients are in the logit or log-odds scale, which can be converted to probabilities as shown in Formula (2).

$$P\left(event\right) = \frac{e^{log-odds}}{1 + e^{log-odds}}$$

Formula 2. Converting log-odds to probability.

The odds were converted to probabilities of harmful algal bloom exceedance for model evaluation and predictive performance evaluation. A comprehensive mathematical overview of INLA SPDE can be found elsewhere (Rue et al., 2009; Lindgren and Rue, 2015). More detailed technical explanations of INLA SPDE applied to ecological and epidemiological modeling are available (Cosandey-Godin et al., 2014; Khana et al., 2018; Myer and Johnston, 2018). See **Supplementary Material** for a general discussion and explanation of the statistical methods used in this study along with definitions and further equations.

The utility of the spatial and temporal effects was assessed by fitting the model with and without random effects. The models were compared using the Deviance Information Criterion (DIC, **Supplementary Formula 7**) to determine if the inclusion of the spatial and temporal effects improved model fit. Model performance was evaluated through holdout cross-validation in which the dataset was divided into three compartments: 80% of the data was randomly selected for training, 20% of the data was held out for validation, and the most recent week of data available at the time of the study was obtained for prediction. The model was created based on the training data only, and then model predictive power was assessed on the validation and prediction datasets. Model predictive power was determined by calculating the Area Under Curve (AUC), and by evaluating the sensitivity (true positive rate, **Supplementary Formula 8**), and specificity (true negative rate, **Supplementary Formula 9**) in predicting the holdout validation and prediction datasets after optimizing the logistic cutoff. Cutoff optimization, which chooses a value for the logistic predictor above which we consider a bloom prediction as positive, was performed by maximizing Youden's index on the validation dataset. Youden's index, sometimes referred to as the J-statistic, is defined in Formula (3).

$$J = sensitivity + specificity - 1$$

Formula 3. Youden's Index, or the J-statistic. Maximizing the value of this statistic provides the maximum overall accuracy for a binomial predictor.

Youden optimization attempts to find the cutoff at which sensitivity and specificity are balanced and at a maximum. All statistical analyses were conducted using R 3.3.4 on a compute cluster with 128 nodes and 4,096 cores.

RESULTS

The likelihood of high-risk cyanoHAB presence was estimated for 103 lakes and waterbodies in Florida. The number of high-risk blooms in individual lakes across Florida ranged from 0 to 146 weeks from 2016 to 2019 (**Figure 2**). During the study period, 22.5% of total bloom weeks were classified as high risk ($n = 3{,}149$ bloom weeks). Average waterbody-wide cyanobacterial concentration in lakes classified as high-risk was 376,504 cells/mL, more than three times the WHO "high" threshold of 100,000 cells/mL.

Model Selection

The model fit of our four candidate models was evaluated using the Deviance Information Criterion (DIC), with lower DIC values indicating better fit (**Table 2**). All four models included the same fixed effect predictors. The first model (M1), a non-hierarchical baseline model that did not incorporate random effects nor correlation features, exhibited a DIC of 14,195 and a ∼7 s computation time. The addition of a temporal effect (M2) improved the DIC value and only slightly increased the computation time. The addition of a spatial component (M3) dramatically improved the DIC value, but approximately quadrupled computation time. The addition of the spatial and temporal autocorrelation structure (M4) further improved the DIC value but increased the computation time to ∼53 s. We concluded that computational time was not an issue of

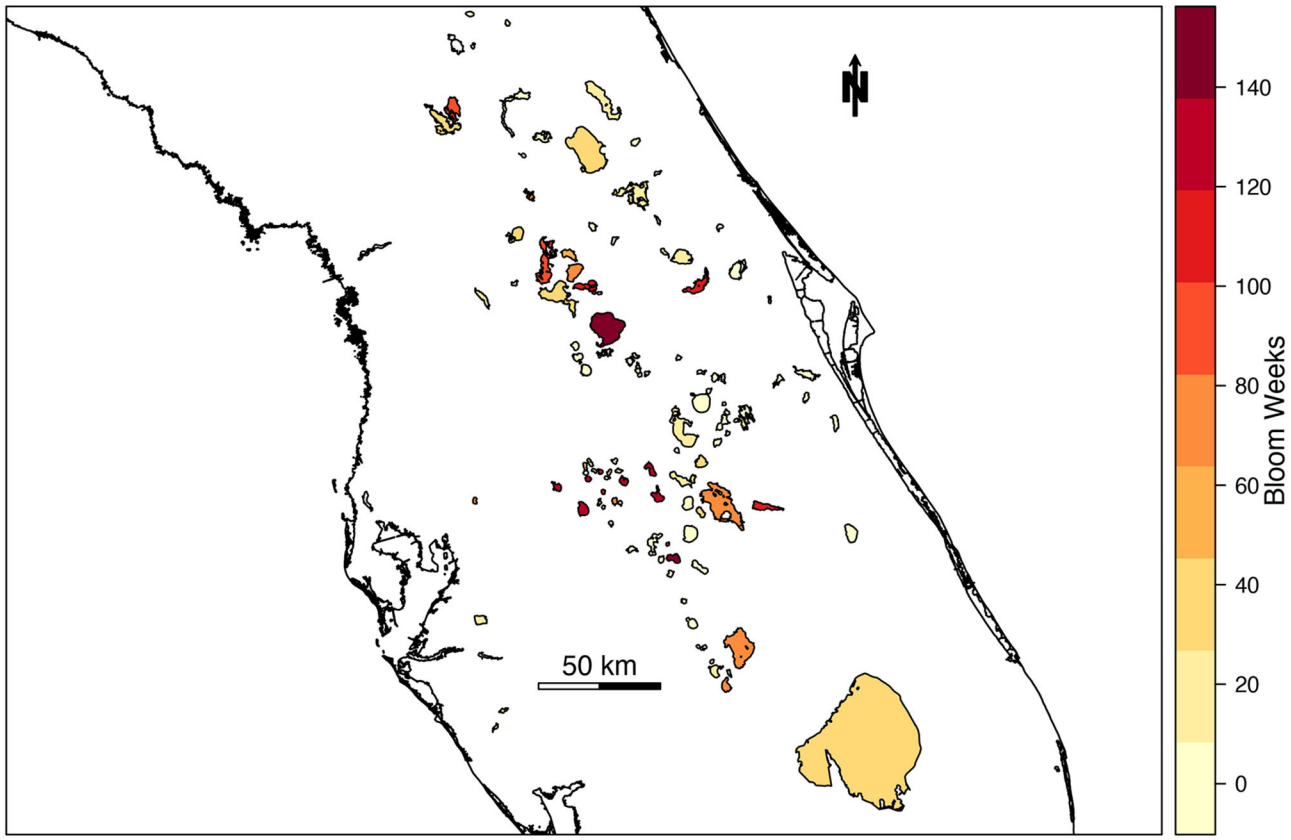

FIGURE 2 | Choropleth map of the number of high-risk bloom weeks in Florida lakes from 2016 to 2019.

TABLE 2 | Models considered with corresponding performance information.

Model	Model description	DIC	Computation time (s)
M1	Non-hierarchical model	21,381	~7
M2	Temporal component only	21,294	~10
M3	Spatial component only	7,758	~45
M4	Spatial + temporal model	7,601	~53

concern with this model, due to the favorable computational characteristics of the INLA SPDE method. Thus, the M4 hierarchical model with a full set of time varying, fixed effect covariates and spatio-temporal correlation effects provided the best model fit and was selected as the best model with subsequent results presented as follows.

Fixed Effect Covariates

The mean posterior coefficients of the fixed effect covariates are presented in log-odds and signify the estimated response to a one standard deviation change in the predictor variable when all other variables are held constant. For the purposes of determining statistical importance, we utilized an alpha level of 0.05 and considered a variable with a 95% credible interval that did not encompass zero to have an important effect on the response. Using stepwise-selection and the resulting AIC values, ambient air temperature, surface water temperature, precipitation, lake area, and mean lake depth were selected as fixed effect predictors in the bloom estimation models (**Supplementary Table 1**). Fixed effect coefficients and 95% Bayesian credible intervals for the covariates included in the full spatio-temporal model (M4) are provided in **Table 3**. Posterior distributions of these fixed effect variables are presented as log-odds of the scaled covariate variables. As expected, a significant positive association is observed between surface water temperature (WTEMP) and high-risk bloom presence in Florida. For a one standard deviation increase in surface water temperature (6.23°C), the expected change in high-risk bloom log odds is 0.17 (or 1.18 times greater odds). Further, mean lake depth (DMEAN) exhibited a significant positive association with high-risk bloom presence, with an increase in one standard deviation (0.75 m) leading to an expected increase in log odds of 2.70 (or 14.88 times greater odds). Ambient air temperature (ATEMP) had a significant and negative effect on the likelihood of high-risk bloom presence in Florida, with a one standard deviation increase in ambient air temperature (4.79°C) resulting in change in high-risk bloom log odds of −0.23 (or 0.79 times lower odds).

TABLE 3 | Posterior estimates (mean, St. Dev., quantiles) for fixed effects.

Variable	Mean posterior	St. Dev.	0.025	0.5	0.975
ATEMP	−0.23	0.07	−0.37	−0.23	−0.08
WTEMP	0.17	0.05	0.08	0.17	0.26
PRECIP	−0.01	0.04	−0.09	−0.01	0.07
AREA	−0.11	0.66	−1.40	−0.11	1.19
DMEAN	2.70	0.52	1.68	2.70	3.72

TABLE 4 | Posterior estimates (mean, St. Dev., quantiles) for random effects.

Parameter (random effect)	Posterior mean	St. Dev.	0.025	0.5	0.975
Temporal variance	0.19	0.09	0.05	0.15	0.62
Spatial variance	38.51	7.85	25.63	37.61	56.35
Spatial correlation range ρ	16.76	3.44	10.72	16.54	24.14
AR (1) parameter α	0.90	0.09	0.68	0.92	0.99

Random Effects and Hyperparameters

The temporal model component (**Figure 3**) shows how the temporal effect on the odds of a high-risk bloom event vary throughout the year. This effect represents residual error that can be attributed to time and can be interpreted as the influence in the model of an unmeasured or unmeasurable predictor that varies in time. The log odds of high-risk bloom presence were higher from spring (week 15, approximately April 6) to late summer (week 35, approximately August 17) all other variables held constant. The posterior mean of the AR (1) parameter indicated an autocorrelation effect of 0.90 (95% CI = 0.68:0.99), which indicates that the temporal effect depends strongly on previous values and does not change quickly throughout the year (**Table 4**).

The spatial random effect (**Figure 4**) indicates that there is a significant amount of spatial variation in the mean concentration of cyanoHABs in lakes across Florida. The spatial random effect represents residual error that can be attributed to location and may reflect the influence of an unmeasured or unmeasurable predictor that varies in space. The posterior estimates (mean, standard deviation, 95% CI) for the random hyperparameters are collected in **Table 4**. The variance of the spatial effect showed a wide posterior distribution (95% CI = 25:56), indicating that the variability in bloom odds attributable to location is high. The posterior mean of the spatial correlation range (the distance at which spatial correlation declines to ∼0.1) was 16.8 km with a standard deviation of 3.4 km. This range indicates the approximate distance between lakes within which the odds of an algal bloom can be considered correlated.

Model Performance

In order to test the performance of the final spatio-temporal model (M4), we used holdout data to determine if M4 correctly estimates the observed data in space and time. Twenty percent (20%) of the data were randomly set aside as a holdout validation dataset (n = 2,775 observations). Instead of using an arbitrary cutoff threshold to assign the predicted high-risk bloom value as positive or negative, we calculated a Youden-optimized cutoff point of 0.365. Traditional logistic model evaluation statistics including Area Under Curve (AUC), sensitivity (true positive rate), and specificity (true negative rate) provide insight into the model performance for both holdout dataset scenarios (**Table 5**). An AUC > 0.5 indicates that the model predicts better than chance alone. The resulting AUC between observations and predictions of the holdout validation dataset was 0.95, sensitivity was 0.88, specificity was 0.88, and accuracy was 0.88.

TABLE 5 | Results of the statistical evaluation metrics obtained using a cutoff point of 0.365.

Metric	Validation dataset	Prediction dataset
AUC	0.95	0.89
Sensitivity	0.88	0.82
Specificity	0.88	0.82
Accuracy	0.88	0.82

Prediction

For practical application reasons, we were also interested in assessing the model's capability to predict or forecast future bloom presence for a week in which the model was untrained. Predictive power of M4 was tested by reserving response and fixed effect data for the most recent week of available data at the time of analysis (May 27th through June 2nd, 2019) as a holdout prediction dataset (n = 103 observations). The resulting AUC between observations and predictions of the holdout prediction dataset is 0.89, sensitivity is 0.82, and specificity is 0.82 (**Table 5**). Our prediction objective was to get a probability of high-risk bloom exceedance, for a given week, using a threshold of 100,000 cyanobacteria cells/mL. As expected, higher exceedance probabilities are detected in lakes with >100 bloom weeks such as Lake Apopka located in central Florida (**Figure 5**).

DISCUSSION

Here we present a hierarchical Bayesian spatio-temporal modeling approach in R-INLA to estimate the likelihood of high-risk cyanoHABs in Florida inland waterbodies. Using DIC to evaluate model performance, the full spatio-temporal model (M4, **Table 2**) was selected as the best model and used to forecast the likelihood of bloom occurrence across Florida lakes for a week outside of the dataset, with AUC 0.93 (**Table 5**). The spatial random effect (**Figure 4**) identified residual error attributed to location that may reflect the influence of an unmeasured or unmeasurable predictor that varies across the landscape. The variance of the spatial effect also indicated the variability in cyanoHAB bloom odds for each lake is high. The distance at which spatial correlation declines below a meaningful threshold (0.1) indicates ∼17 km as the inter-lake distance within which the odds of cyanoHAB can be considered correlated. Because our model did not include any measures of nutrient input or

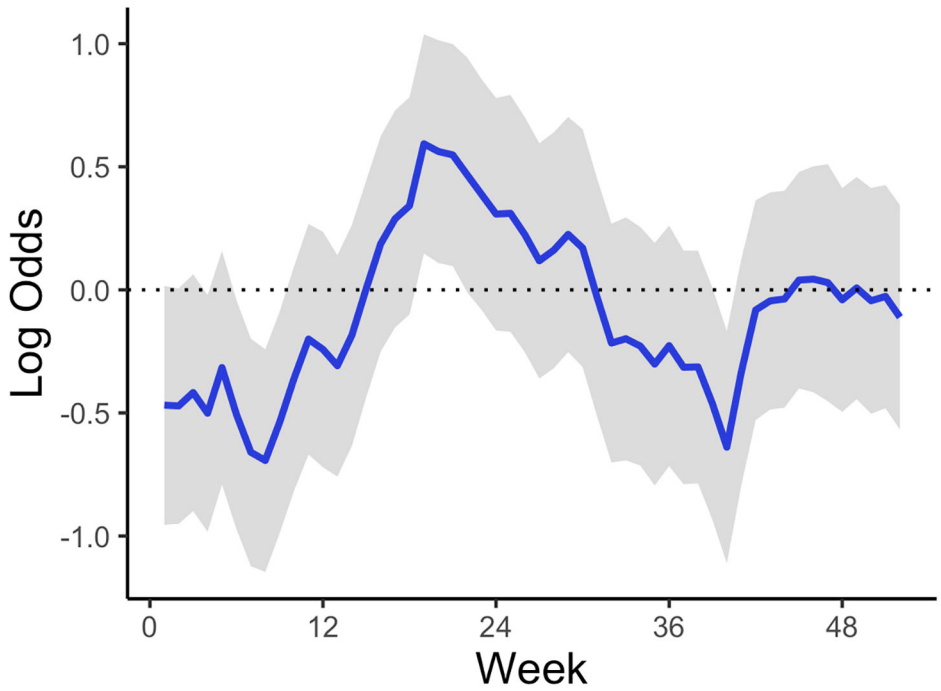

FIGURE 3 | Mean AR (1) temporal trend corresponding to week of year across all study years and lakes. The shaded area represents the 95% credible interval.

land use, we believe that it is likely the spatial component of the model is related to land cover and its resultant effect on eutrophication. This landscape effect varies at long spatial scales and is known to have a significant effect on the likelihood of cyanoHABs (Doubek et al., 2015; Marion et al., 2017). Another related possibility is that the spatial correlation represents the distance between watersheds experiencing similar environmental stressors such as nutrient input, making the lakes fed by those watersheds more similar in terms of cyanoHAB risk.

Water surface temperature had a positive effect on cyanoHAB risk, an association that has been observed in many studies to date (Paerl and Huisman, 2008; Wynne et al., 2010; Kosten et al., 2012; Taranu et al., 2012; Beaulieu et al., 2013; Cha et al., 2017). Several mechanisms operate concurrently to the advantage of cyanobacteria at higher water temperatures. The optimal temperature for cyanobacterial growth and photosynthesis is above 20°C, with some species experiencing optimal growth at 30°C or higher (Konopka and Brock, 1978; Lürling et al., 2013; Giannuzzi et al., 2016; Melina Celeste et al., 2017). At high temperatures cyanobacteria have a competitive advantage over green algae, diatoms, and other phytoplankton which favors cyanobacteria dominance. However, some common species of cyanoHAB in the genus *Microcystis* have been found to produce fewer toxins at high temperatures which may mitigate health risks (Runnegar et al., 1983; Rapala et al., 1997; Melina Celeste et al., 2017), although these findings are disputed (Lehman et al., 2008; Davis et al., 2009). Bloom-forming cyanobacteria contain many cylindrical gas vacuoles that impart buoyancy (Walsby, 1977). This buoyancy causes the cells to float to the surface where they are exposed to more light and can outcompete sinking phytoplankton, and there is evidence that increased water temperature improves the ability of cyanobacteria to stay afloat (Kromkamp et al., 1988; Huisman et al., 2004).

Contrary to our expectations, mean lake depth (DMEAN) was a strongly positive correlate of cyanoHAB bloom odds. Our prior belief was that a shallower lake would have a diminished capacity to buffer changes in nutrient input, leading to a heightened risk for HAB blooms. However, in our data this does not seem to be the case. The lakes in our dataset, and Florida lakes in general, are shallow. The average lake in our study had a mean lake depth of only 0.75 m, and the deepest lake had a mean depth of 3.68 m. To contextualize the large positive coefficient of the lake depth effect, we note that an increase in mean depth of 0.75 m, the unit of increase in our model, represents a doubling in depth for the average lake. Satellite penetration in the red spectrum is 2 m or less in oligotrophic waters (Mishra et al., 2005). Given the focus of our model on cyanoHABs at the >100,000 cells/ml threshold, the penetration depth is likely only a few centimeters. It is possible that optically shallow water could cause bottom reflectance or benthic cyanobacteria could cause artifacts. However, Coffer et al. (2020) found the satellite derived phenology of cyanobacteria in Florida followed well-accepted ecological trends and a few lakes that had a peak of biomass in the winter were supported by independent field observations.

Classic models of lake eutrophication posit a strong effect of mixing between the epilimnion and hypolimnion (O'Melia, 1972; Imboden, 1974). Deep lakes are considered to have a greater inertia with respect to changing nutrient conditions;

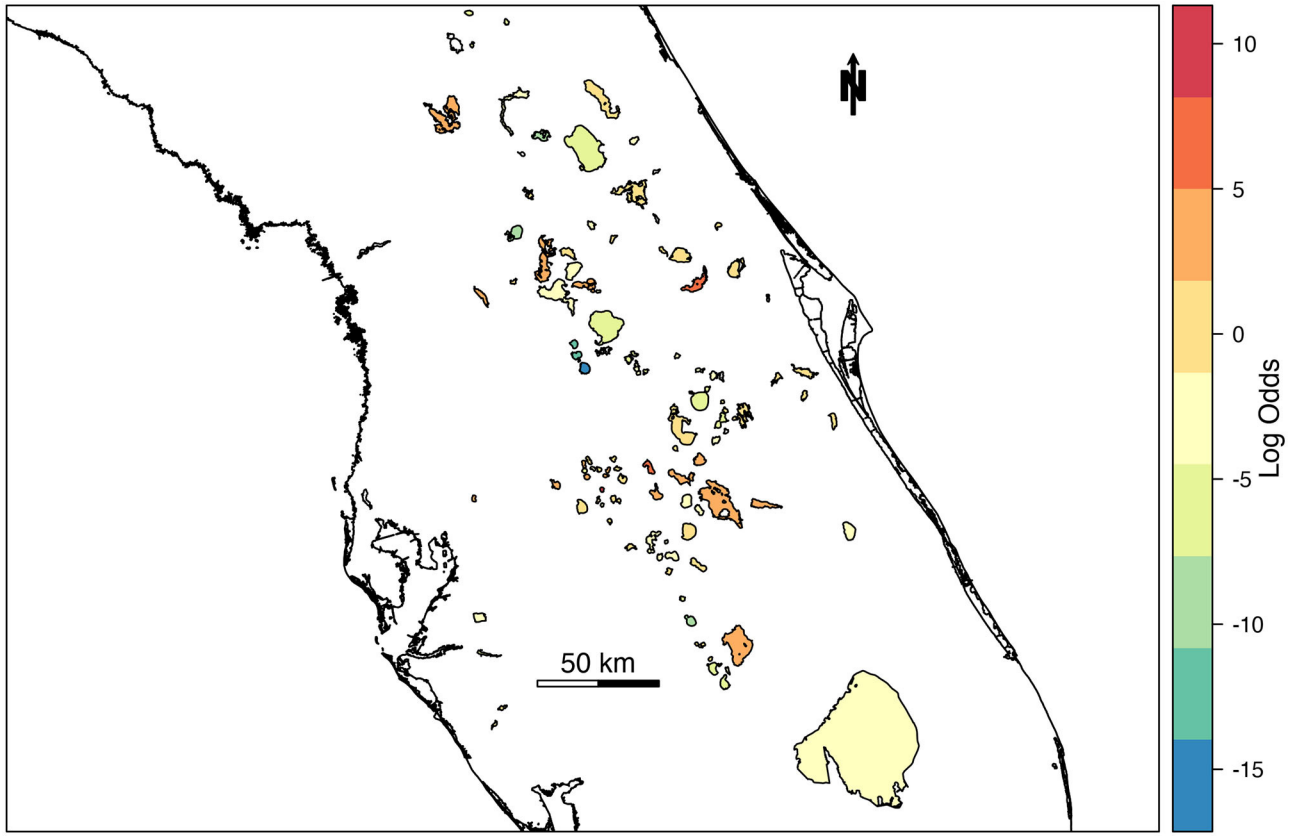

FIGURE 4 | Mean of spatial random effect mapped across lakes in Florida. Lakes with relatively higher log-odds of a high-risk cyanobacteria bloom are indicated with warm colors, while cool colors represent lakes with relatively lower log-odds of high-risk blooms.

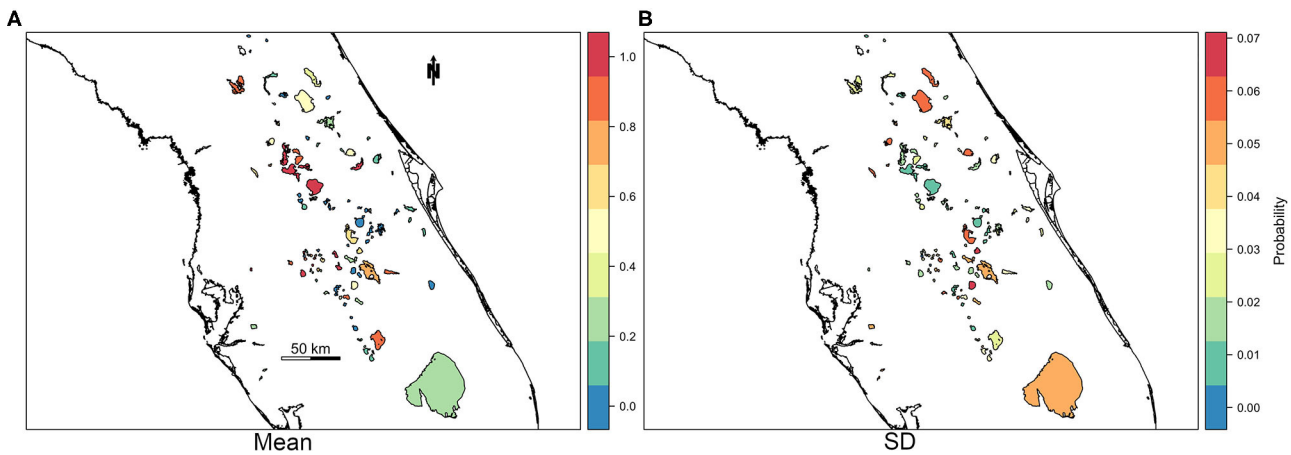

FIGURE 5 | Map of mean **(A)** and standard deviation **(B)** of probability of exceedance of high-risk bloom event for the week of May 27, 2019 through June 2, 2019.

Imboden called this effect a "memory" and found that deep lakes take longer to change from oligotrophy to eutrophy and vice-versa. Shallow lakes do not form the distinctive temperature-delineated layers of a stratified lake and are polymictic: experiencing constant mixing by wind and temperature that leaves the water at a generally homogenous state. This mixing leads to resuspension of nutrients from sediment a higher nutrient load in the water column (Taranu and Gregory-Eaves, 2008; Liu et al., 2012). The lakes in our study are not deep enough to stratify and should be considered polymictic.

Because all of our lakes are shallow, nutrients cannot sequester within the hypolimnion and sediment and the association between depth and oligotrophy found in stratified lakes does not apply.

In a study of cyanobacteria growth in shallow lakes (<6 m), Kosten et al. found similar results to our study, with water temperature predicting a higher proportion of cyanobacteria among the phytoplankton community (Kosten et al., 2012). A study of the National Lake Assessment dataset, containing 1,147 lakes and spanning the continental U.S., found that when lakes were divided into shallow (<6 m) or deep, their models were less able to predict cyanobacterial concentrations in the shallow lakes (Beaulieu et al., 2013). Associations of HAB volume with nitrogen content and water temperature were consistent across all lakes, but there was a decrease of two-thirds in variation explained when lakes were shallow. A national-scale study in the United Kingdom that investigated both shallow and deep lakes suggested that water residence time, a correlate of depth, was a positive predictor of HAB biovolume, especially in lakes with significant opacity (Carvalho et al., 2011). An in-depth study of a shallow (mean depth 1.2 m), warm, polymictic lake in the Mediterranean that was substantially similar to the lakes in our study found that water residence time was a strong predictor of harmful algae concentration (Romo et al., 2013). We propose that in our study, mean lake depth is acting as a correlate of water residence time, explaining its positive association with HAB blooms.

Air temperature had a negative effect on cyanoHAB risk, a result that seems counterintuitive when considered alongside the positive effect of water surface temperature. Our model suggests that cyanoHAB risk is heightened when air temperature is lower relative to surface water temperature, a condition that can occur in shallow lakes during the transition from summer to fall, or when lake temperature is artificially increased by impervious surface runoff or industrial input (Sabouri et al., 2013). In our dataset, the peak mean water temperature was significantly higher than the peak mean air temperature observed (36.5 and 30.3°C, respectively). The higher specific heat of water is responsible for this effect, with lakes serving as a heat sink that can persist after air temperature has cooled.

The predictive accuracy of our model on a holdout dataset was high, with ∼82% of held-out observations for the week of May 27, 2019 predicted correctly. Accuracy was also good in our validation dataset, with 88% of observations correctly classified. The accuracy of our simple model is encouraging but has a few caveats. This model is not expected to remain accurate for more than 2 weeks into the future, because wide spatial coverage meteorological estimates become less reliable beyond that time scale. Additionally, the autocorrelation parameter, or α, was 0.9, indicating that the change in the temporal component of risk of a cyanoHAB is strongly related to the past week's bloom conditions. While this temporal component was not as significant a contribution to model fit as the spatial component that considered lake location (**Table 2**), we caution that interpretation of our model's accuracy should consider that due to system inertia, a fairly accurate prediction of near-future bloom conditions can be made by simply extrapolating that current conditions will continue unchanged.

Although we have developed a reliable model for forecasting cyanoHAB odds for lakes in central Florida lakes for a week of interest outside of the modeled dataset, there are several limitations of this study. While remote sensing provides a continuous cyanoHAB data source, the relatively coarse 300 m sensor resolution, presence of cloud cover, and occasional missing data due to waterbody misclassification, limits our predictive ability in smaller inland waterbodies. Additional satellite limitations are reviewed in Coffer et al. (2020) and Clark et al. (2017). Future work could assess the applicability of higher resolution sensors such as the European Commission's Copernicus Sentinel-2. Our covariates were not all available at the same spatial scale and had to be resampled to the same 300 m resolution as our lake imagery. As a result, lake areas with highly irregular or elongated narrow reaches may be underrepresented vs. lake areas with broader widths. It is possible that CyanoHAB was present in a specific part of the lake, but satellite data didn't capture it because of land proximity. This study incorporated several environmental covariates known to be associated with cyanoHAB occurrence; however, our results showed a strong spatially varying effect, the cause of which is undetermined in the present analysis. Future studies could explore additional environmental determinants such as nutrient loadings. Nutrients certainly play a role related to cyanoHABs and nutrient eutrophication is a "wicked" problem as defined by Thornton et al. (2013), meaning that the issue is convoluted and precludes a simple solution. However, modeling nutrient transport and availability is complex and system specific, with model validation data lacking for most systems. This complexity, specificity and lack of data limits the ability to scale such models across spatial and temporal scales as described in Soranno et al. (2015). Therefore, we limited the model to data that would be readily available and most relevant to cyanoHAB biomass.

In the present study we applied R-INLA for the purpose of mapping/predicting exceedance probability of high-risk cyanoHABs at the level of a whole lake. Future work will apply the spatial-temporal modeling approach at the sub-lake level, particularly in large systems with greater geographic bloom variability such as Lake Okeechobee in South Florida.

DATA AVAILABILITY STATEMENT

The datasets presented in this study can be found in online repositories. The names of the repository/repositories and accession number(s) can be found at: US EPA Environmental Dataset Gateway, https://edg.epa.gov/metadata/catalog/main/home.page. DOI: 10.23719/1518919.

AUTHOR CONTRIBUTIONS

EU and BS developed the project, gathered data, and conducted the initial round of analysis including determining algae levels from remote sensing data. MM and JJ provided editing and technical advice during the initial analysis round. MM conducted

the final analysis. All authors contributed equally to the writing of the final manuscript.

FUNDING

This work was supported by the NASA Ocean Biology and Biogeochemistry Program/Applied Sciences Program (proposal 14-SMDUNSOL14- 0001) and by U.S. EPA, NOAA, U.S. Geological Survey Toxic Substances Hydrology Program, and Oak Ridge Institute for Science and Technology (ORISE).

ACKNOWLEDGMENTS

This article has been reviewed by the US Environmental Protection Agency and approved for publication. Mention of trade names or commercial products does not constitute endorsement or recommendation for use by the U.S. Government. The views expressed in this article are those of the authors and do not necessarily reflect the views or policies of the U.S. EPA. The authors would like to thank internal and journal peer reviewers for many useful comments on the manuscript. Data and R code used in this study are available at the US EPA Science Hub at: https://www.catalog.data.gov/dataset/epa-sciencehub.

SUPPLEMENTARY MATERIAL

The Supplementary Material for this article can be found online at: https://www.frontiersin.org/articles/10.3389/fenvs.2020.581091/full#supplementary-material

REFERENCES

Akaike, H. (1998). "A Bayesian analysis of the minimum AIC procedure," in *Selected Papers of Hirotugu Akaike*, eds E. Parzen, K. Tanabe, and G. Kitagawa (New York, NY: Springer), 275–280.

Beaulieu, M., Pick, F., and Gregory-Eaves, I. (2013). Nutrients and water temperature are significant predictors of cyanobacterial biomass in a 1147 lakes data set. *Limnol. Oceanogr.* 58, 1736–1746. doi: 10.4319/lo.2013.58.5.1736

Beaulieu, M., Pick, F., Palmer, M., Watson, S., Winter, J., Zurawell, R., et al. (2014). Comparing predictive cyanobacterial models from temperate regions. *Can. J. Fisher. Aquat. Sci.* 71, 1830–1839. doi: 10.1139/cjfas-2014-0168

Boyer, G., and FitzPatrick, K. (2016). *Water Quality Final Report*. Available online at: https://www.martin.fl.us/martin-county-services/water-quality-reports (accessed June 14, 2016).

Burns, J. (2008). "Toxic cyanobacteria in Florida waters," in *Cyanobacterial Harmful Algal Blooms: State of the Science and Research Needs*, ed H. K. Hudnell (New York, NY: Springer), 127–137.

Burns, J., Williams, C. D., and Chapman, A. D. (2002). Cyanobacteria and their toxins in Florida surface waters. *Paper presented at the Health Effects of Exposure to Cyanobacteria Toxins: State of the Science* (Sarasota, FL).

Calcagno, V., and de Mazancourt, C. (2010). glmulti: an R package for easy automated model selection with (generalized) linear models. *J. Stat. Softw.* 34, 1–29. doi: 10.18637/jss.v034.i12

Cameletti, M., Lindgren, F., Simpson, D., and Rue, H. (2013). Spatio-temporal modeling of particulate matter concentration through the SPDE approach. *AStA Adv. Stat. Anal.* 97, 109–131. doi: 10.1007/s10182-012-0196-3

Carmichael, W. (1992). *A Status Report of Planktonic Cyanobacteria (Blue-Green Algae) and Their Toxins*. Cincinnati, OH: United States Environmental Protection Agency.

Carvalho, L., Miller, C. A., Scott, E. M., Codd, G. A., Davies, P. S., and Tyler, A. N. (2011). Cyanobacterial blooms: statistical models describing risk factors for national-scale lake assessment and lake management. *Sci. Total Environ.* 409, 5353–5358. doi: 10.1016/j.scitotenv.2011.09.030

Cha, Y., Cho, K. H., Lee, H., Kang, T., and Kim, J. H. (2017). The relative importance of water temperature and residence time in predicting cyanobacteria abundance in regulated rivers. *Water Res.* 124, 11–19. doi: 10.1016/j.watres.2017.07.040

Chapman, A. D., and Schelske, C. L. (1997). Recent appearance of cylindrospemopsis (cyanobacteuia) in five hypereutropic florida lakes. *J. Phycol.* 33, 191–195. doi: 10.1111/j.0022-3646.1997.00191.x

Chorus, E. I., and Bartram, J. (1999). *Toxic Cyanobacteria in Water: A Guide to Their Public Health Consequences, Monitoring and Management*. Geneva: World Health Organization.

Clark, J. M., Schaeffer, B. A., Darling, J. A., Urquhart, E. A., Johnston, J. M., Ignatius, A. R., et al. (2017). Satellite monitoring of cyanobacterial harmful algal bloom frequency in recreational waters and drinking water sources. *Ecol. Indic.* 80, 84–95. doi: 10.1016/j.ecolind.2017.04.046

Coffer, M. M., Schaeffer, B. A., Darling, J. A., Urquhart, E. A., and Salls, W. B. (2020). Quantifying national and regional cyanobacterial occurrence in US lakes using satellite remote sensing. *Ecol. Indic.* 111:105976. doi: 10.1016/j.ecolind.2019.105976

Cook, M., Schott, J., Mandel, J., and Raqueno, N. (2014). Development of an operational calibration methodology for the Landsat thermal data archive and initial testing of the atmospheric compensation component of a Land Surface Temperature (LST) product from the archive. *Remote Sens.* 6, 11244–11266. doi: 10.3390/rs61111244

Cosandey-Godin, A., Krainski, E. T., Worm, B., and Flemming, J. M. (2014). Applying Bayesian spatiotemporal models to fisheries bycatch in the Canadian Arctic. *Can. J. Fisher. Aquat. Sci.* 72, 186–197. doi: 10.1139/cjfas-2014-0159

Daly, C., Taylor, G., and Gibson, W. (1997). "The PRISM approach to mapping precipitation and temperature," in *Proc 10th AMS Conf. on Applied Climatology*. Reno, NV: American Meteorological Society.

Davis, T. W., Berry, D. L., Boyer, G. L., and Gobler, C. J. (2009). The effects of temperature and nutrients on the growth and dynamics of toxic and non-toxic strains of microcystis during cyanobacteria blooms. *Harmful Algae* 8, 715–725. doi: 10.1016/j.hal.2009.02.004

Doubek, J. P., Carey, C. C., and Cardinale, B. J. (2015). Anthropogenic land use is associated with N-fixing cyanobacterial dominance in lakes across the continental United States. *Aquat. Sci.* 77, 681–694. doi: 10.1007/s00027-015-0411-x

Downing, J. A., Watson, S. B., and McCauley, E. (2001). Predicting cyanobacteria dominance in lakes. *Can. J. Fisher. Aquat. Sci.* 58, 1905–1908. doi: 10.1139/f01-143

Florida Fish and Wildlife Conservation Commission (2017). *Cyanobacteria in Florida Waters*. Available online at: http://myfwc.com/research/redtide/general/cyanobacteria/

Giannuzzi, L., Krock, B., Minaglia, M. C. C., Rosso, L., Houghton, C., Sedan, D., et al. (2016). Growth, toxin production, active oxygen species and catalase activity of *Microcystis aeruginosa* (*Cyanophyceae*) exposed to temperature stress. *Comp. Biochem. Physiol. Part C Toxicol. Pharmacol.* 189, 22–30. doi: 10.1016/j.cbpc.2016.07.001

Glibert, P. M., Harrison, J., Heil, C., and Seitzinger, S. (2006). Escalating worldwide use of urea – a global change contributing to coastal eutrophication. *Biogeochemistry* 77, 441–463. doi: 10.1007/s10533-005-3070-5

Havens, K. E., Phlips, E. J., Cichra, M. F., and Li, B.-l. (1998). Light availability as a possible regulator of cyanobacteria species composition in a shallow subtropical lake. *Freshw. Biol.* 39, 547–556. doi: 10.1046/j.1365-2427.1998.00308.x

Havens, K. E., and Steinman, A. D. (2015). Ecological responses of a large shallow lake (Okeechobee, Florida) to climate change and potential future hydrologic regimes. *Environ. Manage.* 55, 763–775. doi: 10.1007/s00267-013-0189-3

Hollister, J., and Stachelek, J. (2017). lakemorpho: Calculating lake morphometry metrics in R. *F1000Res.* 6:1718. doi: 10.12688/f1000research.12512.1

Huisman, J., Sharples, J., Stroom, J. M., Visser, P. M., Kardinaal, W. E. A., Verspagen, J. M. H., et al. (2004). Changes in turbulent mixing shift competition for light between phytoplankton species. *Ecology* 85, 2960–2970. doi: 10.1890/03-0763

Imboden, D. M. (1974). Phosphorus model of lake eutrophication. *Limnol. Oceanogr.* 19, 297–304. doi: 10.4319/lo.1974.19.2.0297

Khana, D., Rossen, L. M., Hedegaard, H., and Warner, M. (2018). A Bayesian spatial and temporal modeling approach to mapping geographic variation in mortality rates for subnational areas with R-INLA. *J. Data Sci.* 16, 147–182. doi: 10.6339/JDS.201801_16(1).0009

Konopka, A., and Brock, T. D. (1978). Effect of temperature on blue-green algae (cyanobacteria) in lake mendota. *Appl. Environ. Microbiol.* 36, 572–576. doi: 10.1128/AEM.36.4.572-576.1978

Kosten, S., Huszar, V. L. M., Bécares, E., Costa, L. S., van Donk, E., Hansson, L.-A., et al. (2012). Warmer climates boost cyanobacterial dominance in shallow lakes. *Glob. Chang. Biol.* 18, 118–126. doi: 10.1111/j.1365-2486.2011.02488.x

Kromkamp, J., Botterweg, J., and Mur, L. R. (1988). Buoyancy regulation in *Microcystis aeruginosa* grown at different temperatures. *FEMS Microbiol. Ecol.* 4, 231–237. doi: 10.1111/j.1574-6968.1988.tb02669.x

Lehman, P., Boyer, G., Satchwell, M., and Waller, S. (2008). The influence of environmental conditions on coffseasonal variation of microcystis abundance and microcystins concentration in San Francisco Estuary. *Hydrobiologia* 600, 187–204. doi: 10.1007/s10750-007-9231-x

Lindgren, F., and Rue, H. (2015). Bayesian spatial modelling with R-INLA. *J. Stat. Softw.* 63, 1–25. doi: 10.18637/jss.v063.i19

Lindgren, F., Rue, H., and Lindstrom, J. (2011). An explicit link between Gaussian fields and Gaussian Markov random fields: the stochastic partial differential equation approach. *J. R. Statist. Soc B.* 73, 763–775. doi: 10.1111/j.1467-9868.2011.00777.x

Liu, W., Li, S., Bu, H., Zhang, Q., and Liu, G. (2012). Eutrophication in the Yunnan Plateau lakes: the influence of lake morphology, watershed land use, and socioeconomic factors. *Environ. Sci. Pollut. Res.* 19, 858–870. doi: 10.1007/s11356-011-0616-z

Lunetta, R. S., Schaeffer, B. A., Stumpf, R. P., Keith, D., Jacobs, S. A., and Murphy, M. S. (2015). Evaluation of cyanobacteria cell count detection derived from MERIS imagery across the eastern USA. *Remote Sens. Environ.* 157, 24–34. doi: 10.1016/j.rse.2014.06.008

Lürling, M., Eshetu, F., Faasen, E. J., Kosten, S., and Huszar, V. L. M. (2013). Comparison of cyanobacterial and green algal growth rates at different temperatures. *Freshw. Biol.* 58, 552–559. doi: 10.1111/j.1365-2427.2012.02866.x

Marion, J. W., Zhang, F., Cutting, D., and Lee, J. (2017). Associations between county-level land cover classes and cyanobacteria blooms in the United States. *Ecol. Eng.* 108, 556–563. doi: 10.1016/j.ecoleng.2017.07.032

Melina Celeste, C. M., Lorena, R., Jorge Oswaldo, A., Sandro, G., Daniela, S., Dario, A., et al. (2017). Mathematical modeling of *Microcystis aeruginosa* growth and [D-Leu1] microcystin-LR production in culture media at different temperatures. *Harmful Algae* 67, 13–25. doi: 10.1016/j.hal.2017.05.006

Michalak, A. M., Anderson, E. J., Beletsky, D., Boland, S., Bosch, N. S., Bridgeman, T. B., et al. (2013). Record-setting algal bloom in Lake Erie caused by agricultural and meteorological trends consistent with expected future conditions. *Proc. Natl. Acad. Sci. U.S.A.* 110, 6448–6452. doi: 10.1073/pnas.1216006110

Millie, D. F., Weckman, G. R., Fahnenstiel, G. L., Carrick, H. J., Ardjmand, E., Young, W. A., et al. (2014). Using artificial intelligence for CyanoHAB niche modeling: discovery and visualization of Microcystis–environmental associations within western Lake Erie. *Can. J. Fisher. Aquat. Sci.* 71, 1642–1654. doi: 10.1139/cjfas-2013-0654

Mishra, D. R., Narumalani, S., Rundquist, D., and Lawson, M. (2005). Characterizing the vertical diffuse attenuation coefficient for downwelling irradiance in coastal waters: implications for water penetration by high resolution satellite data. *ISPRS J. Photogramm. Remote Sens.* 60, 48–64. doi: 10.1016/j.isprsjprs.2005.09.003

Myer, M. H., and Johnston, J. M. (2018). Spatiotemporal Bayesian modeling of West Nile virus: identifying risk of infection in mosquitoes with local-scale predictors. *Sci. Total Environ.* 650, 2818–2829. doi: 10.1016/j.scitotenv.2018.09.397

Obenour, D. R., Gronewold, A. D., Stow, C. A., and Scavia, D. (2014). Using a Bayesian hierarchical model to improve Lake Erie cyanobacteria bloom forecasts. *Water Resour. Res.* 50, 7847–7860. doi: 10.1002/2014WR015616

Oehrle, S., Rodriguez-Matos, M., Cartamil, M., Zavala, C., and Rein, K. S. (2017). Toxin composition of the 2016 *Microcystis aeruginosa* bloom in the St. Lucie Estuary, Florida. *Toxicon* 138, 169–172. doi: 10.1016/j.toxicon.2017.09.005

O'Melia, C. R. (1972). An approach to the modeling of lakes. *Schweizerische Zeitschrift Hydrol.* 34, 1–33. doi: 10.1007/BF02502798

Paerl, H. W., and Huisman, J. (2008). Blooms like it hot. *Science* 320, 57–58. doi: 10.1126/science.1155398

Phlips, E. J., Bledsoe, E., Cichra, M. F., Badylak, S., and Frost, J. (2002). The distribution of potentially toxic cyanobacteria in Florida. *Paper presented at the Health Effects of Exposure to Cyanobacteria Toxins: State of the Science* (Sarasota, FL).

Potzelberger, K. (1990). A characterization of random-coefficient AR(1) models. *Scotchastic Process. Appl.* 34, 171–180. doi: 10.1016/0304-4149(90)90062-W

PRISM Climate Group (2004). Oregon State University. Available online at: http://prism.oregonstate.edu (accessed Febuary 4, 2004).

R Core Team (2015). *R: A Language and Environment for Statistical Computing.* Vienna. Available online at: https://www.R-project.org

Rapala, J., Sivonen, K., Lyra, C., and Niemela, S. I. (1997). Variation of microcystins, cyanobacterial hepatotoxins, in *Anabaena* spp. as a function of growth stimuli. *Appl. Environ. Microbiol.* 63, 2206–2212. doi: 10.1128/AEM.63.6.2206-2212.1997

Ripley, B. (2002). *Modern Applied Statistics With S.* New York, NY: Springer.

Romo, S., Soria, J., Fernandez, F., Ouahid, Y., and Baron-Sola, Á. (2013). Water residence time and the dynamics of toxic cyanobacteria. *Freshw. Biol.* 58, 513–522. doi: 10.1111/j.1365-2427.2012.02734.x

Rue, H., Martino, S., and Chopin, N. (2009). Approximate Bayesian inference for latent Gaussian models by using integrated nested Laplace approximations. *J. R. Stat. Soc. Ser. B* 71, 319–392. doi: 10.1111/j.1467-9868.2008.00700.x

Rue, H., Riebler, A., Sørbye, S. H., Illian, J. B., Simpson, D. P., and Lindgren, F. K. (2017). Bayesian computing with INLA: a review. *Annu. Rev. Stat. Appl.* 4, 395–421. doi: 10.1146/annurev-statistics-060116-054045

Runnegar, M. T. C., Falconer, I. R., Jackson, A. R. B., and McInnes, A. (1983). Toxin production by *Microcystis aeruginosa* cultures. *Toxicon* 21, 377–380. doi: 10.1016/0041-0101(83)90233-7

Sabouri, F., Gharabaghi, B., Mahboubi, A. A., and McBean, E. A. (2013). Impervious surfaces and sewer pipe effects on stormwater runoff temperature. *J. Hydrol.* 502, 10–17. doi: 10.1016/j.jhydrol.2013.08.016

Schaeffer, B. A., Iiames, J., Dwyer, J., Urquhart, E., Salls, W., Rover, J., et al. (2018). An initial validation of Landsat 5 and 7 derived surface water temperature for U.S. lakes, reservoirs, and estuaries. *Int. J. Remote Sens.* 39, 7789–7805. doi: 10.1080/01431161.2018.1471545

Simpson, D., Rue, H., Riebler, A., Martins, T. G., and Sørbye, S. H. (2017). Penalising model component complexity: a principled, practical approach to constructing priors. *Stat. Sci.* 32, 1–28. doi: 10.1214/16-STS576

Smayda, T. J. (1997). What is a bloom? A commentary. *Limnol. Oceanogr.* 42, 1132–1136. doi: 10.4319/lo.1997.42.5_part_2.1132

Soranno, P. A., Cheruvelil, K. S., Wagner, T., Webster, K. E., and Bremigan, M. T. (2015). Effects of land use on lake nutrients: the importance of scale, hydrologic connectivity, and region. *PLoS ONE.* 10:e0135454. doi: 10.1371/journal.pone.0135454

Taranu, Z. E., and Gregory-Eaves, I. (2008). Quantifying relationships among phosphorus, agriculture, and lake depth at an inter-regional scale. *Ecosystems* 11, 715–725. doi: 10.1007/s10021-008-9153-0

Taranu, Z. E., Zurawell, R. W., Pick, F., and Gregory-Eaves, I. (2012). Predicting cyanobacterial dynamics in the face of global change: the importance of scale and environmental context. *Glob. Chang. Biol.* 18, 3477–3490. doi: 10.1111/gcb.12015

Thornton, J. A., Harding, W. R., Dent, M., Hart, R. C., Lin, H., Rast, C. L., et al. (2013). Eutrophication as a 'wicked' problem. *Lakes Reserv.* 18, 298–316. doi: 10.1111/lre.12044

Tomlinson, M. C., Stumpf, R. P., Wynne, T. T., Dupuy, D., Burks, R., Hendrickson, J., et al. (2016). Relating chlorophyll from cyanobacteria-dominated inland waters to a MERIS bloom index. *Remote Sens. Lett.* 7, 141–149. doi: 10.1080/2150704X.2015.1117155

United States Army Corps of Engineers (2016). *Corps to Reduce Flows From Lake Okeechobee.* Available online at: http://www.saj.usace.army.mil/Media/News-Releases/Article/821885/corps-to-reduce-flows-from-lake-okeechobee/

Urquhart, E. A., and Schaeffer, B. A. (2020). Envisat MERIS and sentinel-3 OLCI satellite lake biophysical water quality flag dataset for the contiguous United States. *Data Brief* 28:104826. doi: 10.1016/j.dib.2019.104826

US EPA (2009). *National Lakes Assessment: A Collaborative Survey of the Nation's Lakes.* Washington, DC.

US EPA (2019). *Draft Technical Support Document: Implementing the 2019 Recommended Human Health Recreational Ambient Water Quality Criteria or Swimming Advisories for Microcystins and Cylindrospermopsin.* US Environmental Protection Agency Office of Water.

Visser, P. M., Ibelings, B. W., Bormans, M., and Huisman, J. (2015). Artificial mixing to control cyanobacterial blooms: a review. *Aquat. Ecol.* 43, 12–19. doi: 10.1007/s10452-015-9537-0

Walsby, A. E. (1977). The gas vacuoles of blue-green algae. *Sci. Am.* 237, 90–97. doi: 10.1038/scientificamerican0877-90

Williams, C. D., Aubel, M. T., Chapman, A. D., and D'Aiuto, P. E. (2007). Identification of cyanobacterial toxins in Florida's freshwater systems. *Lake Reserv. Manag.* 23, 144–152. doi: 10.1080/07438140709353917

Williams, C. D., Burns, J., Chapman, A. D., Flewelling, L., Pawlowicz, M., and Carmichael, W. (2001). *Assessment of Cyanotoxins in Florida's Lakes, Reservoirs, and Rivers. 1999. Final Annual Report to the Florida Harmful Algal Bloom Task Force*. St. Petersburg, FL.

World Health Organization (2003). *Guidelines for Safe Recreational Water Environments: Coastal and Fresh Waters.* Vol. 1. Geneva: World Health Organization.

Wynne, T. T., Stumpf, R. P., Tomlinson, M. C., and Dyble, J. (2010). Characterizing a cyanobacterial bloom in western Lake Erie using satellite imagery and meteorological data. *Limnol. Oceanogr.* 55, 2025–2036. doi: 10.4319/lo.2010.55.5.2025

Wynne, T. T., Stumpf, R. P., Tomlinson, M. C., Warner, R. A., Tester, P. A., Dyble, J., et al. (2008). Relating spectral shape to cyanobacterial blooms in the Laurentian Great Lakes. *Int. J. Remote Sens.* 29, 3665–3672. doi: 10.1080/01431160802007640

Conflict of Interest: The authors declare that the research was conducted in the absence of any commercial or financial relationships that could be construed as a potential conflict of interest.

Copyright © 2020 Myer, Urquhart, Schaeffer and Johnston. This is an open-access article distributed under the terms of the Creative Commons Attribution License (CC BY). The use, distribution or reproduction in other forums is permitted, provided the original author(s) and the copyright owner(s) are credited and that the original publication in this journal is cited, in accordance with accepted academic practice. No use, distribution or reproduction is permitted which does not comply with these terms.

frontiers in Environmental Science

ORIGINAL RESEARCH
published: 12 November 2020
doi: 10.3389/fenvs.2020.579856

Branching Algorithm to Identify Bottom Habitat in the Optically Complex Coastal Waters of Atlantic Canada Using Sentinel-2 Satellite Imagery

Kristen L. Wilson, Melisa C. Wong and Emmanuel Devred*

Bedford Institute of Oceanography, Fisheries and Oceans Canada, Dartmouth, NS, Canada

Sentinel-2 satellite imagery has been successfully used to map submerged seagrasses in clear waters, and surface-canopy forming seaweed habitats in a range of water types. We examined the ability to use Sentinel-2 remote sensing reflectance to classify fully submerged seagrass and seaweed habitats in optically complex, temperate waters within a high priority management region in Atlantic Canada. To do so, we determined the "best" Sentinel-2 image available between 2015 and 2019 based on tidal height, absence of sun glint and clouds, and water transparency. Using the full Sentinel-2 tile, we atmospherically corrected the image using ACOLITE's dark spectrum fitting method. Our classification goal was a two-class prediction of vegetation presence and absence. Using information obtained from drop-camera surveys, the image was first partially classified using simple band thresholds based on the normalized difference vegetation index (NDVI), red/green ratio and the blue band. A random forest model was built to classify the remaining areas to a maximum depth of 10 m, the maximum depth at which field surveys were performed. The resulting habitat map had an overall accuracy of 79% and ~231 km^2 of vegetated habitat were predicted to occur (total area 345.15 km^2). As expected, the classification performed best in regions dominated by bright sandy bare substrate, and dense dark vegetated beds. The classification performed less well in regions dominated by dark bare muddy substrate, whose spectra were similar to vegetated habitat, in pixels where vegetation density was low and mixed with other substrates, and in regions impacted by freshwater input. The maximum depth that bottom habitat was detectable also varied across the image. Leveraging the full capacity of the freely available Sentinel-2 satellite series with its high spatial resolution and resampling frequency, provides a new opportunity to generate large scale vegetation habitat maps, and examine how vegetation extent changes over time in Atlantic Canada, providing essential data layers to inform monitoring and management of macrophyte dominated habitats and the resulting ecosystem functions and services.

Keywords: habitat mapping, machine learning, rockweed, satellite remote sensing, seaweed, submerged aquatic vegetation, kelp, seagrass

OPEN ACCESS

Edited by:
Andrea J. Vander Woude, NOAA-Great Lakes Environmental Research Laboratory, United States

Reviewed by:
Eric Jeremy Hochberg, Bermuda Institute of Ocean Sciences, Bermuda
Tiit Kutser, University of Tartu, Estonia

****Correspondence:***
Kristen L. Wilson
kristen.wilson@dfo-mpo.gc.ca

Specialty section:
This article was submitted to Environmental Informatics and Remote Sensing, a section of the journal Frontiers in Environmental Science

Received: *03 July 2020*
Accepted: *15 October 2020*
Published: *12 November 2020*

Citation:
Wilson KL, Wong MC and Devred E (2020) Branching Algorithm to Identify Bottom Habitat in the Optically Complex Coastal Waters of Atlantic Canada Using Sentinel-2 Satellite Imagery. Front. Environ. Sci. 8:579856. doi: 10.3389/fenvs.2020.579856

INTRODUCTION

Seaweeds and seagrasses (marine macrophytes) are submerged aquatic vegetation found in nearshore coastal environments. In Atlantic Canada, seagrasses (primarily eelgrass, *Zostera marina*, rarely widgeon grass, *Ruppia maritima*) occur within subtidal soft-sedimentary habitats and seaweed canopies (dominated by brown algae in the Fucaceae and Laminariaceae families) occur along rocky habitats. In the rocky intertidal zone, *Ascophyllum nodosum* (rockweed), is the dominant habitat forming species in sheltered areas while *Fucus* spp. dominates along exposed areas, with a transition to kelps (e.g., *Laminaria digitata* and *Saccharina latissima*) in the subtidal whose canopy does not reach the surface. Coastal ecosystems which are dominated by seaweeds and seagrasses are some of the most productive habitats globally and provide several important ecosystem functions and services (Barbier et al., 2011). These include acting as ecosystem engineers to provide biogenic habitat structure, providing coastal protection against erosion, absorbing nutrient runoff, providing carbon storage, supporting biodiversity and fisheries, and generally acting as an indicator of overall ecosystem health (Orth et al., 2006; Schmidt et al., 2011; Duarte et al., 2013; Wong and Dowd, 2016; Teagle et al., 2017; Wong and Kay, 2019). In Atlantic Canada, and globally, seaweed and seagrass habitat, and ecological services, are under threat from stressors such as invasive species, climate change, coastal development, and nutrient loading (Waycott et al., 2009; Filbee-Dexter and Wernberg, 2018; Murphy et al., 2019). Tools for mapping and monitoring marine macrophyte distribution are important to understand and quantify habitat changes, particularly to inform decision making related to conservation areas for seaweed and eelgrass habitat, and resource management for commercially important seaweeds.

Satellite remote sensing has been used to map and monitor marine macrophyte distribution globally in optically shallow waters (Duffy et al., 2019; Kutser et al., 2020). Satellites measure the amount of sunlight reflected off of the seafloor at several wavelengths (including water-column attenuation) in sufficiently transparent waters, which can be classified using several approaches including empirical, image-based classification algorithms (e.g., O'Neill and Costa, 2013; Poursanidis et al., 2019), object-based techniques (e.g., Roelfsema et al., 2014; León-Pérez et al., 2019), or physics-based semi-analytical model inversion (e.g., Lee et al., 1999; McKinna et al., 2015). As the light travels from the sun, to the seafloor, and back to the satellite, it interacts with the atmosphere, which amounts to up to 90% of the top-of-atmosphere signal (Wang, 2010), sea surface, and the water column, necessitating the requirements for atmospheric (Vanhellemont and Ruddick, 2016; Vanhellemont, 2019), sun glint (Hedley et al., 2005; Kutser et al., 2009), and water column corrections (Zoffoli et al., 2014). Empirical, image-based classifications, which require *in situ* data to train an algorithm, are widely used to quantify bottom habitat. Historically the maximum likelihood classifier has been the preferred classification algorithm (Richards, 1986), however, machine learning algorithms such as support vector machines (Vapnick, 1995) and random forests (Breiman, 2001) have been recently demonstrated to perform better than the maximum likelihood classification (Marcello et al., 2018; Ha et al., 2020). Empirical methods are less sensitive to rigorous atmospheric and water-column corrections, but are not readily applicable to other regions (Islam et al., 2020). Object-based classifications operate on similar principles as image-based classifications, with the exception that the image is first segmented into many objects, and the classification is performed at the level of the object, opposed to the pixel (Roelfsema et al., 2014; Su and Huang, 2019). This is a hybrid approach, which can include non-spectral data layers during classification. Physics-based semi-analytical inversion models retrieve simultaneously the inherent optical properties (IOPs) of the water column (i.e., absorption and scattering coefficients), water depth and bottom reflectance (e.g., Lee et al., 1999; McKinna et al., 2015). This approach requires the development of spectral libraries for all optically active components but regional *in situ* data are not required for model training given the globality of the spectral libraries (Kutser et al., 2020). Its application to any water body requires highly accurate atmospheric correction to retrieve seafloor reflectance and identify bottom habitat. Satellite remote sensing of seagrass and coral habitat is widely used in tropical clear waters, where bottom habitat is readily detectable to great depths (<40 m) (Hossain et al., 2015; Kovacs et al., 2018; Wicaksono et al., 2019). Satellite remote sensing is also widely used in a range of water types for certain seaweed habitats, when the vegetation canopy reaches the surface, as the measured signal comes from the sea surface, opposed to the seafloor, and there is negligible interaction of the water-leaving signal with the water column (e.g., Schroeder et al., 2019; Bell et al., 2020; Mora-Soto et al., 2020). A more complicated classification question arises for submerged macrophytes in optically complex temperate waters, where high CDOM, suspended particulate matter, and phytoplankton concentration reduce the maximum depth at which the seafloor is visible compared to tropical habitats (3–10 m vs. <40 m). The use of satellite remote sensing in temperate habitats is becoming more common (e.g., Casal et al., 2011; O'Neill and Costa, 2013; Dierssen et al., 2019), and in the process, new methods are being developed to leverage the many benefits of satellite remote sensing to accurately quantify the distribution of marine macrophytes in areas where water transparency still permits bottom habitat mapping with passive sensors.

In the optically complex, temperate waters of Atlantic Canada there has been considerable interest in using remote sensing to classify marine macrophyte habitat using sonar, lidar, and optical satellites. Intertidal rockweed habitat along the south shore of Nova Scotia has been classified with lidar (Webster et al., 2020) and multispectral satellite sensors including Worldview and Quickbird imagery (Macdonald et al., 2012). Rockweed habitat can be easily identified using vegetation indices given its strong signal in the near-infrared (NIR) compared to its environment. In the subtidal zone, completely submerged kelp habitat has been quantified with Landsat along the Gaspé Peninsula in Quebec (Simms and Dubois, 2001), with SPOT-7 along the Mingan Archipelago also in Québec (St-Pierre and Gagnon, 2020) and with lidar along the south shore of Nova Scotia (Webster, 2018). Eelgrass habitat has been quantified

with lidar (Webster et al., 2016), sonar (Vandermeulen, 2014; Barrell et al., 2015), and a variety of multispectral sensors including Worldview, Quickbird, and SPOT (Milton et al., 2009; Barrell et al., 2015; Wilson et al., 2019) at various sites along the exposed Atlantic coast of Nova Scotia and along the Northumberland Straight. The above listed studies used either an image-based classification generally based on the maximum likelihood classifier (Wilson et al., 2019; St-Pierre and Gagnon, 2020; Webster et al., 2020), or object-based classification (Milton et al., 2009; Barrell et al., 2015) to quantify marine macrophyte habitat at bay-wide scales with commercial satellites.

In this study, we were interested in understanding to what extent detailed marine macrophyte habitat could be classified using the freely available Senintel-2 satellite data series and an image-based classification procedure. Varying from previous work in the region, we aimed to classify marine macrophyte habitat at large spatial scales (hundreds of square kilometers), and with the exception of the Landsat study, with a freely available imaging platform, which allows for repeated surveys over yearly to decadal time-scales without prior tasking. We focused on a high-priority management region characterized by complex bathymetry and a multispecies environment, including fully submerged kelp and eelgrass beds, in an optically complex coastal environment. We explored the impact of various preprocessing steps such as water column corrections, and image-based classification algorithms such as maximum likelihood classification and machine learning classifiers. While our original goal was to differentiate between eelgrass and seaweed (primarily brown) habitat this was found not to be possible and maps were produced denoting vegetation presence and absence. The driver of this work was to develop a method framework for using Sentinel-2 data in a systematic manner to classify the large-scale distribution of marine macrophyte habitat, to be able to provide data layers for marine spatial planning, monitor marine macrophytes habitat extent, and consequently inform management decisions in high-priority regions (e.g., conservation). To support this, the final map classification is presented in both a binary presence-absence map, and probability of vegetated habitat to define a level of certainty in the map. To the best of our knowledge, our study is the first to use Sentinel-2 data to quantify marine macrophyte habitats in Atlantic Canada, which includes completely submerged kelp beds and eelgrass meadows.

MATERIALS AND METHODS

Study Area

The Eastern Shore Islands (ESI) are an archipelago located along the Atlantic coast of Nova Scotia, Canada (**Figure 1**). The ESI archipelago is an important management area with most of the land already protected, and the marine environment under consideration for a marine protected area (DFO, 2019). The high management priority is given due to the relative pristine condition of the terrestrial and marine environments including several healthy eelgrass meadows, and rockweed and kelp beds, all important habitat forming species in the region, providing three-dimensional structure and nursery habitat for many marine species (Schmidt et al., 2011; Vercaemer et al., 2018). The ESI archipelago is characterized by a complex coastline including rocky shores, sandy beaches, and salt marshes, each at a varied degree of exposure to the Atlantic Ocean. The numerous islands result in a complex bathymetry with shallow depths (<10 m) extending kilometers offshore. This results in an optically complex environment for satellite remote sensing where bottom substrate and water transparency are highly variable.

Field Surveys

Drop camera field surveys were conducted to characterize bottom type as well as eelgrass and seaweed presence/absence from September to October 2019. Stations ($n = 128$) were pre-identified based on depth (0–10 m) and substrate type (5 classifications ranging from soft mud to hard bottom) to allow stratified sampling across conditions in which both vegetated habitat types are found (hard versus soft substrate). At each station (**Figure 1**), an underwater video system (consisting of a GoPro Hero 7 camera inside a waterproof housing with lasers attached for scaling; Pro Squid, Spot X underwater Vision[1]) was deployed. The system was connected to a topside console that allowed operators to view video feed and record GPS position. The camera was lowered into the water to approximately 1 m above the sea bottom, and the boat was allowed to drift for 1–2 min while the camera video recorded the bottom substrate. Substrate type (i.e., bare, eelgrass, or seaweed) was visually determined from the live feed and then validated from the video at a later date. For image classification, all points were labeled as bare or vegetated following the video validation, as exploratory analysis showed it was not possible to separate eelgrass and seaweed habitat (results not shown).

There was about a 1- to 3-year period between the field surveys (2017–2019) and image acquisition (2016) depending on the source of the *in situ* data. While it is not uncommon to have a temporal gap between the field survey and image acquisition (e.g., O'Neill and Costa, 2013; Poursanidis et al., 2019), we assumed that large-scale vegetation distribution patterns would have minimally changed during the time period, particularly given that both the image acquisition and field survey were obtained in the same season. Yet, given that areas with patchy/mixed habitat types might have undergone slight shifts in vegetation density, particularly since the region was impacted by the passage of Hurricane Dorian in early September 2019, days before the field surveys were performed, an additional data quality control step was performed. The video footage for each field survey point was examined in relation to the true color composite of the satellite imagery and the spectra, to identify areas of mixed habitat types or very low density of vegetation coverage. These stations ($n = 32$) were omitted from image classification resulting in using 96 stations giving 218 data points. Each drift transect consisted of 2–3 observations depending on the number of GPS coordinates obtained. The quality control step was done both to use pure endmembers for model training, and to account for slight shifts in habitat, which are more likely to occur in

[1]https://www.spotx.com.au/

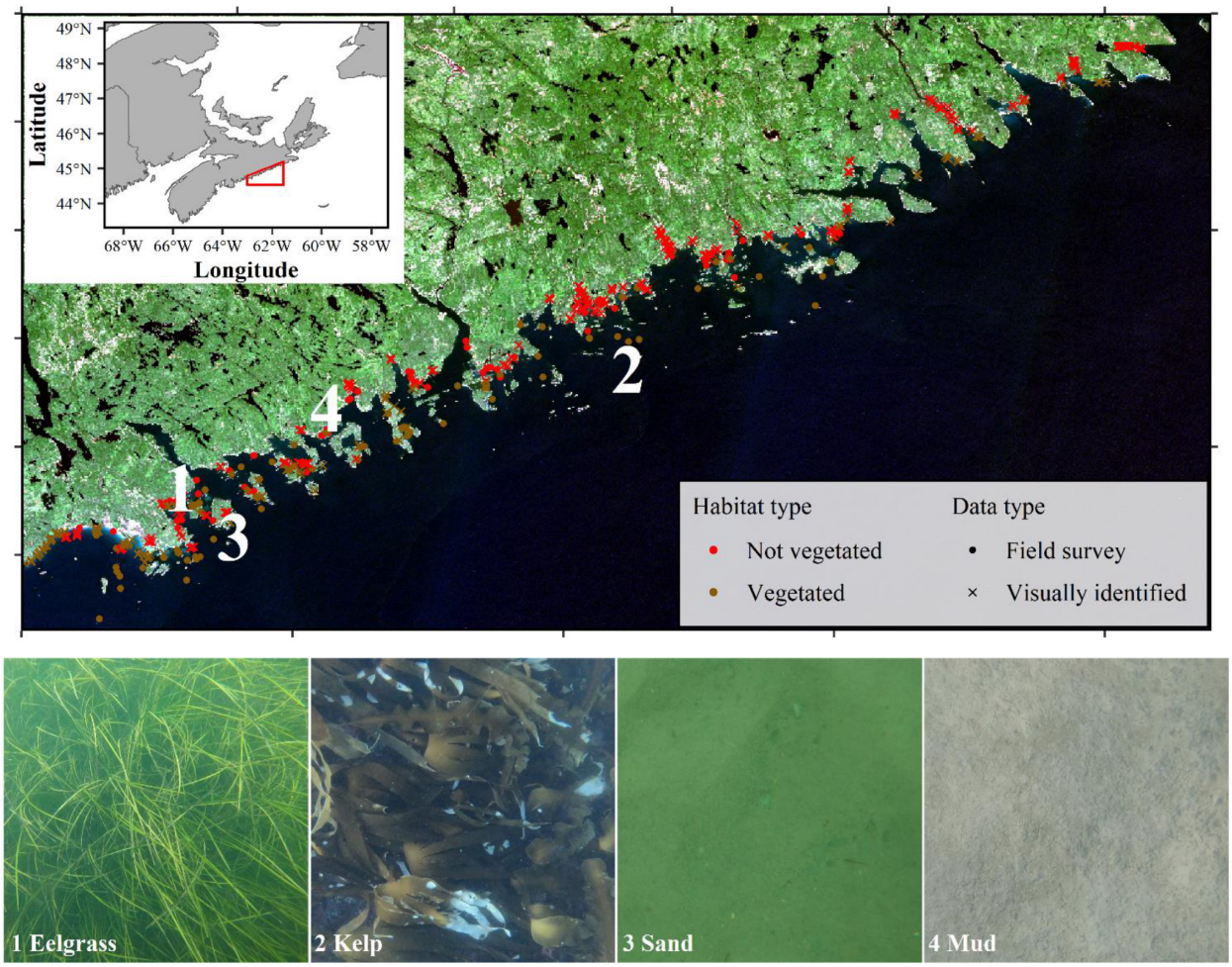

FIGURE 1 | Atmospherically corrected true-color composite of the Sentinel-2 tile (T20NQ) of the Eastern Shore Islands in Nova Scotia, Canada acquired on September 13, 2016. Dots indicate stations where field survey data were collected, triangles indicate visually identified points, colors show where vegetated habitat is known and not known to occur. Numbers relate to image-stills of select habitat types occurring in the region.

fragmented areas. Percent cover was calculated for select video frames per station, and in general average vegetated percent cover was >75%, often higher, in stations that passed quality control. Additionally, a visual assessment between a Worldview-3 image acquired in August 2019 over a large portion of the tile, and the best Sentinel-2 image acquired in 2016 (see section "Satellite Data, Atmospheric Correction, and Land Masking") was performed to ensure that large-scale vegetation patterns were fairly stable between 2016 and 2019.

In addition to the 2019 field survey (n = 218), additional field data from 2017 to 2019 were also included (n = 15; Wong et al. Unpublished data). Lastly some visually identified points from the imagery were added to assist in model training for habitat types missed in the field surveys for shallow bare substrate (n = 294), shallow vegetation (n = 202), and bare sand at moderate depths (n = 50; **Figure 1**). These visually identified points were selected from areas that were easily interpretable, were spaced evenly to cover the entire Sentinel-2 tile, and were added in an iterative approach to provide a more accurate vegetation map (Vahtmäe and Kutser, 2013). All field survey data and visually identified points were labeled as vegetated or non-vegetated for a two-class binary classification of vegetation presence and absence for a total of 779 data points (**Table 1**). Therefore, three separate data sources were used in model building/evaluation to maximize the amount of information available to the classification algorithm. The number of data points used in the current study lies within the number of points used for other coastal Sentinel-2 studies ranging from <150 (e.g., Fauzan et al., 2017; Poursanidis et al., 2019) to >1,000 (e.g., Traganos et al., 2018; Yucel-Gier et al., 2020).

Satellite Data, Atmospheric Correction, and Land Masking

Sentinel-2 is a European observation system composed of two identical satellites (A and B launched in 2015 and 2017, respectively), that provide images every 5 days at the equator and every 2–3 days at 45°N (Drusch et al., 2012). Sentinel-2 has a

TABLE 1 | Number of field survey and visually identified points by habitat type and water depth (m).

Water depth (m)	Habitat type						Total points (%)	Total pixels (%)	Total SA (km^2)
	Field survey points				Visually identified points				
	Eelgrass	Seaweed	Sand	Mud	Vegetated	Bare			
0–1	17	0	0	0	100	221	43.39	14.67	50.63
1–2	8	0	0	16	57	60	18.10	12.07	41.68
2–3	14	0	4	17	30	12	9.88	13.41	46.29
3–4	11	22	7	12	6	2	7.70	7.67	26.46
4–5	0	12	0	4	7	5	3.59	9.13	31.53
5–6	0	10	0	5	2	2	2.44	11.12	38.39
6–7	0	18	3	0	0	8	3.72	7.75	26.76
7–8	0	11	0	8	0	7	3.34	7.08	24.43
8–9	0	0	0	12	0	7	2.44	7.40	25.55
9–10	0	12	4	6	0	20	5.39	9.69	33.44
Total	**50**	**85**	**18**	**80**	**202**	**344**	**100.00**	**100.00**	**345.16**

The sum of all points by depth class represented as a percentage (%) of all points (n = 779) that were available for model building and evaluation (Total Points). The number of pixels in the Sentinel-2 tile by depth class represented as a percentage (%) of all pixels (n = 3,451,533) in the Sentinel-2 tile (Total Pixels). The total surface area (SA; km^2) of each depth class in the Sentinel-2 tile assuming an equal area of 100 m^2 per pixel (Total SA). Only the field survey points which passed quality control are included in this table. Depth was measured in situ for field survey points. Depth was obtained from the 30 m multibeam data for the visually identified points, and the Sentinel-2 pixels. Note the difference in total SA with ***Table 3*** *is due to rounding.*

swath width of 290 km and provides 13 bands at a radiometric resolution of 12-bits and a spatial resolution from 10 to 60-m. At the spatial resolution of 10-m, four bands are available with centered wavelengths of ∼490 nm (band 2 blue), ∼560 nm (band 3 green), ∼665 nm (band 4 red), and ∼833 nm (band 8 NIR). These were the only bands used in the study to take advantage of the high spatial resolution. Level-1C products are geolocated and radiometrically corrected to top-of-atmosphere reflectances in local UTM coordinates and are available in 100 × 100 km tiles. Images can be freely downloaded, pending a registration, from Copernicus Open Access Hub[2].

To determine the best image for classification, we assembled a catalog of available Sentinel-2 imagery for our region of interest between the launch of Sentinel-2 in 2015 to 2019 (see **Supplementary Material 1**). From the first day imagery was available for our region of interest on September 12, 2015 to December 31, 2019, we identified 464 days where the entire region, or a part of it, was imaged by Sentinel-2. Of which, 320 days were immediately discarded due to heavy cloud cover, leaving 144 days, which may be suitable for image classification (**Supplementary Figure 1.1**). All 2015 images were cloud covered, but in general from 2016 to 2019 at least one cloud free image existed per month and year. The tidal height at time of image acquisition varied between low and high tides, and 57 days (out of the 144) were impacted by different degrees of sunglint, both of which can impact classification success. Additionally, it was noted that water transparency varied highly across these cloud-free image dates and bottom habitat was not always visible in the Sentinel-2 imagery. Lastly, due to the various satellite tracks, only 64 days (out of the 144) imaged the entire region, the rest partially imaged the region of interest. This resulted in about 14% of all available images that were potentially suitable for bottom-habitat monitoring.

The best Sentinel-2 image from 2015 to 2019 for our region of interest was selected based on tidal height, the absence of clouds and sun glint, minimal wave action, and low turbidity. This image was acquired on September 13, 2016 at 15:07 UTC, within 10 min of a low tide (15:17 UTC at a tidal height[3] of 0.58 m). The full Sentinel-2 tile (T20NQ) Level 1C image was downloaded for analysis. This image was assumed to represent the best-case scenario for image quality to understand what information about marine macrophyte coverage can optimally be extracted from Sentinel-2 for Atlantic Canada. A method workflow is presented in **Figure 2** and described in Sections "Satellite Data, Atmospheric Correction, and Land Masking" and "Image Classification."

The full tile image was atmospherically corrected with ACOLITE (Python v.20190326.0) using the dark spectrum fitting approach (Vanhellemont and Ruddick, 2016; Vanhellemont, 2019). Previous work with Sentinel-2 in another region of Atlantic Canada explored the use of ACOLITE to atmospherically correct Sentinel-2 images for bottom habitat identification and found the dark spectrum fitting method to be superior to the exponential approach (Wilson and Devred, 2019). Dark spectrum fitting is an entirely automated, image-based approach to aerosol calculation which makes no prior assumptions on which bands should be used to calculate atmospheric properties (for instance the red or NIR signal being negligible). It assumes that a tile contains pixels whose surface reflectance should be approximately zero for at least one band. Using the dark targets, and various aerosol models, a final model is chosen based on the band which defines the lowest atmospheric path reflectance. Rayleigh scattering is accounted for via lookup tables based on

[2]https://scihub.copernicus.eu

[3]waterlevels.gc.ca/eng/station?sid=505

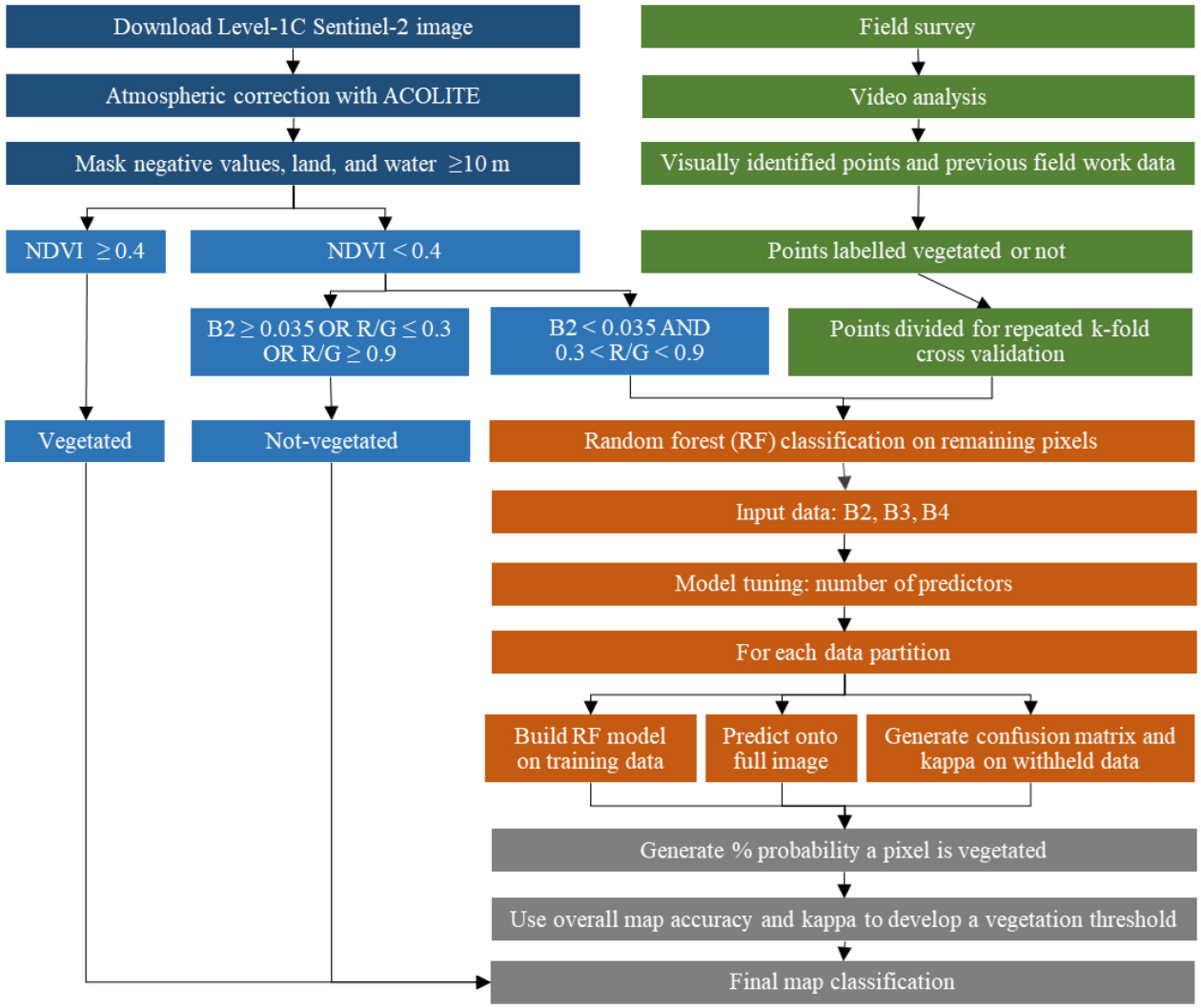

FIGURE 2 | Methods workflow to classify the Sentinel-2 tile.

the 6SV radiative transfer model. All ACOLITE settings were left at their default values except for masking. All l2w_mask settings were disabled to allow for more fine-tuned masking.

Generating accurate land masks is an essential preprocessing step when working with coastal near-shore environments, where sharp transitions in the magnitude of surface reflectance occur. ACOLITE default mask settings define land values where top-of-atmosphere reflectance (ρ_t) in band 11 (SWIR; central wavelength ~1,610 nm; 20-m resolution) are greater than 0.0215. Previous work in another region of Atlantic Canada found this threshold inadequate to define near-shore environments, and that an appropriate threshold was image dependent (Wilson and Devred, 2019). Additionally, as the aim of our study was to eventually use Sentinel-2 for repeated image classification over multiple years, a standard land mask was desired that would not be impacted by tidal height. Therefore, a high tide image of the same tile (T20NQ) was used to generate a standard regional land mask that could be used across multiple image dates (Roelfsema et al., 2009). High-tide was chosen over low-tide to include the entire range of habitat that marine macrophytes exist. This image was acquired on August 24, 2016 at 15:08 UTC corresponding to high tide (15:08 UTC at a tidal height of 1.62 m) and pixels with $\rho_t \geq 0.07$ for band 11 were defined as land based on visual inspection and masked. While SWIR is strongly absorbed by water and therefore provides better delimitation of land and water surfaces than NIR, the different spatial resolution between the 10-m bands used in image classification, and the 20-m band used to generate a land mask should be accounted for. To do so, mixed pixels (i.e., containing both land and water areas) at the 20-m resolution were masked with the Normalized Difference Vegetation Index (NDVI) to identify any vegetated land pixels. Floating algae index (FAI) was not explored as it requires information from the 20-m SWIR bands. The August 24, 2016 image was atmospherically corrected with ACOLITE and surface reflectances of band 4 and band 8 were used to calculate NDVI. Pixels where NDVI ≥ 0.7 were identified as land vegetation based

on visual examination and masked. This threshold was defined as the lowest threshold which did not include rockweed beds, which may float at the surface at high tide. As a final step, areas of freshwater (e.g., lakes) were manually masked.

Our regional land mask was applied to the September 13, 2016 image for the 10-m bands (i.e., bands 2, 3, 4, and 8). Next, all pixels in water depths ≥10 m were masked out to correspond with the maximum depth of the field survey (see section "Field Surveys"). The bathymetry was obtained from the Canadian Hydrographic Services multibeam data (Greenlaw Unpublished data) at a spatial resolution of 30-m and was resampled to a 10-m resolution with bilinear interpolation using the *raster* package (Hijmans, 2019) in R (R Core Team., 2019). As a last quality control step, pixels with at least one negative remote sensing reflectance in any of the four 10-m bands were discarded from the study (25 pixels; <0.001% of total pixels).

No water-column correction was performed on the imagery. While we explored the use of the commonly employed depth invariant indices (Lyzenga, 1978; results not shown here), we could not assume that water transparency was consistent across our study area breaking a key assumption of the approach (Zoffoli et al., 2014). Regardless, water column corrections based on depth invariant indices and more analytical bio-optical modeling have been shown to have mixed effects on image classification success (e.g., Marcello et al., 2018; Poursanidis et al., 2018; Traganos et al., 2018) and are commonly not applied (e.g., Hogrefe et al., 2014; Wicaksono and Lazuardi, 2018). In addition, given that we only used the four wavebands at 10-m resolution, resolving depth, water column and bottom properties might appear as an overoptimistic task.

Image Classification

Our original classification goal was to differentiate between eelgrass and seaweed habitat but this was not found to be possible (results not shown) as their spectral signatures were very similar for the Sentinel-2 three visible bands (see **Figure 3** and section "Results"). We therefore adapted our classification goal from species distribution mapping to detect vegetated versus non-vegetated habitat (see **Figure 2** for an organization of data processing). Three common supervised (i.e., requiring *a priori* knowledge of habitat type), and one unsupervised image classification procedures were tried as a preliminary data exploration (**Supplementary Table 2.1**). All analyses were performed on remote sensing reflectance using R version 3.6.0 (R Core Team., 2019) with the *raster* (Hijmans, 2019), *caret* (Kuhn, 2019), *RSToolbox* (Leutner et al., 2019), *irr* (Gamer et al., 2019), and *readxl* packages (Wickham and Bryan, 2019). The first approach was a supervised statistical classification with maximum likelihood classification (Richards, 1986). Maximum likelihood is a simple approach, which assigns a pixel to the class it has the highest probability of being a member of. Maximum likelihood has been widely used in remote sensing studies; however, it requires many training points across all habitat (class) types, and that the remote sensing reflectance within each class follows a normal distribution. More recently, remote sensing studies have focused on machine learning classifiers that do not make any assumptions on data distributions and require fewer training points, notably support vector machines (SVM) and random forests (e.g., Traganos and Reinartz, 2018b; Poursanidis et al., 2019). The SVM approach differentiates classes based on defining the optimal hyperplane between the classes and can separate non-linearity by applying a kernel function. As such, we explored the use of SVM with a radial basis function kernel (Vapnick, 1995). Random forests build a collection of decision trees, and randomly sample these trees to create a final ensemble model, which is a robust classifier to outliers and noisy training data (Breiman, 2001). We lastly compared the supervised classifiers to an unsupervised *k*-means analysis (MacQueen, 1967). Following this preliminary data exploration (see **Supplementary Material 2**), the random forest algorithm was found to be the preferred classifier. As expected, the supervised classifiers outperformed the *k*-means classification, even when the *k*-means was performed on shallow depths (O'Neill and Costa, 2013), and the machine learning classifiers outperformed the maximum likelihood classification based on maximizing map accuracies and kappa (**Supplementary Tables 2.2, 2.3**; Traganos and Reinartz, 2018b; Ha et al., 2020). While SVM produced higher overall map accuracies and kappa coefficient than random forests (**Supplementary Table 2.3**), no threshold could be identified to correctly classify all data points in the final map (**Supplementary Figure 2.1** and see following paragraphs). Additionally, visual examination of the imagery demonstrated that the random forests and SVM classifications were almost identical (**Supplementary Figure 2.2**). Therefore, the random forests approach was found to be the preferred classifier as it required significantly less model tuning, both in time, number of parameters, and dependency on kernel choice (**Supplementary Table 2.1**). It produced comparable habitat maps to the SVM classification with higher accuracy from the cross-validation runs (**Supplementary Figure 2.2**), and a threshold could be identified in the final map to correctly classify all data points (**Supplementary Figure 2.1**).

The full Sentinel-2 tile was classified as follows (**Figure 2**). First, intertidal, and very shallow subtidal pixels with canopy near-surface vegetation were classified using NDVI. Here, very shallow generally corresponded to depth ≤2 m, although we did not compare canopy height relative to water depth which would provide a more accurate threshold for vegetation detection with NDVI. NDVI was calculated with band 4 and band 8, and all pixels with a value greater or equal to 0.4 were assumed to be vegetated (Barillé et al., 2010). Second, for all pixels with NDVI < 0.4, band thresholds were used to classify some non-vegetated habitats. A threshold for band 2 (blue) of ≥0.035 was assigned to mask out the remaining "bright" pixels, which were assumed to be non-vegetated substrate such as uncovered intertidal areas to very shallow (<2–3 m) sand/rocks, or breaking waves on shore. Shallow to moderate depth bare sediment was classified using the Red/Green ratio (Band 4 divided by Band 3). Pixels with a Red/Green ratio ≤ 0.3 were classified as bare sand as in Dierssen et al. (2019), and pixels with a Red/Green ratio ≥ 0.9 were classified as mud (i.e., dark sediment) or contaminated by fresh tannic water runoff which is common along beaches in the region.

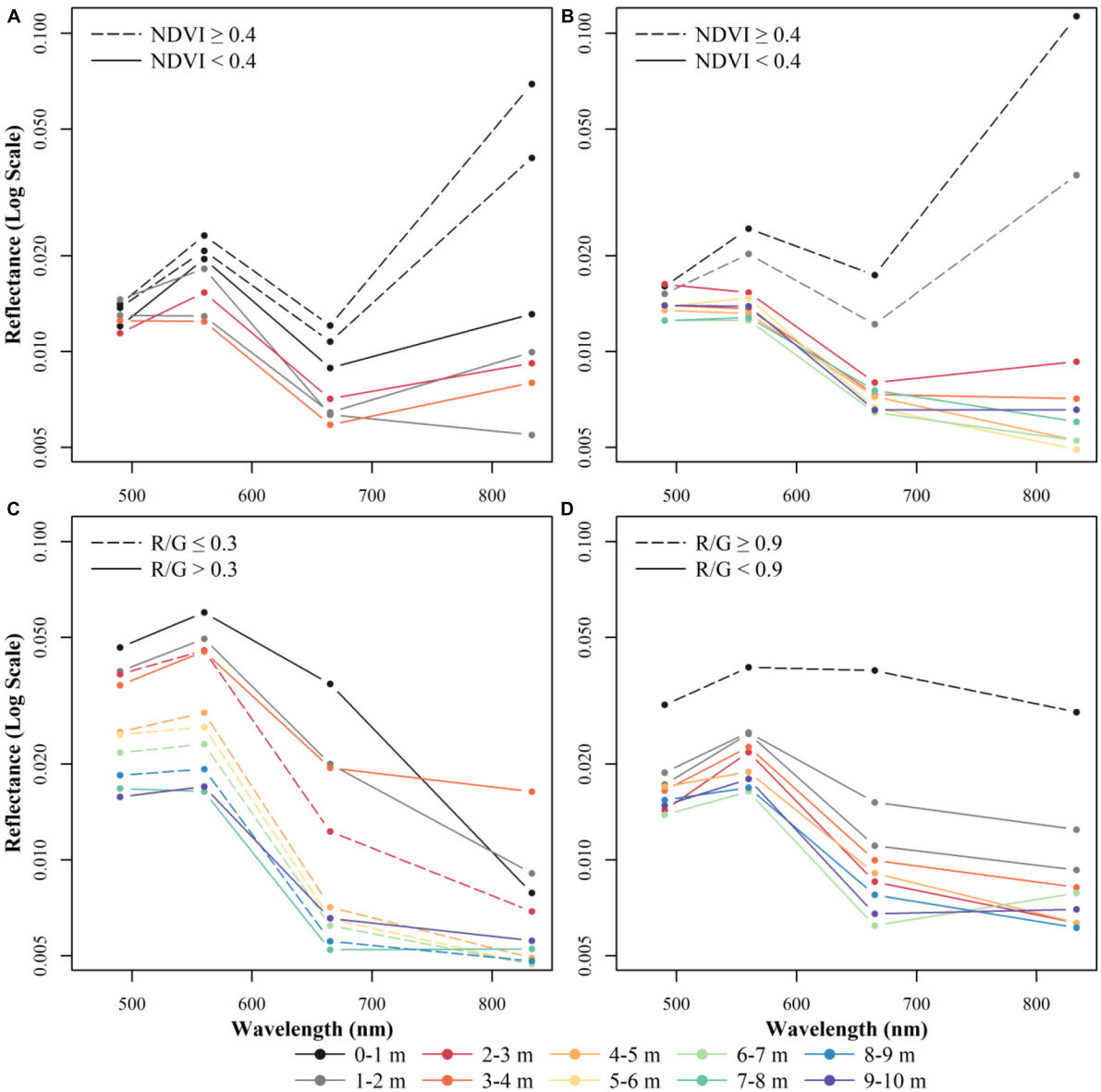

FIGURE 3 | Example spectra from representative field survey points across multiple depths for **(A)** eelgrass, **(B)** seaweed, **(C)** sand, **(D)** mud. Dashed lines indicate pixels that would be classified using the NDVI or R/G band thresholds. Solid lines indicate pixels classified with the random forests model. Note that seaweed at 0–3 m, mud at 0–1 m, and sand at 1–2, 4–7, and 8–9 m of depth is based on visually identified points. No non-patchy eelgrass habitat was sampled at >4 m water depths and visually identified points at these depths could not be labeled with certainty to be an eelgrass bed (instead of a seaweed dominated habitat).

All remaining pixels (i.e., NDVI < 0.4 and Blue < 0.035 and 0.3 < Red/Green < 0.9), were classified using the random forests approach as described in Section "Image Classification" (**Figure 2**). The three visible wavelengths were used in the random forests model (bands 2, 3, 4; blue, green, red) for a two-class binary prediction of vegetation presence from absence. For differentiation of major macrophyte groups (e.g., eelgrass from brown seaweed) in these temperate waters, the maximum depth for image classification would need to be reduced from 10 to 2–3 m, significantly more field survey points at overlapping depths for the various vegetation types would need to be collected, and imagery with greater spectral (e.g., hyperspectral) and/or spatial resolution would be required (Kutser et al., 2020; Vahtmäe et al., 2020). In our study region, the three visible bands at 10-m resolution did not provide enough information to separate seagrass from seaweed dominated habitat.

Random forest model tuning with the "rf" method in R requires defining the number of random predictors to select at each branch of the tree. An initial model was developed with repeated *k*-fold cross-validations with fivefolds repeated 10 times to determine the best number of predictors. With model tuning complete, all training data were partitioned into fivefolds repeated 10 times. A random forests model was built on each partition's training data, then predicted onto the full data set.

For each partition's test data, the withheld points were used to generate a confusion matrix including overall map accuracy, user accuracy, producer accuracy, and a Kappa coefficient with *z*-tests for significance from zero (Foody, 2002). This cumulated in 50 different models, habitat maps, and confusion matrices. A final confusion matrix was calculated based on the average accuracy metrics from the cross-validation runs. To generate the final map classification, the probability that a pixel was classified as vegetation was calculated by summing the number of times a pixel was classified as vegetation, divided by 50 (number of cross-validation runs) and converted to a percentage. Pixels labeled as vegetated with NDVI were labeled as 100%, and pixels labeled as bare habitat with the blue band or Red/Green ratio were labeled as 0%. Delivering a final map classification as a percentage demonstrates the level of confidence an end-user should have when using the vegetation map. Yet, if a binary map classification is required for presence from absence, we explored what vegetation probability threshold choice would maximize overall map accuracy and kappa using all data points in **Table 1**. For instance, if the final map classification was thresholded at 50%, where pixels ≥50% probability were labeled as vegetated and pixels with <50% were labeled as not-vegetated, we then compared how overall map accuracy and kappa would change relative to a 60% threshold.

RESULTS

We examined changes in the spectral signatures of remote sensing reflectance for pixels extracted from the best Sentinel-2 image over four known habitat types: sand, mud, eelgrass, and seaweed (including rockweed and kelp habitat which are structured by vertical zonation patterns; **Figure 3**). As expected, sand had the highest reflectance values, with a clear decrease in magnitude as the wavelength increases (**Figure 3C**). Reflectance spectra from muddy substrate (**Figure 3D**) were dissimilar to the ones from sandy substrate with lower absolute reflectance values at comparable depths, and a weak spectral dependence at all depths, compared to the sharp decrease in the red and NIR for sand. For mud substrate, the red and NIR bands showed the clearest decrease as a function of depth. Both eelgrass (**Figure 3A**) and seaweed (**Figure 3B**) showed lower reflectance in the visible part of the spectrum at comparable depths than the reflectance for both sand and mud bare substrate habitats. Subtle differences are visible between the two vegetation types, where eelgrass has a higher Green/Blue ratio but a lower NIR/Red ratio. However, differences in vegetation type could not be differentiated by any image classifier and limited overlapping field points at comparable depths made a true comparison of the ratios difficult (**Supplementary Figure 3.1** in **Supplementary Material 3**).

To classify the best image, the threshold for NDVI indicating vegetated habitat and the thresholds for non-vegetated habitat were set to perfectly classify (i.e., 100% classification success) the training points located within those values (**Table 2**). A total of 12 data points occurred within NDVI ≥ 0.4, and this threshold classified ∼6% of the pixels in the tile (**Table 3**). A total of 61 data points occurred within the non-vegetated thresholds (**Table 2**) and classified ∼6% of the pixels in the tile (**Table 3**). The remaining pixels (n = 3,031,740) were classified with a random forests model. Following the repeated k-fold cross validation of the random forests model, the final average overall map accuracy was 79% with an average moderate kappa value of 0.57 based on the withheld test data partitions (**Table 2**). Non-vegetated habitat had ∼5% higher user and producer accuracy for non-vegetated habitat, relative to the user and producer accuracy of vegetated habitat, indicating the classification was slightly better at predicting absence of vegetation.

The probability that a pixel was classified as vegetated with the random forests model was determined by summing the number of times a pixel was classified as vegetation, divided by 50 (number of cross-validation runs) and converted to a percentage (**Figure 4A**). In this classification map, 76% of the pixels were always classified the same in all 50 cross-validation runs where 16% (474,937) of the pixels were always classified as bare (non-vegetated) habitat, and 60% (1,831,911) were always classified as vegetated habitat by the random forests model (**Figure 4B**). When the threshold based classified pixels were included in the final classification map as either 0% (non-vegetated thresholds) or 100% (NDVI ≥ 0.4; total n = 3,451,533), we then explored the effect of thresholding the habitat probability map between 1 and 100% on overall map accuracy (**Figure 4C**) and kappa (**Figure 4D**) to determine an appropriate threshold for a binary map classification. When a threshold of 21% was chosen, meaning that any value ≥21% was labeled as vegetated habitat and any value <21% was labeled as non-vegetated, all data points were classified correctly resulting in an overall accuracy of 100% and a kappa of 1. This trend persisted until a vegetated threshold of ≥80%, where at vegetated thresholds >80% (i.e., 81% and higher) overall map accuracy and kappa began to decrease again.

Our classification scheme applied to Sentinel-2 data performed best at identifying bright sandy habitats, and dense vegetated beds (**Figure 5**), which can be expected as they represent the two most distanced endmembers. The blue threshold (0.035) classified bright, bare sandy habitats to depths of 2–3 m (**Figure 3**). The R/G threshold of 0.3 classified bare sandy habitats from 2–3 m to roughly 7–8 m. The NDVI threshold classified both intertidal/shallow seaweed beds and shallow eelgrass beds as vegetated. The random forests classifier was able to differentiate vegetated from non-vegetated habitat to the edge of the 10 m deep water mask (**Figure 5**). However, this maximum depth at which bottom habitat could be classified was not consistent across the tile (**Figure 6**). For instance, in areas affected by freshwater runoff, even bright sand was misclassified at depths >5 m (**Figure 6A**), and in more estuarine regions almost all bottom habitat is classified as vegetated habitat (**Figure 6B**). While limited field survey data are available in estuarine regions to confirm this, it appears that freshwater with high concentrations of CDOM reduces the water depth at which the sea floor is visible due to strong absorption. These areas (i.e., pixels) present reflectance spectra similar to the ones of optically deep water even in regions of very shallow water depths. As the distance from the river increased, water transparency increased, and bottom habitat gradually became visible in seaward estuarine regions (**Figure 6**).

Additionally, the classification performs poorly in bare sediment habitats dominated by muddy substrate (**Figure 7**).

TABLE 2 | Confusion matrix after each classification step has been added in. Overall map accuracy is bolded. Kappa significance indicated by asterisk (*).

Classification stage	Map classification	Field survey data			Kappa
		Not vegetated	Vegetated	User accuracy (%)	
NDVI ≥ 0.4	Not vegetated	0	0	100.00	1.00
	Vegetated	0	12	100.00	
	Producer accuracy (%)	100.00	100.00	**100.00**	
B2 ≥ 0.035 OR R/G ≤ 0.3 OR R/G ≥ 0.9	Not vegetated	61	0	100.00	1.00
	Vegetated	0	12	100.00	
	Producer accuracy (%)	100.00	100.00	**100.00**	
Random forests	Not vegetated	72.42 ± 3.64	17.16 ± 3.95	80.98 ± 3.57	0.57 ± 0.07*
	Vegetated	15.98 ± 3.68	50.24 ± 3.99	76.04 ± 5.85	
	Producer accuracy (%)	81.93 ± 4.16	74.54 ± 5.85	**78.72 ± 3.18**	

First classification stage includes only the vegetated pixels classified with NDVI. Second classification stage includes the vegetated pixels classified with NDVI, and the non-vegetated pixels classified with the blue band or red/green ratio. Third classification stage includes the vegetated pixels classified with NDVI, the non-vegetated pixels classified with the blue band or red/green ratio, and the random forests classified pixels. For the third matrix, the average (±standard deviation) confusion matrix based on the test data partitions from the repeated k-fold cross validation (k = 50) is shown.

TABLE 3 | Number and percentage of pixels and surface area (SA) of habitat classified across various classification steps and water depth.

Max depth (m)	Metric	Tile total	NDVI ≥ 0.4	NDVI < 0.4			
				B2 ≥ 0.035 OR R/G ≤ 0.3 OR R/G ≥ 0.9	B2 < 0.035 AND 0.3 < R/G < 0.9		
					RF average (±SD)	RF 21% threshold	RF 80% threshold
4	Total pixels (#)	1,650,543	211,472	144,101	801,630 ± 14,708	866,892	741,491
	Total pixels (%)	100.00	12.81	8.73	48.57 ± 0.89	52.51	44.92
	SA (km^2)	165.05	21.15	14.41	80.16 ± 1.47	86.69	74.15
10	Total pixels (#)	3,451,533	216,806	202,987	2,208,412 ± 35,334	2,349,498	2,099,200
	Total pixels (%)	100.00	6.28	5.88	63.98 ± 1.02	68.07	60.82
	SA (km^2)	345.15	21.68	20.30	222.08 ± 3.53	234.95	209.92

Tile total indicates the number of pixels across the full tile to be classified (total pixels; #), the percentage of the pixels relative to the total (total pixels;%), and the SA the pixels cover assuming an equal area of 100 m^2 per pixel (SA; km^2). Pixels classified with the NDVI threshold as vegetated habitat (NDV ≥ 0.4). Pixels classified as bare habitat with threshold the blue band (B2) or the red/green ratio (R/G). Pixels classified as bare habitat with the random forests (RF) classification based on the average (±standard deviation, SD) from the k-fold cross-validation, and when the final map classification is thresholded at 21 and 80% probability.

The lower albedo of bare mud presents a spectral shape more similar to vegetated habitat than bare sand at comparable depths (**Figure 7A**). Consequently, around the 4–5 m depth (even shallower in some areas) the classification became "salt-and-peppered" suggesting that the binary classification has become purely random. Lastly, the classification also performed less well in areas of mixed habitat types. In areas of shallow waters with patchy vegetation, the bright reflectance from nearby bare sand overwhelmed the vegetation signal and the spectra of low-density vegetation on sandy substrate has a spectrum comparable to sand (**Figure 8**). This can be seen as a contamination due to the adjacency effect as it occurs in coastal waters close to land, where pixels in the vicinity of a brighter target are contaminated. Increased satellite resolution might address this issue. Therefore, the classification fails for low density or dense but isolated patches of vegetated habitat.

With these limitations in mind, the total surface area coverage of vegetated habitat was calculated (**Table 3**). At the maximum depth of image classification (10 m), ∼231 km^2 (67%) of vegetated habitat were predicted to exist, 21.68 km^2 were calculated with NDVI and 209.92 km^2 calculated from the random forests calculation. Conversely, ∼114 km^2 (33%) were dominated by bare sediment habitat, 20.30 km^2 were calculated with thresholding the blue band and Red/Green ratio, and 93.25 km^2 were calculated with the random forests classifier. There are uncertainties around the random forests surface area values depending on the average used for the cross-validation maps, and if the final map was thresholded. If the image was masked to 4 m, a depth where most of the image was well classified based on visual examination, about 95 km^2 (∼58% of the total area) of the seafloor was vegetated.

DISCUSSION

We used the "best" Sentinel-2 image acquired between 2015 and 2019 for a high priority management region and examined to what detail marine macrophyte habitat could be classified

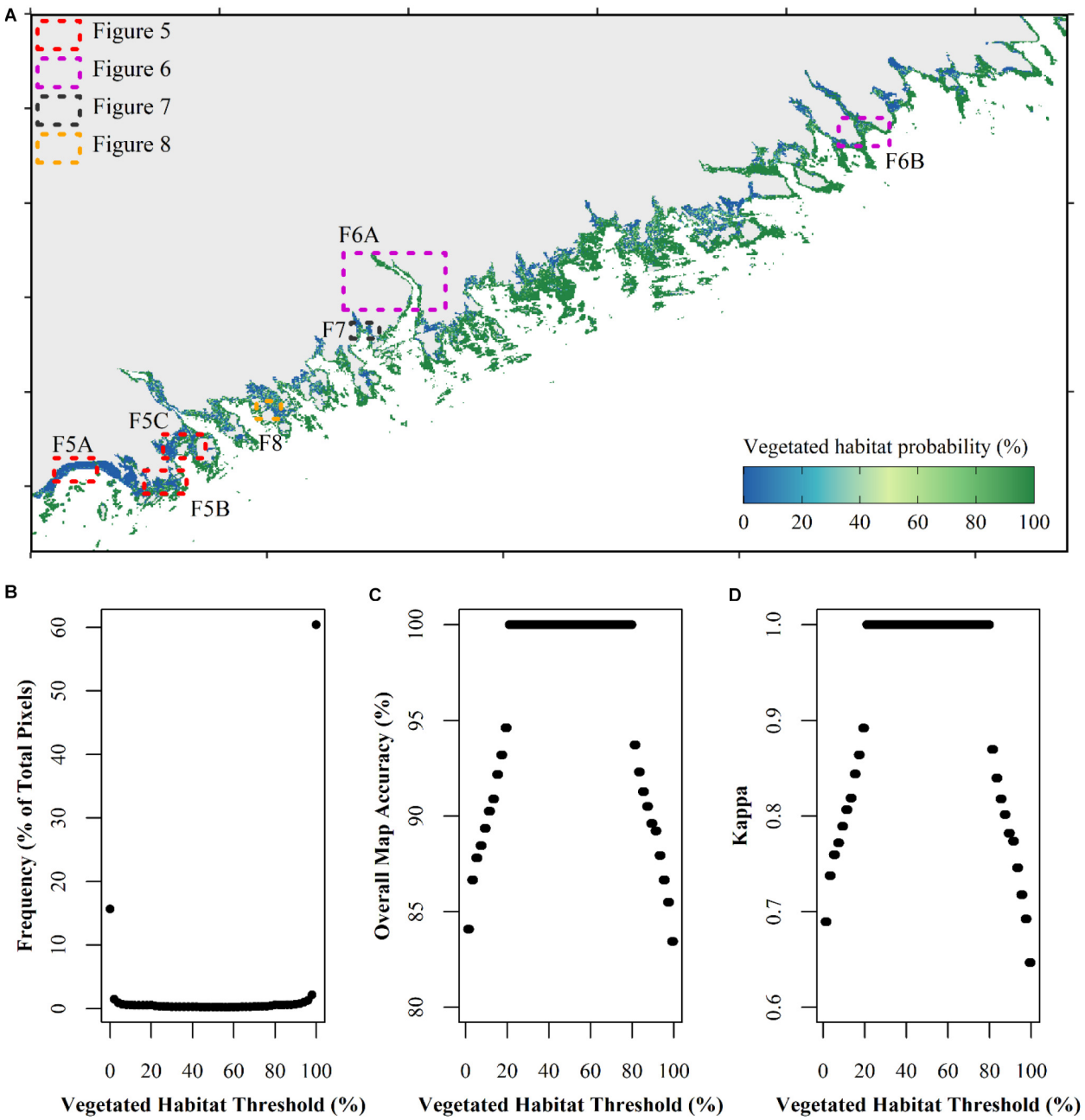

FIGURE 4 | Pre-threshold vegetation map demonstrating the probability that a pixel contains vegetated habitat with land (light gray) and deep water (≥10 m; white) masked **(A)**. Pixels classified as vegetated or non-vegetated with the threshold classification were labeled as 100 or 0%, respectively. All other pixels were classified with the random forests classifier and probability was determined as the number of times a pixel was classified as vegetated divided by 50. Polygons with dashed borders indicate the location of zoomed in boxes in the following figures. The number of pixels at each probability value **(B)**. The effect of various threshold choices for the map in **(A)** on overall map accuracy **(C)** and kappa value **(D)** using all data points (see **Table 1**).

in an optically complex costal environment based on empirical image-based classification procedures. We found that simple band thresholds were effective at classifying very shallow habitats, and bright sandy bare substrate to moderate depths, although a supervised image classifier was required to classify the remaining areas. Vegetated habitat extent was classified at depths shallower than 10 m, with an overall accuracy of 79%, although the maximum depth that bottom habitat was visible varied spatially across the tile (i.e., 4–10 m, due to shifts in water column content and habitat type). While the random forest model developed for our study area cannot be directly applied to other areas (Islam et al., 2020), our method workflow can be readily applied to other images provided that field survey data are available to train the algorithm. In the following section, we discuss the

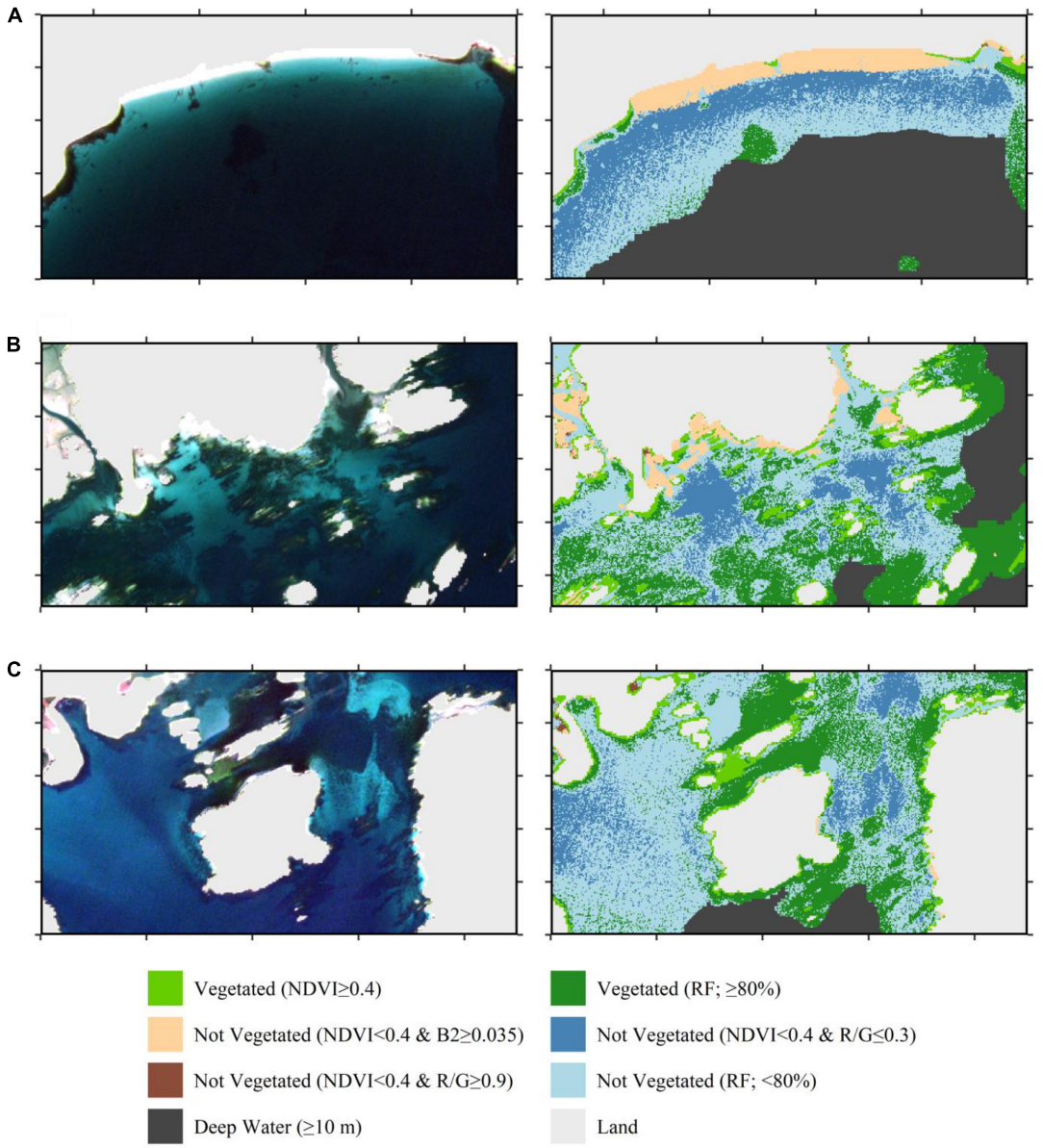

FIGURE 5 | Finalized classification of the Sentinel-2 image from September 13, 2016 highlighting three example regions where the classification performed well including the differences between the classification stages. Left column is the true color composite. Right column is the map classification for the same region. **(A)** A predominantly sandy beach with distinct seaweed patches (F5A in **Figure 4**). **(B)** Mixed seaweed and eelgrass habitat interspersed with sandy habitat (F5B in **Figure 4**). **(C)** Large dense eelgrass meadows and separate kelp forests surrounded by bare substrate (F5C in **Figure 4**). Knowledge of vegetation type was from the field survey data only and not the map classification.

strengths and weaknesses of using Sentinel-2 to classify marine macrophyte habitat in Atlantic Canada, keeping in mind that our findings can be applied to other temperate coastal areas of the world.

Suitability of Sentinel-2 for Benthic Habitat Mapping in Atlantic Canada

Our stepwise approach to image classification is a unique hybrid of other methods of image classification, which generally focus on simple band ratios (e.g., Dierssen et al., 2019; Mora-Soto et al., 2020) or a supervised classifier to quantify bottom habitat (e.g., Traganos and Reinartz, 2018b; Poursanidis et al., 2019), but not both. The ratio approach was applied first to all pixels, and when the threshold was met, pixels were classified with no assumptions made on the other pixels (i.e., the one that did not meet the threshold criteria). These remaining pixels were then classified with random forests. This two-step process is performed in the classification stage, with no post-classification manipulation of pixels and therefore does not require contextual

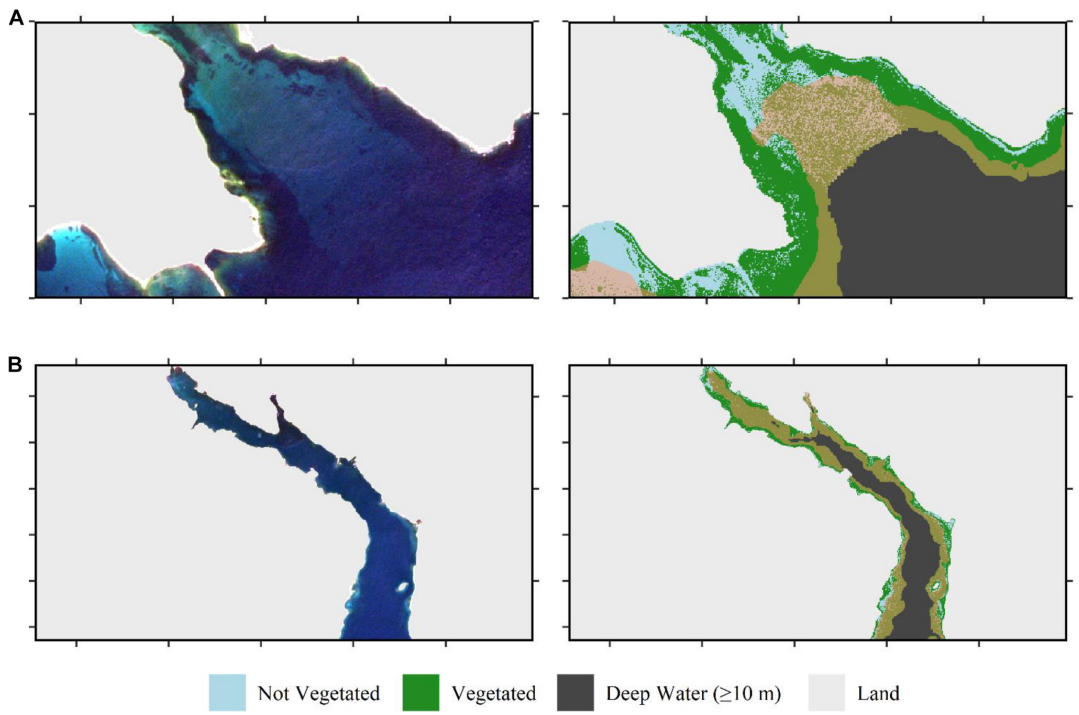

FIGURE 6 | Finalized classification of the Sentinel-2 image from September 13, 2016 highlighting variance in maximum depth the classifier was successful. Left column is the true color composite. Right column is the map classification for the same region thresholded at 80% probability of being vegetated. **(A)** A sandy beach at the edge of an estuary influenced by freshwater input was successfully classified to ∼5 m, waters at depth from 5.5 to 10 m shown with transparent yellow overlay (F6A in **Figure 4**). **(B)** An estuarine brackish environment by freshwater input was successfully classified to ∼2 m, waters at depth from 2.5 to 10 m shown with transparent yellow overlay ("brown" in the figure; F6B in **Figure 4**).

editing as in Mumby et al. (1998). It leverages the simplicity and high accuracy of band ratios in habitats that are relatively straightforward to classify, such as bright sand, and shallow, dense vegetation, with the power of machine learning classifiers in more complex classification schemes. The random forests classification was performed across all depths where the threshold approach had failed.

The band ratios include vegetation indices based on red-edge indices such as NDVI and the Red-Green ratio, which can be effective tools for quantifying intertidal vegetation at low tide or vegetation that floats at, or near, the surface (e.g., Barillé et al., 2010; Dierssen et al., 2019; Mora-Soto et al., 2020). Following Dierssen et al. (2019) we found that the Red-Green ratio could successfully classify bare sand at shallow to moderate depths, albeit at a slightly lower threshold value ($<$0.30 this study, $<$0.35 Dierssen et al., 2019). While no upper threshold could be determined to classify vegetated habitat, an upper threshold could be defined to exclude shallow muddy substrate ($>$0.9). These thresholds were conservatively set to not misclassify any field survey points, which cover a large spatial area, even though the inherent optical properties (IOPs) of the water would vary over this scale. The thresholds could be fine-tuned at smaller spatial scales, where water column properties remain fairly stable. In our study we also found NDVI (Band 4 and 8) to be effective at classifying intertidal to very shallow subtidal habitat ($\sim<$ 2 m). This threshold can be more readily defined from the literature instead of requiring field survey points as there is little impact of the water column in regions where NDVI is effective. No distinctions were made between major species groups, such as rockweed from shallow eelgrass beds. This is in agreement with the study of Mora-Soto et al. (2020) who found that NDVI and FAI based on Sentinel-2 imagery could be used to map Giant Kelp (*Macrocystis pyrifera*) forests, which float at the surface and intertidal green algae, but could not discriminate between the two vegetation types.

Our choice of a specific image classifier (random forests) was based on an initial exploratory analysis (**Supplementary Material 2**), and previous studies which compared different machine learning classifiers to the maximum likelihood classification and found the machine learning classifiers to be the superior image classifier (e.g., Ha et al., 2020). Therefore, our study provides further support for the shift away from the continued use of maximum likelihood. Both SVM and random forests have routinely high overall map accuracies as found in our study and other works (Traganos and Reinartz, 2018b; Poursanidis et al., 2019; Wicaksono et al., 2019). However, we chose to use random forests as it requires less model tuning than SVM. Furthermore, for acoustic seabed classification, random forests was found to be the preferred algorithm compared to *k*-nearest neighbor and *k*-means as it produced the most reliable and repeatable results (Zelada Leon et al., 2020). While the classification choice does have an impact on map accuracy values, we found

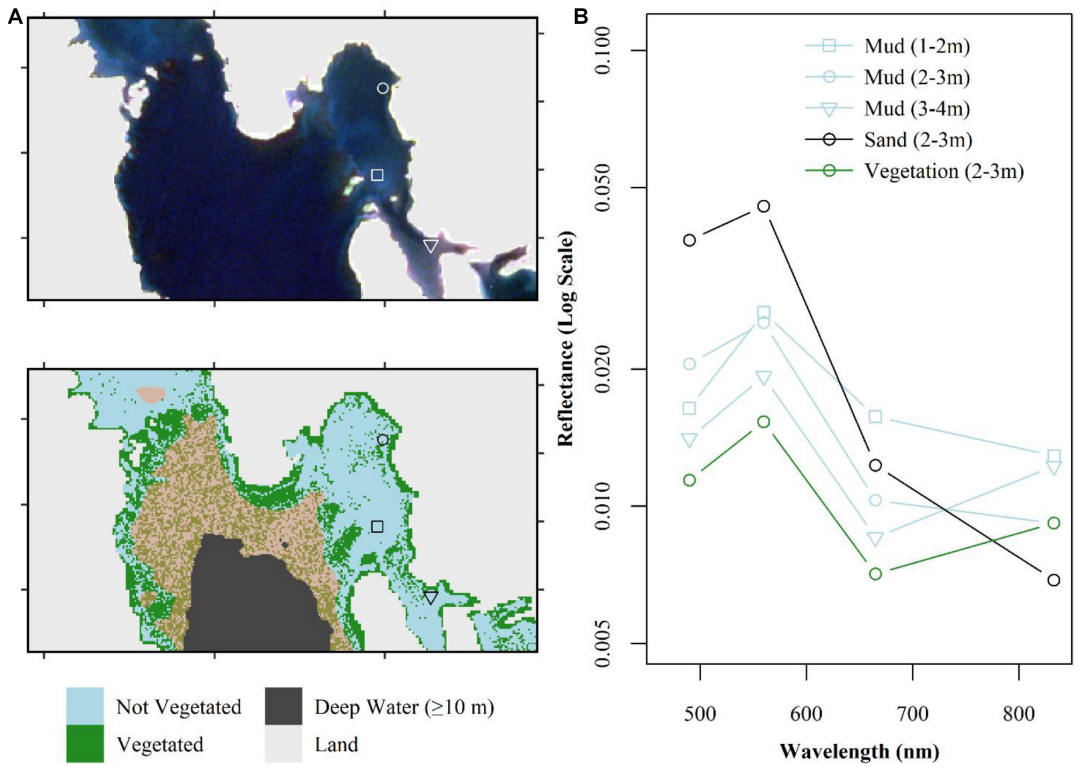

FIGURE 7 | Finalized classification of the Sentinel-2 image from September 13, 2016 highlighting how mud is misclassified at greater depths. **(A)** True color composite and resulting map classification (thresholded at ≥80% probability of being vegetated) indicating location of field survey points of a muddy habitat at 1–2 m (square), 2–3 m (circle), and 3–4 m (triangle). Waters at depth from 5 to 10 m shown with transparent yellow overlay ("brown" in the figure). **(B)** Spectra for the same three survey points, compared to sand and vegetated dominated habitat at 2–3 m of water depth.

that it had no effect on species level discrimination during exploratory analysis. For instance, all four classification types explored in our initial analysis could map vegetated versus non-vegetated habitat, to varying degrees of accuracy, but none could differentiate between eelgrass versus (predominantly brown) seaweed dominated habitat. We therefore had to modify our classification goal from separating eelgrass from seaweed habitat, to only classifying vegetated habitat presence and absence. This is in line with another study based on Sentinel-2 imagery in temperate waters that was also able to only classify vegetation presence from absence (Fethers, 2018). Using SPOT-6/7 imagery, with similar band placements to Sentinel-2 bands 2–4 (blue, green, and red) but at a higher spatial resolution (1.5-m), eelgrass was differentiated from seaweeds in only one of three different images for a bay-wide mapping study in Atlantic Canada (Wilson et al., 2019). Even in tropical clear waters, supervised classifiers with Sentinel-2 have had varying success to differentiate among submerged seagrass species (Kovacs et al., 2018; Traganos and Reinartz, 2018b). Therefore, while Sentinel-2 can produce large-scale coastal benthic habitat maps in Atlantic Canada, it would only be to a level of vegetation presence. If greater class separation is required, hyperspectral imagery (5–10 nm resolution depending on the part of the spectrum) can differentiate between different vegetation types, even in optically complex waters, albeit to much shallower depths (Vahtmäe et al., 2020). Our analysis found that the four 10-m spectral bands on Sentinel-2 were not enough to provide differentiation between eelgrass and seaweeds.

Including appropriate water penetrating bands is essential for developing accurate coastal benthic habitat maps. In the submerged habitat classification using random forests, we excluded the NIR band from the analysis. While the NIR provides critical information along the red-edge, strong absorption by water in this part of the spectrum introduces noise into the classification in all but the shallowest of waters (<2 m; Kutser et al., 2009). Exploratory analysis found that excluding the NIR band (8) increased the maximum depth from ∼5 to ∼10 m at which the classifier could successfully identify bottom habitat at the expense of misclassifying vegetation in very shallow (∼<2 m) waters (Wilson and Devred, 2019). Classifying intertidal/shallow habitat with NDVI provided comparable results in very shallow regions as including NIR in the random forests model, with the benefit of reducing "noise" in the classification allowing for classifying bottom habitat at greater depths. Consequently, we found the best band combination to maximize spectral information available to the classifier, while minimizing noise introduction to the blue, green, and red bands (Bands 2–4). The blue (band 2) and green (band 3) are commonly used in image classification of seagrass habitat with Sentinel-2, generally with a third band either being coastal blue (Traganos et al., 2018;

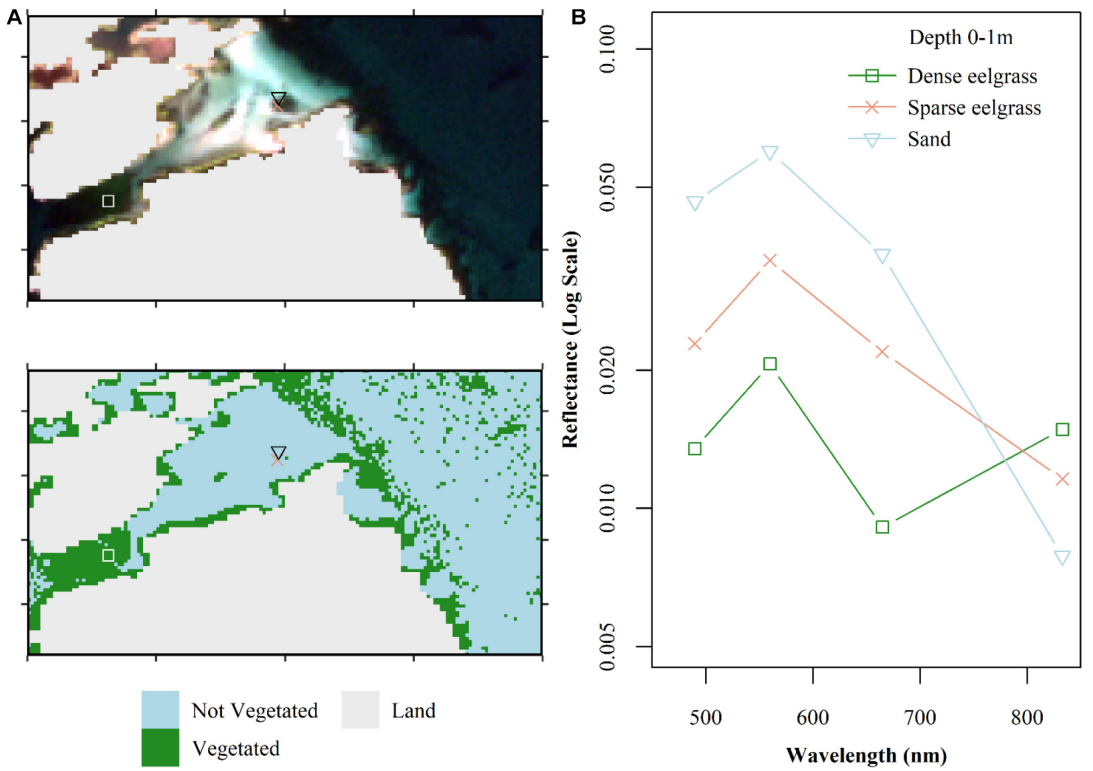

FIGURE 8 | Finalized classification of the Sentinel-2 image from September 13, 2016 highlighting how low-density vegetation is misclassified. **(A)** True color composite and resulting map classification (thresholded at ≥80% probability of being vegetated) indicating location of field survey points of a sandy habitat (black triangle), low density eelgrass (red x), and a large, dense eelgrass bed (white square). **(B)** Spectra for the same three survey points which all are between 0 and 1 m of water depth. Note the low-density eelgrass training point would not have been included in model training (see section "Field Surveys").

Poursanidis et al., 2019) or red (Traganos and Reinartz, 2018b; Ha et al., 2020). In our study, classification performance decreased when the coastal blue band (band 1) was added due to its low spatial resolution (60-m), which was inappropriate for identification of highly heterogeneous habitat such as in our area of interest. Furthermore, while in very clear waters the coastal blue band provides valuable information on bottom habitat across all depths, the presence of CDOM and particulate matter in temperate optically complex waters limits the applicability of the coastal blue band due to their high absorption across these wavelengths (∼450 nm). Classification performance also decreased when the red band was omitted, which is commonly done in tropical studies (Traganos et al., 2018; Poursanidis et al., 2019), indicating that valuable information was still provided at this wavelengths even though it is strongly attenuated by water. Therefore, the optimum bands in temperate, optically complex waters vary compared to the typical band combination used in tropical studies. Classification of seaweed habitat with Sentinel-2 has focused on intertidal species (Kotta et al., 2018), or those with floating canopies such as Giant kelp (Mora-Soto et al., 2020), and can therefore use information about the red-edge for image classification, including the NIR bands.

Effective masking of optically deep water is an important step in image-based classification procedures as bottom reflectance is no longer detected by the satellite. If a poor maximum depth for image classification is chosen, then all habitat below this depth will be classified as vegetated due to the relatively dark spectra compared to optically shallow regions. Generally, the maximum depth is either specified to coincide with the maximum depth that field survey data were collected (Yucel-Gier et al., 2020), or analytical modeling is used to determine the maximum depth bottom reflectance that can be detected (O'Neill and Costa, 2013; Poursanidis et al., 2019). In Nova Scotia, eelgrass beds have been documented up to 12 m deep (DFO, 2009) and kelp beds to 20 m deep (Johnson and Mann, 1988), yet we masked water deeper than 10 m to coincide with the maximum depth at which field survey points were collected during our study. While the external bathymetry file was at a lower spatial resolution then the satellite data (30 versus 10-m), which would cause errors if bathymetry was required for every pixel particularly in shallower (<5 m) waters, it is reasonable to derive a deep water mask based on the 10-m contour. Therefore, most eelgrass habitat was included in our map product but there is an additional ∼333 km^2 of total surface area between 10 and 20 m of water depth where kelp habitat may exist within the study area. While bottom type could be visually distinguished at depths shallower than the 11–12 m isobaths in regions with high albedo (sandy beach) and sharp contrast (sand into dense vegetation patch), this maximum depth was not consistent across the image. In some areas bottom habitat was only detectable for depths shallower than 2 m. It is not

surprising that there is a large range of maximum water depths where bottom habitat can be classified. In the clear waters of the Mediterranean Sea, the seagrass species *Posidonia oceanica* has been consistently mapped with Sentinel-2 to water depths of 16–40 m (Traganos and Reinartz, 2018b; Traganos et al., 2018; Poursanidis et al., 2019). While in optically complex temperate environments, Sentinel-2 has been used to map eelgrass beds to depths of 4–5 m (Fethers, 2018; Dierssen et al., 2019), and retrieve bathymetry to 10-m deep in Ireland (Casal et al., 2020), both studies observed that this maximum depth was highly dependent on image quality, and depth limits were significantly shallower under non-optimal conditions, which is consistent with our results. Lastly, while Sentinel-2 has not previously been used to detect submerged kelp beds, SPOT and Landsat have been used to map vegetated bottom habitat (eelgrass and kelps) to depths of 7–8 m in Atlantic Canada (Simms and Dubois, 2001; Wilson et al., 2019; St-Pierre and Gagnon, 2020) and down to 10 m in turbid waters in Spain (Casal et al., 2011).

It is not surprising that water transparency would vary over a Sentinel-2 tile characterized by a complex coastline subject to river inputs, sediment redistribution and resuspension, CDOM runoff, and differing phytoplankton concentrations, which all impact the optical characteristics of the water column and are highly variable over even small spatial scales. Furthermore, while the 10-m maximum depth at which bottom habitat can be detected using Sentinel-2 provides a cost effective mean to quantify large-scale distribution of marine macrophytes in Nova Scotia, the variance in the maximum depth that bottom habitat is visible should be further explored. On small scales (single seagrass bed or inlet) a maximum depth should be readily detectable for classifying vegetation coverage. But on large-scales (several inlets to full Sentinel-2 tiles) another approach is required. The simplest approach would be to use the minimum water depth that bottom habitat could be consistently detected, although this would limit the extent of habitat maps to the shallowest waters. Another, albeit tedious, technique could involve manually digitizing a deep-water mask accounting for the spatial heterogeneity of water transparency. A more automated approach may involve deriving water column properties with ACOLITE and the use of detectability limits of different substrates (Vahtmäe et al., 2020) to develop contours where water transparency may shift. Furthermore, the high revisiting time of Sentinel-2 (every 2–3 days in Atlantic Canada) allows for multi-scene compositing, opposed to relying on only classifying the overall "best" image, within a time frame for which vegetation extent is expected to remain similar. This would minimize water transparency impacts on image classification as this process has shown promising results for satellite derived bathymetry studies in turbid waters with Sentinel-2 (Caballero and Stumpf, 2020), and coastal habitat classification with Landsat (Knudby et al., 2014). Regardless, our image classifier performed well to a maximum water depth of 10 m, but some interpretation is required to understand where water transparency is limiting the classification performance. As we used a "best" image for classification, we can conclude that marine macrophytes can be detected to the 10 m depth contour in Atlantic Canada under optimal conditions, and in sub-optimal conditions this value likely varies between the 4–8 m depth contour, although further work would be required to define the lower threshold.

The final map classification yielded an overall map accuracy of 79% for the binary classification of vegetation presence and absence. This is comparable to other Sentinel-2 coastal habitat mapping studies for submerged seagrasses in optically complex waters of Denmark (73%; Fethers, 2018) and in clear waters in Turkey (75–78%; Yucel-Gier et al., 2020), Italy (82–88%; Dattola et al., 2018), New Zealand (88%; Ha et al., 2020), and Greece (58–96%; Traganos and Reinartz, 2018b; Traganos et al., 2018; Poursanidis et al., 2019). The large range of accuracy values for the study carried out in the coastal waters of Greece reflects differences in their seascapes. The lowest accuracy values (58%) occurred in a fragmented seascape with large amounts of mixed habitat types (Poursanidis et al., 2019), the highest (96%) occurred in a small ($\sim$3 km^2) study region with large seagrass beds (Traganos and Reinartz, 2018b), and intermediate values (72%) were obtained for a classification encompassing the entire Aegean and Ionian Seas (Traganos et al., 2018). Elsewhere in Atlantic Canada, submerged kelp and eelgrass habitat has been classified using the high-resolution SPOT-6/7 imagery with an overall map accuracy of $\sim$88% at bay-wide scales (Wilson et al., 2019; St-Pierre and Gagnon, 2020). Consequently, our accuracy metrics would likely improve if we focused on smaller spatial scales where classification models can be fine-tuned to specific habitat-types and water column properties. Still, good accuracy metrics were achieved for the full tile classification, providing accurate maps of vegetated areas for marine spatial planning. While the previous Atlantic Canada studies were punctual in space and time, and demonstrated feasibility of using satellite remote sensing to map bottom habitat in Atlantic Canada, this study represents a first step to routinely classify and monitor bottom habitat in Atlantic Canada to inform habitat management policies at effective cost.

This study only explored the limits of empirical, image-based classification procedures to map marine macrophyte habitat with Sentinel-2 in the optically complex waters of Atlantic Canada. Further work includes comparing the results from the image-based classification to a map derived from a semi-analytical inversion models. Inversion methods solve simultaneously for depth, bottom reflectance, and water IOPs but are highly sensitive to atmospheric correction errors and were developed for hyperspectral data (Lee et al., 1999). To date, they have had limited applications for multispectral data due to the high number of unknown parameters (absorption, scattering, depth, and bottom reflectance) relative to the number of spectral bands (Garcia et al., 2020). In the case of Sentinel-2, only three water-penetrating spectral bands are available at a 10-m spatial resolution, which is inadequate to characterize both the water column, depth, and bottom reflectance (Dierssen et al., 2019). To our knowledge, only one study has explored semi-analytical inversion of Sentinel-2 data to map seagrass habitat and derive water column properties in a tropical environment (Traganos and Reinartz, 2018a). To do so, they first solved for water depth with an empirical satellite-derived bathymetry approach by regressing *in situ* measured depth against the coastal blue and green ratio, and then solved for water column properties

and bottom reflectance using the three 10-m bands (blue, green, and red) with the downscaled 60-m coastal blue and 20-m red-edge (740 nm) bands, and the derived depth layer with a modified HOPE (Hyperspectral Optimization Process Exemplar) model (Lee et al., 1999). The addition of the lower-resolution spatial bands in our study region would complicate benthic habitat mapping due to the complex coastline and high spatial heterogeneity of both bottom habitat and water depth.

CONCLUSION

The freely available Sentinel-2 satellite imagery time series provides a new opportunity to generate large scale vegetation habitat maps, and examine how vegetation extent changes over time, at a spatial resolution of about a tenth that of the Landsat imagery series (i.e., 100 m^2 for Sentinel-2 against 900 m^2 for Landsat-8). As such, Sentinel-2 has been used to map the extent of marine macrophytes in single inlets and bays (Traganos and Reinartz, 2018a; Dierssen et al., 2019), regionally (Traganos et al., 2018), and globally (Mora-Soto et al., 2020). Such uses at both small and large spatial scales show promise in Atlantic Canada, provided that accurate water transparency masks are generated. In regions where water transparency limits Sentinel-2 mapping capabilities, gaps in coverage can be addressed with *in situ* approaches such as sonar deployment (Vandermeulen, 2014). Using Sentinel-2, we found that two complimentary approaches provide a unique, robust and efficient classification of bottom habitat. The simple band-ratio thresholds can classify vegetation extent in shallow, sandy waters, and when the thresholds method fails the random forests machine learning classifier successfully denotes the location of vegetated habitat. From the classified habitat maps, estimates of surface area coverage of marine macrophyte habitat can be generated. Although attempted, Sentinel-2 does not have the spectral resolution to distinguish seagrass from seaweed dominated habitats in the optically complex waters of our study region, this finding is in contrast to other studies that took place in tropical waters (e.g., Kovacs et al., 2018). As such, the final vegetation maps can be combined with other data layers including depth, substrate, exposure, species distribution models and/or local ecological knowledge to qualitatively differentiate eelgrass from seaweed habitats (Lauer and Aswani, 2008; Wilson et al., 2019; Beca-Carretero et al., 2020). Benthic habitat maps are an essential data layer to inform the monitoring and management of macrophyte dominated habitats, and Sentinel-2 provides a cost-effective tool to quantify these habitats.

DATA AVAILABILITY STATEMENT

The raw data supporting the conclusions of this article will be made available by the authors, without undue reservation, to any qualified researcher.

AUTHOR CONTRIBUTIONS

MW and ED conceived the study. KW performed all data analysis and drafted the initial manuscript. MW organized field operations. All authors contributed substantially to the manuscript revision and review.

FUNDING

This study was funded by Fisheries and Oceans Canada Strategic Program for Ecosystem-Based Research and Advice (SPERA). The study also benefited from in-kind support from the Oceans and Coastal Management Division, Ecosystem Management Branch.

ACKNOWLEDGMENTS

We thank J. O'Brien and B. Roethlisberger for support in the field and laboratory. We thank V. Stuart and C. Caverhill for reviewing the manuscript and A. Hilborn for IT support. We also thank ESA for freely providing Sentinel-2 data.

SUPPLEMENTARY MATERIAL

The Supplementary Material for this article can be found online at: https://www.frontiersin.org/articles/10.3389/fenvs.2020.579856/full#supplementary-material

REFERENCES

Barbier, E. B., Hacker, S. D., Kennedy, C., Koch, E. W., Stier, A. C., and Silliman, B. R. (2011). The value of estuarine and coastal ecosystem services. *Ecol. Monogr.* 81, 169–193.

Barillé, L., Robin, M., Harin, N., Bargain, A., and Launeau, P. (2010). Increase in seagrass distribution at Bourgneuf Bay (France) detected by spatial remote sensing. *Aquat. Bot.* 92, 185–194. doi: 10.1016/j.aquabot.2009.11.006

Barrell, J., Grant, J., Hanson, A., and Mahoney, M. (2015). Evaluating the complementarity of acoustic and satellite remote sensing for seagrass landscape mapping. *Int. J. Remote Sens.* 36, 4069–4094. doi: 10.1080/01431161.2015.1076208

Beca-Carretero, P., Varela, S., Stengel, D. B., Beca-Carretero, P., Varela, S., and Stengel, D. B. (2020). A novel method combining species distribution models, remote sensing, and field surveys for detecting and mapping subtidal seagrass meadows. *Aquat. Conserv. Mar. Freshw. Ecosyst* 30, 1098–1110. doi: 10.1002/aqc.3312

Bell, T. W., Allen, J. G., Cavanaugh, K. C., and Siegel, D. A. (2020). Three decades of variability in California's giant kelp forests from the Landsat satellites. *Remote Sens. Environ.* 238:110811. doi: 10.1016/j.rse.2018.06.039

Breiman, L. (2001). *Random Forests in Machine Learning*. Berlin: Springer, 5–32.

Caballero, I., and Stumpf, R. P. (2020). Towards routine mapping of shallow bathymetry in environments with variable turbidity: contribution of Sentinel-2A/B satellites mission. *Remote Sens.* 12:451.

Casal, G., Hedley, J. D., Monteys, X., Harris, P., Cahalane, C., and Mccarthy, T. (2020). Satellite-derived bathymetry in optically complex waters using a model inversion approach and Sentinel-2 data. *Estuar. Coast. Shelf Sci.* 241:106814. doi: 10.1016/j.ecss.2020.106814

Casal, G., Sánchez-Carnero, N., Sánchez-Rodríguez, E., and Freire, J. (2011). Remote sensing with SPOT-4 for mapping kelp forests in turbid waters on the south European Atlantic shelf. *Estuar. Coast. Shelf Sci.* 91, 371–378. doi: 10.1016/j.ecss.2010.10.024

Dattola, L., Rende, F. S., Di Mento, R., Dominici, R., Cappa, P., Scalise, S., et al. (2018). Comparison of Sentinel-2 and Landsat-8 OLI satellite images vs. high spatial resolution images (MIVIS and WorldView-2) for mapping *Posidonia oceanica* meadows. *Proc. SPIE* 10784:1078419. doi: 10.1117/12.2326798

DFO (2009). Does eelgrass (*Zostera marina*) meet the criteria as an ecologically significant species? *DFO Can. Sci. Advis. Sec. Sci. Advis. Rep.* 2009/018.

DFO (2019). Biophysical and ecological overview of the Eastern Shore Islands Area of Interest (AOI). *DFO Can. Sci. Advis. Sec. Sci. Advis. Rep.* 2019/016.

Dierssen, H. M., Bostrom, K. J., Chlus, A., Hammerstrom, K., Thompson, D. R., and Lee, Z. (2019). Pushing the limits of seagrass remote sensing in the turbid waters of Elkhorn Slough, California. *Remote Sens.* 11, 1664. doi: 10.3390/rs11141664

Drusch, M., Del Bello, U., Carlier, S., Colin, O., Fernandez, V., Gascon, F., et al. (2012). Sentinel-2: ESA's optical high-resolution mission for GMES operational services. *Remote Sens. Environ.* 120, 25–36. doi: 10.1016/j.rse.2011.11.026

Duarte, C. M., Losada, I. J., Hendriks, I. E., Mazarrasa, I., and Marba, N. (2013). The role of coastal plant communities for climate change mitigation and adaptation. *Nat. Clim. Chang.* 3, 961–968. doi: 10.1038/NCLIMATE1970

Duffy, J. E., Benedetti-Cecchi, L., Trinanes, J., Muller-Karger, F. E., Ambo-Rappe, R., Boström, C., et al. (2019). Toward a coordinated global observing system for seagrasses and marine macroalgae. *Front. Mar. Sci.* 6:317. doi: 10.3389/fmars.2019.00317

Fauzan, M. A., Kumara, I. S. W., Yogyantoro, R., Suwardana, S., Fadhilah, N., Nurmalasari, I., et al. (2017). Assessing the capability of Sentinel-2A data for mapping seagrass percent cover in Jerowaru. *East Lombok. Indones. J. Geogr.* 49, 195–203. doi: 10.22146/ijg.28407

Fethers, J. O. (2018). *Remote sensing of eelgrass using Object Based Image Analysis and Sentinel-2 Imagery*. Master Thesis, Aalborg University, Aalborg.

Filbee-Dexter, K., and Wernberg, T. (2018). Rise of turfs: a new battlefront for globally declining kelp forests. *Bioscience* 68, 64–76. doi: 10.1093/biosci/bix147

Foody, G. M. (2002). Status of land cover classification accuracy assessment. *Remote Sens. Environ.* 80, 185–201. doi: 10.1016/S0034-4257(01)00295-4

Gamer, M., Lemon, J., and Singh, I. F. P. (2019). *irr: Various Coefficients of Interrater Reliability and Agreement*. R package version 0.84.1.

Garcia, R. A., Lee, Z., Barnes, B. B., Hu, C., Dierssen, H. M., and Hochberg, E. J. (2020). Benthic classification and IOP retrievals in shallow water environments using MERIS imagery. *Remote Sens. Environ.* 249:112015. doi: 10.1016/j.rse.2020.112015

Ha, N. T., Manley-Harris, M., Pham, T. D., and Hawes, I. (2020). A comparative assessment of ensemble-based machine learning and maximum likelihood methods for mapping seagrass using Sentinel-2. *Remote Sens.* 12:355.

Hedley, J. D., Harborne, A. R., and Mumby, P. J. (2005). Simple and robust removal of sun glint for mapping shallow-water benthos. *Int. J. Remote Sens.* 26, 2107–2112. doi: 10.1080/01431160500034086

Hijmans, R. J. (2019). *raster: Geographic Data Analysis and Modeling*. R package version 3.0-7

Hogrefe, K. R., Ward, D. H., Donnelly, T. F., and Dau, N. (2014). Establishing a baseline for regional scale monitoring of eelgrass (*Zostera marina*) habitat on the lower Alaska Peninsula. *Remote Sens.* 6, 12447–12477. doi: 10.3390/rs61212447

Hossain, M. S., Bujang, J. S., Zakaria, M. H., and Hashim, M. (2015). The application of remote sensing to seagrass ecosystems: an overview and future research prospects. *Int. J. Remote Sens.* 36, 61–114. doi: 10.1080/01431161.2014.990649

Islam, K. A., Hill, V., Schaeffer, B., Zimmerman, R., and Li, J. (2020). Semi-supervised adversarial domain adaptation for seagrass detection using multispectral images in coastal areas. *Data Sci. Eng.* 5, 111–125. doi: 10.1007/s41019-020-00126-0

Johnson, C. R., and Mann, K. H. (1988). Diversity, patterns of adaptation, and stability of Nova Scotian kelp beds. *Ecol. Monogr.* 58, 129–154.

Knudby, A., Nordlund, L. M., Palmqvist, G., Wikström, K., Koliji, A., Lindborg, R., et al. (2014). Using multiple Landsat scenes in an ensemble classifier reduces classification error in a stable nearshore environment. *Int. J. Appl. Earth Obs. Geoinf.* 28, 90–101. doi: 10.1016/j.jag.2013.11.015

Kotta, J., Valdivia, N., Kutser, T., Toming, K., Rätsep, M., and Orav-Kotta, H. (2018). Predicting the cover and richness of intertidal macroalgae in remote areas: a case study in the Antarctic Peninsula. *Ecol. Evol.* 8, 9086–9094. doi: 10.1002/ece3.4463

Kovacs, E., Roelfsema, C. M., Lyons, M., Zhao, S., and Phinn, S. R. (2018). Seagrass habitat mapping: how do Landsat 8 OLI, Sentinel-2. ZY-3A, and Worldview-3 perform? *Remote Sens. Lett.* 9, 686–695. doi: 10.1080/2150704X.2018.1468101

Kuhn, M. (2019). *caret: Classification and Regression Training*. R package version 6.0-84.

Kutser, T., Hedley, J., Giardino, C., Roelfsema, C. M., and Brando, V. E. (2020). Remote sensing of shallow waters – A 50 year retrospective and future directions. *Remote Sens. Environ.* 240:111619. doi: 10.1016/j.rse.2019.111619

Kutser, T., Vahtmäe, E., and Praks, J. (2009). A sun glint correction method for hyperspectral imagery containing areas with non-negligible water leaving NIR signal. *Remote Sens. Environ.* 113, 2267–2274. doi: 10.1016/j.rse.2009.06.016

Lauer, M., and Aswani, S. (2008). Integrating indigenous ecological knowledge and multi-spectral image classification for marine habitat mapping in Oceania. *Ocean Coast. Manag.* 51, 495–504. doi: 10.1016/j.ocecoaman.2008.04.006

Lee, Z., Carder, K. L., Mobley, C. D., Steward, R. G., and Patch, J. S. (1999). Hyperspectral remote sensing for shallow waters: 2 Deriving bottom depths and water properties by optimization. *Appl. Opt.* 38:3831. doi: 10.1364/ao.38.003831

León-Pérez, M. C., Hernández, W. J., and Armstrong, R. A. (2019). Characterization and distribution of seagrass habitats in a caribbean nature reserve using high-resolution satellite imagery and field sampling. *J. Coast. Res.* 35:937. doi: 10.2112/jcoastres-d-18-00106.1

Leutner, B., Horning, N., and Schalb-Willman, J. (2019). *RStoolbox: Tools for Remote Sensing Data Analysis*. R package version 0.2.6.

Lyzenga, D. R. (1978). Passive remote sensing techniques for mapping water depth and bottom features. *Appl. Opt.* 17:379. doi: 10.1364/ao.17.000379

Macdonald, C., Webster, T., and Livingstone, B. (2012). *Identification and Quantification of Rockweed Using High-Resolution Satellite Imagery*. Report submitted to Acadian SeaPlants Limited.

MacQueen, J. (1967). Some methods for classification and analysis of multivariate observations. Proceedings of 5th Berkeley Symposium on Mathematical Statistics and Probability. *Univ. Calif. Press* 1, 281–297.

Marcello, J., Eugenio, F., Martín, J., and Marqués, F. (2018). Seabed mapping in coastal shallow waters using high resolution multispectral and hyperspectral imagery. *Remote Sens.* 10:1208. doi: 10.3390/rs10081208

McKinna, L. I. W., Fearns, P. R. C., Weeks, S. J., Werdell, P. J., Reichstetter, M., Franz, B. A., et al. (2015). A semianalytical ocean color inversion algorithm with explicit water column depth and substrate reflectance parameterization. *J. Geophys. Res. Ocean.* 120, 1741–1770. doi: 10.1002/2014JC010224

Milton, G. R., Parsons, F. M. G., and McIntyre, L. B. J. H. C. (2009). Interim report of eelgrass classification project. *Nova Sco. Dep. Nat. Resour.* 32.

Mora-Soto, A., Palacios, M., Macaya, E. C., Gómez, I., Huovinen, P., Pérez-Matus, A., et al. (2020). A high-resolution global map of giant kelp (*Macrocystis pyrifera*) forests and intertidal green algae (Ulvophyceae) with Sentinel-2 imagery. *Remote Sens.* 12:694. doi: 10.3390/rs12040694

Mumby, P. J., Clark, C. D., Green, E. P., and Edwards, A. J. (1998). Benefits of water column correction and contextual editing for mapping coral reefs. *Int. J. Remote Sens.* 19, 203–210. doi: 10.1080/014311698216521

Murphy, G. E. P., Wong, M. C., and Lotze, H. K. (2019). A human impact metric for coastal ecosystems with application to seagrass beds in Atlantic Canada. *Facets* 4, 210–237. doi: 10.1139/facets-2018-0044

O'Neill, J. D., and Costa, M. (2013). Mapping eelgrass (*Zostera marina*) in the Gulf Islands National Park Reserve of Canada using high spatial resolution satellite and airborne imagery. *Remote Sens. Environ.* 133, 152–167. doi: 10.1016/j.rse.2013.02.010

Orth, R. J., Carruthers, T. J. B., Denntson, W. C., Duarte, C. M., Fourgurean, J. W., Heck, Jr. K. L, et al. (2006). A global crisis for seagrass ecosystems. *Bioscience* 56, 987–997.

Poursanidis, D., Topouzelis, K., and Chrysoulakis, N. (2018). Mapping coastal marine habitats and delineating the deep limits of the Neptune's seagrass meadows using very high resolution Earth observation data. *Int. J. Remote Sens.* 39, 8670–8687. doi: 10.1080/01431161.2018.1490974

Poursanidis, D., Traganos, D., Reinartz, P., and Chrysoulakis, N. (2019). On the use of Sentinel-2 for coastal habitat mapping and satellite-derived bathymetry estimation using downscaled coastal aerosol band. *Int. J. Appl. Earth Obs. Geoinf.* 80, 58–70. doi: 10.1016/j.jag.2019.03.012

R Core Team. (2019). *R: A Language and Environment for Statistical Computing*. Vienna: R Foundation for Statistical Computing.

Richards, J. A. (1986). *Remote Sensing Digital Image Analysis*. Berlin: Springer-Verlag.

Roelfsema, C. M., Lyons, M., Kovacs, E. M., Maxwell, P., Saunders, M. I., Samper-Villarreal, J., et al. (2014). Multi-temporal mapping of seagrass cover, species and biomass: a semi-automated object based image analysis approach. *Remote Sens. Environ.* 150, 172–187. doi: 10.1016/j.rse.2014.05.001

Roelfsema, C. M., Phinn, S., Udy, N., and Maxwell, P. (2009). An integrated field and remote sensing approach for mapping seagrass cover, moreton bay. *Austr. J. Spat. Sci.* 54, 45–62. doi: 10.1080/14498596.2009.9635166

Schmidt, A. L., Coll, M., Romanuk, T. N., and Lotze, H. K. (2011). Ecosystem structure and services in eelgrass *Zostera marina* and rockweed *Ascophyllum nodosum* habitats. *Mar. Ecol. Prog. Ser.* 437, 51–68. doi: 10.3354/meps09276

Schroeder, S. B., Dupont, C., Boyer, L., Juanes, F., and Costa, M. (2019). Passive remote sensing technology for mapping bull kelp (*Nereocystis luetkeana*): a review of techniques and regional case study. *Glob. Ecol. Conserv.* 19:e00683. doi: 10.1016/j.gecco.2019.e00683

Simms, L., and Dubois, J. M. M. (2001). Satellite remote sensing of submerged kelp beds on the Atlantic coast of Canada. *Int. J. Remote Sens.* 22, 2083–2094. doi: 10.1080/01431160116919

St-Pierre, A. P., and Gagnon, P. (2020). Kelp-bed dynamics across scales: enhancing mapping capability with remote sensing and GIS. *J. Exp. Mar. Bio. Ecol.* 522:151246. doi: 10.1016/j.jembe.2019.151246

Su, L., and Huang, Y. (2019). Seagrass resource assessment using World View-2 imagery in the Redfish Bay, Texas. *J. Mar. Sci. Eng.* 7:98. doi: 10.3390/jmse7040098

Teagle, H., Hawkins, S. J., Moore, P. J., and Smale, D. A. (2017). The role of kelp species as biogenic habitat formers in coastal marine ecosystems. *J. Exp. Mar. Bio. Ecol.* 492, 81–98.

Traganos, D., Aggarwal, B., Poursanidis, D., Topouzelis, K., Chrysoulakis, N., and Reinartz, P. (2018). Towards global-scale seagrass mapping and monitoring using Sentinel-2 on Google Earth Engine: the case study of the Aegean and Ionian Seas. *Remote Sens.* 10, 1–14. doi: 10.3390/rs10081227

Traganos, D., and Reinartz, P. (2018a). Machine learning-based retrieval of benthic reflectance and *Posidonia oceanica* seagrass extent using a semi-analytical inversion of Sentinel-2 satellite data. *Int. J. Remote Sens.* 39, 9428–9452. doi: 10.1080/01431161.2018.1519289

Traganos, D., and Reinartz, P. (2018b). Mapping Mediterranean seagrasses with Sentinel-2 imagery. *Mar. Pollut. Bull.* 134, 197–209. doi: 10.1016/j.marpolbul.2017.06.075

Vahtmäe, E., and Kutser, T. (2013). Classifying the baltic sea shallow water habitats using image-based and spectral library methods. *Remote Sens.* 5, 2451–2474. doi: 10.3390/rs5052451

Vahtmäe, E., Paavel, B., and Kutser, T. (2020). How much benthic information can be retrieved with hyperspectral sensor from the optically complex coastal waters? *J. Appl. Remote Sens.* 14:016504. doi: 10.1117/1.JRS.14.016504

Vandermeulen, H. (2014). Bay-scale assessment of eelgrass beds using sidescan and video. *Helgol. Mar. Res.* 68, 559–569. doi: 10.1007/s10152-014-0412-5

Vanhellemont, Q. (2019). Adaptation of the dark spectrum fitting atmospheric correction for aquatic applications of the Landsat and Sentinel-2 archives. *Remote Sens. Environ.* 225, 175–192. doi: 10.1016/j.rse.2019.03.010

Vanhellemont, Q., and Ruddick, K. (2016). Acolite for Sentinel-2: aquatic applications of MSI imagery. *Eur. Sp. Agency* 740, 9–13.

Vapnick, V. (1995). *The Nature of Statistical Learning Theory*. New York, NY: Springer-Verlag.

Vercaemer, B., Wong, M. C., and Bravo, M. A. (2018). Fish assemblages in rockweed (*Ascophyllum nodosum* (L.) Le Jolis) beds on the Atlantic Coast of Nova Scotia, Canada. *Can. Tech. Rep. Fish. Aquat. Sci* 3249:34.

Wang, M. (2010). Atmospheric correction for remotely-sensed ocean-colour products. *Rep. Monogr. Int. Ocean. Coord. Gr.* 10, 1–78.

Waycott, M., Duarte, C. M., Carruthers, T. J. B., Orth, R. J., Dennison, W. C., Olyarnik, S., et al. (2009). Accelerating loss of seagrasses across the globe threatens coastal ecosystems. *Proc. Natl. Acad. Sci. U.S.A.* 106, 12377–12381. doi: 10.1073/pnas.0905620106

Webster, T. (2018). *Advanced coastal mapping along the South Shore of NS to support Hydrodynamic Modelling*. Final Report. Technical report, Applied Geomatics Research Group, NSCC, Middleton, NS.

Webster, T., MacDonald, C., McGuigan, K., Crowell, N., Lauzon-Guay, J.-S., and Collins, K. (2020). Calculating macroalgal height and biomass using bathymetric LiDAR and a comparison with surface area derived from satellite data in Nova Scotia. *Canada. Bot. Mar.* 63, 43–59. doi: 10.1515/bot-2018-0080

Webster, T., McGuigan, K., Crowell, N., Collins, K., and MacDonald, C. (2016). Optimization of data collection and refinement of post-processing techniques for Maritime Canada's first shallow water topographic-bathymetric lidar survey. *J. Coast. Res.* 76, 31–43. doi: 10.2112/si76-004

Wicaksono, P., Aryaguna, P. A., and Lazuardi, W. (2019). Benthic habitat mapping model and cross validation using machine-learning classification algorithms. *Remote Sens.* 11:1279. doi: 10.3390/rs11111279

Wicaksono, P., and Lazuardi, W. (2018). Assessment of PlanetScope images for benthic habitat and seagrass species mapping in a complex optically shallow water environment. *Int. J. Remote Sens.* 39, 5739–5765. doi: 10.1080/01431161.2018.1506951

Wickham, H., and Bryan, J. (2019). *readxl: Read Excel Files. R Package Version 1.3.1*. Availabel online at: https://cran.rproject.org/package=readxl

Wilson, K. L., and Devred, E. (2019). Exploratory analysis to retrieve biogenic habitat and bottom substrate type from high-resolution satellite imagery in Atlantic Canada. *Can. Tech. Rep. Fish. Aquat. Sci* 3337:56.

Wilson, K. L., Skinner, M. A., and Lotze, H. K. (2019). Eelgrass (*Zostera marina*) and benthic habitat mapping in Atlantic Canada using high-resolution SPOT 6/7 satellite imagery. *Estuar. Coast. Shelf Sci.* 226:106292. doi: 10.1016/j.ecss.2019.106292

Wong, M. C., and Dowd, M. (2016). A model framework to determine the production potential of fish derived from coastal habitats for use in habitat restoration. *Estuaries and Coasts* 39, 1785–1800. doi: 10.1007/s12237-016-0121-1

Wong, M. C., and Kay, L. M. (2019). Partial congruence in habitat patterns for taxonomic and functional diversity of fish assemblages in seagrass ecosystems. *Mar. Biol.* 166:46. doi: 10.1007/s00227-019-3488-2

Yucel-Gier, G., Kocak, G., Akcali, B., Ilhan, T., and Duman, M. (2020). Evaluation of *Posidonia oceanica* map generated by Sentinel-2 image: gulbahce Bay test site. *Turkish J. Fish. Aquat. Sci.* 20, 571–581. doi: 10.4194/1303-2712-v20_7_07

Zelada Leon, A., Huvenne, V. A. I., Benoist, N. M. A., Ferguson, M., Bett, B. J., and Wynn, R. B. (2020). Assessing the repeatability of automated seafloor cassification algorithms, with application in marine protected area monitoring. *Remote Sens.* 12:1572. doi: 10.3390/rs12101572

Zoffoli, M., Frouin, R., and Kampel, M. (2014). Water column correction for coral reef studies by remote sensing. *Sensors* 14, 16881–16931. doi: 10.3390/s140916881

Conflict of Interest: The authors declare that the research was conducted in the absence of any commercial or financial relationships that could be construed as a potential conflict of interest.

Copyright © 2020 Wilson, Wong and Devred. This is an open-access article distributed under the terms of the Creative Commons Attribution License (CC BY). The use, distribution or reproduction in other forums is permitted, provided the original author(s) and the copyright owner(s) are credited and that the original publication in this journal is cited, in accordance with accepted academic practice. No use, distribution or reproduction is permitted which does not comply with these terms.

frontiers in Environmental Science

ORIGINAL RESEARCH
published: 20 November 2020
doi: 10.3389/fenvs.2020.585529

Airborne Radiometry for Calibration, Validation, and Research in Oceanic, Coastal, and Inland Waters

Liane S. Guild[1], Raphael M. Kudela[2], Stanford B. Hooker[3], Sherry L. Palacios[4] and Henry F. Houskeeper[5]*

[1] Biospheric Science Branch, Earth Science Division, NASA Ames Research Center, Moffett Field, CA, United States, [2] Institute of Marine Sciences, Ocean Sciences Department, University of California, Santa Cruz, Santa Cruz, CA, United States, [3] Ocean Ecology Laboratory, NASA Goddard Space Flight Center, Greenbelt, MD, United States, [4] Department of Marine Science, California State University, Monterey Bay, Seaside, CA, United States, [5] Department of Geography, University of California, Los Angeles, Los Angeles, CA, United States

OPEN ACCESS

Edited by:
Xuan Zhu,
Monash University, Australia

Reviewed by:
Mukesh Gupta,
Catholic University of Louvain, Belgium
Claudia Giardino,
National Research Council (IREA-CNR), Italy

***Correspondence:**
Liane S. Guild
liane.s.guild@nasa.gov

Specialty section:
This article was submitted to Environmental Informatics and Remote Sensing, a section of the journal Frontiers in Environmental Science

Received: *20 July 2020*
Accepted: *12 October 2020*
Published: *20 November 2020*

Citation:
Guild LS, Kudela RM, Hooker SB, Palacios SL and Houskeeper HF (2020) Airborne Radiometry for Calibration, Validation, and Research in Oceanic, Coastal, and Inland Waters. Front. Environ. Sci. 8:585529. doi: 10.3389/fenvs.2020.585529

Present-day ocean color satellite sensors, which principally provide reliable data on chlorophyll, sediments, and colored dissolved organic material in the open ocean, are not well suited for coastal and inland water studies for a variety of reasons, including coarse spatial and spectral resolution plus challenges with atmospheric correction. National Aeronautics and Space Administration (NASA) airborne mission concepts tested in 2011, 2013, 2017, and 2018 over Monterey Bay, CA, and nearby inland waters have demonstrated the feasibility of improving airborne monitoring and research activities in case-1 and case-2 aquatic ecosystems through the combined use of state-of-the-art above- and in-water measurement capabilities. These competencies have evolved through time to produce a sensor-web approach: imaging spectrometer, microradiometers, and a sun photometer (airborne) with their analogous algorithms, and with corresponding in-water radiometers and ground-based sun photometry. The NASA airborne instrument suite and mission concept demonstrations, leveraging high-quality above- and in-water data, significantly improves the fidelity as well as the spatial and spectral resolution of observations for studying and monitoring water quality in oceanic, coastal, and inland water ecosystems. The goal of this series of projects was to develop and fly a portable airborne sensor suite for NASA science missions focusing on a gradient of water types from oligotrophic to turbid waters addressing the challenges of an optically complex coastal ocean zone and inland waters. The airborne radiometry in this range of aquatic conditions and sites has supported improved results of studies of water quality and biogeochemistry and provides capabilities for research areas such as ocean productivity and biogeochemistry; aquatic impacts of coastal landscape alteration; coastal, estuarine, and inland waters ecosystem productivity; atmospheric correction; and regional climate variability.

Keywords: ocean color, water quality, atmospheric correction, case-1 waters, case-2 waters

INTRODUCTION

The lack of optimized remote sensing capabilities for coastal and inland waters that can bridge limited spatial coverage and high temporal resolution observations from in-water systems, such as buoys, as well as limited spatial and temporal coverage of ship-based validation with the coarse spatial, temporal, and spectral resolution of satellite data for ocean color products is a significant gap. In contrast to the open ocean, coastal and inland waters are difficult regions to accurately retrieve ocean color radiant flux (Dierssen et al., 2006; Dunagan et al., 2009; Guild et al., 2011, 2019; Turpie et al., 2015, 2016). In coastal areas, the magnitude of the radiance signal in the visible (VIS) range (400–700 nm) is highly variable, ranging from very dark values in clear, deep water, as well as in water dominated by colored dissolved organic matter (CDOM) (e.g., Brezonik et al., 2015; Palmer et al., 2015). For example, typical albedo for deep ocean water is often assumed to be approximately 5% (Moses et al., 2012), but productive and turbid inland waters can easily exceed 25% or more (Kudela et al., 2019). Legacy and presently operational ocean color satellite sensors such as Sea-viewing Wide Field-of-View Sensor (SeaWiFS), Moderate Resolution Imaging Spectrometer (MODIS), Medium Resolution Imaging Spectrometer (MERIS), and the Visible Infrared Imaging Radiometer Suite (VIIRS) are optimally designed for open-ocean imagery. They are calibrated for low spectral water-leaving radiances, $L_W(\lambda)$, and produce coarse spatial (km) and spectral resolution. While more recent sensors, such as the Ocean Land Color Instrument (OLCI), Operational Land Imager (OLI), and Multispectral Instrument (MSI), provide improved spatial and spectral resolution, they are not optimized for retrievals over inland waters (Kudela et al., 2019).

Radiance signals are also highly variable in space and time at the land–sea interface due to the dynamic nature of this region. Low signal-to-noise ratio (SNR) measurements of $L_W(\lambda)$ in the blue spectral domain result in negative values using standard re-processing, leading to poor discrimination of pigments from CDOM and poor estimates in the ultraviolet (UV). Aerosol and trace gas plumes from continental sources complicate the task of atmospheric correction, as does cloud cover. Aerosols and water vapor strongly scatter and absorb light in the same region of the spectrum where some ocean color algorithms are derived (e.g., chlorophyll), compounding the problems associated with atmospheric correction and low SNR. Atmospheric correction schemes are also problematic for productive coastal waters. Issues include the use of non-zero near-infrared (NIR) radiances and poor SNR values, complicating the use of short-wave infrared (SWIR) observations to improve atmospheric correction (Siegel et al., 2000; Shi and Wang, 2009; Werdell et al., 2010). The UV is also potentially useful for discriminating red tides (Kahru and Mitchell, 1998), identifying point sources for pollution (Hooker et al., 2013), and improving atmospheric correction, particularly in turbid coastal waters (Wang et al., 2007; Gao et al., 2009; He et al., 2012). Frequent atmospheric correction failures occur at moderate to high chlorophyll levels, leading to data loss in these dynamic regions (Loisel et al., 2013; Houskeeper and Kudela, 2019), while most existing instruments for calibration, validation, and research (CVR) measurements, as well as spectral radiometers, exhibit poor performance in the UV.

The limited legacy and presently operational ocean color satellites (Groom et al., 2019) having both multiple mid-range spectral bands (500–600 nm) and high spatial resolution spaceborne sensors makes it difficult to detect high biomass events and "red tides" (Dierssen et al., 2006), one of the main targets for coastal and inland water remote sensing. While this can be mitigated to some extent by switching to red or infrared bands (Houskeeper and Kudela, 2019), there can be both over- and under-estimates based on the specific band configuration (Ryan et al., 2014). There is a demonstrable need for high spatial, spectral, and temporal resolution data to meet these challenges. For the foreseeable future, this can be enhanced with airborne instrumentation well suited for smaller water bodies and enabling higher spatial and spectral resolution measurements (Davis et al., 2007; Gholizadeh et al., 2016) and with agility in timing for event response and time of day for science needs. To bridge the gap between open ocean, coastal, and inland waters, innovation and selection of relevant aquatic airborne instruments for CVR and flight planning to support the science and instrument requirements is crucial (Guild et al., 2011, 2019). Further, aligned sensor technology, site coverage, and data collection contemporaneous with in-water observations enable credible CVR in dynamic coastal and inland aquatic environments. To meet these observational and innovative technology needs, next-generation instrument suites, processing, and data products have been tested in coastal and inland waters during several recent airborne missions on the Naval Postgraduate School's (NPS) Twin Otter (TO): (a) 2011 NASA Coastal and Ocean Airborne Science Testbed (COAST); (b) 2013 NASA Ocean Color Ecosystem Assessments using Novel Instruments and Aircraft (OCEANIA); and (c) the 2017 and 2018 Coastal High Acquisition Rate Radiometers for Innovative Environmental Research (C-HARRIER) campaigns (**Table 1**). These airborne mission technology developments advanced from establishing the flight observation requirements for the instruments individually or as a sensor suite, to flight scenarios that address the remote sensing needs of aquatic environments in support of satellite observations (or high-altitude simulations thereof), and including the processing of airborne data for aquatic CVR for ocean, coastal, and inland targets.

NASA COAST initiated the first in a series of airborne CVR concepts for coastal and inland waters and operated in coastal California in 2011, focusing on the greater Monterey Bay region (**Figures 1**, **2**). The goal of the COAST project was to develop and fly a portable airborne sensor suite for NASA science missions addressing the challenges of an optically complex coastal ocean zone in support of research areas such as water quality, ocean productivity and biogeochemistry, coastal landscape alteration, coastal, estuarine, and inland waters ecosystem productivity, atmospheric correction, and regional climate variability (Guild et al., 2011). The COAST instrument suite included a portable Headwall Hyperspectral Imaging System (HIS), the new Coastal Airborne *In situ* Radiometers (C-AIR) bio-optical radiometer package, and the 14-Channel Ames Airborne Tracking Sun (AATS-14) photometer enabling contemporaneous observations

TABLE 1 | Summary of data collection and instrumentation.

Campaign	Date	Airborne sensors	Above- and in-water sensors	Ancillary remote sensing data
COAST	28 October 2011	HIS, AATS-14, C-AIR	C-OPS, HyperPro II, MicroTOPS	MERIS
OCEANIA	30–31 October 2013	C-AIR	C-OPS, HyperPro II, MicroTOPS	AVIRIS
OCEANIA	4, 5 November 2013	C-AIR	C-OPS, HyperPro II, MicroTOPS	MODIS
C-HARRIER	8, 13–14 September 2017	C-AERO	C-OPS, HyperPro II	MODIS, VHRS
C-HARRIER	26 October 2018	C-AERO	C-OPS, HyperPro II	MODIS, VIIRS

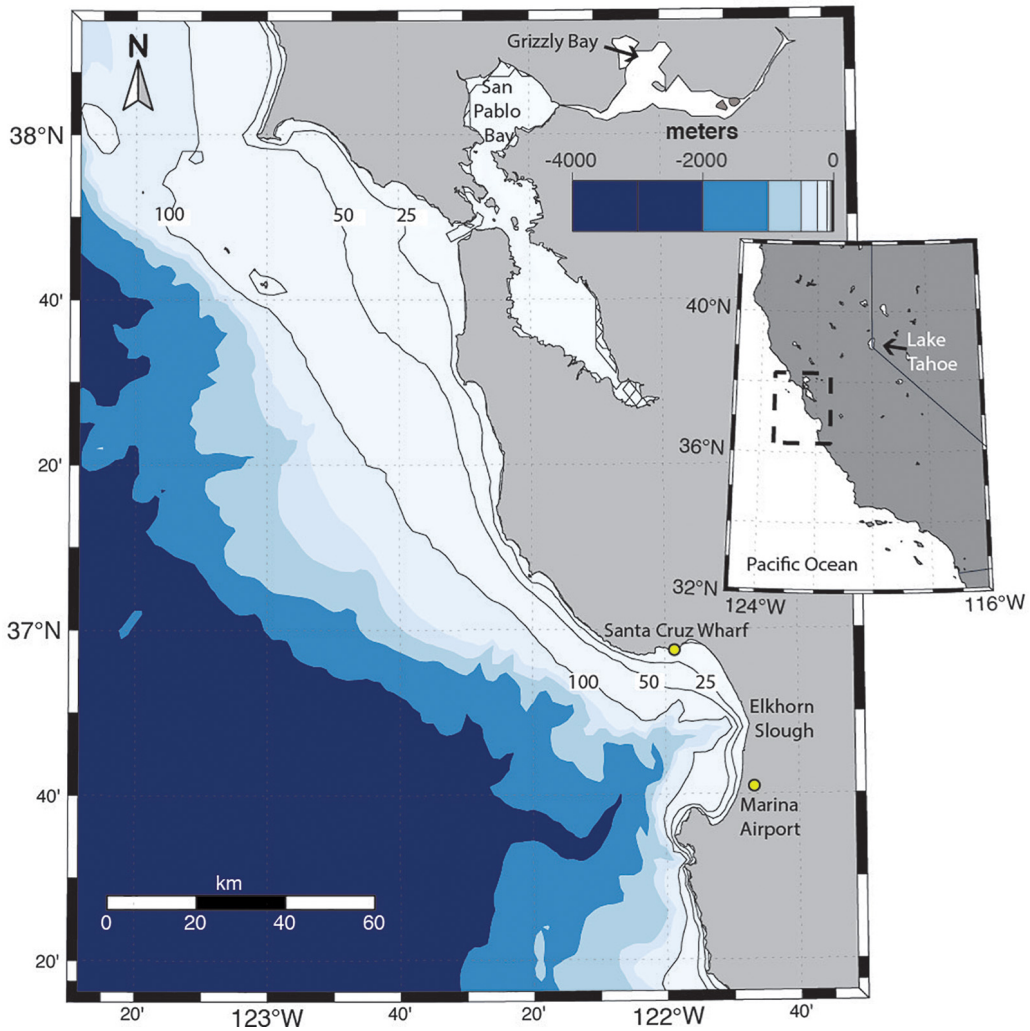

FIGURE 1 | Map of bathymetry and California study site locations of Monterey Bay including Santa Cruz Wharf and Elkhorn Slough, San Pablo Bay, Grizzly Bay, and Lake Tahoe (inset map). The nearby Marina Airport is also identified where the NPS TO is located.

over the same water target for deriving $L_W(\lambda)$ and relevant aerosol optical depth (AOD) to support atmospheric correction schemes. The instrument integration design and flight planning addressed competing instrument observation requirements and solar geometry to optimize instrument measurements. The COAST flight demonstrations advanced opportunities for aquatic ecosystem research and coastal ocean color CVR capabilities by providing a unique airborne payload optimized for remote sensing in optically complex waters.

The 2013 NASA OCEANIA campaign extended the COAST project to focus on apparent optical properties (AOPs) derived from the in-water Compact-Optical Profiling System (C-OPS) built with microradiometers by Biospherical Instruments Inc. (BSI) and from C-AIR flown in COAST aboard the NPS TO aircraft and also built with BSI microradiometers. The OCEANIA project was designed to assess CVR capabilities in support of high-altitude airborne simulation of satellite observations. Flight planning at lowest safe altitude (LSA, e.g.,

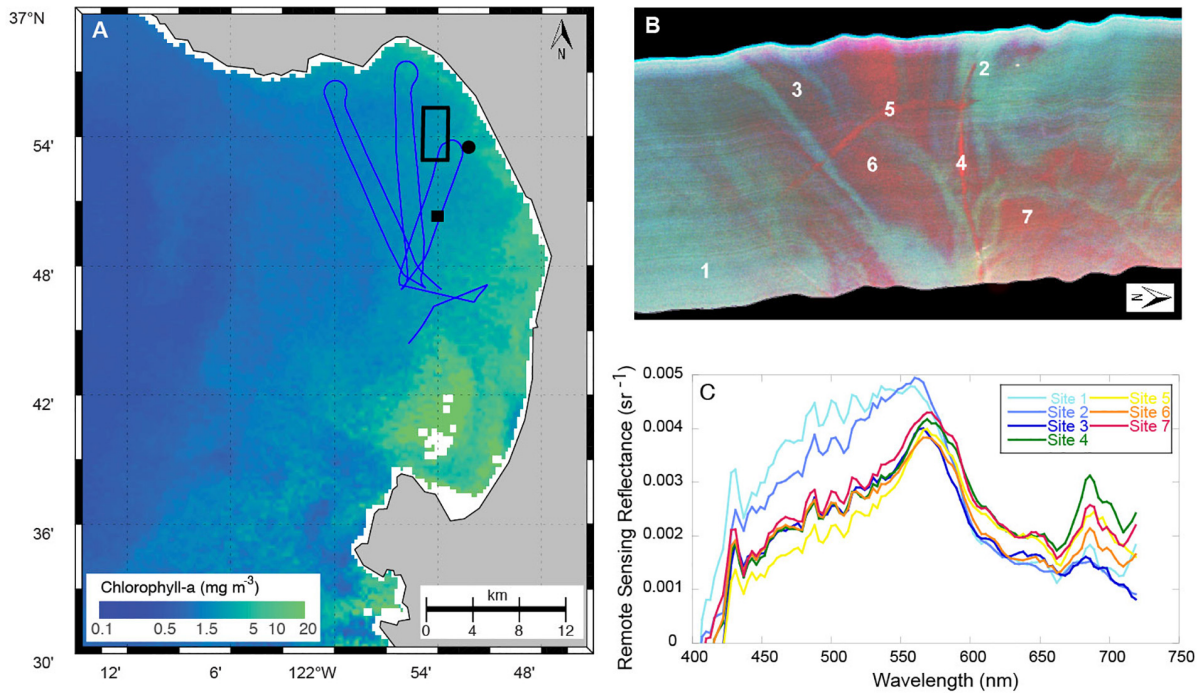

FIGURE 2 | Monterey Bay, CA was the primary target for the airborne missions. **(A)** The MERIS chl *a* image from 28 October 2011 (COAST), with the LSA AATS-14 lines (blue) and the "red tide" (CST17; solid circle) and M0 (CST18; solid square) stations. The rectangular box denotes the region depicted in **(B)**, showing the HIS data as an RGB composite, with red indicating high chlorophyll. **(C)** The spectra from the labels 1–7 in **(B)** from the HIS. The water depths for these seven sites range from approximately 18 to 25 m.

30 m) used flight headings into and out of the principal solar plane during optimal sun elevation to reduce glint, which were coordinated with field measurements and timing of high-altitude aircraft and satellite overpasses, as well as established flight protocols supporting CVR for the radiometers. Both COAST and OCEANIA utilized a sensor-web network approach to enable simultaneous measurements in support of CVR exercises for satellite coastal ocean color products.

The 2017 and 2018 C-HARRIER campaigns built on the technological development and integration of multiple sensors initiated in COAST and OCEANIA CVR activities. The airborne radiometer suite was upgraded to the Compact-Airborne Environmental Radiometers for Oceanography (C-AERO), which was built with the latest generation of BSI microradiometers (Hooker et al., 2018a). The in-water validation data were obtained with a C-OPS instrument equipped with the Compact-Propulsion Option for Profiling Systems (C-PrOPS) accessory, which adds two small digital thrusters to the backplane so it can be maneuvered independently (Hooker et al., 2018a). The thrusters improve the planar and solar geometry of the light apertures, as well as increasing surface loitering while decreasing descent rate. The net effect of these improvements is a vertical sampling resolution (VSR) that is frequently 1 mm or less (Hooker et al., 2020), whereas C-OPS without C-PrOPS typically has a VSR of 1 cm (Hooker et al., 2013).

The C-AERO instrument suite incorporated increased spectral range to collect data at longer wavelengths, a shroud to eliminate stray light, faster data sampling (from 15 Hz in the 2017 mission to 30 Hz in the 2018 mission) to better discretize surface glint from oblique wave facets, and advanced instrument characterization to improve data processing capabilities by using a novel synthetic dark correction approach (c.f. Kudela et al., 2019 and see section "Implementation of Synthetic Dark Corrections for the C-HARRIER Mission"). The increased data acquisition rate of C-AERO enables a rich collection of CVR data within a single satellite pixel as well as more validation data coverage of smaller water targets (e.g., lakes, rivers, and deltas). C-HARRIER will ultimately include a novel airborne sun photometer, also built with microradiometers, called the Sky-Scanning Sun-Tracking Airborne Radiometer (3STAR), thus completing the development of a sensor-web in which radiometric observations can be conducted for airborne, above-water, and in-water modalities using the same hardware and software suite.

Here we document the evolution of the various sensor suites used for COAST, OCEANIA, and C-HARRIER, including mission planning, operational success, and challenges, and the path toward a fully integrated sensor suite. We highlight specific science applications using these data to underscore how an airborne CVR observatory can be used to understand coastal and inland water quality and provide recommendations for airborne missions in support of aquatic remote sensing, including calibration and validation of existing and future satellite platforms.

MATERIALS AND METHODS

The methodology development for this airborne CVR capability was enabled through a NASA mission training activity, subsequent innovation funds to advance focused instrument investigation, and ultimately maturing airborne instrument technology and flight demonstrations over varying water types for science missions. These separate projects advanced the airborne CVR methodology through the team members' expertise in instrument development and ocean biology, ecology, and optics to align science measurement objectives to instrument specifications (Guild et al., 2011, 2019). Further, flight planning on a relevant aircraft to meet science objectives and instrument observation requirements was critical to the success of data acquisition. The following outlines the methodology steps and advances made through each project mission in development of the airborne CVR capability.

First a review of the science requirements supported selection of instruments, or an understanding of their deficiencies, and included identification of relevant channels of the instrument suite aligned to support legacy and next-generation ocean color satellite capabilities. A Science Traceability Matrix (STM) was used to link science objectives and measurements to instrument requirements and performance and provides a conceptual model of the technology threshold needed to meet the measurement objectives. STM science objectives included measurements of aquatic bio-optical properties over spatial extents from less than 1 m to 10 s of meters over coastal waters to capture dynamic coastal phenomena (e.g., blooms and riverine plumes). Corresponding in-water measurements include both apparent (water-leaving radiances) and inherent (absorption, scattering) optical properties at relevant wavelengths (400–800 nm) aligned with satellites used for ocean color (e.g., MERIS, MODIS). These data products form the basis for science questions by deriving relevant ecological and biogeochemical properties from the high-quality water-leaving radiances. Instrument specifications and performance requirements were established in the STM and instruments were evaluated to meet instrument requirements.

For the COAST mission training project, the HIS aligned with the instrument spectral range and was an available test instrument provided by the NASA Ames Research Center (ARC) Airborne Sensor Facility. Additionally, the AATS-14 sun photometer exceeded instrument sensor requirements and was selected for having demonstrated science and flight heritage since 1997 for atmospheric chemistry (Livingston et al., 2003; Redemann et al., 2005, 2009; Russell et al., 2007). The microradiometer instruments (Morrow et al., 2010) provided the instrument channel specifications to align with satellite ocean color sensors and were the underlying foundation of a new CVR radiometric package flying for the first time for COAST and remained the consistent primary instrument suite as the basis for the airborne CVR objective. The flight planning for the AATS-14 sun photometer and HIS were well established; however, the microradiometers were new to integration on an aircraft and flight.

Airborne flight planning over optically dark water targets provides unique challenges from the optically bright targets in terrestrial environments (Mustard et al., 2001; Kudela et al., 2019). Flight plans over water must take into consideration the following: (a) sensor field of view (FOV), integration, and data rate; (b) solar elevation and azimuth to optimize the observational geometry and minimize sun glint; (c) weather mitigation (less than 25% cloud cover); (d) calm wind conditions to simplify water surface roughness modeling, reduce white-cap effects, and facilitate in-water validation measurements; (e) flights $\pm$ 30 min of satellite overpass to capture dynamic changes in water features; (f) coordination with *in situ* validation teams (boat and targets); and (g) for flights including an airborne sun photometer, stacked flight transects at high and low altitudes for full column and intervening layer AOD retrievals.

The TO, operated and maintained by the NPS, was used for all flights. It is a non-pressurized turboprop, twin-engine aircraft. The payload capacity of the TO is 680 kg. The platform endurance is about 5 h in a fully loaded weight configuration. The practical mission ceiling is 5,486 m, or 3,658 m without crew requiring oxygen. Instruments may be installed in racks inside the cabin where a well-characterized community inlet delivers ambient air samples, or in pods either suspended by wing-mounted pylons or mounted on a hard point on the cabin roof. Optical ports and window options for integration are located in certified portals, as well as in the fuselage underside and cabin roof. The NPS has aircraft facility instruments providing position, navigation, time, altitude, groundspeed, heading, pitch, roll, true airspeed, total temperature, dew point, static pressure, dynamic pressure, surface temperature, sky temperature, true wind speed, and wind direction.

COAST Mission Overview

For this study, the COAST project serves as the prime mission model with subsequent extension missions that advanced technical capabilities and methodology in support of improved data quality from airborne observations for aquatics research. The COAST project integrated an instrument suite onboard a platform flown over a location wherein the latter two were trade-study-selected. Examining these trade spaces provided key training opportunities for the team, reflecting typical NASA science flight mission early-phase activities. Following NASA's procedural requirements for missions, the COAST project passed systems engineering and process requirements of Systems Requirements Review, Preliminary Design Review, Critical Design Review, Airworthiness and Flight Readiness Review, and Flight/Mission Readiness Review. This process established the development and integration of the first airborne end-to-end package for simultaneous measurements of ocean color (modified imaging spectrometer), AOD and water vapor column content (sun photometer), and aquatic bio-optical measurements (fixed-wavelength radiometer package) with the airborne components flight-capable on a variety of airborne platforms. All instruments use inputs from an associated precision navigation system during flight, or the onboard cabin navigation data for post-processing after flight. This first deliverable, therefore, provided a fully operational, integrated, and portable airborne instrument suite optimized for coastal and inland water airborne missions.

Flight planning with instrument science and ocean color scientist team members yielded flights that demonstrated CVR protocols (Hooker et al., 2007) for coastal ocean and inland water color through airborne campaigns of the HIS, AATS-14 sun photometer, and C-AIR microradiometer package flown in coordination with satellite and *in situ* observations from ships. The flights produced high spatial resolution (5–10 m), atmospherically corrected and geolocated ocean-color products calibrated to at-sensor radiances and post-processed to derive $L_W(\lambda)$. The primary CVR products from the C-AIR radiometers are $L_W(\lambda)$ and the corresponding normalized forms, e.g., the remote sensing reflectance (R_{rs}); there are numerous applications for these data to produce biogeochemically meaningful products for the coastal ocean as well as inland waters.

COAST Airborne Platform and Instrumentation

The 2011 COAST mission flew at altitudes between approximately 30 and 1,829 m on the NPS TO platform on 28 October 2011 over northern Monterey Bay, California (**Figures 1**, **2**).

The complete COAST flight system included three main instruments, a prototype portable Headwall HIS, AATS-14, and C-AIR, with ancillary supporting instruments (**Table 1**). Sea-truth instrumentation included a MicroTOPS II sun photometer (Solar Light Inc.), C-OPS (BSI), a HyperPro II hyperspectral profiling radiometer (Satlantic), and ancillary supporting instruments including an inherent optical properties (IOP) package consisting of an ac-s (WETLabs), HydroScat-6 (HOBI Labs), and a Conductivity, Temperature, Depth (CTD) instrument (SeaBird Scientific). A detailed comparison of the in-water instruments is provided in Bausell and Kudela (2019) and is not further described here.

Hyperspectral Imaging System

The prototype HIS is a concentric push broom hyperspectral imager of the Offner design optimized in the blue region of the spectrum for marine and freshwater targets. The system was further customized for ocean imaging with a cooled, blue-enhanced charge-coupled device array with 600 × 800 elements and was thermo-electrically cooled to −30°C for increased sensitivity and radiometric stability. The HIS is nadir pointing and mounted on a plate integration design with attachment structures to the seat rails over the nadir port. The HIS was flown at 1,828 m to acquire data at approximately 4 m ground spatial resolution (GSR) with a spectral range of 380–760 nm.

14-Channel Sun Photometer

The AATS-14 measures direct solar-beam transmission (T) at 14 discrete wavelengths from 354 to 2,139 nm, yielding AOD at 13 wavelengths and water vapor column content using T at 940 nm. Azimuth and elevation motors controlled by differential sun sensors rotate the tracking head, keeping the detectors normal to the solar beam. AATS-14 is integrated in a zenith port and on a seat rail mounted truss. AATS-14 has been used extensively to test and improve AOD retrievals by MODIS, SeaWiFS, Multi-angle Imaging SpectroRadiometer (MISR), and many other satellite sensors (Hsu et al., 2002; Livingston et al., 2003; Redemann et al., 2005, 2009; Russell et al., 2007), and to test water vapor retrievals by the Atmospheric Infrared Sounder (AIRS) and MODIS (Livingston et al., 2007). AATS-14-measured AODs have successfully been used in atmospheric correction of satellite data (Spanner et al., 1990; Wrigley et al., 1992).

Airborne Radiometers

Coastal Airborne *In situ* Radiometers was a new airborne radiometer instrument package flown for the first time for the COAST mission in 2011. Based on microradiometers (Morrow et al., 2010), like C-OPS, C-AIR consists of three 19-channel radiometers: one measuring global solar irradiance (E_s) and fitted with a cosine collector, plus two radiance instruments oriented to measure the indirect sky radiance (L_i) and the total surface radiance (L_T). The spectral range of each 19-channel radiometer bundle includes selected 10 nm channels centered around 320, 340, 380, 412, 443, 490, 510, 532, 555, 589, 625, 670, 683, 710, 780, and 875 nm, seven of which match satellite ocean color (MODIS) bands. The sampling data rate was 15 Hz. Application-specific sensors are included such as UV-bands for CDOM or atmospheric correction, bands targeting phycocyanin and phycoerythrin pigments for flights over reservoirs and terrestrial waters (blue-green algae detection), or bands targeting natural fluorescence (for red tide, high sediment load, and primary production applications). The microradiometer detectors have 10 decades of dynamic range and are sensitive enough to detect moonlight in global irradiance. The physical FOV radiance instrument is 2.5° full-angle and 0.7° slope angle. The E_s and L_i radiometers are mounted within a fairing on top of the aircraft and the L_i radiometer is mounted 40° off zenith, normal to the path of the aircraft. The L_T radiometer is mounted at 40° off nadir, pointed normal to the path of the aircraft, and located alongside the imaging spectrometer in a seat rail structure in an underside nadir port. This configuration eliminated any competing observation requirements between the HIS and C-AIR during flight.

COAST Flight Plan

Flight planning considered the FOV of each instrument and integration on the aircraft. To optimize observations from the hyperspectral imager and radiometer, the aircraft was flown into and out of the principal solar plane and 30–45° solar elevations to avoid sun glint. For the Monterey Bay coastal region in California, this enabled 2–3 h flight windows in the morning and afternoon around solar noon in October. Flight lines were flown in parallel at 1,829 m and spaced with 20% overlap for the HIS. The C-AIR L_T radiometer, pointing 40° from nadir, was pointing at the next adjacent line flown or the previous line flown depending on the heading. LSA flights supported the AATS-14 sun photometer and radiometers observations. Approximately every 20 min, the aircraft spiraled down in concentric circles to LSA and then flew a line under the high-altitude lines and then spiraled up in concentric circles to continue the high-altitude lines. These flight spirals, from high altitude lines down to LSA and back to the high-altitude flight lines, sampled the full atmospheric column and intervening layer for AOD retrievals. Pilots controlled aircraft pitch to not exceed radiometer

tolerance requirements which also optimized the hyperspectral imager observations. Flights over Monterey Bay included flight restrictions. The NPS TO was permitted to fly at 30 m altitude outside one nautical mile (including National Marine Sanctuary) from shore and 152 m over vessels.

OCEANIA Mission

The 2013 OCEANIA mission, extended the COAST project to focus on AOPs from in-water (C-OPS) and from the TO airborne platform (C-AIR) to evaluate CVR capabilities in support of high-altitude airborne simulation of satellite observations. OCEANIA did not include the HIS or AATS-14 sensors. C-OPS was upgraded to include small digital thrusters (Hooker et al., 2018a) that improve the VSR to 1 mm or less (Hooker et al., 2020). Driving requirements for flight planning emphasized C-AIR observations without competing requirements from another sensor, as experienced with AATS-14 in COAST and C-AIR E_s, L_i, and L_T radiometer configuration and integration was unchanged. Given successful data acquisition associated with flight planning for COAST, C-AIR was flown at LSA over Monterey Bay at approximately 30 m (150 m over vessels) as well as at 305 m altitude on the NPS TO. Flight headings remained into and out of the sun with 30–45° solar elevations. The low altitude flight plans minimized effects of AOD on C-AIR $L_W(\lambda)$ derivations consistent with the COAST mission. OCEANIA was flown on 30–31 October and 5 November 2013. The 31 October 2013 flight was coordinated with the Hyperspectral Infrared Imager (HyspIRI) Airborne Preparatory Campaign, which provided coincident imagery from the Airborne Visible Infrared Imaging Spectrometer (AVIRIS) sensor aboard the NASA ER2 platform at approximately 19,810 m (c.f. Palacios et al., 2015).

C-HARRIER 2017 and 2018 Missions

The 2017 NASA C-HARRIER campaign collected measurements in the San Francisco Bay Delta, northern Monterey Bay and Pinto Lake on 8 September, Lake Tahoe on 13 September, and northern Monterey Bay and Pinto Lake on 14 September 2017. The same instrument suite was used as for OCEANIA, but the C-AIR system was upgraded to use C-AERO. As described in Kudela et al. (2019), the principal differences between the two embodiments are that the above-water C-AERO instrument suite has wavelengths spanning 320–1,640 nm (SWIR channels 1,020, 1,245, and 1,640 nm with 10, 15, and 30 nm bandwidths, respectively). This allows for atmospheric correction studies that emphasize long wavelengths. C-AERO includes a shroud to eliminate sun glint in SWIR channels. The sampling frequency remained at 15 Hz. Data were collected from the NPS TO at LSA (approximately 30 m above the water surface). For the 2018 NASA C-HARRIER mission, the C-AERO L_T radiometer was upgraded to a 30 Hz data sampling rate. This upgrade enables additional valid data points following data filtering of sub-optimal airborne data collection and rejection of glint-contaminated data. The resultant data collection increases statistical robustness for 1% radiometry requirements for vicarious calibration and enables a greater number of observations of small water targets such as small lakes, rivers, and estuaries.

Ancillary Imagery

For the scheduled mission flight date windows, available satellite overpass timing options for MERIS (operational for COAST only), MODIS, VIIRS, Landsat 8 OLI, and Sentinel-2 MSI were identified for flight planning purposes. Based on requirements of flights within 30 min of satellite overpass, data from COAST, OCEANIA, and C-HARRIER were compared to contemporaneous imagery from the MERIS sensor, MODIS, and from AVIRIS flown as part of the NASA HyspIRI Airborne Preparatory Campaign (Hochberg et al., 2015; Lee et al., 2015) (**Table 1**). Data were accessed as Level-1A (L1A) radiances and Level-2 (L2) atmospherically corrected water-leaving radiance products from the NASA repositories. Details of the atmospheric corrections applied are provided in Section "Data Processing."

Field Sites and *in situ* Measurements

Our primary coastal field sites are the northern part of Monterey Bay, CA (**Figure 1**) with secondary sites including Lake Tahoe and San Pablo, Grizzly Bays located in the northern San Francisco Bay. Based on past project experience and typical conditions, a fall flight window maximized data collection days, minimized cloud cover, and provided a range of scientifically interesting features including tidal exchange with Elkhorn Slough (a tidally driven coastal estuary along the Monterey Bay), red tides, fall transition, upwelling versus oceanic conditions, and, potentially, a "first flush" rain event. Actual observations focused on bloom events as both time periods (2011 and 2013) corresponded with seasonally low river flow with no observed salinity anomalies indicative of river plumes at our field sites. Monterey Bay is well characterized oceanographically, provides rich historical and ongoing observations, and has been used in the past for CVR airborne operations (e.g., Ryan et al., 2005a,b, 2008, 2009, 2010; Dierssen et al., 2006; Davis et al., 2007; Chien et al., 2009) including the October 2011 NASA COAST mission (**Figure 2**) (Guild et al., 2011). In-water validation data were collected aboard the R/V *John Martin* for COAST and OCEANIA, and from the Santa Cruz Municipal Wharf for C-HARRIER. Instrumentation (**Table 1**) included the C-OPS and HyperPro II profiling radiometers, MicroTOPS II sun photometer, and ancillary measurements of water quality parameters including total chlorophyll *a* (TChl *a*; Van Heukelem and Thomas, 2001), phytoplankton composition via microscopy (Lund et al., 1958), CDOM (Hooker et al., 2020), IOP, and standard oceanographic parameters (temperature, salinity) as described in Bausell and Kudela (2019) and Hooker et al. (2020). Suspended Particulate Material (SPM) was not collected, but a United States Geological Survey (USGS) cruise in San Francisco Bay provided a range of concentrations from the same time period of 14.6–126.3 mg L^{-1} ($n = 6$) for San Pablo and Suisun bays (Grizzly Bay is in northern Suisun; **Figure 1**).

Data Processing

The radiometric and ancillary data were processed using the Processing of Radiometric Observations of Seawater using Information Technologies (PROSIT) software package (Hooker et al., 2018b) to provide estimates of L_W and R_{rs} from above- and

in-water measurements (Hooker et al., 2018c). As described in Kudela et al. (2019), a full atmospheric correction is not applied given the low flight altitude for OCEANIA and C-HARRIER, but skylight reflectance is removed as per standard NASA above-water reflectance protocols. For COAST, the HIS data were processed using both Tafkaa Tabular, hereafter referred to as Tafkaa, and the vector version of the Second Simulation of the Satellite Signal in the Solar Spectrum (6SV). The 6S code generally is used for atmospheric correction to obtain top of atmosphere (TOA) estimates of radiance and is not optimized to retrieve target water reflectances. Our use of 6SV to perform inverse modeling to obtain a target water reflectance has been used for similar purposes in some aquatic remote sensing studies (e.g., Bélanger et al., 2007; Allan et al., 2011). The aquatic hyperspectral community uses both correction algorithms, e.g., Palacios et al. (2015) corrected high altitude airborne imagery using Tafkaa, and Vanhellemont and Ruddick (2015) generated lookup tables using 6SV. Tafkaa is an atmospheric correction algorithm based on the Atmospheric Removal (ATREM, 4.0) algorithm. In this study, Tafkaa ingests at-sensor radiance of the entire image from the HIS and solves for a number of water-leaving quantities. For the purpose of this study, we used the remote sensing reflectance (R_{rs}) output. For complete details of the algorithm, see Gao and Davis (1997), Gao et al. (2000), and Montes et al. (2001, 2003). 6SV computes the scattering and absorptive effects of the particles and gases in the atmosphere in order to model the atmosphere from the target reflectance to the sensor (forward modeling approach) or to remove the atmospheric radiance from the at-sensor radiance (inverse modeling approach) to obtain surface reflectance. For the purposes of this study, 6SV was used in the inverse modeling approach, with R_{rs} derived through division of the dimensionless reflectance by pi following Eq. 3 in Allan et al. (2011). For complete details related to computations used by 6SV, see Vermote et al. (1997), Kotchenova et al. (2006), and Kotchenova and Vermote (2007).

Satellite (MERIS) imagery were processed by the NASA Ocean Biology Processing Group (OBPG) and were accessed as L1A and L2 files. MODIS utilized L2 products with no modification to the standard atmospheric correction. For comparison with the COAST data, the MERIS imagery were reprocessed from L1A data using SeaDAS (v7.3.2). Reprocessing included use of directly measured atmospheric components by applying a fixed AOD model with measured AOD and column water vapor from the AATS-14 LSA dataset (**Figures 3**, **4**). For the HIS data, a sensitivity analysis was performed using both Tafkaa and 6SV. For this analysis, the at-sensor radiance was atmospherically corrected using three atmospheric models (Coastal, Coastal-a, and Maritime) with AOD and column water vapor values from the NASA OBPG processing, MicroTOPS, and AATS-14 (**Figure 5**). MODIS Aqua data were also examined for indications of upwelling-induced suspended sediments (e.g., Ryan et al., 2012) using the Particulate Inorganic Carbon (PIC) standard product; there was no indication of elevated suspended sediment concentration (SSC) at any of our sites.

Implementation of Synthetic Dark Corrections for the C-HARRIER Mission

A difficulty with autonomous systems, like airborne instrument suites, is the radiometer apertures are not accessible during flight. Consequently, if environmental parameters change significantly with respect to pre- or post-flight conditions when the apertures are accessible, new more representative dark currents cannot be measured. Because dark currents are an order-one term in the calibration equation, accurate dark measurements are a requirement for maintaining an uncertainty budget. The traditional method for measuring dark currents (Hooker, 2014) is to cover the apertures of the radiometers with opaque

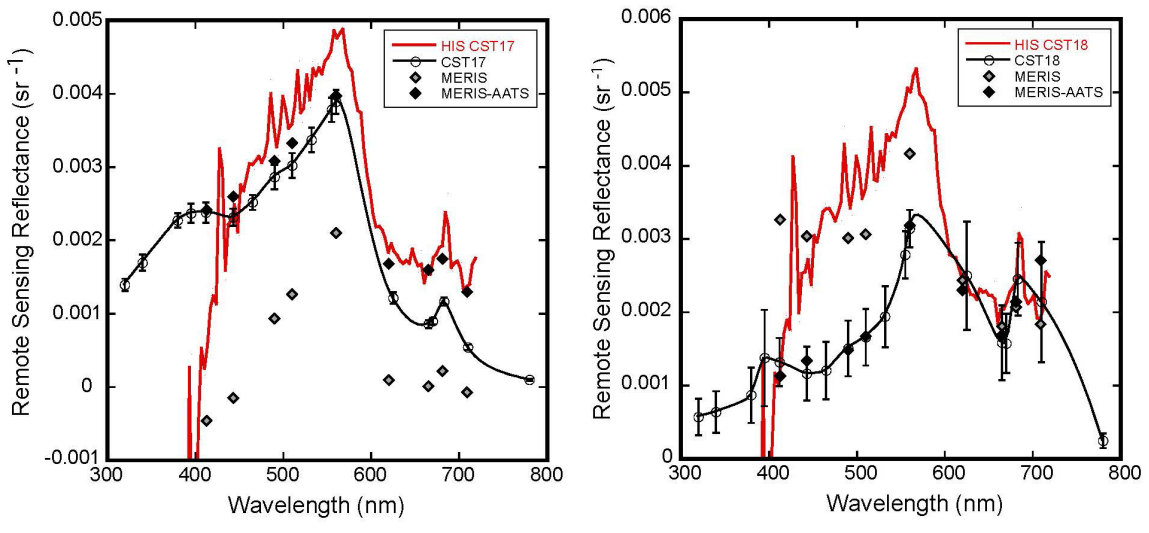

FIGURE 3 | Remote sensing reflectance (R_{rs}, sr^{-1}) is plotted for CST17 and CST18 stations, for the HIS (red line), C-OPS in-water profiler (open circles), and MERIS with standard atmospheric correction (open diamonds) and with AATS-14-derived atmospheric correction (solid diamonds). Error bars on the C-OPS data indicate one standard deviation from three consecutive casts.

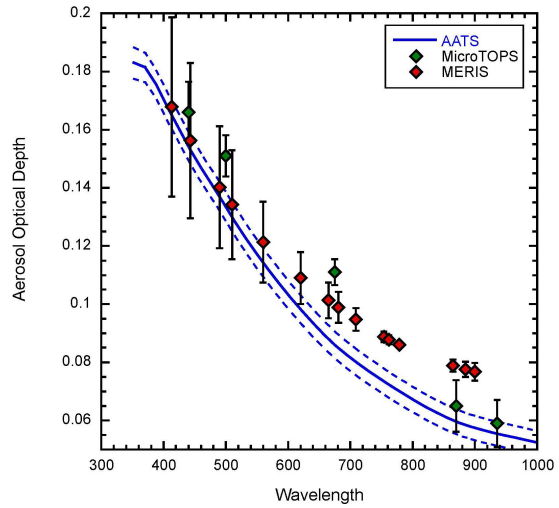

FIGURE 4 | Aerosol optical depth (AOD) derived from the average of all LSA AATS-14 measurements (blue), the average MicroTops II values for two stations, CST17 and CST18 (green), and the default MERIS AOD from SeaDAS parameters (red). Error bars indicate standard deviations for the two stations (green) and for the full MERIS image (red).

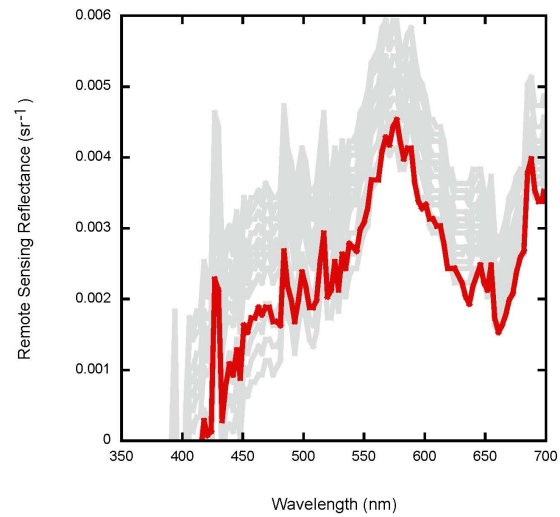

FIGURE 5 | A sensitivity analysis of the atmospheric correction for CST18 from the COAST 2011 mission was performed. The red line indicates the best retrieval (compared to C-AIR and C-OPS) from HIS, while the gray lines indicate retrievals using three atmospheric models in Tafkaa and 6SV with measured AOD values. The best fit falls within the range of reasonable spectra, but without direct measurement of in-water (C-OPS) or LSA data (C-AIR), there is no basis for quantitatively selecting the best spectrum.

caps and then to collect dark current observations for each microradiometer gain stage (nominally three). Typically, 1,024 data records are obtained at each gain stage, so quality assurance statistics can be obtained.

A synthetic or predictive dark current (PDC) was developed for each C-AERO radiometer based on a laboratory characterization of the individual microradiometers in each instrument. The laboratory characterization subjected each instrument to an operational range of parameters inside an environmental chamber while acquiring dark currents. The high and low values for each parameter range were based on the performance specifications of the instruments, e.g., temperature ranged from −2 to 40°C. The PDC was validated for the flight certified C-AERO instrument suite using a combination of airborne data and field trials, with the latter obtained with a manual pointing system (Hooker, 2014).

Predictive dark current dark characterization can be applied in three different configurations, based on the environmental parameters for the time period involved, as follows: 1. Equivalent pre- and post-flight caps dark files (called equivalent darks); 2. Along-track flight segment dark files at a temporal interval define by the operator, e.g., 15, 30, 45, and 90 s (called segment darks); and 3. Sample-by-sample corrections at instrument sampling rates of 15 or 30 Hz (called sample darks). The three configurations are evaluated using a combination of airborne and field data partitioned in the spectral domain, as follows: (a) 300–400 nm, UV; (b) 400–600 nm, BGr; (c) 600–700 nm, Red; (d) 700–800 nm, NIR1, (e) 800–900 nm, NIR2, and (f) 900–1,700 nm, SWIR.

RESULTS

Data are presented sequentially from the COAST, OCEANIA, and C-HARRIER airborne campaigns (refer to **Table 1** for airborne, field, and available high altitude and satellite data). Presented results were chosen to highlight mission accomplishments and the iterative improvements in the sensor-web approach.

COAST 2011

Data were successfully collected on 28 October 2011 over northern Monterey Bay (**Figure 2A**). The day of the overflight had calm seas and low winds, with good atmospheric visibility. At that time, there was a large "red tide" present in the bay (**Figure 2B**), with surface TChl *a* samples ranging from 4.8 to 75.0 mg m^{-3}. The bloom was dominated by the dinoflagellate genera *Akashiwo*, *Ceratium*, and *Prorocentrum* with TChl *a* at Stations 17 and 18 (**Figure 2A**) of 6.8 and 52.8 mg m^{-3} and site location depths of 24 and 84 m, respectively. **Figure 1** provides bathymetry for the entire region. The biomass was distributed heterogeneously (**Figure 2B**), with substantial spatial and temporal variability and corresponding variability in R_{rs} (**Figure 2C**). Despite the heterogeneity, comparable matchups between in-water and remotely sensed instrumentation were achieved, with a MERIS overpass at 1855 (UTC), AATS-14 and HIS data collected over the two stations at 2022 and 2024, and in-water observations at 1852 and 2040, or within less than a 2 h window (**Figure 3**). SPM samples were not collected but given the lack of river plumes or upwelling-induced suspended sediments, it was assumed that SPM was a minor contribution to the optical signals. The elevated red (approximately 555 nm) peak observed at several sites (**Figures 3**, **5**, **6**) was attributed to high algal

biomass rather than SPM, which typically shifts further toward 600 nm with increasing concentration (Dierssen et al., 2006).

Direct comparisons of R_{rs} between the C-OPS, HIS, and MERIS showed similar spectral shapes, but with large discrepancies for several wavelengths (**Figure 3**). Specifically, MERIS data obtained directly from NASA exhibited severe underestimates (including negative reflectances) at Station 17 and overestimates at Station 18, while HIS generally overestimated R_{rs} compared to C-OPS with significant sensor noise and very poor sensitivity and performance for blue and red spectral end members. To assess whether the remotely sensed data could be improved with a regionally tuned atmospheric correction, the MERIS data were reanalyzed using a fixed aerosol model and directly measured AOD and column water vapor from both a MicroTOPS II handheld sun photometer deployed aboard the ship and the average AOD and column water vapor values from LSA flight lines using AATS-14 (**Figure 2A** and **Table 2**). While the AOD values were similar between sensors (**Figure 4**), the overestimation of AOD beyond 600 nm resulted in substantial discrepancies in calculated R_{rs} (**Figure 3**), highlighting the utility of coincident airborne AOD measurements.

For quantitative assessment of the data, the relative percent difference (RPD) was calculated for R_{rs} at the MERIS wavelengths for C-OPS (considered to be the most accurate; Kudela et al., 2019) and MERIS. The average RPD for all MERIS wavelengths was −87% for CST 17 and 18% for CST 18 with standard processing. Using MicroTOPS data improved the RPD for CST 17 but not CST 18, with RPD of 35 and 36%, while the RPD for AATS-14-corrected imagery was 29 and 0.9%, respectively.

For the HIS data, a sensitivity analysis was performed using both Tafkaa and 6SV. For this analysis, the at-sensor radiance was atmospherically corrected using three atmospheric models (Coastal, Coastal-a, and Maritime) with AOD and column water vapor values from the NASA OBPG processing, MicroTOPS, and AATS-14 (**Figure 5**). While both models produce reasonable values, the R_{rs} spectra span a considerable range (factor of two) with no ability to *a priori* identify any particular combination as the "best" solution.

Following the COAST mission, the prototype HIS was removed from the instrument package because significant engineering issues (poor calibration results, not blue-optimized, significant noise, difficulty integrating the data stream) were discovered. C-AIR flew successfully on the TO during COAST but was not collecting adequate time series of data at LSA with optimal headings due to the driving priority of the flight planning for the AATS-14 and was therefore not used for demonstration of the airborne CVR activity during COAST.

OCEANIA 2013

The OCEANIA mission focused on supporting airborne CVR through the collection of coincident data from the TO at LSA using C-AIR and from in-water observations using C-OPS with small digital thrusters. Both instrument packages employ single-channel microradiometers, allowing sensor calibration, data collection, and post-processing to occur using the same workflow and identical hardware components (Hooker et al., 2018a,b,c). Data were again collected over northern Monterey Bay on 5 November 2013 (**Figure 6A** showing MODIS Aqua Chl *a*; see also Palacios et al., 2015; Bausell and Kudela, 2019) with clear skies, good visibility, and low winds. TChl *a* was comparable to COAST with a value of 8.3 mg m^{-3}. Red tides were prominent in September and October of that year (Palacios et al., 2015), with the dinoflagellate genera *Cochlodinium*, *Prorocentrum*, and *Ceratium* dominating at the OCEANIA station on 5 November 2013. AVIRIS data were acquired over the same location immediately prior to OCEANIA on 31 October 2013, for which the Pajaro River Mouth (PRM) station in Palacios et al. (2015) was coincident with OCEANIA. As noted above, there was no indication of significant concentrations of SPM from the river or from upwelling at these sites.

In-water data were collected with the C-OPS profiler within the red tide (**Figure 6**). C-OPS data were collected from 2025 to 2032 (UTC) while the closest matching C-AIR data collected at LSA from the TO were collected at 1914, and a MODIS Aqua image was captured at 2110, approximately a 2 h window for all observations. A comparison of data products derived from above- and in-water measurements is presented in **Figure 6B**, with normalized forms obtained following published NASA Ocean Optics protocols wherein bidirectionally corrected spectra were derived and presented in normalized forms to account for the

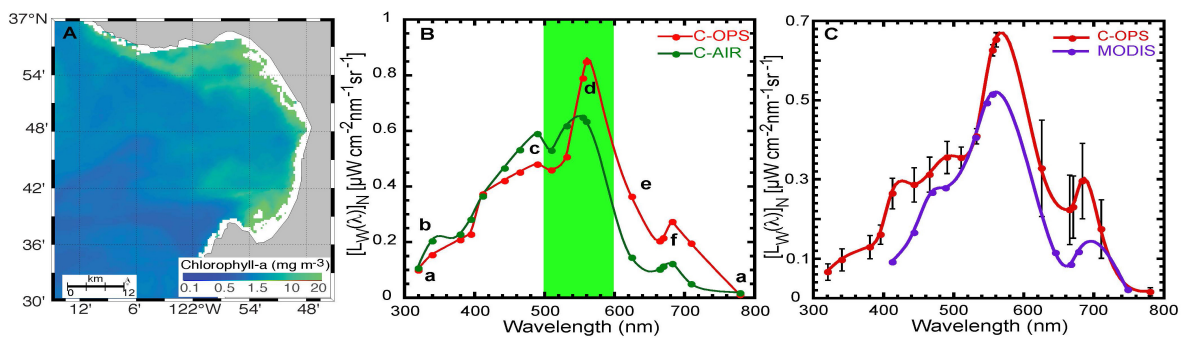

FIGURE 6 | MODIS Aqua Chl *a* from 5 November 2013 (OCEANIA) is shown in **(A)**, processed at 250 m resolution, with a comparison of C-OPS (in-water) and C-AIR (airborne) within the red tide in **(B)**, and the corresponding C-OPS versus MODIS data in **(C)** processed at 1 km resolution. Error bars in **(C)** represent the standard deviation of three consecutive C-OPS profiles. Station location is indicated in **Figure 2A** (solid circle).

TABLE 2 | Summary of atmospheric parameters used for correction of the HIS imagery.

Platform	Column water Vapor (g cm^{-2})	Humidity (%)	AOD (520 nm)
MERIS	1.58	29%	0.121
MicroTOPS II	1.02	39%	0.128
AATS	1.3	63%	0.111

solar illumination and geometry (Hooker et al., 2002, 2004). Products obtained by deploying C-OPS from a small ship are shown in red and products obtained from the C-AIR instrument on the NPS TO are shown in green. The data compare the nearest in-water station to the nearest airborne observation. The plot shows the in-water data were obtained more substantially inside the red tide, because the highest amplitude peak in the green domain is with the C-OPS data. Six spectral features spanning the entire spectral domain (UV to NIR) demonstrate the good agreement achieved between the two sensor systems: (a) the UV and NIR spectral end members are in agreement; (b) the expected UV shoulder for the type of coastal water sampled is in both spectra, with the C-OPS data showing the anticipated UV suppression from the more intense bloom conditions; (c) the expected blue shoulder for higher productivity coastal water in both spectra, with the in-water data showing greater blue suppression from the more intense bloom conditions; (d) the expected peak in the green domain is in both spectra with the higher in-water peak establishing the C-OPS data were obtained more substantially in the red tide; (e) the expected higher elevation of the red domain for the in-water spectrum (which was obtained in more intense bloom conditions); and (f) the expected fluorescence peak is present in both spectra, with the in-water peak being larger as expected.

Spectra from the MODIS image was comparable to C-AIR and C-OPS (**Figure 6C**), although it should be noted that the 488 nm band exhibited negative radiance, presumably due to poor atmospheric correction. In contrast to the MODIS data, AVIRIS data collected a week prior (31 October 2013) were unable to produce accurate retrievals of ocean color due to a combination of poor SNR and suboptimal atmospheric correction (Palacios et al., 2015).

C-HARRIER 2017 and 2018

The C-HARRIER 2017 and 2018 missions focused primarily on flight planning and highlight incremental improvements to the C-AERO sensor including a shroud and expanded spectral range from 320 to 1,640 nm. Specifically, sampling rates were increased from 15 to 30 Hz for the 2018 mission for the downward-viewing L_T radiometer (total radiance from the surface). A new "synthetic dark" method was developed to apply dark corrections to the instruments during flight (rather than before and after flight).

In 2017, flight planning was enhanced to include additional sites demonstrating data collection in varying water types and feasibility of sorties to inland waters such as the San Francisco Bay and Lake Tahoe. Grizzly Bay and San Pablo Bay represented the turbid waters of San Francisco Bay. Lake Tahoe represented oligotrophic (e.g., oceanic) conditions, a clear water type.

For 2018, the primary field target was northern Monterey Bay. A short segment was collected near the Santa Cruz Municipal Wharf, and after processing (including the use of synthetic darks) the data were reduced from 30 to 15 Hz and the SNR was calculated as per Kudela et al. (2019) (**Figure 7**). Absolute values of SNR were comparable but use of the 30 Hz data increased SNR approximately 1–9%, depending on wavelength, with greatest improvement in the NIR and SWIR region (**Figure 7**). It is also notable that increasing the sampling rate effectively decreases the ground sampling distance (GSD) without adjusting other flight characteristics. In this example, the GSD decreased from 3.4 to 1.7 m at 15 and 30 Hz, respectively, for an LSA of 30 m and a speed over ground of 185 kph.

A PDC method described in Section "Implementation of Synthetic Dark Corrections for the C-HARRIER Mission" was used to apply dark corrections to the 2017 and 2018 data collections (**Figure 8**). Processing existing airborne C-AERO data with caps darks versus equivalent darks results in data products that agree at all wavelengths to within 0.1%. For manually pointed C-AERO data, the use of equivalent darks produces data products that agree with an in-water C-OPS instrument suite as follows: UV −4.2, BGr −2.9, Red −1.7, NIR1 −2.8, and NIR2 7.9%, which is similar to the combined uncertainty for sensor calibration (about 3%) plus temporal variance during station work (5% or less, but without an estimate of spatial variance), except for NIR2. Pearson's statistical correlation coefficient, ρ, for the two relevant match-up spectra in **Figure 8** is shown for the SPB, GB, MB, and LT sites. The overall average value is ρ = 0.991, which

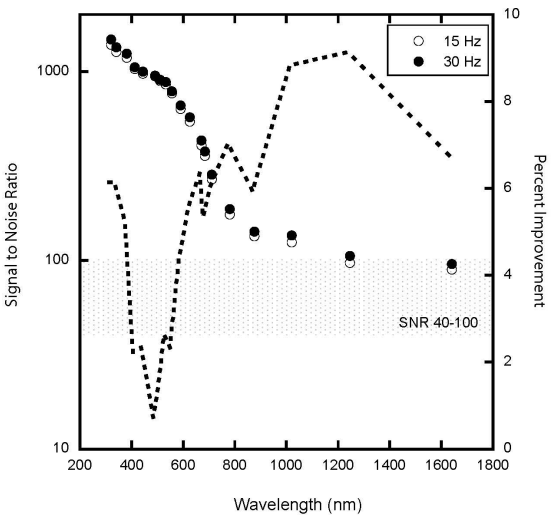

FIGURE 7 | Effective signal-to-noise ratio (SNR) calculated at LSA for C-AERO data over Monterey Bay, CA collected 26 October 2018 (C-HARRIER) with C-AERO at 15 and 30 Hz. The stippled region identifies an optimal SNR of 40–100, while the dashed line provides the percent difference in SNR for 15 versus 30 Hz otherwise processed using the same methods. The percent improvement (as percent increase in SNR when collecting at 15 versus 30 Hz) is shown as the dashed line.

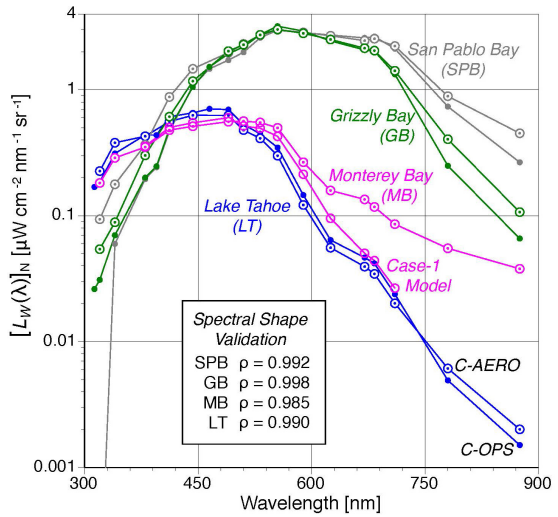

FIGURE 8 | C-AERO was validated using *in situ* data obtained with a C-OPS equipped with digital thrusters (C-PrOPS) except in Monterey Bay (30 Hz L_T data), wherein a case-1 model was used. The matchups between C-AERO and C-OPS are based on minimizing the distance between the two sampling sites. For the Monterey Bay comparison, the TChl *a* concentration obtained at the Santa Cruz Wharf was used to derive the case-1 model results and compared to the spatially nearest C-AERO observation. The correlations (ρ) in spectral shape for each site are provided, demonstrating excellent retrieval of spectral information from the airborne observations.

means more than 99% of the variance in the shape is explained. These data span a large range of bio-optical complexity, from very blue water (Lake Tahoe) to estuarine waters dominated by both CDOM and non-algal particles (Grizzly Bay). The excellent agreement in spectral shape for all sites translates directly into reduced error for derived products such as chl *a* that rely on band-ratios (i.e., spectral shape and magnitude). Estimation of the absolute percent difference using the standard maximum band ratio approach yields uncertainty of 5.9% in Tchl *a* for the data in **Figure 8**, well within the range of acceptable uncertainty for existing satellite sensors (Kudela et al., 2019).

Processing existing airborne C-AERO data with segment darks results in no negative calibrated radiometric values, whereas the use of caps darks (either pre- or post-flight) can produce negative calibrated radiances over dim targets in the middle of a long flight. For the airborne data used herein, the amount of data that is lost due to negative calibrated radiances if caps darks are used is less than 1.8% (no field data is lost for caps darks, because the deployments are relatively short in duration). A larger percentage of the SWIR data is improved by using segment darks. Approximately 3.5% of the data are sufficiently changed by the use of segment darks to influence data products at the 1% level or more. None of the data obtained in other wavelength domains are improved sufficiently to influence data products at the 1% level or more, but this is likely a function of the water bodies that were sampled.

Processing existing airborne C-AERO data with segment darks versus sample darks results in data products that agree at all wavelengths to within 0.2%; the agreement is to within 1% at all wavelengths for field data. The reason for the excellent agreement is due to the relative short time periods used to define a flight segment. The longest flight segment is 90 s, so the opportunity for environmental or performance changes during a flight segment for an aircraft operating at near-constant LSA is small.

DISCUSSION

Aquatic remote sensing provides a cost-effective, synoptic method for deriving information about the ecologically relevant constituents of the coastal ocean (IOCCG, 2000), because ocean color provides a depth integrated measurement of the biotic and abiotic constituents that interact with light in the ocean. What has historically been challenging is partitioning this signal into relevant biogeochemical parameters (Dierssen et al., 2006; Dunagan et al., 2009; Gregg and Casey, 2010; Guild et al., 2011, 2019). The magnitude of L_W is spectrally, spatially, and temporally variable, ranging from very dark values in clear, deep water to very bright values at water's edge. The spatial (1 km) and temporal (daily) resolution from legacy instruments is of marginal use in coastal waters (Aurin et al., 2013; Dekker et al., 2018). Further, low SNR measurements of L_W in the blue spectral domain contribute to poor discrimination of pigments from CDOM and poor estimates in the UV (Kudela et al., 2019). Continental sources of aerosols and trace gas plumes may not be well represented by atmospheric models used in atmospheric correction approaches. Also, for productive coastal waters, the use of non-zero NIR radiances and poor SNR values complicate atmospheric correction schemes based on SWIR wavelengths (Siegel et al., 2000; Shi and Wang, 2009; Werdell et al., 2010).

NASA Ocean Optics Protocols require CVR uncertainties as follows: calibration data to within 5%, validation data to within 10% error, and research data to within 25% (Hooker and McClain, 2000). A fundamental limitation using historical airborne and satellite data is that sensors such as AVIRIS, the primary instrument (for example) in the HyspIRI Preparatory Airborne Campaign, has poor SNR and calibration issues (Palacios et al., 2015; Thompson et al., 2015), with SNR at 400 nm as low as 20:1, compared to a next-generation requirement of 400:1 for the Plankton, Aerosol, Cloud, ocean Ecosystem (PACE) sensor. Second, in-water calibration data are needed, limiting the improved correction to specific targets (Moses et al., 2012). Next-generation satellite sensors are also required to meet 3.5% absolute accuracy, with 1% absolute radiometry for validation (Hooker et al., 2007), which is challenging at best for existing airborne and satellite platforms (Kudela et al., 2019). A fundamental goal of COAST, OCEANIA, C-HARRIER, and related campaigns was to demonstrate the evolution of the capability to meet these exacting requirements in coastal ocean and inland waters while simultaneously moving away from the traditional paradigm of relying on a limited number of fixed locations for CVR data [e.g., AErosol RObotic NETwork Ocean Color (AERONET-OC), Zibordi et al., 2009].

A primary obstacle for the remote sensing of coastal and inland waters is atmospheric correction. The COAST campaign demonstrated the utility of collecting high-quality atmospheric

and oceanic data simultaneously from an airborne platform by collocating a science-grade sun photometer and ocean color radiometers. Traditional processing of MERIS satellite data resulted in both over- and underestimation of R_{rs} and was greatly improved with the addition of AOD collected either from a fixed platform (MicroTOPS aboard the research vessel) or from the TO. A clear advantage of the airborne approach is that considerable additional spatial information is provided for AOD, as well as an ability to collect columnar atmospheric data by varying flight altitude. The improved horizontal and vertical resolution provided by the airborne perspective is most useful for heterogeneous air masses, which often correspond to inland (i.e., compared with marine) environments.

A sensitivity analysis of the HIS atmospheric correction reinforces the requirement for highly accurate atmospheric information for post-processing of imagery. For this analysis, we focused primarily on calibration and validation and therefore primarily analyzed the data from the two locations where in-water measurements were available. The spatially explicit AOD data, like that from the AATS-14 aboard the TO, would enable future missions coupling a sun photometer with imaging spectrometers to conduct a pixel-by-pixel atmospheric correction, which would presumably greatly improve data collection for any mission study airborne simulation programs supporting PACE, the Surface Biology and Geology (SBG) hyperspectral mission study (Schneider et al., 2019), and the past HyspIRI precursor study (Hochberg et al., 2015), where AVIRIS atmospheric correction issues varied dramatically across a space of a few kilometers for Monterey Bay (Palacios et al., 2015). While the HIS had significant engineering and data processing issues, COAST also highlighted the desirability to capture the two-dimensional structure of the surface ocean to put the more limited shipboard data into spatial context (**Figure 2B**).

The OCEANIA campaign highlighted the usefulness of a high SNR sensor with expanded spectral range (C-AIR) flown at LSA, relevant to coastal remote sensing. For example, while AATS-14 was not available for OCEANIA, there was also no requirement for atmospheric correction of the C-AIR data at LSA, as demonstrated by the very good agreement between the C-OPS and C-AIR spectra over the red tide (**Figure 6B**). It was recognized that next-generation sensors for missions such as PACE and SBG would challenge existing CVR instrumentation by requiring radiometric measurements extending into the UV and NIR and shortwave infrared, where legacy instruments are challenged by noise and sensitivity issues (e.g., Kudela et al., 2019). The C-AERO instrument was, therefore, designed around the same microradiometers used in C-AIR but with extended spectral range (320–1,640 nm) and addition of a shroud to reduce long wavelength scattering at the sensor aperture (Hooker et al., 2018a). For C-HARRIER, the C-AERO sensor was further upgraded between 2017 (Kudela et al., 2019) and 2018 by increasing the sampling frequency from 15 to 30 Hz. This effectively decreases GSD while doubling the data volume, allowing post-processing to exclude noisy features such as glint and whitecaps that would be included in the data for instruments sampling at slower rates.

Following OCEANIA, it was also recognized that inexpensive and easy to deploy sun-tracking photometers were lacking, given the high demand and frequent unavailability of systems such as AATS-14. The same microradiometer systems were therefore used to develop a portable fixed-platform system, the Compact-Optical Sensors for Planetary Radiant Energy (C-OSPREy) sun photometer mounted on a tracker with a quad detector, supported by a solar reference (E_s) with a shadow band, documented in Hooker et al. (2018b), and initial development of the microradiometer-based 3STAR sun-tracking photometer, based on the same design and engineering as the C-AIR radiance sensor. The C-OSPREy system was not deployed in Monterey for C-HARRIER, because 3STAR was not flight certified, but is considered to be at NASA technical readiness level (TRL) 9 after successful deployments on multiple campaigns (Hooker et al., 2018c). At this time, all engineering and flight-readiness tests for 3STAR aboard the TO are completed, but 3STAR has not conducted a science mission. Consequently, the capabilities of 3STAR are not evaluated within this manuscript.

With the completion of engineering tests for 3STAR in 2019, all the components for a fully operational coastal in-water and airborne "sensor-web" approach were established. All of the radiometer instruments (C-OPS, CAIR, C-AERO, C-OSPREy, and 3STAR) are based on the same core set of microradiometers (albeit using different generations of microradiometers with C-AERO and C-OSPREy being the most recent) with National Institute of Standards and Technology traceable absolute calibration and 10 decades of dynamic range. This approach is fundamentally different from traditional calibration methods which typically rely on fixed location and custom-built above- and in-water optical sensor packages maintained in one location, e.g., the Marine Optical Buoy (MOBy) and *Bouée pour l'acquisition de Séries Optiques à Long Terme* (BOUSSOLE) projects (Clark et al., 2003; Antoine et al., 2008, respectively) which cannot be opportunistically deployed across different regions and are generally not optimized for measurement of shallower and more complex inland water bodies. The approach described here provides calibration-level performance for ocean color from fixed platforms as well as airborne observatories; when flown at LSA, the requirement for complex atmospheric correction is removed, while the 10-decade dynamic range allows the same sensors to operate equally effectively in water ranging from extremely clear to highly turbid, including red tides (Hooker et al., 2018a,b,c; Kudela et al., 2019), and across an expanded spectral range that improves algorithm performance for a global range of water bodies (Hooker et al., 2020; Houskeeper et al., 2021). The 15 Hz version of C-AERO already met or exceeded all recommendations for SNR from the aquatic remote sensing community (Kudela et al., 2019), while the recent upgrade to 30 Hz sampling for the downward-viewing (L_T) radiometer has substantially increased the realized SNR for coastal waters. Implementation of the synthetic or predicted darks correction (PDC) improved the radiometric accuracy at all wavelengths, with the greatest improvements at the longer NIR and SWIR wavebands most relevant to atmospheric correction.

A unique capability of this approach is that calibration and validation targets are no longer limited to a handful of ground- or ship-based sun photometer locations. For example, during the C-HARRIER mission, calibration-quality data were collected over a 300 km span covering Monterey Bay, San Francisco Bay,

and Lake Tahoe, CA in a matter of days, with the primary limitation being the availability of personnel and instrumentation for the in-water measurements. We estimate that for a similar payload, the TO used in these studies could extend this range to 1,300 km with flight altitudes ranging from LSA to 3,048 m. This capability opens up the possibility of collecting high-quality CVR data nearly anywhere a suitable airborne platform is available, thus providing data quickly and cost effectively from oligotrophic case-1 waters to bright coastal, estuarine, and inland water targets in the same mission, or multiple revisits of the same location to support the calibration and validation of geostationary sensors, e.g., the Geosynchronous Littoral Imaging and Monitoring Radiometer (Geosynchronous Littoral Imaging and Monitoring Radiometer [GLIMR], 2019) instrument recently selected for development. This approach opens the potential for rapidly acquiring calibration-quality data in a variety of environments in consideration of maintaining sites such as MOBy and greatly reducing the time required to generate appropriate datasets that cover the required range of variability (Bailey et al., 2008). Similarly as noted by Mouw et al. (2015), the primary network used for calibration and validation of aquatic atmospheric correction is AERONET-OC which consists of only a handful of locations (Zibordi et al., 2009), has limited spectral bands, and insufficient resolution in the red to NIR for coastal and inland waters. Recent improvements have increased the spectral resolution and range of above-water instrument suites relevant to calibration (e.g., Vansteenwegen et al., 2019), but are still limited by expanded (compared with C-AERO) integration times and by the spatial limitations of a fixed-location approach. Through the development of a microradiometer-based sensor suite, CVR can be achieved for both the aquatic and atmospheric components anywhere in the world that a suitable airborne platform is available.

To summarize, optically complex coastal and inland waters pose unique challenges for remote sensing. The optical heterogeneity of coastal and inland waters is the result of a diversity of influences such as river plumes, algal blooms, benthic habitats, and resuspension of sediments over shallow shelves—all of which can be further influenced by climatic changes, e.g., drought and flooding. Inland waters are predominantly smaller spatial targets and challenging for satellite remote sensing. The overlying atmosphere is also variable due to terrestrial inputs of aerosols (dust, particulates, and smoke), water vapor, and trace gases, while changes in elevation require modification of atmospheric correction protocols. Improved sensor SNR, spectral range and resolution, spatial coverage, and temporal resolution (to capture water circulation dynamics of features) are needed to support aquatic observations and correction of the atmospheric influences on these observations to fill gaps in coastal and inland waters research. While not a focus of this paper, the same instrumentation used herein also meets or exceeds criteria for case-1 open ocean waters. As demonstrated in the evolving airborne microradiometer instruments used in the COAST, OCEANIA, and C-HARRIER missions, such airborne observatories can readily support local coverage of coastal and inland waters and bridge the high-fidelity CVR quality observations to relevant high altitude airborne and satellite observations.

DATA AVAILABILITY STATEMENT

The raw data supporting the conclusions of this article will be made available by the authors, without undue reservation.

AUTHOR CONTRIBUTIONS

LG served as the principal investigator on the COAST, OCEANIA, and C-HARRIER projects and managed the flight planning and airborne mission flight data collection. LG, RK, and SH contributed to the conception and design of the study. LG and RK wrote the initial draft of the manuscript. RK and SH served as co-investigators on the various NASA projects, participated in data collection for all field campaigns, writing and revision of the manuscript, and preparation of figures. SP participated in field data collection during COAST and OCEANIA, flight planning for OCEANIA, hyperspectral image processing, atmospheric correction sensitivity analysis in Takfaa and 6SV of hyperspectral imagery, and revision of the manuscript. HH participated in data collection during C-HARRIER, processing of field data, preparation of figures, and revision of the manuscript. All authors contributed to the article and approved the submitted version.

FUNDING

The authors declare that this study received funding from NASA. The funder had the following involvement with the study: missions, advancing the airborne instrument technology, data collection, and data analyses. LG, RK, SH, SP, HH, and NASA ARC, UCSC, University of Miami, and BSI project team members received support from the following NASA Programs: (1) HOPE COAST project by NASA Headquarters (HQ) awards from the Science Mission Directorate (SMD) and Office of Chief Engineer Hands-On Project Experience (HOPE) 2010 Training Opportunity For NASA Personnel; (2) Remote Sensing of Water Quality (NNH12ZDA001N-WATER A.32), Earth Science Division (ESD), SMD (High Quality Optical Observations, H-Q2O, for data analysis of COAST and OCEANIA missions); (3) 2013 NASA-ARC Science Innovation Fund (SIF), NASA HQ Office of Chief Scientist, SMD (OCEANIA mission); (4) 2016 NASA-ARC SIF, NASA HQ Office of Chief Scientist (advancing instrument technology); and (5) Airborne Instrument Technology Transition (NNH16ZDA001N-AITT A.26), ESD, SMD (advancing instrument technology, C-HARRIER missions, and data analyses).

ACKNOWLEDGMENTS

We would like to recognize John Morrow, Biospherical Instruments, Inc., as one of the original team members who

conceived of the airborne CVR competency and provided expertise in the radiometry and aquatic bio-optics science for all the airborne missions presented. Also, we acknowledge the significant contributions of Stephen Dunagan and James Eilers who developed the design and implemented the integration of the airborne instruments flying for the first time or flying in the suite configurations for the first time as well as developing flight plans. This engineering activity was innovative in itself. We would like to thank the two reviewers whose thoughtful review has strengthened the contribution of this manuscript.

REFERENCES

Allan, M. G., Hamilton, D. P., Hicks, B. J., and Brabyn, L. (2011). Landsat remote sensing of chlorophyll a concentrations in central North Island lakes of New Zealand. *Intern. J. Remote Sens.* 32, 2037–2055. doi: 10.1080/01431161003645840

Antoine, D., d'Ortenzio, F., Hooker, S. B., Bécu, G., Gentili, B., Tailliez, D., et al. (2008). Assessment of uncertainty in the ocean reflectance determined by three satellite ocean color sensors (MERIS, SeaWiFS and MODIS-A) at an offshore site in the Mediterranean Sea (BOUSSOLE project). *J. Geophys. Res. Oceans* 113:2007JC004472. doi: 10.1029/2007JC004472

Aurin, D., Mannino, A., and Franz, B. (2013). Spatially resolving ocean color and sediment dispersion in river plumes, coastal systems, and continental shelf waters. *Remote Sens. Environ.* 137, 212–225. doi: 10.1016/j.rse.2013.06.018

Bailey, S. W., Hooker, S. B., Antoine, D., Franz, B. A., and Werdell, P. J. (2008). Sources and assumptions for the vicarious calibration of ocean color satellite observations. *Appl. Opt.* 47, 2035–2045. doi: 10.1364/AO.47.002035

Bausell, J., and Kudela, R. (2019). Comparison of two in-water optical profilers in a dynamic coastal marine ecosystem. *Appl. Opt.* 58, 7319–7330. doi: 10.1364/AO.58.007319

Bélanger, S., Ehn, J. K., and Babin, M. (2007). Impact of sea ice on the retrieval of water-leaving reflectance, chlorophyll a concentration and inherent optical properties from satellite ocean color data. *Remote Sens. Environ.* 11, 51–68. doi: 10.1016/j.rse.2007.03.013

Brezonik, P. L., Olmanson, L. G., Finlay, J. C., and Bauer, M. E. (2015). Factors affecting the measurement of CDOM by remote sensing of optically complex inland waters. *Remote Sens. Environ.* 157, 199–215. doi: 10.1016/j.rse.2014.04.033

Chien, S., Doubleday, J., Tran, D., Thompson, D., Mahoney, D., and Chao, Y. (2009). "Towards an autonomous space in-situ marine sensorweb," in *Proceedings of the AIAA Infotech@Aerospace Conference, 6-9 April 2009*, Seattle, WA.

Clark, D. K., Yarbrough, M. A., Feinholz, M., Flora, S., Broenkow, W., Kim, Y. S., et al. (2003). "MOBy, a radiometric buoy for performance monitoring and vicarious calibration of satellite ocean color sensors: measurement and data analysis protocols," in *Ocean Optics Protocols for Satellite Ocean Color Sensor Validation, Revision 4, Volume VI: Special Topics in Ocean Optics Protocols and Appendices*, eds J. L. Mueller, G. S. Fargion, and C. R. McClain (Greenbelt, MD: NASA Goddard Space Flight Center), 3–34.

Davis, C. O., Kavanaugh, M., Letelier, R., Bissett, W. P., and Kohler, D. (2007). "Spatial and spectral resolution considerations for imaging coastal waters," in *Proceedings of the SPIE 6680, Coastal Ocean Remote Sensing*, San Diego, CA.

Dekker, A. G., Pinnel, N., Gege, P., Briottet, X., Court, A., Peters, S., et al. (2018). "Feasibility study for an aquatic ecosystem earth observing system, version 2.0," in *Proceedings of the Committee on Earth Observation Satellites (CEOS)*, Canberra.

Dierssen, H. M., Kudela, R. M., Ryan, J. P., and Zimmerman, R. C. (2006). Red and black tides: quantitative analysis of water-leaving radiance and perceived color for phytoplankton, colored dissolved organic matter, and suspended sediments. *Limnol. Oceanogr.* 51, 2646–2659. doi: 10.4319/lo.2006.51.6.2646

Dunagan, S., Baldauf, B., Finch, P., Guild, L., Hochberg, E., Jaroux, B., et al. (2009). "Small satellite and UAS assets for coral reef and algal bloom monitoring," in *Proceedings of the 33rd International Remote Sensing of Environment, May 4-8, 2009*, Stresa.

Gao, B.-C., and Davis, C. O. (1997). "Development of a line-by-line-based atmosphere removal algorithm for airborne and spaceborne imaging spectrometers," in *Proceedings of the Imaging Spectrometry III SPIE*, San Diego, CA.

Gao, B.-C., Montes, M. J., Ahmad, Z., and Davis, C. O. (2000). Atmospheric correction algorithm for hyperspectral remote sensing of ocean color from space. *Appl. Opt.* 39, 887–896. doi: 10.1364/ao.39.000887

Gao, B.-C., Montes, M. J., Davis, C. O., and Goetz, A. F. (2009). Atmospheric correction algorithms for hyperspectral remote sensing data of land and ocean. *Remote Sens. Environ.* 113, S17–S24. doi: 10.1016/j.rse.2007.12.015

Geosynchronous Littoral Imaging and Monitoring Radiometer [GLIMR] (2019). *Geosynchronous Littoral Imaging and Monitoring Radiometer (EVI-5) (GLIMR)*. Available online at: https://eospso.nasa.gov/missions/geosynchronous-littoral-imaging-and-monitoring-radiometer-evi-5 (accessed May 9, 2020).

Gholizadeh, M. H., Melesse, A. M., and Reddi, L. (2016). A comprehensive review on water quality parameters estimation using remote sensing techniques. *Sensors* 16:1298. doi: 10.3390/s16081298

Gregg, W. W., and Casey, N. W. (2010). Improving the consistency of ocean color data: a step toward climate data records. *Geophys. Res. Lett.* 37:893. doi: 10.1029/2009GL041893

Groom, S., Sathyendranath, S., Ban, Y., Bernard, S., Brewin, R., Wang, M., et al. (2019). Satellite ocean colour: current status and future perspective. *Front. Mar. Sci.* 6:485. doi: 10.3389/fmars.2019.00485

Guild, L., Dungan, J., Edwards, M., Russell, P., Hooker, S., Myers, J., et al. (2011). "NASA's Coastal and ocean airborne science testbed (COAST)," in *Proceedings of the 34th International Remote Sensing of Environment*, Sydney.

Guild, L., Morrow, J., Kudela, R., Myers, J., Palacios, S., Torres-Perez, J., et al. (2019). *Airborne Calibration, Validation, and Research Instrumentation for Current and Next Generation Satellite Ocean Color Observations*. San Jose, CA: Hyperspectral Imaging and Sounding of the Environment.

He, X., Bai, Y., Pan, D., Tang, J., and Wang, D. (2012). Atmospheric correction of satellite ocean color imagery using the ultraviolet wavelength for highly turbid waters. *Opt. Express.* 20, 20754–20770. doi: 10.1364/OE.20.020754

Hochberg, E. J., Roberts, D. A., Dennison, P. E., and Hulley, G. C. (2015). Special issue on the Hyperspectral Infrared Imager (HyspIRI): emerging science in terrestrial and aquatic ecology, radiation balance and hazards. *Remote Sens. Environ.* 167, 1–5. doi: 10.1016/j.rse.2015.06.011

Hooker, S. B. (2014). *Mobilization Protocols for Hybrid Sensors for Environmental AOP Sampling (HySEAS) Observations*. NASA Tech. Pub. 2014–217518, Greenbelt, MD: NASA Goddard Space Flight Center.

Hooker, S. B., Lazin, G., Zibordi, G., and McLean, S. (2002). An evaluation of above- and in-water methods for determining water-leaving radiances. *J. Atmos. Ocean. Technol.* 19, 486–515. doi: 10.1175/1520-0426(2002)019<0486:aeoaai>2.0.co;2

Hooker, S. B., Lind, R. N., Morrow, J. H., Brown, J. W., Suzuki, K., Houskeeper, H. F., et al. (2018a). *Advances in Above- and In-Water Radiometry, Vol. 1: Enhanced Legacy and State-of-the-Art Instrument Suites*. NASA Tech. Pub. 2018–219033/Vol. 1, Greenbelt, MD: NASA Goddard Space Flight Center.

Hooker, S. B., Lind, R. N., Morrow, J. H., Brown Kudela, R. M., Houskeeper, H. F., and Suzuki, K. (2018b). *Advances in Above- and In-Water Radiometry, Vol. 2: Autonomous Atmospheric and Oceanic Observing Systems*. NASA Tech. Pub. 2018–219033/Vol. 2, Greenbelt, MD: NASA Goddard Space Flight Center.

Hooker, S. B., Lind, R. N., Morrow, J. H., Brown Kudela, R. M., Houskeeper, H. F., and Suzuki, K. (2018c). *Advances in Above- and In-Water Radiometry, Vol. 3: Hybridspectral Next-Generation Optical Instruments*. NASA Tech. Pub. 2018–219033/Vol. 3, Greenbelt, MD: NASA Goddard Space Flight Center.

Hooker, S. B., Matsuoka, A., Kudela, R. M., Yamashita, Y., Suzuki, K., and Houskeeper, H. F. (2020). A global end-member approach to derive aCDOM(440) from near-surface optical measurements. *Biogeoscience* 17, 475–497. doi: 10.5194/bg-17-475-2020

Hooker, S. B., and McClain, C. R. (2000). The calibration and validation of SeaWiFS data. *Prog. Oceanogr.* 45, 427–465. doi: 10.1016/s0079-6611(00)00012-4

Hooker, S. B., McClain, C. R., and Mannino, A. (2007). *NASA Strategic Planning Document: A Comprehensive Plan for the Long-Term Calibration and Validation*

of Oceanic Biogeochemical Satellite Data. NASA Special Pub. 2007–214152, Greenbelt, MD: NASA Goddard Space Flight Center.

Hooker, S. B., Morrow, J. H., and Matsuoka, A. (2013). The 1% and 1 cm perspective in deriving and validating AOP data products. *Biogeoscience* 10, 511–527.

Hooker, S. B., Zibordi, G., Berthon, J. F., and Brown, J. W. (2004). Above-water radiometry in shallow coastal waters. *Appl. Opt.* 43, 4254–4268. doi: 10.1364/ao.43.004254

Houskeeper, H. F., Hooker, S. B., and Kudela, R. M. (2021). Spectral range within global aCDOM(440) algorithms for oceanic, coastal, and inland waters with application to airborne measurements. *Remote Sens. Environ.* 252C. doi: 10.1016/j.rse.2020.112155

Houskeeper, H. F., and Kudela, R. M. (2019). Ocean color quality control masks contain the high phytoplankton fraction of coastal ocean observations. *Remote Sens.* 11:2167. doi: 10.3390/rs11182167

Hsu, N. C., Tsay, S., Herman, J., and Holben, B. (2002). Comparisons of satellite retrieval of aerosol properties from SeaWiFS and TOMS to the AERONET measurements. *EOS Trans. AGU* 82:47.

IOCCG (2000). "Remote sensing of ocean colour in coastal, and other optically-complex waters," in *Reports of the International Ocean-Colour Coordinating Group, No. 3*, ed. S. Sathyendranath (Dartmouth, NS: IOCCG).

Kahru, M., and Mitchell, B. G. (1998). Spectral reflectance and absorption of a massive red tide off southern California. *J. Geophys. Res. Ocean.* 103, 21601–21609. doi: 10.1029/98JC01945

Kotchenova, S. Y., and Vermote, E. F. (2007). Validation of a vector version of the 6S radiative transfer code for atmospheric correction of satellite data. Part II. Homogeneous lambertian and anisotropic surfaces. *Appl. Opt.* 46, 4455–4464. doi: 10.1364/ao.46.004455

Kotchenova, S. Y., Vermote, E. F., Matarrese, R., and Klemm, F. J. Jr. (2006). Validation of a vector version of the 6S radiative transfer code for atmospheric correction of satellite data. Part I: path radiance. *Appl. Opt.* 45, 6762–6774. doi: 10.1364/ao.45.006762

Kudela, R. M., Hooker, S. B., Houskeeper, H. F., and McPherson, M. (2019). The influence of signal to noise ratio of legacy airborne and satellite sensors for simulating next-generation coastal and inland water products. *Remote Sens.* 11:2071. doi: 10.3390/rs11182071

Lee, C. M., Cable, M. L., Hook, S. J., Green, R. O., Ustin, S. L., Mandl, D. J., et al. (2015). An introduction to the NASA Hyperspectral InfraRed Imager (HyspIRI) mission and preparatory activities. *Remote Sens. Environ.* 167, 6–19. doi: 10.1016/j.rse.2015.06.012

Livingston, J., Schmid, B., Redemann, J., Russell, P. B., Ramirez, S. A., Eilers, J., et al. (2007). Comparison of water vapor measurements by airborne Sun photometer and near-coincident in situ and satellite sensors during INTEX/ITCT 2004. *J. Geophys. Res.* 112:D12S16. doi: 10.1029/2006JD007733

Livingston, J. M., Russell, P. B., Reid, J. S., Redemann, J., Schmid, B., Allen, D., et al. (2003). Airborne sunphotometer measurements of aerosol optical depth and columnar water vapor during the Puerto Rico Dust Experiment, and comparison with land, aircraft, and satellite measurements. *J. Geophys. Res.* 108:8588. doi: 10.1029/2002JD002520

Loisel, H., Vantrepotte, V., Jamet, C., and Dat, D. N. (2013). "Challenges and new advances in ocean color remote sensing of coastal waters," in *Topics in Oceanography*, ed. E. Zambianchi (Greer, SC: InTech).

Lund, J. W. G., Kipling, C., and Le Cren, E. D. (1958). The inverted microscope method of estimating algal numbers and the statistical basis of estimations by counting. *Hydrobiologia* 11, 143–170. doi: 10.1007/BF00007865

Montes, M. J., Gao, B.-C., and Davis, C. O. (2001). "A new algorithm for atmospheric correction of hyperspectral remote sensing data," in *Proceedings of SPIE - The International Society for Optical Engineering*, Orlando, FL.

Montes, M. J., Gao, B.-C., and Davis, C. O. (2003). "Tafkaa atmospheric correction of hyperspectral data," in *Proceedings of SPIE - The International Society for Optical Engineering*, San Diego, CA.

Morrow, J. H., Hooker, S. B., Booth, C. R., Bernhard, G., Lind, R. N., and Brown, J. W. (2010). *Advances in Measuring the Apparent Optical Properties (AOPs) of Optically Complex Waters*. NASA Tech. Memo. 2010-215856, Greenbelt, MD: NASA Goddard Space Flight Center.

Moses, W. J., Bowles, J. H., Lucke, R. L., and Corson, M. R. (2012). Impact of signal-to-noise ratio in a hyperspectral sensor on the accuracy of biophysical parameter estimation in case II waters. *Opt. Express.* 20, 4309–4330. doi: 10.1364/OE.20.004309

Mouw, C. B., Greb, S., Aurin, D., DiGiacomo, P. M., Lee, Z., Twardowski, M., et al. (2015). Aquatic color radiometry remote sensing of coastal and inland waters: challenges and recommendations for future satellite missions. *Remote Sens. Environ.* 160, 15–30. doi: 10.1016/j.rse.2015.02.001

Mustard, J. F., Staid, M., and Fripp, W. J. (2001). A semianalytical approach to the calibration of AVIRIS data to reflectance over water. *Remote Sens. Environ.* 75, 335–349. doi: 10.1016/S0034-4257(00)00177-2

Palacios, S. L., Kudela, R. M., Guild, L. S., Negrey, K. H., Torres-Perez, J., and Broughton, J. (2015). Remote sensing of phytoplankton functional types in the coastal ocean from the HyspIRI Preparatory Flight Campaign. *Remote Sens. Environ.* 167, 269–280. doi: 10.1016/j.rse.2015.05014

Palmer, S. C. J., Kutser, T., and Hunter, P. D. (2015). Remote sensing of inland waters: challenges, progress and future directions. *Remote Sens. Environ.* 157, 1–8. doi: 10.1016/j.rse.2014.09.021

Redemann, J., Schmid, B., Eilers, J. A., Kahn, R. A., Levy, R. C., Russell, P. B., et al. (2005). Suborbital measurements of spectral aerosol optical depth and its variability at sub-satellite grid scales in support of CLAMS, 2001. *J. Atmos. Sci.* 62, 993–1007. doi: 10.1175/JAS3387.1

Redemann, J., Zhang, Q., Livingston, J., Russell, P., Shinozuka, Y., Clarke, A., et al. (2009). Testing aerosol properties in MODIS Collection 4 and 5 using airborne sunphotometer observations in INTEX-B/MILAGRO. *Atmos. Chem. Phys.* 9, 8159–8172. doi: 10.5194/acp-9-8159-2009

Russell, P. B., Livingston, J. M., Redemann, J., Schmid, B., Ramirez, S. A., Eilers, J., et al. (2007). Multi-grid-cell validation of satellite aerosol property retrievals in INTEX/ITCT/ICARTT 2004. *J. Geophys. Res.* 112:D12S09. doi: 10.1029/2006JD007606

Ryan, J., Davis, C., Tufillaro, N., Kudela, R., and Gao, B.-C. (2014). Application of the Hyperspectral Imager for the Coastal Ocean to Phytoplankton Ecology Studies in Monterey Bay, CA, USA. *Remote Sens.* 6, 1007–1025. doi: 10.3390/rs6021007

Ryan, J. P., Chavez, F. P., and Bellingham, J. G. (2005a). Physical-biological coupling in Monterey Bay, California: topographic influences on phytoplankton ecology. *Mar. Ecol. Prog. Ser.* 287, 23–32. doi: 10.3354/meps287023

Ryan, J. P., Dierssen, H. M., Kudela, R. M., Scholin, C. A., Johnson, K. S., Sullivan, J. M., et al. (2005b). Coastal ocean physics and red tides: an example from Monterey Bay, California. *Oceanography* 18, 246–256. doi: 10.5670/oceanog.2005.58

Ryan, J. P., Fischer, A. M., Kudela, L., McManus, M. A., Myers, J. S., Paduan, J. D., et al. (2010). Recurrent frontal slicks of a coastal ocean upwelling shadow. *J. Geophys. Res.* 115:C12070. doi: 10.1029/2010JC006398

Ryan, J. P., Fischer, A. M., Kudela, R. M., Gower, J. F. R., King, S. A., Marin, R., et al. (2009). Influences of upwelling and downwelling winds on red tide bloom dynamics in Monterey Bay, California. *Continent. Shelf Res.* 29, 785–795. doi: 10.1016/j.csr.2008.11.006

Ryan, J. P., Gower, J. F. R., King, S. A., Bissett, W. P., Fischer, A. M., Kudela, R. M., et al. (2008). A coastal ocean extreme bloom incubator. *Geophys. Res. Lett.* 35:L12602. doi: 10.1029/2008GL034081

Ryan, J. P., Tufillaro, N. B., and Davis, C. O. (2012). *HICO Observations of Biological and Sediment-Transport Processes in Monterey Bay, California*. Washington, DC: Optical Society of America.

Schneider, F. D., Ferraz, A., and Schimel, D. (2019). Watching Earth's interconnected systems at work. *EOS* 100:205. doi: 10.1029/2019EO136205

Shi, W., and Wang, M. (2009). An assessment of the black ocean pixel assumption for MODIS SWIR bands. *Remote Sens. Environ.* 113, 1587–1597. doi: 10.1016/j.rse.2009.03.011

Siegel, D. A., Wang, M., Maritorena, S., and Robinson, W. (2000). Atmospheric correction of satellite ocean color imagery: the black pixel assumption. *Appl. Opt.* 39, 3582–3591. doi: 10.1364/ao.39.003582

Spanner, M. A., Wrigley, R. C., Pueschel, R. F., Livingston, J. M., and Colburn, D. S. (1990). Determination of atmospheric optical properties during the First international satellite land surface climatology project field experiment. *J. Spacecraft.* 27, 373–379. doi: 10.2514/3.26153

Thompson, D. R., Seidel, F. C., Gao, B. C., Gierach, M. M., Green, R. O., Kudela, R. M., et al. (2015). Optimizing irradiance estimates for coastal and inland

water imaging spectroscopy. *Geophys. Res. Lett.* 42, 4116–4123. doi: 10.1002/2015GL063287

Turpie, K. R., Ackelson, S., Bell, T., Dierssen, H. M., Goodman, J., Green, R. O., et al. (2016). Global Observations of Coastal and Inland Aquatic Habitats, white paper submission in response to a 'Request for Information' issued on behalf of the steering committee for the National Academies of Science, Engineering, and Medicine study, Earth Science and Applications from Space. doi: 10.13140/RG.2.2.15839.66729

Turpie, K. R., Allen, D. W., Ackelson, S., Bell, T., Dierssen, H. M., Cavanaugh, K., et al. (2015). New Need to Understand Changing Coastal and Inland Aquatic Services, white paper submission in response to a 'Request for Information' issued on behalf of the steering committee for the National Academies of Science, Engineering, and Medicine study, Earth Science and Applications from Space. doi: 10.13140/RG.2.1.5162.6007

Van Heukelem, L., and Thomas, C. S. (2001). Computer-assisted high-performance liquid chromatography method development with applications to the isolation and analysis of phytoplankton pigments. *J. Chromatogr. A* 910, 31–49. doi: 10.1016/S0378-4347(00)00603-4

Vanhellemont, Q., and Ruddick, K. (2015). Advantages of high quality SWIR bands for ocean colour processing: examples from Landsat-8. *Remote Sens. Environ.* 161, 89–106. doi: 10.1016/j.rse.2015.02.007

Vansteenwegen, D., Ruddick, K., Cattrijsse, A., Vanhellemont, Q., and Beck, M. (2019). The Pan-and-Tilt hyperspectral radiometer system (PANTHYR) for autonomous satellite validation measurements—prototype design and testing. *Remote Sens.* 11:1360. doi: 10.3390/rs11111360

Vermote, E. F., Tanré, D., Deuze, J. L., Herman, M., and Morcette, J. J. (1997). Second simulation of the satellite signal in the solar spectrum, 6S: an overview. *IEEE Trans. Geosci. Remote Sens.* 35, 675–686. doi: 10.1109/36.581987

Wang, Z., King, K. L., Ramsdell, J. S., and Doucette, G. J. (2007). Determination of domoic acid in seawater and phytoplankton by liquid chromatography-tandem mass spectrometry. *J. Chromatogr. A* 1163, 169–176. doi: 10.1016/j.chroma.2007.06.054

Werdell, P. J., Franz, B. A., and Bailey, S. W. (2010). Evaluation of shortwave infrared atmospheric correction for ocean color remote sensing of Chesapeake Bay. *Rem. Sens. Env.* 114, 2238–2247. doi: 10.1016/j.rse.2010.04.027

Wrigley, R. C., Spanner, M. A., Sly, R. E., Pueschel, R. F., and Aggarwal, O. (1992). Atmospheric correction of remotely sensed image data by a simplified model. *J. Geophys. Res.* 97, 18797–18814. doi: 10.1029/92JD01347

Zibordi, G., Mélin, F., Berthon, J.-F., Holben, B., Slutsker, I., Giles, D., et al. (2009). AERONET-OC: a network for the validation of ocean color primary products. *J. Atmos. Ocean. Technol.* 26, 1634–1651. doi: 10.1175/2009JTECHO654.1 doi: 10.1175/2009jtecho654.1

Conflict of Interest: The authors declare that the research was conducted in the absence of any commercial or financial relationships that could be construed as a potential conflict of interest.

Copyright © 2020 Guild, Kudela, Hooker, Palacios and Houskeeper. This is an open-access article distributed under the terms of the Creative Commons Attribution License (CC BY). The use, distribution or reproduction in other forums is permitted, provided the original author(s) and the copyright owner(s) are credited and that the original publication in this journal is cited, in accordance with accepted academic practice. No use, distribution or reproduction is permitted which does not comply with these terms.

frontiers in Environmental Science

ORIGINAL RESEARCH
published: 03 December 2020
doi: 10.3389/fenvs.2020.599030

Analysis and Classification of Stormwater and Wastewater Runoff From the Tijuana River Using Remote Sensing Imagery

Mariam Ayad[1], Jingjing Li[1], Benjamin Holt[2] and Christine Lee[2]*

[1] Department of Geosciences and Environment, California State University, Los Angeles, Los Angeles, CA, United States,
[2] Jet Propulsion Laboratory, California Institute of Technology, Pasadena, CA, United States

Urban runoff represents the primary cause of marine pollution in the Southern California coastal oceans. This study focuses on water quality issues originating from the Tijuana River watershed, which spans the southwest border of the United States and Mexico. Frequent discharge events into the coastal ocean at this boundary include stormwater and wastewater. This study focuses on differences in spectral features, as assessed by RapidEye, Sentinel-2 A/B, and Landsat-8 satellite data, along with physical and biological *in situ* data, to characterize and classify plumes into four key categories: stormwater, wastewater, open ocean/no plume, and mixed (when both types of plumes are present). Key spectral differences in the visible to NIR bands showed that stormwater had elevated reflectance (0.02 to 0.09), followed by mixed (0 to 0.08), wastewater (0 to 0.05), and open ocean/no plume (0 to 0.03) events. We also examined biophysical parameters and found that stormwater events had the highest values in remote sensing based estimates of colored dissolved organic matter (CDOM) (0.98 to 2.1 m^{-1}) and turbidity (12.4 to 45.7 FNU) and also had a large range for *in situ* variables of enterococcus bacteria and flow rates. This study also finds that the use of spectral features in a hierarchical cluster analysis can correctly classify stormwater from wastewater plumes when there is a dominant type. These results of this study will enable improved determination of the transport of both types of plumes and transboundary monitoring of coastal water quality across the Southern California/Baja California region.

Keywords: satellite remote sensing, marine pollution, water quality, RapidEye, wastewater, runoff plumes

OPEN ACCESS

Edited by:
Andrea J. Vander Woude, NOAA Great Lakes Environmental Research Laboratory, United States

Reviewed by:
Dulcinea Avouris, University of California, Merced, United States
Milton Kampel, National Institute of Space Research (INPE), Brazil

****Correspondence:***
Mariam Ayad
maayad@ucsc.edu;
mayad2@calstatela.edu

Specialty section:
This article was submitted to Environmental Informatics and Remote Sensing, a section of the journal Frontiers in Environmental Science

Received: *26 August 2020*
Accepted: *06 November 2020*
Published: *03 December 2020*

Citation:
Ayad M, Li J, Holt B and Lee C (2020) Analysis and Classification of Stormwater and Wastewater Runoff From the Tijuana River Using Remote Sensing Imagery. Front. Environ. Sci. 8:599030. doi: 10.3389/fenvs.2020.599030

INTRODUCTION

The coastal regions of Southern California are susceptible to coastal pollution from urban drainage. With respect to stormwater, a buildup of pollutants on land during the dry summer months are transported to coastal oceans during wet season events (Bay et al., 2003; DiGiacomo et al., 2004; Svejkovsky et al., 2010; Holt et al., 2017). Stormwater runoff from a large urban coastal environment contains sediments as well as bacteria, oil, fuel, and tire particles from automobiles, anthropogenic components from sewage, and fertilizer from agriculture (Reifel et al., 2009; Svejkovsky et al., 2010). This represents a hazard for the ecosystem and for public health in this coastal region, particularly during the rainy season (Ackerman and Weisberg, 2003). Often, during these events, bacteria levels

of fecal indicator bacteria (FIB) and enterococcus (ENT) are as high as 15,000 CFU/100 mL in the ocean which can lead to significant health issues for beachgoers and surfers (Ackerman and Weisberg, 2003). EPA guidelines recommend FIB and ENT should not be greater than 100 CFU/100 mL[1]. Recreational water activities should be avoided for at least 3 days after a rain event (Ackerman and Weisberg, 2003) since studies have shown an increase risk of gastrointestinal or other acute illness in surfers within that time period (Schiff et al., 2016; Arnold et al., 2017).

Analysis of stormwater runoff and wastewater plumes, for purposes of managing and minimizing health impacts to beach communities, with observational datasets are generally limited to *in situ* data collections and fixed stations. Remote sensing based assessments of plumes in Southern California have used various multispectral sensors with varying resolution including SeaWiFS optical radiometer (Nezlin and DiGiacomo, 2005), MODIS (1 km), Landsat-8 (15 to 30 m), and NOAA's Advanced Very High-Resolution Radiometer (AVHRR) (1 km) (Nezlin et al., 2007; Warrick et al., 2007; Lahet and Stramski, 2010; Svejkovsky et al., 2010), all of which have significant limitations in terms of spatial, temporal and spectral resolution and cloud cover. In Holt et al. (2017), both SAR (5 to 150 m) and MODIS imagery were used to study stormwater runoff in the Southern California Bight. In Devlin et al. (2015), MODIS was also used to investigate the impact of stormwater plumes on coral reefs in the Great Barrier Reef.

Publicly operated wastewater treatment facilities in Southern California typically discharge treated wastewater offshore at depth, with the effluent largely mixing at depth and remaining below the thermocline. During limited occasions, maintenance requirements to a facility's discharge system required the temporary diversion of treated wastewater closer to shore and at shallower depths. During such diversions, significant collections of both *in situ* and spaceborne remote sensing provided an opportunity to improve understanding of wastewater plume dynamics and impacts (Gierach et al., 2017; Trinh et al., 2017) as well as the biological response to increased nutrient levels (Reifel et al., 2009; Caron et al., 2017). The Tijuana River watershed is about 1,750 square miles of area that spans across the California – Mexico border (**Figure 1**). About 75 percent of the watershed is in Mexico, while the remainder is on the California side near Imperial Beach including the river mouth. Stormwater runoff plumes have been observed after rain events at the Tijuana River outlet. In addition, the frequent release of treated and untreated wastewater into the Tijuana River watershed has been documented to occur since the late 1990s. Both types of coastal plumes have been shown to impact the San Diego, CA, United States coastal region as well as the closely adjacent Mexico region, causing health concerns for beachgoers and residents. The two wastewater treatment plants of interest are the South Bay International Wastewater Treatment Plant (SBIWTP) located in San Diego, CA, United States and the San Antonio de los Buenos Wastewater Treatment Plant located in Tijuana, Mexico shown in **Figure 1**.

Stormwater runoff is largely tied to rain events, often carrying along multiple type of material and contaminants as mentioned earlier, and is monitored by a flow gauge station. The Tijuana River has raised particular attention due to the increasing occurrence of untreated wastewater released up river closer to the Tijuana population center that contains a high level of FIB effluent into the coastal area[2] as well as the reference of human fecal markers. The transport of both type of plumes is dependent on the nearshore circulation, with the San Diego coastal population notably greater than on the Mexico coastal side. For example, the San Diego Regional Water Quality Control Board reported wastewater pollution in the Tijuana River Watershed on February 6-23, 2017, where there was an incident of an estimated 28 million gallons (MG) of untreated wastewater released into the Tijuana River (see text footnote 2). This has caused major water quality and health issues particularly when transported northward into the large urban population in the San Diego area that live near the coast. In another recent case, during December 11–14, 2018, there was a wastewater spill of 7 million gallons per day, totaling an estimated 28 million gallons (see text footnote 2). More recently, from January 18–30, 2019, there were 610 million gallons that spilled in this region (see text footnote 1). In 2018, the San Diego Regional Water Quality Control Board sent a letter of intent to sue the United States Section of the International Boundary and Water Commission (USIBWC) for violations of the Clean Water Act and seeking improvements to the treatment of wastewater and reduction of accidental releases. Both the United States and Mexico are working toward a solution since the watershed is shared by both countries and continues to be an ongoing transboundary water issue.

The studies on stormwater and wastewater focused on the detection, extent, and impact of known separately occurring events and resultanting plumes but did not differentiate between plume types based on sensor responses. The only known studies on the detection and possible classification of wastewater in a coastal environment with remote sensing were in DiGiacomo et al., 2004; Marmorino et al., 2010; Seegers et al., 2017; Trinh et al., 2017; Gierach et al., 2017. In Gierach et al. (2017), Moderate Resolution Imaging Spectrometer (MODIS) and Satellite Aperture Radar (SAR) data were used to detect wastewater plumes during two diversion events in Southern California. The results showed that wastewater plumes could be identified by a decrease in sea surface temperature (SST) from MODIS and changes in the surface roughness from SAR. Another study by Trinh et al. (2017) utilized Landsat 8 Operational Land Imager (OLI) and MODIS imagery to derive SST and chlorophyll-a to investigate wastewater impacts and transport within Santa Monica Bay, California, after a third diversion event. We know of no published study using remote sensing that has successfully identified stormwater plumes from treated wastewater or raw wastewater plumes.

The goal of this study is to determine if the wastewater and stormwater plumes are optically distinct from each other, by examining differences in spectral reflectance and derived

[1]https://www.epa.gov/sites/production/files/2015-10/documents/rwqc2012.pdf

[2]http://www.waterboards.ca.gov/sandiego/water_issues/programs/tijuana_river_valley_strategy/sewage_issue.html

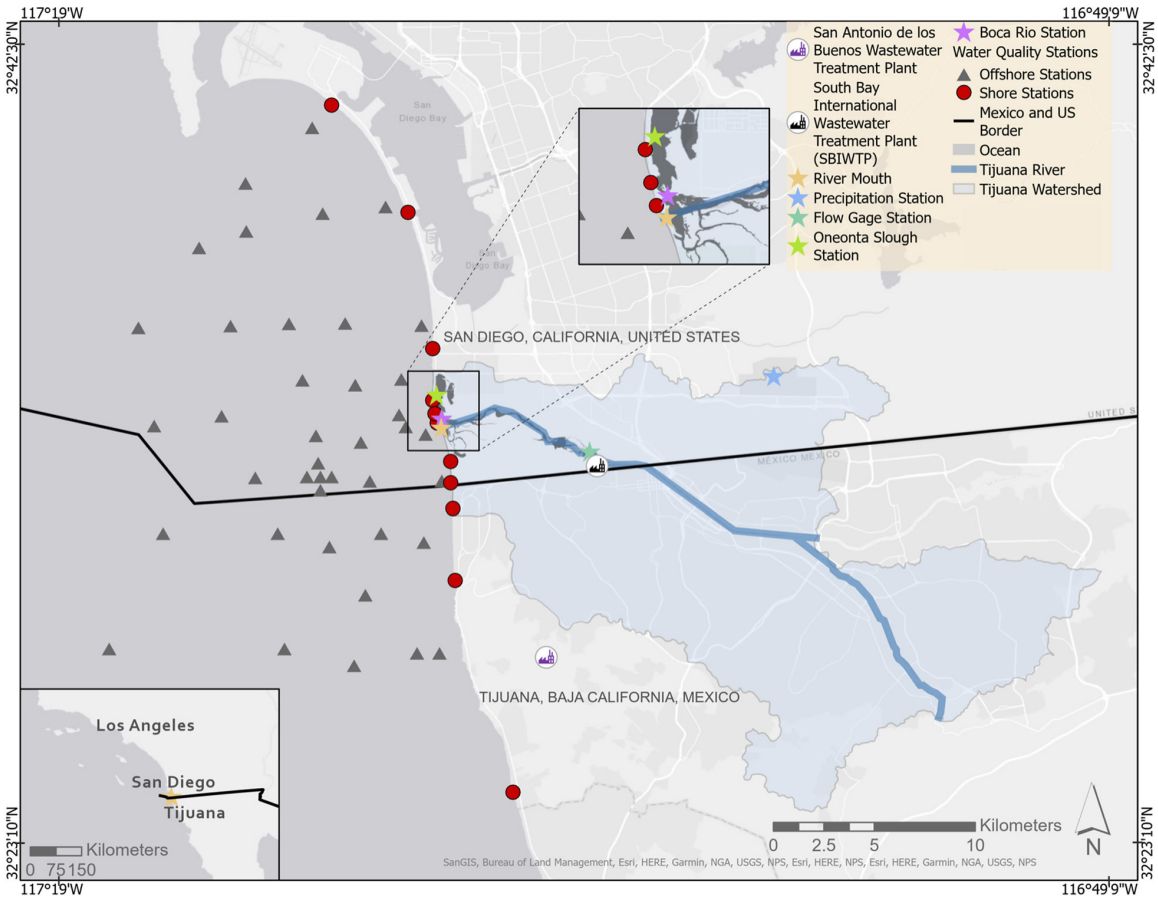

FIGURE 1 | The Tijuana River Watershed. The water quality sampling stations from The City of San Diego Public Utilities are denoted by red points and gray triangles. Automatic water quality sampling stations from the NOAA National Estuarine Research Reserve System (NERRS) located in the estuary are symbolized as a purple (Boca Rio Station) and light green star (Oneonta Slough Station). The Tijuana River mouth is symbolized as a yellow star and the flow gauge station is a green star near the United States Mexico border. The precipitation station is the blue star located at the Brown Field Municipal Airport. The South Bay International Wastewater Treatment Plant (SBIWTP) is located in San Diego, CA near the United States Mexico border. The San Antonio de los Buenos Wastewater Treatment Plant is located in Tijuana, Mexico situated south of the watershed.

parameters, such as turbidity and colored dissolved organic matter (CDOM), in combination with *in situ* data, such as precipitation, enterococcus (ENT), and flow discharge rate. We hypothesize that these two plume types will have distinct spectral properties because stormwater plumes are likely to be dominated by sediments (Corcoran et al., 2010) and that wastewater is likely to be dominated by organic matter (DiGiacomo et al., 2004; Nezlin et al., 2008; Marmorino et al., 2010). This hypothesis will be evaluated within the context of a regional use case at the southwest border of United States and Mexico, in the coastal ocean downstream of the Tijuana River Watershed.

DATA AND METHODS

Identification and Selection of Plume Events

A stormwater plume is identified by precipitation event(s) that occurred at least 1–3 days prior to a remote sensing observation with no reported concurrent wastewater events occurring. Gauge data are used to identify high flow conditions following precipitation events. A wastewater plume is identified based on a reported wastewater spill from the San Diego Regional Water Quality Control Board with no reported concurrent precipitation events occurring within 3 days of precipitation prior to the spill (dry event). Sewage reports indicate that these spills are a combination of treated and untreated wastewater (see text footnote 2). Mixed events are a combination of precipitation 1–3 days prior and a reported wastewater spill. A no-plume event is defined when there is no precipitation or wastewater spill for the prior 2 weeks.

Optical Imagery and Surface Reflectance Profiles

Data Sources

The primary remote sensing sensor used in this study is RapidEye imagery available from Planet.com and complemented

by European Space Agency Sentinel 2A/B and NASA/USGS Landsat 8. While RapidEye has limited spectral information, its revisit rate of 5 days and higher spatial resolution of 5 m were critical to capturing plume events. This imagery has been acquired over this region since 2009 through March 2020, when sensor operations ended. RapidEye is made available by Planet.com under the Education and Research Program for non-commercial access to Planet and Rapid Eye imagery. Sentinel 2 A/B (high revisit rate) and PlanetScope (high spatial resolution) sensors are key alternatives for future studies since RapidEye has been discontinued. Revisit time, spatial resolution, swath width, data source, and spectral characteristics of the sensors used in this study are shown in **Table 1**.

The Copernicus Sentinel-2A and Sentinel-2B missions were launched on June 23, 2015 and March 7, 2017, respectively, and are operated by the European Space Agency (ESA). Each instrument consists of 12 spectral bands and a swath width of 290 km, and a spatial resolution of 10 m. The Landsat 8 mission carrying the Operational Land Imager (OLI) and the Thermal Infrared Sensor (TIRS) is operated by the USGS and was launched on February 11, 2013. The OLI has 9 spectral bands and a swath width of 185 km. The spatial resolution of Landsat 8 is 30 m for the multispectral bands. Sentinel 2 A/B and Landsat 8 were used to calculate CDOM since they have the required bands to apply the Quasi-Analytical Algorithm (QAA) of Lee et al. (2002).

We utilize these sensors to examine and characterize the optical properties of both types of coastal plumes with the intent of separately classifying each type of plume. Since these plumes disperse after a day or two, a sensor that has a high spatial and temporal resolution is crucial (DiGiacomo et al., 2004).

A total of 40 RapidEye images were identified during these periods and separated into four groups (10 stormwater, 10 wastewater, 10 mixed (a combination of both), and 10 open ocean/no plume) and were then analyzed for differences in surface reflectance in five bands and other biochemical parameters such as turbidity and CDOM. We also utilize *in situ* data such as flow rate, precipitation, ENT, and plume color to differentiate between these groups. **Supplementary Table 1** provides more detailed information on each RapidEye image and its output. RapidEye was used for all the outputs of spectral reflectance for consistency. Information on how the spectral reflectances values were extracted are in section "Spectral Profiles."

Atmospheric Correction

For RapidEye, Sentinel-2, and Landsat-8 data, an atmospheric correction scheme was applied using ACOLITE software. The open-source program ACOLITE (Vanhellemont and Ruddick, 2018) was used to process these images with atmospheric corrections (Eq. 1) and to generate output parameters including remote sensing reflectance (*Rrs*), chlorophyll-a concentration (*chla*), CDOM (*a443*), suspended matter concentration, and turbidity (Vanhellemont, 2019a). ACOLITE can be downloaded from the GitHub repository for RapidEye imagery[3] and Sentinel-2 and Landsat-8 imagery[4]. Atmospheric correction was calculated for all imagery using the following:

$$REF\,(i) = \frac{RAD\,(i)\,\pi d^2}{ESI(i)\,\cos\theta_s} \quad (1)$$

where *REF* is the reflectance value for the top of atmosphere (TOA) reflectance, *RAD* is the radiance value, *i* is the number

[3]https://github.com/acolite/acolite_mr/

[4]https://github.com/acolite/acolite

TABLE 1 | Optical satellite specifications for RapidEye, Sentinel-2 A/B, and Landsat 8.

	RapidEye	Sentinel 2 A/B	Landsat 8
			OLI and TIRS
Revisit time (days)	5	5	16
Spatial resolution (m/pixel)	5	10	30
Swath width (km)	77	290	290
Data access	Planet Labs (https://planet.com)	Copernicus (https://sentinels.copernicus.eu/web/sentinel/sentinel-data-access)	USGS (https://earthexplorer.usgs.gov)
Spectral band info (lists of bands used in this study)	Band 1: Blue (440–510 nm)	Band 1: Coastal aerosol (443–452 nm)	Band 1: Coastal aerosol (433–453 nm)
	Central wavelength: 475 nm	**Central wavelength: 443 nm**	**Central wavelength: 440 nm**
		Band 2: Blue (458–523 nm)	Band 2: Blue (450–515 nm)
		Central wavelength: 490 nm	**Central wavelength: 480 nm**
	Band 2: Green (520–590 nm)	Band 3: Green (543–578 nm)	Band 3: Green (525–600 nm)
	Central wavelength: 555 nm	**Central wavelength: 560 nm**	**Central wavelength: 560 nm**
	Band 3: Red (630–685 nm)	Band 4: Red (650–680 nm)	Band 4: Red (630–680 nm)
	Central wavelength: 658 nm	**Central wavelength: 665 nm**	**Central wavelength: 655 nm**
	Band 4: Red Edge (690–730 nm)		
	Central wavelength: 710 nm		
	Band 5: Near-infrared (760–850 nm)		
	Central wavelength: 805 nm		

Central wavelength corresponds to the peak wavelength for each band in nanometers.

of the spectral band, d is the earth-sun distance at the day of acquisition in astronomical units (AU), *ESI* is the extraterrestrial solar irradiance, and θ_s is the solar zenith angle in degrees (90° – sun elevation). More information on calculating TOA reflectance and ESI values for each band can be found on the Planet Labs website[5]. *REF* is corrected using the Dark Spectrum Fitting (DSF) algorithm for the five RapidEye bands (Vanhellemont, 2019b). The DSF algorithm is an aerosol correction algorithm and is used to estimate surface reflectance (see text footnote 3). All imagery was atmospherically corrected using the DSF algorithm.

Remote Sensing Based Analyses

Spectral Profiles

We utilize a region of interest polygon (circle) to define the area of interest (AOI) for all RapidEye images with a size of 1.28 km^2 (51,076 pixels) to maintain consistency when examining spectral properties for different plume events. An example of the AOI is symbolized as a white circle in **Figure 2**. The surface reflectance values, after the atmospheric correction, were extracted from the AOI and were spatially averaged to obtain the mean surface reflectance value for each band in the AOI. The same process was done for all 10 events for each of the four groups.

Derived Turbidity

Turbidity is the measure of water clarity in a body of water. High turbidity is often due to high concentrations of suspended particles from sediments, CDOM, or algae and has units of Formazine Nephelometric Units (FNU) or Nephelometric Turbidity Unit (NTU). The bands that can detect turbidity are red, red-edge, or near-infrared (NIR) since turbidity has the optical properties of scattering light in these bands (Dogliotti et al., 2015; Hafeez et al., 2018). Turbidity is computed using the following equation (Nechad et al., 2009):

$$T = \frac{A\ \rho_w}{1 - \frac{\rho_w}{C}} \quad (2)$$

where T is the algorithm derived turbidity, ρw is the surface reflectance after atmospheric correction, and A and C are constant coefficients associated with inherent optical properties. Vanhellemont (2019b) shows excellent agreement from using RapidEye's red and red-edge bands after comparing seven sites (sites in Northern California, North Sea, and the Irish Sea) of *in situ* turbidity with derived turbidity. We decided to use RapidEye's red band for ρw since it gave the best results according to the Vanhellemont (2019b) study. We used the default A and C values, 247.10 and 0.1697, respectively, for the red band based on recommendations from Nechad et al. (2009) and Vanhellemont (2019b).

Derived Colored Dissolved Organic Matter

Colored dissolved organic matter is a yellow substance, gelbstoff, from the mixing of organic matter such as remains of plants and animals. High concentrations of CDOM arise from the breakdown of dead organisms and organic matter. The color of CDOM can range from yellow to brown in nearshore waters (Aurin et al., 2018). To calculate CDOM, we implement the Quasi-Analytical Algorithm (QAA) from Lee et al. (2002). Bands that are needed to calculate CDOM (a443) have a wavelength of 443, 490, 560, and 665 nm. Sentinel-2 A/B and Landsat 8 were used since they have all the required bands to derive CDOM. RapidEye has only one band from 410 to 510 nm (blue band) and may not give an estimate for CDOM. From the multistep process (shown in **Supplementary Table 4**), we obtain absorption outputs: a443, a490, a560, and a665. CDOM absorption can also be observed in the blue band since it absorbs in the UV and visible (blue light) spectrum range. The most recent updates to the QAA algorithm are in both version 5 (Lee et al., 2009) and version 6 (Lee et al., 2014) which incorporate Rrs (670 nm) (remote sensing reflectance in band 670 nm) since most sensors (MODIS, Sentinel-2, Landsat 8) have a band near this wavelength. ACOLITE applies either version 5 or version 6 depending on if Rrs (670nm) is less than 0.0015. **Supplementary Table 4** displays the equations to calculate a443 (CDOM). CDOM is calculated for 5 stormwater, 5 wastewater, 5 mixed, and 5 open ocean/no plume events from the AOI using Landsat 8 and Sentinel 2 A/B imagery (**Supplementary Table 3**).

Water Quality *in situ* Data

The NOAA National Estuarine Research Reserve System (NERRS)[6], a long-term monitoring program to protect estuarine ecosystems, has 28 stations across the United States collecting water quality, meteorological, nutrient, and pigment data. Each station is located near an estuary with an automatic sampler that collects data every 15 min (every 30 min prior to 2007). Two NOAA stations are used in this study, with one located at the mouth of the Tijuana River (Boca Rio: purple star in **Figure 1**) and the other inside the estuary (Oneonta Slough: light green star in **Figure 1**). Water quality parameters of interest are turbidity (FNU/NTU) and chlorophyll fluorescence (ug/L). The visual observations are also reported at each shore station including water color, water clarity, and human or animal activity (**Supplementary Table 2**). We used these visual observations to validate the plume color and water clarity observed from the true color imagery.

Wastewater spill data is from the City of San Diego (see text footnote 2) under Spill Reports, which provides the amount of wastewater spills and when the spills occurred. We also incorporate enterococcus (ENT) (CFU/100 mL) from The City of San Diego Public Utilities[7] to check the bacteria levels during a wastewater or stormwater event. Bacteria levels of ENT that go above 100 CFU/100mL are deemed harmful by the EPA standards (see text footnote 1). ENT is commonly used as an indicator of harmful bacteria and viruses that can cause illnesses in swimmers and surfers (Schiff et al., 2016). These data are used to characterize and compare the impact of wastewater and stormwater plumes with respect to turbidity and ENT.

[5]https://www.planet.com/products/satellite-imagery/files/160625-RapidEye%20Image-Product-Specifications.pdf

[6]http://cdmo.baruch.sc.edu

[7]https://www.sandiego.gov/public-utilities/sustainability/ocean-monitoring/data/south-bay

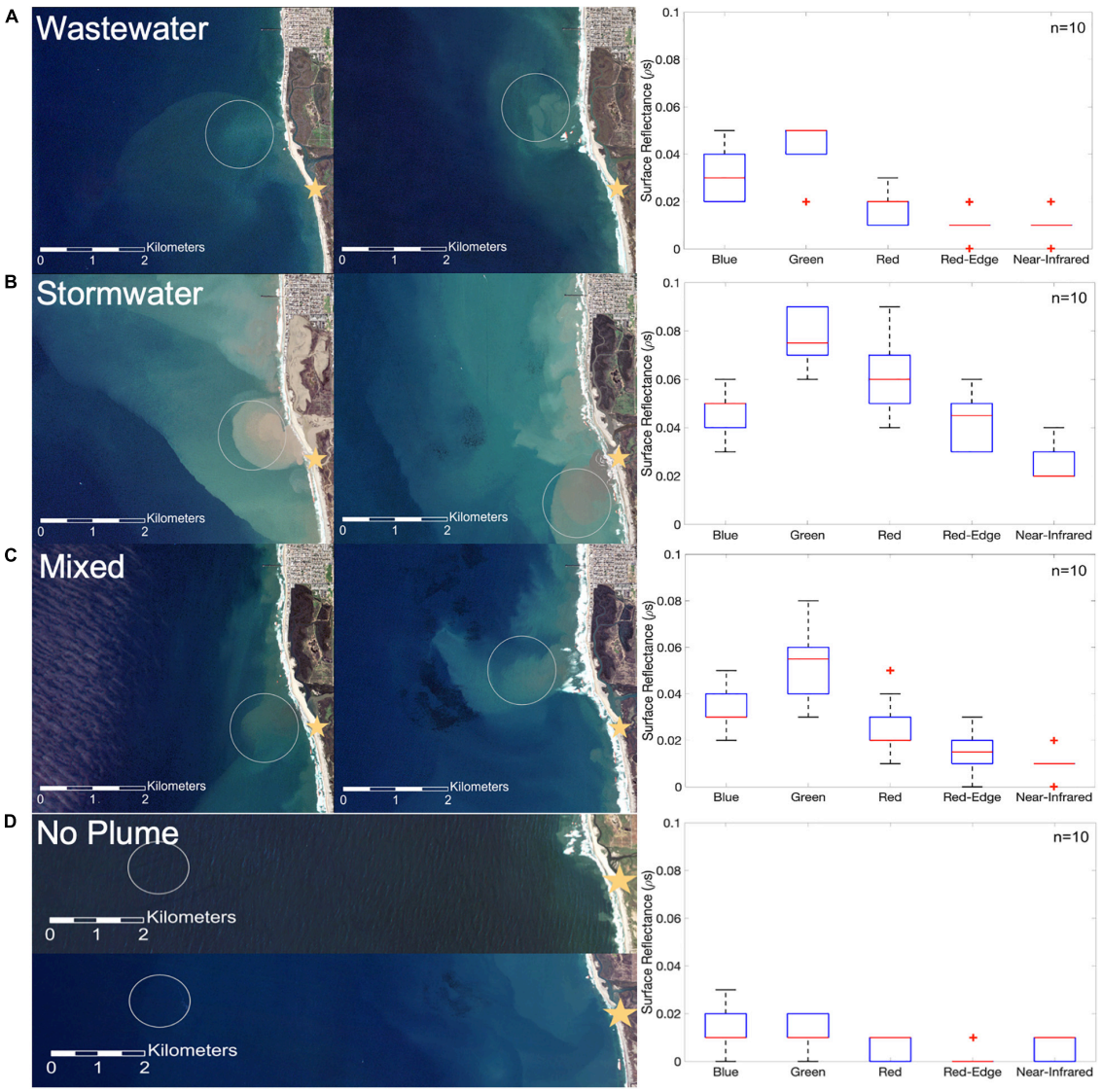

FIGURE 2 | Surface Reflectances for **(A)** Wastewater, **(B)** Stormwater, **(C)** Mixed, and **(D)** No event/No Plume. Images are the true color imagery from RapidEye with AOI circled. Box plots are the surface reflectance values for each plume type (10 events per type). A yellow star denotes the Tijuana River mouth. **(A)** Wastewater Plume Events: on 1/24/19 (left image): 610 million gallons (MG) of raw wastewater (occurred on 1/18 and ended on 1/30). 12/11/18 (right image): 147.7 MG of raw wastewater (occurred on 12/11 and ended on 12/24). **(B)** Stormwater Plume Events: 12/7/18 (left image): precipitation amount was 1.07 inches (2.7 cm) on 12/6/18 and flow rate hourly mean was 158.3 cms. 1/28/10 (right image): precipitation amount was 0.07 inches (0.18 cm) on 1/26/10 and no data available for flow rate. **(C)** Mixed Plume Events: 2/9/17 (left image): 143 MG of raw wastewater (occurred on 2/6/17 and ended on 2/23/2017), precipitation amount on 2/7 was 0.19 inches (0.48 cm), and flow rate hourly mean was 2.4 cms. 1/24/16 (right image): 23.7 MG of raw wastewater (occurred on 1/16/16 and ended on 1/24/16), precipitation amount on 1/23/16 was 0.4 inches (1 cm), and flow rate hourly mean was 0.2 cms. **(D)** No Plume Events: 3/23/17 (top image) and 12/16/15 (bottom image): no wastewater or precipitation events for at least a month. The AOI is extracted offshore due to natural sedimentation near the coast, which may influence surface reflectance values. For each box plot, the median is shown by the red mark, the whiskers correspond to the maximum and minimum values, the red plus signs show the outliers outside of the 25–75 percentile range shown by the box.

Precipitation and Flow Gauge Data

Precipitation data are acquired from NOAA[8] from 2010 to 2019, which is collected at the precipitation station at the Brown Field Municipal Airport marked as the blue star in **Figure 1**. Precipitation values for all stormwater events were plotted using MATLAB and are shown in **Supplementary Figure 2**. The units for the daily precipitation amount are in inches. Flow gauge data is from the International Boundary & Water Commission (IBWC)[9], whose station is marked as the green star in **Figure 1**. The units for flow rate are in cubic meters per second (cms) and the flow rate is the hourly mean of 12 h prior to the satellite

[8]https://www.ncdc.noaa.gov/orders/qclcd/

[9]https://www.ibwc.gov/Water_Data/Index.html

acquisition time. We use the hourly mean for the 12-h window since the flow gauge station is located upstream on the river approximately 6.4 km from the river mouth.

Analyses and Comparison of Plumes

Plume Comparison Using Spectral Data and *in situ* Data

To compare spectral reflectance information for each plume type, we created a box plot for each band using all 10 events shown in **Figure 2**. **Figure 2A** is an example of two wastewater plumes coming out of the Tijuana River Mouth on January 24, 2019 (147 million gallons of wastewater) and December 7, 2019 (610 million gallons of wastewater). **Figure 2B** is an example of two stormwater plumes on December 7, 2018 (1.07 inches of precipitation) and January 28, 2010 (0.07 inches of precipitation). **Figure 2C** is an example of two mixed plumes on February 9, 2017 (0.19 inches of precipitation and 143 million gallons of wastewater) and January 24, 2016 (0.4 inches of precipitation and 23.7 million gallons of wastewater). **Figure 2D** is an example of no plume events on March 23, 2017 and December 16, 2015. For both events, there is no wastewater or precipitation amounts. We compared the ranges of the reflectance values for each band to observe spectral differences across all bands. A line graph of these surface reflectance values was plotted with ± 1 standard deviation from the average spectral value for each plume type shown in **Figure 3**. Box plots of mean derived CDOM and turbidity from the AOI, and the *in situ* mean hourly flow rate and ENT (**Supplementary Table 2**) values were generated for each plume group. We implemented a one-way analysis of variance (ANOVA) test to determine if the means are different for each group.

Hierarchical Cluster Analysis and Principal Component Analyses

Two approaches were utilized to investigate how spectral data can be used to assess coastal plume classes. First, we applied a principal component analysis (PCA) (Jolliffe and Cadima, 2016) to our dataset of surface reflectance and derived turbidity values from the defined AOI. This was done directly on raw data (with the exception of averaging over an area of interest) to preserve variability in the dataset and account for interrelatedness of surface reflectance values between bands and because turbidity is derived from spectral information. PCA has been conducted on numerous studies of the natural and built environment in various capacities (Gašparović and Jogun, 2018; Judice et al., 2020) and is especially used for simplifying high dimensionality datasets and for classification applications. The principal components (PC1 and PC2) were then plotted to see whether groups of coastal plume classes were clearly clustered or not.

The second methodology applied here was the hierarchical cluster analysis (HCA) in a complete-linkage clustering approach (Revelle, 1979). The purpose of utilizing an alternate approach was to see if both modes of analysis would reinforce the observed spectrally dependent differentiation of coastal plume types. HCA performed in this study uses an agglomerative scheme that considers each sample as its own individual cluster. Clusters that are considered more similar (i.e., shortest distance) are then used to generate larger clusters. Previous work has demonstrated the utility of HCA on water quality classifications and aquatic properties (Brezonik et al., 2005; Kamble and Vijay, 2011; Reynolds and Stramski, 2019).

Both HCA and PCA utilized input data from 30 separate coastal plume events – 10 were considered "no plume" or open ocean, 10 were considered sewage spill plumes, and 10 were considered stormwater plumes. Pixels for the AOI were averaged for each of these events, the events are summarized in **Supplementary Table 1**.

RESULTS

Plume Comparison Using Spectra Data of AOI (Surface Reflectance, Turbidity, and CDOM)

Figure 2A shows wastewater plume reflectance values ranged from low-medium reflectance in the blue to green bands and low reflectance in the red-NIR bands. Stormwater plumes had medium reflectance in the blue band, medium-high reflectance in the green to red-edge bands, and low-medium reflectance in the NIR shown in **Figure 2B**. The results show that the stormwater plumes have the highest reflectance in the green-red region (500–700 nm) which could potentially be due to increased sediment loading. **Figure 2C** shows there is considerable overlap of mixed plumes in the green and red bands, especially with both the stormwater and wastewater plumes only, indicating varying concentrations and extent of both wastewater and sediments shown. Wastewater and mixed plumes reflect mostly in the green band (500–600 nm) which may be due to CDOM or chlorophyll. Open ocean/no plume has the lowest reflectance across all wavelengths considered as shown in **Figure 2D**. Wastewater plumes are clearly separated from stormwater plumes in all five bands.

The line graph in **Figure 3** shows the surface reflectances of 10 stormwater plumes, 10 wastewater plumes, 10 mixed plumes, and 10 open ocean/no plume events. Each plot represents the average reflectance value and the bounding bars indicate ± 1 standard deviation. These surface reflectance values are shown in **Supplementary Figure 1**.

We conducted an HCA and a PCA on 30 independent plume images, where 10 images were associated with stormwater, 10 for wastewater, and 10 for open ocean/no plume events. Mixed plumes were excluded from this analysis because their spectral signature overlapped with wastewater plumes. As seen in **Figure 4A**, there are three primary branches that correspond with each of the coastal plume classes evaluated in this analysis: O (Open Ocean/No Plume – in red); WW (Wastewater – in green); and SW (Stormwater – in blue). Three of the open ocean samples (O8, O9, and O10) were clustered into the wastewater plumes branch, indicating that 27 out of 30 events were classified into their matching plume class (90% correct classification).

In the PCA analysis, (**Figure 4B**) we see two distinct groups [(1) Open Ocean/Wastewater and (2) Stormwater], differentiated across PC1, the component that accounts for the majority of the

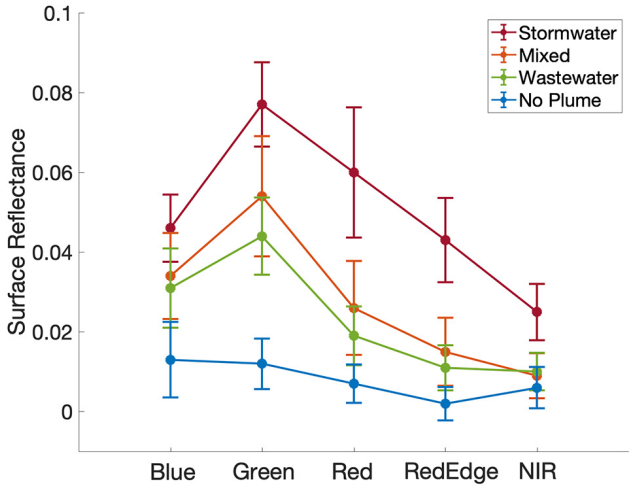

FIGURE 3 | Line graph of surface reflectances for 10 stormwater plumes, 10 wastewater plumes, 10 mixed plumes, and 10 open ocean events. The *y*-axis indicates the surface reflectance values and the *x*-axis is the wavelength. The bounding bars are the ±1 standard deviation from the average spectral value.

variance (89.1%) and less clear distinction across the *y*-axis/PC2 for open ocean and wastewater, with PC2 explaining about 6.8% of the variance. While O9 and O10 are in closest proximity to the WW samples, O3 a slightly closer than O8 is, which is a slight difference between HCA and PCA evaluations. PC1 and PC2 are plotted here to help evaluate the similarities and distributions in sample types relative to their classes.

We utilize the a443 parameter (Lee et al., 2002) from ACOLITE that derives CDOM to compare the CDOM concentrations between plume types. **Figure 5A** is the derived CDOM (a443) parameter from 5 stormwater, 5 wastewater, 5 mixed, and 5 open ocean/no plume events (**Supplementary Table 3**). Since CDOM can only be calculated using Landsat 8 and Sentinel 2 imageries, we were only able to acquire a limited number of these events for comparison. From **Figure 5A**, the mean CDOM values for our AOI ranged from 0.06 to 0.32 m^{-1} (low CDOM) for open ocean/no plume, 0.3 to 0.59 m^{-1} (low-medium CDOM) for wastewater, 0.39 to 0.96 m^{-1} (medium-high CDOM) for mixed, and 0.98 to 2.1 m^{-1} (high CDOM) for stormwater. The *P*-value from ANOVA test is 8.96e-6 for CDOM. CDOM has the 2nd highest variance compared to turbidity, ENT, and flow rate. Overall, we observed that the wastewater plumes have less CDOM compared to the stormwater plumes (**Supplementary Table 3**).

Figure 5B shows derived turbidity (mean of AOI) from Eq. 2 for all four groups. The turbidity mean values ranges from 0.5 to 3.1 FNU (low turbidity) for open ocean/no plume, 1.83 to 8 FNU (low-medium turbidity) for wastewater, 3.5 to 17.1 FNU (medium-high turbidity) for mixed, and 12.38 to 45.65 FNU (high turbidity) for stormwater. In **Figure 5B**, we observed that turbidity existed for all 3 types of plume events. The *P*-value from ANOVA test is 3.24e-10 for turbidity. Turbidity has the highest variance compared to CDOM, ENT, and flow rate.

Plume Comparison Using *in situ* Data (Plume Color, Flow Rate, and ENT)

In situ water quality data was acquired from the water quality station monitoring reports for 7 stormwater, 6 mixed, 5 wastewater, and 2 open ocean/no plume events that match with our RapidEye imagery. There are several sampling locations for each event (**Figure 1**: offshore and shore stations). We extracted the station data that are within each plume or closest to the river mouth (more information: **Supplementary Table 2**). **Figure 5C** shows that the average ENT for the open ocean/no plume events is low (3.2 CFU/100 mL), wastewater average ENT is medium (890 CFU/100 mL), mixed average ENT is relatively high (1314.1 CFU/100 mL), and stormwater average ENT is high (3440.5 CFU/100 mL). The *P*-value from ANOVA test is 1.45e-4 for ENT.

We also see differences in plume color for wastewater and stormwater plumes. Wastewater plumes are green while stormwater plumes are brown based on the true color imagery (**Supplementary Table 1**). Mixed plumes are a combination of greenish-brown and open ocean/no plumes are dark blue in the imagery. Such color difference was also captured by the visual observations in the water quality station monitoring reports (offshore and shore stations in **Figure 1**) for the events in **Supplementary Table 2**. Wastewater events reported that the water color was green and included: sewage like odor, turbid water, and debris. Stormwater events reported that the water color was brown and included: turbid water, sewage like odor, debris, and detergent-like odor. Mixed events reported that the water color was green or brown and included: sewage like odor, water turbid, and foam present. Open ocean/no plume events reported that the water color was greenish-blue and no comments included in visual observations.

Figure 5D shows the hourly mean flow rate from the flow gauge station (green star) in **Figure 1**. Stormwater flow rates from events 1–4 (**Supplementary Table 1**) are missing since there are no data available during those dates. Flow rate includes all 10 events for wastewater, mixed, and open ocean/no plume events. **Figure 5D** shows that the flow rate values for open ocean/no plume range from 0.1 to 1.3 cms (low flow), 0 to 2.7 cms for wastewater (low flow), 0 to 16 cms for mixed (medium flow), and 2.2 to 158.3 cms for stormwater (high flow). The stormwater events typically exhibit relatively higher flow rates, which is consistent with being associated with precipitation events. The *P*-value from ANOVA test is 1.3e-4 for flow rate. ENT and flow rate have similar variances since these values are closer to the mean compared to turbidity and CDOM. Since all *p*-values from the ANOVA test for all parameters are less than the significance level of 0.05, we reject the null hypothesis that four groups have equal means.

Evaluation of Satellite-Derived Turbidity

Satellite-derived turbidity values for RapidEye were compared with those collected from *in situ* stations in the Tijuana River to assure the accuracy of the satellite measurements. It should

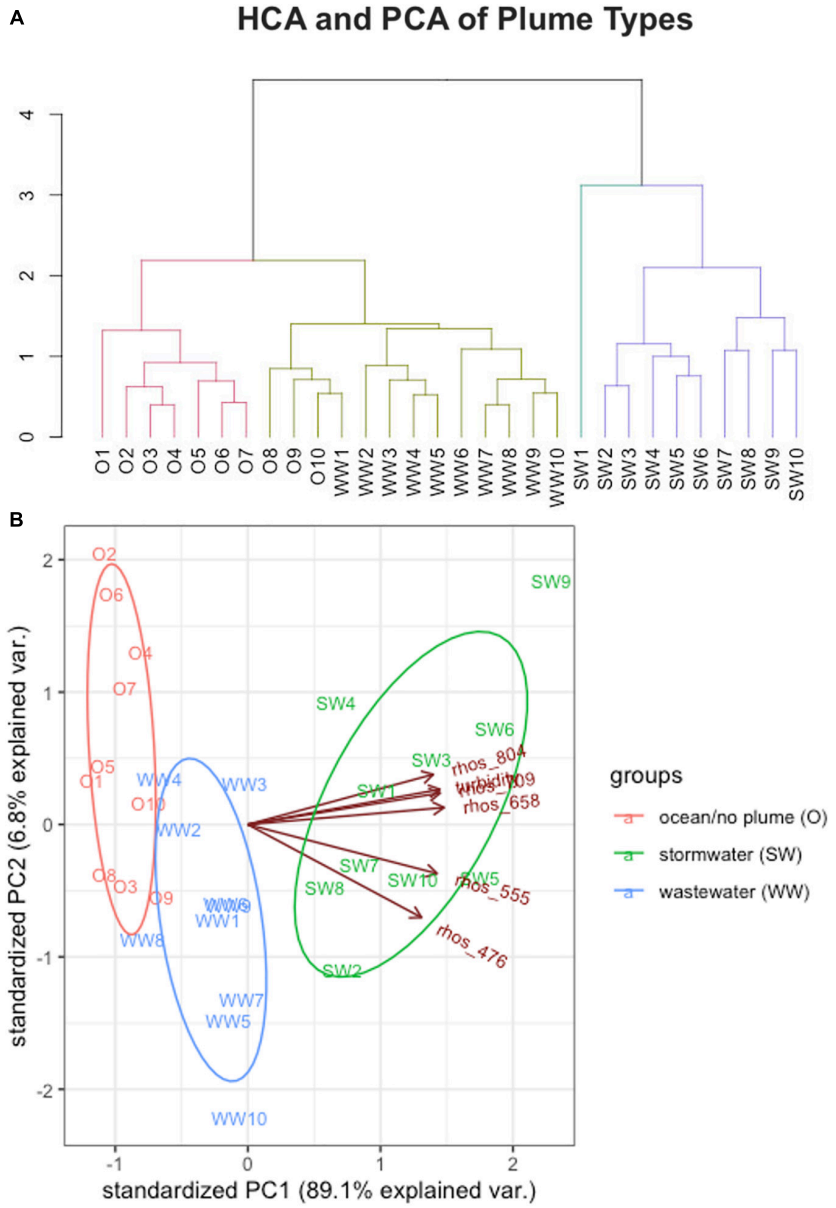

FIGURE 4 | HCA and PCA Analysis. **(A)** A dendrogram tree from the HCA. **(B)** PCA result of PC1 on the *x*-axis, and PC2 on the *y*-axis. The arrows indicate the relative influence of the parameters used in the underlying data (surface reflectance and derived turbidity).

be noted that *in situ* data for CDOM and spectral data were not available for evaluation. The *in situ* water quality stations are from the NOAA NERRS and are located at the mouth of the Tijuana River (Boca Rio: purple star in **Figure 1**) and inside the estuary (Oneonta Slough: light green star in **Figure 1**).

We compared the turbidity from water quality station at Oneonta Slough (**Figure 6A**) to the algorithm derived turbidity from 40 images listed in the **Supplementary Table 1**, including 10 wastewater events, 10 stormwater events, 10 mixed events, and 10 open ocean/no plume. We extracted a 3 × 3 pixel area surrounding the Oneonta Slough Station to compute the average derived turbidity. This average derived turbidity is compared with the *in situ* hourly average turbidity (4 of the 15-min turbidity values are averaged). The same methods were applied to the Boca Rio station (**Figure 6B**). The high peaks of turbidity from **Figures 6A,B** are from stormwater (SW) events, moderate values of turbidity are from wastewater (WW), and mixed (M) events, and low turbidity values are from open ocean/no plume events (O). Oneonta Slough has an R^2 of 0.94, and the Boca Rio station has an R^2 of 0.71 with a sample size of 40 for each station. **Figures 6C,D** are the regression line plots for the Oneonta Slough Station and Boca Rio Station, respectively.

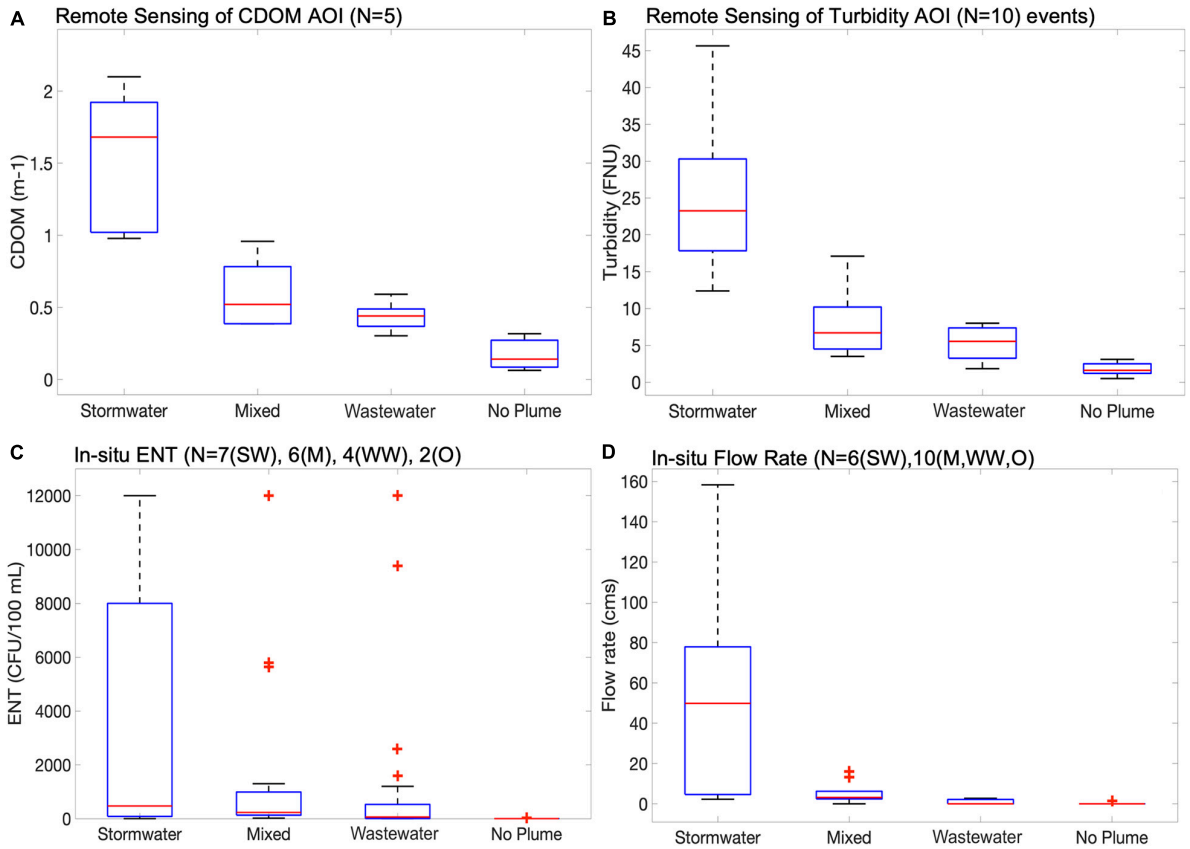

FIGURE 5 | Box plots of CDOM and turbidity derived from remote sensing data, and ENT and flow rate from *in situ* measurements. **(A)** Mean derived CDOM from AOI (Lee et al., 2002) for 5 stormwater, 5 mixed, 5 wastewater, and 5 no plume events using Landsat 8 and Sentinel 2 A/B data (more information: **Supplementary Table 3**). **(B)** Mean derived turbidity from AOI (Nechad et al., 2009) for 10 stormwater, 10 wastewater, 10 mixed, and 10 no plume events using RapidEye data. **(C)** Enterococcus (ENT) counts for 7 stormwater, 6 mixed, 4 wastewater, and 2 no plume events (more information: **Supplementary Table 2**). **(D)** Mean flow rate from gauge station (**Figure 1**: green star) in cubic meters per second (cms) from 12 h prior to the satellite revisit time for 6 stormwater events and 10 wastewater, 10 mixed, and 10 no plume events). For each box plot, the median is shown by the red mark, the whiskers correspond to the maximum and minimum values, the red plus signs show the outliers outside of the 25–75 percentile range shown by the box.

DISCUSSION AND CONCLUSION

Previous remote sensing studies focused on tracking, dispersal, detection, and impacts of stormwater plumes (Warrick et al., 2007; Lahet and Stramski, 2010; Svejkovsky et al., 2010; Brando et al., 2015; Holt et al., 2017). There are limited studies on remote sensing of wastewater plumes (DiGiacomo et al., 2004; Marmorino et al., 2010; Gierach et al., 2017; Trinh et al., 2017). However, no known studies have performed the classification of these plume types. Our study differentiated the wastewater and stormwater events based on the different characteristics presented in the plumes. These parameters include spectral profile, CDOM, turbidity, flow rate, plume color, and bacteria level (ENT).

Stormwater plumes reflectance values are consistent with other studies where we see highest reflectance values in the blue to red ranges (Hafeez et al., 2018; Wang et al., 2019). The wastewater plumes reflect most strongly in the green wavelength which shows similar reflectance signatures as CDOM and chlorophyll. Mixed events show a wide range of reflectance, which depends on a case by case basis on having "more stormwater" or "more wastewater" in the mixed plumes. Through conducting HCA and PCA of surface reflectance values, we were able to classify stormwater, wastewater, and open ocean/no plume in nearly all cases (90% success rate). HCA and PCA managed to cluster these events into 3 groups by finding similar surface reflectance values for each group. However, HCA misclassified three ocean samples to wastewater and PCA misclassified two wastewater samples to open ocean/no plume and one open ocean/no plume to wastewater. The majority of the samples show that wastewater and ocean (low-moderate reflectance in the visible) are more related to each other as compared to stormwater (high reflectance in the visible). This might be due to some open ocean/no plume events also having small concentrations of CDOM or chlorophyll, which reflects in the blue-green band ranges. Another issue may be the amount of wastewater and its varying concentration and properties that could influence the surface reflectance values. For example, the wastewater amounts range from 172,000 gallons to 610 million gallons. These wastewater events are also comprised of treated wastewater, untreated wastewater, or

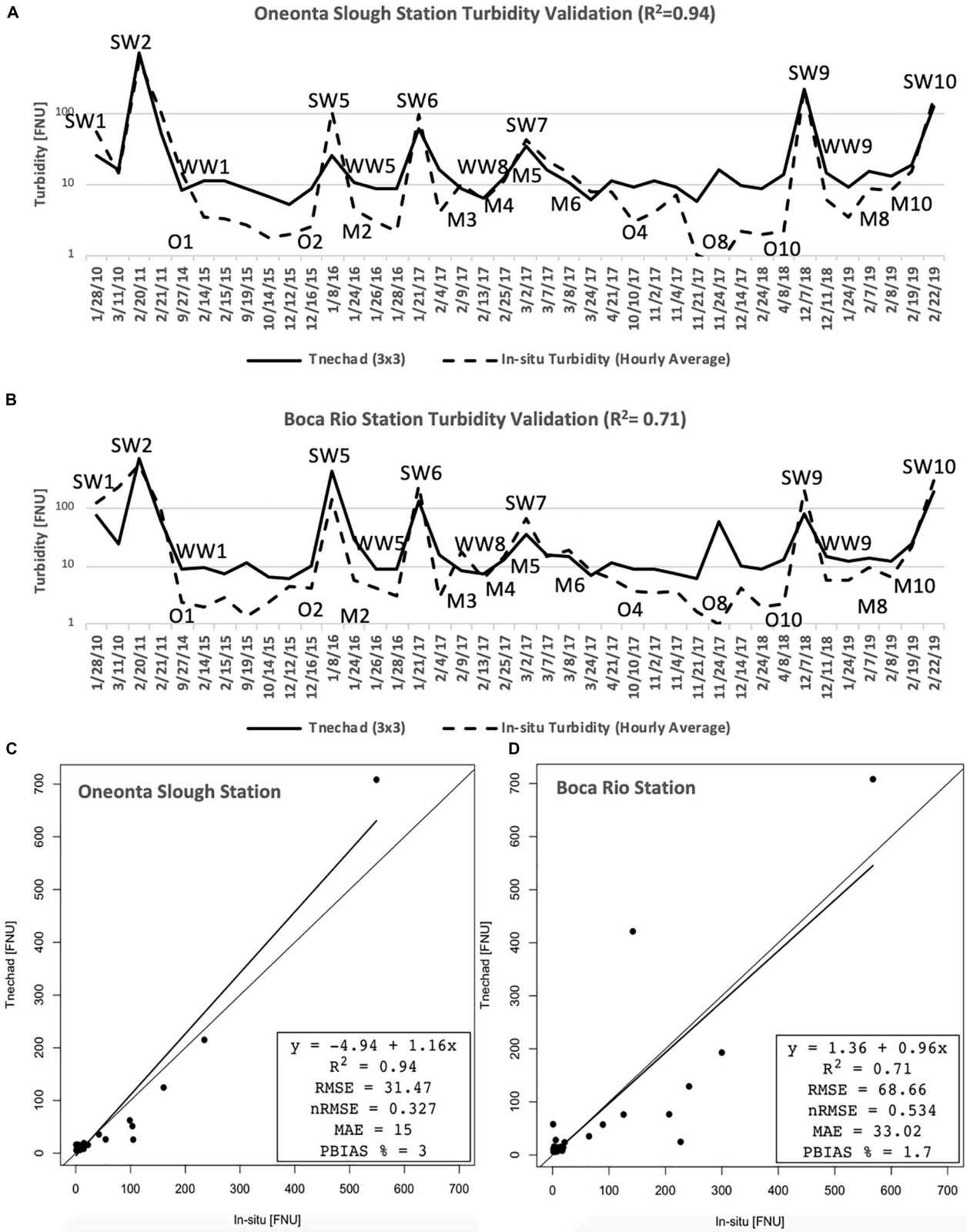

FIGURE 6 | Turbidity validation at the **(A)** Oneonta Slough Station and **(B)** Boca Rio Station. **(C,D)** The regression plots for both stations. Both stations have 40 points each: 10 stormwater, 10 wastewater, 10 mixed, and 10 no plume events.

a combination of both (see text footnote 1). The plumes that were misclassified were WW4 and WW8 and we included the end times of each spill in **Supplementary Table 1**. There may have been less wastewater for WW4 since the reported spill ended 4 h prior to the satellite acquisition time. WW8 might have been less wastewater as well since it was in the middle date of a spill that lasted 17 days. The wastewater amount was significant (143 MG) but occurred throughout these days. Overall, the majority of the highest reflectances values were those with the highest reported wastewater amounts. There were higher amounts of CDOM in stormwater (0.98 to 2.1 m^{-1}) and lower CDOM values for wastewater (0.3 to 0.59 m^{-1}) (shown in **Figure 5A**). Mixed plumes are in-between ranging from 0.39 to 0.96 m^{-1}. Studies have shown variable concentrations of CDOM in wastewater plumes, which may be due to the dilution and transport of these plumes (Marmorino et al., 2010; Gierach et al., 2017).

Validation was only implemented for turbidity since no *in situ* data was available for reflectance or CDOM. Turbidity validation showed high correlations for both the Oneonta Slough ($R^2 = 0.94$) and Boca Rio ($R^2 = 0.71$) stations. The Oneonta Slough station obtained the best results due to the station being in quieter waters with low wave energy (in the estuary) compared to the Boca Rio station located at the river mouth. At the Boca Rio station there may be high energy waves which can fluctuate the turbidity values. In Vanhellemont (2019b), the turbidity deriving algorithm (Nechad et al., 2009) was validated for RapidEye in several sample sites with 84 smart Buoys and 129 USGS sites that matched with RapidEye imagery. The algorithm was able to achieve R^2 of 0.78 and 0.81 in the validation of these sites using the red band. Both Vanhellemont (2019b) and this study have shown that RapidEye imagery can be used to derive meaningful and accurate turbidity results based on the Nechad et al. (2009) algorithm.

Turbidity existed in our 3 water groups: stormwater, wastewater, and mixed (**Figure 5B**). Stormwater showed the highest turbidity (ranging from 12.38 to 45.65 FNU) out of all the groups due to the high amount of sediments in these plumes. Since mixed plumes are a combination of wastewater and stormwater, the average turbidity ranges from 3.5 to 17.1 FNU. Wastewater turbidity values are on the lower end ranging from 1.83 to 8 FNU. Open ocean/no plume has almost no turbidity ranging from 0.5 to 3.1 FNU. Flow rate (**Figure 5D**) showed a similar pattern as turbidity: high flow rate values for stormwater, low-medium flow rate for mixed, low flow rate for wastewater, and almost no flow rate for open ocean/no plume. High flow amounts are most common when there is runoff from precipitation which is why there are higher flow rates for stormwater events. Other studies have reported high flow rates (Corcoran et al., 2010; Holt et al., 2017) and turbidity (Washburn et al., 2003) for stormwater plumes due to increases in sediments, dirt, oil, and other pollutants. For wastewater, results found that the flow rate is low which may be due to the gauge not being able to accurately estimate the flow. A report from IBWC[10] found that the flow gauge accuracy is ± 5% and is not able to detect low flow rates. It is unclear why the wastewater flow rate is almost undetected since some spills report millions of gallons of wastewater discharged into the Tijuana River. The IBWC report mentions that this is due to silt and solid sediments in the river.

Plume color differences are seen in the true-color imagery: wastewater plume is green while the stormwater plume is brown. Mixed plumes are a combination of both (greenish-brown) and open ocean/no plume is dark blue. The water quality station monitoring reports observed that wastewater plumes are green, stormwater plumes are brown, mixed plumes are green or brown, and no plume waters are greenish-blue. Depending on whether a wastewater spill is treated (less ENT), stormwater plumes often result in high ENT since this is an unregulated non-point source. This is shown in **Figure 5C** with stormwater showing high ENT (average: 3440.5 CFU/100 mL) for reported events while wastewater showed lower ENT (average: 890 CFU/100 mL). The average ENT for mixed was 1314.1 CFU/100 mL and for open ocean/no plume was 3.2 CFU/100 mL.

We depend primarily on spectral data from RapidEye, which is highly limited in terms of spectral information but still useful enough to help classify between plumes at a reasonably good rate (90% correct). The uncertainties with utilizing remote sensing to study these optically complex waters come from variations in CDOM, chlorophyll-a, sun glint, bottom reflectance, and suspended sediments (Trinh, et al. 2017). Several studies (Kahru et al., 2012; Dogliotti et al., 2015; Ruddick et al., 2016; Trinh et al., 2017; Zheng and DiGiacomo, 2017; Vanhellemont, 2019a) have shown challenges in determining accurate chlorophyll-a concentrations in these optically complex waters. This is due to increases in CDOM and sediments near the coast. In this study, CDOM in stormwater plumes may be overestimated due to an increase in suspended sediment particles. However, without a more complete *in situ* data archive, we are unable to validate these parameters, such as CDOM and surface reflectance. Some of the limitations can be addressed by looking at more detailed spectral profiles, such as what might be offered by Landsat 8 and Sentinel-2 which we were only able to use in a limited way in this study. There are also opportunities to do data fusion or downscale by combining Landsat 8 and Sentinel-2 with RapidEye and PlanetScope, which might provide us more opportunity to address tradeoffs between spectral, temporal, and spatial resolutions. Another essential aspect to consider is understanding the hydrodynamics of wastewater plumes once they enter the ocean since there is little known on the residence time and dilution rates of wastewater.

It is also crucial to understand where these point and non-point sources are originating from. An example of a point source is a wastewater spill since it can be traced back to the wastewater treatment effluent. Stormwater plumes are a non-point source since this runoff can come from a variety of sources. A report from the City of San Diego[11] found that there are several potential non-point sources in this region such as agricultural operations, erosion due to unimproved roadways, homeless encampments, and natural sources of sediment. Moreover, since this watershed

[10]https://www.ibwc.gov/Files/Report_Trans_Bypass_Flows_Tijuana_033117.pdf

[11]https://www.sandiego.gov/sites/default/files/legacy/stormwater/pdf/TJR_WaterQualityImprovementPlan_021715.pdf

is both on the U.S-Mexico border, there are also pollutants from Mexico that contribute to this runoff. It is important to understand the origin of these sources and classify them in order to regulate harmful pollutants entering our waterways. *In situ* sampling in combination with remote sensing is necessary to tackle these complex problems and protect public health and the marine environment. Wastewater spills are becoming more common due to an increasing amount of people living in the Tijuana area; our techniques can be applied in order to help coastal managers detect and classify plume types in areas where there is less extensive monitoring of water quality.

DATA AVAILABILITY STATEMENT

The raw data supporting the conclusions of this article will be made available by the authors, without undue reservation.

AUTHOR CONTRIBUTIONS

JL, BH, and CL provided the guidance on designing and planning the study. All authors contributed and approved the final version of the manuscript.

FUNDING

This work was funded by the NASA Minority University Research and Education Project (MUREP) Institutional Research Opportunity under Grant (NNX15AQ06A). This work was performed at the California State University, Los Angeles and the Jet Propulsion Laboratory, California Institute of Technology, under contract with the National Aeronautics and Space Administration. The NASA DIRECT-STEM program was the primary support for this research.

ACKNOWLEDGMENTS

We would like to acknowledge Planet Labs for allowing access to RapidEye imagery for this study from the Education and Research Program and the Open California Program.

SUPPLEMENTARY MATERIAL

The Supplementary Material for this article can be found online at: https://www.frontiersin.org/articles/10.3389/fenvs.2020.599030/full#supplementary-material

REFERENCES

Ackerman, D., and Weisberg, S. B. (2003). Relationship between rainfall and beach bacterial concentrations on Santa Monica Bay beaches. *J. Water Health* 1, 85–89. doi: 10.2166/wh.2003.0010

Arnold, B. F., Schiff, K. C., Ercumen, A., Benjamin-Chung, J., Steele, J. A., and Griffith, J. F. (2017). Acute illness among surfers after exposure to seawater in dry-and wet-weather conditions. *Am. J. Epidemiol.* 186, 866–875. doi: 10.1093/aje/kwx019

Aurin, D., Mannino, A., and Lary, D. J. (2018). Remote sensing of CDOM, CDOM spectral slope, and dissolved organic carbon in the global ocean. *Appl. Sci.* 8:2687. doi: 10.3390/app8122687

Bay, S., Jones, B. H., Schiff, K., and Washburn, L. (2003). Water quality impacts of stormwater discharges to Santa Monica Bay. *Mar. Environ. Res.* 56, 205–223. doi: 10.1016/S0141-1136(02)00331-8

Brando, V. E., Braga, F., Zaggia, L., Giardino, C., Bresciani, M., and Matta, E. (2015). High-resolution satellite turbidity and sea surface temperature observations of river plume interactions during a significant flood event. *Ocean Sci.* 11:909. doi: 10.5194/os-11-1-2015

Brezonik, P., Menken, K. D., and Bauer, M. (2005). Landsat-based remote sensing of lake water quality characteristics, including chlorophyll and colored dissolved organic matter (CDOM). *Lake Reserv. Manag.* 21, 373–382. doi: 10.1080/07438140509354442

Caron, D. A., Gellene, A. G., Smith, J., Seubert, E. L., Campbell, V., and Sukhatme, G. S. (2017). Response of phytoplankton and bacterial biomass during a wastewater effluent diversion into nearshore coastal waters. *Estuar., Coast. Shelf Sci.* 186, 223–236. doi: 10.1016/j.ecss.2015.09.013

Corcoran, A. A., Reifel, K. M., Jones, B. H., and Shipe, R. F. (2010). Spatiotemporal development of physical, chemical, and biological characteristics of stormwater plumes in Santa Monica Bay, California (USA). *J. Sea Res.* 63, 129–142. doi: 10.1016/j.seares.2009.11.006

Devlin, M. J., Petus, C., Da Silva, E., Tracey, D., Wolff, N. H., and Waterhouse, J. (2015). Water quality and river plume monitoring in the Great Barrier Reef: an overview of methods based on ocean colour satellite data. *Remote Sens.* 7, 12909–12941. doi: 10.3390/rs71012909

DiGiacomo, P. M., Washburn, L., Holt, B., and Jones, B. H. (2004). Coastal pollution hazards in southern California observed by SAR imagery: stormwater plumes, wastewater plumes, and natural hydrocarbon seeps. *Mar. Pollu. Bull.* 49, 1013–1024. doi: 10.1016/j.marpolbul.2004.07.016

Dogliotti, A. I., Ruddick, K. G., Nechad, B., Doxaran, D., and Knaeps, E. (2015). A single algorithm to retrieve turbidity from remotely-sensed data in all coastal and estuarine waters. *Remote Sens. Environ.* 156, 157–168. doi: 10.1016/j.rse.2014.09.020

Gašparović, M., and Jogun, T. (2018). The effect of fusing Sentinel-2 bands on land-cover classification. *Int. J. Remote Sens.* 39, 822–841. doi: 10.1080/01431161.2017.1392640

Gierach, M. M., Holt, B., Trinh, R., Pan, B. J., and Rains, C. (2017). Satellite detection of wastewater diversion plumes in Southern California. *Estuar. Coast. Shelf Sci.* 186, 171–182. doi: 10.1016/j.ecss.2016.10.012

Hafeez, S., Wong, M. S., Abbas, S., Kwok, C. Y., Nichol, J., Lee, K. H., et al. (2018). Detection and monitoring of marine pollution using remote sensing technologies. *Monitor. Mar. Pollut.* 2018, 81657. doi: 10.5772/intechopen.81657

Holt, B., Trinh, R., and Gierach, M. M. (2017). Stormwater runoff plumes in the Southern California Bight: A comparison study with SAR and MODIS imagery. *Marine Pollution.* 118, 141–154. doi: 10.1016/j.marpolbul.2017.02.040

Jolliffe, I. T., and Cadima, J. (2016). Principal component analysis: a review and recent developments. *Philos. Transac. R. Soc. A* 374:20150202. doi: 10.1098/rsta.2015.0202

Judice, T. J., Widder, E. A., Falls, W. H., Avouris, D. M., Cristiano, D. J., and Ortiz, J. D. (2020). Field−validated detection of Aureoumbra lagunensis brown tide blooms in the Indian River Lagoon, Florida using Sentinel−3A OLCI and ground−based hyperspectral spectroradiometers. *GeoHealth* 4, e2019GH000238. doi: 10.1029/2019GH000238

Kahru, M., Kudela, R. M., Manzano-Sarabia, M., and Mitchell, B. G. (2012). Trends in the surface chlorophyll of the California Current: Merging data from multiple ocean color satellites. *Deep Sea Res.* 77, 89–98. doi: 10.1016/j.dsr2.2012.04.007

Kamble, S. R., and Vijay, R. (2011). Assessment of water quality using cluster analysis in coastal region of Mumbai. India. *Environ. Monitor. Assess.* 178, 321–332. doi: 10.1007/s10661-010-1692-0

Lahet, F., and Stramski, D. (2010). MODIS imagery of turbid plumes in San Diego coastal waters during rainstorm events. *Remote Sens. Environ.* 114, 332–344. doi: 10.1016/j.rse.2009.09.017

Lee, Z. P., Lubac, B., and Werdell, J. (2014). *Update of the Quasi-Analytical Algorithm (QAA_v6). International Ocean Color Group Software Report,*. http://www.ioccg.org/groups/Software_OCA/QAA_v6_2014209.pdf

Lee, Z., Carder, K. L., and Arnone, R. A. (2002). Deriving inherent optical properties from water color: a multiband quasi-analytical algorithm for optically deep waters. *Appl. Opt.* 41, 5755–5772. doi: 10.1364/ao.41.005755

Lee, Z., Lubac, B., Werdell, J., and Arnone, R. (2009). *An update of the quasi-analytical algorithm (QAA_v5). International Ocean Color Group Software Report*, 1-9. https://www.ioccg.org/groups/Software_OCA/QAA_v5.pdf

Marmorino, G. O., Smith, G. B., Miller, W. D., and Bowles, J. (2010). Detection of a buoyant coastal wastewater discharge using airborne hyperspectral and infrared imagery. *J. Appl. Remote Sens.* 4:043502. doi: 10.1117/1.3302630

Nechad, B., Ruddick, K. G., and Neukermans, G. (2009). Calibration and validation of a generic multisensor algorithm for mapping of turbidity in coastal waters. *Remote Sens. Ocean, Sea Ice Large Water Reg.* 7473:74730H.

Nezlin, N. P., and DiGiacomo, P. M. (2005). Satellite ocean color observations of stormwater runoff plumes along the San Pedro Shelf (southern California) during 1997–2003. *Contin. Shelf Res.* 25, 1692–1711. doi: 10.1016/j.csr.2005.05.001

Nezlin, N. P., DiGiacomo, P. M., Diehl, D. W., Jones, B. H., Johnson, S. C., and Mengel, M. J. (2008). Stormwater plume detection by MODIS imagery in the southern California coastal ocean. *Estuar. Coast. Shelf Sci.* 80, 141–152. doi: 10.1016/j.ecss.2008.07.012

Nezlin, N. P., Weisberg, S. B., and Diehl, D. W. (2007). Relative availability of satellite imagery and ship-based sampling for assessment of stormwater runoff plumes in coastal southern California. *Estuar. Coast. Shelf Sci.* 71, 250–258. doi: 10.1016/j.ecss.2006.07.016

Reifel, K. M., Johnson, S. C., DiGiacomo, P. M., Mengel, M. J., Nezlin, N. P., and Warrick, J. A. (2009). Impacts of stormwater runoff in the Southern California Bight: Relationships among plume constituents. *Cont. Shelf Res.* 29, 1821–1835. doi: 10.1016/j.csr.2009.06.011

Revelle, W. (1979). Hierarchical cluster analysis and the internal structure of tests. *Multivar. Behav. Res.* 14, 57–74. doi: 10.1207/s15327906mbr1401_4

Reynolds, R. A., and Stramski, D. (2019). Optical characterization of marine phytoplankton assemblages within surface waters of the western Arctic Ocean. *Limnol. Oceanogr.* 64, 2478–2496. doi: 10.1002/lno.11199

Ruddick, K., Vanhellemont, Q., Dogliotti, A., Nechad, B., Pringle, N., and Van der Zande, D. (2016). "New opportunities and challenges for high resolution remote sensing of water colour," in *Proceedings of the Ocean Optics XXIII*, (Victoria, BC), 23–28.

Schiff, K., Griffith, J., Steele, J., Arnold, B., Ercumen, A., and Benjamin-Chung, J. (2016). The surfer health study: a three-year study examining illness rates associated with surfing during wet weather. *SCCWRP Technol. Rep.* 2016:943.

Seegers, B. N., Teel, E. N., Kudela, R. M., Caron, D. A., and Jones, B. H. (2017). Glider and remote sensing observations of the upper ocean response to an extended shallow coastal diversion of wastewater effluent. *Estuar. Coast. Shelf Sci.* 186, 198–208. doi: 10.1016/j.ecss.2016.06.019

Svejkovsky, J., Nezlin, N. P., Mustain, N. M., and Kum, J. B. (2010). Tracking stormwater discharge plumes and water quality of the Tijuana River with multispectral aerial imagery. *Estuar. Coast. Shelf Sci.* 87, 387–398. doi: 10.1016/j.ecss.2010.01.022

Trinh, R. C., Fichot, C. G., Gierach, M. M., Holt, B., Malakar, N. K., and Hulley, G. (2017). Application of Landsat 8 for monitoring impacts of wastewater discharge on coastal water quality. *Front. Mar. Sci.* 4:329. doi: 10.3389/fmars.2017.00329

Vanhellemont, Q. (2019a). Adaptation of the dark spectrum fitting atmospheric correction for aquatic applications of the Landsat and Sentinel-2 archives. *Remote Sens. Environ.* 225, 175–192. doi: 10.1016/j.rse.2019.03.010

Vanhellemont, Q. (2019b). Daily metre-scale mapping of water turbidity using CubeSat imagery. *Opt. Exp.* 27, A1372–A1399. doi: 10.1364/OE.27.0A1372

Vanhellemont, Q., and Ruddick, K. (2018). Atmospheric correction of metre-scale optical satellite data for inland and coastal water applications. *Remote Sens. Environ.* 216, 586–597. doi: 10.1016/j.rse.2018.07.015

Wang, D., Ma, R., Xue, K., and Loiselle, S. A. (2019). The assessment of Landsat-8 OLI atmospheric correction algorithms for inland waters. *Remote Sens.* 11:169. doi: 10.3390/rs11020169

Warrick, J. A., DiGiacomo, P. M., Weisberg, S. B., Nezlin, N. P., Mengel, M., and Jones, B. H. (2007). River plume patterns and dynamics within the Southern California Bight. *Cont. Shelf Res.* 27, 2427–2448. doi: 10.1016/j.csr.2007.06.015

Washburn, L., McClure, K. A., Jones, B. H., and Bay, S. M. (2003). Spatial scales and evolution of stormwater plumes in Santa Monica Bay. *Mar. Environ. Res.* 56, 103–125. doi: 10.1016/S0141-1136(02)00327-6

Zheng, G., and DiGiacomo, P. M. (2017). Uncertainties and applications of satellite-derived coastal water quality products. *Prog. Oceanogr.* 159, 45–72. doi: 10.1016/j.pocean.2017.08.007

Conflict of Interest: The authors declare that the research was conducted in the absence of any commercial or financial relationships that could be construed as a potential conflict of interest.

Copyright © 2020 Ayad, Li, Holt and Lee. This is an open-access article distributed under the terms of the Creative Commons Attribution License (CC BY). The use, distribution or reproduction in other forums is permitted, provided the original author(s) and the copyright owner(s) are credited and that the original publication in this journal is cited, in accordance with accepted academic practice. No use, distribution or reproduction is permitted which does not comply with these terms.

frontiers in Environmental Science

ORIGINAL RESEARCH
published: 17 February 2021
doi: 10.3389/fenvs.2020.587354

An Automated Method for Mapping Giant Kelp Canopy Dynamics from UAV

Katherine C. Cavanaugh[1]*, *Kyle C. Cavanaugh*[1], *Tom W. Bell*[2] and *Evan G. Hockridge*[3]

[1]Department of Geography, University of California, Los Angeles, CA, United States, [2]Earth Research Institute, University of California, Santa Barbara, CA, United States, [3]Department of Organismic and Evolutionary Biology, Harvard University, Cambridge, MA, United States

Satellite and aerial imagery have been used extensively for mapping the abundance and distribution of giant kelp (*Macrocystis pyrifera*) in southern California. There is now great potential for using unoccupied aerial vehicles (UAVs) to map kelp canopy at very high resolutions. However, tides and currents have been shown to affect the amount of floating kelp canopy on the water surface, and the impacts of these processes on remotely sensed kelp estimates in this region have not been fully quantified. UAVs were used to map fine-scale changes in canopy area due to tidal height and current speed at kelp forests off the coast of Palos Verdes, CA and Santa Barbara, CA. An automated method for detecting kelp canopy was developed that was 67% accurate using red-green-blue (RGB) UAV imagery and 93% accurate using multispectral UAV imagery across a range of weather, ocean, and illumination conditions. Increases in tidal height of 1 m reduced the amount of floating kelp canopy by 15% in Santa Barbara and by over 30% in Palos Verdes. The effect of current speed on visible kelp canopy was inconclusive, but there was a trend towards lower canopy area with increased current speed. Therefore, while tidal height and current speed can introduce significant variability to estimates of kelp abundance, the magnitude of this variability is site specific. Still, UAVs are a valuable tool for mapping of kelp canopy and can provide greater spatial resolution and temporal coverage than is possible from many satellite sensors. This data can provide insight into the patterns and drivers of high frequency fluctuations in kelp abundance.

Keywords: drones, kelp classification, kelp mapping, spatial variability, tidal height, current speed, ecological succession

OPEN ACCESS

Edited by:
Sherry L. Palacios, California State University, Monterey Bay, United States

Reviewed by:
Maycira Costa, University of Victoria, Canada
Greg M. Silsbe, University of Maryland Center for Environmental Science (UMCES), United States
Anna Windle, University of Maryland Center for Environmental Science (UMCES), in collaboration with reviewer GS

***Correspondence:**
Katherine C. Cavanaugh
kccavanaugh@g.ucla.edu

Specialty section:
This article was submitted to Environmental Informatics and Remote Sensing, a section of the journal Frontiers in Environmental Science

Received: *25 July 2020*
Accepted: *24 December 2020*
Published: *17 February 2021*

Citation:
Cavanaugh KC, Cavanaugh KC, Bell TW and Hockridge EG (2021) An Automated Method for Mapping Giant Kelp Canopy Dynamics from UAV. Front. Environ. Sci. 8:587354. doi: 10.3389/fenvs.2020.587354

INTRODUCTION

Giant kelp (*Macrocystis pyrifera*) serves as the structural and nutritional foundation for globally distributed and highly productive nearshore ecosystems (Dugan et al., 2003; Graham et al., 2007; Miller et al., 2018). Giant kelp forests offer great societal and economic value through the support of fisheries, recreation, and a wide range of products including cosmetics, food, fertilizer, and biofuels (Gentry et al., 2017, Gentry et al., 2019). Accordingly, monitoring the abundance and distribution of this valuable resource is particularly important in the face of global climate change, as marine ecosystems are especially susceptible to the effects of climatic disturbances (Harley et al., 2006).

Fixed to subtidal, rocky reefs with a holdfast, giant kelp fronds extend vertically towards the sea surface to form dense, floating canopies, which are visible from above. Satellite imagery has shown

great potential for monitoring kelp populations, as floating kelp canopies are visible with multispectral spaceborne sensors (Cavanaugh et al., 2011; Bell et al., 2015a, Bell et al., 2020; Mora-Soto et al., 2020). Repeated global measurements provide a comprehensive view of changes in kelp canopy area through time, enabling the roles of seasonal (e.g., wave disturbance and nutrient availability) to decadal scale (e.g., the El Niño-Southern Oscillation (ENSO) and the North Pacific Gyre Oscillation (NPGO)) drivers to be evaluated across a wide range of spatial scales. Satellites with moderate spatial resolution (10–30 m) can be used to accurately estimate the area and biomass of continuous kelp canopies on the order of hundreds of sq. meters in size (Cavanaugh et al., 2011), yet are unable to detect sparse stands of kelp that cover less than 15% of a pixel (i.e., 135 m^2 for a 900 m^2 Landsat pixel; Hamilton et al., 2020). Additionally, shallow kelp forests can be difficult to differentiate from land, especially when pixels contain a mixture of land, water, and kelp (Schroeder et al., 2019a; Bell et al., 2020; Hamilton et al., 2020). These issues limit the suitability of moderate resolution satellite imagery for monitoring giant kelp habitat in regions where kelp beds are small, sparse and/or found close to the shoreline (e.g., British Columbia; Nijland et al., 2019).

Tidal height and surface currents introduce additional complexity into aerial estimates of kelp canopy area (Britton-Simmons et al., 2008). The amount of kelp exposed on the water surface periodically fluctuates with incoming and outgoing tides. Portions of the canopy submerge and reemerge as tidal height increases and decreases, and at high tide, deeply submerged individuals become undetectable with aerial and satellite-based sensors. Similarly, strong currents can temporarily immerse floating canopies, changing the shape and coverage of the forest when viewed from above.

In southern California, satellite and aerial imagery have been used extensively for monitoring the drivers of giant kelp biomass dynamics, kelp physiological condition, and synchrony and metapopulation dynamics (Jensen et al., 1980; Deysher 1993; Stekoll et al., 2006; Cavanaugh et al., 2011; Cavanaugh et al., 2013; Cavanaugh et al., 2014; Cavanaugh et al.,2019; Bell et al., 2015a; Bell et al., 2015b; Bell et al., 2020; Castorani et al., 2015; Castorani et al., 2017). Despite this widespread use, it is unclear how tidal height and surface currents impact apparent bed size in this region. Britton-Simmons et al. (2008) demonstrated a significant impact of tides and currents on bull kelp (*Nereocystis luetkeana*) canopy using oblique-angle, shore-based photography, however these impacts have not been quantified for giant kelp, which has a different morphology from bull kelp. In addition, there are limitations with estimating area from oblique-angle imagery, and the sensitivity of this imagery to tides and currents may be different than that of nadir imagery.

Unoccupied aerial vehicles (UAVs) present a low-cost, versatile solution to the challenges and limitations associated with using satellite imagery to study small or sparse kelp beds. Offering spatial resolutions on the order of centimeters, UAVs not only provide the fine resolution necessary to monitor environmental processes on fine spatial scales, but they also present the flexibility in timing of image capture (Whitehead and Hugenholtz 2014; Whitehead et al., 2014). Additionally, sensor systems with varying spectral capabilities have been developed for UAV platforms, ranging from digital color cameras, containing red, green, and blue channels (RGB) to hyperspectral (Whitehead and Hugenholtz 2014). While emergent giant kelp canopy prominently reflects in the near infrared (NIR), seawater has a high absorption (Jensen et al., 1980; Schroeder et al., 2019a), and so NIR imagery is useful for detecting surface canopy (Cavanaugh et al., 2010) but has limited ability to detect subsurface kelp.

UAV imagery has been successfully implemented in the detection and mapping of both floating and submerged seaweed communities, yet sun glint, crashing waves, shadows, and spectral noise have made automated classification schemes problematic, necessitating manual image classifications (Kellaris et al., 2019; Taddia and Russo 2019; Thomsen et al., 2019). Here, we present a novel automated canopy detection algorithm that can be applied consistently to UAV imagery collected across varying conditions. We then quantify the influence of tides and currents on estimates of floating giant kelp canopy area in southern California using these methods. Using this automated detection method, we introduce field collection methods used to create a time series of kelp canopy area from multispectral UAV imagery. This dataset allows for the local scale assessment of giant kelp canopy area at 10 cm resolution every two weeks for one year while controlling for tides. The time series provides insight to patterns and drivers of high-frequency variability in giant kelp abundance in southern California.

MATERIALS AND METHODS

Field Data Collection

The study area included two kelp forests located on the southern California coast: Arroyo Quemado (34°28.127′N, 120° 07.285′W) west of Santa Barbara, and Honeymoon Cove (33°45.906′N, 118° 25.392′W) at Palos Verdes (**Figure 1**). Both kelp forests experience tidal fluctuations ranging from~−0.55 m to 2.2 m.

Flights were conducted throughout the tidal range (hereafter referred to as tidal surveys) on January 2, 2018 at Arroyo Quemado (−0.52 m–2.15 m) and on July 9, 2018 (0.64 m–1.96 m) and July 18, 2018 (0.25 m–1.56 m) at Honeymoon Cove to capture the tidal responses of kelp beds with different structural properties (**Supplementary Table S1**). The Arroyo Quemado kelp forest is located offshore of an open coast, and one discrete stand was sampled within the forest~400 m from the shoreline. The Honeymoon Cove kelp forest extends throughout a sheltered cove, with thicker stands of kelp fringing the coastline and sparser stands of kelp covering the rest of the cove. Flights were only conducted within the cove, but the kelp forest continuously extended past the section that was surveyed. The flight duration for each site was approximately 20–30 min. For each tidal survey, hourly flights were performed across the tidal amplitude (approximately 6 h). Wind speeds were less than 8 km/h during all tidal survey flights.

A separate series of UAV flights were conducted at Arroyo Quemado in order to isolate the effects of currents. These consisted of one flight per day at the same tidal stage (bottom of

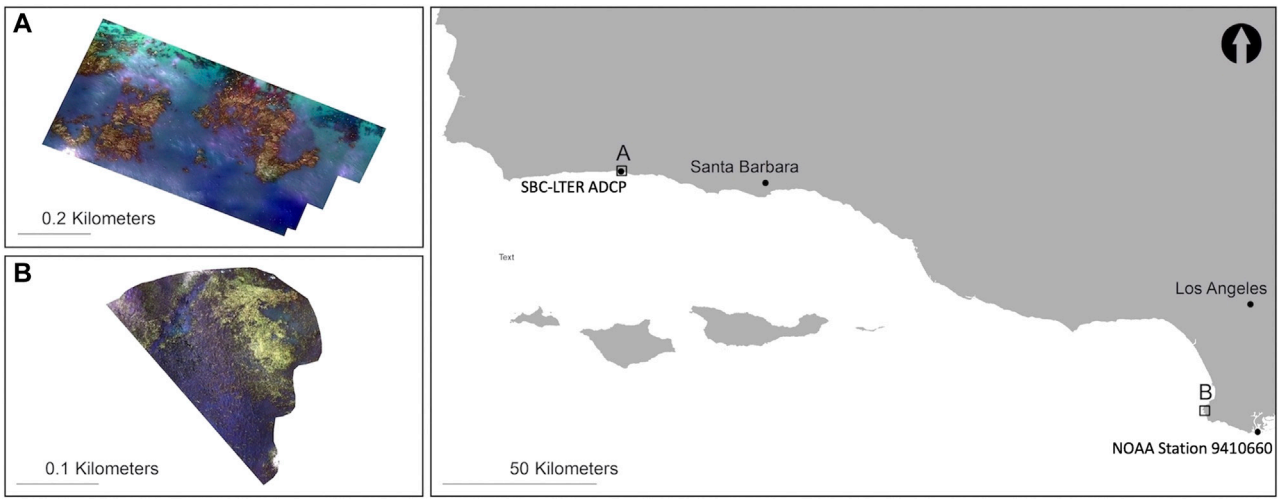

FIGURE 1 | Santa Barbara, California study site: Arroyo Quemado **(A)** with associated SBC-LTER ADCP and Palos Verdes, California study site: Honeymoon Cove **(B)** with associated NOAA station 9410660.

low tide) across a 5 day span (June 26, 2019 to June 30, 2019) with varying wind and current speeds (**Supplementary Table S1**).

A MicaSense RedEdge sensor mounted on a DJI Matrice 100 quadcopter was used to survey the kelp bed at Honeymoon Cove. The RedEdge simultaneously captures data in five spectral channels, the blue (475 nm center, 20 nm bandwidth), green (560 nm center, 20 nm bandwidth), red (668 nm center, 10 nm bandwidth), red-edge (717 nm center, 10 nm bandwidth), and NIR (840 nm center, 40 nm bandwidth). Sun angle and illumination conditions varied temporally across each survey, and while the RedEdge was equipped with a downwelling light sensor (DLS), DLS data were omitted in image processing as sensor measurements during flight vary with the pitch and roll of the UAV (Hakala et al., 2018). To calibrate reflectance for each flight, a spectral calibration panel with known reflectance was imaged before and after each flight. The along-track overlap between consecutive images was set to 80%, and the side-track overlap between consecutive flight lines was set to a minimum of 75%. Sun glint distorted the reflectance of pixels in the middle and edges of images taken when the sun was at or close to zenith. To increase pixel coverage unaffected by sun glint, the side-track overlap was increased to 85% during these flights. Due to UAV and sensor availability between collaborators, a MicaSense Altum sensor mounted on a DJI Matrice 200 quadcopter was used to survey the kelp bed at Arroyo Quemado. The Altum simultaneously captures data in five channels similar to the RedEdge, the blue (475 nm center, 32 nm bandwidth), green (560 nm center, 27 nm bandwidth), red (668 nm center, 14 nm bandwidth), red-edge (717 nm center, 13 nm bandwidth), and NIR (840 nm center, 57 nm bandwidth). All other settings remained consistent to those used with the RedEdge sensor.

A moored CTD and Acoustic Doppler Current Profiler (ADCP) from the Santa Barbara Coastal Long Term Ecological Research (SBC LTER) program (http://sbc.lternet.edu) were located within the Arroyo Quemado kelp forest, allowing for simultaneous *in situ* depth and current measurement comparisons with each Arroyo Quemado flight. These data included north velocity, east velocity, and water depth, which were provided in 20 min intervals. Velocity data were collected at 16 different heights in the water column, from 2.5 m to 17.5 m from the bottom. Measurements from 12.5 m readings were used for this study, as measurements taken above 12.5 m from the bottom often yielded no data values at low tide. Both depth and current measurements were linearly interpolated to one min intervals to match both the tidal height and current speed at the midpoint (from UAV launch to landing) of the time each kelp forest was imaged. NOAA/NOS/CO-OPS one min tidal measurements (https://tidesandcurrents.noaa.gov/1mindata.html) were used from Station 9410660 for simultaneous *in situ* depth measurement comparisons with each Honeymoon Cove flight.

UAV Image Data Processing

Before analyzing the UAV images, raw pixel values were converted from digital numbers (DN) to reflectance using the recommended MicaSense processing steps (https://github.com/micasense/imageprocessing). A dark pixel correction was applied to reduce sensor noise, an imager specific radiometric calibration function was calculated to account for radiometric inaccuracies, vignette effects were removed from image corners, and each pixel was divided by image gain, exposure time, and a sensor-specific calibration coefficient (all imager and sensor specific calibrations were provided by MicaSense). For each band, the pixels within the inner 75% of reflectance panel images captured before and after each flight were extracted and averaged to account for any illumination changes from launch to landing. The provided Lambertian panel for the RedEdge and Altum have a known reflectance for each band, which were used to convert DN to reflectance.

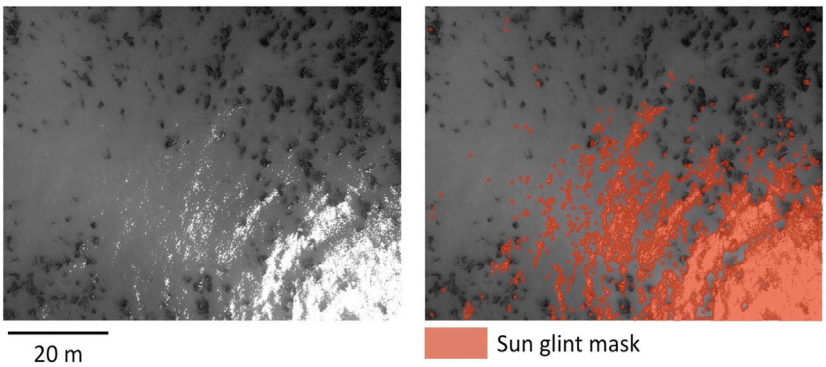

FIGURE 2 | Unprocessed, grayscale UAV image **(left)** and corresponding sun glint mask **(right)**. All reflectance pixels found within the sun glint mask were removed during photogrammetric processing to improve mosaicking success.

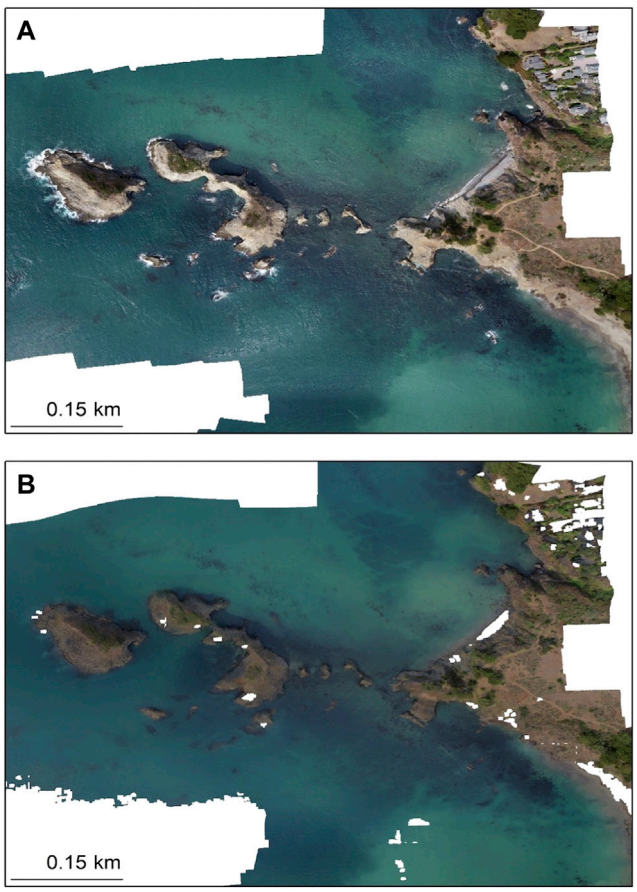

FIGURE 3 | Example of a UAV-based orthomosaic export from Agisoft Metashape Pro without the glint correction applied **(A)** and with the glint correction applied **(B)**. Land areas that were erroneously removed with the glint correction are apparent–masks containing coastline can be excluded to reduce this effect.

Pixels altered by sun glint and crashing waves introduce distortion into individual images, as these pixels are inconsistent across space and time, making image mosaicking difficult. To reduce distortion, these pixels were masked from each band of pre-mosaicked reflectance images using gray-level co-occurrence matrices (GLCM), which have been successful in a variety of remote sensing-based classifications (Changhui et al., 2013; Huang et al., 2014; Zheng et al., 2018). GLCMs yield textural features from images by calculating the spatial distribution of the gray-level variations of individual band values (Haralick et al., 1973). The function *graycomatrix* in MATLAB (2018) creates a GLCM by describing pixel spatial dependency, or the frequency at which a pixel with value *i* occurs adjacent to a pixel with value *j* (MATLAB, 2018).

In the blue portion of the visible spectrum, dense kelp has a relatively low reflectance, while water has a relatively high reflectance (**Supplementary Figure S1**; Schroeder et al., 2019b). As a result, graycomatrix was applied to the blue band of each image to help isolate glint pixels and to reduce the potential for misclassification between glint and kelp. The brightest pixel grouping within each matrix was used to identify glint and wave pixels within all images containing 100% water. If masks were applied to images with land, this process may accidentally mask land and coastal pixels as well. A 5-pixel buffer was placed around any pixels classified as glint, and the resulting masks were exported for each individual UAV image (**Figure 2**).

Reflectance images were mosaicked into orthomosaics using the structure from motion photogrammetric software Agisoft Metashape Pro (formerly Agisoft Photoscan Pro; Agisoft Photoscan Pro version 1.4.5 through Metashape Pro version 1.6.2 were used for processing; Agisoft, St. Petersburg, Russia). Metashape Pro allows users to directly import binary masks that are associated with raw UAV image files (i.e., Metashape will correspond images with their respective masks if the files share

TABLE 1 | Blue (B), green (G), red (R), red-edge (Re), and near infrared (NIR) band combinations for each of the vegetation indices tested for the separability analysis of kelp and water pixels.

Description	Equation	References
Red-Blue	$R - B$	
Normalized Difference of Red and Blue (NDRB)	$\frac{R-B}{R+B}$	
Modified Green Red Vegetation Index (MGVI)	$\frac{G^2-R^2}{G^2+R^2}$	Bendig et al. (2015)
Modified Photochemical Reflectance Index (MPRI)	$\frac{G-R}{G+R}$	Yang et al. (2008)
Red Green Blue Vegetation Index (RGBVI)	$\frac{G-B*R}{G^2+B*R}$	Bendig et al. (2015)
Green Leaf Index (GLI)	$\frac{2G-R-B}{2G+R+B}$	Louhaichi et al. (2001)
Greenness Index (GI)	$\frac{G}{R}$	Smith et al., 2005
Blue/Red	$\frac{B}{R}$	
Excess of Green (ExG)	$2G - R - B$	Woebbecke et al. (1995)
Visible Atmospherically Resistant Index (VARI)	$\frac{G-R}{G+R-B}$	Gitelson et al. (2002)
Triangular Vegetation Index (TVI)	$\frac{120(Re-G)-200(R-G)}{2}$	Broge and Leblanc (2001)
Normalized Difference Vegetation Index (NDVI)	$\frac{NIR-R}{NIR+R}$	Tucker (1979)
Green Normalized Difference Vegetation Index (Green NDVI)	$\frac{NIR-G}{NIR+G}$	Gitelson et al. (1996)
Normalized Difference Blue Index (Blue NDVI)	$\frac{NIR-B}{NIR+B}$	Zerbe and Liew (2004)
Renormalized Difference Vegetation Index (RDVI)	$\frac{NIR-R}{\sqrt{NIR+R}}$	Roujean and Breon (1995)
Normalized Difference Red-edge Blue (NDREB)	$\frac{Re-B}{Re+B}$	
Enhanced Vegetation Index (EVI)	$2.5\left[\frac{NIR-R}{NIR+6*R-7.5*B+1}\right]$	Huete et al. (2002)
Green Chlorophyll Index (CIG)	$\frac{NIR}{G} - 1$	Gitelson et al. (2005)
Blue/Red-edge	$\frac{B}{Re}$	
Blue/NIR	$\frac{B}{NIR}$	

the same file name), and the software will exclude masked areas when finding tie points for photogrammetric stitching. As a result, only the pixels unaffected by glint will be incorporated into the final orthomosaic (**Figure 3**). To account for error in measurements of the UAV's onboard GPS, each orthomosaic GeoTiff was manually georeferenced. An arbitrary UAV image from Honeymoon Cove and Arroyo Quemado were selected as the base image, and ten coordinates located along the shoreline of each site were located. All subsequent images were georeferenced to these ten points to ensure that our images were referenced to one another through time. Once images were georeferenced, they were resampled to 10 cm × 10 cm, and all land and coastal pixels within 10 m of the low-tide line were removed.

UAV-Based Kelp Area Detection

Twenty vegetation indices were compared to determine which was best at separating kelp from water in UAV imagery. These included both previously published indices as well as simple additive and multiplicative band combinations. Ten indices were restricted to RGB wavelengths, and ten indices included either the red-edge or NIR band (**Table 1**). To compare the performance of various vegetation indices in detecting kelp canopy, kelp and water pixels were manually identified and digitized using ESRI ArcMap 10.7 software across 10 dates from the Honeymoon Cove time series with varying sun angles, wind speeds, wave conditions, water clarity, and kelp health to cover a wide range of conditions experienced in the field. For this manual classification and all further discussion in this paper, submerged fronds were classified as "water". The number of identified kelp and water pixels varied from image to image, and to keep samples consistent, 500 pixels were randomly selected from each class within each image for a total of 5,000 pixels per class. Two parametric separability measures, the transformed divergence (TD) separability measure and the Jeffries-Matusita distance (JM), were used to assess the ability of each index to differentiate kelp from water. JM and TD are both statistical mechanisms for testing the ability to distinguish two classes. TD (**Eq. 2**) relies on the divergence (D) equation (**Eq. 1**), while JM (**Eq. 4**) relies on the Bhattacharyya distance (BD) equation (**Eq. 3**). Each is bound between 0 and 2, with 0 being no separability between classes and 2 being complete class separability as:

$$\boldsymbol{D} = \frac{1}{2}\boldsymbol{tr}\left[(\boldsymbol{C}_1 - \boldsymbol{C}_2)(\boldsymbol{C}_1^{-1} - \boldsymbol{C}_2^{-1})\right] + \frac{1}{2}\boldsymbol{tr}\left[(\boldsymbol{C}_1^{-1} - \boldsymbol{C}_2^{-1}) \times (\boldsymbol{\mu}_{1-}\boldsymbol{\mu}_2)(\boldsymbol{\mu}_{1-}\boldsymbol{\mu}_2)^T\right], \quad (1)$$

$$\boldsymbol{TD} = 2\left[1 - \exp\left(-\frac{\boldsymbol{D}}{8}\right)\right], \quad (2)$$

$$\boldsymbol{BD} = \frac{1}{8}(\boldsymbol{\mu}_{2-}\boldsymbol{\mu}_1)^T\left[\frac{\boldsymbol{C}_1 + \boldsymbol{C}_2}{2}\right]^{-1}(\boldsymbol{\mu}_{2-}\boldsymbol{\mu}_1) + \frac{1}{2}\boldsymbol{ln}\frac{\left|\frac{C_1+C_2}{2}\right|}{\sqrt{|\boldsymbol{C}_1||\boldsymbol{C}_2|}}, \quad (3)$$

$$\boldsymbol{JM} = \sqrt{2\left[1 - \exp(-\boldsymbol{BD})\right]}. \quad (4)$$

where C_1 and C_2 are the covariance matrices of class 1 and class 2, μ_1 and μ_2 are the mean vectors of class 1 and class 2, *tr* is the matrix trace function, and *T* is the matrix transpose function. JM and TD are the transformed divergence and Jeffries-Matusita distances between class 1 and class 2, respectively (Jensen 1996; Huang et al., 2016).

Because JM and TD are only indicative of separability in cases of normality, the Shapiro-Wilk Normality test was used to determine whether the kelp and water pixel samples were normally distributed after each index was applied. The Shapiro-Wilk Normality test is most reliable with small

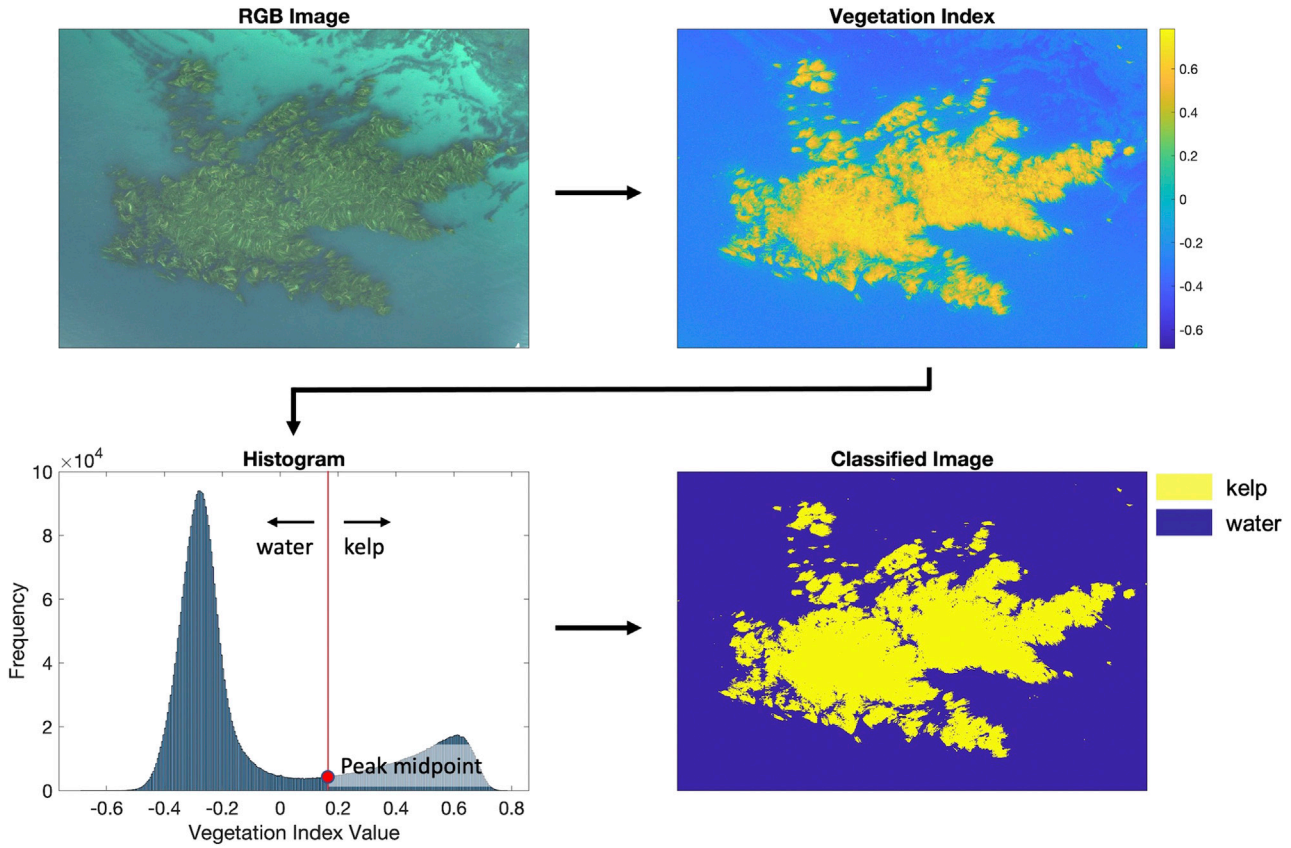

FIGURE 4 | Methodology used in the detection of the presence or absence of kelp in each pixel. For each image, we applied the vegetation index (Red-Blue and NDREB) and calculated histograms to find unique thresholds for image classifications.

sample sizes, and accordingly, ten iterations of the Shapiro-Wilk Normality test were computed, each extracting 100 random samples from the 500 kelp samples and 500 water samples from each image acquisition and spectral index (Huang et al., 2016).

In order to identify kelp using a vegetation index, a threshold was identified, and pixels above this threshold were considered kelp canopy. Ideally, a single threshold would have been used for all images, but differing sensors, illumination conditions, and kelp condition necessitated a more dynamic approach. For each image, histograms were calculated from vegetation index values (**Figure 4**). For images containing both kelp and water, histograms displayed a bimodal signature, with one peak characterizing kelp pixels and the other characterizing water. The locations of the "kelp" peak and the "water" peak were identified using the function findpeaks in MATLAB (2018). The value of the vegetation index at the midpoint between these two peaks was calculated, and this vegetation index value was used as the unique, image-based classification threshold (**Figure 4**). If only one peak was identified (i.e., the image was dominated by either kelp or water pixels), the function gradient was applied in MATLAB (2018) to identify potential shoulders within the histogram. In these images, the vegetation index value at the midpoint between the shoulder and the peak was used as the unique, image-based classification threshold (**Supplementary Figure S2**).

Using the separability measures, the best performing RGB-based index (Red-Blue, see results) and the best performing red-edge or NIR-based index (Normalized Difference Red-edge Blue (NDREB), see Results) were identified. An accuracy assessment was performed to compare the automated classifications from these two indices. Using the same 10 images used within the TD and JD separability analysis, 50 random points within each image were sampled for a total of 500 random points (211 kelp points, 289 water points). The points were manually determined to be either a kelp or water pixel, the number of pixels each index accurately classified was calculated.

NDREB yielded the highest accuracy, and the NDREB histogram-based automated classification was applied to each image in Honeymoon Cove tidal surveys, Arroyo Quemado tidal surveys, Arroyo Quemado current surveys, and Honeymoon Cove time series (**Supplementary Figures S3–S6**). The number of kelp pixels in each classified image was multiplied by the area of each pixel (10 cm × 10 cm) to calculate kelp canopy area for each image. For the tidal analysis, the identified kelp canopy area from Arroyo Quemado was compared to ADCP tidal measurements from the SBC LTER project, and the identified kelp area from Honeymoon Cove was compared to NOAA/NOS/CO-OPS 1 min tidal measurements. The station-measured tidal height at the midpoint of each flight

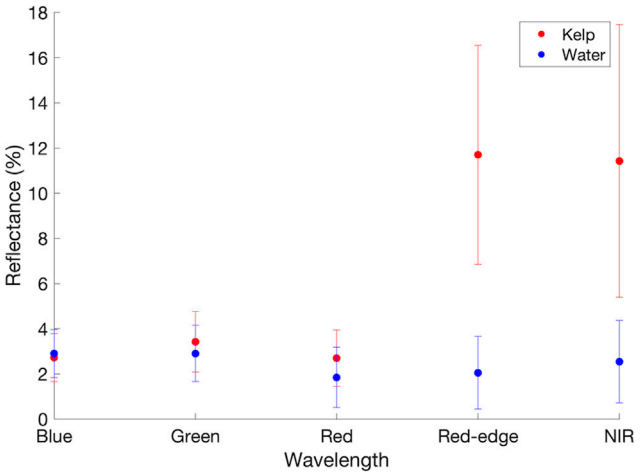

FIGURE 5 | Mean and standard deviation for the manually classified and digitized kelp and water pixels for from the blue, green, red, red-edge, and NIR bands. These values were used as inputs to the vegetation indices used in the parametric separability analysis.

was used for comparison. For the current analysis, the identified kelp area from Arroyo Quemado was compared to ADCP current measurements from the SBC LTER project taken within the kelp forest at 12.5 m (from the bottom). The ADCP-measured current speed at the midpoint of each flight was used for comparison.

Seasonal Variability in Kelp Abundance

Biweekly imagery at Honeymoon Cove was collected from June 2018 to August 2019 for a total of 25 images. All flights were conducted at mid-tide (~1 m) to reduce the impact of tides on surface canopy measurements. Flights were not restricted due to time of day or cloud coverage, however, flights were canceled if wind speeds exceeded 16 km/h or if there was any precipitation.

For qualitative comparisons between seasonal variations in kelp canopy area and environmental variables, SST measurements were collected from the NOAA National Data Buoy Center Station 9410660 and the measurements were aggregated to daily means. Additionally, maximum wave height data were collected from the Coastal Data Information Program's (CDIP) nowcast alongshore wave-propagation model (O'Reilly et al., 2016). The model uses various parameters from sites located at 100 m intervals along the backbeach to calculate hourly estimates of maximum wave height at a depth of 10 m along the California coastline. Five sites that incorporated calculations from the backbeach within Honeymoon Cove (sites L0389–L0394) were selected and averaged by date and time. The daily maximum wave height was calculated for analysis.

Statistical Analyses

Tidal height and current speed can be strongly correlated, and as a result, several statistical analyses were performed to detect and separate the effects of tides and currents on variations in kelp canopy area (Britton-Simmons et al., 2008). For each tidal survey (both Honeymoon Cove surveys and the Arroyo Quemado survey), a simple linear regression was applied to determine whether tidal height (independent variable) was significantly correlated with kelp canopy area (dependent variable). To test for potential differences between the Honeymoon Cove tidal surveys due to current speed, a one-way analysis of covariance (ANCOVA) was used to determine whether the Honeymoon Cove simple linear regression slopes from the two tidal survey dates were equal. To test for potential differences in the relationship between tidal height and kelp canopy area at Honeymoon Cove and Arroyo Quemado, an ANCOVA was used to determine if the simple linear regression slopes between the two sites were significantly different from each other.

For the Arroyo Quemado tidal and current surveys, multiple linear regression was used to determine whether tidal height and current speed (independent variables) were significantly correlated with kelp area (dependent variable; Britton-Simmons et al., 2008). Additionally, partial correlation coefficients were calculated to partition the variance in canopy area explained by tidal height or current speed (Britton-Simmons et al., 2008). Partial correlation coefficients measure the correlation between two variables while holding a specified covariate constant (i.e., correlation between tidal height and kelp canopy area while holding current speed constant, and the correlation between current speed and kelp canopy area while holding tidal height constant; Sokal and Rohlf, 1981). These additional analyses were performed to help distinguish the effect of tides and currents on kelp canopy area during the tidal and current surveys. Current data were only available at the Arroyo Quemado kelp forest (current data were not available during the Honeymoon Cove tidal surveys), and as a result, the multiple linear regression analysis and partial correlation coefficients were only calculated at this site.

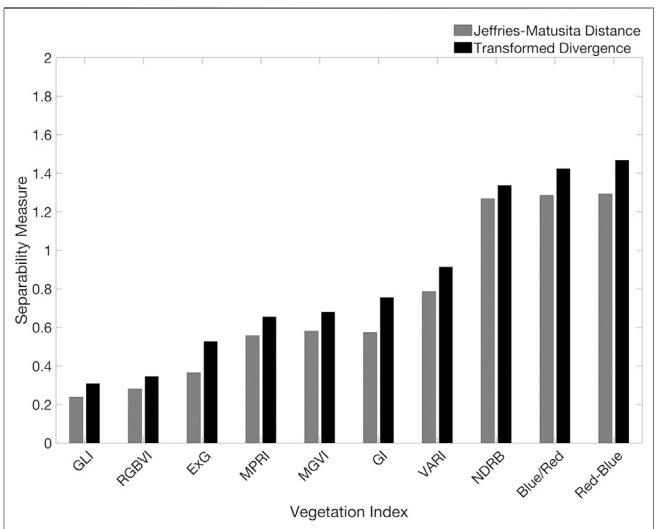

FIGURE 6 | JM and TD values for the 10 RGB vegetation indices, with 0 being no separability between classes and 2 being complete separability.

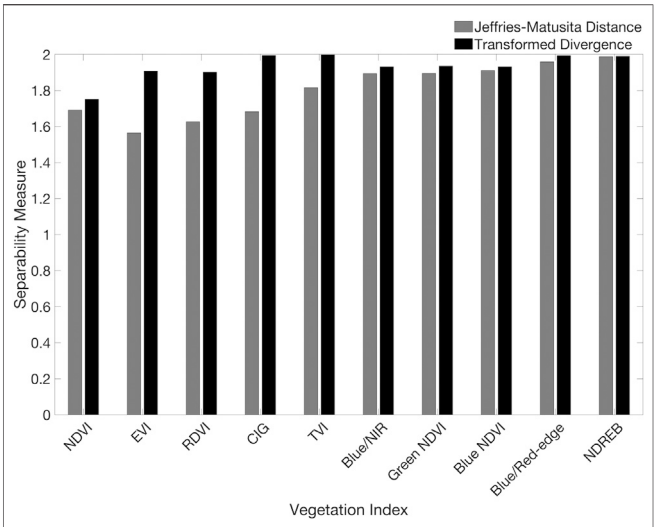

FIGURE 7 | JM and TD values for the 10 red-edge or NIR-based vegetation indices, with 0 being no separability between classes and 2 being complete separability.

RESULTS

Kelp and Water Separability Analysis

The twenty vegetation indices yielded variable performances in the parametric separability analysis of kelp and water pixel samples (**Figure 5**). *p*-values from the Shapiro-Wilk Normality test, which indicate whether the data come from a normally distributed population, varied within and between the ten iterations performed on each vegetation index. All of the data were not considered to be normally distributed (with *p*-values ranging from <0.001 to 0.35 for kelp and from <0.001 to 0.46 for water), which may introduce bias into the JM and TD tests. However, these results were only used to help inform the optimal vegetation index for analysis. For the RGB-based vegetation indices, Red-Blue exhibited the highest cumulative JM and TD values (1.29 and 1.47, respectively), while Blue/Red exhibited the next highest cumulative values (1.29 and 1.42, respectively; **Figure 6**). None of the RGB-based vegetation indices yielded completely separable results. For vegetation indices that included either the red-edge or NIR band, each index exceeded separability scores of 1.5 or greater for both JM and TD. NDREB exhibited the highest cumulative JM and TD values (1.99 and 1.99, respectively), while Blue/Red-edge exhibited the next highest cumulative values (1.96 and 1.99, respectively; **Figure 7**).

Automated Classification Accuracy Assessment

The Red-Blue and NDREB performances in separating kelp and water pixel samples led to further analysis of these vegetation indices for use in the histogram-based automated classification. Red-Blue exhibited an overall accuracy of 67% in identification of the randomly selected 500 pixels, with an accuracy of 76.3% for kelp and 60.2% for water. The index NDREB exhibited an overall accuracy of 93%, with an accuracy of 88.6% for kelp and 96.2% for water. Red-Blue consistently classified submerged fronds as floating canopy, as exemplified by the lower classification accuracy for water. Additionally, Red-Blue often classified visible substrate (i.e., on a day with high water clarity) as floating kelp canopy.

Both indices were sensitive to water surface features (ripples and waves), remnant glint artifacts, shadows (i.e., from steeply sloped shoreline), often mis-classifying these features as kelp. Darkly shaded kelp fronds and remnant glint on kelp fronds were often mis-classified as water. Overall, NDREB was more robust and was able to accurately classify kelp and water pixels across a wide variety of environmental conditions and was used to distinguish kelp from water in all further analyses.

Tidal Analyses

A simple linear regression showed tidal height was significantly correlated with kelp canopy area in both Honeymoon Cove tidal surveys ($F(1,5) = 213.19$, $p < 0.001$ and $F(1,4) = 10.39$, $p = 0.03$, respectively) and in the Arroyo Quemado tidal survey ($F(1,5) = 134.69$, $p < 0.001$; **Figure 8**). Tides had a large impact on the amount of kelp canopy exposed in southern California aerial imagery, as a 1 m increase in tidal height resulted in a 30.26% and 32.30% decrease in kelp canopy area during the first and second Honeymoon Cove tidal surveys, respectively, and a 15.67% decrease in kelp canopy area at the Arroyo Quemado kelp forest (**Figure 8**).

The reduction in canopy area with increasing tidal height was similar between the two Honeymoon Cove tidal surveys, as the slopes of the Honeymoon Cove regression lines (one for each tidal survey date) were not significantly different ($F(1,9) = 0.02$, $p = 0.90$). The reduction in canopy area with increasing tidal height was greater in both Honeymoon Cove surveys than it was at Arroyo Quemado ($F(1,10) = 60.18$, $p < 0.001$ and $F(1,9) = 6.83$, $p = 0.02$, respectively).

Current Analyses

Analysis of Currents During Tidal Surveys at Arroyo Quemado

During the Arroyo Quemado tidal survey, current speeds generally increased as tidal heights reached their minimum (**Figure 9**). During this survey, tidal height was significantly correlated with current speed ($F(1,5) = 23.6$, $p = 0.005$). However, the relationship between tidal height and current speed was variable at the Santa Barbara site, and over the course of the two weeks following the tidal height survey, tides and currents were not correlated ($R^2 = 0.0009$). The multiple regression analysis from the Arroyo Quemado tidal survey showed a significant negative relationship between tidal height and kelp area ($p = 0.01$; **Table 2**). The relationship between current speed and kelp area was positive but insignificant ($p = 0.65$; **Table 2**). The partial correlation analysis showed that when the effects of current speed were controlled, tidal height explained 86.90% of the observed variation in and kelp canopy area. By contrast, contribution of current velocity explained only 5.7% of the observed variation in canopy area, and this result was not significant ($p = 0.65$; **Table 2**).

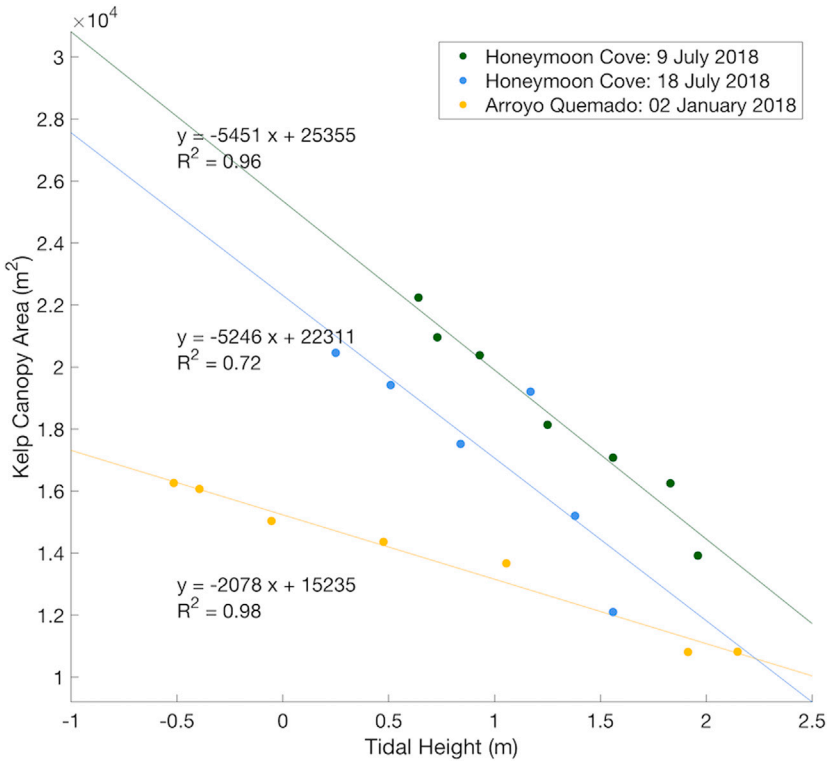

FIGURE 8 | Regression analysis between kelp canopy area and tidal height for each tidal survey completed at Honeymoon Cove (n = 7, n = 6) and Arroyo Quemado (n = 7).

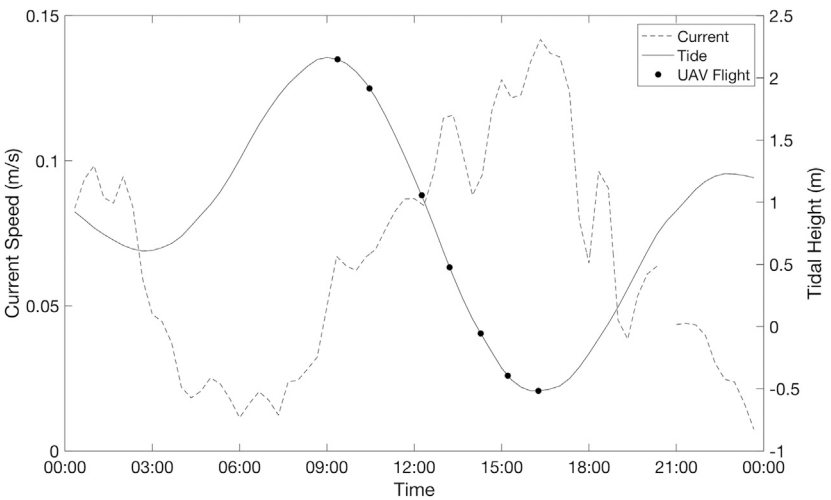

FIGURE 9 | Temporal variations in tidal height and current speed during each flight of the single-day Arroyo Quemado tidal survey.

Analysis of Currents During Multi-Day UAV Surveys at Arroyo Quemado

Current speeds ranged from 0.02 to 0.13 m/s across the five dates, which was representative of average conditions in the Arroyo Quemado kelp forest during 2019 as a whole (**Figure 10**; annual average of 0.085 ± 0.066 m/s). Current speed exhibited a negative linear relationship with kelp canopy area, with canopy area declining by 31.99% for a 0.1 m/s increase in current velocity (F (1,5) = 6.05, p = 0.09; **Figure 11**). While this relationship was not highly

TABLE 2 | Multiple regression and partial correlation analysis results from the Arroyo Quemado tidal survey.

Multiple regression analysis				Partial correlation analysis			
Coefficients				Tide effect		Current effect	
Intercept	Tide	Current	R^2	r	R^2	r	R^2
14,441.5*	−1913.3*	6,912.3	0.98	−0.932*	0.869	0.238	0.057

*Indicates statistical significance.

significant, the magnitude of the current effect was relatively large.

During these five dates, there was no consistent relationship between tidal height and current speed (**Figure 10**) and the two were not significantly correlated (F (1,5) = 1.92, p = 0.23). The multiple regression analysis from the Arroyo Quemado current survey showed neither a significant effect of current speed on kelp area, nor a significant effect of tidal height (F (2,5) = 2.01, p = 0.33). The partial correlation analysis showed that variability in current speed accounted for a large amount of variability in kelp area during the current survey, this relationship was not statistically significant (p = 0.26), likely due to the limited number of data points (n = 5).

Honeymoon Cove Time Series

The mean kelp canopy area in Honeymoon Cove from June 2018 to August 2019 was 6,763.2 m^2, but there was a high amount of variability about this mean. With a standard deviation of 7,104.6 m^2, the coefficient of variation across the 25 surveys was 105%. Changes in kelp canopy area occurred over a seasonal cycle with kelp area maximums in mid-summer and minimums in winter (**Figure 12**). There was also pronounced seasonal variability, as patch level declines and increases in kelp canopy each progressed for about four months (from late summer to fall and from spring to early summer, respectively) before reaching maximum or minimum values (**Figure 12**). These gradual changes coincided with SST patterns, with kelp area declining to 3.14% of the overall time series mean area in mid-September after mean SST increased during the summer months (20.34 ± 1.20°C). Kelp canopy recovered to 104.48% of the mean kelp canopy area in June after mean SST decreases in the winter (15.64 ± 0.61°C; **Figure 12**) persisted through May. Rapid changes also occurred within seasonal time spans, as evidenced by kelp recovery from late October to late November (212.15 m^2–8,990.92 m^2) once the mean SST began to cool during the fall months (19.24 ± 0.36°C), followed by a rapid decline in kelp area to 169.87 m^2 that corresponded to large wave events that began in late November (maximum wave height of 2.87 m). Kelp canopy area persisted below 10% of the mean kelp canopy area until April, when wave events began to subside and SST remained low (**Figure 12**).

DISCUSSION

UAV Data Collection, Processing, and Classification

Our results demonstrate strong potential for using UAVs for repeat monitoring of floating kelp canopy on local scales. Flights were conducted for our area of interest using one battery set (20–30 min flights), allowing for relatively quick data collection. Additionally, mostly automated processing workflows (reflectance corrections, photogrammetry workflow, and classifications) allowed for dataset manageability, as processing took about 5 h from start to finish (about 4.5 h were automated). This time would decrease with more computing power and/or GPU processing.

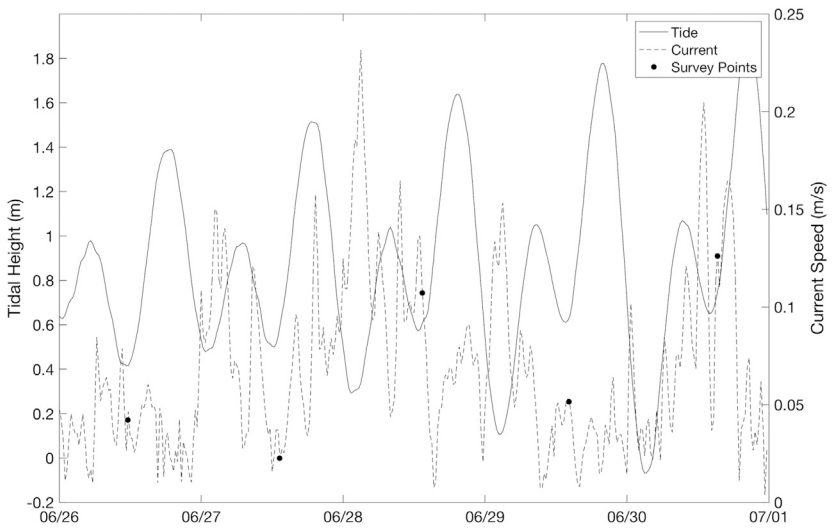

FIGURE 10 | Temporal variations in tidal height and current speed during each flight of the multi-day Arroyo Quemado current surveys.

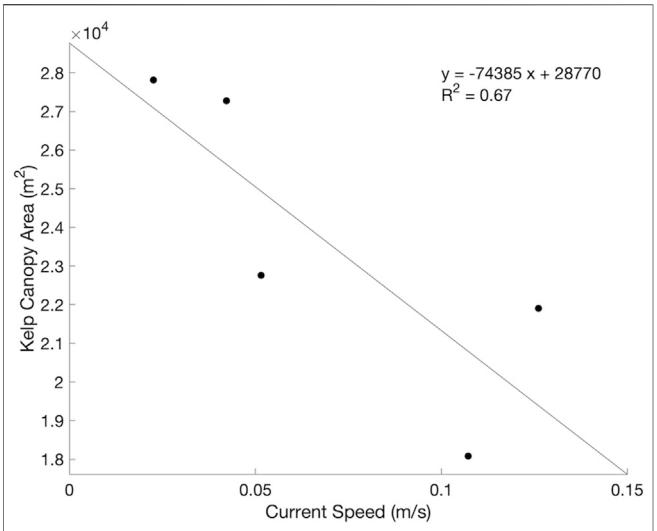

FIGURE 11 | Regression analysis between kelp canopy area and current speed during the Arroyo Quemado current surveys.

Our automated method for detecting kelp canopy can be applied to both multispectral and RGB UAV imagery and is accurate across a range of weather, ocean, and illumination conditions. This robustness is important as there are a number of challenges associated with UAV-based remote sensing in coastal zones (Hodgson et al., 2013; Bevan et al., 2016; Schaub et al., 2018). Weather conditions, including precipitation and high wind, are common limiting factors in UAV deployment. Sun can also be a limiting factor for marine applications, as glint features on the water surface are challenging for photogrammetric software packages to manage. During stitching, the software may use glint artifacts as tie points to stitch two non-neighboring images in error, or it may be unable to find tie points altogether due to the lack of viable pixels. Additionally, any remaining glint in orthomosaics can introduce spectral noise and bias classification efforts. Sun glint can be reduced or avoided by collecting data on overcast days or by flying when the sun is at lower angles in the sky, but this is not always possible as flights may need to be conducted at a certain tidal stage. By introducing sun glint masks into our image processing workflow, photogrammetry alignment success increased in almost every flight and the presence of sun glint greatly decreased in final orthomosaics.

Another challenge of using UAV imagery for analysis in marine ecosystems includes changing illumination conditions within flights (i.e., on a partly cloudy day when the sun continuously emerges and disappears behind clouds) and between flights (i.e., flying on an overcast day and flying on a sunny day). Despite spectral corrections with reflectance panels, these variations impact output reflectance values and cause spectral inconsistencies. As a result, using supervised classification schemes to distinguish kelp from water is difficult, as the training data often do not adequately cover the spectral ranges observed through each flight (Taddia and Russo 2019). Additionally, while vegetation indices help to distinguish kelp from water, the threshold for separation

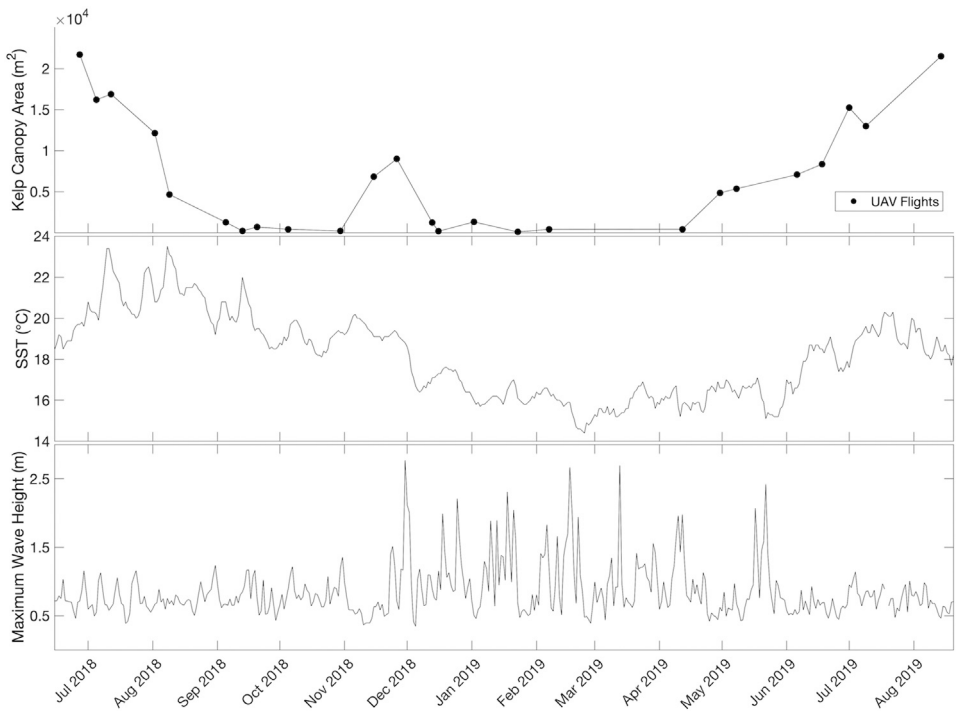

FIGURE 12 | Honeymoon Cove UAV-derived time series of kelp canopy area from June 2018 to August 2019.

strongly depends on image-specific spectral values, in turn necessitating image-specific thresholds (Taddia and Russo 2019). Our dynamic thresholding procedure removed the subjectivity and visual bias involved with manual threshold selection and produced a classification that was highly accurate in classifying both kelp and water.

Our highest accuracies were achieved using multispectral imagery, and a number of other studies have demonstrated the utility of multispectral imagery in detecting kelp canopy (Jensen et al., 1980; Cavanaugh et al., 2010). While many traditional floating algae indices depend on the NIR band (Tucker 1979; Hu 2009; Cavanaugh et al., 2010; Xing and Hu 2016), the NDREB index, our highest preforming index, takes advantage of the high red-edge and low blue reflectance of kelp, as compared to the higher blue and lower red-edge reflectance of water, resulting in a stronger separation potential than traditional NDVI. Giant kelp is a brown alga, and spectrally differs from both green vegetation and green algae, as it lacks the chlorophyll *b* pigment. There is high reflectance between the absorption peaks of chlorophyll *a* and chlorophyll *c* (the orange-edge; Bell et al., 2015b; Schroeder et al., 2019b). Combined with the high reflectance of seawater in the blue portion of the visible spectrum, there is a larger difference between the blue and red-edge/NIR than there is between the red and red-edge/NIR.

Additionally, accuracies of >60% could be achieved using RGB imagery using a simple subtraction between the red and the blue band. This indicates potential for kelp mapping using accessible low-cost UAV platforms that come with digital cameras. However, users should be aware that RGB imagery is more sensitive to the misclassification of submerged kelp fronds and visible substrate (i.e., on a day with high water clarity).

Floating kelp canopy appears similar to submerged canopy in the visible range of the spectrum, yet the magnitude of NIR reflectance is much greater for floating canopy than for submerged canopy (Schroeder et al., 2019a, Schroeder et al., 2019b). As a result, RGB-based indices may have a hard time distinguishing between floating and submerged canopy when submerged canopy is visible. However, this could be a benefit for certain applications, as it indicates potential for mapping of submerged fronds using RGB imagery. While we lose submerged canopy data in the NIR, the variability in water clarity, environmental conditions, and the amount of floating canopy result in an inconsistent ability to detect submerged canopy–even when the NIR is excluded during detection efforts. Using the NIR reduces the error associated with this variability and allows us to isolate floating canopy.

While both indices misclassified surface features (ripples and waves), remnant glint artifacts, and shadows (i.e., from steeply sloped shoreline) as kelp, Red-Blue was much more prone to these errors. The difference in magnitude between kelp pixels and water pixels in the red-edge and the blue band is much larger than the difference in magnitude between kelp pixels and water pixels in the red and blue band (**Figure 5**). As a result, using the histogram approach, problematic features are more easily distinguishable from kelp with red-edge or NIR-based indices, as the signature of kelp is very strong in these histograms despite the added noise. With RGB-based indices, the kelp signal in Red-Blue is often small and can be masked by the noise.

Effects of Tidal Height and Current Speed on Exposed Canopy

The amount of kelp canopy mapped on the water surface at both Honeymoon Cove and Arroyo Quemado declined significantly with tidal height, suggesting that tides can bias aerial-derived metrics of kelp canopy. The effect of tide was not consistent between the two sites and was almost twice as strong at Honeymoon Cove, which may be the result of differing bed structures between the two sites. The Arroyo Quemado kelp forest is comprised of large discrete, offshore stands, while the Honeymoon Cove kelp forest is comprised of both large, dense kelp stands as well as small, sparse stands. At Arroyo Quemado, the depth linearly slopes downward from the shoreline (from about −1.5 m to −16.5 m), but the extensive rocky reef along the gradient allows for a continuous, dense canopy. Increases in tidal height submerged the edges of the canopy but did not submerge any central canopy features. At Honeymoon Cove, the depth slopes downward from the outer edges of the cove to the center (from about 0 m to −8 m). There is extensive and continuous rocky reef along the shallow edges of the cove, but the reef in the center is much more fragmented. As a result, dense aggregates of kelp grow along edges, and these behave similarly to the beds at Arroyo Quemado as tidal height increases. However, the patchy, fragmented aggregates in the center of the cove often only consist of a few individuals, and these become fully submerged as the tide increases (**Figure 1**). Kelp forest demographics might also influence the impacts of tides by controlling the fraction of canopy vs. subsurface fronds.

A region's tidal range will clearly influence the degree to which UAV estimates of canopy area are affected by tides. Southern California has a generally low tidal range (~2 m) compared to some other global regions (i.e., Southeast Alaska, ~9 m). Yet, even this small range impacted kelp canopy coverage by over 15% at Arroyo Quemado and over 30% at Honeymoon Cove. This result disagrees with previous work that estimated the weak tidal fluctuations in Santa Barbara had no effect on kelp canopy coverage estimates from Landsat satellite imagery (Cavanaugh et al., 2010, 2011). However, the higher resolution of the UAV imagery and experimental design aimed at isolating the effects of tides likely enabled us to more clearly detect the tidal effect. Bell et al. (2020) also used Landsat imagery for kelp canopy detection and found inconsistencies in kelp biomass estimates between Landsat TM and ETM + sensors, which was attributed to the 8 day repeat difference between the satellites imaging at different points in the tidal cycle. Aggregating Landsat biomass estimates (30 m resolution) to a seasonal scale (3 months) was sufficient for correcting for tidal effects (Bell et al., 2020).

Tidal height explained 87% of the variation in kelp canopy area during the Arroyo Quemado tidal survey, which is consistent with findings from other regions with similar tidal signals, such as San Juan Island, WA (Britton-Simmons et al., 2008). Kelp beds

adjacent to San Juan Island experience tidal ranges of 2–3 m and are mainly comprised of bull kelp (*Nereocystis luetkeana*). Britton-Simmons et al. (2008) found that tidal height explained between 67% and 95% of observed variability in kelp area across six different sites near San Juan Island, which included differing kelp densities, bathymetry, coastline shapes, and current strength. While both giant kelp and bull kelp form floating canopies, they exhibit unique morphological features. Each giant kelp blade is attached to a pneumatocyst that buoys it to the surface (Graham et al., 2007), while bull kelp blades for one individual grow from a single, large (15 cm diameter) pneumatocyst (Amsler and Neushul, 1989; Schroeder et al., 2019a). As a result, giant kelp canopies consist of stipes, pneumatocysts, and blades, while bull kelp canopies mainly consist of stipes and pneumatocysts; bull kelp fronds often remain submerged (Schroeder et al., 2019a). While these morphological differences responded similarly to tidal fluctuations in southern California and San Juan Island, they may exhibit different effects in regions with more extreme tidal fluctuations. Additionally, currents and tides are often related, and these factors have the ability to interact and impact the amount of canopy visible to the sensor. Currents and tides were significantly correlated during the Arroyo Quemado tidal survey, and while multiple regression and partial correlation coefficients show that variations in kelp canopy were likely due to tidal fluctuations, it remains difficult to concretely separate the effect of either tides or currents on floating canopy area.

Canopy area was not significantly correlated (at the $p = 0.05$ level) with current speed during the tidal surveys or in the surveys conducted across multiple days at similar tidal stages. However, the relationship may have been significant if more samples were included in the study. While the p-value for this relationship was above 0.05 ($p = 0.09$), the effect size was large, as a 0.1 m/s increase in current speed reduced the amount of floating canopy by over 31%. More data is needed to determine whether there is in fact a relationship between these relatively low current speeds and visible canopy area. In their study of bull kelp along San Juan Island, Britton-Simmons et al. (2008) found that for a bed where current speeds never exceeded 0.4 m/s, there was no significant relationship between current speed and the amount of visible kelp on the water surface (Britton-Simmons et al., 2008). In contrast, the effects of current speed on the canopy areas of the other five kelp beds from Britton-Simmons et al., 2008 were found to be highly significant, but current speeds ranged much higher at these sites (>1 m/s). While low current speeds may impact giant kelp and bull kelp similarly, the relationship may change as current speed increases. Bull kelp blades begin to stream laterally with moderate amounts of current, resulting in larger floating canopies. As a result, the relationship between the percentage of bull kelp bed visible and current speed is often non-linear and difficult to quantify, as it varies with geographic shading, coastline shape, and bathymetry (Britton-Simmons et al., 2008). The spatial variation in current dynamics around kelp beds is extremely dynamic, and necessitates site-specific corrections–especially in places with high current ranges (Britton-Simmons et al., 2008).

UAV Kelp Canopy Time Series

Our UAV time series dataset represents a high-resolution assessment of high-frequency variability in kelp canopy area. Previous studies have demonstrated the effectiveness of deriving time series of kelp canopy biomass or area from aerial and satellite imagery, but many of these analyze data on quarterly or annual time scales, which limits the potential for characterizing seasonal dynamics (Jensen et al., 1980; Deysher 1993; Berry et al., 2005; Stekoll et al., 2007; Cavanaugh et al., 2010; Cavanaugh et al., 2011; Cavanaugh et al., 2019; Bell et al., 2015b; Bell et al., 2020; Pfister et al., 2018; Rogers-Bsennett and Catton 2019; Schroeder et al., 2019a). This UAV dataset provides a novel view into the feasibility for collecting long-term datasets at high spatial and temporal resolution, and the potential for understanding the rapid, sub-seasonal variations in canopy dynamics.

The Honeymoon Cove time series displayed a high degree of intra-annual variability in giant kelp abundance. Previous studies in southern and central California have found that kelp canopies and standing crop in wave exposed locations typically exhibit a seasonal cycle with maximums in the late summer to early fall and minimums in late winter to early spring (Graham et al., 1997; Reed et al., 2008; Cavanaugh et al., 2011). This pattern has been attributed to wave disturbance in the winter followed by recovery during the spring and summer. However, nutrient availability can be low in southern California during summer months, which can lead to reduced growth rates and canopy dieback (Clendenning and Sargent, 1971; Zimmerman and Kremer, 1986). Our time series of canopy showed evidence of both of these processes superimposed on one another. Increased temperature and decreased nutrients in the late summer were associated with gradual declines in kelp coverage. However, water temperatures decreased in the fall before the onset of major wave disturbance, and this was associated with a short-lived increase in kelp cover (**Figure 12**). This increase may have been linked to increased nutrient levels, however, a number of other factors may have been involved, including increased light availability and an increase in unoccupied substrate following the late fall kelp decline. The first large wave event of the winter yielded immediate kelp declines, and abundance remained low until wave events began to subside in the spring. As temperature and nutrient conditions became more favorable, kelp abundance continued to increase until reaching a peak in late summer.

One of the benefits of UAV-based monitoring is the flexibility in timing of data collection. For example, repeated UAV surveys provide one way for characterizing variability in the phenology of giant kelp abundance across sites and years. The timing of kelp growth and dieback is likely to be important as it might influence cycles of reproduction and growth of species that depend on kelp for food, e.g., sea urchins. UAV surveys can also be used to document the effect of discrete disturbances such as large wave events or marine heatwaves. Logistically, UAVs allow the operator to mitigate the impacts of environmental conditions such as clouds, tides, and wind on data quality. Cloud cover limits satellite acquisitions while UAVs can be flown below clouds or surveys can be planned for clear days. Here we have shown the potential impacts of tides on canopy area estimates and the difficulty of applying a universal correction factor across different sites. UAV surveys can be planned around tidal cycles to reduce the need to correct for tides.

CONCLUSION

The spatial and temporal capabilities of UAV imagery make these platforms useful for local mapping of giant kelp canopies at high spatial resolution, but the potential effects of tides and current should be considered when planning UAV surveys. Collecting repeated measurements of kelp canopy area at a relatively small spatial scale (e.g., less than a few m^2) is challenging, as diving efforts require extensive data collection, and estimates from most satellite platforms do not provide suitable resolutions (Britton-Simmons et al., 2008; Reed et al., 2008, Reed et al., 2009; Schroeder et al., 2019a). UAVs provide the ability to collect data over larger areas than would be possible with other *in situ* methods and provide much higher resolution than most satellite datasets. In addition, they are typically much more cost effective than occupied aerial surveys. Therefore, UAVs can be used to map kelp in small, sparse beds close to the coast, to create high spatial resolution time series, and to examine the impacts of discrete events such as large wave events. This high spatial resolution comes at the expense of the broad spatial coverage of satellites, and neither method can fully replace the other. Ultimately, the choice of which method to use is highly dependent on the ecological questions being asked.

DATA AVAILABILITY STATEMENT

The raw data supporting the conclusions of this article will be made available by the authors, without undue reservation. A conservation institution has used the glint masking methods developed in this study to produce an open-access tool for glint removal of aerial imagery (https://doi.org/10.21966/3cpa-2e10).

AUTHOR CONTRIBUTIONS

KaC, KyC, and TB conceived the study. KaC, KyC, TB, and EH performed UAV flight planning and conducted UAV flights. KaC and EGH processed the data. KaC led algorithm development. KaC and KyC led the analysis and wrote the manuscript. All authors contributed to results interpretation and manuscript draft revisions.

FUNDING

Funding was provided by the U.S. Department of Energy ARPA-E (grant number DE-AR0000922), the U.S. National Science Foundation which provided funding for the SBC LTER (grant number OCE 1831937), and the Nature Conservancy (grant number 02042019-5719).

ACKNOWLEDGMENTS

The content of this manuscript has been published as part of the thesis of KaC. We would like to thank the field and laboratory technicians who helped in the collection and processing of the UAV data.

SUPPLEMENTARY MATERIAL

The Supplementary Material for this article can be found online at: https://www.frontiersin.org/articles/10.3389/fenvs.2020.587354/full#supplementary-material.

REFERENCES

Amsler, C. D., and Neushul, M. (1989). Diel periodicity of spore release from the kelp *Nereocystis luetkeana*. *J. Exp. Mar. Biol. Ecol.* 134, 117–127.

Bell, T. W., Allen, J. G., Cavanaugh, K. C., and Siegel, D. A. (2020). Three decades of variability in California's giant kelp forests from the Landsat satellites. *Remote Sens. Environ.* 238, 110811. doi:10.1016/j.rse.2018.06.039

Bell, T. W., Cavanaugh, K. C., Reed, D. C., and Siegel, D. A. (2015a). Geographical variability in the controls of giant kelp biomass dynamics. *J. Biogeogr.* 42, 2010–2021. doi:10.1111/jbi.12550

Bell, T. W., Cavanaugh, K. C., and Siegel, D. A. (2015b). Remote monitoring of giant kelp biomass and physiological condition : an evaluation of the potential for the Hyperspectral Infrared Imager (HyspIRI) mission. *Remote Sens. Environ.* 167, 218–228. doi:10.1016/j.rse.2015.05.003

Bendig, J., Yu, K., Aasen, H., Bolten, A., Bennertz, S., Broscheit, J., et al. (2015). Combining UAV-based plant height from crop surface models, visible, and near infrared vegetation indices for biomass monitoring in barley. *Int. J. Appl. Earth Obs. Geoinf.* 39, 79–87. doi:10.1016/j.jag.2015.02.012

Berry, H. D., Mumford, T. F., and Dowty, P. (2005). Using historical data to estimate changes in floating kelp (nereocystis luetkeana and macrocystis integrifolia) in puget sound (Available at:http://depts.washington.edu/uwconf/2005psgb/2005proceedings/papers/F7_BERRY.pdf%0Apapers3://publication/uuid/A9C39740-8651-46F0-A52A-D1E89664AF5C.

Bevan, E., Wibbels, T., and Najera, B. M. Z. (2016). Using unmanned aerial vehicle (UAV) technology for locating, identifying, and monitoring courtship and mating behavior in the green turtle (*Chelonia mydas*) Techniques. *Tech. 27 Herpetol. Rev.* 47, 27–32.

Britton-Simmons, K., Eckman, J. E., and Duggins, D. O. (2008). Effect of tidal currents and tidal stage on estimates of bed size in the kelp Nereocystis luetkeana. *Mar. Ecol. Prog. Ser.* 355, 95–105. doi:10.3354/meps07209

Broge, N. H., and Leblanc, E. (2001). Comparing prediction power and stability of broadband and hyperspectral vegetation indices for estimation of green leaf area index and canopy chlorophyll density. *Remote Sens. Environ.* 76, 156–172. doi:10.1016/S0034-4257(00)00197-8

Castorani, M. C., Reed, D. C., Alberto, F., Bell, T. W., Simons, R. D., Cavanaugh, K. C., et al. (2015). Connectivity structures local population dynamics: a long-term empirical test in a large metapopulation system. *Ecology.* 96, 3141–3152. doi:10.1890/15-0283.1

Castorani, M. C., Reed, D. C., Raimondi, P. T., Alberto, F., Bell, T. W., Cavanaugh, K. C., et al. (2017). Fluctuations in population fecundity drive variation in demographic connectivity and metapopulation dynamics. *Proc. Biol. Sci.* 284. doi:10.1098/rspb.2016.2086

Cavanaugh, K. C., Kendall, B. E., Siegel, D. A., Reed, D. C., Alberto, F., and Assis, J. (2013). Synchrony in dynamics of giant kelp forests is driven by both local recruitment and regional environmental controls. *Ecology.* 94, 499–509. doi:10.1890/12-0268.1

Cavanaugh, K. C., Siegel, D. A., Raimondi, P. T., and Alberto, F. (2014). Patch definition in metapopulation analysis: a graph theory approach to solve the mega-patch problem. *Ecology.* 95, 316–328. doi:10.1890/13-0221.1

Cavanaugh, K. C., Reed, D. C., Bell, T. W., Castorani, M. C. N., Beas-luna, R., and Barrett, N. S. (2019). Spatial variability in the resistance and resilience of giant kelp in southern and baja California to a multiyear heatwave. *Front. Mar. Sci.* 6, 1–14. doi:10.3389/fmars.2019.00413

Cavanaugh, K. C., Siegel, D. A., Kinlan, B. P., and Reed, D. C. (2010). Scaling giant kelp field measurements to regional scales using satellite observations. *Mar. Ecol. Prog. Ser.* 403, 13–27. doi:10.3354/meps08467

Cavanaugh, K. C., Siegel, D. A., Reed, D. C., and Dennison, P. E. (2011). Environmental controls of giant-kelp biomass in the Santa Barbara channel, California. *Mar. Ecol. Prog. Ser.* 429, 1–17. doi:10.3354/meps09141

Changhui, Y., Yuan, Y., Minjing, M., and Menglu, Z. (2013). "Cloud detection method based on feature extraction in remote sensing images Int. Arch. Photogramm. Remote Sens. Spat. Inf. Sci. XL-2/W1," in , 8th International Symposium on Spatial Data Quality, Hong Kong, China, May 30–June 1, 2013, 173–177.

Clendenning, K. A., and Sargent, M. C. (1971). Photosynthesis and general development in Macrocystis. *Nova Hedwigia* 32, 169–190.

Deysher, L. E. (1993). Evaluation of remote sensing techniques for monitoring giant kelp populations. *Hydrobiologia*. 260–261, 307–312. doi:10.1007/BF00049033

Dugan, J. E., Hubbard, D. M., Mccrary, M. D., and Pierson, M. O. (2003). The response of macrofauna communities and shorebirds to macrophyte wrack subsidies on exposed sandy beaches of southern California. *Estuar. Coast. Shelf Sci.* 58, 25–40. doi:10.1016/S0272-7714(03)00045-3

Gentry, R. R., Froehlich, H. E., Grimm, D., Kareiva, P., Parke, M., Rust, M., et al. (2017). Mapping the global potential for marine aquaculture. *Nat. Ecol. Evol.* 1, 1317–1324. doi:10.1038/s41559-017-0257-9

Gentry, R. R., Alleway, H. K., Bishop, M. J., Gillies, C. L., Waters, T., and Jones, R. (2019). Exploring the potential for marine aquaculture to contribute to ecosystem services. *Rev. Aquacult.*, 499–512. doi:10.1111/raq.12328

Gitelson, A. A., Kaufman, Y. J., and Merzlyak, M. N. (1996). Use of a green channel in remote sensing of global vegetation from EOS- MODIS. *Remote Sens. Environ.* 58, 289–298. doi:10.1016/S0034-4257(96)00072-7

Gitelson, A. A., Kaufman, Y. J., Stark, R., and Rundquist, D. (2002). Novel algorithms for remote estimation of vegetation fraction, *Remote Sens. Environ.* 80 76–87. doi:10.1016/S0034-4257(01)00289-9

Gitelson, A. A., Viña, A., Ciganda, V., Rundquist, D. C., and Arkebauer, T. J. (2005). Remote estimation of canopy chlorophyll content in crops. *Geophys. Res. Lett.* 32, 1–4. doi:10.1029/2005GL022688

Graham, M. H., Harrold, C., Lisin, S., Light, K., Watanabe, J. M., and Foster, M. S. (1997). Population dynamics ofgiant kelp Macrocystis pyrifera along awave exposure gradient. *Marine Ecol. Prog. Ser.* 148, 269–279. doi:10.3354/meps148269

Graham, M. H., Vásquez, J. A., and Buschmann, A. H. (2007). Global ecology of the giant kelp Macrocystis : from ecotypes to ecosystems. *Oceanogr. Mar. Biol.* 45, 39–88. doi:10.1201/9781420050943.ch2

Hakala, T., Markelin, L., Id, E. H., Scott, B., Theocharous, T., Id, O. N., et al. (2018). Direct reflectance measurements from Drones : sensor absolute radiometric calibration and system tests for forest reflectance characterization. *Sensors (Basel).* 18 (5), 14–17. doi:10.3390/s18051417

Hamilton, S. L., Bell, T. W., Watson, J. R., Grorud-Colvert, K. A., and Menge, B. A. (2020). Remote sensing: generation of long-term kelp bed data sets for evaluation of impacts of climatic variation. *Ecology*., 1–13. doi:10.1002/ecy.3031

Haralick, R. M., Shanmugam, K., and Dinstein, I. (1973). Textural features for image classification. *IEEE Trans. Syst. Man Cybern. SMC.* 3, 610–621, doi:10.1109/TSMC.1973.4309314

Harley, C. D., Hughes, A. R., Hultgren, K. M., Miner, B. G., Sorte, C. J., Thornber, C. S., et al. (2006). The impacts of climate change in coastal marine systems. *Ecol. Lett.* 9, 228–241. doi:10.1111/j.1461-0248.2005.00871.x

Hodgson, A., Kelly, N., and Peel, D. (2013). Unmanned aerial vehicles (UAVs) for surveying Marine Fauna: a dugong case study. *PLoS One*. 8, e79556–15. doi:10.1371/journal.pone.0079556

Hu, C. (2009). A novel ocean color index to detect floating algae in the global oceans. *Remote Sens. Environ.* 113, 2118–2129. doi:10.1016/j.rse.2009.05.012

Huang, H., Roy, D. P., Boschetti, L., Zhang, H. K., Yan, L., Kumar, S. S., et al. (2016). Separability analysis of Sentinel-2A Multi-Spectral Instrument (MSI) data for burned area discrimination. *Rem. Sens.* 8 (10). doi:10.3390/rs8100873

Huang, X., Liu, X., and Zhang, L. (2014). A multichannel gray level Co-occurrence matrix for multi/hyperspectral image texture representation. *Rem. Sens.* 6 (9). 8424–8445. doi:10.3390/rs6098424

Huete, A., Didan, K., Miura, T., Rodriguez, E. P., Gao, X., and Ferreira, L. G. (2002). Overview of the radiometric and biophysical performance of the MODIS vegetation indices. *Rem. Sens.* 83, 195–213. doi:10.1080/0965156x.2013.836857

Jensen, J. R., Estes, J. E., and Tinney, L. (1980). Remote sensing techniques for kelp surveys. *Photogramm. Eng. Rem. Sens.* 46, 743–755.

Kellaris, A., Badia, I. M., Gil, A., Neto, A., and Amaral, R. (2019). *Using low.–cost drones to monitor heterogeneous submerged seaweed habitats : a case study in the Azores*. New Jercy, NJ: Wiley. doi:10.1002/aqc.3189

Louhaichi, M., Borman, M. M., and Johnson, D. E. (2001). Spatially located platform and aerial photography for documentation of grazing impacts on wheat. *Geocarto Int.* 16, 65–70. doi:10.1080/10106040108542184

MATLAB (2018). version 9.4 (R2018a). Natick, MA: The MathWorks Inc.

Miller, R. J., Lafferty, K. D., Lamy, T., Kui, L., Rassweiler, A., Reed, D. C., et al. (2018). Giant kelp, Macrocystis pyrifera, increases faunal diversity through physical engineering. *Proc. Biol. Sci.* 285 (1874), 20172571 doi:10.1098/rspb.2017.2571

Mora-Soto, A., Palacios, M., Macaya, E. C., Gómez, I., Huovinen, P., Pérez-Matus, A., et al. (2020). A high-resolution global map of giant kelp (macrocystis pyrifera) forests and intertidal green. 1–20 12 (4), 2-20. doi:10.3390/rs12040694

Nijland, W., Reshitnyk, L., and Rubidge, E. (2019). Satellite remote sensing of canopy-forming kelp on a complex coastline: a novel procedure using the Landsat image archive. *Remote Sens. Environ.* 220, 41–50. doi:10.1016/j.rse.2018.10.032

O'Reilly, W. C., Olfe, C. B., Thomas, J., Seymour, R. J., and Guza, R. T. (2016). The California coastal wave monitoring and prediction system. *Coast. Eng.* 116, 118–132. doi:10.1016/j.coastaleng.2016.06.005

Pfister, C. A., Berry, H. D., and Mumford, T. (2018). The dynamics of kelp forests in the northeast pacific ocean and the relationship with environmental drivers. *J. Ecol.* 106, 1520–1533. doi:10.1111/1365-2745.12908

Reed, D., Rassweiler, A., and Arkema, K. (2009). Density derived estimates of standing crop and net primary production in the giant kelp. *Mar. Biol.* 156, 2077–2083. doi:10.1007/s00227-009-1238-6

Reed, D. C., Rassweiler, A., and Arkema, K. K. (2008). Biomass rather than growth rate determines variation in net primary production by giant kelp. *Ecology*. 89, 2493–2505. doi:10.1890/07-1106.1

Rogers-Bennett, L., and Catton, C. A. (2019). Marine heat wave and multiple stressors tip bull kelp forest to sea urchin barrens. *Sci. Repor.* 9 (1). doi:10.1038/s41598-019-51114-y

Roujean, J. L., and Breon, F. M. (1995). Estimating PAR absorbed by vegetation from bidirectional reflectance measurements. *Remote Sens. Environ.* 51, 375–384. doi:10.1016/0034-4257(94)00114-3

Schaub, J., Hunt, B. P. V., Pakhomov, E. A., Holmes, K., Lu, Y., and Quayle, L. (2018). Using unmanned aerial vehicles (UAVs) to measure jellyfish aggregations. *Mar. Ecol. Prog. Ser.* 591, 29–36. doi:10.3354/meps12414

Schroeder, S. B., Boyer, L., Juanes, F., and Costa, M. (2019a). Spatial and temporal persistence of nearshore kelp beds on the west coast of British Columbia, Canada using satellite remote sensing. *Remote Sens. Ecol. Conserv.* 6, 327–343. doi:10.1002/rse2.142

Schroeder, S. B., Dupont, C., Boyer, L., Juanes, F., and Costa, M. (2019b). Passive remote sensing technology for mapping bull kelp (Nereocystis luetkeana): a review of techniques and regional case study. *Glob. Ecol. Conserv.* 19, e00683. doi:10.1016/j.gecco.2019.e00683

Sokal, R. R., and Rohlf, F. J. (1981). Biometry. 2nd Edn. San Francisco, CA: Freeman and Company.

Stekoll, M. S., Deysher, L. E., and Hess, M. (2006). A remote sensing approach to estimating harvestable kelp biomass. *J. Appl. Phycol.* 18, 323–334. doi:10.1007/s10811-006-9029-7

Stekoll, M. S., Deysher, L. E., and Hess, M. (2007). Eighteenth international seaweed symposium. *Eighteenth Int. Seaweed Symp*. doi:10.1007/978-1-4020-5670-3

Taddia, Y., and Russo, P. (2019). *Multispectral UAV monitoring of submerged seaweed in shallow water*.

Thomsen, M. S., Mondardini, L., Alestra, T., Gerrity, S., Tait, L., South, P. M., et al. (2019). Local extinction of bull kelp (durvillaea spp). *Due to a Marine Heatwave*. 6, 1–10. doi:10.3389/fmars.2019.00084

Tucker, C. J. (1979). Red and photographic infrared linear combinations for monitoring vegetation. *Remote Sens. Environ.* 8, 127–150. doi:10.1016/0034-4257(79)90013-0

Whitehead, K., Hugenholtz, C. H., Myshak, S., Brown, O., LeClair, A., Tamminga, A., et al. (2014). Remote sensing of the environment with small unmanned aircraft

systems (UASs), part 2: scientific and commercial applications. *J. Unmanned Veh. Syst.* 02, 86–102. doi:10.1139/juvs-2014-0006

Whitehead, K., and Hugenholtz, C. H. (2014). Remote sensing of the environment with small unmanned aircraft systems (UASs), part 1: a review of progress and challenges. *J. Unmanned Veh. Syst.* 02, 69–85. doi:10.1139/juvs-2014-0006

Woebbecke, D. M., Meyer, G. E., Von Bargen, K., and Mortensen, D. A. (1995). Shape features for identifying young weeds using image analysis. *Trans. Am. Soc. Agric. Eng.* 38, 271–281. doi:10.13031/2013.27839

Xing, Q., and Hu, C. (2016). Mapping macroalgal blooms in the Yellow Sea and East China Sea using HJ-1 and Landsat data: application of a virtual baseline reflectance height technique. *Remote Sens. Environ.* 178, 113–126. doi:10.1016/j.rse.2016.02.065

Yang, Z., Willis, P., and Mueller, R. (2008). *Impact of band-ratio enhanced awifs image to crop classification accuracy*. Colorado, CO: Pecora Corporation.

Zerbe, L. M., and Liew, S. C. (2004). Reevaluating the traditional maximum NDVI compositing methodology: the normalized difference blue index. *Int. Geosci. Remote Sens. Symp.* 4, 2401–2404. doi:10.1109/igarss.2004.1369774

Zheng, G., Li, X., Member, S., Zhou, L., Yang, J., Ren, L., et al. (2018). Development of a gray-level Co-occurrence matrix-based texture orientation estimation method and its application in sea surface wind direction retrieval from SAR imagery. *IEEE Trans. Geosci. Rem. Sens.* 56, 5244–5260. doi:10.1109/TGRS.2018.2812778

Zimmerman, R. C., and Kremer, J. N. (1986). In situ growth and chemical composition of the giant kelp, Macrocystis pyrifera: response to temporal changes in ambient nutrient availability. *Marine Ecol. Prog. Ser.* 27 (3), 277–285. doi:10.3354/meps027277

Conflict of Interest: The authors declare that the research was conducted in the absence of any commercial or financial relationships that could be construed as a potential conflict of interest.

Copyright © 2021 Cavanaugh, Cavanaugh, Bell and Hockridge. This is an open-access article distributed under the terms of the Creative Commons Attribution License (CC BY). The use, distribution or reproduction in other forums is permitted, provided the original author(s) and the copyright owner(s) are credited and that the original publication in this journal is cited, in accordance with accepted academic practice. No use, distribution or reproduction is permitted which does not comply with these terms.

frontiers in Environmental Science

ORIGINAL RESEARCH
published: 10 March 2021
doi: 10.3389/fenvs.2021.587660

Potential for High Fidelity Global Mapping of Common Inland Water Quality Products at High Spatial and Temporal Resolutions Based on a Synthetic Data and Machine Learning Approach

Jeremy Kravitz[1,2]*, *Mark Matthews*[3], *Lisl Lain*[1], *Sarah Fawcett*[1] *and Stewart Bernard*[4]

[1]Department of Oceanography, University of Cape Town, Cape Town, South Africa, [2]Biospheric Science Branch, NASA Ames Research Center, Mountain View, CA, United States, [3]CyanoLakes (Pty) Ltd, Cape Town, South Africa, [4]Earth Systems Earth Observation Division, CSIR, Cape Town, South Africa

OPEN ACCESS

Edited by:
Sherry L Palacios,
California State University, Monterey Bay, United States

Reviewed by:
Hongtao Duan,
Nanjing Institute of Geography and Limnology (CAS), China
John Hedley,
Numerical Optics Ltd., United Kingdom

***Correspondence:**
Jeremy Kravitz
jeremy.kravitz@gmail.com

Specialty section:
This article was submitted to Environmental Informatics and Remote Sensing, a section of the journal Frontiers in Environmental Science

Received: 27 July 2020
Accepted: 18 January 2021
Published: 10 March 2021

Citation:
Kravitz J, Matthews M, Lain L, Fawcett S and Bernard S (2021) Potential for High Fidelity Global Mapping of Common Inland Water Quality Products at High Spatial and Temporal Resolutions Based on a Synthetic Data and Machine Learning Approach. Front. Environ. Sci. 9:587660. doi: 10.3389/fenvs.2021.587660

There is currently a scarcity of paired *in-situ* aquatic optical and biogeophysical data for productive inland waters, which critically hinders our capacity to develop and validate robust retrieval models for Earth Observation applications. This study aims to address this limitation through the development of a novel synthetic dataset of top-of-atmosphere and bottom-of-atmosphere reflectances, which is the first to encompass the immense natural optical variability present in inland waters. Novel aspects of the synthetic dataset include: 1) physics-based, two-layered, size- and type-specific phytoplankton inherent optical properties (IOPs) for mixed eukaryotic/cyanobacteria assemblages; 2) calculations of mixed assemblage chlorophyll-a (chl-a) fluorescence; 3) modeled phycocyanin concentration derived from assemblage-based phycocyanin absorption; 4) and paired sensor-specific top-of-atmosphere reflectances, including optically extreme cases and the contribution of green vegetation adjacency. The synthetic bottom-of-atmosphere reflectance spectra were compiled into 13 distinct optical water types similar to those discovered using *in-situ* data. Inspection showed similar relationships of concentrations and IOPs to those of natural waters. This dataset was used to calculate typical surviving water-leaving signal at top-of-atmosphere, and used to train and test four state-of-the-art machine learning architectures for multi-parameter retrieval and cross-sensor capability. Initial results provide reliable estimates of water quality parameters and IOPs over a highly dynamic range of water types, at various spectral and spatial sensor resolutions. The results of this work represent a significant leap forward in our capacity for routine, global monitoring of inland water quality.

Keywords: eutrophication, Earth observation, water quality, inland waters, machine learning, radiative transfer modeling, cyanobacteria, optics

INTRODUCTION

Widespread increase of lake phytoplankton blooms is causing global eutrophication to intensify (Ho et al., 2019). The substantial increase in eutrophication will potentially increase methane emissions from these systems by 30–90% over the next century, substantially contributing to global warming (Beaulieu et al., 2019). Recent advancements in sensor technology and algorithm development have allowed for improved measurements of coastal and inland waters (Hu, 2009; Matthews et al., 2012; Palmer et al., 2015b; Smith et al., 2018; Pahlevan et al., 2020). Given the increased attention placed on retrieving eutrophication metrics for inland water bodies, numerous studies have attempted radiometric retrieval of chlorophyll-a (chl-a) or phycocyanin (PC), the diagnostic pigment within cyanobacteria, with varying degrees of success (see reviews by Ogashawara, 2020; Odermatt et al., 2012; Blondeau-Patissier et al., 2014; Matthews, 2011; Gholizadeh et al., 2016). Retrieval of chl-a concentration has been significantly developed, and is generally more robust for trophic delineation; however, PC is highly specific to cyanobacteria and is thus a better indicator of potential water toxicity (Stumpf et al., 2016). Given the fine-scale horizontal and vertical heterogeneity of productive waters (Kutser, 2004; Kutser et al., 2008; Kravitz et al., 2020) and lack of standardization of field methods, laboratory procedures, and analysis for mixed freshwater phytoplankton assemblages, it is difficult to conduct high impact optical sensitivity studies. Consequently, trustworthy *in-situ* data for productive coastal and inland waters is limited compared to combined global datasets for ocean calibration and validation, which critically hinders our capacity to execute global baseline studies, as well as to identify global trends using archival imagery. It is therefore imperative that we develop suitable algorithms for optical constituent retrieval for current and planned missions, with a full understanding of the associated uncertainties and limitations.

Machine learning (ML) and deep learning (DL) approaches are quickly becoming recognized as state-of-the-art for classification and regression type problems, and remote sensing is ideally suited to such approaches (Ma et al., 2019, and references therein). The majority of ML and DL development and application have been within the terrestrial remote sensing community (Ball et al., 2017; Li et al., 2018; Maxwell et al., 2018; Ghorbanzadeh et al., 2019), although recent research reveals the benefit of ML and DL approaches for aquatic purposes (Pahlevan et al., 2020; Balasubramanian et al., 2020; Watanabe et al., 2020; Sagan et al., 2020; Peterson et al., 2020; Hafeez et al., 2019; Ruescas et al., 2018). While these studies generally found better performance of ML and DL approaches over traditional empirical or semi-analytical methods, most note that the advanced models were trained on too few datapoints, and would greatly benefit from expanded datasets. DL architectures in particular substantially benefit from greater volumes of high-quality training data. Vastly more coincident reflectance—biophysical parameter pairs, PC in particular, are required to train new and improved multi-parameter inversions for synoptic image analysis at global scales.

Radiative transfer modeling (RTM) has proven instrumental to furthering our understanding of coastal aquatic optical relationships in the form of numerous parameterized case studies (Dall'Olmo and Gitelson, 2005; Dall'Olmo and Gitelson, 2006; Gilerson et al., 2007; Gilerson et al., 2008; Lain et al., 2014; Lain et al., 2016; Evers-King et al., 2014). Few, however, have expanded these analyses to cyanobacteria dominated inland waters (Kutser, 2004; Metsamma et al., 2006; Matthews and Bernard, 2013; Kutser et al., 2006). RTM has proved advantageous for the development of large synthetic datasets to address the scarcity of valid *in-situ* data available to train neural network (NN) retrieval models (Doerffer and Schiller, 2008; Arabi et al., 2016; Brockmann et al., 2016; Fan et al., 2017; Hieronymi et al., 2017). While a few of these algorithms such as the Case 2 Extreme OLCI Neural Network Swarm (ONNS, Hieronymi et al., 2017) and Case 2 Regional Coast Color (C2RCC, Brockmann et al., 2016) include samples for extremely absorbing and scattering cases due to global instances of elevated colored dissolved organic matter (CDOM) and non-algal particles (NAP), the phytoplankton component of these models is not optimized for adequate pigment retrieval in optically complex eutrophic inland water (Palmer et al., 2015a; Kutser et al., 2018; Kravitz et al., 2020).

The fundamental building blocks of aquatic RTM rely on accurate parameterization of the inherent optical properties (IOPs; i.e., absorption and scattering properties) of all light altering constituents in a volume of water. Fan et al. (2017) and C2RCC utilize chlorophyll-specific phytoplankton absorption (a^*_{phy}) measurements directly from the NASA bio-Optical Marine Algorithm Dataset (NOMAD), while ONNS uses five a^*_{phy} shapes derived from cluster and derivative analysis of various phytoplankton cultures (Xi et al., 2015). These studies rely heavily on phytoplankton absorption characteristics as the main driver for resulting functional type and biomass related differences in modeled reflectances. Such an assumption is generally adequate for oligotrophic to mesotrophic water conditions, whereas the absence of a wavelength dependent, phytoplankton-specific backscattering term, or the use of backscattering relating only to gross particulate, is too simplistic for eutrophic conditions and generally underperforms in more productive waters (Lain et al., 2014; Lain et al., 2016). The scattering phase function, critical for fully realizing the underwater light field, is generally approximated as a simple functional form for mathematical simplicity (Mobley et al., 2002) or derived from Mie theory, which over-generalizes phytoplankton particles as spherical homogenous structures. Indeed, some studies that characterized the backscattering properties of various monospecific cultures have found a prominent deviation from the homogenous sphere model, which yields a poor simplification of the complex cellular structures found in bloom-forming phytoplankton (Quirantes and Bernard, 2004; Vaillancourt et al., 2004; Whitmire et al., 2007; Zhou et al., 2012; Matthews and Bernard, 2013). This is particularly important for productive inland waters where blooms of potentially toxic cyanobacteria are becoming more prevalent. Cyanobacteria, *Mycrocystis aeruginosa* especially, appear to be extremely efficient backscatterers (Zhou

et al., 2012), which has been attributed to their internal gas vacuoles (Matthews and Bernard, 2013). Due to strong effects of gas vacuoles on attenuation, rather than absorption, drastic differences in water-leaving reflectance occur in mixed cyanobacteria assemblages. Thus, vacuolate induced spectral scattering (Ganf et al., 1989; Walsby et al., 1995) cannot be overlooked when parameterizing RTMs for inland water application. To address these over-simplifications, the Equivalent Algal Populations (EAP) model provides an alternative assemblage-based particle modeling approach, simulating phytoplankton IOPs derived from differences in cell and assemblage size distributions, dominant pigmentation, cell composition, and ultrastructure (Bernard et al., 2009; Lain et al., 2014).

While Pahlevan et al. (2020) and Balasubramanian et al. (2020) present highly convincing results for the transition to ML based models for aquatic particle retrievals using multi-spectral sensors, the authors note that adequate atmospheric correction (AC) of top of atmosphere (TOA) radiances to bottom of atmosphere (BOA) reflectances remains one of the largest hurdles to robust, operational space-based water quality retrievals. Baseline type algorithms, which have proven to be robust estimators of trophic status, and relatively insensitive to poor AC, have been utilized on partially corrected bottom-of-Rayleigh reflectance (BRR) in an attempt to bypass the requirement for a full AC (Binding et al., 2011; Matthews et al., 2012; Palmer et al., 2015c). This approach is indeed helpful for smaller water bodies where AC-induced uncertainty remains very high (Kravitz et al., 2020). Thus, it follows that ML type models should also perform adequately when utilized on TOA data for inland water pixels. However, relatively few studies have quantified the actual fraction of the isolated water-leaving signal that reaches the satellite sensor over productive inland water bodies. Utilizing TOA data is theoretically more feasible for turbid waters due to the elevated water signal from increased particulate backscattering compared to "darker" oligotrophic waters, which are dominated by water absorption. It is quite often cited that of the total radiance signal reaching a satellite over water, roughly 10% is due to the upwelling water-leaving radiance (L_w), with atmospheric aerosols and molecular (Rayleigh) scattering contributing the majority of the signal. However, in a localized modeling study, Martins et al. (2017) found that L_w had the potential to reach ~43% of the total signal for red-edge bands of Sentinel-2 MSI over turbid lakes in the Amazon. It is important to understand the extent of the water signal at TOA and its sensitivity to certain water and atmospheric parameters in order to more thoroughly evaluate models that use TOA data.

Here, we aim to explore the potential for developing quick, robust multi-parameter aquatic retrieval models for both multi-spectral and hyper-spectral sensor specifications using a combined synthetic data and ML approach for productive inland waters. Our goal is to begin to simulate the immense natural optical variability of inland waters and to address the issues described above. Novel aspects of the synthetic dataset presented here include: 1) physics-based, two-layered, size and type specific phytoplankton IOPs for mixed eukaryotic/cyanobacteria assemblages, 2) calculations of mixed assemblage chl-a fluorescence, 3) modeled PC concentration, 4) and paired sensor-specific TOA reflectances, which include optically extreme cases and contribution of green vegetation adjacency. Below, we first describe the parameterization of RTM, followed by an examination of typical survived L_w signal at TOA, a description and assessment of state-of-the-art ML retrieval models, and application to multi-spectral imagery with a semi-quantitative validation against *in-situ* data.

PARAMETERIZATION OF RADIATIVE TRANSFER MODEL

Aquatic RTM

For consistency with natural optical relationships, the IOPs of four datasets were compiled based on the domination of a particular optical constituent. The EcoLight RTM was then used to derive water-leaving reflectances from the IOP builds. The first dataset is modeled as typical Case 1 waters where water and phytoplankton provide the bulk of the optical signal and represent oligotrophic conditions. The bio-optical model in this dataset closely follows that of Lee (2003), wherein other optical constituents co-vary with phytoplankton biomass. The other three datasets resemble cyanobacteria dominated inland waters, CDOM dominated waters, and inorganic sediment dominated waters where more complex optical relationships persist and optical constituents do not tend to co-vary (Brewin et al., 2017). A four-component bio-optical model was used to generate the IOPs of these hypothetical inland water cases to be used in the EcoLight RTM (Lee, 2006; Gilerson et al., 2007):

$$a(\lambda) = a_w(\lambda) + a_g(\lambda) + a_{phy}(\lambda) + a_{nap}(\lambda) \quad (1)$$

where $a_w(\lambda)$, $a_g(\lambda)$, $a_{phy}(\lambda)$, and $a_{nap}(\lambda)$ represent the spectral absorptions of water, a combined CDOM/detritus term, phytoplankton, and non-algal particles (NAP), respectively (refer to **Supplementary Appendix A, Table A1**, for a full list of definitions of symbols and units used throughout this manuscript). Except for the Case 1 dataset, which is defined solely on chlorophyll-a concentration (C_{chl}) and relationships governing the co-variation of other constituents with C_{chl}, the three other datasets are defined by independent values of C_{chl}, the concentration of nonalgal particles (C_{nap}), and the absorption of CDOM at 440 nm ($a_g(440)$). Great care was taken to ensure that constituent ranges were appropriate and based on natural populations from the LIMNADES *in-situ* inland water dataset (Spyrakos et al., 2018). A table of mode values and standard deviations used for the lognormal distributions within each dataset can be found in **Supplementary Appendix A, Table A3**. To generate synthetic datasets representative of natural waters, values of all constituents were randomly selected from the described lognormal distributions. Derivation and equations used in modeling components other than phytoplankton are common to studies that have parameterized models for Case 2 waters (Bukata, 1995; Twardowski et al., 2001; Gilerson et al., 2007) and can also be found in **Supplementary Appendix A, Table A2**.

Phytoplankton Component

The total spectral phytoplankton component in **Eq. 1** is modeled as a product of C_{chl} and the specific chlorophyll absorption spectrum.

$$a_{phy}(\lambda) = C_{chl} * a^*_{chl}(\lambda) \quad (2)$$

where $a^*_{chl}(\lambda)$ is the spectral specific chlorophyll absorption spectrum in m^2/mg. Phytoplankton specific IOPs (SIOPs) for this work are based on the physics-based two-layered spherical Equivalent Algal Population (EAP) model, where population-specific refractive indices are used to derive IOPs (Bernard et al., 2009; Lain and Bernard, 2018). The two-layered spherical geometry consists of a core sphere, acting as the cytoplasm, and a shell sphere acting as the chloroplast. The EAP model calculates, from first principles, biophysically-linked phytoplankton absorption and scattering characteristics from particle refractive indices reflecting the primary light-harvesting pigments of various phytoplankton groups (Lain et al., 2014; Lain and Bernard, 2018). IOPs are calculated at 5 nm spectral resolution between 200 and 900 nm and integrated over an entire equivalent size distribution represented by effective diameters (D_{eff}) between 1 and 50 μm (Bernard et al., 2007; Lain et al., 2016). For a hypothetical eukaryotic population, refractive indices are derived from blooms in the Benguela upwelling off southern Africa, which is typically dominated by chlorophyll-a (chl-a) and the carotenoid pigments, fucoxanthin and peridinin, which are the main light harvesting pigments in diatoms and dinoflagellates, respectively. Because there are minimal differences within carotenoid pigment refractive indices and absorption, these two groups were combined into a generalized set of chl-a—carotenoid IOPs (Bernard et al., 2009; Organelli et al., 2017). The EAP model has been consistently validated and is considered an accurate phytoplankton model for coastal and inland waters (Evers-King et al., 2014; Mathews and Bernard, 2013; Lain et al., 2016; Smith et al., 2018).

The EAP two-layered sphere model has also been used to derive IOPs for the optically complex cyanobacteria *M. aeruginosa* (Matthews and Bernard, 2013). In this instance, the core layer is assigned to a highly scattering vacuole, while the shell layer acts as the chromatoplasm. *M. aeruginosa* is modeled with a D_{eff} of 5 μm for consistency with natural populations. For derivation of the complex refractive indices, influence of gas vacuolation, and tuning of the two-layered model for cyanobacteria, see Matthews and Bernard (2013). IOPs for the cyanobacteria *Aphanizomenon, Anabaena cirinalis* and non-vacuolate *Nodularia spumigena*, which were measured in the laboratory, are also included in the dataset (Kutser et al., 2006). The final phytoplankton SIOPs used in the RTM can be found in **Supplementary Appendix A, Figure A1**.

To account for optical variation due to mixed populations, the $a^*_{chl}(\lambda)$ term in **Eq. 2** is modeled as an admixture of eukaryotic and cyanobacteria SIOPs based on a series of weighting factors. Total $a^*_{chl}(\lambda)$ is therefore calculated as the sum of the cyanobacteria and eukaryotic populations:

$$a^*_{chl}(\lambda) = S_f\left(a^*_{cy}(\lambda)\right) + \left(1 - S_f\right)\left(a^*_{euk}(\lambda)\right) \quad (3)$$

where S_f = [0.1,0.2,0.3,0.4,0.5,0.6,0.7,0.8,0.9,1.0], a^*_{cy} is the chlorophyll-specific absorption of the cyanobacteria population and a^*_{euk} is the chlorophyll-specific absorption for the carotenoid containing eukaryotic population. Total scattering and backscattering coefficients of the phytoplankton component ($b_{phy}(\lambda)$ and $b_{bphy}(\lambda)$, respectively) are calculated in a similar manner using EAP derived spectral chlorophyll-specific scattering and backscattering terms (**Supplementary Appendix A**).

The admixture weighting factor and input D_{eff} for the eukaryotic population were also randomly varied for the RTM, albeit with some constraints. Several studies have shown that for natural populations of oligotrophic to mesotrophic waters, a^*_{euk} tends to decrease with increasing C_{chl} (Bricaud et al., 1995; Babin et al., 1996). This rule is not as strict in more complex inland and coastal waters, but rough relationships have been observed (Matthews and Bernard, 2013). Due to the nature of the EAP model, the magnitudes of the resulting SIOPs are highly dependent on the particle size. To generalize this natural relationship in our RTM, input phytoplankton SIOPs of the carotenoid containing population were constrained by D_{eff} as: $5 < D_{eff} < 20$ μm for $0 < C_{chl} < 20$ mg/m^3, $15 < D_{eff} < 35$ μm for $20 < C_{chl} < 50$ mg/m^3, and $30 < D_{eff} < 45$ μm for $C_{chl} > 50$ mg/m^3.

Ranges for appropriate cyanobacteria admixture weighting must also be comparable to natural variations as a function of phytoplankton biomass. Randomization of weighting factors was constrained based on *in-situ* phytoplankton abundance and biomass collected from South African inland waters between 2016 and 2018 (Kravitz et al., 2020). For a comparison of the fraction of cyanobacteria abundance as a function of chl-a concentration for both field data and ranges used in the RTM, see **Supplementary Figure S1**. Given the field data, it was assumed that if cyanobacteria are part of the phytoplankton population, they will tend to dominate at higher biomass (i.e., it is rare to find low fractions of cyanobacteria as C_{chl} rises to extremely hypertrophic levels, if cyanobacteria are present). *M. aeruginosa* is known to produce extremely high biomass blooms, with the potential to form floating scum mats that can reach C_{chl} upwards of 20,000 mg/m^3 (Matthews and Bernard, 2013). Extremely hypertrophic cases are reflected in the RTM. For C_{chl} greater than 500 mg/m^3, only *M. aeruginosa* is included as there are no data showing blooms of such an extent for other species.

Chl-a Fluorescence

Chl-a fluorescence is potentially an important source of information regarding phytoplankton physiology, size, and/or identification (Greene et al., 1992; Behrenfeld et al., 2009), although to what extent remains uncertain. While an integral component of phytoplankton physiology, fluorescence is often omitted from RTMs [as in the case of Hieronymi et al. (2017) and Fan et al. (2017)] or is modeled as a simplistic Gaussian term centered at 685 nm with a full width half max (FWHM) of 25 nm (Gilerson et al., 2007; Huot et al., 2007). The magnitude of the depth-integrated radiance contribution by chl-a fluorescence at 685 nm has traditionally been calculated as in **Eq. 4** (Huot et al.,

2005; Huot et al., 2007; refer to **Supplementary Appendix A** for definitions of symbols and units).

$$L_f(685) = 0.54 L_f^-(685) = 0.54 \frac{1\varnothing_f}{4\pi C_f} Q_a^*[Chl] \int_{400}^{700} \frac{a_{chl}^*(\lambda) E_o^-(\lambda)}{K(\lambda) + K_{Lu}(685)} d\lambda \quad (4)$$

This modeling approach is an oversimplification for natural coastal and cyanobacteria dominated waters. The approach above assumes a purely eukaryotic, photosynthetic carotenoid-containing phytoplankton assemblage. In other words, it assumes that the modeled population contains all intracellular chl-a in the fluorescing photosystem II (PSII). Emission spectra of chl-a are a response to photosynthetic pigments that harvest light in PSII. However, cyanobacteria generally contain only 10–20% of their total cellular chl-a in PSII, with no accessory chlorophylls or carotenoids, and with the remaining cellular chl-a located in non-fluorescing photosystem I (PSI) (Johnsen and Sakshaug, 2007; Simis et al., 2012). A second oversimplification pertains to the shape of the modeled Gaussian fluorescence emission. In reality, while chl-a fluorescence does indeed have a major fluorescence emission around 685 nm, it also has an adjacent vibrational satellite emission centered around 730–740 nm (Govindjee, 2004 and references therein; Lu et al., 2016). Although generally smaller in amplitude due to increased absorption from water farther into the near-infrared (NIR), this 730–740 nm fluorescence emission can potentially contribute to the water leaving radiance. **Supplementary Appendix B.1** details an updated mathematical derivation for the shape and magnitude of the chl-a fluorescence signal associated with mixed algal populations, which takes into account differences in PSII physiology for cyanobacteria and eukaryotic populations. Equations B1, B2, and B3 were applied to every synthetic spectra to calculate, and add, the modeled chl-a fluorescence spectrum.

Phycocyanin Concentration

While the EcoLight radiative transfer code allows C_{chl} to be defined as an input to the model, C_{pc} must be modeled independently. The calculation of C_{pc} can be accomplished as follows (Simis et al., 2005):

$$\text{Cpc} = a_{pc}(620) / a_{pc}^*(620) \quad (5)$$

where $a_{pc}(620)$ is the total absorption due to PC at 620 nm and $a_{pc}^*(620)$ is the specific absorption coefficient of PC at 620 nm. The $a_{pc}(620)$ term must be corrected for the absorption of all other optical constituents and pigments at 620 nm. Most existing methods only correct for absorption at 620 nm due to chl-a and not due other accessory pigments; thus, studies suggest that at low PC concentrations (<50 mg/m^3), estimated $a_{pc}(620)$ is not fully corrected for other pigment or constituent absorptions, resulting in overestimated C_{pc} (Simis et al., 2007; Yacobi et al., 2015). The mathematical logic for removal of the absorption due to chl-a and its accessory pigments, chl-b and chl-c, is further detailed in **Supplementary Appendix B.2**.

While the source of variability of $a_{pc}^*(620)$ in nature is still not entirely clear, we can assume that first order variation can result from variable algal/cyanobacteria composition and biomass effects. Thus, varying $a_{pc}^*(620)$ based on cyanobacteria dominance according to the admixture for each sample is a reasonable approach. Previous studies have generally relied on a fixed $a_{pc}^*(620)$ value for PC estimation models. Considering that $a_{pc}^*(620)$ has the potential to vary by a factor of 60 in nature (see Table 4 in Yacobi et al., 2015), holding it constant is a major oversimplification, especially for lower C_{pc} or for cases when cyanobacteria is not the dominant species. In particular, using an invariant $a_{pc}^*(620)$ can result in a dramatic increase in error of PC retrieval when PC:chl-a < 0.5 (Simis et al., 2005; Randolph et al., 2008; Hunter et al., 2010; Li et al., 2015; Yacobi et al., 2015) or when C_{pc} < 50 mg/m^3 (Simis et al., 2005; Ruiz-Verdu et al., 2008; Yacobi et al., 2015). By employing a model that allows $a_{pc}^*(620)$ to vary based on cyanobacteria dominance, more appropriate values of $a_{pc}^*(620)$ can be applied to situations of lower PC concentration. Given the consensus that a PC:chl-a ratio ≥0.5 (mg/m^3) implies a cyanobacteria dominant water target (Simis et al., 2005; Hunter et al., 2010; Yacobi et al., 2015), our admixture of 0–1 was scaled to a PC:chl-a between 0 and 4, where an admixture of 0.6 (60% dominance by cyanobacteria in population) is equal to a PC:chl-a of 0.5. A strong non-linear relationship was found between PC:chla-a and $a_{pc}^*(620)$ using *in-situ* data (**Figures 1A,B**), and is used in conjunction with each sample's scaled admixture parameter to define a sample specific $a_{pc}^*(620)$ as:

$$a_{pc}^*(620) = 0.0093 (S_{ad})^{-0.717} \quad (6)$$

where S_{ad} is the scaled admixture parameter. Once both $a_{pc}(620)$ and $a_{pc}^*(620)$ are known, **Eq. 5** can be used to calculate a final PC concentration.

Modeled values for $a_{pc}^*(620)$ using this methodology resulted in a mean and median $a_{pc}^*(620)$ of 0.013 ± 0.017 and 0.0041, respectively. Simis et al. (2005) used an average value of 0.0095 m^2 (mg PC)$^{-1}$ calculated from their *in-situ* data while Matthews and Bernard (2013) found the mean $a_{pc}^*(620)$ of various inland water bodies to range between 0.0072 and 0.0122. Yacobi et al. (2015) found that with C_{pc} > 10 mg/m^3, $a_{pc}^*(620)$ tended to converge on 0.007 m^2 (mg PC)$^{-1}$, but noted that this value is potentially too high. Other studies suggest $a_{pc}^*(620)$ values between 0.004 and 0.005 m^2 (mg PC)$^{-1}$ (Li et al., 2015; Mishra et al., 2013; Simis and Kauko, 2012; Jupp et al., 1994). These values are more similar to our modeled absorption ranges, indicating that our calculated $a_{pc}^*(620)$ are reasonable (**Figure 1**). At modeled PC concentrations >50 mg/m^3, mean and median $a_{pc}^*(620)$ stabilized at 0.0042 ± 0.002 and 0.0034, respectively. The majority of variability in modeled $a_{pc}^*(620)$ occurred at a PC:chl-a < 0.5 or a C_{pc} < 50 mg/m^3, consistent with previous findings (Mishra et al., 2013; Yacobi et al., 2015). The resulting PC:chl-a of the modeled synthetic data ranged between 0 and 4 mg/m^3.

Atmospheric RTM Parameterization

The MODTRAN 5.0 radiative transfer software was used to propagate both L_w and R_{rs} from the aquatic modeling to OLCI

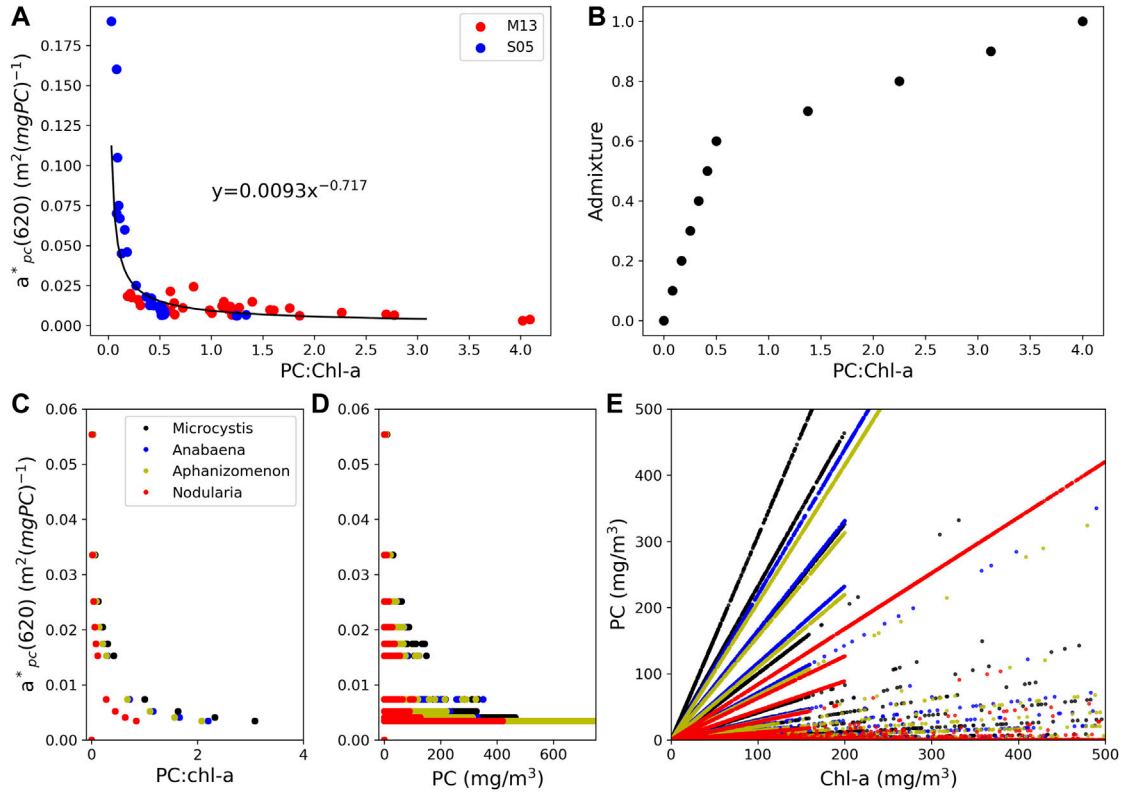

FIGURE 1 | (A) $a^*_{pc}(620)$ plotted as a function of PC:chl-a from Matthews and Bernard (2013) and Simis et al. (2005), denoted as M13 and S05, with best fit line in black, **(B)** Visual of admixture scaling, where an admixture of 0.6 (60% dominance by cyanobacteria in population) is equal to a PC:chl-a of 0.5, **(C)** $a^*_{pc}(620)$ for four cyanobacteria groups plotted as a function of PC:chl-a for modeled synthetic data, **(D)** $a^*_{pc}(620)$ plotted as a function of PC concentration, **(E)** PC plotted as function of chl-a concentration.

at-sensor radiances. The radiance received by an optical sensor can be defined in simple terms following Bulgarelli et al. (2014) as:

$$L_{tot} = L_{path} + L_{BG} + tL_u \quad (7)$$

where L_{tot} is the total radiance received by the sensor, L_{path} is the path radiance, which defines the photons scattered into the instantaneous field of view (FOV) by the atmosphere alone, L_{BG} is the background radiance from neighboring pixels, which are diffusely scattered into the sensor FOV, L_u is the combined sky reflected and water leaving radiance at the sensor, and t is the diffuse transmittance. L_{BG} is considered as the radiance introduced due to the adjacency effect (AE), which can lead to large errors in derived products if inter-pixel non-uniformity is very large as in the case for neighboring vegetation, sand, or snow (Bulgarelli et al., 2017). Optical properties for a hypothetical atmospheric column for defining the RTM were compiled from level-2 (L2) derived products from the global Aerosol Robotic Network (AERONET) database (https://aeronet.gsfc.nasa.gov/). The parameters that were directly varied for the RTM included aerosol optical thickness at 550 nm (AOT550), the angstrom extinction coefficient (Ext), single scattering albedo (SSA), the altitude of the hypothetical water target (Alt), water vapor (H_2O), and percent adjacency of green grass vegetation (Adj). A tropospheric canned model was used to define the initial Mie-generated phase functions and asymmetry parameter, while Ext, SSA, and AOT550 were used to tweak the model based on randomly selected values from the L2 AERONET database. The ranges for these parameters are evident in **Supplementary Figure S3**. For each aquatic R_{rs} measurement, two random atmospheres were modeled, and for each atmosphere, a second identical run was performed with a random contribution of green grass adjacency between 0.5 and 50%, totaling four atmospheric radiative transfer runs per R_{rs} measurement. Spectral radiance reaching the satellite sensor was calculated as follows:

1. The weighted mean of mixed spectral albedo curves was computed based on the Adj parameter.
2. The atmospheric model was compiled in MODTRAN by tweaking the standard tropospheric canned model using randomly selected parameters (AOT550, SSA, H_2O, Ext, Alt, Adj).
3. L_u and L_w from Ecolight output were multiplied by atmospheric path transmittance (t) from MODTRAN output to obtain L_u and L_w at TOA (L_uTOA and L_wTOA, respectively).
4. Total radiance at TOA (L_{tot}TOA) was calculated by adding L_uTOA to the MODTRAN derived atmospheric L_{path}, which is the radiance contribution from a scattering atmosphere.
5. All computations up to this point were performed at full MODTRAN 5 spectral resolution. The sensor specific

spectral response functions (SRFs) were then applied to compute channel radiances.
6. Fraction of surviving L_w reaching the satellite sensor was calculated as $L_wTOA/L_{tot}TOA$.

Radiance at TOA was converted to reflectance using an analytical derivation as in Hu et al. (2004):

$$\rho_t = \pi L_t^* / (F_0 cos\theta_0) \quad (8)$$

where ρ_t is sensor reflectance at TOA, L_t^* is the calibrated at-sensor radiance after adjustment for ozone and gaseous absorption, F_0 is the extraterrestrial solar irradiance, and θ_0 is the solar zenith angle. Adjustment for ozone and molecular species profiles are inherent to the MODTRAN RTM based on the specified atmospheric model used (Tropical, Mid-Latitude Summer, or Mid-Latitude Winter).

DATA PREPARATION AND TRAINING

Data Smoothing and Clustering

Roughly 70,000 R_{rs} spectra were modeled with coincident C_{chl}, C_{pc}, C_{nap}, and associated IOPs. A clustering procedure was undertaken to identify distinct optical clusters with respect to reflectance within the dataset. Clustering of water types on the basis of optical properties has been commonly employed since the 1970s as a method to direct the application of Earth observation (EO) for aquatic purposes (Moore et al., 2001; Moore et al., 2009; Moore et al., 2014; Vantrepotte et al., 2012; Spyrakos et al., 2018). Clustering of optical data has historically been beneficial for demonstrating underlying bio-optical relationships and variability, and guiding the development and application of retrieval models. For consistency with previous clustering applications in coastal and inland waters, the functional data analysis (FDA) approach of Spyrakos et al. (2018) was closely followed, although only briefly discussed here. A full analysis of historical clustering techniques is beyond the scope of this paper, and readers are directed to Spyrakos et al. (2018 and references therein) for a more comprehensive overview of clustering approaches. A comprehensive guide to FDA can also be found in Ramsay and Silverman (2006).

Prior to clustering, all R_{rs} spectra were normalized by their respective integrals, as a way to standardize amplitude variation attributed to concentrations of optically active constituents. Each spectrum was deconvolved into 26 cubic basis functions, of which a linear combination results in a smoothed R_{rs} spectra (**Supplementary Figure S4**). The same *B*-spline representation was used here as in Spyrakos et al. (2018), with the inclusion of one extra knot in the 800–900 nm region. The actual clustering by *k*-means was then performed on the 26 basis coefficients from the cubic functions. This acts as a method of dimensional reduction that removes excessive local variability, keeps independence among variables, and allows for a customizable smoothing approach through number and placement of knots. *k*-means was used to cluster the dataset of basis coefficients into 13 distinct clusters. Information on how the number of clusters was chosen can be found in **Supplementary Material**. Median curves were defined by band depth, a metric determining the centrality of each curve to the cluster, and are presented in **Figure 2** along with ranges of C_{chl}, C_{pc}, a_{nap} (440), a_g (440), and PC:chl-a. We note that the aim of this paper was not necessarily to determine the most optimal set of optical water types (OWTs) for inland waters. Rather, the clustering analysis was used to demonstrate that RTM can be used to produce OWTs representative of those observed in nature.

The 13 clusters were then condensed into seven manually defined OWTs with ecological relevance. Median R_{rs} spectra of the seven OWTs are shown in **Figure 3**, where "Mild" represents low to medium biomass mixed blooms (C2, C5, C11), "NAP" represents waters with relatively high non-algal particle loads (C1, C12), "CDOM" represents waters with relatively high CDOM absorption (C8, C13), "Euk" represents eukaryotic algal blooms (C7), "Cy" represents cyanobacteria blooms (C6, C9), "Scum" represents Microcystis floating scum conditions (C3), and "Oligo" represents oligotrophic to slightly mesotrophic waters (C4, C10). The resulting median R_{rs} spectra from each manually defined OWT are shown in **Figure 4** and match exceptionally well with *in-situ* water types in Kravitz et al. (2020; their **Figure 4**) for productive South African waters.

Machine Learning Models

K-Nearest Neighbors

The K-nearest neighbor (KNN) algorithm (Altman, 1992) is a non-parametric, lazy learning model, that can be used for regression (KNR) and classification (KNC). The model is "lazy" in that all training data are used in the testing phase. This allows for faster training times, but slower and costlier testing and prediction. The core of the KNN model is based on identifying similarity between datapoints, which is done by calculating distance or proximity of all points to each other, and assuming similar datapoints are close to each other. The model is tuned by choosing the optimal number for K, which defines the number of training samples closest in distance to the new point, followed by a value prediction. How distance between points is calculated can also be defined. KNN has become popular for its simplicity and fast training with minimal tuning; however, predictions take much longer with increasing training data or number of features.

Random Forest

The random forest (RF) algorithm (Ho, 1998; Breiman, 2001) is an extension of the decision tree model, which, in simple terms, constructs a series of yes/no questions about the data until an answer is reached and can be used for classification (RFC) or regression (RFR). RF is an ensemble method that builds tens to thousands of decision trees based on random sampling of training subsets and features, and averages (or majority voting for classification) all the results for a final product. There are a number of tunable hyperparameters that generally differ in how the questions are formed and define the depth of the trees. Training can be computationally expensive with extremely large datasets; however, prediction is much faster than can be achieved using KNN.

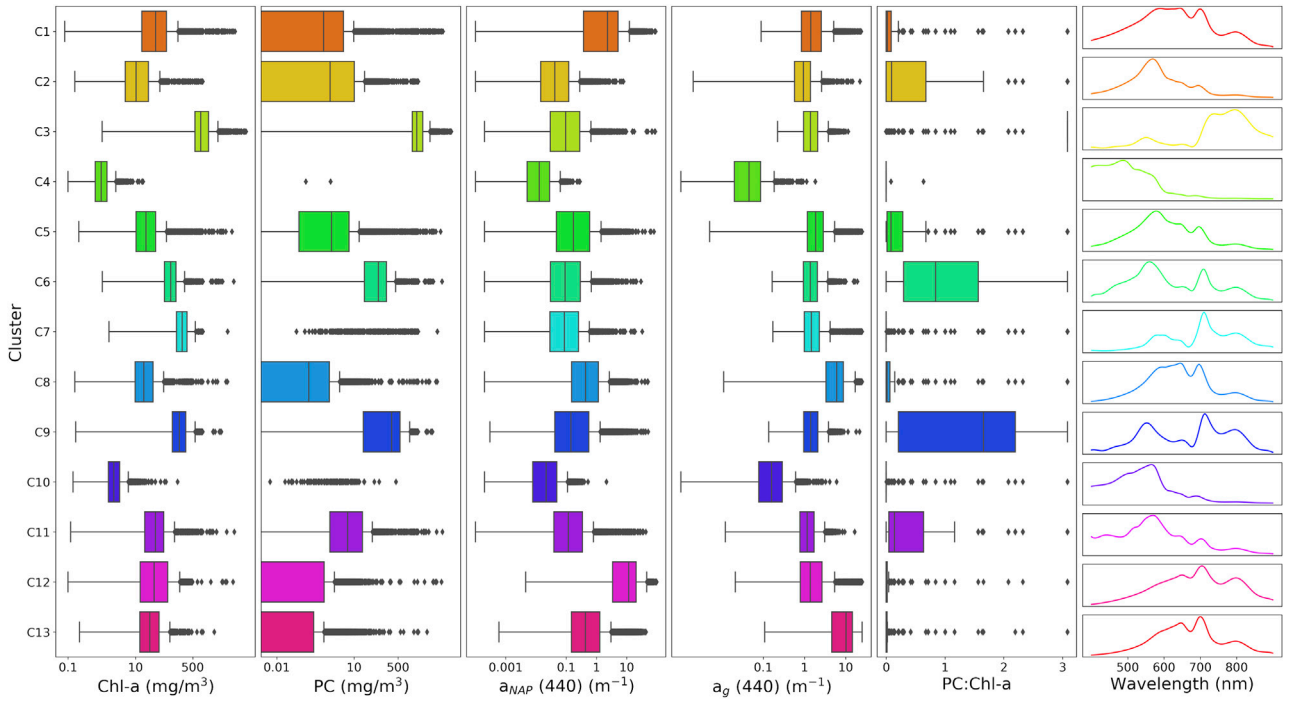

FIGURE 2 | Ranges of C_{chl}, C_{pc}, a_{nap} (440), a_g (440), and PC:chl-a for each defined synthetic cluster along with median R_{rs} spectra. Additional IOP ranges can be found in **Supplementary Material**.

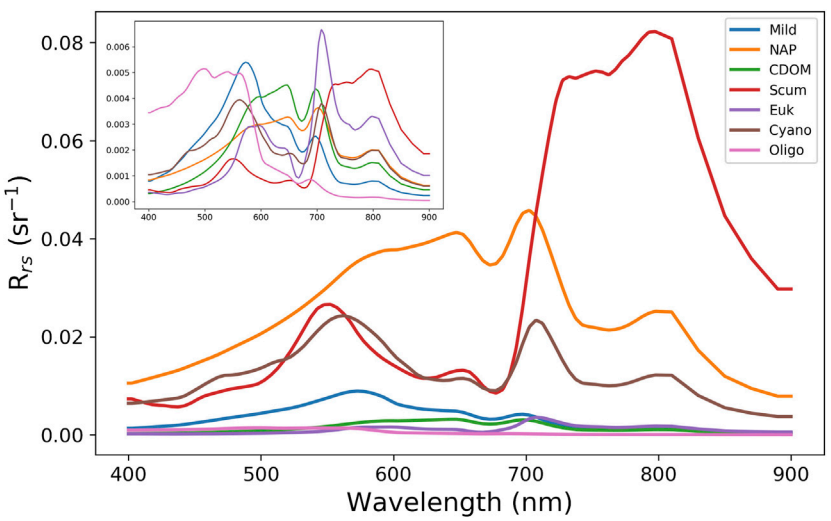

FIGURE 3 | Median R_{rs} spectra of the seven manually defined OWTs derived from the set of 13 clusters. The inset shows the same spectra on a standardized scale, achieved by removing the mean and scaling to unit variance in order to better show shape variation.

XGBoost

The extreme gradient boosting (XGBoost) framework (Chen and Guestrin, 2016) advances the RF model by including gradient boosted decision trees. This ensemble method builds new, weak models sequentially by minimizing errors from previous models and increasing the influence of higher performing models (boosting), until no further model improvements can be made. Gradient boosting then uses the gradient descent algorithm to minimize the loss when adding new models. XGBoost runs exceptionally well on tabulated data for classification or regression purposes and has dominated data science competitions in recent years due to its efficiency and power.

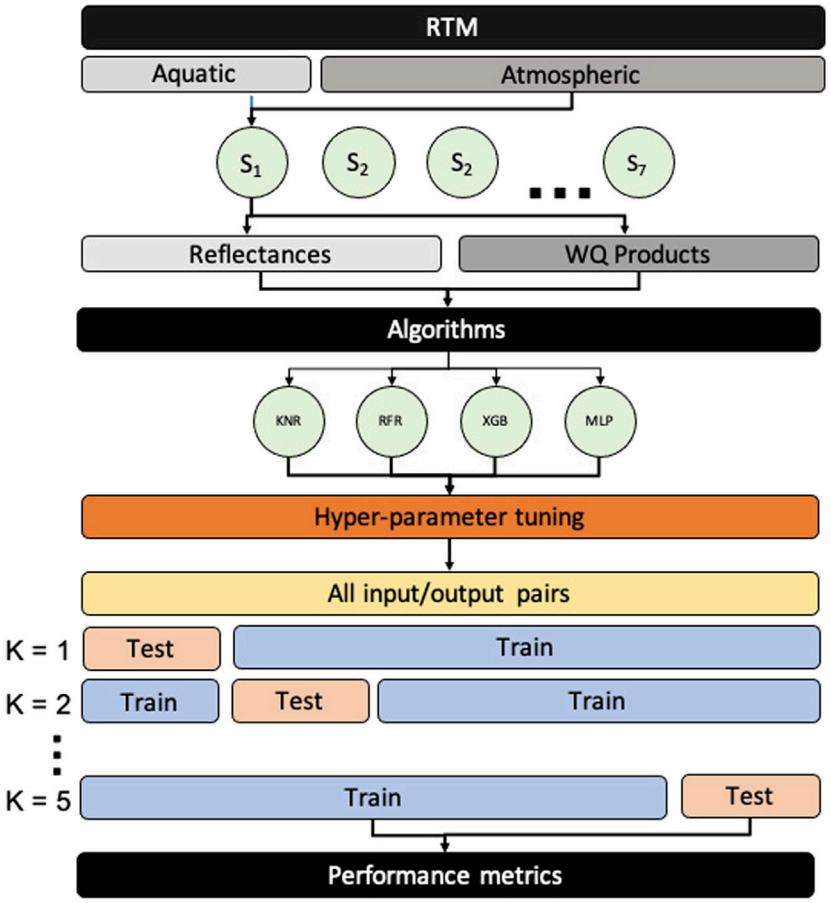

FIGURE 4 | A technical flowchart showing the summarized data development and training stages of ML algorithms to retrieve water quality products ("WQ Products"). S_x indicates one of the seven band configurations used in data preparation. K represents the specific iteration of k-fold cross validation.

Multi-Layer Perceptron

The multi-layer perceptron (MLP) is a type of classical artificial neural network (ANN) that is capable of learning any non-linear mapping function and can be thought of as a universal approximation algorithm. The fundamental units of MLPs are artificial neurons, each with their own weighting and activation functions. The activation function maps the summed weighted inputs to the output of the neuron. Individual neurons can be merged into networks of neurons, generally in the form of a visible input layer and subsequent hidden layers, including the output layer. The activation function of the output layer constrains the model for the specific type of problem (i.e., regression or classification). With increasing computational resources, deep multi-layer networks composed of multiple layers of hundreds of neurons can now be constructed for highly complex problems.

Cross Validation

Model Inputs and Outputs

The primary input to each ML algorithm is the visible and near infrared channel TOA reflectances or R_{rs} of the specific sensor and band configuration. The modeled synthetic data were resolved to six multispectral and hyperspectral sensor specifications: Sentinel 3 Ocean and Land Colour Imager (S3-OLCI), Sentinel 2 multi-spectral imager (S2-MSI) at the sensor's 60, 20, and 10 m band configurations, Landsat 8 operational land imager (L8-OLI), the moderate resolution imaging spectroradiometer (MODIS), and a hypothetical hyperspectral configuration based on the hyperspectral imager for the coastal ocean (HICO). As a means of dimensionality reduction, the seventh configuration consisted of the scores from the first ten EOF modes from a singular value decomposition (SVD) of the entire dataset for HICO bands. In this instance, the ten scores were used as input to the ML model, replacing the channel reflectances. See **Table 1** for a list of all sensor band configurations.

Inputs to each model consist of three sets of features: 1) the visible and near infrared (NIR) bands of the specific sensor configuration, 2) the Sun and sensor geometry if the model is applied to TOA reflectance, and 3) a selection of feature interactions, which include band ratios and spectral derivative type indices (**Table 1**). Feature tuning and extraction can have dramatic effects on resulting model errors or accuracies. Generally, interactions among variables can supplement the individual predictor variables to enhance the feature space to

TABLE 1 | Inputs for ML models. Inputs are the same for the four ML models used in this study, except for Sun and sensor geometries, which were only used on TOA models. References from 1 to 13 (Gower et al., 2008; Hu, 2009; Dall'Olmo and Gitelson, 2005; Mishra and Mishra, 2012; Gower et al., 1999; Moses et al., 2009; Qi et al., 2014; Matthews et al., 2012; Hunter et al., 2010; Mishra et al., 2013; Liu et al., 2017; Dekker, 1993; Shi et al., 2015):

Sensor	Bands	Geometries	Feature interactions
L8-OLI	B1, B2, B3, B4, B5	OZA, OAA, SZA, SAA	B4/B3, B4/B2, B4/B1, B3/B2, B3/B1, B2/B1
S2-MSI 10 m	B2, B3, B4, B8		B4/B3, B4/B2, B3/B2
S2-MSI 20 m	B2, B3, B4, B5, B6, B7, B8, B8A		B5/B4, B5/B3, B5/B2, B4/B3, B4/B2, B3/B2, MCI[1], FAI[2], D3b[3], NDCI[4]
S2-MSI 60 m	B1, B2, B3, B4, B5, B6, B7, B8, B8A		B5/B4, B5/B3, B5/B2, B4/B3, B4/B2, B3/B2, MCI, FAI, D3b, NDCI
S3-OLCI	Oa1, Oa2, Oa3, Oa4, Oa5, Oa6, Oa7, Oa8, Oa9, Oa10, Oa11, Oa12, Oa16, Oa17, Oa18		FLH[5], MCI, FAI, M2b[6], D3B, NDCI, PCI[7], SIPF[8], H103b[9], M133b[10], L4b[11], D93[12]
MODIS	B1, B2, B3, B4, B8, B9, B10, B11, B12, B13, B14, B15, B16		FLH, SIPF, FAI, Shi15[13]
HICO	All bands 400–900 nm		None
HICO-SVD	EOF modes 1–10		None

improve the predictive capability of the models. This has been confirmed for aquatic cases (Ruescas et al., 2018; Hafeez et al., 2019) where including band interactions such as band ratios or line height models has improved model performance. Model outputs are concentrations of chl-a, PC, and NAP in mg/m^3, as well as a_{phy} in m^{-1}, and the OWT.

The R_{rs} dataset contains roughly 70,000 samples, while the TOA reflectance dataset contains roughly 260,000 samples. For each dataset, models were evaluated using k-fold cross validation where the data were split into 80% for training and 20% for testing for five folds in order to avoid sampling bias (**Figure 4**). Performance metrics used in the evaluation consist of both linear and log-transformed root mean squared error (RMSE and RMSELE, respectively), relative RMSE (rRMSE), bias, and median absolute percent error (MAPE).

Hyper-Parameter Tuning

To obtain results of the highest fidelity possible, ML models require optimization of their respective hyper-parameters before training of the actual ML model for product retrieval. The hyper-parameters govern the training process itself and define the model architecture. These parameters are not updated during the learning process and are used to configure the model in various ways. In this study, hyper-parameter tuning was accomplished using a grid search, which builds a model for each possible combination of all hyper-parameters provided, evaluates each model, and selects the architecture with the lowest mean squared error (MSE) for regression models, or accuracy for classification models. The best performing combination of hyper-parameters is then applied to train the ML model using the entire dataset. Computational requirements for extensive hyper-parameter tuning can be very high, especially when dealing with more complex or deep models. The models used here were trained with minimal hyper-parameter tuning, as conducting an exhaustive grid search exercise for every trained model explored in this study would be very computationally expensive. However, a brief hyper-parameter tuning exercise was performed to optimize each of the models' most sensitive hyperparameters. Final model hyper-parameters are listed in the **Supplementary Material**. A technical roadmap of the data development and training stages is shown in **Figure 4**. All the analyses were performed using a personal laptop equipped with 16 GB of RAM.

RESULTS

Surviving L_w at TOA

The average percent contributions of the surviving water signal at L_{tot} for the seven manually defined OWTs derived above for specific visible and NIR bands are shown in **Figure 5**. The high inter- and intra-variability of the percent contribution of the L_w signal is evident. Relatively low contribution from the 443 nm band is common amongst OWTs. This region encompasses high amounts of absorption amongst the different aquatic optical constituents as well as significant interference from atmospheric molecular Rayleigh scattering. Consequently, this band only reaches above 20% contribution in extremely scattering conditions containing relatively low amounts of blue absorption due to decreased phytoplankton and CDOM. There is a general increase in surviving aquatic signal with increased inorganic sediment, as well as with a more dominant phytoplankton component. The fraction of L_w at TOA is also relatively elevated in OWTs comprising greater concentrations of PC, particularly the red edge band. When cyanobacteria dominate, L_w at TOA fractions have the potential to reach 40% for red/NIR bands with chl-a concentrations as low as 10 mg/m^3, while maxing out at an average of roughly 60% for the 709 nm band just above 100 mg/m^3 (data not shown). When eukaryotic algae dominate, average surviving L_w at TOA fraction only exceeds 20% for the NIR bands and at highly elevated chl-a concentrations. This relationship is also apparent when comparing subdued L_w at TOA fractions of the eukaryotic bloom OWT ("Euk"), which represents high biomass eukaryotic algae blooms, vs. the "Cy" OWT dominated by cyanobacteria and containing much higher PC:chl-a ratios (**Figure 6**). OWTs consisting of relatively high mineral concentrations ("NAP" OWT) yield broadly elevated surviving L_w at TOA, with fractions ranging from 20 to 60% for the green to NIR bands.

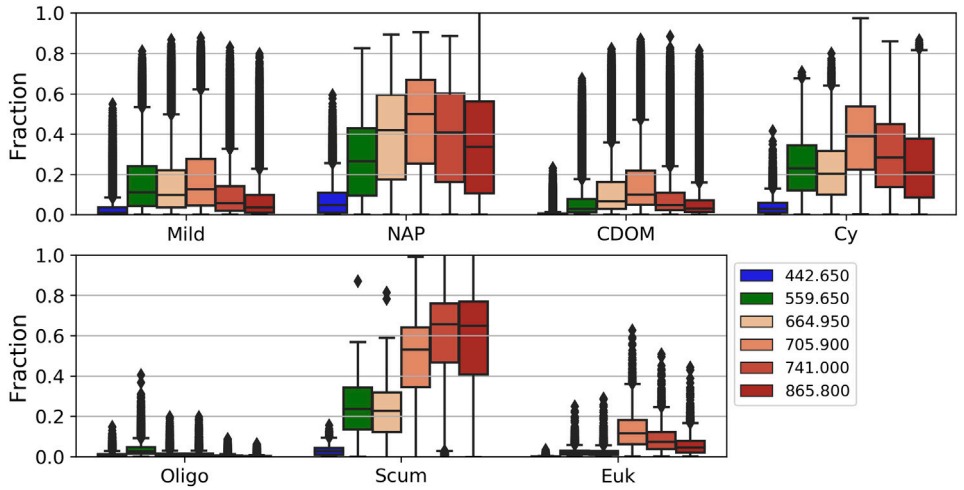

FIGURE 5 | Fraction of surviving L_w at L_{tot} for specific wavelengths for each derived OWT.

Model Performance Against Synthetic Dataset

Evaluation of overall model performance applied to TOA reflectance or R_{rs} spectral data, per sensor, can be found in **Supplementary Appendix C** for retrieval of chl-a, PC, and NAP concentrations, and $a_{phy}(440)$. The MLP overwhelmingly outperforms the other ML models in almost every case in terms of MAPE and RMSELE when evaluated against the entire dataset using R_{rs} data. A lower MAPE/RMSELE would signify better performance (**Supplementary Appendix Figure C1**). When applied to TOA reflectance, MLP still generally performs the best, although with exceptions in specific cases. The KNR model generally performs the worst for retrievals when applied to both R_{rs} and TOA reflectance. Considering the variability of these products within the synthetic dataset, the MLP shows promising predictive capabilities for all trophic states.

Figure 6 shows the MAPE of the MLP algorithm retrievals by OWT for each sensor using both R_{rs} and TOA reflectance data. Significant differences can be observed in the capability of the MLP algorithm for chl-a, PC, and NAP concentration retrievals, as well as retrievals for absorption at 440 nm by phytoplankton and CDOM, due to the different band configurations. The OWT can also significantly affect retrieval performance differently among sensors. When using R_{rs} data, product retrievals by sensor do not show much intra-variability within OWTs, and on average, yield errors ranging from 20 to 40% amongst OWTs. Exceptions to this include errors >50% for C_{nap} retrieval, and <20% for chl-a and PC in OWTs dominated by cyanobacteria (Scum and Cy). Phytoplankton absorption at 440 nm is also retrievable with <20% error at R_{rs} amongst the different band configurations. S3-OLCI shows considerably better retrieval performance of PC than other multi-spectral sensors, in-line with HICO retrieval performance.

Examining product retrieval errors using TOA reflectance by sensor shows more intra-variability within OWTs as compared to R_{rs}. OWTs that result in lower proportions of surviving L_w signal at TOA, such as the Oligo or Euk water types, experience the greatest difference in product retrieval error when comparing retrievals at R_{rs} or TOA. When comparing sensor configurations, L8-OLI generally observes the largest discrepancies between product retrievals at R_{rs} and TOA, most significantly for pigment retrievals and a_{phy} (440). That said, L8 produces smaller errors at TOA in oligotrophic to mesotrophic waters (Oligo OWT) when compared to the S2-MSI 10 m and 20 m band configurations. Other than for the Oligo OWT, the difference in error between $a_g(440)$ retrievals at R_{rs} and TOA are relatively consistent between sensor configurations.

Case Study Application

Hartbeespoort Dam, South Africa

To assess the spatial integrity of retrieval products as well as test cross-sensor consistency, a semi-quantitative examination of productive freshwater scenes was undertaken. **Figure 7** shows the results of MLP products retrievals using S2-MSI in the 10 m band configuration and L8 TOA reflectances (refer to **Table 1** for band configurations). The scene focuses on Hartbeespoort Dam, South Africa, on October 27, 2016. Hartbeespoort Dam is a small, optically complex reservoir that experiences frequent cyanobacteria and floating aquatic macrophyte blooms. The dam is traditionally a very difficult remote sensing target due to its small size and the optically complex nature of the water. While both sensor configurations have similar, limited spectral resolution, L8-OLI provides the advantage of an additional coastal/aerosol band at 440 nm, while S2-MSI at 10 m provides the advantage of a band situated at the red edge of 705 nm. Values of same-day *in-situ* matchup points for chl-a are overlayed on the product as a qualitative validation. Information regarding sample collection can be found in Kravitz et al. (2020).

Unfortunately, only *in-situ* chl-a could be quantified; however, other products are also show to illustrate product relationships (**Figure 7**). Strong consistency between the two sensor retrievals

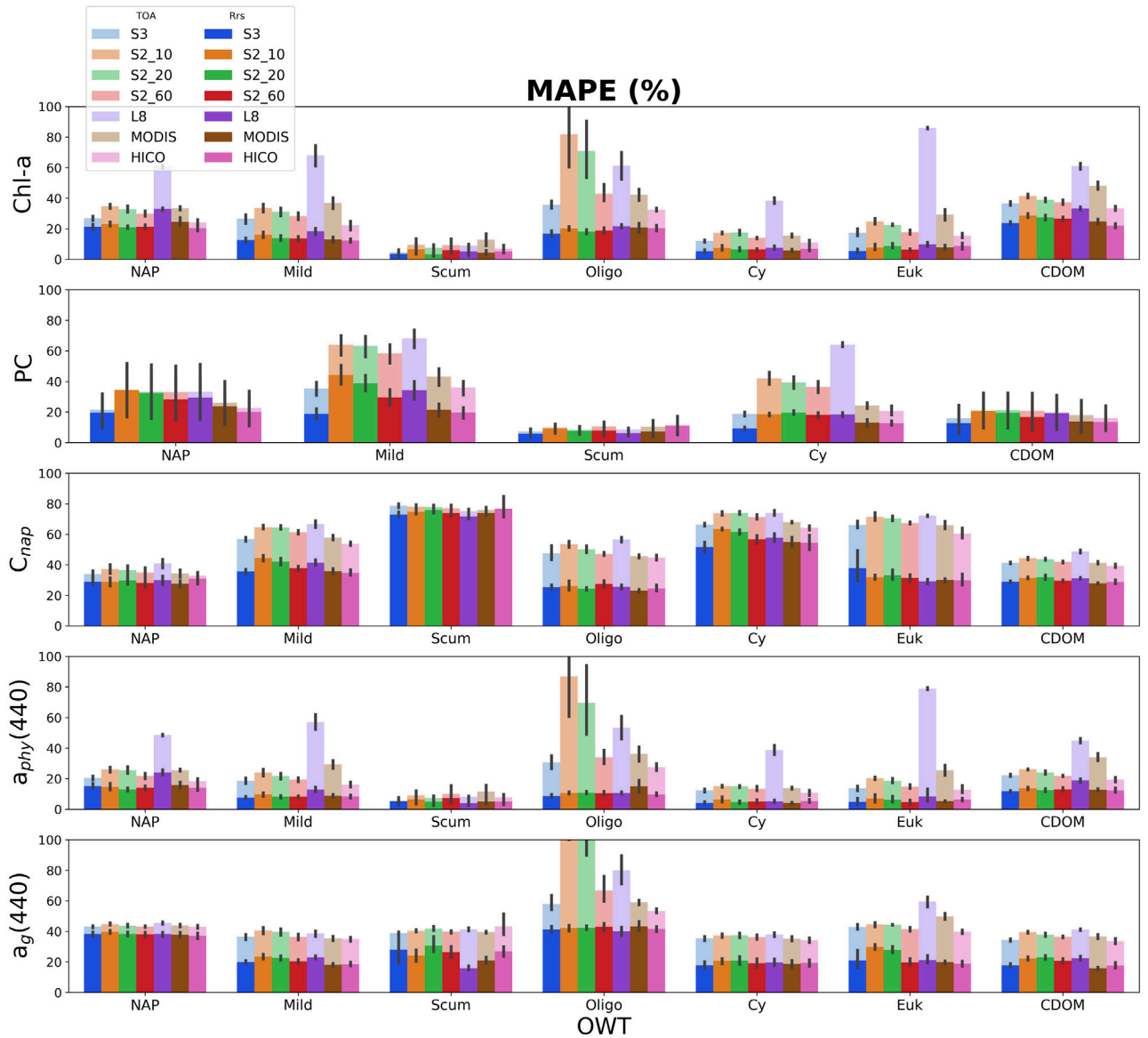

FIGURE 6 | Median absolute percent error (MAPE) for MLP derived products (from top-to-bottom: chl-a, PC, and NAP concentrations, absorption of phytoplankton, and a_g at 440 nm). Retrieval errors using R_{rs} are in solid bright colors, while retrieval errors using TOA reflectance are stacked in corresponding opaque colors. Lower MAPE corresponds to better performance. Error bars represent the standard deviation for the five-fold cross validation.

is apparent. L8 slightly underestimates chl-a outside of the intense bloom in the western part of the dam relative to the S2 retrieval. The PC and $a_{phy}(440)$ retrievals, although not validated with *in-situ* data, depict realistic relationships and ranges associated with the chl-a product. Strong consistency between the two sensors is also evident. Inter-comparison of products also depicts the de-coupling of PC and chl-a estimation, as evidenced by strong spatial consistency between chl-a and $a_{phy}(440)$, while PC is more drastically concentrated in the Western basin, and substantially lower in the Eastern basin. The scene demonstrates the capability for extremely dynamic ranges of water quality product retreivals. Water type classification using the two configurations is also remarkably consistent. Depicting a gradient of scum conditions, to cyanobacteria dominated conditions, to milder sub-surface blooms in the Eastern basin. This can also be visualized in the RGB as fading of the intensity of the green color, where the absorption of the water becomes stronger due to less phytoplankton biomass. S2 appears to differentiate scum and high cyanobacteria concentrations more effectively than L8. This is potentially the result of a combination between the inclusion of the red-edge band utilized for S2, as well as smaller pixel size. AC over intense bloom waters such as these are error prone and can lead to large uncertainties in retrieval products (Kravitz et al., 2020). As the AC and product retrieval are essentially performed together in the inversion, the strong water-leaving signal at TOA allows for very reasonable product retrieval estimates.

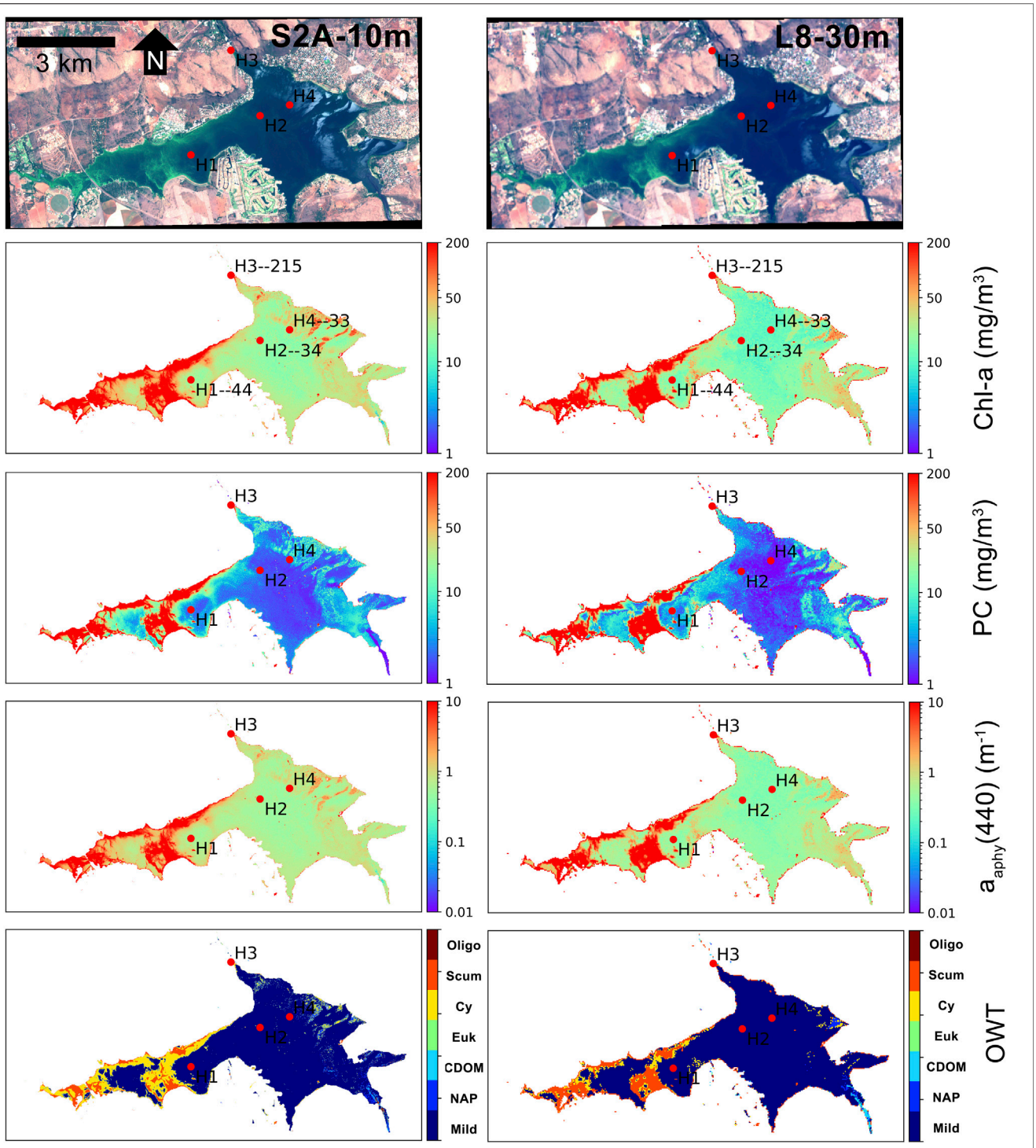

FIGURE 7 | MLP product retrievals over Hartbeespoort Dam on October 27, 2016. The left column shows retrievals using S2 10 m configuration while the right column is the L8 retrievals. All products are derived from TOA reflectance. On the chl-a panels, *in-situ* sampling points (red dots) are labeled with the station name followed by the measured quantity of chl-a, in units of mg/m^3 (e.g., H1--44 indicates station H1 with a measured *in-situ* chl-a concentration of 44 mg/m^3). *In-situ* data are from Kravitz et al. (2020).

Figure 8 displays another instance of same-day chl-a retrievals at Hartbeespoort Dam on March 29, 2017. A large water hyacinth bloom had begun spreading from the North-Eastern basin which can be visualized in the RGB image and is consequently flagged out in product retrievals. This poses a very difficult scenario for medium resolution sensors, with potential for strong signal

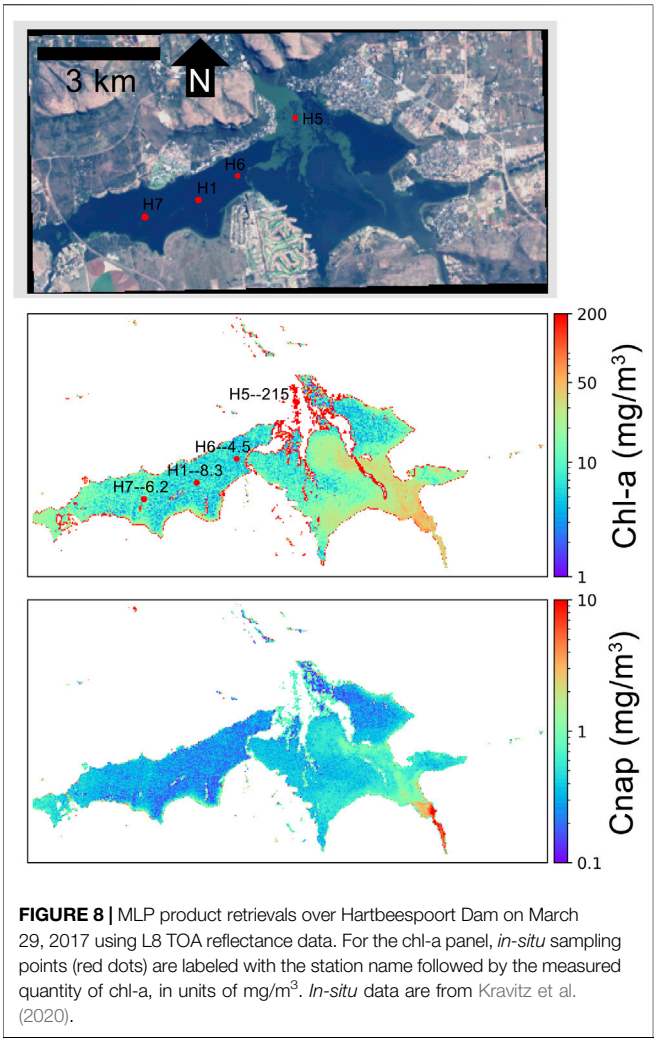

FIGURE 8 | MLP product retrievals over Hartbeespoort Dam on March 29, 2017 using L8 TOA reflectance data. For the chl-a panel, *in-situ* sampling points (red dots) are labeled with the station name followed by the measured quantity of chl-a, in units of mg/m^3. *In-situ* data are from Kravitz et al. (2020).

contamination for less productive water pixels from adjacent bright vegetation pixels. Chl-a product retrieval estimates correlate very well with *in-situ* measurements, even adjacent to the water hyacinth. Product estimations of C_{nap}, although not validated with *in-situ* data, show a realistic de-coupling of organic and inorganic material, with high NAP concentrations displayed in the sediment-laden South Eastern arm of the dam.

Lake Erie, United States

A separate semi-quantitative validation of MLP retrieval products was conducted for the western basin of Lake Erie, USA. **Figures 9**,**10** show product retrievals during a mild cyanobacteria bloom on August 13, 2018 using S2 TOA reflectances in the 60 m and 10 m band configurations, respectively. Retrieval products are qualitatively validated with *in-situ* measurements of chl-a, PC, C_{nap}, and $a_g(440)$ collected and distributed by the National Oceanographic and Atmospheric Administration (NOAA) Great Lakes Environmental Research Laboratory (GERL) and National Centers for Environmental Information (NCEI) (https://www.glerl.noaa.gov/res/HABs_and_Hypoxia/habsMon.html). Comparison of the two figures demonstrates the capability of multi-parameter inversion using only four bands in the 10 m configuration (**Figure 10**), while the 60 m configuration uses nine bands in the vis/NIR (**Figure 9**). Despite the five spectral band difference, product consistency is very strong and respectably correlated with *in-situ* measurements. The higher spatial resolution in the 10 m configuration also demonstrates the de-coupling of water quality products for a slick of disturbed water emanating from the lower western basin. The high spatial resolution captures the elevated dissolved organic and non-algal content in the disturbed water.

A short time-series analysis was conducted at station WE4 of Lake Erie during the bloom period of 2018 between June and October. *In-situ* field data are plotted along with product retrievals for S3, S2 in both 10 m and 60 m configurations, and L8, all using TOA reflectance data (**Figure 11**). All non-cloudy images available for each sensor during the time period were downloaded from either the United States Geological Survey (USGS) Earth Explorer (https://earthexplorer.usgs.gov/), or the European Space Agency (ESA) Copernicus Open Access Hub (https://scihub.copernicus.eu/). Considering the highly dynamic nature of bloom and water dynamics in the western basin, the multi-spectral sensors were able to adequately track the progress of two subsequent cyanobacteria blooms during the time period. Other than some outlying instances of apparent model failure using S3, which would inquire further inspection, **Figure 11** demonstrates the capability of a multi-sensor approach to fill temporal gaps due to clouds and revisit times.

Figure 12 displays the results of MLP product retrievals using L8-OLI and S2-MSI plotted against same-day *in-situ* field data for three images of South African waters, which only include chl-a validation, and two images of Lake Erie, which also include PC, $a_g(440)$, and C_{nap}, for a total of 72 chl-a matchups and 46 matchups for each of PC, $a_g(440)$, and C_{nap}, totaling 216 total point matchups. Although it is not conventional to aggregate multiple sensors and their associated products, the figure provides an estimation of total error, as calculated using the MAPE, for the three sensor configurations on a limited number of validation points. A combined MAPE of 52% was achieved for the four products at three multi-spectral sensor configurations using TOA reflectance. The error adequately corresponds to results achieved using synthetic data in **Figure 6** for these water types, as well as results from other studies using ML trained on *in-situ* data (Balasubramanian et al., 2020; Pahlevan et al., 2020).

DISCUSSION

Machine Learning Models

Four out-of-the-box ML models were trained using synthetic data and applied to EO data using the Python programming language. We note that the aim of this study was not to produce an optimal, finalized retrieval model for operational use, but rather to explore the capacity of a range of well documented ML models to make adequate predictions of water quality variables, trained from synthetic optical and radiometric data. ML has proven an extremely powerful tool that is now more accessible and easier to implement than ever before. This study confirms other reports

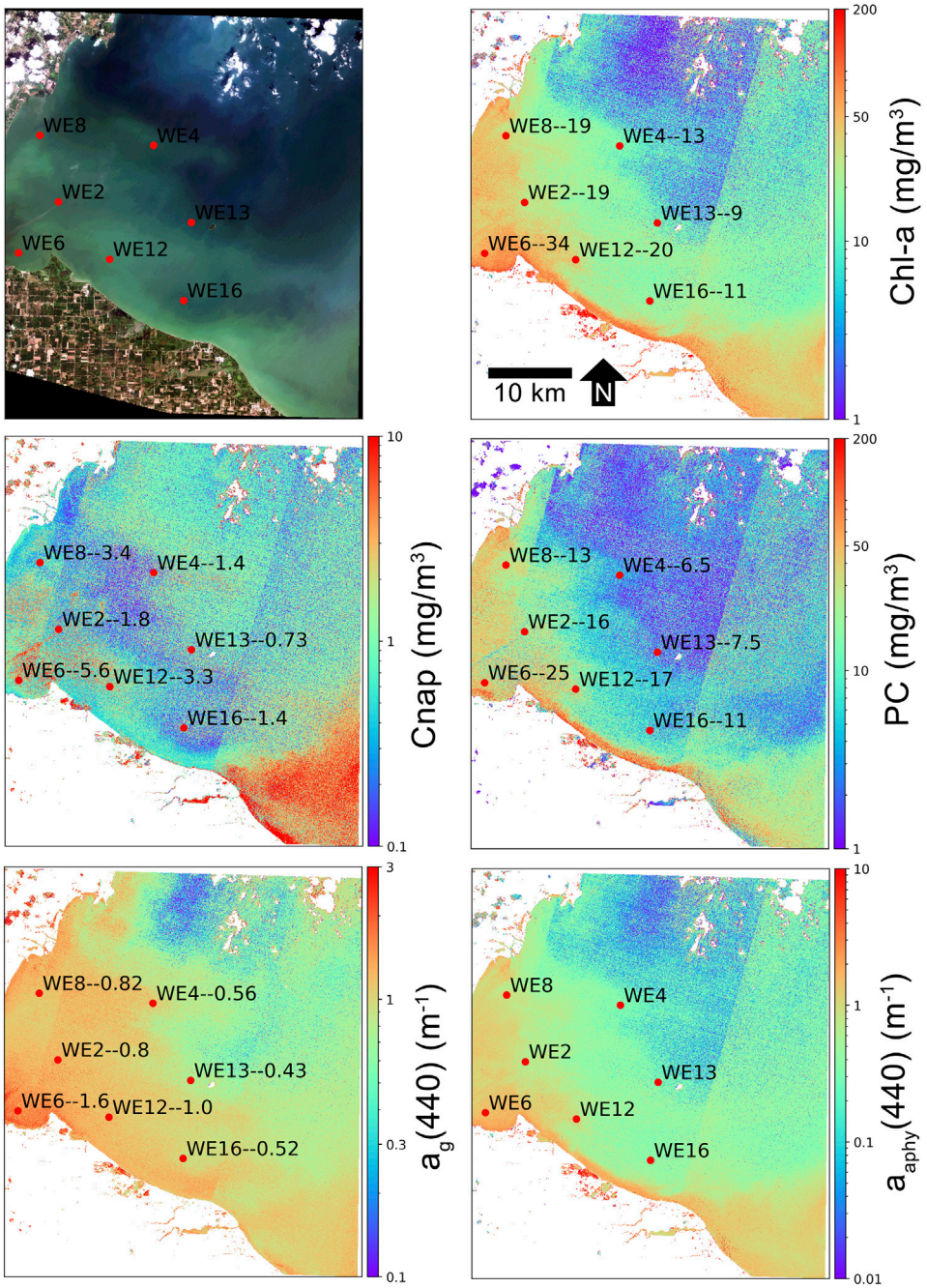

FIGURE 9 | MLP product retrievals over the western basin of Lake Erie on August 13, 2018 using S2 60 m band configuration TOA reflectance data. *In-situ* sampling points (red dots) are labeled with the station name followed by the measured quantity of that particular variable, in units shown on the y-axis. *In-situ* data are from NOAA GERL and NCEI.

of ANNs outperforming other "shallow" ML models such as decision trees or support vector machines (SVM) (Peterson et al., 2018; Hafeez et al., 2019). Other ML techniques utilized in recent aquatic work such as feature fusion (Peterson et al., 2019) were also implemented to a degree in this study. Multiple "feature interactions" in the form of band ratios or line height indices were included in model training along with sensor visible and NIR bands. Ruescas et al. (2018) found increasing model performance by including more feature interactions for a ML model for CDOM retrieval. Although the results are not shown here, we trained a subset of ML models with and without the inclusion of feature interactions; the significant increase in performance when feature interactions were included led us to include them for all models.

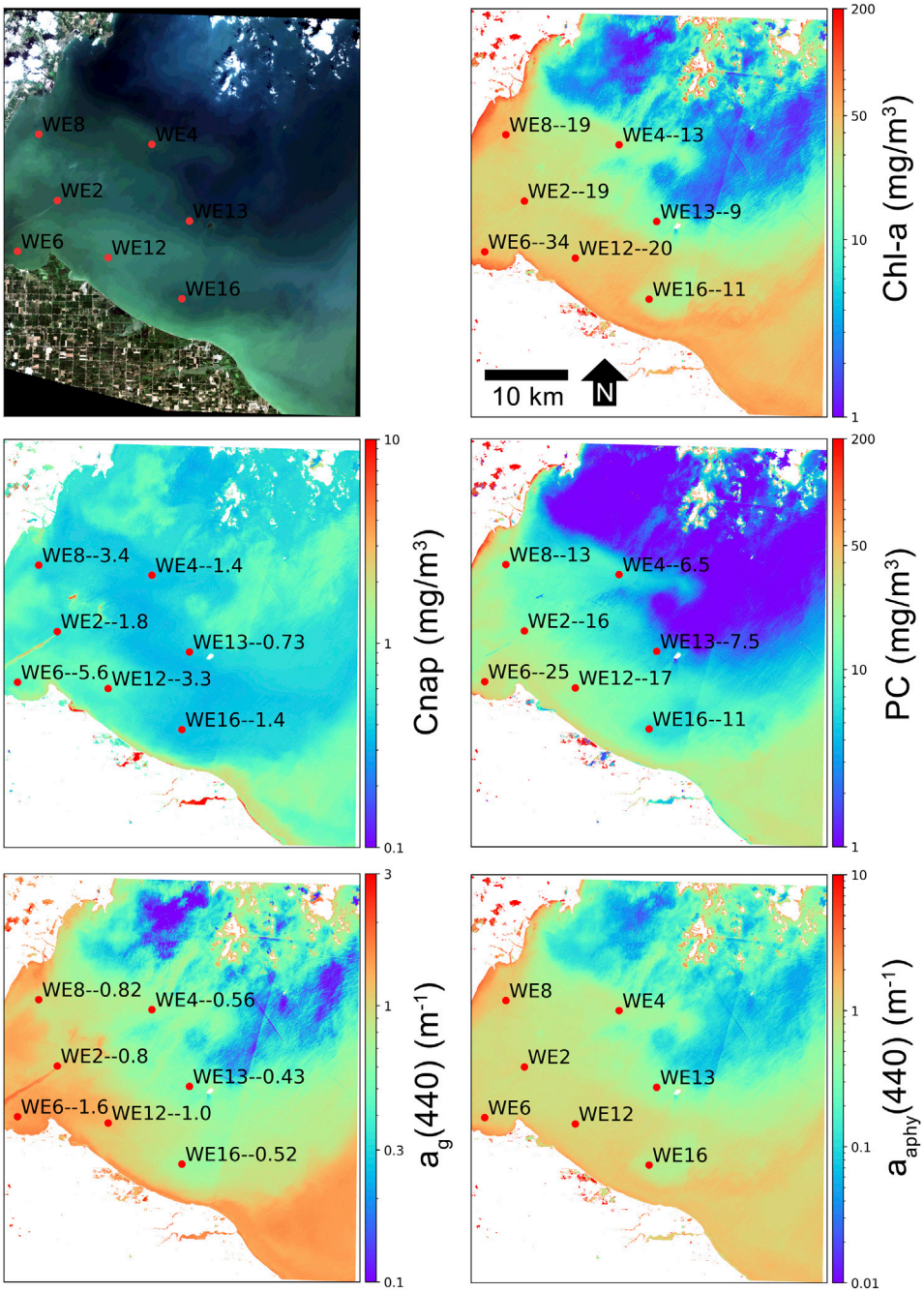

FIGURE 10 | MLP product retrievals over the western basin of Lake Erie on August 13, 2018 using S2 10 m band configuration TOA reflectance data. *In-situ* sampling points (red dots) are labeled with the station name followed by the measured quantity of that particular variable, in units shown on the y-axis. *In-situ* data are from NOAA GERL and NCEI.

Pahlevan et al. (2020) and Balasubramanian et al. (2020) found that a mixture density network (MDN), which is essentially an ANN with the final layer mapped to a mixture of distributions, produced extremely robust results for chl-a and suspended solid material. MDNs would theoretically be the optimal choice for aquatic parameter retrievals, as one can design a highly efficient deep neural network (DNN) while also addressing the signal ambiguity problem of optical remote sensing through the addition of a mixture of parameterized Gaussians. Such an approach was attempted here; however, it took considerably longer for training and cross validation, and produced roughly similar results to the MLP model, such that it was discarded. Future work, with access to higher computational resources, should include training of deeper NNs and the inclusion of mixture distributions.

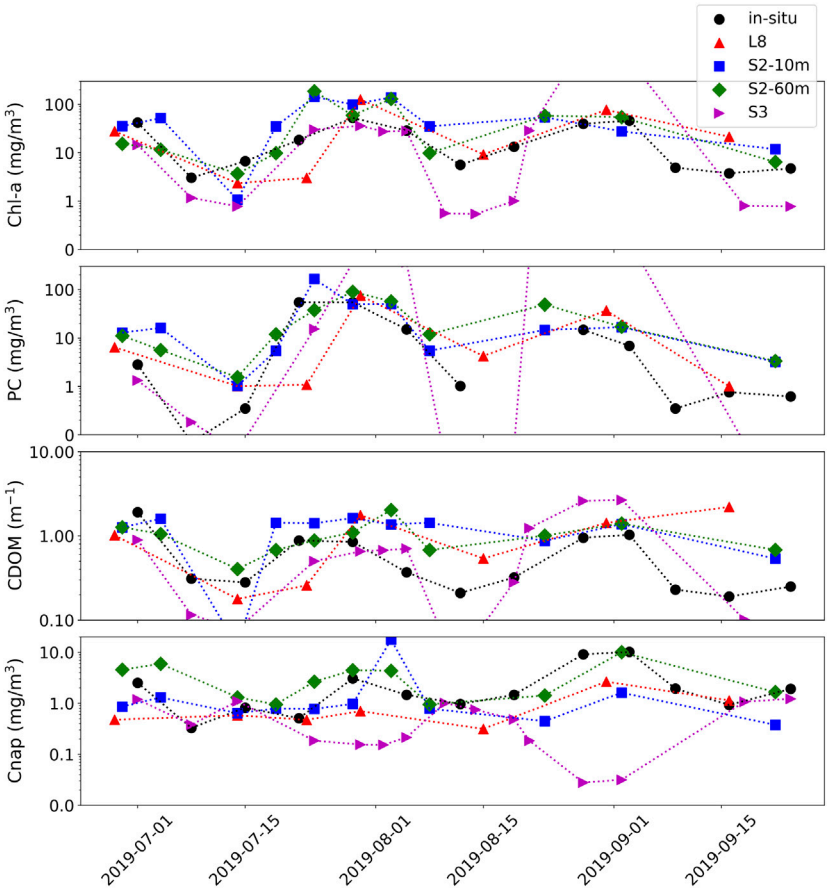

FIGURE 11 | Time-series of station WE4 from western Lake Erie. Product retrievals are derived from MLP from S3, S2, and L8 using TOA reflectance data (colors) plotted with *in-situ* data (black) from NOAA GERL and NCEI.

Shallow ML models such as Random Forest and XGBoost require far less parameterization and computational resources but still provide relatively robust results. We note that all models were both trained and validated using mainly the synthetic database with only the MLP model validated against a limited *in-situ* dataset. Future work will entail validating products against available *in-situ* data. It is speculated that performance will decline somewhat when validated against field data due to spatial inconsistencies and uncertainty introduced by field methods.

Product Consistency

Pahlevan et al. (2020) note AC to still be one of the major challenges for operational inland and coastal remote sensing. The present study explores the capability of product retrievals from TOA reflectances. We find that water types for turbid or productive inland waters have substantially higher percentages of surviving water-leaving radiances reaching the satellite sensor than oligotrophic waters or waters dominated by eukaryotic algae (**Figure 5**). The separation of MLP performance by OWT confirms that water types with stronger bulk scattering signals have smaller discrepancy between product retrievals from TOA reflectance and R_{rs} (**Figure 6**). An OWT based framework could be used to run AC only on oligotrophic pixels where AC processors are more ideally suited, with product retrievals made from TOA in more productive or scattering water types. Due to uncertainties inherent to current AC processors, especially for smaller water bodies, the product maps shown here (e.g., **Figures 7–10**) were made using TOA reflectance data. Nevertheless, promising AC processors have been developed using a combined synthetic data/NN approach (Fan et al., 2017), and the dataset developed here could be used in future to train an appropriate AC.

The water bodies shown in this manuscript have the potential to experience high spatial and temporally dynamic blooms. Sensor requirements for operational monitoring of such waters are recommended to be <60 m spatial resolution with daily to tri-weekly revisit times (Hestir et al., 2015; Mouw et al., 2015; Muller-Karger et al., 2018). The case studies presented in *Case Study Application* Section demonstrate the fine-scale spatial distributions of cyanobacteria blooms. MLP products at different spatial resolutions demonstrate how spatial smoothing from just 10–60 m can cause significant differences in product retrievals. Reasonable comparisons of *in-situ* data against highly consistent product maps between S2 10 m and 60 m configurations provide a promising justification of the capability of ML to exploit information from just a few sensor bands. Extreme temporal dynamics can additionally be visualized

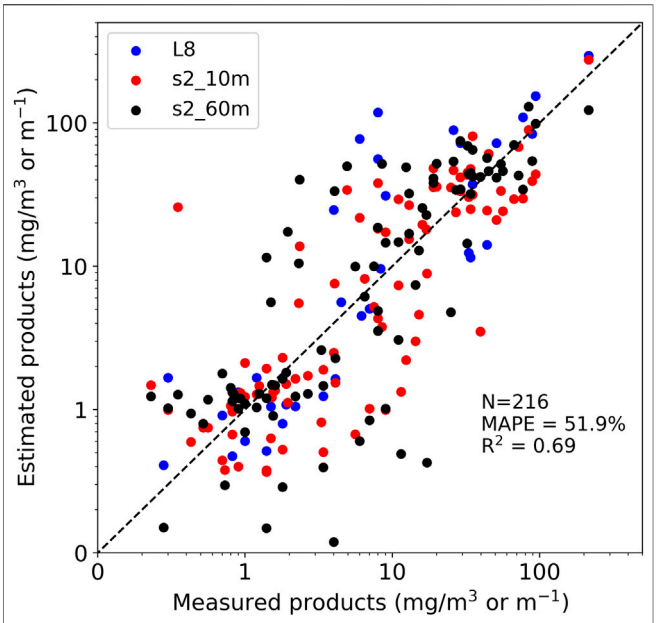

FIGURE 12 | Measured vs. estimated products; chl-a (N = 72), PC (N = 46), $a_g(440)$ (N = 46), and C_{nap} (N = 46) for same day matchups from L8 and S2.

in the short time-series shown in **Figure 11**, where a multi-sensor approach was adequately able to trace fine temporal dynamics of cyanobacteria blooms in Lake Erie.

Product Integrity

The magnitude and fraction of the water-leaving radiance surviving to TOA can also have a significant impact on the resulting sensor signal-to-noise ratio (SNR). There is a trade-off in sensor design concerning spatial and spectral resolution and resulting sensor radiometric quality. For example, sensor configurations such as S2-MSI or L8-OLI sacrifice SNR for the sake of higher spatial resolution. Narrower band widths can also compromise SNR. Numerous investigations have concluded that errors in both AC and geophysical retrievals only become acceptable (<100%) at SNRs of 300 – 500 at visible wavelengths and >100 at NIR wavelengths for water quality applications (Moses et al., 2015; Wang and Gordon, 2018; Qi et al., 2017; Jorge et al., 2017). Some studies suggest SNR for NIR bands to be >600 if used in AC schemes (Wang and Gordon, 2018; Qi et al., 2017). A brief examination of typical SNR values for S2-MSI for the OWTs defined here is presented in **Figure 13**. The SNR in this instance applies solely to the water-leaving radiance reaching TOA (L_w) rather than to the total radiance signal at TOA, which includes the atmosphere (L_{tot}), that the aforementioned studies primarily use. Using SNR for L_w provides an SNR more relevant to the investigator as it pertains directly to the signal of interest (Kudela et al., 2019). Kudela et al. (2019) proposed a set of theoretical SNR thresholds described as a theoretical research limit (SNR = 2), a theoretical validation limit (SNR = 8), and a theoretical calibration limit (SNR = 50). The SNR ranges depicted in **Figure 13** follow similar patterns and relationships as in **Figure 5** for that of surviving L_w at TOA. Only water types with a strong bulk scattering signal such as cyanobacteria- or NAP dominated waters appear to reach a theoretical validation limit of 8, on average (**Figure 13**). Waters types with more subdued signal strength have difficulty reaching even a theoretical research limit of SNR of 2 in visible bands. Thus, unless dealing with extremely scattering waters, MSI SNRs are considerably lower than the recommended radiometric requirements for aquatic application, which can lead to large uncertainties in product retrieval. The synthetic dataset approach could be used in future to perform robust sensor and algorithm specific uncertainty analysis per OWT.

The adjacency effect (AE), whereby strong spatial heterogeneity from surrounding terrestrial sources contaminates the water signal, has the potential to induce considerable errors in retrieved products (Bulgarelli et al., 2017). Contamination by green terrestrial vegetation at TOA was incorporated into the synthetic modeling in an attempt to mitigate this issue. **Figure 14** shows an S2 scene over a small dam in South Africa that was found to be affected by considerable adjacency by Kravitz et al. (2020). The predicted contribution of adjacency to water pixels based on a simple RF model trained using the synthetic dataset is illustrated. The plot shows realistic gradation of increasing adjacency contribution towards the edges of the dam in the darker waters, as well as in instances near bright surface cyanobacteria blooms. Areas of intense algal surface bloom would be less affected by green vegetation adjacency since they exhibit similar reflectance patterns in the red and NIR, and would themselves be potentially contaminating nearby "less bright" water pixels. While more quantitative validation is required, the fact that the model demonstrates reasonable patterns of the AE gives confidence that other retrieval products would be inherently corrected for this effect. Future work should incorporate more sources of adjacency and could also include other sources of signal contamination such as Sun glint.

Outlook

While this study is more proof-of-concept than finalized product, the results suggest the potential for using a synthetic dataset and ML approach to develop operational global freshwater monitoring products. Expansion of the synthetic dataset by incorporating more diverse phytoplankton IOPs and other sources of signal contamination is the logical next step. While the amount of synthetic data generated here (~260,000 TOA spectra) is quite small with respect to current advances in Big Data analytics, the development of extremely large synthetic datasets containing tens and hundreds of millions of datapoints from which advanced deep learning networks can be trained, would be feasible with access to high powered computing resources. Validation of models using global *in-situ* datasets would then be the final step to compare product outputs trained from synthetic data to outputs trained on field data as in Pahlevan et al. (2020) and Balasubramanian et al. (2020). That said, it is very promising that the model performance described here relates so well to the results detailed in the aforementioned studies. Further research should also include parameterized sensitivity studies identifying the most optimal spectral and

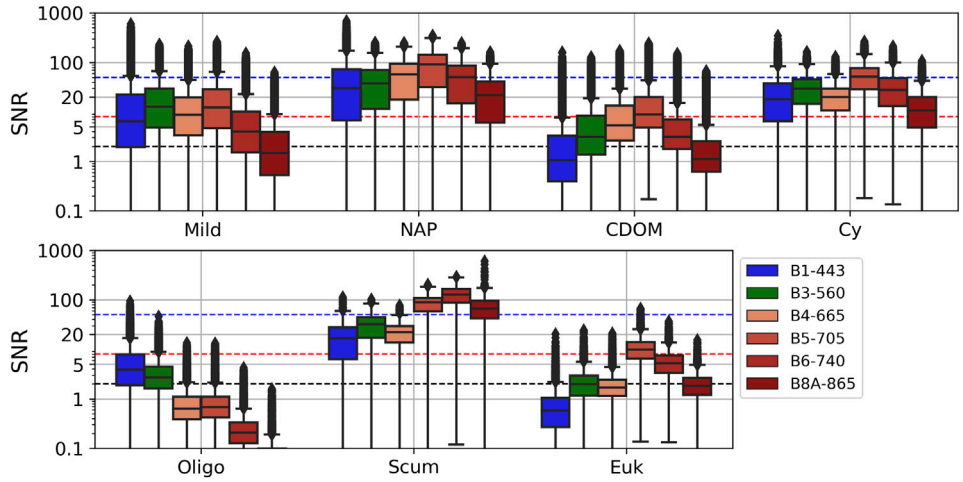

FIGURE 13 | SNR for water-leaving radiance (L_w) for S2-MSI developed using the ESA Sentinel 2 radiometric uncertainty tool (Gorroño et al., 2017; 2018) for the OWTs defined in this study. The black, red, and blue dashed lines represent the theoretical research, validation, and calibration limits described in Kudela et al. (2019).

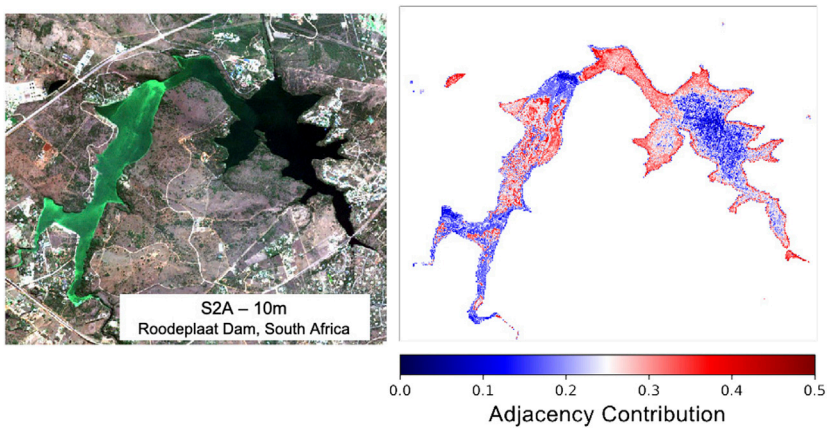

FIGURE 14 | Percent adjacency contribution derived using RF regression over Roodeplaat Dam, South Africa, using TOA reflectance data.

radiometric resolutions that ML can exploit. Having a large, high quality synthetic dataset would also be an asset for sensitivity studies pertaining to upcoming satellite missions such as NASA's Surface, Biology, and Geology (SBG) mission.

This study suggests that both L8 and S2 at its various sensor configurations contain enough spectral information at TOA, to produce reasonable estimates of various aquatic products for productive water bodies. Highly consistent product outputs were found for S2 at 60 m and 10 m resolutions, which is significant considering the five additional NIR spectral bands in the 60 m configuration. This observation has potential implications for future sensor design as it suggests that more resources could be invested in increasing SNR or spatial resolutions of sensors while spectral resolution remains fairly low, at least for the water types investigated here. Finally, our findings suggest that relevant bands for assessing wide ranging trophic levels should at least include a short wavelength blue band around 440 nm as in L8 for more oligotrophic instances and highly absorbing scenarios, a band around 620 nm to aid in cyanobacteria detection and quantification, and a band in the red edge around 710 nm to capture the phytoplankton scattering peak.

CONCLUSION

A state-of-the-art synthetic dataset of R_{rs} and at-sensor reflectances for various sensor configurations with coincident measurements of associated IOPs and optical constituent concentrations was developed using novel techniques suited to high biomass, complex optical systems and cyanobacteria dominated waters. The parameterization of the RTM describing the synthetic dataset utilizes our most current understanding of optical properties and relationships related to eutrophic and cyanobacteria dominated waters and includes four prominent novel aspects: 1) two-layered,

size and type-specific phytoplankton IOPs; 2) mixed assemblage chl-a fluorescence; 3) assemblage based modeled PC concentrations; and 4) paired sensor-specific TOA reflectances, which includes green vegetation adjacency. R_{rs} spectra modeled through the RTM were compiled into 13 distinct clusters using a functional data analysis and k-means clustering approach, and the 13 clusters were then condensed into seven manually defined OWTs. The water types are similar to those discovered using *in-situ* data by Spyrakos et al. (2018) and Kravitz et al. (2020). Manual inspection of synthetic OWTs showed relationships and ranges in the concentrations of water constituents and IOPs that were similar to *in-situ* derived OWTs. Four types of current ML architectures were tested and trained using the synthetic dataset. Major points of interest resulting from the training and application of machine learning models in this study can be summarized as follows:

1. Surviving L_w fraction at TOA is significantly increased by increased bulk scattering such as in NAP or cyanobacteria dominated waters.
2. An artificial neural network produced the most promising results among all sensors and retrieval products when compared to other machine learning methods.
3. The 620 nm band of OLCI, which aligns with the maximum absorption peak of PC, appears to provide a significant advantage over other multispectral sensors for the quantification of cyanobacteria.
4. The 443 nm band present in L8-OLI, but not in the S2-MSI 10 m and 20 m configurations, appears to aid significantly in pigment retrieval in oligotrophic waters.
5. The red-edge band, present in MSI and OLCI, aids significantly in pigment retrieval in bloom waters.
6. Water types containing higher fractions of surviving L_w at TOA experience significantly smaller differences in product retrieval errors when comparing retrieval results from TOA reflectance and R_{rs}.
7. Application to EO imagery provides realistic concentration gradients of chl-a, PC, NAP, and absorption due to CDOM at 440 nm for wide ranging trophic scenarios for small inland water bodies using TOA reflectance data, corroborated by *in-situ* field data.
8. Product retrievals from low spectral resolution configurations such as L8-OLI and S2-MSI at 10 m resolution produce as consistent results as product retrievals from higher spectral resolution configurations such as S2-MSI at 60 m, OLCI, and MODIS.

With a combination of current and past sensor spatial resolutions ranging from 10 m to 4 km scales, a synergistic evaluation of water constituents, with known uncertainties by OWT, may assist in improving global-scale capability for monitoring fine scale ecological dynamics of coastal and inland waters. The synthetic dataset produced and interrogated here represents the first step towards this goal. It is by no means an exhaustive compilation of all possible natural values and relationships found in inland waters; however, it works as a proof-of-concept to show the capability of these techniques for creating accurate simulations of real-world aquatic environments.

DATA AVAILABILITY STATEMENT

The raw data supporting the conclusion of this article will be made available by the authors, without undue reservation.

AUTHOR CONTRIBUTIONS

JK: Conceptualization, Methodology, Software, Formal Analysis, Investigation, Data Curation, Writing - Original Draft, Writing - Review and Editing, Visualization, Project Administration, MM: Resources, Writing - Review and Editing, Supervision, Funding acquisition, SB: Resources, Supervision, Funding Acquisition, LL: Software, Writing- Review and Editing, Supervision, SF: Supervision, Funding Acquisition.

FUNDING

Financial support for this project was provided through the South Africa Water Research Commission Grant K5/2518 and Grant K5/2458, NRF SANAP Grant 105539 and 110735, UCT Vice Chancellor's Future Leaders 2030 Award, and Royal Society/ African Academy of Sciences Future Leaders-Africa Independent Researcher Fellowship.

SUPPLEMENTARY MATERIAL

The Supplementary Material for this article can be found online at: https://www.frontiersin.org/articles/10.3389/fenvs.2021.587660/full#supplementary-material.

REFERENCES

Altman, N. S. (1992). An introduction to kernel and nearest-neighbor nonparametric regression. *Am. Stat.* 46 (3), 175–185. doi:10.1080/00031305.1992.10475879

Arabi, B., Salama, M., Wernand, M., and Verhoef, W. (2016). MOD2SEA: a coupled atmosphere-hydro-optical model for the retrieval of chlorophyll-a from remote sensing observations in complex turbid waters. *Remote Sensing* 8 (9), 722. doi:10.3390/rs8090722

Babin, M., Morel, A., and Gentili, B. (1996). Remote sensing of sea surface sun-induced chlorophyll fluorescence: consequences of natural variations in the optical characteristics of phytoplankton and the quantum yield of chlorophyll a fluorescence. *Int. J. ;Remote Sensing* 17 (12), 2417–2448. doi:10.1080/01431169608948781

Balasubramanian, S. V., Pahlevan, N., Smith, B., Binding, C., Schalles, J., Loisel, H., et al. (2020). Robust algorithm for estimating total suspended solids (TSS) in inland and nearshore coastal waters, *Remote Sensing Environ.*, 246, 111768. doi:10.1016/j.rse.2020.111768

Ball, J. E., Anderson, D. T., and Chan, C. S. (2017). Comprehensive survey of deep learning in remote sensing: theories, tools, and challenges for the community. *J. Appl. Remote Sensing* 11 (4), 042609. doi:10.1117/1.jrs.11.042609

Beaulieu, J. J., DelSontro, T., and Downing, J. A. (2019). Eutrophication will increase methane emissions from lakes and impoundments during the 21st century. *Nat. Commun.* 10 (1), 1–5. doi:10.1038/s41467-019-09100-5

Behrenfeld, M. J., Westberry, T. K., Boss, E. S., O'Malley, R. T., Siegel, D. A., Wiggert, J. D., et al. (2009). Satellite-detected fluorescence reveals global physiology of ocean phytoplankton. *Biogeosciences* 6 (5), 779. doi:10.5194/bg-6-779-2009

Bernard, S., Probyn, T. A., and Quirantes, A. (2009). Simulating the optical properties of phytoplankton cells using a two-layered spherical geometry. *Biogeosci. Discuss.* 6 (1).

Bernard, S., Shillington, F. A., and Probyn, T. A. (2007). The use of equivalent size distributions of natural phytoplankton assemblages for optical modeling. *Opt. Exp.* 15 (5), 1995–2007.

Bidigare, R. R., Ondrusek, M. E., Morrow, J. H., and Kiefer, D. A. (1990). *In-vivo* absorption properties of algal pigments. *Int. Soc. Opt. Photon.* 1302, 290–302.

Binding, C. E., Greenberg, T. A., and Bukata, R. P. (2011). Time series analysis of algal blooms in Lake of the Woods using the MERIS maximum chlorophyll index. *J. Plankton Res.* 33 (12), 1847–1852. doi:10.1093/plankt/fbr079

Blondeau-Patissier, D., Gower, J. F. R., Dekker, A. G., Phinn, S. R., and Brando, V. E. (2014). A review of ocean color remote sensing methods and statistical techniques for the detection, mapping and analysis of phytoplankton blooms in coastal and open oceans. *Prog. Oceanogr.* 123, 123–144. doi:10.1016/j.pocean.2013.12.008

Breiman, L. (2001). Random forests. *Machine Learn.* 45 (1), 5–32. doi:10.1023/a:1010933404324

Brewin, R. J. W., Tilstone, G. H., Jackson, T., Cain, T., Miller, P. I., Lange, P. K., et al. (2017). Modelling size-fractionated primary production in the Atlantic Ocean from remote sensing. *Prog. Oceanogr.* 158, 130–149. doi:10.1016/j.pocean.2017.02.002

Bricaud, A., Roesler, C., and Zaneveld, J. R. V. (1995). *In situ* methods for measuring the inherent optical properties of ocean waters. *Limnol. Oceanogr.* 40 (2), 393–410. doi:10.4319/lo.1995.40.2.0393

Brockmann, C., Doerffer, R., Peters, M., Kerstin, S., Embacher, S., and Ruescas, A. (2016). Evolution of the C2RCC neural network for Sentinel 2 and 3 for the retrieval of ocean colour products in normal and extreme optically complex waters. *Living Planet. Symp.* 740 (54), 393.

Bukata, R. P. (1995). The effects of chlorophyll, suspended mineral, and dissolved organic carbon on volume reflectance. *Opt. Prop. Remote Sensing* 64, 135–166.

Bulgarelli, B., Kiselev, V., and Zibordi, G. (2017). Adjacency effects in satellite radiometric products from coastal waters: a theoretical analysis for the northern Adriatic Sea. *Appl. Opt.* 56 (4), 854–869. doi:10.1364/ao.56.000854

Bulgarelli, B., Kiselev, V., and Zibordi, G. (2014). Simulation and analysis of adjacency effects in coastal waters: a case study. *Appl. Opt.* 53 (8), 1523–1545. doi:10.1364/ao.53.001523

Carlson, R. E., and Simpson, J. (1996). A coordinator's guide to volunteer lake monitoring methods, *North Am. Lake Manag. Soc.* 96. 305.

Chen, T., and Guestrin, C. (2016). Xgboost: a scalable tree boosting system, in Proceedings of the 22nd ACM SIGKDD international conference on knowledge discovery and data mining, 785–794.

Dall'Olmo, G., and Gitelson, A. A. (2006). Effect of bio-optical parameter variability and uncertainties in reflectance measurements on the remote estimation of chlorophyll-a concentration in turbid productive waters: modeling results. *Appl. Opt.* 45 (15), 3577–3592. doi:10.1364/ao.45.003577

Dall'Olmo, G., and Gitelson, A. A. (2005). Effect of bio-optical parameter variability on the remote estimation of chlorophyll-a concentration in turbid productive waters: experimental results. *Appl. Opt.* 44 (3), 412–422.

Dekker, A. G. (1993). *Detection of optical water quality parameters for eutrophic waters by high resolution remote sensing.*

Doerffer, R., and Schiller, H. (2008). *MERIS lake water algorithm for BEAM—MERIS algorithm theoretical basis document. V1.0, 10 June 2008.* Geesthacht, Germany: GKSS Research Center.

D. R. Mishra, I. Ogashawara, and A. A. Gitelson (2017). in *Bio-optical modeling and remote sensing of inland waters* (New York, NY: Elsevier).

Evers-King, H., Bernard, S., Lain, L. R., and Probyn, T. A. (2014). Sensitivity in reflectance attributed to phytoplankton cell size: forward and inverse modelling approaches. *Opt. Expr.* 22 (10), 11536–11551. doi:10.1364/oe.22.011536

Fan, Y., Li, W., Gatebe, C. K., Jamet, C., Zibordi, G., Schroeder, T., et al. (2017). Atmospheric correction over coastal waters using multilayer neural networks. *Rem. Sensing Environ.* 199, 218–240. doi:10.1016/j.rse.2017.07.016

Fischer, J., and Kronfeld, U. (1990). Sun-stimulated chlorophyll fluorescence 1: influence of oceanic properties. *Int. J. Remote Sensing* 11 (12), 2125–2147. doi:10.1080/01431169008955166

Ganf, G., Oliver, R., and Walsby, A. (1989). Optical properties of gas-vacuolate cells and colonies of Microcystis in relation to light attenuation in a turbid, stratified reservoir (Mount Bold Reservoir, South Australia). *Mar. Freshw. Res.* 40 (6), 595–611. doi:10.1071/mf9890595

Gholizadeh, M., Melesse, A., and Reddi, L. (2016). A comprehensive review on water quality parameters estimation using remote sensing techniques. *Sensors* 16 (8), 1298. doi:10.3390/s16081298

Ghorbanzadeh, O., Blaschke, T., Gholamnia, K., Meena, S., Tiede, D., and Aryal, J. (2019). Evaluation of different machine learning methods and deep-learning convolutional neural networks for landslide detection. *Remote Sensing* 11 (2), 196. doi:10.3390/rs11020196

Gilerson, A., Zhou, J., Hlaing, S., Ioannou, I., Amin, R., Gross, B., et al. (2007). Fluorescence contribution to reflectance spectra for a variety of coastal waters. *Coast. Ocean Rem. Sensing* 6680, 66800C.

Gilerson, A., Zhou, J., Hlaing, S., Ioannou, I., Gross, B., Moshary, F., et al. (2008). Fluorescence component in the reflectance spectra from coastal waters. II. Performance of retrieval algorithms. *Opt. Express* 16 (4), 2446–2460. doi:10.1364/oe.16.002446

Gorroño, J., Fomferra, N., Peters, M., Gascon, F., Underwood, C., Fox, N., et al. (2017). A radiometric uncertainty tool for the Sentinel 2 mission. *Rem. Sensing* 9 (2), 178. doi:10.3390/rs9020178

Gorroño, J., Hunt, S., Scanlon, T., Banks, A., Fox, N., Woolliams, E., et al. (2018). Providing uncertainty estimates of the Sentinel-2 top-of-atmosphere measurements for radiometric validation activities. *Eur. J. Remote Sensing* 51 (1), 650–666. doi:10.1080/22797254.2018.1471739

Govindjee, G. (2004). *Chlorophyll a fluorescence: a bit of basics and history.* Chlorophyll a fluorescence: a signature of photosynthesis. Dordrecht: Springer, 1–42.

Gower, J. F. R., Doerffer, R., and Borstad, G. A. (1999). Interpretation of the 685nm peak in water-leaving radiance spectra in terms of fluorescence, absorption and scattering, and its observation by MERIS. *Int. J. Remote Sensing* 20 (9), 1771–1786. doi:10.1080/014311699212470

Gower, J., King, S., and Goncalves, P. (2008). Global monitoring of plankton blooms using MERIS MCI. *Int. J. Remote Sensing* 29 (21), 6209–6216. doi:10.1080/01431160802178110

Greene, R. M., Geider, R. J., Kolber, Z., and Falkowski, P. G. (1992). Iron-induced changes in light harvesting and photochemical energy conversion processes in eukaryotic marine algae. *Plant Physiol.* 100 (2), 565–575. doi:10.1104/pp.100.2.565

Hafeez, S., Wong, M., Ho, H., Nazeer, M., Nichol, J., Abbas, S., et al. (2019). Comparison of machine learning algorithms for retrieval of water quality indicators in case-II waters: a case study of Hong Kong. *Remote Sensing* 11 (6), 617. doi:10.3390/rs11060617

Hestir, E. L., Brando, V. E., Bresciani, M., Giardino, C., Matta, E., Villa, P., et al. (2015). Measuring freshwater aquatic ecosystems: the need for a hyperspectral global mapping satellite mission. *Rem. Sensing Environ.* 167, 181–195. doi:10.1016/j.rse.2015.05.023

Hieronymi, M., Müller, D., and Doerffer, R. (2017). The OLCI Neural Network Swarm (ONNS): a bio-geo-optical algorithm for open ocean and coastal waters. *Front. Mar. Sci.* 4, 140. doi:10.3389/fmars.2017.00140

Ho, J. C., Michalak, A. M., and Pahlevan, N. (2019). Widespread global increase in intense lake phytoplankton blooms since the 1980s. *Nature*, 574, 667. doi:10.1038/s41586-019-1648-7

Ho, T. K. (1998). The random subspace method for constructing decision forests. *IEEE Trans. Pattern Anal. Mach. Intell.* 20 (8), 832–844.

Hu, C. (2009). A novel ocean color index to detect floating algae in the global oceans. *Rem. Sensing Environ.* 113 (10), 2118–2129. doi:10.1016/j.rse.2009.05.012

Hu, C., Chen, Z., Clayton, T. D., Swarzenski, P., Brock, J. C., and Muller–Karger, F. E. (2004). Assessment of estuarine water-quality indicators using MODIS medium-resolution bands: initial results from Tampa Bay, FL. *Rem. Sensing Environ.* 93 (3), 423–441. doi:10.1016/j.rse.2004.08.007

Hunter, P. D., Tyler, A. N., Carvalho, L., Codd, G. A., and Maberly, S. C. (2010). Hyperspectral remote sensing of cyanobacterial pigments as indicators for cell populations and toxins in eutrophic lakes. *Rem. Sensing Environ.* 114 (11), 2705–2718. doi:10.1016/j.rse.2010.06.006

Huot, Y., Brown, C. A., and Cullen, J. J. (2005). New algorithms for MODIS sun-induced chlorophyll fluorescence and a comparison with present data products. *Limnol. Oceanogr. Methods* 3 (2), 108–130. doi:10.4319/lom.2005.3.108

Huot, Y., Brown, C. A., and Cullen, J. J. (2007). Retrieval of phytoplankton biomass from simultaneous inversion of reflectance, the diffuse attenuation coefficient, and Sun-induced fluorescence in coastal waters. *J. Geophys. Res. Oceans* 112 (C6), 94. doi:10.1029/2006jc003794

Johnsen, G., and Sakshaug, E. (2007). Biooptical characteristics of PSII and PSI in 33 species (13 pigment groups) of marine phytoplankton, and the relevance for pulse-amplitude-modulated and fast-repetition-rate fluorometry 1. *J. Phycol.* 43 (6), 1236–1251. doi:10.1111/j.1529-8817.2007.00422.x

Jorge, D. S., Barbosa, C. C., De Carvalho, L. A., Affonso, A. G., Lobo, F. D. L., and Novo, E. M. D. M. (2017). Snr (signal-to-noise ratio) impact on water constituent retrieval from simulated images of optically complex amazon lakes. *Remote Sens.* 9 (7), 644.

Jupp, D., Kirk, J., and Harris, G. (1994). Detection, identification and mapping of cyanobacteria—using remote sensing to measure the optical quality of turbid inland waters. *Mar. Freshw. Res.* 45 (5), 801–828. doi:10.1071/mf9940801

Kravitz, J., Matthews, M., Bernard, S., and Griffith, D. (2020). Application of Sentinel 3 OLCI for chl-a retrieval over small inland water targets: successes and challenges. *Remote Sensing Environ.* 237, 111562. doi:10.1016/j.rse.2019.111562

Kudela, R. M., Hooker, S. B., Houskeeper, H. F., and McPherson, M. (2019). The influence of signal to noise ratio of legacy airborne and satellite sensors for simulating next-generation coastal and inland water products. *Remote Sensing* 11 (18), 2071. doi:10.3390/rs11182071

Kutser, T., Metsamaa, L., and Dekker, A. G. (2008). Influence of the vertical distribution of cyanobacteria in the water column on the remote sensing signal. *Coast. Shelf Sci.* 78 (4), 649–654. doi:10.1016/j.ecss.2008.02.024

Kutser, T., Metsamaa, L., Strömbeck, N., and Vahtmäe, E. (2006). Monitoring cyanobacterial blooms by satellite remote sensing. *Estuarine Coast. Shelf Sci.* 67 (1-2), 303–312.

Kutser, T. (2004). Quantitative detection of chlorophyll in cyanobacterial blooms by satellite remote sensing. *Limnol. Oceanogr.* 49 (6), 2179–2189. doi:10.4319/lo.2004.49.6.2179

Kutser, T., Soomets, T., Toming, K., Uiboupin, R., Arikas, A., Vahter, K., et al. (2018). Assessing the Baltic sea water quality with Sentinel-3 OLCI imagery, in 2018 IEEE/OES Baltic International Symposium (BALTIC), IEEE, 1–6.

Lain, L., and Bernard, S. (2018). The fundamental contribution of phytoplankton spectral scattering to ocean colour: implications for satellite detection of phytoplankton community structure. *Appl. Sci.* 8 (12), 2681. doi:10.3390/app8122681

Lain, L. R., Bernard, S., and Evers-King, H. (2014). Biophysical modelling of phytoplankton communities from first principles using two-layered spheres: equivalent Algal Populations (EAP) model. *Opt. express* 22 (14), 16745–16758.

Lain, L. R., Bernard, S., and Matthews, M. W. (2016). Biophysical modelling of phytoplankton communities from first principles using two-layered spheres: equivalent Algal Populations (EAP) model: erratum. *Opt. Express* 24 (24), 27423–27424. doi:10.1364/oe.24.027423

Lee, Z. P. (2003). Models, parameters, and approaches that used to generate wide range of absorption and backscattering spectra. *Ocean Color Algorithm Working Group IOCCG*. doi:10.1920/wp.cem.2003.1303

Lee, Z. (2006). *Remote sensing of inherent optical properties: fundamentals, tests of algorithms, and applications*.

Li, L., Li, L., and Song, K. (2015). Remote sensing of freshwater cyanobacteria: an extended IOP Inversion Model of Inland Waters (IIMIW) for partitioning absorption coefficient and estimating phycocyanin. *Remote Sensing Environ.* 157, 9–23. doi:10.1016/j.rse.2014.06.009

Li, Y., Zhang, H., Xue, X., Jiang, Y., and Shen, Q. (2018). Deep learning for remote sensing image classification: a survey. *WIREs Data Min. Knowl. Discov.* 8 (6), e1264. doi:10.1002/widm.1264

Liu, G., Simis, S. G., Li, L., Wang, Q., Li, Y., Song, K., et al. (2017). A four-band semi- analytical model for estimating phycocyanin in inland waters from simulated MERIS and OLCI data. *IEEE Trans. Geosci. Remote Sensing* 56 (3), 1374–1385.

Lu, Y., Li, L., Hu, C., Li, L., Zhang, M., Sun, S., et al. (2016). Sunlight induced chlorophyll fluorescence in the near-infrared spectral region in natural waters: interpretation of the narrow reflectance peak around 761 nm. *J. Geophys. Res. Oceans* 121 (7), 5017–5029. doi:10.1002/2016jc011797

Ma, L., Liu, Y., Zhang, X., Ye, Y., Yin, G., and Johnson, B. A. (2019). Deep learning in remote sensing applications: a meta-analysis and review. *ISPRS J. Photogram. Rem. sensing* 152, 166–177. doi:10.1016/j.isprsjprs.2019.04.015

Martins, V., Barbosa, C., de Carvalho, L., Jorge, D., Lobo, F., and Novo, E. (2017). Assessment of atmospheric correction methods for Sentinel-2 MSI images applied to Amazon floodplain lakes. *Rem. Sensing* 9 (4), 322. doi:10.3390/rs9040322

Matthews, M., and Bernard, S. (2013). Characterizing the absorption properties for remote sensing of three small optically-diverse South African reservoirs. *Rem. Sensing* 5 (9), 4370–4404. doi:10.3390/rs5094370

Matthews, M. W. (2011). A current review of empirical procedures of remote sensing in inland and near-coastal transitional waters. *Int. J. Rem. Sensing* 32 (21), 6855–6899. doi:10.1080/01431161.2010.512947

Matthews, M. W., Bernard, S., and Robertson, L. (2012). An algorithm for detecting trophic status (chlorophyll-a), cyanobacterial-dominance, surface scums and floating vegetation in inland and coastal waters. *Rem. Sensing Environ.* 124, 637–652. doi:10.1016/j.rse.2012.05.032

Maxwell, A. E., Warner, T. A., and Fang, F. (2018). Implementation of machine-learning classification in remote sensing: an applied review. *Int. J. Remote Sensing* 39 (9), 2784–2817. doi:10.1080/01431161.2018.1433343

Metsamma, L., Kutser, T., and Strömbeck, N. (2006). Recognising cyanobacterial blooms based on their optical signature: a modelling study. *Boreal Environ. Res.* 11 (6), 493–506.

Mishra, S., Mishra, D. R., Lee, Z., and Tucker, C. S. (2013). Quantifying cyanobacterial phycocyanin concentration in turbid productive waters: a quasi-analytical approach. *Rem. Sensing Environ.* 133, 141–151. doi:10.1016/j.rse.2013.02.004

Mishra, S., and Mishra, D. R. (2012). Normalized difference chlorophyll index: a novel model for remote estimation of chlorophyll-a concentration in turbid productive waters. *Rem. Sensing Environ.* 117, 394–406. doi:10.1016/j.rse.2011.10.016

Mobley, C. D., Sundman, L. K., and Boss, E. (2002). Phase function effects on oceanic light fields. *Appl. Opt.* 41 (6), 1035–1050. doi:10.1364/ao.41.001035

Moore, T. S., Campbell, J. W., and Dowell, M. D. (2009). A class-based approach to characterizing and mapping the uncertainty of the MODIS ocean chlorophyll product. *Rem. Sensing Environ.* 113 (11), 2424–2430. doi:10.1016/j.rse.2009.07.016

Moore, T. S., Campbell, J. W., and Hui Feng, H. (2001). A fuzzy logic classification scheme for selecting and blending satellite ocean color algorithms. *IEEE Trans. Geosci. Rem. Sensing* 39 (8), 1764–1776. doi:10.1109/36.942555

Moore, T. S., Dowell, M. D., Bradt, S., and Ruiz Verdu, A. (2014). An optical water type framework for selecting and blending retrievals from bio-optical algorithms in lakes and coastal waters. *Rem. Sensing Environ.* 143, 97–111. doi:10.1016/j.rse.2013.11.021

Moses, S. A., Janaki, L., Joseph, S., and Joseph, J. (2015). Water quality prediction capabilities of WASP model for a tropical lake system. *Lakes Reserv. Res. Manag.* 20 (4), 285–299. doi:10.1111/lre.12110

Moses, W. J., Gitelson, A. A., Berdnikov, S., and Povazhnyy, V. (2009). Estimation of chlorophyll-a concentration in case II waters using MODIS and MERIS data—successes and challenges. *Environ. Res. Lett.* 4 (4), 045005. doi:10.1088/1748-9326/4/4/045005

Mouw, C. B., Greb, S., Aurin, D., DiGiacomo, P. M., Lee, Z., Twardowski, M., et al. (2015). Aquatic color radiometry remote sensing of coastal and inland waters: challenges and recommendations for future satellite missions. *Remote Sensing Environ.* 160, 15–30. doi:10.1016/j.rse.2015.02.001

Muller-Karger, F. E., Hestir, E., Ade, C., Turpie, K., Roberts, D. A., Siegel, D., et al. (2018). Satellite sensor requirements for monitoring essential biodiversity variables of coastal ecosystems. *Ecol. Appl.* 28 (3), 749–760. doi:10.1002/eap.1682

Odermatt, D., Gitelson, A., Brando, V. E., and Schaepman, M. (2012). Review of constituent retrieval in optically deep and complex waters from satellite imagery. *Rem. Sensing Environ.* 118, 116–126. doi:10.1016/j.rse.2011.11.013

Ogashawara, I. (2020). Determination of phycocyanin from space—a Bibliometric analysis. *Rem. Sensing* 12 (3), 567. doi:10.3390/rs12030567

Organelli, E., Claustre, H., Bricaud, A., Barbieux, M., Uitz, J., D'Ortenzio, F., et al. (2017). Bio-optical anomalies in the world's oceans: an investigation on the diffuse attenuation coefficients for downward irradiance derived from Biogeochemical Argo float measurements. *J. Geophys. Res. Oceans* 122 (5), 3543–3564. doi:10.1002/2016jc012629

Pahlevan, N., Smith, B., Schalles, J., Binding, C., Cao, Z., Ma, R., et al. (2020). Seamless retrievals of chlorophyll-a from Sentinel-2 (MSI) and Sentinel-3

(OLCI) in inland and coastal waters: a machine-learning approach, *Rem. Sensing Environ.* 240, 111604. doi:10.1016/j.rse.2019.111604

Palmer, S. C. J., Hunter, P. D., Lankester, T., Hubbard, S., Spyrakos, E., Tyler, A. N., et al. (2015a). Validation of Envisat MERIS algorithms for chlorophyll retrieval in a large, turbid and optically-complex shallow lake. *Rem. Sensing Environ.* 157, 158–169. doi:10.1016/j.rse.2014.07.024

Palmer, S. C. J., Odermatt, D., Hunter, P. D., Brockmann, C., Présing, M., Balzter, H., et al. (2015c). Satellite remote sensing of phytoplankton phenology in Lake Balaton using 10 years of MERIS observations. *Rem. Sensing Environ.* 158, 441–452. doi:10.1016/j.rse.2014.11.021

Palmer, S. C., Kutser, T., and Hunter, P. D. (2015b). *Remote sensing of inland waters: Challenges, progress and future directions*.

Peterson, K., Sagan, V., Sidike, P., Cox, A., and Martinez, M. (2018). Suspended sediment concentration estimation from Landsat Imagery along the Lower Missouri and Middle Mississippi Rivers using an extreme learning machine. *Rem. Sensing* 10 (10), 1503. doi:10.3390/rs10101503

Peterson, K. T., Sagan, V., Sidike, P., Hasenmueller, E. A., Sloan, J. J., and Knouft, J. H. (2019). Machine learning-based ensemble prediction of water-quality variables using feature-level and decision-level fusion with proximal remote sensing. *Photogram. Eng. Rem. Sensing* 85 (4), 269–280. doi:10.14358/pers.85.4.269

Peterson, K. T., Sagan, V., and Sloan, J. J. (2020). Deep learning-based water quality estimation and anomaly detection using Landsat-8/Sentinel-2 virtual constellation and cloud computing. *GIScience Rem. Sensing* 57 (4), 510–525. doi:10.1080/15481603.2020.1738061

Qi, L., Hu, C., Duan, H., Cannizzaro, J., and Ma, R. (2014). A novel MERIS algorithm to derive cyanobacterial phycocyanin pigment concentrations in a eutrophic lake: theoretical basis and practical considerations. *Rem. Sensing Environ.* 154, 298–317. doi:10.1016/j.rse.2014.08.026

Qi, L., Lee, Z., Hu, C., and Wang, M. (2017). Requirement of minimal signal-to-noise ratios of ocean color sensors and uncertainties of ocean color products. *J. Geophys. Res. Oceans* 122 (3), 2595–2611. doi:10.1002/2016jc012558

Quirantes, A., and Bernard, S. (2004). Light scattering by marine algae: two-layer spherical and nonspherical models. *J. Quant. Spectrosc. Radiat. Transf.* 89 (1), 311–321. doi:10.1016/j.jqsrt.2004.05.031

Ramsay, J. O., and Silverman, B. (2006). *Functional data analysis*. Hoboken.

Randolph, K., Wilson, J., Tedesco, L., Li, L., Pascual, D. L., and Soyeux, E. (2008). Hyperspectral remote sensing of cyanobacteria in turbid productive water using optically active pigments, chlorophyll a and phycocyanin. *Rem. Sensing Environ.* 112 (11), 4009–4019. doi:10.1016/j.rse.2008.06.002

Roesler, C. S., and Perry, M. J. (1995). *In situ* phytoplankton absorption, fluorescence emission, and particulate backscattering spectra determined from reflectance. *J. Geophys. Res.* 100 (C7), 13279–13294. doi:10.1029/95jc00455

Ruescas, A., Hieronymi, M., Mateo-Garcia, G., Koponen, S., Kallio, K., and Camps-Valls, G. (2018). Machine learning regression approaches for colored dissolved organic matter (CDOM) retrieval with S2-MSI and S3-OLCI simulated data. *Rem. Sensing* 10 (5), 786. doi:10.3390/rs10050786

Ruiz-Verdu, R., Koponen, S., Heege, T., Doerffer, R., Brockmann, C., Kallio, K., et al. (2008). *Development of MERIS lake water algorithms: validation results from Europe*.

Sagan, V., Peterson, K. T., Maimaitijiang, M., Sidike, P., Sloan, J., Greeling, B. A., et al. (2020). Monitoring inland water quality using remote sensing: potential and limitations of spectral indices, bio-optical simulations, machine learning, and cloud computing. *Earth-Science Rev.* 10, 3187.

Shi, K., Zhang, Y., Zhu, G., Liu, X., Zhou, Y., Xu, H., et al. (2015). Long-term remote monitoring of total suspended matter concentration in Lake Taihu using 250 m MODIS-Aqua data. *Rem. Sensing Environ.* 164, 43–56. doi:10.1016/j.rse.2015.02.029

Simis, S. G. H., Huot, Y., Babin, M., Seppälä, J., and Metsamaa, L. (2012). Optimization of variable fluorescence measurements of phytoplankton communities with cyanobacteria. *Photosynth. Res.* 112 (1), 13–30. doi:10.1007/s11120-012-9729-6

Simis, S. G. H., and Kauko, H. M. (2012). *In vivo* mass-specific absorption spectra of phycobilipigments through selective bleaching. *Limnol. Oceanogr. Methods* 10 (4), 214–226. doi:10.4319/lom.2012.10.214

Simis, S. G. H., Peters, S. W. M., and Gons, H. J. (2005). Remote sensing of the cyanobacterial pigment phycocyanin in turbid inland water. *Limnol. Oceanogr.* 50 (1), 237–245. doi:10.4319/lo.2005.50.1.0237

Simis, S. G. H., Ruiz-Verdú, A., Domínguez-Gómez, J. A., Peña-Martinez, R., Peters, S. W. M., and Gons, H. J. (2007). Influence of phytoplankton pigment composition on remote sensing of cyanobacterial biomass. *Rem. Sensing Environ.* 106 (4), 414–427. doi:10.1016/j.rse.2006.09.008

Smith, M. E., Lain, L. R., and Bernard, S. (2018). An optimized Chlorophyll a switching algorithm for MERIS and OLCI in phytoplankton-dominated waters. *Rem. Sensing Environ.* 215, 217–227. doi:10.1016/j.rse.2018.06.002

Spyrakos, E., O'Donnell, R., Hunter, P. D., Miller, C., Scott, M., Simis, S. G., et al. (2018). Optical types of inland and coastal waters. *Limnol. Oceanogr.* 63 (2), 846–870. doi:10.1002/lno.10674

Stumpf, R. P., Davis, T. W., Wynne, T. T., Graham, J. L., Loftin, K. A., Johengen, T. H., et al. (2016). Challenges for mapping cyanotoxin patterns from remote sensing of cyanobacteria. *Harmful Algae* 54, 160–173. doi:10.1016/j.hal.2016.01.005

Twardowski, M. S., Boss, E., Macdonald, J. B., Pegau, W. S., Barnard, A. H., and Zaneveld, J. R. V. (2001). A model for estimating bulk refractive index from the optical backscattering ratio and the implications for understanding particle composition in case I and case II waters. *J. Geophys. Res.* 106 (C7), 14129–14142. doi:10.1029/2000jc000404

Vaillancourt, R. D., Brown, C. W., Guillard, R. R., and Balch, W. M. (2004). Light backscattering properties of marine phytoplankton: relationships to cell size, chemical composition and taxonomy. *J. Plankt. Res.* 26 (2), 191–212. doi:10.1093/plankt/fbh012

Vantrepotte, V., Loisel, H., Dessailly, D., and Mériaux, X. (2012). Optical classification of contrasted coastal waters. *Rem. Sensing Environ.* 123, 306–323. doi:10.1016/j.rse.2012.03.004

Walsby, A. E., Hayes, P. K., and Boje, R. (1995). The gas vesicles, buoyancy and vertical distribution of cyanobacteria in the Baltic Sea. *Eur. J. Phycol.* 30 (2), 87–94. doi:10.1080/09670269500650851

Wang, M., and Gordon, H. R. (2018). Sensor performance requirements for atmospheric correction of satellite ocean color remote sensing. *Opt. Expr.* 26 (6), 7390–7403. doi:10.1364/oe.26.007390

Watanabe, F. S., Miyoshi, G. T., Rodrigues, T. W., Bernardo, N. M., Rotta, L. H., Alcântara, E., et al. (2020). Inland water's trophic status classification based on machine learning and remote sensing data. *Rem. Sens. Appl.* 54, 100326.

Whitmire, A. L., Boss, E., Cowles, T. J., and Pegau, W. S. (2007). Spectral variability of the particulate backscattering ratio. *Opt. Expr.* 15 (11), 7019–7031. doi:10.1364/oe.15.007019

Xi, H., Hieronymi, M., Röttgers, R., Krasemann, H., and Qiu, Z. (2015). Hyperspectral differentiation of phytoplankton taxonomic groups: a comparison between using remote sensing reflectance and absorption spectra. *Rem. Sensing* 7 (11), 14781–14805. doi:10.3390/rs71114781

Yacobi, Y. Z., Köhler, J., Leunert, F., and Gitelson, A. (2015). Phycocyanin-specific absorption coefficient: eliminating the effect of chlorophylls absorption. *Limnol. Oceanogr. Methods* 13 (4), 157–168. doi:10.1002/lom3.10015

Zhou, W., Wang, G., Sun, Z., Cao, W., Xu, Z., Hu, S., et al. (2012). Variations in the optical scattering properties of phytoplankton cultures. *Opt. Expr.* 20 (10), 11189–11206. doi:10.1364/oe.20.011189

Conflict of Interest: Author MM was employed by the company CyanoLakes (Pty) Ltd.

The remaining authors declare that the research was conducted in the absence of any commercial or financial relationships that could be construed as a potential conflict of interest.

Copyright © 2021 Kravitz, Matthews, Lain, Fawcett and Bernard. This is an open-access article distributed under the terms of the Creative Commons Attribution License (CC BY). The use, distribution or reproduction in other forums is permitted, provided the original author(s) and the copyright owner(s) are credited and that the original publication in this journal is cited, in accordance with accepted academic practice. No use, distribution or reproduction is permitted which does not comply with these terms.

frontiers in Environmental Science

ORIGINAL RESEARCH
published: 01 April 2021
doi: 10.3389/fenvs.2021.642906

UAV to Inform Restoration: A Case Study From a California Tidal Marsh

John Haskins[1], Charlie Endris[2], Alexandra S. Thomsen[1,3], Fuller Gerbl[1,2], Monique C. Fountain[1] and Kerstin Wasson[1,4]*

[1] Elkhorn Slough National Estuarine Research Reserve, Watsonville, CA, United States, [2] Moss Landing Marine Laboratories, Moss Landing, CA, United States, [3] Department of Applied Environmental Science, California State University, Monterey Bay, Seaside, CA, United States, [4] Ecology and Evolutionary Biology, University of California, Santa Cruz, Santa Cruz, CA, United States

Monitoring of environmental restoration is essential to communicate progress and improve outcomes of current and future projects, but is typically done in a very limited capacity due to budget and personnel constraints. Unoccupied aerial vehicles (UAVs) have been used in a variety of natural and human-influenced environments and have been found to be time- and cost-efficient, but have not yet been widely applied to restoration contexts. In this study, we evaluated the utility of UAVs as an innovative tool for monitoring tidal marsh restoration. We first optimized methods for creating high-resolution orthomosaics and Structure from Motion digital elevation models from UAV imagery by conducting experiments to determine an optimal density of ground control points (GCPs) and flight altitude for UAV monitoring of topography and new vegetation. We used elevation models and raw and classified orthomosaics before, during, and after construction of the restoration site to communicate with various audiences and inform adaptive management. We found that we could achieve 1.1 cm vertical accuracy in our elevation models using 2.1 GCPs per hectare at a flight altitude of 50 m. A lower flight altitude of 30 m was more ideal for capturing patchy early plant cover while still being efficient enough to cover the entire 25-hectare site. UAV products were valuable for several monitoring applications, including calculating the volume of soil moved during construction, tracking whether elevation targets were achieved, quantifying and examining the patterns of vegetation development, and monitoring topographic change including subsidence, erosion, and creek development. We found UAV monitoring advantageous for the ability to survey areas difficult to access on foot, capture spatial variation, tailor timing of data collection to research needs, and collect a large amount of accurate data rapidly at relatively low cost, though with some compromise in detail compared with field monitoring. In summary, we found that UAV data informed the planning, implementation and monitoring phases of a major landscape restoration project and could be valuable for restoration in many habitats.

Keywords: remote sensing, tidal marsh, restoration, topography, digital elevation model, image classification, unmanned aerial vehicle, unoccupied aerial systems

OPEN ACCESS

Edited by:
Wesley Moses, United States Naval Research Laboratory, United States

Reviewed by:
Kristin B. Byrd, United States Geological Survey (USGS), United States
Tom William Bell, University of California, Santa Barbara, United States

***Correspondence:**
Alexandra S. Thomsen
thomsen.alexandra@gmail.com

Specialty section:
This article was submitted to Environmental Informatics and Remote Sensing, a section of the journal Frontiers in Environmental Science

Received: *17 December 2020*
Accepted: *02 March 2021*
Published: *01 April 2021*

Citation:
Haskins J, Endris C, Thomsen AS, Gerbl F, Fountain MC and Wasson K (2021) UAV to Inform Restoration: A Case Study From a California Tidal Marsh. Front. Environ. Sci. 9:642906. doi: 10.3389/fenvs.2021.642906

INTRODUCTION

Human activities including land conversion, resource exploitation, pollution, species introductions, and hydrologic alteration have changed ecosystems globally (Halpern et al., 2008; Gedan et al., 2009). Loss of foundation species is particularly concerning because these species provide habitat and modulate ecosystem processes (Dayton, 1972; Ellison, 2019). In response to negative anthropogenic effects on landscapes, land managers are increasingly undertaking restoration projects to support recovery of ecosystems and the valuable services they provide (Gedan et al., 2009; Palmer et al., 2016). A key element of environmental restoration is recovery of foundation species due to their influential ecological roles (Pastorok et al., 1997). When foundation species distributions are limited by environmental gradients such as moisture or salinity, restoration managers must design sites with appropriate landscape characteristics so that the desired species can successfully establish (Pastorok et al., 1997; Yando et al., 2019).

Monitoring is a critical component of any type of restoration (Pastorok et al., 1997). Restoration projects are often required by funders or permitters to set quantitative targets and monitor progress toward those goals (McDonald et al., 2016). Using monitoring data, restoration managers and scientists can conduct adaptive management and better understand the ecological processes driving restoration success (McDonald et al., 2016). Managers can also leverage monitoring data to engage community audiences by sharing information about local projects. In the past, monitoring tools consisted primarily of traditional field survey techniques, which are often time-consuming (Chabot and Bird, 2013), or remote sensing products available from airplanes or satellites, which are often only available at low spatial and temporal resolution (Roegner et al., 2008; Anderson and Gaston, 2013; Johnston, 2019). Despite its importance, monitoring of many restoration projects is fairly limited. Managers may only be able to conduct the minimum amount of monitoring that satisfies permit requirements (Zedler, 2000b) due to staffing limitations or funding restrictions that limit the amount or percentage of funds available. Unoccupied aerial vehicles (UAVs) offer a less expensive alternative to traditional methods, and UAV methods are beginning to be explored in restoration projects (Knoth et al., 2013; Marteau et al., 2017; Buters et al., 2019a; Padró et al., 2019a; Reis et al., 2019; Pérez et al., 2020).

Restoration monitoring across a variety of habitat types often includes both physical and biological elements (Pastorok et al., 1997; Roegner et al., 2008). Elevation is a major physical monitoring component in restoration (Roegner et al., 2008) given its key role in structuring ecological communities (Watson, 1835). Microtopography (variability on the scale of ∼1 cm to 1 m) and drainage patterns are also critical in restoration planning and monitoring. These factors influence hydrologic conditions (Jarzemsky et al., 2013), soil moisture and temperature (Diefenderfer et al., 2018), with implications for survival of plantings and natural colonization in restoration (Barry et al., 1996). Foundation species are a key biological monitoring target because in providing habitat for other species, they have a strong impact on the outcome of restoration (Pastorok et al., 1997).

Tidal marshes are a major habitat type targeted for restoration due to extensive losses globally (Gedan et al., 2009). Halophytic plants are important foundation species in marshes, with most only flourishing in a very narrow range of elevation, between mean high water and mean higher high water (Larson, 2001). Human activities that cause the landscape elevation to decrease, including diking and draining and groundwater overdraft, are common drivers of tidal marsh loss (Kennish, 2001; Kirwan and Megonigal, 2013). Accelerated sea level rise and restrictions to sediment supply also lead to loss of elevation relative to water levels (Kirwan and Megonigal, 2013; Weston, 2014; Watson et al., 2017). Therefore, a major component of marsh restoration is establishing appropriate elevation of the marsh landscape relative to sea level (Cahoon et al., 2019). Post-restoration monitoring informs success by tracking whether that elevation is met and maintained (Roegner et al., 2008). Sediment or soil addition is the main mechanism for restoring "elevation capital," the accumulated material that establishes wetland height in the tidal frame (Cahoon et al., 2019), enhancing marsh resilience to relative sea level rise. The amount of added material may vary depending on the initial condition of the degraded marsh, continued human impacts, and project goals (Raposa et al., 2020). In soil addition projects, elevation monitoring informs how much vertical gain is needed to create a resilient restoration site. Dense creek networks are another key consideration in marsh restoration to avoid waterlogging of plants while allowing for sufficient inundation (Zedler et al., 1999). Tidal creek size and distribution in marshes affect plant species distributions (Zedler et al., 1999; Sanderson et al., 2001), height and density (Wu et al., 2020). Monitoring the tidal creek network is therefore important to understand drainage and vegetation patterns (Roegner et al., 2008; Jarzemsky et al., 2013). In addition to the physical factors influencing it, vegetation itself is also a key monitoring metric often used to evaluate restoration success (Roegner et al., 2008; McDonald et al., 2016).

Our goal was to develop and test techniques for using UAVs as a monitoring tool for tidal marsh restoration, using a major tidal marsh restoration project in California, United States as a model system. While studies in mature marshes (Kalacska et al., 2017), restored drylands (Pérez et al., 2020), and simulated restoration contexts (Buters et al., 2019b) have provided some proof-of-concept for fine-scale restoration monitoring, we know of no published studies that have implemented UAV monitoring of topography or early colonization at marsh restoration sites, and therefore generated appropriate protocols ourselves. Because elevation and topography are major components of marsh restoration, the underlying backbone of our UAV monitoring was establishing calibration procedures that enable accurate detection of topography changes. This involved establishing an appropriate network of ground control points (GCPs) to tie UAV imagery to known locations, an essential step in creating accurate elevation products (Harwin and Lucieer, 2012; Marteau et al., 2017; Sturdivant et al., 2017). We also needed to ensure that newly colonized plants were detectable in UAV

imagery, which involved testing different flight altitudes (a major determinant of image resolution; Cruzan et al., 2016). In addition to piloting technical approaches to UAV monitoring, we developed imagery and analysis products designed to inform restoration stakeholders. We conducted UAV monitoring before, during, and after construction to inform restoration work and track success. Our specific objectives were to monitor construction progress, estimate the amount of soil used during construction, detect topography changes in tidal creeks and on the marsh plain following construction, and track development of vegetation cover. We compared various inputs and attributes of UAV monitoring with field methods — terrestrial laser scanner (TLS) and surface elevation tables (SET) — and with airborne light detection and ranging (LIDAR) to evaluate the relative benefits of different topography monitoring methods. Overall, we developed, tested and implemented novel monitoring protocols for application of UAV to tidal marsh restoration monitoring and used UAV products to communicate about the restoration with a wide range of stakeholders, including project managers, funders, scientists and the public.

MATERIALS AND METHODS

Study System

We conducted this study at a tidal marsh restoration site in Elkhorn Slough, an estuary in Monterey Bay, Central California, United States (**Figure 1**). Because wetland area on California's coast is relatively limited, Elkhorn Slough's marsh area is particularly significant for providing benefits including habitat for hundreds of species and water quality improvement (Caffrey et al., 2002). Unfortunately, over half of Elkhorn Slough's intact marsh area has been lost over the past 150 years, primarily due to diking and draining (Van Dyke and Wasson, 2005). Much of Elkhorn Slough's remaining marsh area sits low in the tidal frame and is therefore highly vulnerable to inundation-related loss under projected sea level rise scenarios (Wasson et al., 2012).

In 2004, the Elkhorn Slough National Estuarine Research Reserve (ESNERR) initiated the Tidal Wetland Program, an ecosystem-based management initiative, to address rapid changes in the estuary. The result of the decision-making process, which involved input from numerous stakeholders, was prioritization of marsh restoration (Wasson et al., 2015). ESNERR completed construction on a 25-hectare restoration project at Hester Marsh on the southern side of Elkhorn Slough in 2018 (**Figure 1**). Tidal exchange was cut off during the construction period of restoration and resumed when construction ended on August 8, 2018. Construction activities involved approximately 250,000 cubic yards of soil addition on a degraded and subsided marsh, which had converted mostly to unvegetated mudflat following human impacts such as diking and draining. Most of the soil used to elevate the marsh plain originated from an adjacent hillside that was formerly used for agriculture, was scraped during construction to provide soil, and is being restored to native grassland. The largest tidal creeks were left intact and secondary and tertiary creeks were excavated to resemble the historical creek network following soil addition.

Objectives for the restoration project addressed elements including marsh plain elevation, tidal creeks, and the marsh community. The construction target for initial elevation was 1.95 m NAVD88, near the upper limit of marsh plant distributions in Elkhorn Slough, and the marsh plain was expected to settle over time to a long-term target elevation of 1.89 m NAVD88. While some natural changes and minor developments to the tidal creek network were expected, main objectives for creeks were to mimic natural drainage patterns and limit bank erosion. High vegetation cover was another key objective, representing development of a healthy marsh community (Fountain et al., 2020). The Hester Marsh restoration project provided an opportunity for pilot testing of UAV methods for monitoring to evaluate progress toward these goals.

UAV Equipment

In October 2015, Tombolo Mapping Lab & Center for Habitat Studies at Moss Landing Marine Labs used a fixed-wing UAV (E384; Event 38 Unmanned Systems, Inc., Richfield, OH, United States) with a Canon SX260 HS 12-megapixel camera (Canon Inc., Tokyo, Japan) to collect aerial imagery at the study site. For all flights during and after site construction, we collected imagery with a DJI Phantom 4 Pro quadcopter (SZ DJI Technology Co., Ltd., Shenzhen, China) equipped with a 20-megapixel camera that collects visible spectrum (RGB) data. The quadcopter also carries a near infrared (NIR) and red-edge sensor (Double 4k sensor, Sentera Inc., Minneapolis, MN, United States), but use of these data was limited to testing of vegetation monitoring methods, where inclusion of NIR data was evaluated for one flight.

Establishing Methods for Topography Monitoring

We created digital elevation models (DEMs) to monitor topography using UAV-collected photos and field-surveyed GCPs. The DEMs we used throughout our monitoring were digital surface models (DSMs), which by nature represent the elevation of the surface and thus, where there is dense vegetation or other features, the top of those features (Cruzan et al., 2016). We did not expect the use of DSMs to be an issue for our topography monitoring, as vegetation was absent or minimal in most of our imagery.

In order to determine the optimal flight altitude coupled with the minimum number of GCPs that maximized the accuracy of the results, we conducted a GCP density experiment involving a series of flights over an area of roughly 6.25 hectares within the restoration site. We compared vertical accuracy of DEMs created with varying densities of GCPs (0 – 6.4 GCPs/ha) and collected imagery at four flight altitudes (50 m, 75 m, 100 m, and 116 m; **Table 1**), resulting in a total of 34 DEMs that were assessed for accuracy. We encountered processing issues for the 75 m imagery georeferenced with 0 GCPs and 2 GCPs per hectare, so excluded these from our analysis. We sought to determine the threshold above which increased GCP density did not lead to notable decrease in root mean squared error in the vertical direction (RMSE; Coveney and Roberts, 2017).

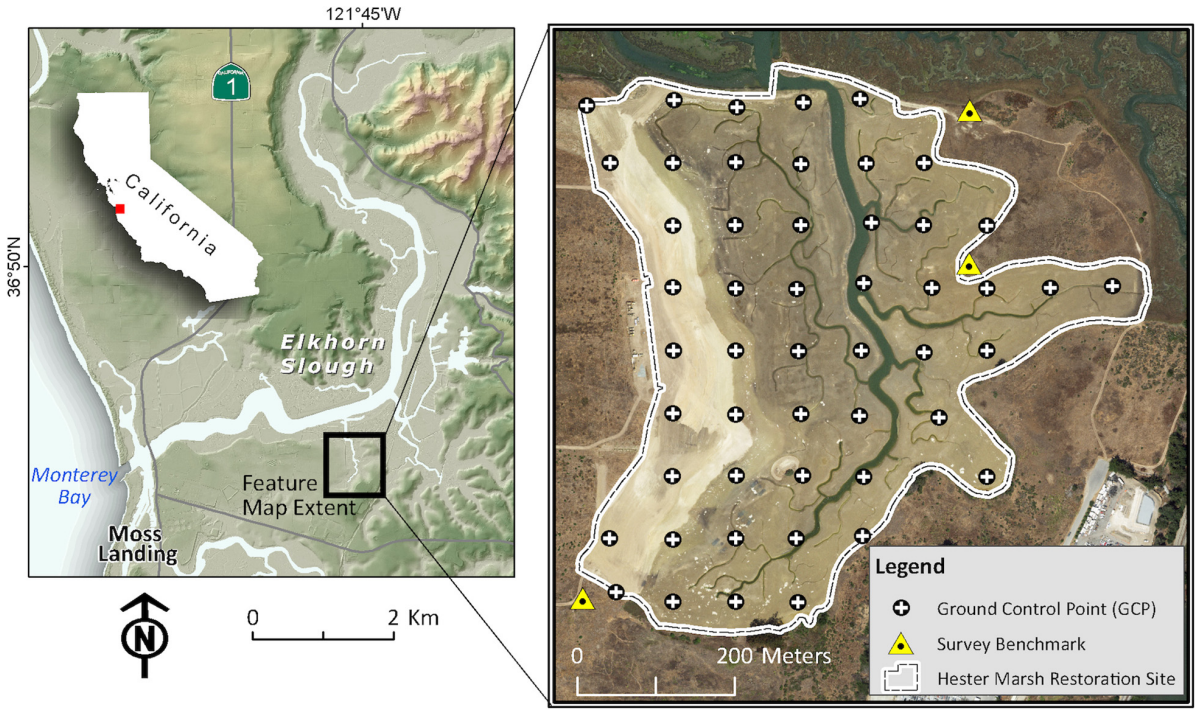

FIGURE 1 | Map of the Hester Marsh restoration site in Elkhorn Slough, an estuary in Central California, United States. A grid of ground control points (GCPs) was established for linking UAV imagery to known locations on the ground. Elevations were surveyed at GCPs and referenced to survey benchmarks to create digital elevation models.

TABLE 1 | General information for UAV flights conducted at six different altitudes for the GCP density and vegetation-flight altitude experiments.

Altitude (m)	Flight time (min/ha)	Orthomosaic resolution (cm)	Images per ha (#)	Total file size of all images (MB)	Total file size of orthomosaic (MB)
10	18.8	0.74	742	8850	1800
30	5.6	0.76	119 (95*)	1410 (170*)	1780
50	0.9	1.5	83	2012	790
75	0.4	1.9	12	1190	125
100	0.3	2.5	5.6	570	81
116	0.2	2.9	4.2	430	84

*One flight altitude used in the vegetation-flight altitude experiment is omitted (60 m) because of similarity with the 50 m flight.Values for the 10 m and 30 m flights are scaled from flights covering 1.6 ha; for the remaining flights, values are scaled from flights originally covering 13.8 hectares. Values assume an overlap of 75% frontal and 70% side overlap. Flight time will vary based on geometry of the area surveyed and flight path of the UAV. Image size and orthomosaic resolution will vary based on camera resolution. *Additional images and file size for near infrared data in parentheses.*

The test site was a portion of the restoration site that had recently been filled with upland soils, creating a mostly level and unvegetated patch of ground. Using ArcGIS (v. 10.3; Esri, Redlands, CA, United States), we established a "fishnet" grid of 40 points spaced approximately 35 – 50 m apart. We created forty GCPs using numbered, 12" round white and black five-gallon bucket lids, and deployed them in the field using a handheld Trimble GPS. We used a Trimble VX TLS (Trimble Navigation, Sunnyvale, CA, United States) to survey the horizontal and vertical position of each GCP, as well as 66 randomly spaced check points. Elevation was referenced to a local tidal benchmark (NAVD88). Vertical accuracy of the TLS survey data was approximately ± 1 cm, slightly better than expected from a traditional RTK survey which would also require use of a base station, rover, and radio antenna.

Imagery was collected with 75% frontal and 65% side overlap, the default in our flight planning software (DroneDeploy, San Francisco, CA, United States). We used Agisoft Metashape software (v. 1.6.3 10732; Agisoft LLC, St. Petersburg, Russia) to create orthomosaics and digital elevation models (DEMs) using Structure from Motion (SfM) principles. We used Agisoft's batch processing function to build orthomosaics and DEMs from the images collected during each UAV flight (details in **Supplementary Table 1**). All images (58 – 274 per flight) were georeferenced with coordinate system WGS84 / UTM zone 10N. Photos were manually georeferenced with GCPs in Agisoft

Metashape. We used these basic processing steps to produce all DEMs and orthomosaics described throughout this study (except for the vegetation-flight altitude experiment), using the GCP density identified through this experiment for all flights beginning in August 2018. To evaluate vertical accuracy, check point elevations collected in the field were used to extract elevations from the DEMs using ArcMap Spatial Analyst. We calculated the difference between the field-surveyed check point elevations and DEM elevations and computed the accuracy (measured as RMSE) for the 34 resulting DEMs. We also evaluated horizontal accuracy (RMSE) for select images by creating points representing the center locations of the GCPs visible in orthoimagery and used the Point Distance tool to calculate the horizontal offset from the TLS-derived positions. We calculated additional error metrics for the highest-resolution (50 m altitude) imagery.

Comparison of UAV and Other Topography Monitoring Methods

We compared three variations of UAV topography data collection with traditional field methods – TLS and SETs – and with airborne LIDAR to evaluate relative benefits of different approaches. The three UAV methods we evaluated used different georeferencing techniques: 1) UAV with onboard uncorrected global navigation satellite systems (GNSS), referred to as UAV–GNSS; 2) UAV with GCPs, surveyed using real-time kinematic (RTK) positioning and evaluated using independent check points, referred to as UAV–GCP; and 3) UAV with post-processed kinematic (PPK) dual-frequency differential GNSS corrected using either a base station in the study area or a nearby CORS station (Continuously Operating Reference Station), referred to as UAV–PPK. We compared these methods based on spatial coverage, vertical ($RMSE_z$) and horizontal ($RMSE_r$) accuracy, initial cost investment, training requirements, time and personnel required for one survey, and temporal and spatial resolution. Training requirements are categorized as "Low" (no prior experience or certification needed), "Moderate" (some experience with the equipment and specific licensing), or "High" (extensive field experience with the equipment and specific licensing).

We report horizontal and vertical error values for the UAV–GNSS and UAV–GCP methods from our GCP density experiment. The values for the UAV–GCP method are based on the GCP density and flight altitude we selected as optimal through this experiment. For the UAV–GNSS method, we used horizontal and vertical error values from imagery collected at that same flight altitude, not georeferenced using any GCPs. The horizontal error value for the UAV–PPK method is from a study comparing UAV georeferencing techniques (Padró et al., 2019b). The authors report horizontal accuracy as error in the radial direction, which includes both X and Y error. Suggested spatial resolution is the DEM cell size we believe to be appropriate based on horizontal error values.

To estimate costs of the different UAV approaches, we considered the aircraft and key accessories, software, and ground control points and equipment to survey them (for details see **Supplementary Table 2**). Although one-time rental fees may greatly reduce the investment costs of UAV equipment, the need for repeat surveys for long-term monitoring makes purchasing equipment less costly. To estimate time requirements for the UAV methods, we considered mission preparation (Haskins, 2020), the flight itself, GCP layout and surveying, and post-processing (details in **Supplementary Table 3**). Passive computer processing time to create the orthomosaics and DEMs is not included in the table since it will vary considerably depending on computer hardware, processing software and specific processing parameters. All UAV flight times assume a 65 m flight altitude covering a 42 ha area with the Phantom 4 Pro quadcopter. Spatial coverage will vary significantly based on the UAV type, total available battery life, flight altitude, and ability to maintain line of sight. The value we report is based on our experience with the Phantom 4 Pro quadcopter, flying at an altitude of 65 m with three batteries available and is intended to give the reader a reference.

To determine TLS error values for comparison with other methods, we identified horizontal and vertical errors during repetitive Trimble VX Spatial Station setups that measured coordinates of established control points. Suggested spatial resolution is based on accuracy of digital surface models created from surveyed point clouds, which is directly related to point spacing. Initial investment cost is based on a 2020 estimate of purchasing the survey equipment new and includes the spatial station, survey controller, batteries, tripods, target reflectors, survey rod, and carrying cases. Daily rental costs, alternatively, may range between $300 and $600. Spatial coverage assumes a survey area measuring 80 m × 80 m with two or more station setups and a point cloud spacing of approximately 10 cm. Time and personnel requirements include a minimum of one survey technician for a daily survey of an area this size and for post-processing.

Accuracy values for SET monitoring are based on the fact that SET pins measure the exact same location on the marsh surface during each successive survey. Unlike the other survey methods that produce dense point clouds and DSMs, SETs are generally limited to a few locations in a marsh and are not intended to be used for broad spatial analyses. Therefore, both spatial resolution and spatial coverage represent the approximate total area covered by a single SET. Initial investment cost includes the cost of one deep rod SET table, fiberglass pins, stainless steel receiver, and approximately 12 meters of stainless steel rods used to establish the SET monument. Time required for a survey includes reading the SET pins and recording measurements, and does not include initial setup time of the SET, which may take several additional hours.

Reported LIDAR accuracy can vary widely based on different instrumentation and landscape variations. We include vertical accuracy values ($RMSE_z$) for an airborne LIDAR-derived DEM in a marsh setting, reported by Hladik and Alber (2012). Horizontal accuracy is based on horizontal point spacing for airborne LIDAR reported by Beland et al. (2019), and spatial resolution is based on this point spacing and general convention. Initial investment cost is an estimated value for acquisition and processing of airborne LIDAR data by a professional LIDAR contractor, and covering an area up to 1000 ha in size (Beland et al., 2019). While airborne

LIDAR can cover a larger area, this will result in increased cost. Temporal resolution will vary according to location, and is an approximation based on local (Central California coast) LIDAR surveys. We assumed that LIDAR data would be collected by an external party and downloaded in a ready-to-use format by the user, so we did not include time or personnel requirements for this method.

Establishing Methods for Vegetation Monitoring

We conducted a second experiment to determine the optimal flight altitude for fine-scale vegetation monitoring. For this vegetation-flight altitude experiment, we examined the accuracy of vegetation cover classification, and the visibility of plants of different sizes, from orthomosaics collected at 10 m, 30 m, and 60 m flight altitudes covering a one-hectare area (**Table 1**). One orthomosaic at each altitude included visible spectrum (RGB) data only, while an additional orthomosaic at 30 m altitude also included near-infrared (NIR) data. All imagery was collected on May 29, 2019. We used red 12" round five-gallon bucket lids to mark plants for visibility assessment, mark plots for percent cover analysis, and georeference orthomosaics. Orthomosaics were stitched by and downloaded from DroneDeploy and georeferenced in ArcGIS (v. 10.7).

To determine the visibility of different sizes of plants in imagery collected at different flight altitudes, we marked 60 plants by placing bucket lids next to them and measured each plant in the field. We marked 20 plants in each of three size classes based on their longest diameter (<10 cm, 10 – 20 cm, and 20 – 50 cm). Half of all plants in each size class were *Salicornia pacifica* (pickleweed, the dominant marsh plant) and half were *Spergularia marina* (a common early marsh plain colonist). We viewed each marked location in true color RGB imagery for each flight altitude in ArcGIS and considered a plant "visible" if it could be distinguished from the background and identified as a plant. We did not evaluate NIR imagery in this portion of the vegetation-flight altitude experiment due to lower resolution of the NIR camera.

To evaluate the accuracy of vegetation cover estimates from classified UAV imagery, we measured percent cover at 24 plots in the field, classified each of the four orthomosaics (10 m RGB, 30 m RGB, 30 m RGBNIR, 60 m RGB) into vegetated and unvegetated areas, and compared the classified vegetation cover to field-measured cover in those plots. Each plot covered one square meter, grouped into six larger 2 m × 2 m plots. We chose plot locations that represented a range of vegetation cover values and included both of the main vegetation species present, *Salicornia* and *Spergularia*. We surveyed cover in the field by placing a one-square-meter gridded quadrat over each plot. We assessed ground cover at intercepts within the grid by recording all vegetation species, or bare ground, touched by a metal rod when dropped at each intercept. To calculate percent cover, we totaled the number of intercept "hits" for each species or bare ground within the plot, divided by total intercepts surveyed in the plot and multiplied by 100. There were no intercepts where both plant species were encountered, so overall vegetation cover in a plot was the sum of *Salicornia* and *Spergularia* cover. Number of intercepts surveyed per plot varied between 16 and 25 because we collected data along the edges of some quadrats. We weighted our analysis to account for these unequal intercept numbers.

We classified imagery in ArcGIS Pro (v. 2.3) in order to calculate UAV-based estimates of vegetation cover. We experimented with both pixel-based and object-based classification methods, but present results using pixel-based classification with a maximum likelihood classifier, which we found to be the most consistent method for our imagery. We updated training polygons as needed to optimize each classification, until making additional changes to the set of training samples only resulted in minor changes in the final classified image. We used a total of nine classes in each classification, representing the two vegetation species, varying shades of mud, and the red bucket lids used for marking. However, because none of our classifications were able to distinguish between vegetation species accurately, we evaluated accuracy of overall vegetation cover only.

We used a weighted Nash-Sutcliffe Efficiency (NSE) coefficient to measure how close classified vegetation cover was to field-measured vegetation cover in each plot. To calculate classified vegetation cover, we tabulated the area of each class in each of the 24 plots using ArcGIS tools, summed the area covered by *Salicornia* and *Spergularia*, divided the sum by the total quadrat area, and multiplied by 100. The weighted NSE equation is as follows:

$$NSE = 1 - \frac{\sum_{i=1}^{n} W_i (E_i - M_i)^2}{\sum_{i=1}^{n} W_i \left(M_i - \overline{M}\right)^2}$$

where n is the number of sampled plots, E is estimated cover from classified imagery, M is measured cover from the field survey, and W is the number of intercept sampling points (weight). NSE is a normalized coefficient that determines how well the relationship between estimated and measured data fits the 1:1 line (Nash and Sutcliffe, 1970; Trescott and Park, 2013). We computed a weighted NSE to account for the different numbers of sampling points in each plot.

Imagery Products

We collected UAV imagery during multiple stages of the restoration process. During construction, we collected and reviewed UAV imagery to monitor progress and coordinate with contractors. Flights were conducted approximately monthly, typically at an altitude of 60 m and sometimes up to 100 m. Following construction, we used UAV imagery to monitor revegetation. We conducted image classification to estimate vegetation cover across the entire site and investigated the patterns of vegetation development by examining classified vegetation cover in relation to elevation, a key factor structuring marsh vegetation communities (Zedler et al., 1999).

Our main analysis of new vegetation relied on UAV imagery collected in October 2019, using the flight altitude we determined to be optimal in our vegetation-flight altitude experiment. We classified the imagery into vegetated and unvegetated areas using a pixel-based maximum likelihood approach in ArcGIS Pro (v. 2.3). We evaluated accuracy of the classification by

creating a confusion matrix in ArcGIS to compare how well the classification matched a visual assessment of the high-resolution orthomosaic at 99 points (56 vegetated and 43 unvegetated points). We computed the true skill statistic (TSS), a metric based on the true positive and true negative rates for each class taken from the confusion matrix, to represent classification accuracy (Allouche et al., 2006). We examined classified vegetation cover in relation to elevation data collected with UAV to determine whether there was an elevation range that was particularly favorable for new colonization. We only examined classified vegetation cover at elevations < 2.0 m to exclude most upland vegetation.

Elevation Products

We used UAV-generated DEMs to monitor changes in topography over various time periods during restoration (**Table 2**). To determine whether UAV data are appropriate for calculating earthwork volume (the volume of soil moved during construction), we calculated the change in soil volume using UAV-derived DEMs collected before (October 2015) and after (June 2018) construction, and compared this value to the earthwork volume determined by professional surveyors.

Because the pre-construction DEM (DSM) included areas with tall weeds, we corrected for vegetation-related errors by calculating the difference in elevation measurements between the 2015 DEM and a 2014 TLS field survey. The TLS survey was conducted using a Trimble VX Spatial Station at 302 points, with elevations referenced to local NOAA tidal benchmarks (vertical accuracy approximately ± 1 cm). We multiplied the mean elevation difference by the size of the hillside area to estimate the total vegetation-related error in the DEM. Vegetation error was not an issue in the post-restoration imagery because the area was bare following soil scraping. We subtracted the 2018 DEM from the 2015 DEM to create a DEM of Difference (DoD; a process known as DEM differencing) using ArcGIS raster calculator. We summed the difference values in each cell of the scraped area, and multiplied this sum by the cell size to calculate the uncorrected volume change. Subtracting the vegetation error from this value resulted in the actual soil volume change. We compared our value for earthwork volume with a value determined by professional surveyors, who conducted RTK field surveys at over 200 points on the hillside area before and after construction and calculated volume change in AutoCAD software.

After construction, we established a network of GCPs based on results of our GCP density experiment and continued to track topography changes using UAV DEMs and DoDs (**Table 2**). We also created a baseline DEM representing Day 0 that assumes a consistent elevation value of 1.95 m for all pixels, prior to the first post-construction UAV survey. We corroborated this assumption using the surveyors' post-construction RTK survey at 310 points on the marsh plain. We examined topographic changes on the marsh plain and in tidal creeks using DEM differencing. We also used UAV data to evaluate the effectiveness of a bank stabilization method to minimize erosion. During construction, bay mud was dug up from the old marsh plain using a long reach excavator and compacted on the west bank of the main channel at the Hester restoration site to create a firm channel edge to reduce bank erosion. We examined DoDs and extracted vertical profiles from UAV DEMs to compare changes on the stabilized bank with the non-stabilized bank on the other side of the main channel.

RESULTS

Establishing Methods for Topography Monitoring

Our GCP density experiment revealed that both GCP density and flight altitude had an effect on DEM accuracy, though GCP density drove most variation in accuracy. Accuracy was lowest (RMSE highest) at the lowest GCP density we tested for all flight altitudes (0 GCPs per hectare; **Figure 2**). Accuracy increased sharply with initial increases in GCP density, but changed very little once GCP density increased beyond 2.1 GCPs per hectare for all flight altitudes (accuracy metrics for 50 m flight in **Table 3**). We selected a density of 1.9 GCPs per hectare (50 total GCPs for our site) for our repeated monitoring to maximize accuracy while minimizing the time required for repeated GCP surveys. We initially used a flight altitude of 60 m, which required a relatively short flight time (45 min to cover 42 ha), but later adjusted flight altitude to 30 m based on our vegetation-flight altitude experiment.

Comparison of UAV and Other Topography Monitoring Methods

We found substantial variation in accuracy and time requirements within the suite of UAV methods we compared, as well as variation in many parameters among UAV and the other topography monitoring methods (TLS, SET, and airborne LIDAR; **Table 4**). Coverage varied from under one hectare with both field-based methods to up to 1000 hectares with LIDAR, with all UAV methods covering a maximum of 42 hectares based on our selected flight altitude (65 m) and battery constraints (three batteries). We did not compare fixed-wing drones here, which typically offer better flight efficiency and maximum coverage (Johnston, 2019).

Horizontal error ($RMSE_r$) was 10 cm or less for all methods except UAV–GNSS and LIDAR, indicating that those two methods should only be used for coarser analyses. While SET horizontal error is minimal (1 mm), having only one or a few SETs results in low spatial resolution and coverage. Although TLS offsets may also be very low (<1 cm vertical and horizontal), DEMs created from surveyed point clouds will produce larger errors (5 – 10 cm vertical and horizontal) that are directly related to the point spacing. For this reason, we suggest a spatial resolution of a minimum of 10 cm for most TLS-derived DEMs. Vertical error values ($RMSE_z$) suggest that neither UAV–GNSS (1.4 m RMSE) nor LIDAR (0.16 m RMSE) would be sufficiently accurate for detecting the fine-scale changes valuable for marsh restoration monitoring. UAV–GCP, UAV–PPK, and SET are the most appropriate methods for this type of monitoring based on vertical error.

TLS was by far the most expensive method, whereas all other methods required an initial investment cost of approximately

TABLE 2 | Dates and basic methods for UAV-derived elevation products.

UAV model	Georeferencing method	Dates (month/year)	Elevation products	Relevant monitoring examples
E384	RTK-surveyed GCPs (n = 16)	10/2015	DEM, DoD	Calculating hillside volume change
Phantom 4 Pro	TLS-surveyed GCPs (n = 26)	06/2018	DEM, DoD	Calculating hillside volume change
Phantom 4 Pro	RTK-surveyed GCPs (n = 50)	08/2018, 05/2019, 08/2019, 10/2020	DEM, DoD	Monitoring post-construction changes in marsh elevation

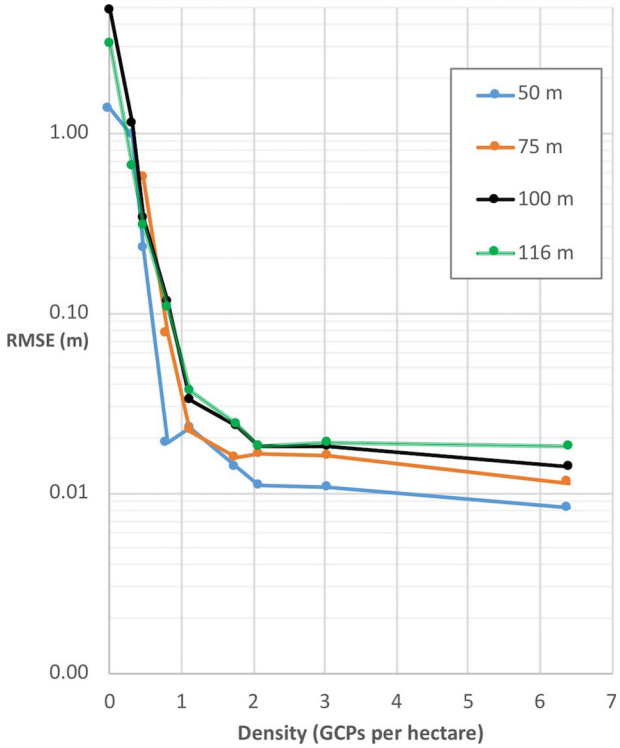

FIGURE 2 | Relationship between vertical DEM error (measured as RMSE) and GCP density, plotted for data collected at four different flight altitudes.

$13,000 or less. TLS involved the greatest time requirement, despite covering only a relatively small area. All UAV methods required less time to cover a much larger area, though time for UAV–GCP and UAV–PPK methods will vary depending on whether GCPs are permanently deployed or require removal after placement on the day of flight. While nearly all methods can collect data on a user-defined schedule, LIDAR may only be available every 5 – 10 years.

Establishing Methods for Vegetation Monitoring

Our vegetation-flight altitude experiment revealed an expected decrease in image resolution (increase in pixel size) with increasing flight altitude (**Table 1**). While individual plants were very well-defined in imagery collected at 10 m altitude, plants appeared blurrier and harder to identify in imagery collected at 60 m altitude (**Figure 3**). Plant visibility increased with decreasing flight altitude for all size classes (**Table 5**). However, we were not able to detect most small plants in UAV imagery regardless of flight altitude. Plant detection was particularly difficult in areas where the substrate was more heterogeneous (dark cracks in mud, or pockets of darker mud).

Accuracy of vegetation cover estimates based on image classification decreased with increasing flight altitude for the RGB imagery (**Figure 3**). While all four classified images represented the vegetated and unvegetated areas fairly well, the higher-altitude (60 m) flight performed the poorest in accuracy tests (NSE = 0.63) and classification of this imagery failed to capture many small plants (**Figure 3**). Classification of the imagery that included RGB and NIR data was best (NSE = 0.74) despite being collected at intermediate flight altitude (30 m), followed by 10 m RGB imagery (NSE = 0.71) and 30 m RGB imagery (NSE = 0.69). Based on these results, we mapped vegetation across the entire site with a 30 m altitude flight in October 2019 because we deemed the improvements in plant visibility and vegetation cover accuracy over the 60 m imagery to be worth the extra flight time and battery requirements. The time required to fly at 10 m altitude made this altitude infeasible for surveying the whole site (**Table 1**).

Imagery Products

We used UAV imagery throughout the course of the restoration project to communicate with various audiences, track construction progress, and assess restoration success. Imagery from before construction showed the degraded marsh, which was mostly unvegetated mudflat covered in algal wrack with a relatively small amount of healthy marsh vegetation on the edges (**Figure 4A**). Immediately after construction, imagery showed a bare marsh plain free of algal wrack (**Figure 4B**). During construction, managers used UAV imagery to view the entire site and evaluate whether progress matched intended plans (**Figure 5**).

Classification of imagery collected in October 2019, roughly a year after construction ended, revealed a total of 6.8% vegetation cover on the marsh plain and patchy patterns of new colonization that we explored in relation to microtopography (**Figure 6A**). Graphing classified vegetation cover and topography data from UAV DEMs revealed greatest vegetation cover at the highest elevations that we examined (1.95 – 2.00 m NAVD88; king tide line is around 2.15 m NAVD88), moderate cover at low elevations (1.75 – 1.80 m), and lowest vegetation cover at mid-elevations (1.85 – 1.90 m; **Figure 6B**).

Elevation Products

In addition to imagery, UAV-derived DEMs were also used for communications and outreach. A 2015 DEM clearly showed how

TABLE 3 | DEM vertical error for imagery collected at 50 m altitude over a 6.25-hectare area. All error values are in meters.

Total GCPs	0	2	3	5	7	11	13	19	40
GCPs per hectare	0	0.32	0.48	0.80	1.12	1.76	2.08	3.04	6.40
Max positive error	3.175	2.140	0.629	0.029	0.028	0.043	0.024	0.022	0.025
Max negative error	−0.167	−1.443	−0.217	−0.057	−0.080	−0.025	−0.021	−0.025	−0.013
Mean error	1.068	0.290	0.104	−0.003	−0.007	0.003	0.001	0.001	0.002
SD	0.846	0.927	0.204	0.019	0.022	0.014	0.011	0.011	0.008
95% CI	0.208	0.228	0.050	0.005	0.005	0.003	0.003	0.003	0.002
RMSE	1.358	0.964	0.227	0.019	0.023	0.014	0.011	0.011	0.008

TABLE 4 | Comparison of different topography data collection methods, including UAV with onboard uncorrected GNSS (UAV–GNSS), UAV georeferenced using 50 surveyed GCPs (UAV–GCP), UAV equipped with PPK (UAV–PPK), terrestrial laser scanning (TLS), surface elevation table (SET), and airborne LIDAR.

	UAV–GNSS	UAV–GCP	UAV–PPK	TLS	SET	LIDAR
$RMSE_r$ (m)	0.79	0.013	0.036*	0.03 – 0.10	0.001	0.2 – 2$^+$
$RMSE_z$ (m)	1.36	0.011	0.036*	0.03 – 0.10	0.001	0.16^
Approx. initial investment cost ($)	$2,700	$3,200	$13,100	$48,000	$2,000	$10,000$^+$
Time required (hrs)	1 – 1.5	7 – 8	2 – 3	≥ 12	≥1	-
Personnel required	≥ 1	≥2	≥ 2*	≥1	≥ 1	-
Training required	Moderate	High	High	High	Low	-
In situ ground support	No	Yes	Yes*	Yes	Yes	No
Temporal resolution (yrs)	User-defined	User-defined	User-defined	User-defined	User-defined	5 – 10
Suggested spatial resolution (m)	≥ 1	≥0.02	≥ 0.05*	≥0.10	1	≥ 1
Spatial Coverage (ha)	< 42	<42	< 42	<0.65	0.0001	< 1000$^+$

*RMSE values are from derived DEMs for all methods except for SET. *Padró et al., 2019b; $^+$Beland et al., 2019; ^Hladik and Alber, 2012.*

subsided the pre-restoration marsh plain was in comparison to healthy nearby marsh (**Figure 4C**). Most of the area was between mean tide level (MTL) and mean high water (MHW; 1.50 m NAVD88 according to Van Dyke, 2012), an elevation range that is inundated too frequently to support the dominant marsh vegetation, *Salicornia* (Larson, 2001). In contrast, the 2018 DEM collected after construction ended showed how high the new marsh plain was in comparison to the former subsided marsh plain and the nearby healthy marsh, with the entire restored marsh plain above mean higher high water (MHHW; 1.72 m NAVD88 in Van Dyke, 2012; **Figure 4D**).

DEM differencing to measure earthwork volume clearly highlighted the upland area of negative elevation change where soil was removed during construction (**Figure 7**). Our UAV-derived estimate of earthwork volume based on the DEM of Difference (DoD) corrected for vegetation-related error was 165,312 m^3, which was very similar to the surveyors' estimate of 166,673 m^3. Before correcting for vegetation, DEM differencing indicated a volume change of 178,604 m^3. The 2014 TLS survey used to correct for vegetation recorded similar elevations to the 2015 DEM in areas lacking ground vegetation (68 of 302 survey points had a difference of < 3 cm between TLS and DEM data). However, the mean difference between TLS and DEM elevations was 14 cm, with greater elevations in the DEM in areas of dense vegetation. We estimated the error due to vegetation to be 13,292 m^3.

Post-construction topography monitoring of the marsh plain with UAV revealed that the marsh plain elevation target was met and maintained, with the expected relatively slight subsidence. The RTK field survey corroborated the assumption of a consistent 1.95 m elevation for the Day 0 DEM, showing a mean elevation of 1.951 m at 310 points. The first post-construction UAV DEM collected at the Hester Marsh restoration site (21 days after construction ended) indicated a mean elevation of 1.915 m on the marsh plain, which was between the initial target elevation of 1.95 m and the long-term target elevation of 1.89 m.

DEM differencing revealed that there was < 0.05 m of elevation change across most of the marsh plain, with some spatial variation including greater subsidence in some areas and elevation gains in others (**Figures 8A,B**). Greater magnitude and area of negative elevation change in the first DoD (0 – 21 days following the end of construction and return of tidal exchange; **Figure 8A**) indicates that most subsidence occurred over the first 3 weeks compared with the following 9 months (21 – 285 days; **Figure 8B**). This temporal trajectory of subsidence and spatial variation is also shown in the values extracted from DoDs at the field survey points. These data show a drop in mean elevation of about 3 cm over the first 21 days and little change thereafter (**Figure 8D**). Some areas show greater drops in elevation over that initial period, around 12 cm, while others show slighter and more gradual loss in elevation (**Figure 8D**).

Post-construction monitoring of creeks using UAV showed that the tidal creek network was developing, with limited bank erosion. A DoD representing vertical change that occurred between the first month following construction (August 2018) and the following year (October 2019) indicated deepening of smaller tidal creeks over time, particularly where they connect with larger creeks (**Supplementary Figure 1**). The DoD also

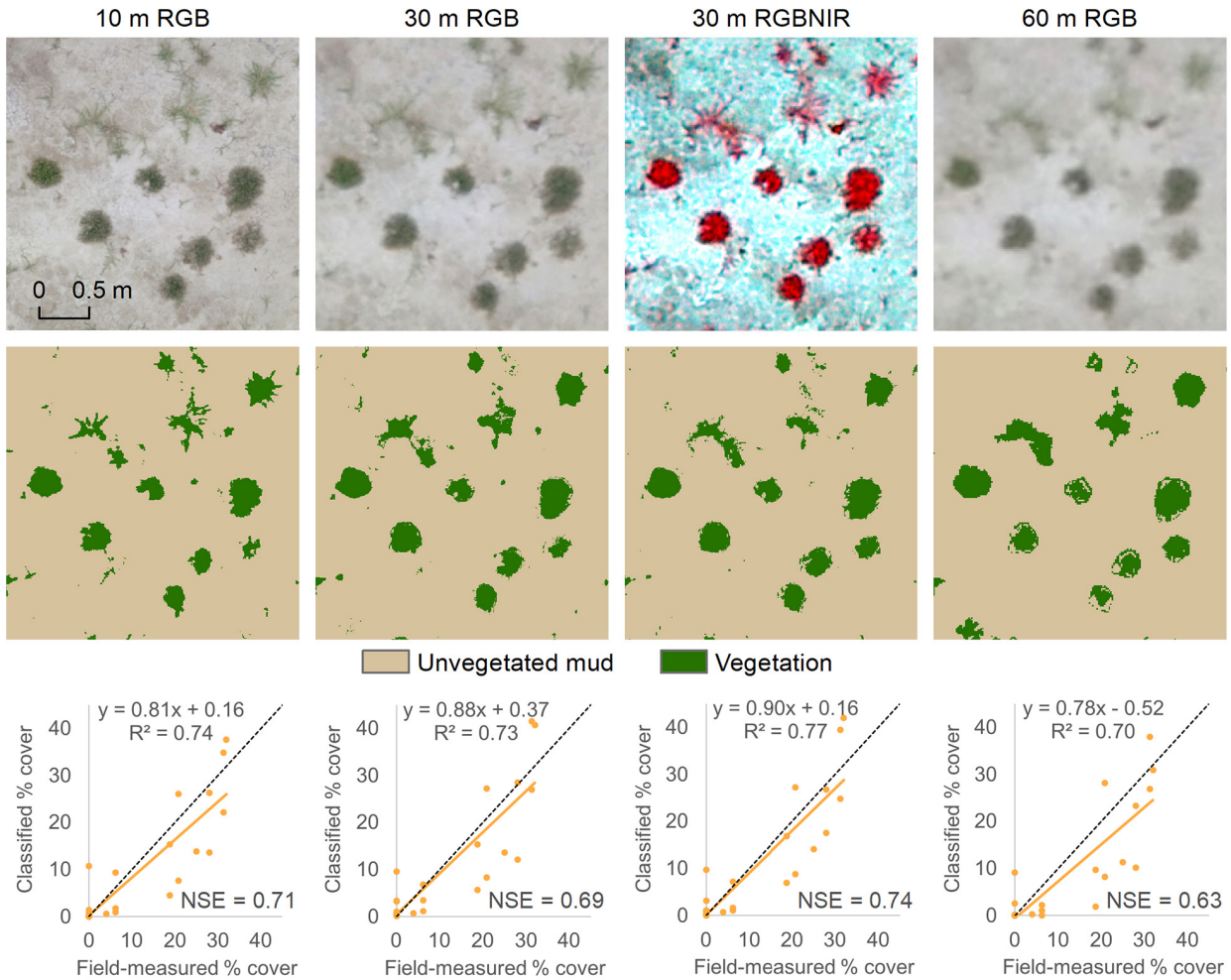

FIGURE 3 | UAV imagery, classified vegetation, and percent cover accuracy assessments for three different flight altitudes (10, 30, and 60 m). Visible spectrum (RGB) imagery is shown in true color, while the imagery including visible and near-infrared bands (RGBNIR) is shown in false color. Accuracy was assessed by comparing percent cover of classified vegetation with field-measured cover in 24 plots and calculating the Nash-Sutcliffe Efficiency (NSE) coefficient, which measures closeness to the 1:1 (dashed) line.

TABLE 5 | Visibility of plants in imagery collected at different flight altitudes. Plants were grouped into size classes based on their longest diameter.

	Percent of plants visible		
Size class	**10 m imagery**	**30 m imagery**	**60 m imagery**
Small (<10 cm)	45%	25%	5%
Mid-size (10–20 cm)	85%	50%	35%
Large (20–50 cm)	95%	90%	70%

shows development of new small creeks, with some limited erosion on the banks of the larger creeks. Some minor areas of positive elevation change in the DoD correspond to dense, large plants that colonized over the first year and are visible in October 2019 imagery.

Examining a DoD and elevation profiles of the main channel banks at different time points revealed differences in bank erosion between the stabilized and non-stabilized banks (**Figures 9A–C**). While the transects across the stabilized (west) bank edge showed similar or even slightly higher elevation profiles one year after construction (October 2019) compared with the initial profiles (August 2018), the transects across the non-stabilized (east) bank showed elevation loss on the non-stabilized bank edge. Orthomosaics and field observations suggest that the elevation increases may reflect vegetation colonization and growth (**Figure 9A**).

DISCUSSION

We successfully developed and implemented methods for UAV monitoring of marsh restoration, and for creating products useful to restoration stakeholders. Below, we share methodological recommendations and illustrate the diversity of applications of UAV data in restoration

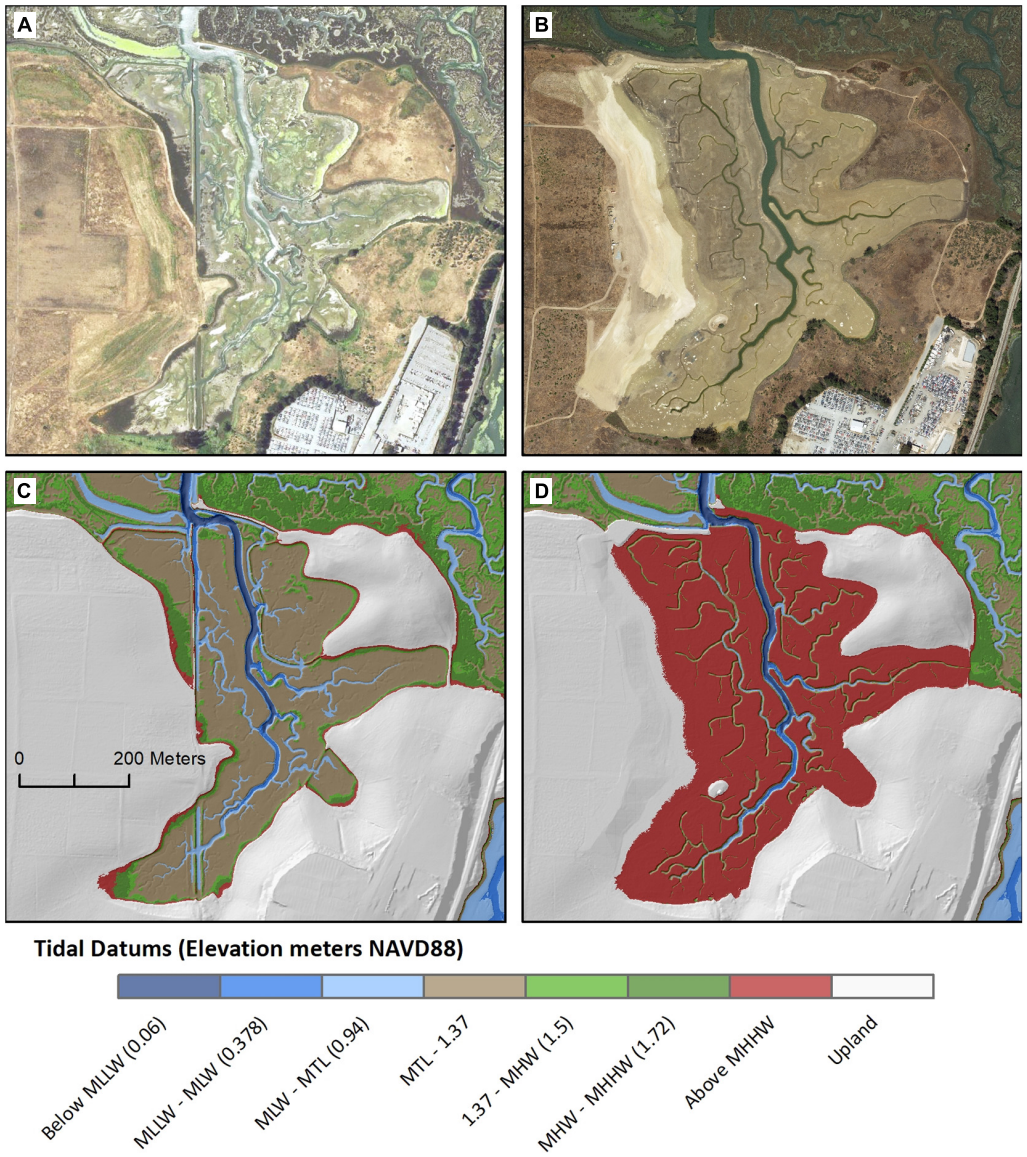

FIGURE 4 | UAV-collected orthomosaics of Hester Marsh showing **(A)** the degraded marsh prior to construction in 2015, and **(B)** the initially bare marsh after construction was completed in 2018. UAV DEMs showing the change between **(C)** pre-construction elevation in 2015, and **(D)** post-construction elevation in 2018.

monitoring. While we focus on our case study of a California tidal marsh restoration project, the general lessons learned can inform UAV-based restoration monitoring in a variety of other habitats.

Recommendations for Topography and Vegetation Monitoring Methods

Overall, the methods we developed were effective for monitoring elevation and vegetation at the scale and spatiotemporal resolution needed for our project, where detecting small changes in elevation over time, and evaluating colonization by small new plants was essential for monitoring restoration success. Our experiments evaluating different UAV methodologies resulted in several recommendations for monitoring topography and vegetation using UAV.

Our first recommendation is to explicitly plan for UAV monitoring before, during, and after restoration monitoring (**Figure 10**). While we developed our topography and vegetation monitoring methods during and after construction, others may find it optimal to determine these methods prior to construction. Surveying at reference sites may be an appropriate way to determine a specific protocol for monitoring ground cover and topography at the restoration site. An important benefit of determining how to make accurate DEMs early on, particularly in soil addition marsh restoration projects, is enabling creation of accurate pre-restoration topography maps. At our site, we conducted an earthmoving volume assessment that relied on a

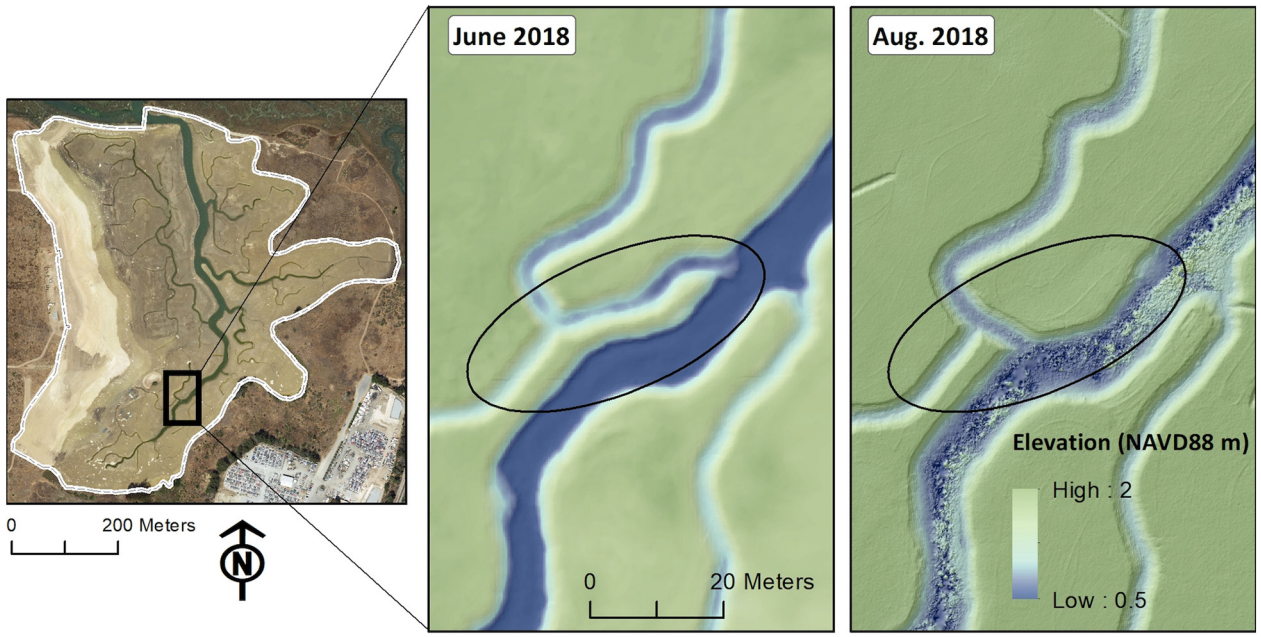

FIGURE 5 | Maps collected during construction (June 2018) and at the end of construction (August 2018) showing a narrow peninsula that was constructed following old creek network designs, and then changed to reflect updated designs. We primarily used orthomosaics to monitor construction, but present DEMs here to make the change more easily visible. Note lower DEM resolution in the June 2018 imagery due to different processing technique with no GCPs.

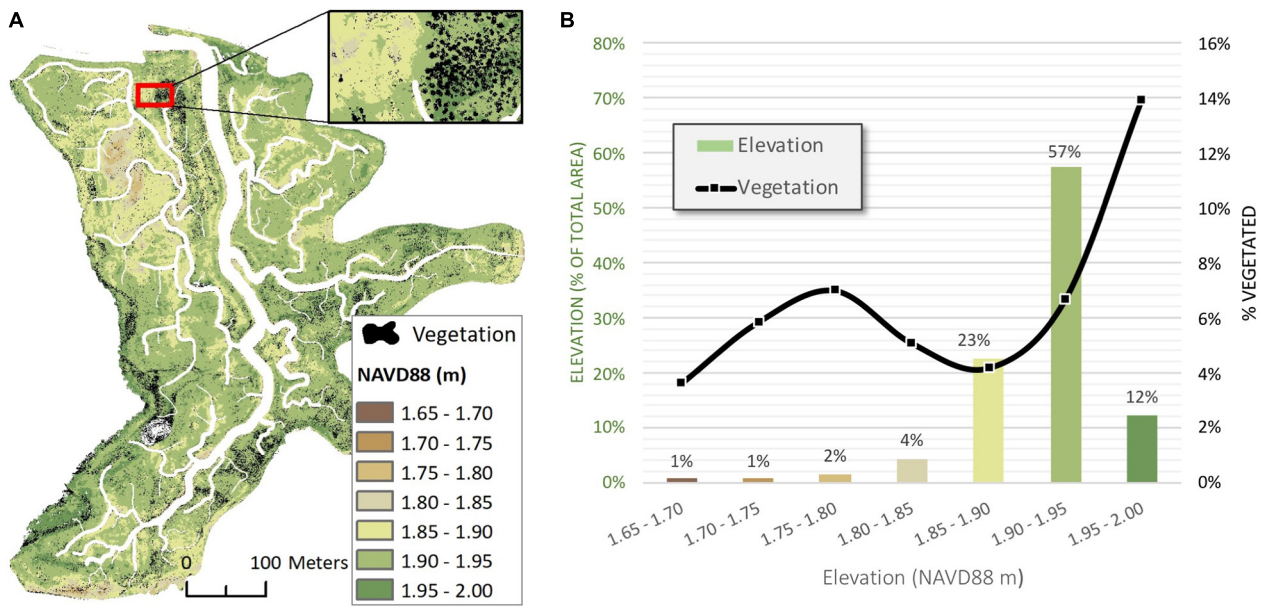

FIGURE 6 | (A) Map of classified vegetation on top of an August 2018 DEM showing elevation in 5 cm increments. **(B)** Percent of total area (histogram) and percent vegetated area (line) in each elevation bin. Percent vegetated area is the area of classified vegetation in an elevation bin out of the total area in that bin.

non-bare-earth DEM collected prior to restoration (**Figure 7**), and an accurate calculation of soil volume change required correcting for vegetation using a field survey. Carrying out pre-restoration flights for method development could also be valuable for determining limitations of using UAV in a given system, such as whether species of interest can be distinguished from each other and from the background substrate, and for identifying potential risks and hazards (Haskins, 2020).

Secondly, we recommend that sites with similar fine-scale topography monitoring goals use a similar GCP density to the

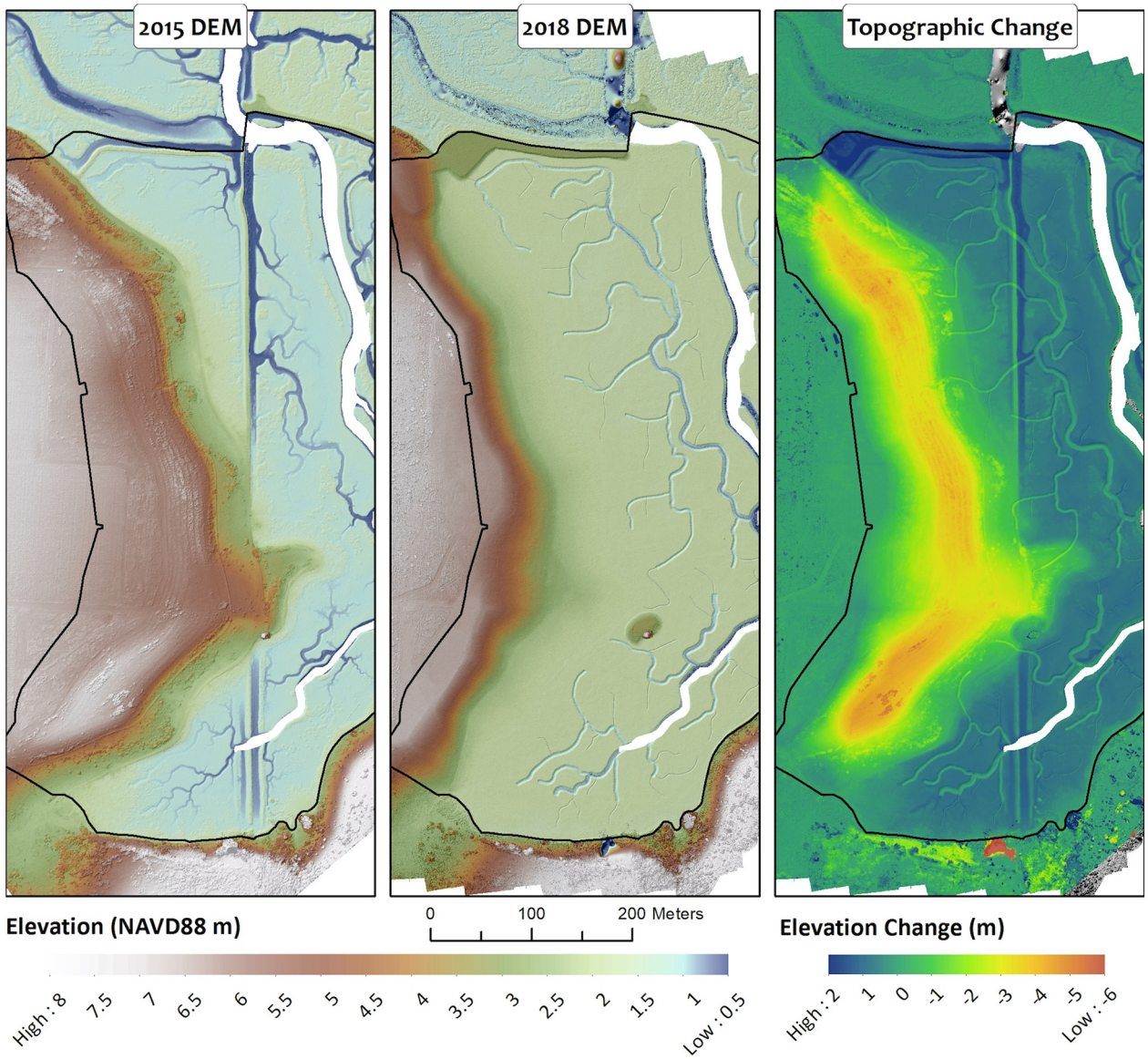

FIGURE 7 | Maps showing elevation change on the western side of the restoration site, where soil was scraped from the hillside to elevate the marsh plain. A DEM of Difference (right) represents topographic change between pre-construction (2015 DEM, left) and post-construction (2018 DEM, middle) and was used to calculate the volume of soil moved from the hillside during construction.

one we determined to be optimal in our experimentation. Our methods for topography monitoring generated highly accurate DEMs (1.1 cm RMSE) and can likely be applied to other sites of a similar size. We found that a GCP density of about 2 GCPs per hectare was ideal, and that increasing GCP density above that level would not result in substantially greater accuracy but would increase field survey time. Flight altitude did not have as strong an influence on DEM accuracy, so we initially flew at an altitude of 60 m, which enabled rapid data acquisition. We later reduced the flight altitude to 30 m in order to better capture recently colonized vegetation. Where vegetation became larger and denser, we noticed errors in the DEM because, as a DSM, it represented the top of the vegetation canopy in these areas rather than the ground (**Supplementary Figure 1**). One way to correct this is by incorporating additional processing steps to filter out vegetation from the DSM (for example, see Cunliffe et al., 2016). The methods we utilized to create DEMs could be valuable for other types of restoration, particularly when microtopographic variation is important to capture. While other studies may choose to use a similar approach to ours in terms of flight altitude and GCP density, researchers at sites of different sizes, or with different accuracy needs, may find it helpful to conduct an experiment similar to ours to determine their optimal methods.

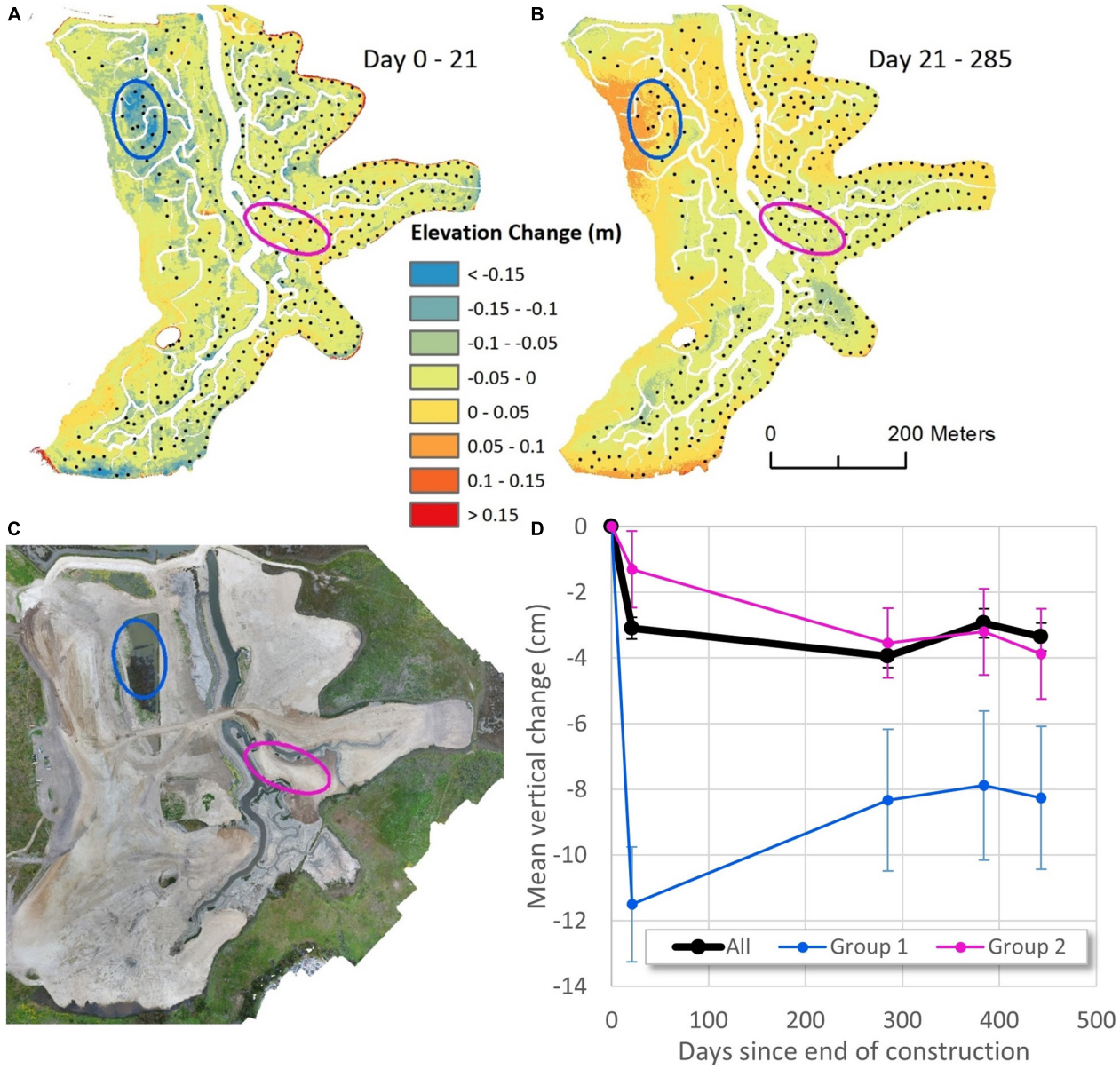

FIGURE 8 | Spatial and temporal patterns of elevation change at Hester Marsh. **(A)** DoD showing elevation change in the first 21 days following construction, assuming a consistent Day 0 elevation of 1.95 m. Black points show locations of the RTK survey completed at the end of construction in 2018. **(B)** DoD showing elevation change between Day 21 and Day 285. **(C)** UAV orthomosaic captured in May 2018 showing an area where excess water was contained during construction (blue oval) and where soil was compacted early on as part of a construction vehicle route (fuchsia oval). **(D)** Mean difference in original RTK-surveyed elevations and elevation values extracted from four post-construction DEMs at those surveyed positions. The black line represents elevation change at all RTK-surveyed positions, blue line represents the subset of locations within the blue oval in all maps, and fuchsia line represents the subset of locations within the fuchsia oval in all maps.

Our third recommendation is to use UAV imagery to track revegetation of the restoration site, using the approach we successfully piloted for data collection, modified as needed for different habitats or sites of different size. At our site, a flight altitude of 30 m enabled sufficiently accurate calculation of vegetation cover compared with field measurements (NSE = 0.69 using RGB imagery), and subsequent exploration of the relationship between new vegetation cover and elevation. While we decided the longer flight time to collect imagery at 30 m altitude was worthwhile for detecting more individual plants and therefore minimizing the need for ground-truthing in the field, a 60 m flight altitude may be sufficient when most plants are larger and less sparse. Other studies comparing UAV flight altitude/image resolution for detecting and classifying small plants have also reported that accuracy increases with greater image resolution, collected at lower flight altitude, but this

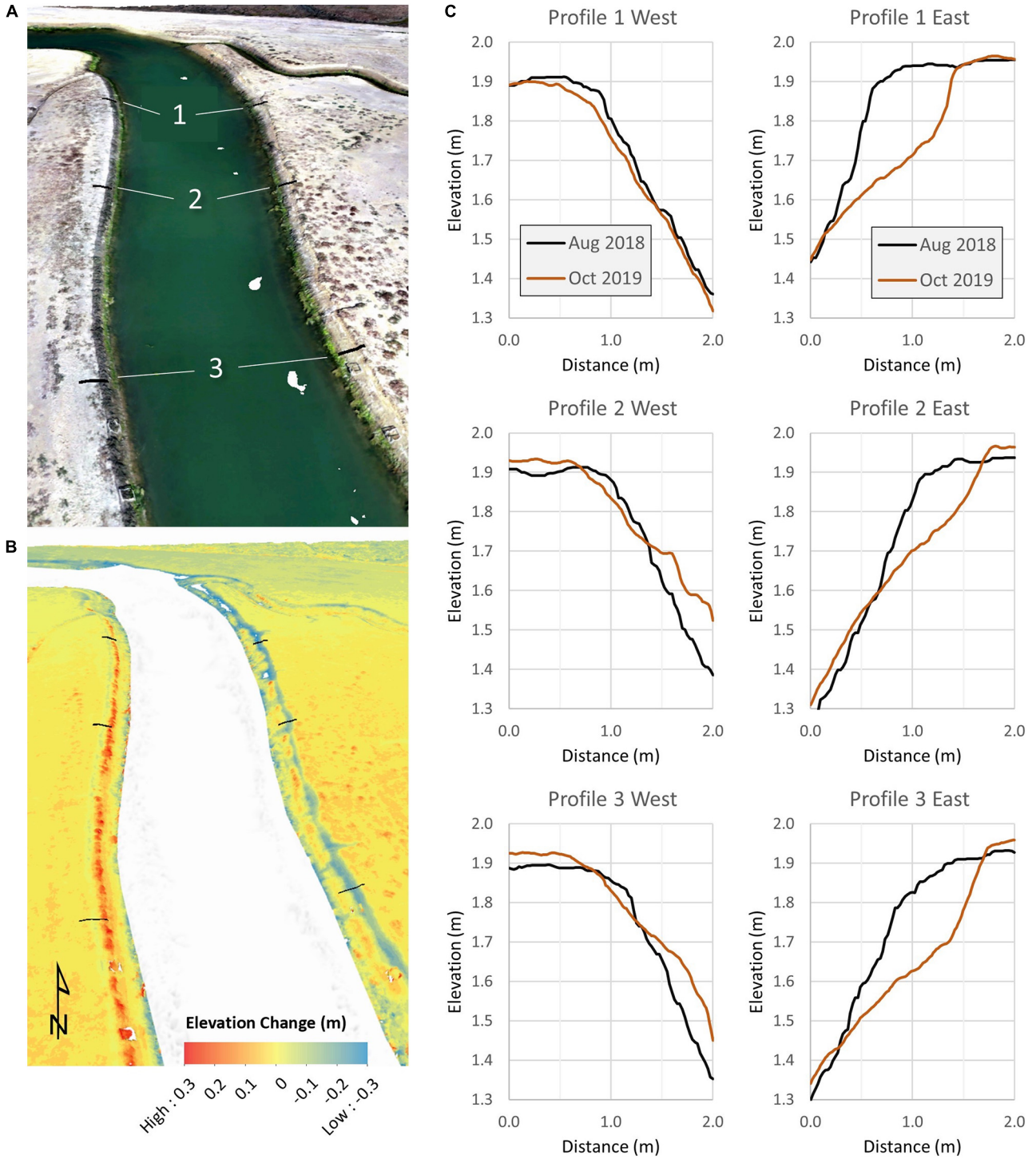

FIGURE 9 | A portion of the Hester Marsh main channel shown in **(A)** an October 2019 orthomosaic, and **(B)** a DoD between August 2018 and October 2019. The west bank of the channel was reinforced with mud excavated from the former wetland; the east bank had no reinforcement. **(C)** Vertical profiles extracted from UAV DEMs were used to evaluate erosion of the main channel banks between August 2018 and October 2019.

increase is sometimes marginal (Torres-Sánchez et al., 2014; Buters et al., 2019b). Others have also found that detection of small plants is easier on more homogenous substrates (Buters et al., 2019b), a conclusion that our findings support. We recommend collecting NIR data in addition to RGB data, which improved vegetation cover estimates in 30 m imagery

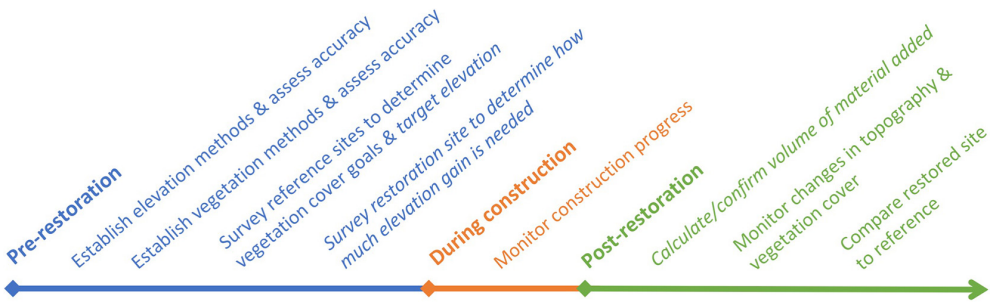

FIGURE 10 | Recommendations for timing of UAV monitoring, generally applicable to all restoration (regular text) and specific to sediment/soil addition projects (italic text).

(NSE = 0.74), but we had issues with either sensor capture or file management that prevented us from using NIR data in our classification of October 2019 imagery covering the entire restoration site. In projects that compare imagery between sites or dates, researchers should collect calibration images that capture a reflectance target before, during, and/or after each flight to calibrate imagery (Assmann et al., 2018).

To elaborate on the third recommendation above, we used image classification to estimate vegetation cover and examine spatial variation from UAV imagery, and suggest that others optimize the specific classification method based on their software and imagery. While the pixel-based maximum likelihood classification we used for UAV-based vegetation cover estimates was adequate for our purposes, many other classification options exist and could improve the accuracy of percent cover estimates. For example, object-based classification methods can incorporate additional factors such as shape and texture of distinct objects, which may be beneficial for distinguishing plants from mud (Dronova, 2015). While we were unable to distinguish between species in our classifications, this type of distinction might be possible with modifications to the data collection and/or classification method. For example, imagery can be collected during times of year when the species appear more different due to flowering or other phenological changes (Gilmore et al., 2008). Some studies also incorporate elevation data into image classification, which can help distinguish between similar-looking vegetation classes when they occupy different vertical zones (Sturdivant et al., 2017; Padró et al., 2019a). Our methods for UAV monitoring of new plants using image classification will work well on initially bare sites when vegetation is easily distinguished from the background, and separating different species or vegetation types is not critical. Given many site-specific factors in vegetation monitoring, the accuracy values we achieved in classifying vegetation cover may not translate to other systems and conducting test flights should be considered essential.

Tradeoffs Between UAV and Traditional Methods for Restoration Monitoring

Determining an appropriate monitoring method is vital for ensuring that lessons are learned from restoration without exceeding limited budgets (Roegner et al., 2008). Our comparison of UAV with TLS, SET, and airborne LIDAR methods for topography monitoring, and our firsthand experience monitoring vegetation and topography at this site using both field and UAV methods, revealed some key benefits of UAV over field monitoring as well as a few drawbacks.

A clear benefit of UAV monitoring includes its capacity to generate high spatial resolution data across an entire site including hard-to-access areas. Our construction monitoring benefitted from the ease of monitoring areas with UAV that were not easily accessible on foot. For example, midway through the construction period, we detected a narrow, erosion-prone peninsula in the interior of the site that had been constructed according to an old creek network design (**Figure 5**). Rapid detection of this issue in UAV imagery enabled us to update construction in this area to shorten the peninsula. The comprehensive spatial coverage of UAV data was also valuable for detecting and analyzing spatial patterns, which field sampling could miss if not distributed well across the whole site. For example, field surveys of subsidence would provide an incomplete or misleading picture if coverage was too limited or certain key areas were missed (**Figures 8A–D**).

Customization of temporal resolution of data is another valuable attribute of UAV monitoring, enabling data collection to be easily tailored to monitoring needs and research questions (Easterday et al., 2019). Temporal resolution is least customizable for aerial or satellite data (e.g., LIDAR), and is customizable for field data but with spatial coverage limitations (**Table 4**). At our site, the ability to collect frequent topographic data with UAV enabled us to determine that most subsidence occurred in the first few weeks of tidal exchange (**Figure 8D**).

There are notable differences among UAV methods in cost and time efficiency as well as accuracy of products (**Table 4**). While two of three UAV methods were comparable in cost to SET monitoring (the cheapest topography monitoring method in our comparison), UAV–PPK involved greater initial investment cost. However, this industry has been evolving rapidly over the past decade, and costs for all UAV methods may continue to decline. Compared with UAV–GCP (the most accurate UAV method), UAV–PPK required less time for one survey and accuracy of this method was only slightly reduced. The most rapid and inexpensive UAV method (UAV–GNSS) was not accurate enough

for our monitoring purposes. While UAV monitoring was more efficient than the field methods we use to regularly survey both topography and vegetation at our site, one notable drawback in comparison to many field methods is the lower level of detail captured in UAV data. Field survey time to collect both vegetation and topography data at our site required a minimum of 2.5 person-hours to fly the UAV (at 30 m altitude, covering the 25 ha site and adjacent areas) compared with 22 person-hours for field data collection (10 h for vegetation cover, 12 for elevation at 100 quadrats). Reduced detail was evident in our inability to distinguish between species, upland vs. marsh plants, or native vs. non-native plants in classification of UAV imagery. For elevation, we found our UAV DEMs to be highly accurate, but note that using SETs is more accurate by an order of magnitude (**Table 4**).

Another drawback of UAV as well as TLS monitoring is the moderate to high training required (**Table 4**). While SET monitoring can be accomplished with low training, all UAV methods require at least moderate training (some experience operating the equipment as well as a FAA 107 drone operator license) and the most accurate UAV methods have high training requirements. Because of the many different considerations when choosing a monitoring methodology, and the lack of a clear winner across all categories, monitoring decisions should be made based on anticipated applications of the data.

Applications of Imagery and Elevation Products

Tracking and communicating about restoration progress is critical for generating public support for restoration, meeting permitting and funding requirements, maintaining institutional support, making management changes to improve outcomes, and informing decisions for future projects (McDonald et al., 2016). Aerial imagery is one powerful tool to accomplish these goals and maximize the benefits of restoration projects. Other restoration studies in a variety of habitats are beginning to use UAV, primarily for post-restoration vegetation cover monitoring (Knoth et al., 2013; Buters et al., 2019a; Padró et al., 2019a; Reis et al., 2019; Pérez et al., 2020). For restoration in more densely vegetated habitats, UAV-derived elevation data has also been used to monitor canopy structure (Zahawi et al., 2015). Other than vegetation monitoring, UAVs have also been found to be useful for monitoring geomorphic change and spatial patterns of erosion and aggradation in restoration of intermittent streams (Marteau et al., 2017). However, few prior studies using UAV at restoration sites focus on the early stages of restoration, which involves collecting data of sufficiently high spatial resolution to capture small, sparse plants and subtle variations in elevation.

We frequently relied on imagery collected using UAV to communicate with the broader community about the restoration project, including the public, funders, and other stakeholders (**Figures 4A–D**). Estuarine habitats are hard to access, so imagery helps to share progress of projects with the public, builds excitement for successes like seeing plants return, and helps generate support for marsh conservation and restoration. We used UAV imagery in many presentations about the restoration project, as well as in teacher training workshops illustrating how marsh restoration can enhance resilience to sea level rise by building new habitat at a high elevation in the tidal frame (**Figure 4D**). UAV products were also valuable for communicating with specific audiences like funders, to whom we reported whether goals were met on metrics including elevation, hydrology, and vegetation.

Monitoring was also valuable for informing adaptive management and planning for future restoration projects. During construction, rapid detection of the erosion-prone peninsula in UAV imagery enabled contractors to make changes while equipment was onsite, preventing potentially large future costs (**Figure 5**). Our UAV-based assessment of the volume of soil moved from the hillside onto the marsh plain during construction was used to verify the surveyor's assessment and was a critical corroboration because earthwork volume is an important determinant of restoration construction costs (**Figure 7**). Accuracy of this UAV volume assessment method indicates that it can be used to estimate construction costs during planning of future projects, serve as an alternative to the more traditional field methods used by surveyors, or corroborate surveyors' assessments.

Repeated topography monitoring following construction revealed some areas of subsidence (**Figures 8A,B**), where water was pooling and plants were not readily colonizing, some of which we were able to target for filling by contractors. Future analyses can take advantage of UAV-collected imagery and topography data to examine whether the spatial variation in subsidence is tied to previous land use or construction methods, such as areas that were used for containing excess water during construction (**Figure 8C**). Understanding how much subsidence occurred, and spatial patterns, enables managers to adjust the initial elevation and construction methods of future soil addition projects. The observed topography changes on a stabilized and non-stabilized bank suggested that bank stabilization not only successfully reduced erosion but also potentially promoted vegetation growth (**Figures 9A–C**). These findings led to implementation of bank stabilization on a larger scale in a new, adjacent marsh restoration area under construction in 2020.

Ultimately, tidal marsh restoration aims to create favorable conditions for redevelopment of the biotic community, including vegetation (Zedler, 2000a; Roegner et al., 2008). Monitoring revegetation using classified UAV imagery helped us understand factors that influence vegetation cover, such as microtopography (**Figure 6**), with the goal of preventing conditions that inhibit colonization at future sites. The applications we have described could be implemented in many different types of habitat restoration, supporting the critical communication of restoration progress with key stakeholders and ensuring knowledge is gained from restoration projects to inform both adaptive management and future planning (McDonald et al., 2016).

DATA AVAILABILITY STATEMENT

The datasets presented in this study can be found in online repositories. The names of the repository/repositories and

accession number(s) can be found below: https://doi.org/10.6084/m9.figshare.c.5226785.v1 (Figshare).

AUTHOR CONTRIBUTIONS

AT created the first draft of the manuscript and literature review, and conducted the vegetation-flight altitude analysis. JH, CE, and FG conducted the topography method development, carried out repeated monitoring, and contributed most of the figures. MF and KW secured funding and provided oversight. All authors contributed to idea development, writing, and editing of the manuscript.

FUNDING

The Hester Marsh restoration project was coordinated by ESNERR's Tidal Wetland Program and funded by grants from California Department of Water Resources (4600009727), California Department of Fish and Wildlife Greenhouse Gas Program (P1496007), California Coastal Conservancy (16-019), USFWS National Coastal Wetlands Conservation Program (16-019), Ocean Protection Council (P01-2-04), and the Wildlife Conservation Board (WC-1522SM) to the Elkhorn Slough Foundation on behalf of ESNERR. The UAV monitoring of Hester, including analyses and manuscript preparation, was funded in part by these sources as well as NOAA's Office for Coastal Management (NA20NOS4200097, NA19NOS4200050, NA18NOS4200075, NA17NOS4200041, and NA16NOS4200073), and the NOAA Office of Education Educational Partnership Program award (NA16SEC4810009). The contents of this manuscript are solely the responsibility of the award recipients and do not necessarily represent the official views of the funding organizations.

ACKNOWLEDGMENTS

A. Lapides assisted with UAV and topographic data collection and was extremely helpful in establishing protocols for UAV processing. N. Maher and H. G. Greene generously offered their time and UAV equipment for the very first flights over the restoration site in 2015. I. Aiello assisted with TLS data collection and processing. R. Kwan-Davis and J. Mejia-Muñoz assisted with evaluating accuracy of classified vegetation cover to inform UAV flight altitude. F. Watson advised on data analysis for the vegetation-flight altitude experiment. AT completed the vegetation-flight altitude experiment as a graduate fellow with the NOAA Center for Coastal and Marine Ecosystems program at California State University Monterey Bay.

SUPPLEMENTARY MATERIAL

The Supplementary Material for this article can be found online at: https://www.frontiersin.org/articles/10.3389/fenvs.2021.642906/full#supplementary-material

REFERENCES

Allouche, O., Tsoar, A., and Kadmon, R. (2006). Assessing the accuracy of species distribution models: prevalence, kappa and the true skill statistic (TSS). *J. Appl. Ecol.* 43, 1223–1232. doi: 10.1111/j.1365-2664.2006.01214.x

Anderson, K., and Gaston, K. J. (2013). Lightweight unmanned aerial vehicles will revolutionize spatial ecology. *Front. Ecol. Environ.* 11:138–146. doi: 10.1890/120150

Assmann, J. J., Kerby, J. T., Cunliffe, A. M., and Myers-Smith, I. H. (2018). Vegetation monitoring using multispectral sensors—Best practices and lessons learned from high latitudes. *J. Unmanned Veh. Syst.* 7, 54–75. doi: 10.1139/juvs-2018-0018

Barry, W. J., Garlo, A. S., and Wood, C. A. (1996). Duplicating the mound-and-pool microtopography of forested wetlands. *Restor. Manag. Notes* 14, 15–21. doi: 10.3368/er.14.1.15

Beland, M., Parker, G., Sparrow, B., Harding, D., Chasmer, L., Phinn, S., et al. (2019). On promoting the use of lidar systems in forest ecosystem research. *For. Ecol. Manag.* 450:117484. doi: 10.1016/j.foreco.2019.117484

Buters, T. M., Bateman, P. W., Robinson, T., Belton, D., Dixon, K. W., and Cross, A. T. (2019a). Methodological ambiguity and inconsistency constrain unmanned aerial vehicles as a silver bullet for monitoring ecological restoration. *Remote Sens.* 11:1180. doi: 10.3390/rs11101180

Buters, T. M., Belton, D., and Cross, A. (2019b). Seed and seedling detection using unmanned aerial vehicles and automated image classification in the monitoring of ecological recovery. *Drones* 3:53. doi: 10.3390/drones3030053

Caffrey, J. M. Brown, M., Tyler, W.B., Silberstein, M., (ed.) (2002). *Changes in a California Estuary: A Profile of Elkhorn Slough*. Elkhorn Slough Foundation. Moss Landing, CA

Cahoon, D. R., Lynch, J. C., Roman, C. T., Schmit, J. P., and Skidds, D. E. (2019). Evaluating the relationship among wetland vertical development, elevation capital, sea-level rise, and tidal marsh sustainability. *Estuaries Coasts* 42, 1–15. doi: 10.1007/s12237-018-0448-x

Chabot, D., and Bird, D. M. (2013). Small unmanned aircraft: precise and convenient new tools for surveying wetlands. *J. Unmanned Veh. Syst.* 1, 15–24. doi: 10.1139/juvs-2013-0014

Coveney, S., and Roberts, K. (2017). Lightweight UAV digital elevation models and orthoimagery for environmental applications: data accuracy evaluation and potential for river flood risk modelling. *Int. J. Remote Sens.* 38, 3159–3180. doi: 10.1080/01431161.2017.1292074

Cruzan, M. B., Weinstein, B. G., Grasty, M. R., Kohrn, B. F., Hendrickson, E. C., Arredondo, T. M., et al. (2016). Small unmanned aerial vehicles (micro-UAVs, drones) in plant ecology. *Appl. Plant Sci.* 4:1600041. doi: 10.3732/apps.1600041

Cunliffe, A. M., Brazier, R. E., and Anderson, K. (2016). Ultra-fine grain landscape-scale quantification of dryland vegetation structure with drone-acquired structure-from-motion photogrammetry. *Remote Sens. Environ.* 183, 129–143. doi: 10.1016/j.rse.2016.05.019

Dayton, P. K. (1972). "Toward an understanding of community resilience and the potential effects of enrichments to the benthos at McMurdo Sound, Antarctica," in *Proceedings of the Colloquium on Conservation Problems in Antarctica*, Lawrence, KS: Allen Press, 81–96.

Diefenderfer, H. L., Sinks, I. A., Zimmerman, S. A., Cullinan, V. I., and Borde, A. B. (2018). Designing topographic heterogeneity for tidal wetland restoration. *Ecol. Eng.* 123, 212–225. doi: 10.1016/j.ecoleng.2018.07.027

Dronova, I. (2015). Object-based image analysis in wetland research: a review. *Remote Sens.* 7, 6380–6413. doi: 10.3390/rs70506380

Easterday, K., Kislik, C., Dawson, T. E., Hogan, S., and Kelly, M. (2019). Remotely sensed water limitation in vegetation: insights from an experiment with unmanned aerial vehicles (UAVs). *Remote Sens.* 11:1853. doi: 10.3390/rs11161853

Ellison, A. M. (2019). Foundation species, non-trophic interactions, and the value of being common. *Iscience* 13, 254–268. doi: 10.1016/j.isci.2019.02.020

Fountain, M., Jeppesen, R., Endris, C., Woolfolk, A., Watson, E., Aiello, I., et al. (2020). *Hester Marsh Restoration. Annual Report 2020. Elkhorn Slough National Estuarine Research Reserve*. Available online at: http://www.elkhornslough.org/tidal-wetland-program/hester-marsh-restoration/ (accessed December 9, 2020).

Gedan, K. B., Silliman, B. R., and Bertness, M. D. (2009). Centuries of human-driven change in salt marsh ecosystems. *Annu. Rev. Mar. Sci.* 1, 117–141. doi: 10.1146/annurev.marine.010908.163930

Gilmore, M. S., Wilson, E. H., Barrett, N., Civco, D. L., Prisloe, S., Hurd, J. D., et al. (2008). Integrating multi-temporal spectral and structural information to map wetland vegetation in a lower Connecticut River tidal marsh. *Remote Sens. Environ.* 112, 4048–4060. doi: 10.1016/j.rse.2008.05.020

Halpern, B. S., Walbridge, S., Selkoe, K. A., Kappel, C. V., Micheli, F., D'Agrosa, C., et al. (2008). A global map of human impact on marine ecosystems. *Science* 319, 948–952.

Harwin, S., and Lucieer, A. (2012). Assessing the accuracy of georeferenced point clouds produced via multi-view stereopsis from unmanned aerial vehicle (UAV) imagery. *Remote Sens.* 4, 1573–1599. doi: 10.3390/rs4061573

Haskins, J. (2020). *Unoccupied Aerial Systems: Procedures Manual. Elkhorn Slough Technical Report Series 2020:4*. Available online at: http://www.elkhornslough.org/research-program/technical-report-series/ (accessed December 15, 2020).

Hladik, C., and Alber, M. (2012). Accuracy assessment and correction of a LIDAR-derived salt marsh digital elevation model. *Remote Sens. Environ.* 121, 224–235. doi: 10.1016/j.rse.2012.01.018

Jarzemsky, R. D., Burchell, M. R. II, and Evans, R. O. (2013). The impact of manipulating surface topography on the hydrologic restoration of a forested coastal wetland. *Ecol. Eng.* 58, 35–43. doi: 10.1016/j.ecoleng.2013.06.002

Johnston, D. W. (2019). Unoccupied aircraft systems in marine science and conservation. *Annu. Rev. Mar. Sci.* 11, 439–463. doi: 10.1146/annurev-marine-010318-095323

Kalacska, M., Chmura, G. L., Lucanus, O., Bérubé, D., and Arroyo-Mora, J. P. (2017). Structure from motion will revolutionize analyses of tidal wetland landscapes. *Remote Sens. Environ.* 199, 14–24. doi: 10.1016/j.rse.2017.06.023

Kennish, M. J. (2001). Coastal salt marsh systems in the US: a review of anthropogenic impacts. *J. Coast. Res.* 17, 731–748.

Kirwan, M. L., and Megonigal, J. P. (2013). Tidal wetland stability in the face of human impacts and sea-level rise. *Nature* 504, 53–60. doi: 10.1038/nature12856

Knoth, C., Klein, B., Prinz, T., and Kleinebecker, T. (2013). Unmanned aerial vehicles as innovative remote sensing platforms for high-resolution infrared imagery to support restoration monitoring in cut-over bogs. *Appl. Veg. Sci.* 16, 509–517. doi: 10.1111/avsc.12024

Larson, E. J. (2001). "Coastal wetlands-emergent marshes," in *California's Living Marine Resources: A Status Report*, eds W. S. Leet, C. M. Dewees, R. Klingbeil, and E. J. Larson (Sacramento, CA: California and California Department of Fish and Game), 483–486.

Marteau, B., Vericat, D., Gibbins, C., Batalla, R. J., and Green, D. R. (2017). Application of Structure-from-Motion photogrammetry to river restoration. *Earth Surf. Process. Landf.* 42, 503–515. doi: 10.1002/esp.4086

McDonald, T., Gann, G., Jonson, J., and Dixon, K. (2016). *International Standards for the Practice of Ecological Restoration–Including Principles and Key Concepts*. Washington, DC: Society for Ecological Restoration *Soil-Tec, Inc.,© Marcel Huijser, Bethanie Walder*.

Nash, J. E., and Sutcliffe, J. V. (1970). River flow forecasting through conceptual models part I—A discussion of principles. *J. Hydrol.* 10, 282–290. doi: 10.1016/0022-1694(70)90255-6

Padró, J. C., Carabassa, V., Balagué, J., Brotons, L., Alcañiz, J. M., and Pons, X. (2019a). Monitoring opencast mine restorations using Unmanned Aerial System (UAS) imagery. *Sci. Total Environ.* 657, 1602–1614. doi: 10.1016/j.scitotenv.2018.12.156

Padró, J. C., Muñoz, F. J., Planas, J., and Pons, X. (2019b). Comparison of four UAV georeferencing methods for environmental monitoring purposes focusing on the combined use with airborne and satellite remote sensing platforms. *Int. J. Appl. Earth Observ. Geoinf.* 75, 130–140. doi: 10.1016/j.jag.2018.10.018

Palmer, M. A., Zedler, J. B., and Falk, D. A. (2016). "Ecological theory and restoration ecology," in *Foundations of Restoration Ecology*, eds M. A. Palmer, J. B. Zedler, and D. A. Falk (Washington, DC: Island Press), 3–26. doi: 10.5822/978-1-61091-698-1_1

Pastorok, R. A., MacDonald, A., Sampson, J. R., Wilber, P., Yozzo, D. J., and Titre, J. P. (1997). An ecological decision framework for environmental restoration projects. *Ecol. Eng.* 9, 89–107. doi: 10.1016/s0925-8574(97)00036-0

Pérez, D. R., Pilustrelli, C., Farinaccio, F. M., Sabino, G., and Aronson, J. (2020). Evaluating success of various restorative interventions through drone-and field-collected data, using six putative framework species in Argentinian Patagonia. *Restor. Ecol.* 28, A44–A53.

Raposa, K., Wasson, K., Nelson, J., Fountain, M., West, J., Endris, C., et al. (2020). *Guidance for Thin-Layer Sediment Placement as a Strategy to Enhance Tidal Marsh Resilience to Sea-Level Rise*. Silver Spring, MD: collaboration with the National Estuarine Research Reserve System Science Collaborative.

Reis, B. P., Martins, S. V., Fernandes Filho, E. I., Sarcinelli, T. S., Gleriani, J. M., Leite, H. G., et al. (2019). Forest restoration monitoring through digital processing of high resolution images. *Ecol. Eng.* 127, 178–186. doi: 10.1016/j.ecoleng.2018.11.022

Roegner, G. C., Diefenderfer, H. L., Borde, A. B., Thom, R. M., Dawley, E. M., Whiting, A. H., et al. (2008). *Protocols for Monitoring Habitat Restoration Projects in the Lower Columbia River and Estuary* (No. PNNL-15793). Richland, WA: Pacific Northwest National Lab.(PNNL).

Sanderson, E. W., Foin, T. C., and Ustin, S. L. (2001). A simple empirical model of salt marsh plant spatial distributions with respect to a tidal channel network. *Ecol. Modell.* 139, 293–307. doi: 10.1016/s0304-3800(01)00253-8

Sturdivant, E. J., Lentz, E. E., Thieler, E. R., Farris, A. S., Weber, K. M., Remsen, D. P., et al. (2017). UAS-SfM for coastal research: geomorphic feature extraction and land cover classification from high-resolution elevation and optical imagery. *Remote Sens.* 9:1020. doi: 10.3390/rs9101020

Torres-Sánchez, J., Pena, J. M., de Castro, A. I., and López-Granados, F. (2014). Multi-temporal mapping of the vegetation fraction in early-season wheat fields using images from UAV. *Comput. Electron. Agric.* 103, 104–113. doi: 10.1016/j.compag.2014.02.009

Trescott, A., and Park, M. H. (2013). Remote sensing models using Landsat satellite data to monitor algal blooms in Lake Champlain. *Water Sci. Technol.* 67, 1113–1120. doi: 10.2166/wst.2013.661

Van Dyke, E. (2012). *Water Levels, Wetland Elevations, And Marsh Loss.* Elkhorn Slough Technical Report Series 2012:2. Available online at: http://www.elkhornslough.org/research-program/technical-report-series/ (accessed December 1, 2020).

Van Dyke, E., and Wasson, K. (2005). Historical ecology of a central California estuary: 150 years of habitat change. *Estuaries* 28, 173–189. doi: 10.1007/bf02732853

Wasson, K., Suarez, B., Akhavan, A., McCarthy, E., Kildow, J., Johnson, K. S., et al. (2015). Lessons learned from an ecosystem-based management approach to restoration of a California estuary. *Mar. Policy* 58, 60–70. doi: 10.1016/j.marpol.2015.04.002

Wasson, K., Watson, E. B., Van Dyke, E., Hayes, G., and Aiello, A. (2012). *A Novel Approach Combining Rapid Paleoecological Assessments With Geospatial Modeling and Visualization to Help Coastal Managers Design Salt Marsh Conservation Strategies in the Face of Environmental Change.* Elkhorn Slough Technical Report Series 2012:1. Available online at: http://www.elkhornslough.org/research-program/technical-report-series/ (accessed June 28, 2020).

Watson, E. B., Wigand, C., Davey, E. W., Andrews, H. M., Bishop, J., and Raposa, K. B. (2017). Wetland loss patterns and inundation-productivity relationships prognosticate widespread salt marsh loss for southern New England. *Estuaries Coasts* 40, 662–681. doi: 10.1007/s12237-016-0069-1

Watson, H. C. (1835). *Remarks on the Geographical Distribution of British Plants: Chiefly in Connection with Latitude, Elevation, and Climate*. London: Longman, Rees, Orme, Brown, Green, and Longman, Paternoster-Row.

Weston, N. B. (2014). Declining sediments and rising seas: an unfortunate convergence for tidal wetlands. *Estuaries Coasts* 37, 1–23. doi: 10.1007/s12237-013-9654-8

Wu, Y., Liu, J., Yan, G., Zhai, J., Cong, L., Dai, L., et al. (2020). The size and distribution of tidal creeks affects salt marsh restoration. *J. Environ. Manag.* 259:110070. doi: 10.1016/j.jenvman.2020.110070

Yando, E. S., Osland, M. J., Jones, S. F., and Hester, M. W. (2019). Jump-starting coastal wetland restoration: a comparison of marsh and mangrove foundation species. *Restor. Ecol.* 27, 1145–1154. doi: 10.1111/rec.12963

Zahawi, R. A., Dandois, J. P., Holl, K. D., Nadwodny, D., Reid, J. L., and Ellis, E. C. (2015). Using lightweight unmanned aerial vehicles to monitor tropical forest recovery. *Biol. Conserv.* 186, 287–295. doi: 10.1016/j.biocon.2015.03.031

Zedler, J. B. (2000a). *Handbook for Restoring Tidal Wetlands*. Boca Raton, FL: CRC press.

Zedler, J. B. (2000b). Progress in wetland restoration ecology. *Trends Ecol. Evol.* 15, 402–407. doi: 10.1016/s0169-5347(00)01959-5

Zedler, J. B., Callaway, J. C., Desmond, J. S., Vivian-Smith, G., Williams, G. D., Sullivan, G., et al. (1999). Californian salt-marsh vegetation: an improved model of spatial pattern. *Ecosystems* 2, 19–35. doi: 10.1007/s100219900055

Conflict of Interest: The authors declare that the research was conducted in the absence of any commercial or financial relationships that could be construed as a potential conflict of interest.

Copyright © 2021 Haskins, Endris, Thomsen, Gerbl, Fountain and Wasson. This is an open-access article distributed under the terms of the Creative Commons Attribution License (CC BY). The use, distribution or reproduction in other forums is permitted, provided the original author(s) and the copyright owner(s) are credited and that the original publication in this journal is cited, in accordance with accepted academic practice. No use, distribution or reproduction is permitted which does not comply with these terms.

frontiers in Environmental Science

ORIGINAL RESEARCH
published: 15 April 2021
doi: 10.3389/fenvs.2021.612934

Quantifying Scales of Spatial Variability of Cyanobacteria in a Large, Eutrophic Lake Using Multiplatform Remote Sensing Tools

Samantha L. Sharp[1,2]*, *Alexander L. Forrest*[1,2], *Keith Bouma-Gregson*[3], *Yufang Jin*[4], *Alicia Cortés*[1,2] *and S. Geoffrey Schladow*[1,2]

[1]*Department of Civil and Environmental Engineering, University of California, Davis, CA, United States,* [2]*Tahoe Environmental Research Center, University of California, Davis, CA, United States,* [3]*Office of Information Management and Analysis, California State Water Resources Control Board, Sacramento, CA, United States,* [4]*Department of Land, Air and Water Resources, University of California, Davis, CA, United States*

Harmful algal blooms of cyanobacteria are increasing in magnitude and frequency globally, degrading inland and coastal aquatic ecosystems and adversely affecting public health. Efforts to understand the structure and natural variability of these blooms range from point sampling methods to a wide array of remote sensing tools. This study aims to provide a comprehensive view of cyanobacterial blooms in Clear Lake, California — a shallow, polymictic, naturally eutrophic lake with a long record of episodic cyanobacteria blooms. To understand the spatial heterogeneity and temporal dynamics of cyanobacterial blooms, we evaluated a satellite remote sensing tool for estimating coarse cyanobacteria distribution with coincident, *in situ* measurements at varying scales and resolutions. The Cyanobacteria Index (CI) remote sensing algorithm was used to estimate cyanobacterial abundance in the top portion of the water column from data acquired from the Ocean and Land Color Instrument (OLCI) sensor on the Sentinel-3a satellite. We collected hyperspectral data from a handheld spectroradiometer; discrete 1 m integrated surface samples for chlorophyll-*a* and phycocyanin; multispectral imagery from small Unmanned Aerial System (sUAS) flights (~12 cm resolution); Autonomous Underwater Vehicle (AUV) measurements of chlorophyll-*a*, turbidity, and colored dissolved organic matter (~10 cm horizontal spacing, 1 m below the water surface); and meteorological forcing and lake temperature data to provide context to our cyanobacteria measurements. A semivariogram analysis of the high resolution AUV and sUAS data found the Critical Scale of Variability for cyanobacterial blooms to range from 70 to 175 m, which is finer than what is resolvable by the satellite data. We thus observed high spatial variability within each 300 m satellite pixel. Finally, we used the field spectroscopy data to evaluate the accuracy of both the original and revised CI algorithm. We found the revised CI algorithm was not effective in estimating cyanobacterial abundance for our study site. Satellite-based remote sensing tools are vital to researchers and water managers as they provide consistent, high-coverage data at a low cost and sampling effort. The findings of this research support continued development and refinement of remote sensing tools, which are essential for satellite monitoring of harmful algal blooms in lakes and reservoirs.

Keywords: cyanobacteria, harmful algal blooms (HABs), remote sensing, Clear Lake, critical scales of variability (CSV), autonomous underwater vehicles (AUV), small unmanned aerial systems (sUAS), inland waters

OPEN ACCESS

Edited by:
Sherry L. Palacios, California State University, Monterey Bay, United States

Reviewed by:
Mark Harrison Myer, United States Environmental Protection Agency (EPA), United States
Joseph Daniel Ortiz, Kent State University, United States

***Correspondence:**
Samantha L. Sharp
ssharp@ucdavis.edu

Specialty section:
This article was submitted to Environmental Informatics and Remote Sensing, a section of the journal Frontiers in Environmental Science

Received: *01 October 2020*
Accepted: *02 February 2021*
Published: *15 April 2021*

Citation:
Sharp SL, Forrest AL, Bouma-Gregson K, Jin Y, Cortés A and Schladow SG (2021) Quantifying Scales of Spatial Variability of Cyanobacteria in a Large, Eutrophic Lake Using Multiplatform Remote Sensing Tools. Front. Environ. Sci. 9:612934. doi: 10.3389/fenvs.2021.612934

INTRODUCTION

Harmful algal blooms of toxin-producing cyanobacteria (cyanoHABs) are increasing in magnitude and frequency globally, both degrading aquatic ecosystems and posing a risk to public health (Havens, 2008; Cheung et al., 2013; Taranu et al., 2015; Huisman et al., 2018; Ho et al., 2019). Monitoring these cyanoHABs is necessary to track their development and mitigate their effects in the context of a changing climate (Paerl et al., 2016; Visser et al., 2016). Monitoring cyanoHABs is challenging because they exhibit substantial spatial and temporal variability (Kutser, 2009; Carey et al., 2014) making it difficult to link complex bloom dynamics with the underlying drivers for these systems (Paerl et al., 2011; Ho and Michalak, 2015).

CyanoHABs demonstrate high spatial variability, which complicates bloom measurement (Kutser, 2009). Drivers of this spatial patchiness include winds and currents, with higher concentrations of cyanobacteria typically observed at downwind sites (Carey et al., 2014; Liu et al., 2019a). Additionally, some cyanobacterial species have gas vacuoles, which allow cells to control their buoyancy and rise and fall in the water column creating spatial variability with depth (Oliver et al., 2012). Even though spatial variability of cyanoHABs is a known issue with regards to remote sensing of blooms as measurements can vary substantially within a satellite pixel (Kutser, 2009), satellite remote sensing tools remain one of the key tools for monitoring cyanoHABs because of their global coverage.

Remote sensing methods have the benefit of offering high spatial and temporal coverage across large scales. Remote sensing of cyanobacteria is possible due to the differences in spectral signatures for cyanobacteria and other types of phytoplankton. Phytoplankton contains chlorophyll-*a* as the main photosynthetic pigment. This pigment demonstrates absorption features in its spectral profile at 440 and 675 nm (Ruiz-Verdú et al., 2008; Stumpf et al., 2016). Cyanobacteria contain the secondary photosynthetic pigment phycocyanin in addition to chlorophyll-*a* (Bryant, 1982; Matthews, 2011). Due to its unique spectral signature (including an absorption peak ~620 nm and a reflectance peak ~650 nm) and limitation to cyanobacteria and rhodophytes, phycocyanin concentrations are often used to distinguish cyanobacteria from freshwater phytoplankton (Kutser, 2009).

Many satellite remote sensing tools for monitoring harmful algal blooms have been developed (see reviews by Kutser, 2009; Matthews, 2011; and Gholizadeh et al., 2016). In this study we use the Cyanobacterial Index (CI) remote sensing tool, which is a spectral shape algorithm based on the tendency of *Microcystis* (a common genus of cyanobacteria) to demonstrate weak chlorophyll-*a* fluorescence compared to other phytoplankton (Wynne et al., 2008; Wynne et al., 2010; Stumpf et al., 2016). This results in an observed reflectance sag in the satellite data at wavelengths of 681 nm. The CI algorithm uses the multispectral MERIS sensor mounted on the Envisat satellite and the Ocean and Land Color Instrument (OLCI) sensor on Sentinel-3 because they have the correct spectral resolution to differentiate cyanobacteria from other phytoplankton. While satellite remote sensing allows for repeated sub-weekly observation of the conditions at the same location, the spatial resolution is usually coarse, ranging from 30 to 1,000 m (Kutser, 2009; Hunter et al., 2017), with most cyanobacteria-specific algorithms utilizing the MERIS and OLCI sensors, which have a resolution of 300 m. This issue is further exacerbated by pixel contamination close to the shoreline. Additionally, cloud coverage is problematic, creating instances where no useful data are obtainable from a satellite pixel. Finally, coarse resolution satellites are not well suited to detect spatial variability of cyanobacteria as the bloom density can vary by up to two orders of magnitude within one satellite pixel (Kutser, 2009).

Given the coarse spatial resolution of satellite tools aimed at detecting cyanobacteria, other high spatial resolution sampling methods are more apt at measuring the spatial variability of cyanoHABs. Many field deployable platforms such as Autonomous Underwater Vehicles and small Unmanned Aerial Systems, can collect data at high spatial resolution. AUVs equipped with fluorescence sensors and/or on-board samplers have been used to measure algal and cyanobacterial blooms, (e.g. Robbins et al., 2006; Blackwell et al., 2008). sUAS carrying Red-Green-Blue, multispectral, and sometimes hyperspectral cameras have also been used for detecting blooms (see review paper by Kislik et al., 2018). These sampling methods have clear benefit due to their high spatial resolution, but do not offer the repeat high temporal measurements offered by satellite platforms.

When satellite tools are combined with other high resolution monitoring tools, they augment the observer's ability to both monitor and study blooms (Vander Woude et al., 2019). Additionally, the high spatial resolution methods, (e.g. AUV and sUAS) may be used to quantify the spatial heterogeneity of cyanoHABs, specifically to determine their Critical Scale of Variability (CSV). CSVs (as defined by Blackwell et al., 2008) are the length scales necessary to resolve the spatial variability of a bloom. The CSV of a cyanobacterial bloom defines the distance required between samples to observe the spatial "patchiness" or changes in bloom concentration across space. The CSV also helps define the spatial extent at which biological and physical processes may occur (Fraschetti et al., 2006). The CSV is important for designing sampling plans by selecting the sampling resolution necessary to adequately characterize a bloom (Vander Woude et al., 2019).

In this study, we measure cyanobacterial bloom density using several methods at varying spatial scales and spatial resolutions to understand how bloom density changes across scales. We collected discrete water samples; hyperspectral measurements from a handheld spectroradiometer; coarse spatial resolution multispectral reflectance data from the OLCI sensor on the Sentinel-3a satellite; high spatial resolution multispectral reflectance data collected using a sUAS; and high spatial resolution scattering and fluorescence data from an AUV. This multiplatform approach provides a synoptic view of cyanobacterial density across multiple spatial scales. The collected data were used to 1) understand the spatial and temporal trends at our study site; 2)

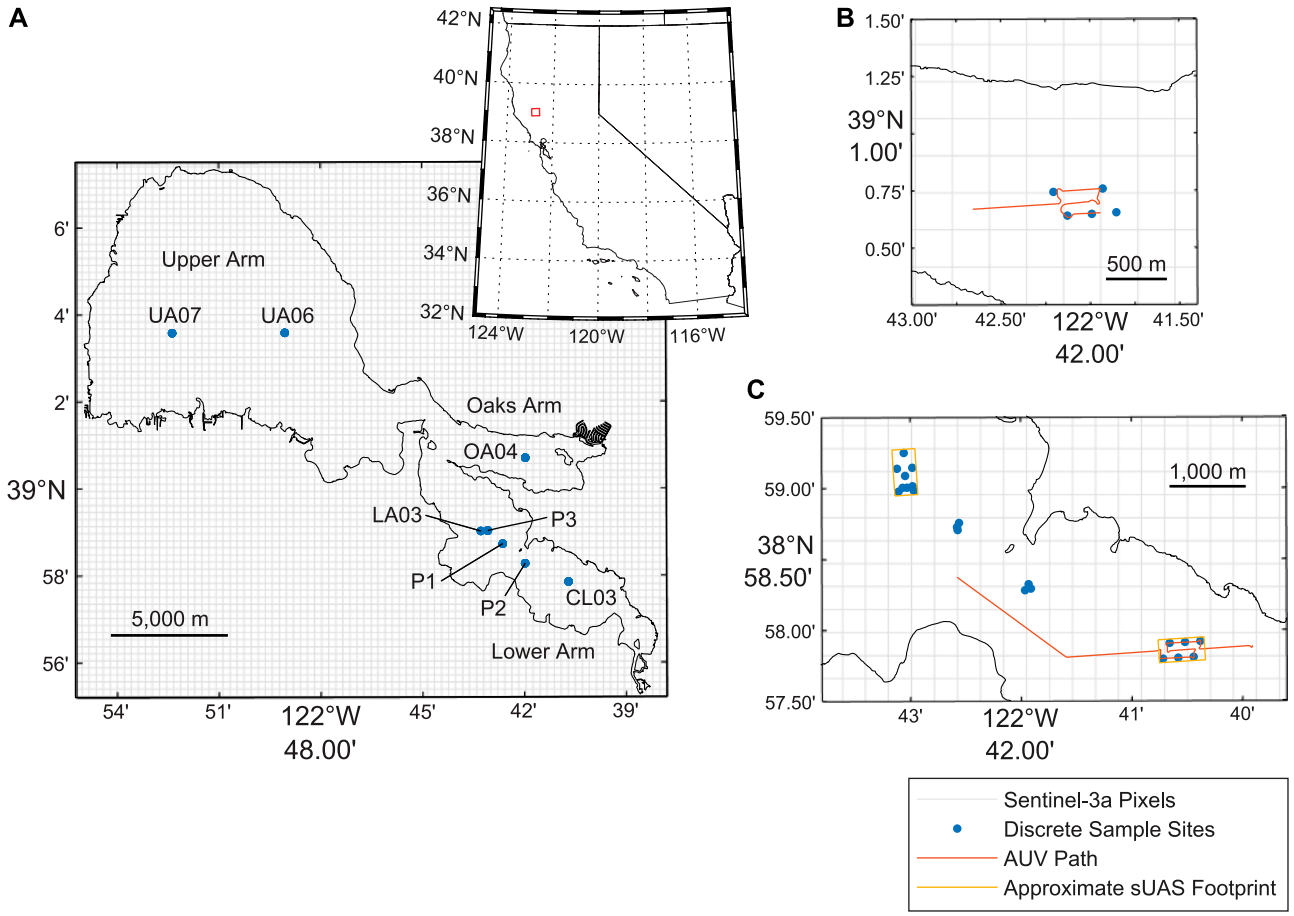

FIGURE 1 | Sample site locations in Clear Lake **(A)** is an overview map of Clear Lake **(B)** shows the sampling locations in the Oaks Arm **(C)** shows the sampling locations in the Lower Arm. The 300 × 300 m outlines of the Sentinel-3a pixels are also shown.

quantify the CSV for cyanobacteria blooms; and 3) evaluate the accuracy of the CI algorithm. Key recommendations stemming from this work are consideration of the CSV of cyanobacteria blooms when designing sampling plans and future satellite remote sensing sensors, and continued refinement of the CI algorithm for improved detection of low concentration blooms.

METHODS

Study Site

This study was conducted at Clear Lake, California, a large (approximately 160 km^2 in surface area) and shallow lake (average depth 8 m, maximum depth 15 m). Clear Lake is comprised of three basins–the Upper Arm, Oaks Arm, and Lower Arm (**Figure 1**). All three basins are deep enough to be thermally stratified but shallow enough to vertically mix fully several times a year and partially mix almost daily, (i.e. polymictic) (Rueda and Schladow, 2003). Clear Lake is naturally eutrophic and supports large fish and waterfowl populations. Algal blooms have been documented to occur primarily in the late spring, summer, and fall (Winder et al., 2010). Past research has identified the phytoplankton community to be cyanobacteria dominated for most of the year (Horne, 1975). CyanoHABs have increased in frequency at Clear Lake since the mid-1900s to create nuisance scums and odors, which cause public and environmental health concerns (Richerson et al., 1994).

Data Collection and Data Processing

Data were collected in Clear Lake using several methods (**Table 1**; **Figure 1**). The *in situ* data collection methods include collection of discrete samples, hyperspectral data measurements using a handheld spectroradiometer, multispectral imaging from a sUAS, and fluorescence and scattering meter measurements from an AUV. Additionally, cyanobacteria index (CI) was calculated from Level 3 OLCI sensor data from the Sentinel-3a satellite. Finally, meteorological and lake temperature data were obtained to provide context to our cyanobacteria measurements.

Discrete Samples

Discrete water samples were collected across 32 sampling sites on Clear Lake (**Table 1**; **Figure 1**), generally located near existing

TABLE 1 | Summary of data collection. Sampling sites CL03 (a, b, c, d, e, f), LA03 (a, b, c, d, e, f), P1 (S1, S2, S3), P2 (S1, S2, S3), and P3 (S1, S2, S3) are in the Lower Arm of Clear Lake, OA04 (a, b, c, d, f) is in the Oaks Arm, and UA06 (a, b, c) and UA07 (a, b, c) are in the Upper Arm.

Date	Sampling sites	Sampling method				
		Chl-*a*	PC	Rad	AUV	sUAS
12-Jul-2019	CL03 (a, b, c), LA03 (a, b, c), OA04 (a, b, c), UA06 (a, b, c), UA07 (a, b, c)	X	X			
07-Aug-2019	P1 (S1, S2, S3), P2 (S1, S2, S3), P3 (S1, S2, S3)	X		X		
16-Aug-2019	OA04 (a, b, c), OA04 (d, f)	X	X	X	X	
	LA03 (a, b, c), LA03 (d, e, f)	X	X	X		X
	CL03 (a, b, c), CL03 (d, e, f)	X	X	X	X	X
08-Oct-2019	CL03 (a, b, c), LA03 (a, b, c), OA04 (a, b, c), UA06 (a, b, c), UA07 (a, b, c)	X	X	X		

Chl-a: discrete sample for chlorophyll-a; PC: discrete sample for phycocyanin; Rad: spectroradiometer.

sampling sites in routine water quality monitoring programs. These existing sampling sites were selected to allow for future comparison between the data collected in this study with data collected in routine water quality monitoring programs; those comparisons were not included with this research. To enable comparisons between discrete samples and satellite CI values, the sample sites are located within 19 separate Sentinel-3a pixels near the centers of each Clear Lake basin to avoid shoreline contamination of the satellite pixels. The samples were planned such that three sample sites would be located within one corresponding Sentinel-3a pixel, (e.g. CL03a, CL03b, and CL03c were planned within the same Sentinel-3a pixel and are all located nearby the routine CL03 water quality monitoring site). However, due to an unknown projection issue associated with the Sentinel-3a CI product obtained from the San Francisco Estuary Institute (SFEI) and the National Oceanic and Atmospheric Administration (NOAA) HAB Tool (see https://fhab.sfei.org/; Stumpf et al., 2015) at the time of planning, the sampling sites did not all necessarily occur in the same pixel and more pixels were sampled than originally planned (19 pixels sampled vs. 10 pixels planned). This projection issue was corrected in data processing and analysis.

Discrete water samples were collected during four sampling events in July, August, and October 2019 (**Table 1**). The sampling dates were chosen to correspond with Sentinel-3a satellite overpasses and with expected summer and fall algal blooms in Clear Lake. The first sampling event in July 2019 included grab sampling from 0.1 m depth. The sampling method was later refined for the remaining sampling events in August and October 2019 to include collection of an integrated depth sample of the top 1 m of the water column. No correction was made to the data despite the differences in sampling method depth. Surface scums were not present at our study sites during sampling so errors arising from the difference in sampling method depth are believed to be minimal. Discrete samples were filtered through pre-combusted (500°C for 2 h) Whatman GF/F filters (0.7 μm nominal pore size). The filters from all four sampling events were analyzed for chlorophyll-*a* by sample processing by extraction in 90% acetone at −20°C for 24 h following a modified EPA method 445.0 (Arar and Collins, 1997) and sample analysis on a Turner Designs 10 AU fluorometer. The filters from three sampling events (July 12, 2019, August 16, 2019, and October 08, 2019) were analyzed for phycocyanin following modified methods developed by Kasinak et al. (2015); Konopko (2007); Siegelman and Kycia (1978) with sample processing by extraction in 10 mM phosphate buffer (pH 6.8) with three freeze-thaw cycles and then sample analysis using a Turner Designs TD700 fluorometer. The sampling event on August 07, 2019 did not include analysis for phycocyanin because this sample was collected with a different sampling program that does not include sampling and analysis for phycocyanin.

Due to unforeseen complications, only one set of sample filters from the July 12, 2019 and August 16, 2019 sampling events was available for laboratory analysis. These filters were cut in half to analyze both chlorophyll-*a* and phycocyanin from a single filter. Prior to analysis of the Clear Lake samples, a test was run on split filters vs. whole filter analysis with five replicate samples from another site (surface samples collected from Pinto Lake, CA on October 24, 2019). Three sets of filters were prepared from each sample, with one set of filters analyzed for chlorophyll-*a*, one set of filters analyzed for phycocyanin, and one set of filters cut in half, with one half analyzed for chlorophyll-*a* and one half analyzed for phycocyanin. A paired-sample *t*-test on the whole and half filter data resulted in *p*-values of 0.42 and 0.77 for the chlorophyll-*a* and phycocyanin data, respectively. Additionally, the means of the replicates were found to be within a standard deviation of one another. Given the statistically insignificant difference between whole and half-filters, the half-filter method was decided to be not ideal but acceptable in the absence of other measurements.

Spectroscopy Data

High resolution spectral measurements were collected at eight sampling sites on Clear Lake during three sampling events in August and October 2019 (**Table 1**; **Figure 1**). Spectral measurements were not made during the July 2019 sampling event because the sampling equipment was not available on that date. The sampling locations were selected such that one sampling site out of every cluster of three discrete sample sites had spectroscopy measurements completed. We could not collect spectral measurements at every discrete sample site due to time constraints. We used a Malvern Panalytical FieldSpec Handheld two Pro spectroradiometer with a 7.5° fore optic angular field of view. The spectroradiometer has a spectral resolution of <3 nm

across a range of wavelengths from 375 to 1,075 nm, with a total of 575 spectral bands (discrete wavelengths). At each site, three to four measurements were taken following standard methods (Tomlinson et al., 2016). Measurements over a 10% calibrated spectralon reflectance plate and at the sky were also collected to convert the radiance measurements to dimensionless reflectance during post-processing (Mobley, 1999; Tomlinson et al., 2016).

Sentinel-3a Data

Satellite-derived cyanobacteria index (CI) was calculated from Level 3 data obtained from NOAA for the multispectral OLCI sensor on the Sentinel-3a satellite. Level 3 data products include ρ_s, which is a dimensionless reflectance product generated from Level 2 data (calibrated and georeferenced) with additional correction for scattering and absorption through the atmosphere (Wynne et al., 2018). CI is calculated from ρ_s (herein referred to as "reflectance") using the CI algorithm (**Eqs 1**, **2**) (Wynne et al., 2008; Wynne et al., 2010). The CI algorithm is a spectral shape algorithm for multispectral data from the MERIS sensor mounted on the Envisat satellite and OLCI sensor on Sentinel-3a. The CI algorithm was developed based on the spectral shape (SS) at wavelength 681 nm (SS{681}) observed in the satellite data as follows (Wynne et al., 2010):

$$\mathrm{CI} = -\mathrm{SS}\{681\}, \tag{1}$$

$$\mathrm{SS}\{\lambda\} = \rho_s\{\lambda\} - \rho_s\{\lambda^-\} - \left(\rho_s\{\lambda^+\} - \rho_s\{\lambda^-\}\right) \times \frac{\lambda - \lambda^-}{\lambda^+ - \lambda^-} \tag{2}$$

where, $\lambda = 681\,\mathrm{nm}$, $\lambda^+ = 709\,\mathrm{nm}$, and $\lambda^- = 665\,\mathrm{nm}$. This algorithm was later refined to incorporate an exclusionary criterion for the spectral shape at 665 nm (SS{665}), where, $\lambda = 665\,\mathrm{nm}$, $\lambda^+ = 681\,\mathrm{nm}$, and $\lambda^- = 620\,\mathrm{nm}$ (Matthews et al., 2012; Lunetta et al., 2015; Coffer et al., 2020). The SS{665} exclusionary criterion targets the 620 nm band, which is a phycocyanin absorption feature (Lunetta et al., 2015). This exclusionary criterion categorizes CI as containing cyanobacteria when SS{665} > 0 and as not containing cyanobacteria when SS{665} < 0 (Lunetta et al., 2015). This research used both the original CI equation and the revised CI equation with the addition of the SS{665} exclusionary criterion. The CI algorithm (both original and revised) was also applied to the spectroradiometer reflectance data.

Using the approach in Tomlinson et al. (2016), a locally tuned equation comparing chlorophyll-*a* and phycocyanin to CI was determined for our study site. Previous proposed equations relating CI to chlorophyll-*a* are shown below (**Eq. 3** from Tomlinson et al., 2016 and **Eq. 4** from Stumpf et al., 2015).

$$\mathrm{chla}\ (\mu\mathrm{g/L}) = 4050\ (\pm 271) \times \mathrm{CI} + 20\ (\pm 3), \tag{3}$$

$$\mathrm{chla}\ (\mu\mathrm{g/L}) = 4000 \times \mathrm{CI} + 10. \tag{4}$$

A least-squares linear regression approach was used to model the relationship between CI and both chlorophyll-*a* and phycocyanin specific to Clear Lake.

Small Unmanned Aerial System Data

Very high spatial resolution multispectral imagery was collected from the two Lower Arm sites (CL03 and LA03) on August 16, 2019 (**Table 1**; **Figure 1**). The sampling date was chosen as a larger effort sampling event when coincident discrete samples, satellite measurements, sUAS, and AUV data could be collected. The sUAS and AUV tools were only available on this sampling date due to resource limitations. The intention was to collect measurements at three locations (two in the Lower Arm and one in the Oaks Arm). These basins were selected for sampling by the sUAS and AUV because at the time of mission planning, they demonstrated the most cyanobacterial activity. However, due to vehicle piloting difficulties only the two Lower Arm sites could be sampled by the sUAS.

We used a MicaSense RedEdge multispectral camera mounted on a Matrice 100 sUAS and operated using DJI GS Pro software using standard methods (Liu et al., 2019b). The MicaSense RedEdge camera, like other commercial multispectral cameras, has individual lenses for each band with discrete exposure times that optimize the radiometric range depending on the target (Kim et al., 2020). Aerial flights were conducted with this sUAS at an average height of 120 m above ground level, resulting in images at a resolution of 8.2 cm/pixel. The flight lines had front and side overlaps of 60%. Before and after each sUAS flight, standard reflectance panel images were captured by the MicaSense camera for later calibration of the data. Individual images were georectified and stitched into a single orthomosaic of multispectral reflectance (true geometrically correct and mosaicked image) using Pix4Dfields software. The planned sUAS flights were intended to cover an area aligned with and equivalent two Sentinel-3a pixels (300 m × 300 m each). However, as previously mentioned, due to an unknown projection issue with the data used in planning, the sUAS flights overlapped with several Sentinel-3a pixels, but none of them were fully covered.

The MicaSense multispectral camera captures reflectance data at five bands: blue (center λ = 475 nm with 20 nm bandwidth Full Width at Half Maximum or FWHM), green (center λ = 560 nm with 20 nm bandwidth FWHM), red (center λ = 668 nm with 10 nm bandwidth FWHM), near infrared (center λ = 840 nm with 40 nm bandwidth FWHM), and red edge (center λ = 717 nm with 10 nm bandwidth FWHM). Chlorophyll-*a* was derived from the reflectance data using the approach in Ha et al. (2017). Ha et al. (2017) found an exponential equation using a green-red band ratio yielded the best results for their study site (**Eq. 5**, where B3 = green band and B4 = red band).

$$\mathrm{chla}\ (\mu\mathrm{g/L}) = 0.80 \times \exp\left(0.35 \times B3/B4\right). \tag{5}$$

We attempted to determine a locally tuned band ratio equation computing chlorophyll-*a* for our study site by using the coincident discrete sample results (n = 6); however, a clear relationship was not found and the published equation (**Eq. 5**) was used instead. The chlorophyll-*a* concentrations determined from **Eq. 5** were scaled to the discrete sample chlorophyll-*a* measurements, where the scaling factor was equal to the ratio of

the average of the discrete sample chlorophyll-*a* results to the average of the sUAS-derived chlorophyll-*a* values. See **Supplementary Section S1** for more information on sUAS data processing.

Autonomous Underwater Vehicle Data

High resolution data were collected using an Autonomous Underwater Vehicle from one Lower Arm site (CL03) and one Oaks Arm site (OA04) on August 16, 2019 (**Table 1**; **Figure 1**). The sampling date and sampling locations are discussed in the sUAS data section above. Additionally, the AUV sample locations intended to include two Lower Arm sites and one Oaks Arm site. However, due to vehicle deployment difficulties and time constraints, only one Lower Arm site and the Oaks Arm site could be sampled.

The AUV used is a small *Gavia*-class AUV. The instruments mounted on the AUV include a Seabird Electronics SBE-49 CTD (Conductivity, Temperature, Depth) sensor and a WETLabs ECO Triplet BBFL2 combination scattering meter and fluorometer. The BBFL2 determines turbidity through measurement of red light scattering at 700 nm; colored dissolved organic matter (CDOM) through fluorescence with excitation at 370 nm and response measurement at 460 nm; and chlorophyll-*a* through fluorescence with excitation at 470 nm and response measurement at 695 nm. The detection ranges for the BBFL2 sensors are 0–50 μg/L for chlorophyll-*a*, 0–375 ppb for CDOM, and 0–5 m^{-1} for the scattering meter. The AUV is also equipped with a navigation system including a combined Teledyne RD Instruments workforce navigator Doppler velocity log (DVL) and a Kearfott inertial navigation system (INS). The AUV was deployed at a cruising speed of 1.5–2 m/s. The AUV mission was designed to have the vehicle run at a constant depth of 0.5 m below the lake surface. A tolerance of three standard deviations from the mean depth was allowed for each mission and all data outside this set tolerance was disregarded during post-processing (Yu et al., 2002; Blackwell et al., 2008; Forrest et al., 2008). The CTD sampled at 16 Hz, the combination scattering meter and fluorometer sampled at approximately 0.9 Hz, and the navigation system records data at 1 Hz. The three datasets were merged with data points interpolated using a linear approach and the fastest sampling rate. The data were then bin averaged to a bin size greater than the slowest sampled dataset. The recorded scattering and fluorescence measurements were converted to turbidity (NTU), CDOM (ppb), and chlorophyll-*a* (μg/L) using the factory determined dark count offsets (false positives read by the sensor in absolute zero light) and scaling factors. The [back] scattering meter was not calibrated in turbidity (NTU) units using a turbidity solution. An approximate conversion from the sensor single-angle scattering scale factor (m^{-1} sr^{-1}) to a turbidity value (NTU) was used to report the turbidity measurements. The chlorophyll-*a* data were further scaled to the results of the adjacent discrete samples to account for differences in the field fluorometry measurements and the laboratory chlorophyll-*a* extraction measurements. Although scaling the AUV chlorophyll-*a* measurements by the discrete samples does not ensure accuracy of the AUV results, it allows for easier comparison of the two datasets. As the main purpose of this study is to evaluate the variability of cyanobacteria blooms rather than the magnitude, we feel this approach is acceptable. See **Supplementary Section S1** for more information on AUV data processing.

Meteorology and Lake Temperature Data

Meteorological forcing and lake temperature data were acquired for Clear Lake for our sampling dates at multiple locations across the lake's basins (Cortés and Schladow, 2020). To measure meteorological conditions, a network of seven Davis Instruments Wireless Vantage Pro2 Plus stations installed at the shoreline around the perimeter of Clear Lake measured air temperature, relative humidity, and wind speed and direction every 15 min (see station map in UC Davis Tahoe Environmental Research Center, 2020). Lake surface temperature was determined from a network of Onset Water Temp Pro loggers installed along the near-shore and adjacent to all but one of the meteorological stations (~0.5 m below lake water level) and also installed on three permanent offshore navigation markers (within the top 2 m of the water column). The thermistors sample every 10 min with 0.2°C accuracy and 0.02°C resolution. Lake water clarity was characterized at each sampling site (**Table 1**; **Figure 1**) using a Secchi disk.

Data Analysis

Critical Scales of Variability

CSVs of cyanobacteria were determined for this study using a semivariogram analysis of the AUV and sUAS data using the GeoR Package in R following similar methods as Blackwell et al. (2008) and as described in Diggle and Ribeiro (2007). The CSV is considered the "apparent range" (Blackwell et al., 2008) or the "practical range" (Diggle and Ribeiro, 2007) at which the semivariance levels off, forming the "sill" of the semivariogram. This value was determined by visual examination of the log-log plot of the semivariogram at the point where there is a noticeable change in the slope of the line (see Figure 2 of Moses et al., 2016), which corresponds to the point of leveling off in the semivariogram. The semivariograms were computed for the AUV-acquired chlorophyll-*a* measurements and the sUAS-derived chlorophyll-*a* measurements. Two semivariograms were produced for the AUV missions in the Lower Arm and in the Oaks arm. Initially semivariograms were examined for every 500th pixel row and column, (i.e. lines) of sUAS data subsampled from the mosaic of pixel values. A subset of data (every 100th pixel row of the lines 2,500–4,500) were further examined to determine the CSV from the sUAS data. The pixel column data did not produce meaningful results to determine the CSV, likely because the columns are shorter that the rows for our data set. See **Supplementary Section S1** for more information on the data processing for the CSV data analysis.

Coefficients of Variation

We calculated the coefficients of variation of the datasets as an additional metric to quantify the variability of the bloom. The coefficient of variation is equal to the ratio of the standard deviation to the mean.

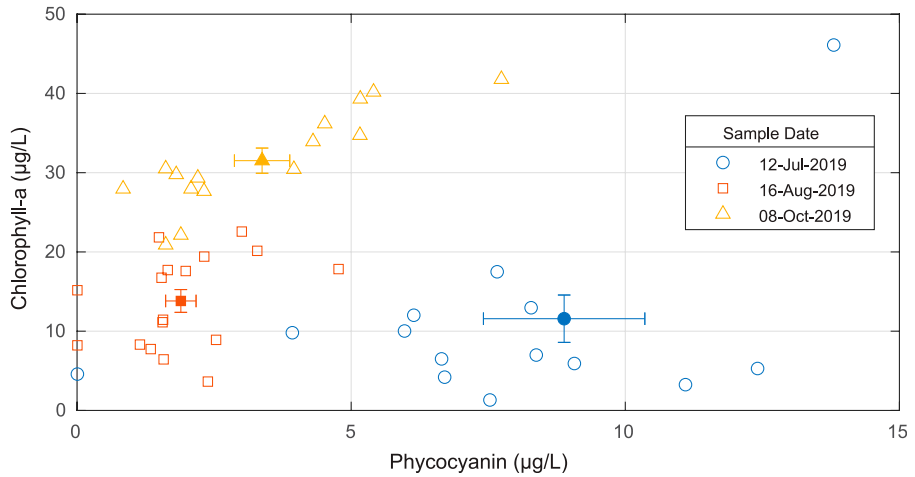

FIGURE 2 | Phycocyanin and chlorophyll-*a* concentrations in discrete samples collected on July 12, 2019, August 16, 2019, and October 08, 2019. The July 12, 2019 sampling event observed a higher average phycocyanin to chlorophyll-*a* ratio compared to the other sampling dates. The averages for each sampling date are shown as the solid symbols with the vertical error bars representing the standard error of the chlorophyll-*a* measurements and the horizontal error bars representing the standard error of the phycocyanin measurements. There is an outlier (phycocyanin = 25.6 µg/L and chlorophyll-*a* = 27.2 µg/L) from July 12, 2019 that is not shown in this plot for visualization purposes.

RESULTS

We measured cyanobacteria over four sampling dates in the Summer and Fall 2019 at different sampling locations in Clear Lake, CA (**Table 1**; **Figure 1**). The central aim of this work was to characterize the CSV of cyanobacteria. We used five methods to quantify cyanobacteria in the water: 1) laboratory analysis of discrete samples for chlorophyll-*a* and phycocyanin; 2) hyperspectral radiance measurements from a handheld spectroradiometer; 3) coarse spatial resolution multispectral reflectance data from the OLCI sensor on Sentinel-3a; 4) high spatial resolution multispectral reflectance data collected using a sUAS; and, 5) high spatial resolution scattering and fluorescence data of turbidity, CDOM, and chlorophyll-*a* collected using an AUV.

Discrete Sampling

The average chlorophyll-*a* concentration of all the samples was approximately four times larger than the average phycocyanin value, with mean ± standard deviation of 18.7 ± 12.0 µg/L and 4.60 ± 4.55 µg/L for chlorophyll-*a* and phycocyanin, respectively. For individual samples, maximum values of phycocyanin (25.6 µg/L) were about half the maximum chlorophyll-*a* concentrations (46.1 µg/L). The mean of the ratio of phycocyanin to chlorophyll-*a* was 0.57 ± 1.04. The correlation coefficients for the relationship between chlorophyll-*a* and phycocyanin are 0.54, 0.36, and 0.87 for the July 12, 2019, August 16, 2019, and October 08, 2019 sampling dates, respectively.

As time progressed over the three sampling dates, we observed increasing chlorophyll-*a* concentrations relative to the concentration of phycocyanin (**Figure 2**). Chlorophyll-*a* concentrations were highest on October 08, 2019 (31.5 ± 6.16 µg/L), while the July 12, 2019 and August 16, 2019 concentrations were similar, 11.6 ± 11.6 µg/L and 13.8 ± 5.93 µg/L, respectively. The August 16, 2019 and October 08, 2019 sampling events had comparable phycocyanin concentrations of 1.89 ± 1.14 µg/L and 3.37 ± 1.95 µg/L, respectively. The largest phycocyanin concentrations were obtained on July 12, 2019 (8.88 ± 5.70 µg/L). As a result, the July 12, 2019 sampling event observed a higher average phycocyanin to chlorophyll-*a* ratio of 1.48 compared to average ratios of 0.19 and 0.10 for the August 16, 2019 and October 08, 2019 events, respectively. Only chlorophyll-*a* was measured on August 07, 2019 and the mean ± standard deviation was 23.0 ± 6.54 µg/L (n = 9). The coefficients of variation for chlorophyll-*a* are 100.0, 28.4, 42.9, and 19.5% for July 12, 2019, August 07, 2019, August 16, 2019, and October 08, 2019, respectively. The coefficient of variation for chlorophyll-*a* for just the CL03 sites in the Lower Arm on August 16, 2019, where coincident AUV and sUAS were taken, is 33%. The coefficients of variation for phycocyanin are 64.2, 60.4, and 57.9% for July 12, 2019, August 16, 2019, and October 08, 2019, respectively. In addition to the chlorophyll-*a* and phycocyanin measurements on August 16, 2019 and October 08, 2019, we also identified the dominant genera of cyanobacteria as *Dolichospermum*, *Gleotrichia*, and *Microcystis*. The authors would like to note that the results from the July 12, 2019 and August 16, 2019 sampling dates are believed to be underestimated. This is because the sample filters from those dates arrived at room temperature after transfer from lab to another.

To provide context to our measurements of cyanobacteria, we measured meteorological forcing and lake surface temperature data. Meteorological variables and lakes surface temperatures were variable between the different basins (**Table 2**). Generally, the Lower and Oaks arms were windier than the Upper Arm. During our sampling dates, wind direction was generally from the Northwest direction. The air and lake surface temperature results

TABLE 2 | Meteorological forcing and lake surface temperature data results. Data provided (columns from left to right) include sampling date, basin sampled, air temperature, relative humidity, wind speed, wind direction, Secchi depth, and lake surface temperature. Generally, the Lower and Oaks arms were windier and have warmer air temperature than the Upper Arm during our sampling events. The Oaks Arm consistently has the lowest clarity based on the Secchi depths.

Date	Basin	Air temp (°C)	RH (%)	Wind v (ms^{-1})	Wind dir	Secchi z^a (m)	Lake surface temp (°C)
Daily average							
12-Jul-2019	UA	22.8	57	0.1	N	–	25
	LA	26.2	48	1.8	NW	–	24
	OA	25.6	47	2.2	NW	–	24.4
07-Aug-2019	LA	21.8	49	1.8	WSW	–	26.9
16-Aug-2019	LA	28.2	38	0.9	WSW	–	26.2
	OA	27.7	43	1.3	NW	–	26.8
08-Oct-2019	UA	16.9	44	4.0	SW	–	18.7
	LA	18.6	51	2.2	WNW	–	19
	OA	18.6	50	2.2	WNW	–	18.7
Value at 12:00 PDT							
12-Jul-2019	UA	24.2	69	0.1	N	2.9	24.8
	LA	29.6	52	0.1	NE	2.6	24.2
	OA	27.5	51	2.2	W	2.0	24.8
07-Aug-2019	LA	27.8	41	2.7	NW	2.5	27.1
16-Aug-2019	LA	29.7	45	1.8	NW	2.6	26.7
	OA	31.1	40	0.1	WSW	1.2	27.5
08-Oct-2019	UA	22.7	39	0.1	W	1.2	20.6
	LA	21.5	42	1.8	W	1.1	20.2
	OA	21.5	42	1.8	W	1.0	20.4

[a]*Secchi depths are single values measured at time of sampling. 12-Jul-2019 Secchi depth measured on 13-Jul-2019; 08-Oct-2019 Secchi depth measured on 11-Oct-2019.*

are varied but there appears to be some tendency of the Lower and Oaks Arms to have warmer air temperature than the Upper Arm. The relative humidity results also do not show a clear trend. Finally, each basin has similar Secchi depths, but the Oaks Arm consistently had the lowest clarity.

In Situ and Satellite-Based Spectra and Cyanobacteria Index Values

We calculated hyperspectral reflectance data from spectroradiometer measurements at several locations on August 07, 2019, August 16, 2019, and October 08, 2019 along with concurrent multispectral satellite reflectance data for all sampling locations and times. Paired hyperspectral/multispectral reflectance data from the spectroradiometer measurements and corresponding Sentinel-3a pixels on August 07, 2019, August 16, 2019 and October 08, 2019 were examined across the spectrum 600–750 nm, where most of the spectral features for phycocyanin and chlorophyll-*a* occur (**Figure 3**). The *in situ* measurements yield a much smoother curve with 150 bands of spectroradiometer data across the range of wavelengths (600–750 nm). Sentinel-3a captured reflectance across 21 bands, and thus, yielded coarser curves. The spectra are presented across the full visible spectrum (400–750 nm) in **Supplementary Figure S1**.

The hyperspectral measurements demonstrate spectral signatures expected from algal and cyanobacteria-laden waters including strong chlorophyll-*a* absorption of red light at ~675 nm (**Figures 3A,C,E**). A slight phycocyanin absorption feature (characterized by reflectance trough) is observed at 615–630 nm as well as the reflectance peak at ~650 nm. The absorption feature at 615–630 nm is more prominently observed in the data for the two August sampling dates.

The coarser reflectance plots (**Figures 3B,D,F**) of the multispectral satellite data do not show the absorption and reflectance features specific to phycocyanin and chlorophyll-*a* as strongly as the hyperspectral reflectance plots. The absorption feature by chlorophyll-*a* of red light (674 nm) is present, while the phycocyanin spectral features at 620 and 650 nm are absent. The reflectance values from the satellite data are higher than the reflectance values from the spectroradiometer data particularly for the August 07, 2019 sampling date, which has the highest satellite reflectance values of any of the sampling dates.

The CI calculated from the spectroradiometer measurements (Field CI) were compared to the corresponding CI from satellite measurements (Satellite CI) (**Figure 4**). CI was calculated both using the original equation defined by Wynne et al. (2008 and 2010) and the revised equation which includes an exclusionary criterion for the spectral shape around wavelength 665 nm defined by Matthews et al. (2012) and validated for lakes in the eastern US by Lunetta et al. (2015). CI without the exclusionary criterion shows some seasonal trend with the highest CI observed on August 07, 2019 with decreasing CI until the lowest values on October 08, 2019 (**Figure 4A**). This trend is consistent between the Field CI and the Satellite CI. We obtained the highest CI values using satellite measurements, which were four-fold larger than the overall mean Satellite CI, and only two-fold larger when using field measurements. The Field CI are generally higher than the Satellite CI for August 07, 2019 whereas the reverse is true for October 08, 2019. The standard deviation was 1.04×10^{-3} for all the calculated CI values. All field reflectance data failed to exceed the SS{665} exclusionary criterion threshold, resulting in Field CI values of zero (**Figure 4B**). The same is true for the October 08, 2019 satellite data.

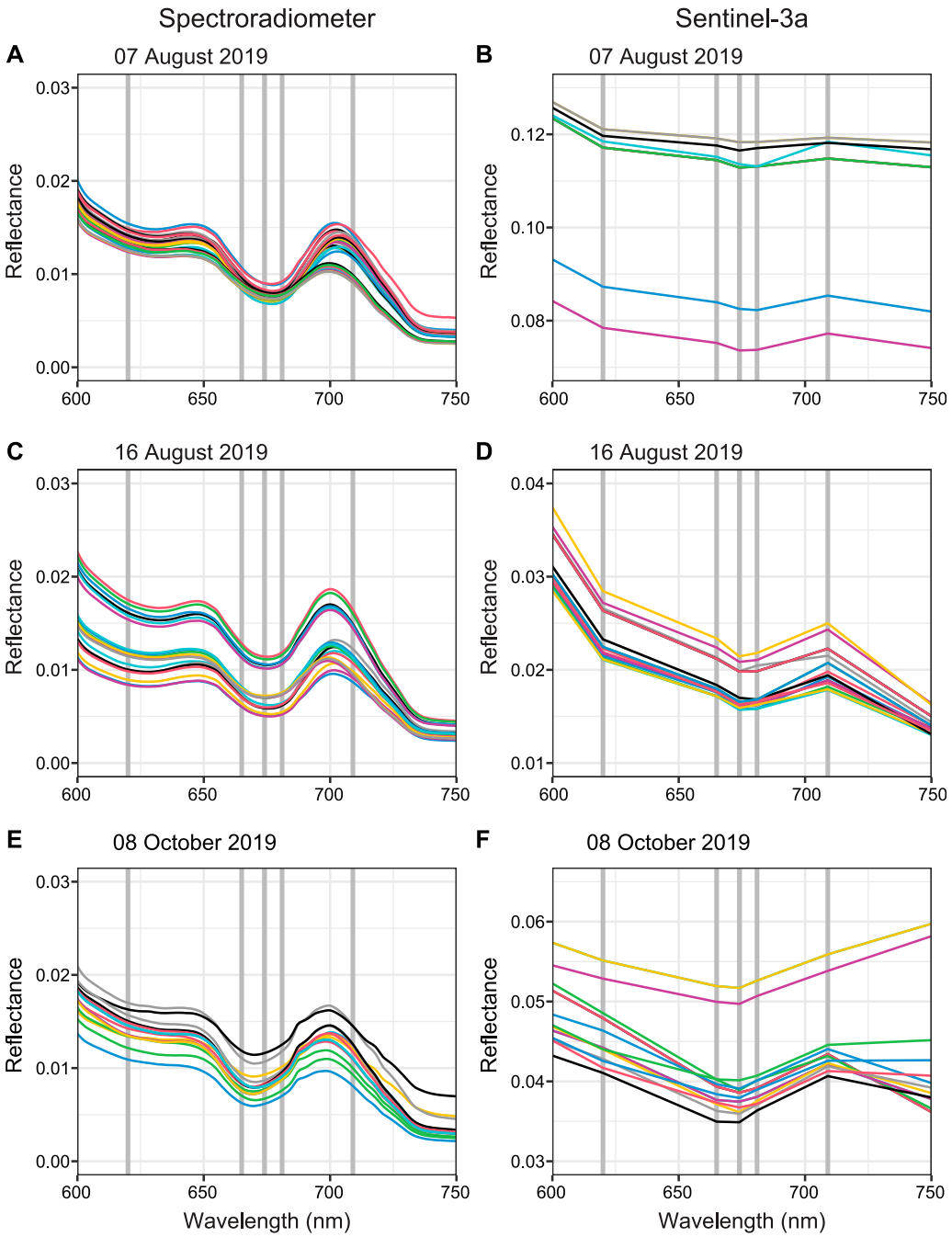

FIGURE 3 | Spectra from *in situ* spectroradiometer **(A, C, E)** and Sentinel-3 pixel data **(B, D, F)** for different sampling dates **(A–B)** August 07, 2019 **(C–D)** August 16, 2019, and **(E–F)** October 08, 2019. The field spectra demonstrate spectral features for phycocyanin and chlorophyll-*a* which are less discernable in the coarser satellite data. Each colored line represented the results from a different discrete sample site (n = 61 total over three sampling dates) for the spectroradiometer data and a different pixel (n = 42 total over three sampling dates) for satellite data. The vertical gray lines represent the spectral band centers of Sentinel-3a. Note the difference in the *y*-axis range between the reflectance plots. Reflectance is dimensionless.

Relationship Between Cyanobacteria Index, Chlorophyll-*a*, and Phycocyanin

The relationship between Field CI and chlorophyll-*a* was significant ($p < 0.05$) on only one sampling day (August 07, 2019). For Satellite CI and chlorophyll-*a*, the relationship was significant for three sampling days, and there was a significantly positive relationship across all sampling days (**Figures 5A,B**). The October 08, 2019 did not fit the same trend as the other dates for Field CI vs. chlorophyll-*a*.

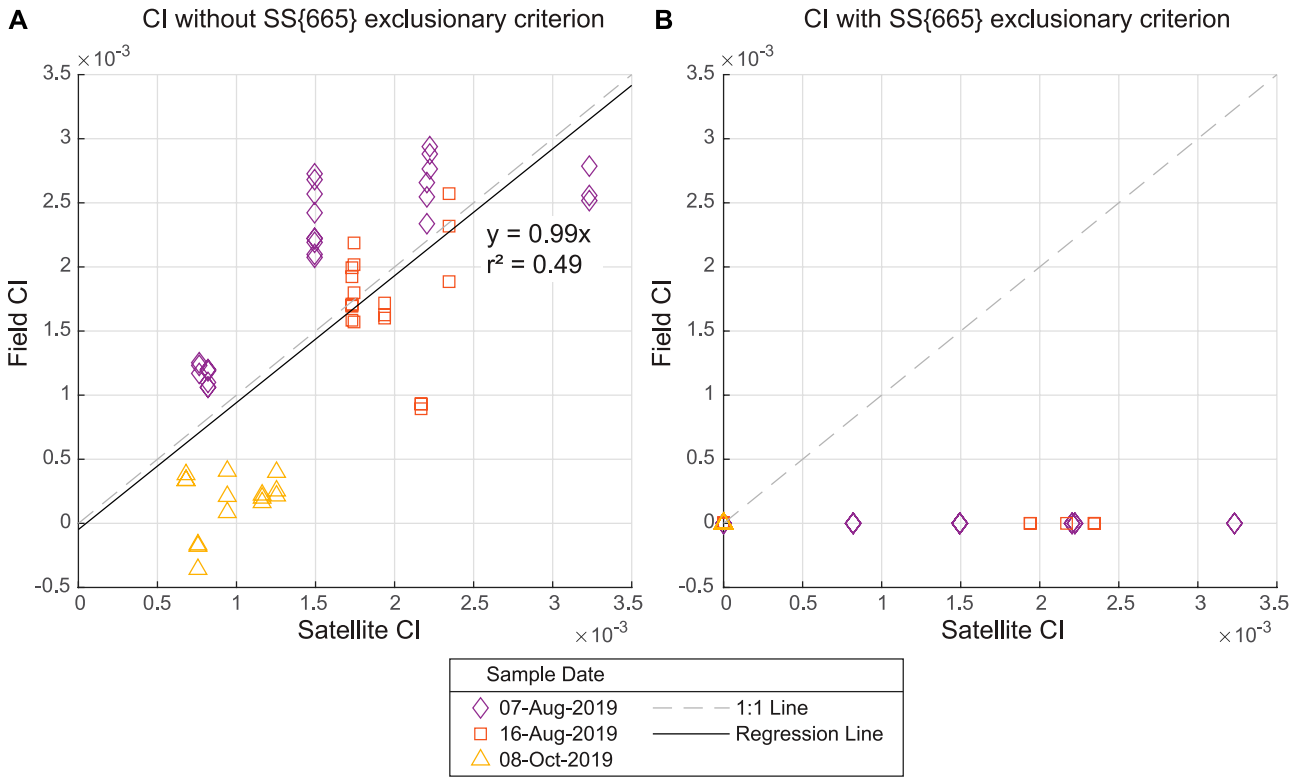

FIGURE 4 | (A) CI without the SS{665} exclusionary criterion for field spectroradiometer measurements (*y*-axis) and the Sentinel-3 measurements (*x*-axis) for the same sampling dates **(B)** CI with the SS{665} exclusionary criterion for field spectroradiometer measurements (*y*-axis) and the Sentinel-3 measurements (*x*-axis) for the same sampling dates. The CI calculated without the SS{665} exclusionary criteria demonstrates good correlation between the field CI and satellite CI. The CI calculated with the exclusionary criteria for the field measurements resulted in CI equal to zero in all cases. The CI calculated with the exclusionary criteria for the satellite measurements resulted in CI equal to zero for all of October 08, 2019 data.

For this date, we observe the highest chlorophyll-*a* concentrations but also the lowest Field CI (**Figure 5A**). The Satellite CI to chlorophyll-*a* does not show this same trend with the October 08, 2019 Satellite CI values similar to the other sampling dates (**Figure 5B**). The CI to phycocyanin relationship is less clear, although there is a positive linear trend evident in the July 12, 2019 data (only Satellite CI is available for this date) (**Figures 5C,D**).

We found significant relationships (corrected *p*-value < 0.05, where *p*-value is corrected using Benjamini and Hochberg False Discovery Rate procedure) for only six out of sixteen evaluated linear models between Field and Satellite CI to chlorophyll-*a* and phycocyanin for all the available data as well as each individual sampling date. Of those significant relationships, we found moderately low to moderate correlation (r^2 values between 0.08–0.39) for most of the linear models (**Table 3**). The linear model between Field CI and chlorophyll-*a* for August 07, 2019 and Satellite CI and chlorophyll-*a* for July 12, 2019 both demonstrated moderately high correlation with r^2 values of 0.68 and 0.65, respectively (**Table 3**).

Small Unmanned Aerial System Measurements

Conditions on the day of sUAS deployment were clear and calm, with sunny skies and low to no cloud cover. The sUAS-derived chlorophyll-*a* ranged from 0 to 39.7 μg/L. For image presentation of the data the upper and lower bounds were set to the 99.7 percentile (3σ = 18.2 μg/L) and 0.3 percentile (−3σ = 11.7 μg/L), respectively (**Figure 6**). The chlorophyll-*a* concentrations are variable throughout the site with higher concentrations observed near the northern portions and through an area in the eastern portion of the site. The average calculated chlorophyll-*a* value was 15.3 mg/L ± 0.90 μg/L. The coefficient of variation for the sUAS-derived chlorophyll-*a* is 5.92%.

Autonomous Underwater Vehicle Measurements

Concurrent with the sUAS flights, an AUV was deployed on August 16, 2019 in the Lower and Oaks Arms of Clear Lake. Sensors mounted on the AUV collected continuous measurements of turbidity, chlorophyll-*a*, and CDOM during deployment at an average depth below the free water surface of ~0.6 m in the Lower Arm and ~0.9 m in the Oaks Arm (**Figure 7**). Conditions were mild on the day of deployment with low winds (<5 kph) and low wave heights (<10 cm). Lake clarity was low, similar to other observations made for our

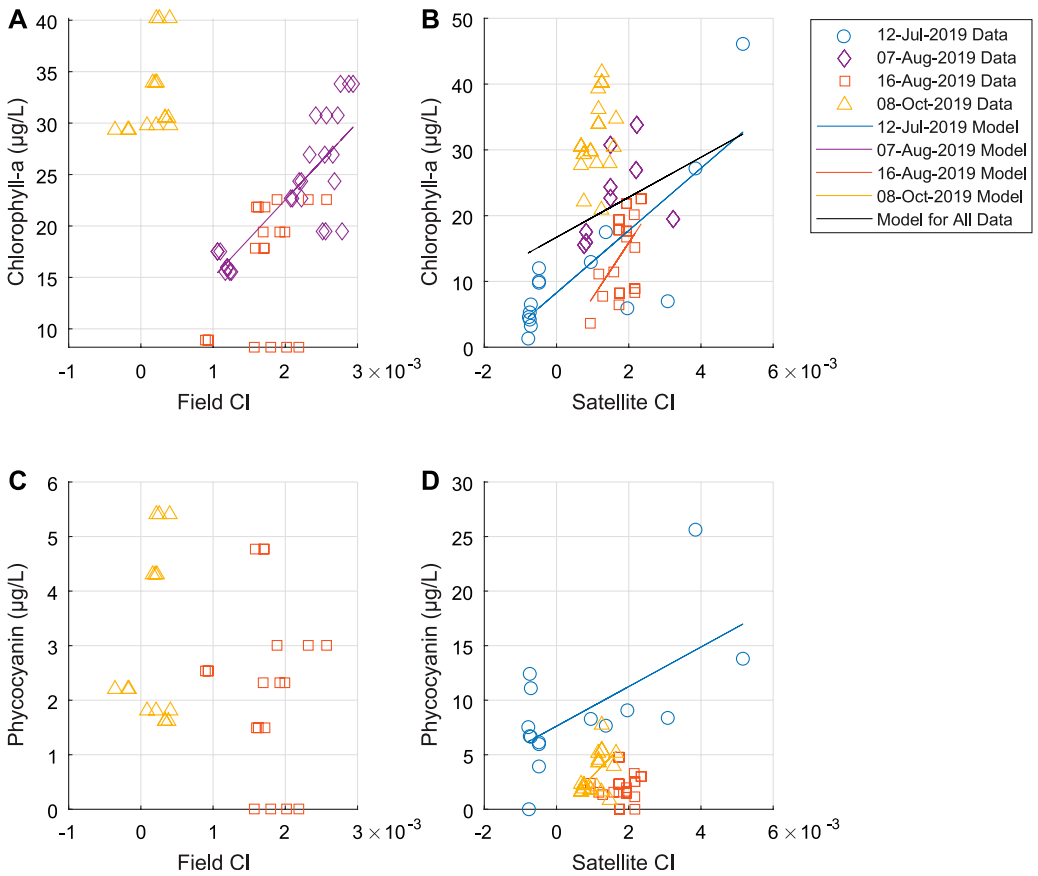

FIGURE 5 | Relationship of **(A)** CI from field spectroradiometer data to chlorophyll-*a* concentration **(B)** CI from satellite data to chlorophyll-*a* concentration **(C, D)** as **(A, B)** except for to phycocyanin concentration. Note the difference in axes ranges between each plot. Linear models are shown for those relationships that are significant (corrected *p*-value < 0.05, where *p*-value is corrected using Benjamini and Hochberg False Discovery Rate procedure). Few of the modeled relationships are significant.

TABLE 3 | Linear model parameters as well as the model performances of results of least-squares linear regression analysis relating the calculated CI to observed chlorophyll-a and phycocyanin concentrations. Only the linear models Field CI vs Chlorophyll-*a* (07-Aug-2019), Satellite CI vs Chlorophyll-*a* (All Data, 12-Jul-2019, and 16-Aug-2019), and Phycocyanin vs Satellite CI (12-Jul-2019 and 8-Oct-2019) are significant (corrected *p*-value < 0.05, where *p*-value is corrected using Benjamini and Hochberg False Discovery Rate procedure). The significant models have positive linear slopes. The significant models have moderately low to moderately high correlation.

	Field CI vs Chlorophyll-*a*		Satellite CI vs Chlorophyll-*a*	
Date	**Linear model**	r^2	**Linear model**	r^2
All data	chla (µg/L) = −1991 × CI + 26.2	0.05	chla (µg/L) = 3040 × CI + 16.7	0.08
12-Jul-2019	NA	NA	chla (µg/L) = 4733 × CI + 8.3	0.65
07-Aug-2019	chla (µg/L) = 7539 × CI + 7.5	0.68	chla (µg/L) = 3438 × CI + 17.4	0.19
16-Aug-2019	chla (µg/L) = 6297 × CI + 5.2	0.21	chla (µg/L) = 8336 × CI − 0.8	0.21
08-Oct-2019	chla (µg/L) = 6858 × CI + 31.6	0.14	chla (µg/L) = 7342 × CI + 24.2	0.15
	Field CI vs Phycocyanin		**Satellite CI vs Phycocyanin**	
Date	**Linear model**	r^2	**Linear model**	r^2
All data	chla (µg/L) = −457 × CI + 3.1	0.06	chla (µg/L) = 452 × CI + 3.3	0.01
12-Jul-2019	NA	NA	chla (µg/L) = 1813 × CI + 7.6	0.39
16-Aug-2019	chla (µg/L) = −353 × CI + 2.8	0.01	chla (µg/L) = 466 × CI + 1.1	0.01
08-Oct-2019	chla (µg/L) = 1276 × CI + 2.9	0.04	chla (µg/L) = 3468 × CI − 0.4	0.32

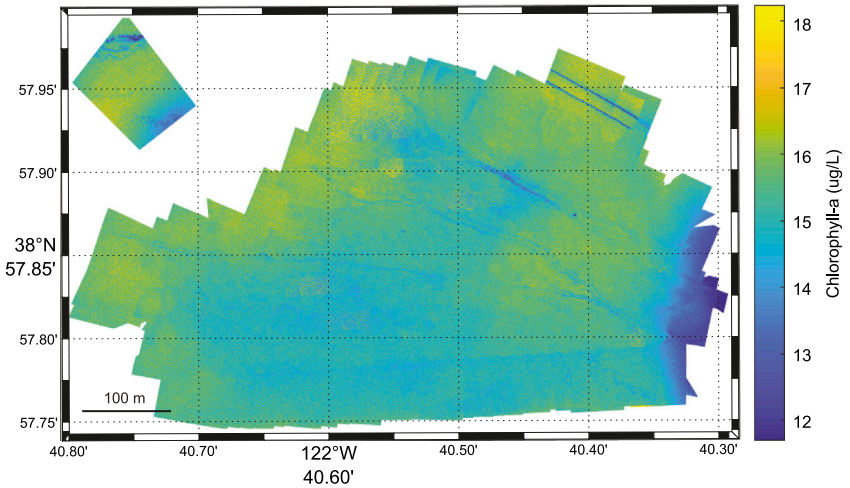

FIGURE 6 | sUAS-derived chlorophyll-*a* (μg/L) image from August 16, 2019. Spatial variability is observed in the sUAS-derived chlorophyll-*a* image with higher concentrations observed near the northern portions and through an area in the eastern portion of the site.

other sampling events. Due to technical difficulties during operations, data were only obtained from the Lower Arm site CL03 and the Oaks Arm site OA04. Additionally, AUV and sensor hardware issues during deployment may have resulted in strings of zero values, which were subsequently removed from the dataset (**Figure 7**).

The turbidity, chlorophyll-*a*, and CDOM results from the AUV mission showed spatial variability varied among the basins. Turbidity was higher in the Oaks Arm than in the Lower Arm, with averages of 1.58 ± 1.13 NTU and 0.57 ± 0.72 NTU, respectively, and maximum values approximately double in the Oaks Arm (**Figures 7A,B**). The coefficients of variation for turbidity are 127% in the Lower Arm and 71.4% in the Oaks Arm. The chlorophyll-*a* results had higher maxima in the Lower Arm than in the Oaks Arm (58.6 μg/L and 23.8 μg/L, respectively), but higher average chlorophyll-*a* concentrations in the Oaks Arm compared to the Lower Arm (18.7 μg/L and 9.26 μg/L, respectively) (**Figures 7C,D**). The coefficients of variation for chlorophyll-*a* are 119% in the Lower Arm and 15.2% in the Oaks Arm. The CDOM concentrations in the Lower Arm were below detection. This occurs because the factory determined offset and scaling factor can result in some CDOM values calculated from the fluorescence counts to be below the detection limit, which we interpret as zero values. The CDOM concentrations ranged from 0 to 9.12 ppb in the Oaks Arm and averaged of 2.78 ± 1.55 ppb (**Figures 7E,F**). The coefficient of variation for CDOM in the Oaks Arm is 56.0%.

Co-Located and Coincident Measurements

We used the concurrent and co-located measurements to obtain a more complete characterization of a cyanobacteria bloom in the Lower Arm of Clear Lake on August 16, 2019 (**Figure 8**). There is observed variability in the measurements between the different sensors and platforms employed at the site. As seen in the southwest corner of the site, the lowest discrete sample result is observed (8.21 μg/L chlorophyll-*a*), whereas the adjacent AUV fluorometry results indicate chlorophyll-*a* levels with concentrations as high as 54.3 μg/L. The range of average ± standard deviation of chlorophyll-*a* values for this site on this sampling date were 15.3 ± 5.02 μg/L for the discrete samples, 9.26 ± 11.1 μg/L for the AUV fluorometer results, and 15.3 ± 0.90 μg/L for the sUAS-derived chlorophyll-*a* results. In addition to variance between platforms, high spatial heterogeneity is also observed inside each satellite pixel. At sampling site (CL03) on August 16, 2019, the discrete sample chlorophyll-*a* results range from 8.21 to 22.6 μg/L; the AUV chlorophyll-*a* results range from 1.06 to 58.6 μg/L; and the sUAS-derived chlorophyll-*a* results range from 0 to 39.7 μg/L.

Critical Scales of Variability

Chlorophyll-*a* concentrations are spatially autocorrelated in the AUV and sUAS data. The semivariograms have a mostly asymptotic shape with the value of semivariance increasing with distance and then leveling off (**Figure 9**). The spatial autocorrelation is stronger in the AUV data than the sUAS, and especially in the AUV mission in the Lower Arm where the variation overall is very low between measurements. From the semivariograms of the AUV-acquired chlorophyll-*a* measurements (**Figures 9A,B**) and also considering their log-log plots, we find the CSV occurs at distances of 70–100 m. From the semivariograms and the log-log plots of the sUAS-derived chlorophyll-*a* measurements, we find the CSV occurs at roughly 175 m on average with the CSV ranging from 70 to 300 m for the 21 lines evaluated (**Figures 9C,D**).

A semivariogram analysis was also completed on the AUV turbidity and CDOM data. The semivariogram analysis on the CDOM data did not yield any meaningful results for the Lower Arm and the Oaks Arm mostly demonstrated a leveling off pattern (see **Supplementary Figure S2**). The CSV for the CDOM is estimated to be ~100 m based on the semivariogram

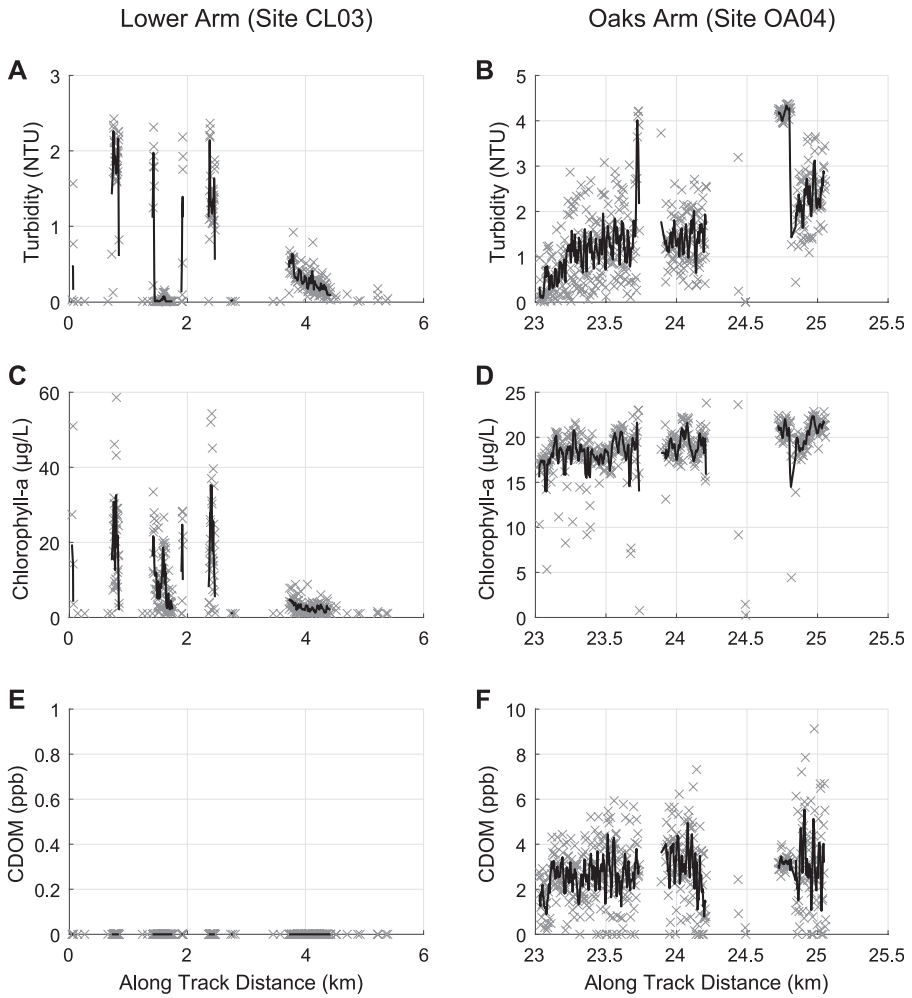

FIGURE 7 | AUV data results for **(A, B)** turbidity (NTU) **(C, D)** chlorophyll-*a* (µg/L), and **(E, F)** CDOM (ppb) for **(A, C, E)** the Lower Arm and **(B, D, F)** the Oaks Arm. Running averages (5 consecutive results) are shown for each plot in black. Turbidity is higher in the Oaks Arm than the Lower Arm. The maximum chlorophyll-*a* concentrations are higher in the Lower Arm while the average concentrations are roughly twice as high in the Oaks Arm. CDOM values were zero in the Lower Arm and averaged 2.7 ppb in the Oaks Arm.

for the Oaks Arm data. The semivariogram for the turbidity data were similar to those for chlorophyll-*a* (see **Supplementary Figure S3**). The CSV for Turbidity is estimated to be between 90 and 100 m.

DISCUSSION

While satellite tools have clear advantages with early detection of cyanoHABs, which has quantifiable socioeconomic benefits (Stroming et al., 2020), they do not adequately characterize bloom spatial variability (Kutser, 2009). This study used a multiplatform sampling approach to measure cyanoHABs to characterize spatial variability of the blooms. Each sampling method provides a perspective of a cyanobacteria bloom from a different vantage point. Satellite imagery provides high coverage and temporal resolution of the bloom. sUAS-acquired imagery provides good coverage and high spatial resolution of the surface of the bloom. Measurements from the AUV provides high spatial resolution measurements of the blooms underwater. Finally, the discrete samples and spectroradiometer measurements provide context and validation of the other methods as well as an understanding of the surface forcing conditions.

Synoptic View of Cyanobacterial Blooms

Each of cyanobacteria sampling methods employed was a compromise of the sampling scale and spatial, temporal, and, in some cases, spectral resolution. While previous studies have used AUV, (e.g. Robbins et al., 2006; Blackwell et al., 2008) and sUAS platforms, (e.g. Kislik et al., 2018), a more complete picture of cyanobacterial blooms is obtained if these high resolution platforms are deployed concurrently, which, to our knowledge, has not been done to date. When comparing the measurements from the discrete samples, AUV, and sUAS, we find the discrete samples fail to capture the spatial variability in chlorophyll-*a* concentrations (**Figure 8**). Based on their coefficients of

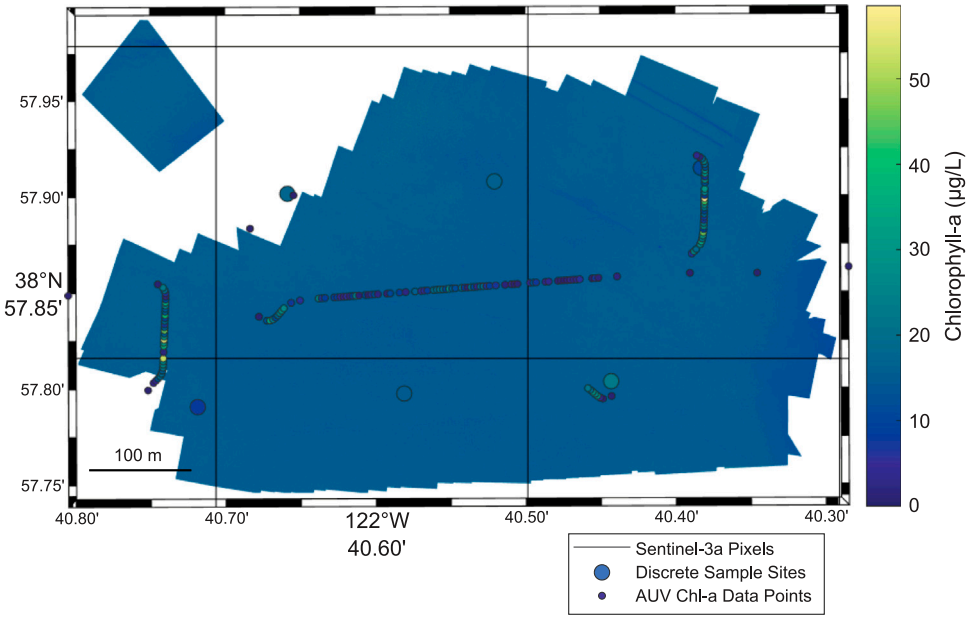

FIGURE 8 | Concurrent measurements of cyanobacteria bloom in the Lower Arm of Clear Lake (site CL03) on August 16, 2019. Variability is observed in the chlorophyll-*a* measurements between the different sampling platforms. Also, there is high intra-pixel variability of the chlorophyll-*a* measurements. Image includes grab sample chlorophyll-*a* observations (large circles), AUV chlorophyll-*a* measurements (small circles), and sUAS-derived chlorophyll-*a* as background image. Sentinel-3a satellite pixels shown as dark grey outlines.

variation, the discrete samples only capture 28% of the variability measured by the AUV. The discrete samples are limited to six disparate locations and only represent the chlorophyll-*a* concentration for each discrete point. However, these sample results can be scaled up to the higher spatial resolution provided by the AUV and sUAS measurements by providing accurate measurements to scale the AUV results to (**Figures 7C,D**) and by informing models relating the sUAS measurements to chlorophyll-*a* concentrations (**Figure 6**). These higher resolution measurements demonstrate the inherent spatial variability of these blooms and how discrete sampling under resolves bloom dynamics.

The high spatial variability is also observed within each satellite pixel. The intra-pixel variability is reflected in the standard deviation of the AUV chlorophyll-*a* measurements within each pixel, which was on average 5.37 µg/L (n = 10, only pixels with a minimum of 20 AUV points were included). Using this average standard deviation, we find at least 28 discrete samples are needed to estimate the chlorophyll-a concentrations of a bloom (95% confidence interval with 2 µg/L margin of error) within a 300 × 300 m pixel (Israel, 1992). Collecting this many samples is impractical for many research and monitoring programs, which highlights the need for calibrated multi-platform measurement programs to more precisely measure and track bloom densities.

The inter-basin variability is observed with respect to the meteorological data. Generally, and although the observed differences are slight, the meteorological and lake surface temperature data (**Table 2**) near the time of sampling (values at 12:00 local time) show the air and lake water surface temperatures were warmer and the wind speeds were calmer (thus lower mixing) for the basins that demonstrated the highest ratio of phycocyanin to chlorophyll-*a* for that sampling date, which indicates dominance by cyanobacteria over phytoplankton. These include the Upper Arm for July 12, 2019, Oaks Arm for August 16, 2019, and the Upper Arm for October 08, 2019. These observations are consistent with the understanding that cyanobacteria favor warm temperatures and calm, stratified lake conditions, and in such conditions will outcompete phytoplankton (Paerl and Huisman, 2008). Our results support the concern that cyanobacteria blooms are expected to increase with increasing global temperatures associated with climate change (Paerl and Huisman, 2009).

Critical Scales of Variability of Cyanobacterial Blooms

CSVs of cyanobacterial blooms are the length scales necessary for detecting the spatial variability or "patchiness" observed in blooms. Previous phytoplankton and cyanobacteria bloom CSVs have been less than the spatial resolution for Sentinel-3a (300 m). Wrigley and Horne (1974) visually identified length scales on the orders of meters for detecting the microstructure variation of cyanoHABs in Clear Lake. They further identified complex patterns of cyanoHABs as not being detectable by conventional boat-based sampling techniques. Blackwell et al. (2008) computed the CSV for fluorescence measurements from an AUV-platform at sub-kilometer scales ranging from 23 to 170 m in coastal systems. While the work of Blackwell et al. (2008) was not in a freshwater system, they used a similar vehicle and instrumentation as in this study. Moses et al. (2016) evaluated scales of variability of ocean color

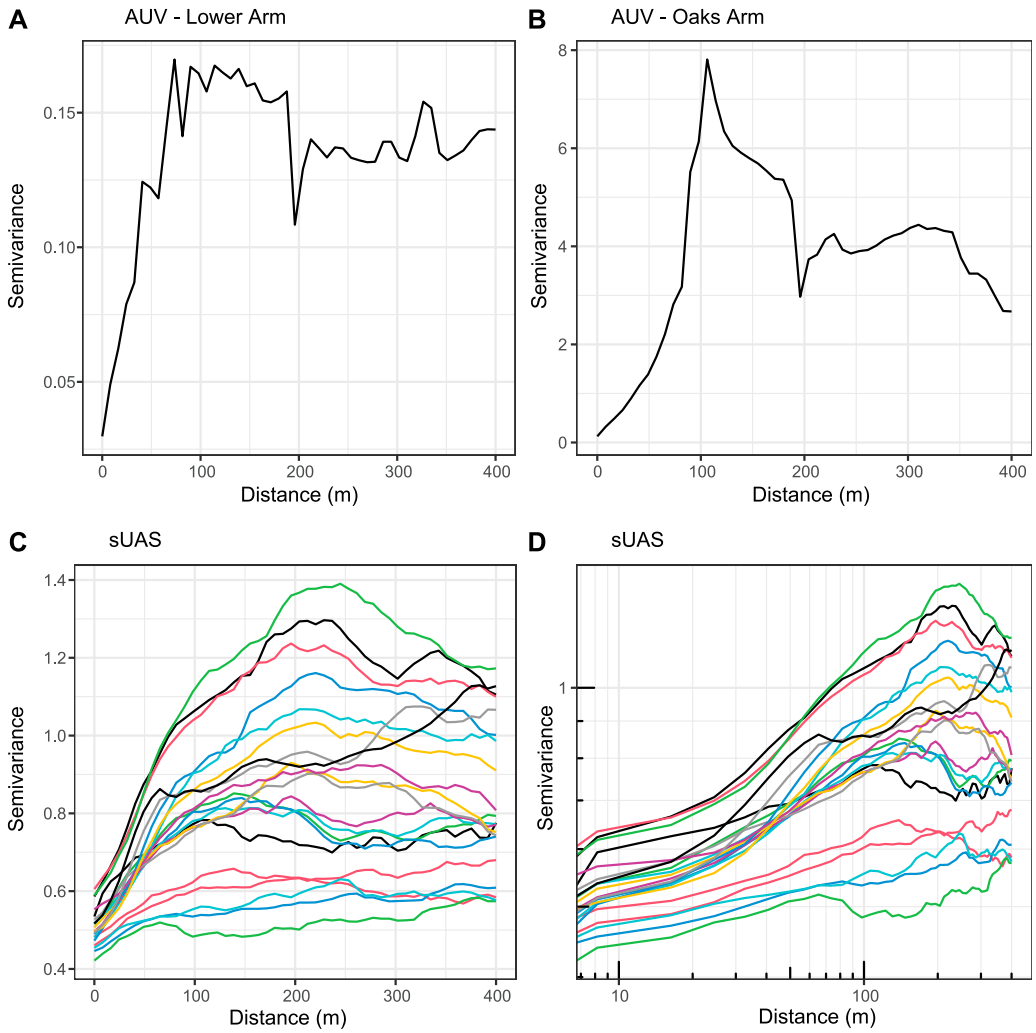

FIGURE 9 | Semivariograms of chlorophyll-*a* measurements from **(A)** AUV Missions in Lower Arm **(B)** AUV Mission in Oaks Arm; and **(C)** lines extracted from sUAS data in Lower Arm. Panel **(D)** shows the log-log scale of the sUAS semivariograms shown in panel **(C)**, which is used for determining the CSV. Semivariograms demonstrate spatial autocorrelation with close data points having less variation. The semivariograms level off at the CSV at roughly 70–100 m for the AUV data and at 175 m on average for the sUAS data, with values ranging from 70 to 300 m for the 21 lines evaluated.

parameters (including phytoplankton) in coastal systems by determining the distance at a critical change in slope for the plot of distance vs. coefficient of variance using ship-based, airborne, and satellite data. They found scales of variability between 75 and 600 m, with an average distance of 200 m. Finally, Vander Woude et al. (2019) identified scales of variability for cyanoHABs in the Great Lakes from hyperspectral data using decorrelation scales. They found scales of variability ranged from 8 to 335 m.

The CSV is necessary to improve sampling plans by selecting the sampling resolution necessary to adequately characterize a bloom (Vander Woude et al., 2019). We find the AUV fluorometer results correspond to a CSV of 70–100 m and the sUAS-derived chlorophyll-*a* concentrations correspond to a CSV of approximately 175 m. These length scales of variability are less than the 300 m pixel size of the OLCI-derived CI. The CSV found by this and other studies (e.g. Blackwell et al., 2008; Moses et al., 2016; Vander Woude et al., 2019) should be used to inform how distant to sample for cyanobacteria to ensure the bloom is adequately resolved. Additionally, the CSV may inform sensor specifications for future satellite development to have spatial resolutions equal to or finer than this CSV while maintaining similar temporal and spectral scales to Sentinel-3 to adequately monitor cyanobacterial blooms (such as those found by Moses et al., 2016 for sensor design over coastal targets).

Challenges of Multimodal Platform Sampling

Despite being able to characterize cyanobacteria blooms, there are significant challenges associated with each method detailed in this

work. Firstly, as shown in the CSV analysis, one of the biggest disadvantages of using satellite imagery is that the CSV for cyanobacteria blooms are finer than the Sentinel-3a pixel size of 300 m. Secondly, the results of this research also indicate poor performance of the revised CI algorithm for Clear Lake. Despite these challenges, this and other satellite-based remote sensing tools are invaluable for water managers and researchers because of their repeat measurements at high temporal frequency and spatial coverage, which provides data on cyanoHABs where monitoring programs are currently lacking (Matthews, 2011). Furthermore, even without calibration and validation, we speculate the CI algorithm still provides valuable information on development and trends of cyanoHABs.

As shown in **Figure 4A**, the CI algorithm without the exclusionary criterion demonstrates good performance as the results of the CI follow a 1:1 line on the plot. In contrast, the revised CI algorithm using the exclusionary criterion, as suggested for best practice (Stumpf et al., 2015; Wynne et al., 2018), produces false negatives. The CI with the exclusionary criterion calculated from the spectroradiometer measurements results in all CI values equal to zero (**Figure 4B**). Additionally, the CI with the exclusionary criterion calculated from the satellite measurements from October 08, 2019 results in all CI values equal to zero. Visual observations in the field and microscopy confirmed that cyanobacteria were present on the sampling dates, in contradiction to the CI results equal to zero.

The exclusionary criteria of SS{665} is less sensitive than the original SS{681} CI algorithm of spectral shape around 681 nm, and thus does not adequately capture low-level cyanobacteria blooms (Urquhart et al., 2017). The spectral shape around 665 nm (SS{665}) is influenced by increased absorption of the 620 nm band by phycocyanin compared to chlorophyll-*a* (Lunetta et al., 2015). Our results show an absorption feature at 615–630 nm (**Figures 3A,C,E**), however, the depression is not significant enough to change SS{665} from negative to positive in order for the revised CI algorithm with the exclusionary criterion to identify cyanobacteria. Although the cyanobacteria blooms during our sampling dates were not as large as has been observed on Clear Lake in other years, there were still cyanobacteria present despite not being detected using the CI algorithm with the exclusionary criterion. The SS{665} exclusionary criteria is designed to reduce the rate of false-positives (Lunetta et al., 2015), however, as seen in our results, it also increases the rate of false-negatives by failing to detect low-concentration blooms. These low detections of cyanobacteria are still valuable (Matthews et al., 2012) as they allow water managers to observe and prepare for the onset of blooms. We recommend continued data collection and research to tune the exclusionary criterion for improved performance at Clear Lake, and likely other lakes and reservoirs. The exclusionary criterion could be tuned by adjusting the zero threshold so that low level blooms would result in a SS{665} greater than the revised threshold. This adjustment could improve the algorithm results for detection of low level cyanobacteria blooms.

In addition to evaluating the performance of the CI algorithm, we evaluated the relationship of CI to chlorophyll-*a* and phycocyanin. Previous research has shown mixed success when comparing CI to chlorophyll-*a* and to phycocyanin. Poor correlations between CI and phycocyanin and chlorophyll-*a* have been reported by Kudela et al. (2015) and Xu et al. (2019), respectively. However, there has been better success by others (Tomlinson et al., 2016 found an $r^2 = 0.95$ for the relationship of CI to chlorophyll-*a*). Additionally, on a continental scale, the CI has shown good correlation to cyanobacterial abundance (cells/mL) (Lunetta et al., 2015; Clark et al., 2017). We feel the mixed success of establishing a relationship of CI to chlorophyll-*a* and phycocyanin in this study may be due to limitations, both in scope and robustness, of our dataset. Our dataset does not validate nor disprove the CI algorithm, rather our work shows that more research is needed.

Inland waters are optically complex (Ortiz et al., 2019) meaning the application of remote sensing tools is challenging. Use of spectral decomposition methods aimed at identifying the specific components of a bloom may prove more useful for some inland waters, where spectral shape algorithms such as the CI are unsuccessful. This is shown by Avouris and Ortiz (2019) with their use of varimax-rotated principal component analysis to partition the spectral components of a bloom, although they also acknowledge that further research is needed. The confounding factors for use of remote sensing methods in optically complex waters and our findings in the variation in the CI to chlorophyll-*a* and phycocyanin relationship emphasize the need to better understand how CI performs on specific waterbodies of interest when making decisions based on CI values.

On a finer scale, one of the main challenges associated with using a fluorometer sensor on an AUV is the effect of non-photochemical quenching (NPQ) on chlorophyll-*a* measurements. NPQ is the process by which plants and algae dissipate excess light energy than is needed for photosynthesis (Müller et al., 2001). NPQ is also known to occur in cyanobacteria and reduces chlorophyll-*a* fluorescence (Humbert and Törökné, 2017). Therefore, ground truthing data using fluorometry for comparison to satellite remote sensing products must account for the of decrease in daytime chlorophyll-*a* fluorescence due to NPQ (Carberry et al., 2019). *In situ* data collected for comparison to satellite products is ideally collected near the surface of the water and close to the time of daytime satellite overpass, which in the case of Sentinel-3a for Clear Lake is approximately 12:00 pm (local time). This directly conflicts with collection of chlorophyll-*a* data using fluorometry to avoid the impacts of NPQ, which occur closer to the water surface and follow the diurnal parabolic pattern of shortwave radiation (see the results of Austin, 2019). Further research into alleviating and/or accounting for the impacts of NPQ on fluorescence measurements for satellite validation is needed. However, even without this NPQ correction applied to fluorescence datasets, we find AUV-acquired fluorescence data are useful for determining the CSV of the blooms even if the relative magnitude of chlorophyll-*a* concentrations remains poorly quantified.

In addition to the challenges associated with fluorometry measurements on the AUV, we found difficulties with the other remote sensing methods employed in this research. Although aerial imaging with sUAS flights provides a larger coverage and higher spatial resolution view of a cyanobacterial bloom, there are challenges associated with the sUAS multispectral imaging method. One challenge is that there may be uncertainty in the sUAS measurements due to a potentially lower signal to noise ratio of the MicaSense camera over a water body, due to the lower radiance

level than typical terrestrial targets (Kim et al., 2020). Additionally, the coarser spectral resolution of the typical multiband multispectral camera limits the ability to capture the fine and narrower absorption features observed for phycocyanin and chlorophyll-*a* in the hyperspectral spectroradiometer data (**Figure 3**). The MicaSense camera used for our study has very few bands at limited wavelengths, and this did not allow for calculation of the CI from the sUAS data, although it did allow for calculation of chlorophyll-*a* from a known band ratio relationship (Ha et al., 2017). A locally tuned chlorophyll-*a* band ratio equation could not be determined for Clear Lake because there were not enough coincident measurements (n = 6). There are consequences of using a published equation tuned to another study site (Lake Ba Be in Vietnam in the case of Ha et al., 2017). We speculate that a locally tuned relationship would yield more accurate results. In the case of this study, the unscaled sUAS-derived chlorophyll-*a* measurements using the published equation were much lower than the discrete sample chlorophyll-*a* results. For this reason, we scaled the sUAS-derived chlorophyll-*a* results so that the average equals the average of the adjacent discrete samples. This allowed for easier comparison of the datasets. Additionally, the main purpose of this study is to evaluate the variability of cyanobacteria blooms and not necessarily the magnitude of the chlorophyll-*a* results. Thus, we acknowledge that the sUAS-derived chlorophyll-*a* results without a locally tuned equation, although scaled to the discrete sample results, should not be used to directly consider the magnitude of the concentrations individually. Further research with additional discrete sampling coincident to sUAS flights is needed to develop a locally tuned equation relating chlorophyll-*a* to a reflectance band ratio for this site in order for the magnitudes of the sUAS chlorophyll-*a* results to be meaningful. Finally, we encountered challenges with photomosaicing the sUAS images over water because there are limited static reference points for image matchups and further challenges due to wave action. Due to these challenges, we were not successful in photomosaicing the images from the second sUAS site (LA03) and that data is not presented in this paper.

CONCLUSION

This research used a multiplatform sampling approach to evaluate the spatial variability including the CSV of cyanobacteria blooms. We find the CSV for cyanobacteria blooms is on the order of 70–175 m, which should be considered when planning sampling efforts. A multiplatform approach provides a more holistic view of a cyanobacteria bloom as each sampling method is completed at different sampling scales and resolutions. We found high intra-pixel variability and also variability between methods at discrete sampling locations. Based on intra-pixel variability of our measurements, we determined a sample size of 28 discrete samples per 300 × 300 m pixel is necessary to adequately characterize the variability of a bloom. Finally, we find low sensitivity of the revised CI algorithm with exclusionary criteria, which failed to detect cyanobacteria at Clear Lake during our sampling events. As such, the exclusionary criterion should be tuned for Clear Lake and potentially for all lakes across California, with the zero threshold adjusted to improve the algorithm results for low level cyanobacteria blooms.

With many lakes across the globe experiencing an increase in the frequency and severity of harmful algal blooms of cyanobacteria (Taranu et al., 2015; Ho et al., 2019), there is a need to develop of tools for water managers to understand and predict their inception. Satellite-based remote sensing tools have emerged as a solution for water managers to monitor the onset and development of harmful algal blooms (Coffer et al., 2020). This research provides data for ground-truthing and algorithm validation, which is essential before widespread use and data interpretation of these satellite products can take place. However, this higher resolution data from autonomous platforms also demonstrates that satellite measurements under-resolve the spatial variability of cyanoHABs. Therefore, strategies will need to be used to scale data between these different platforms. Validation of remote sensing tools will also allow for high temporal resolution cyanobacteria data to be easily accessible by water managers which will aid as a decision support tool. This data will reveal daily, seasonal, and interannual trends, which will be useful to researchers with understanding the drivers of cyanobacteria blooms and determining appropriate engineering solutions to manage large scale harmful algal blooms.

DATA AVAILABILITY STATEMENT

The raw data supporting the conclusion of this article will be made available by the authors, without undue reservation.

AUTHOR CONTRIBUTIONS

SLS conceived the presented idea with contributions from AF and SGS. SLS, AF, and KG planned and conducted the field work, and YJ provided support. SLS lead the data analysis under the supervision of AF with additional feedback from KG and AC. SLS took the lead in writing the manuscript. All authors provided critical feedback and helped shape the research, analysis, and manuscript.

FUNDING

This study was made possible by funding from the California Department of Fish and Wildlife through California State Assembly Bill 707 (2017), the UC Davis Tahoe Environmental Research Center, and the State Water Resources Control Board. Samantha Sharp is funded through a NASA OSE graduate student fellowship awarded in 2020 (Grant Number 80NSSC20K1458).

ACKNOWLEDGMENTS

The authors would like to acknowledge contribution to this research by Ben Daniels, Nick Framsted, Matthew Krause, Doug Kubota, Drew Stang, Micah Swann, and Andy Wong and for data collection, Erica Kono and Lindsay Vaughan for sampling preparation and sample filtering, Brandon Berry and Andy Wong for AUV and sUAS mission planning and data processing, Randy Turner for technical assistance, and to Sarah Ryan and the Big Valley Band of

Pomo Indians for sharing their cyanobacteria data results collected during our sampling events. The authors acknowledge the Clear Lake Blue Ribbon Committee for their leadership role in the efforts to restore Clear Lake. The authors acknowledge the two reviewers for their thorough and thoughtful review.

SUPPLEMENTARY MATERIAL

The Supplementary Material for this article can be found online at: https://www.frontiersin.org/articles/10.3389/fenvs.2021.612934/full#supplementary-material.

REFERENCES

Arar, E. J., and Collins, G. B. (1997). *Method 445.0: in vitro determination of chlorophyll a and pheophytin a in marine and freshwater algae by fluorescence* (Ohio, United States: United States Environmental Protection Agency, Office of Research and Development, National Exposure Research Laboratory).

Austin, J. A. (2019). Observations of radiatively driven convection in a deep lake. *Limnol. Oceanogr.* 64 (5), 2152–2160. doi:10.1002/lno.11175

Avouris, D. M., and Ortiz, J. D. (2019). Validation of 2015 Lake Erie MODIS image spectral decomposition using visible derivative spectroscopy and field campaign data. *J. Great Lakes Res.* 45 (3), 466–479. doi:10.1016/j.jglr.2019.02.005

Blackwell, S. M., Moline, M. A., Schaffner, A., Garrison, T., and Chang, G. (2008). Sub-kilometer length scales in coastal waters. *Continental Shelf Res.* 28 (2), 215–226. doi:10.1016/j.csr.2007.07.009

Bryant, D. A. (1982). Phycoerythrocyanin and phycoerythrin: properties and occurrence in cyanobacteria. *Microbiology* 128 (4), 835–844. doi:10.1099/00221287-128-4-835

Carberry, L., Roesler, C., and Drapeau, S. (2019). Correcting *in situ* chlorophyll fluorescence time-series observations for nonphotochemical quenching and tidal variability reveals nonconservative phytoplankton variability in coastal waters. *Limnol. Oceanogr. Methods* 17 (8), 462–473. doi:10.1002/lom3.10325

Carey, C. C., Weathers, K. C., Ewing, H. A., Greer, M. L., and Cottingham, K. L. (2014). Spatial and temporal variability in recruitment of the cyanobacterium Gloeotrichia echinulatain an oligotrophic lake. *Freshw. Sci.* 33 (2), 577–592. doi:10.1086/675734

Cheung, M. Y., Liang, S., and Lee, J. (2013). Toxin-producing cyanobacteria in freshwater: a review of the problems, impact on drinking water safety, and efforts for protecting public health. *J. Microbiol.* 51 (1), 1–10. doi:10.1007/s12275-013-2549-3

Clark, J. M., Schaeffer, B. A., Darling, J. A., Urquhart, E. A., Johnston, J. M., Ignatius, A., et al. (2017). Satellite monitoring of cyanobacterial harmful algal bloom frequency in recreational waters and drinking source waters. *Ecol. Indic.* 80, 84–95. doi:10.1016/j.ecolind.2017.04.046

Coffer, M. M., Schaeffer, B. A., Darling, J. A., Urquhart, E. A., and Salls, W. B. (2020). Quantifying national and regional cyanobacterial occurrence in US lakes using satellite remote sensing. *Ecol. Indic.* 111, 105976. doi:10.1016/j.ecolind.2019.105976

Cortés, A., and Schladow, S. G. (2020). Lake temperature, dissolved oxygen and meteorological data in Clear Lake, CA, USA (2019–2020). *Knowledge Network for Biocomplexity*. doi:10.5063/F1C827P7

Diggle, P. J., and Ribeiro, P. J. (2007). *Model-based geostatistics*. New York, NY, United States: Springer.

Forrest, A. L., Laval, B. E., Pieters, R., and Lim, D. S. S. (2008). Convectively driven transport in temperate lakes. *Limnol. Oceanogr.* 53 (5part2), 2321–2332. doi:10.4319/lo.2008.53.5_part_2.2321

Fraschetti, S., Terlizzi, A., Bevilacqua, S., and Boero, F. (2006). The distribution of hydroids (Cnidaria, Hydrozoa) from micro- to macro-scale: spatial patterns on habitat-forming algae. *J. Exp. Mar. Biol. Ecol.* 339 (2), 148–158. doi:10.1016/j.jembe.2006.07.007

Gholizadeh, M. H., Melesse, A. M., and Reddi, L. (2016). A comprehensive review on water quality parameters estimation using remote sensing techniques. *Sensors (Basel)* 16 (8), 1298. doi:10.3390/s16081298

Ha, N. T. T., Thao, N. T. P., Koike, K., and Nhuan, M. T. (2017). Selecting the best band ratio to estimate chlorophyll-a concentration in a tropical freshwater lake using sentinel 2A images from a case study of Lake Ba Be (Northern Vietnam). *Ijgi* 6 (9), 290. doi:10.3390/ijgi6090290

Havens, K. (2008). Cyanobacteria blooms: effects on aquatic ecosystems, *Adv. Exp. Med. Biol.* 619, 733–747. doi:10.1007/978-0-387-75865-7_33

Ho, J. C., Michalak, A. M., and Pahlevan, N. (2019). Widespread global increase in intense lake phytoplankton blooms since the 1980s. *Nature* 574 (7780), 667–670. doi:10.1038/s41586-019-1648-7

Ho, J. C., and Michalak, A. M. (2015). Challenges in tracking harmful algal blooms: a synthesis of evidence from Lake Erie. *J. Great Lakes Res.* 41 (2), 317–325. doi:10.1016/j.jglr.2015.01.001

Horne, A. J. (1975). The ecology of Clear Lake phytoplankton. Clear Lake Algal Research Unit, 1–116.

Huisman, J., Codd, G. A., Paerl, H. W., Ibelings, B. W., Verspagen, J. M. H., and Visser, P. M. (2018). Cyanobacterial blooms. *Nat. Rev. Microbiol.* 16 (8), 471–483. doi:10.1038/s41579-018-0040-1

Humbert, J. F., and Törökné, A. (2017). "New tools for the monitoring of cyanobacteria in freshwater ecosystems," in *Handbook of Cyanobacterial Monitoring and Cyanotoxin Analysis*. Editors J. Meriluoto, L. Spoof, and G. A. Codd (Chichester, United Kingdom: John Wiley and Sons), 84–88. doi:10.1002/9781119068761.ch8

Hunter, P. D., Matthews, M. W., Kutser, T., and Tyler, A. N. (2017). "Remote sensing of cyanobacterial blooms in inland, coastal, and ocean waters," in *Handbook of Cyanobacterial Monitoring and Cyanotoxin Analysis*. Editors J. Meriluoto, L. Spoof, and G. A. Codd (Chichester, United Kingdom: John Wiley and Sons), 89–99. doi:10.1002/9781119068761.ch9

Israel, G. D. (1992). Determining sample size. IFAS extension, *PEOD-6*. Gainesville, FL, United States: University of Florida.

Kasinak, J.-M. E., Holt, B. M., Chislock, M. F., and Wilson, A. E. (2015). Benchtop fluorometry of phycocyanin as a rapid approach for estimating cyanobacterial biovolume. *J. Plankton Res.* 37 (1), 248–257. doi:10.1093/plankt/fbu096

Kim, W., Jung, S., Moon, Y., and Mangum, S. C. (2020). Morphological band registration of multispectral cameras for water quality analysis with unmanned aerial vehicle. *Remote Sensing* 12 (12), 2024. doi:10.3390/rs12122024

Kislik, C., Dronova, I., and Kelly, M. (2018). UAVs in support of algal bloom research: a review of current applications and future opportunities. *Drones* 2 (4), 35. doi:10.3390/drones2040035

Konopko, E. A. (2007). *Development of a flow-through fluorometric system for the detection of phycocyanin in the lower Great Lakes*. Syracuse, NY, United Staes: State University of New York College of Environmental Science and Forestry.

Kudela, R. M., Palacios, S. L., Austerberry, D. C., Accorsi, E. K., Guild, L. S., and Torres-Perez, J. (2015). Application of hyperspectral remote sensing to cyanobacterial blooms in inland waters. *Remote Sensing Environ.* 167, 196–205. doi:10.1016/j.rse.2015.01.025

Kutser, T. (2009). Passive optical remote sensing of cyanobacteria and other intense phytoplankton blooms in coastal and inland waters. *Int. J. Remote Sensing* 30 (17), 4401–4425. doi:10.1080/01431160802562305

Liu, H., Dahlgren, R., Larsen, R., Devine, S., Roche, L., O' Geen, A., et al. (2019a). Estimating rangeland forage production using remote sensing data from a small unmanned aerial system (sUAS) and PlanetScope satellite. *Remote Sensing* 11 (5), 595. doi:10.3390/rs11050595

Liu, H., Zheng, Z. C., Young, B., and Harris, T. D. (2019b). Three-dimensional numerical modeling of the cyanobacterium Microcystis transport and its population dynamics in a large freshwater reservoir. *Ecol. Model.* 398, 20–34. doi:10.1016/j.ecolmodel.2019.01.022

Lunetta, R. S., Schaeffer, B. A., Stumpf, R. P., Keith, D., Jacobs, S. A., and Murphy, M. S. (2015). Evaluation of cyanobacteria cell count detection derived from MERIS imagery across the eastern United States. *Remote Sensing Environ.* 157, 24–34. doi:10.1016/j.rse.2014.06.008

Matthews, M. W. (2011). A current review of empirical procedures of remote sensing in inland and near-coastal transitional waters. *Int. J. Remote Sensing* 32 (21), 6855–6899. doi:10.1080/01431161.2010.512947

Matthews, M. W., Bernard, S., and Robertson, L. (2012). An algorithm for detecting trophic status (chlorophyll-a), cyanobacterial-dominance, surface scums and floating vegetation in inland and coastal waters. *Remote Sensing Environ.* 124, 637–652. doi:10.1016/j.rse.2012.05.032

Mobley, C. D. (1999). Estimation of the remote-sensing reflectance from above-surface measurements. *Appl. Opt.* 38 (36), 7442–7455. doi:10.1364/AO.38.007442

Moses, W. J., Ackleson, S. G., Hair, J. W., Hostetler, C. A., and Miller, W. D. (2016). Spatial scales of optical variability in the coastal ocean: implications for remote sensing and *in situ* sampling. *J. Geophys. Res. Oceans* 121 (6), 4194–4208. doi:10.1002/2016JC011767

Müller, P., Li, X. P., and Niyogi, K. K. (2001). Non-photochemical quenching. A response to excess light energy. *Plant Physiol.* 125 (4), 1558–1566. doi:10.1104/pp.125.4.1558

Oliver, R. L., Hamilton, D. P., Brookes, J. D., and Ganf, G. G. (2012). "Physiology, blooms and prediction of planktonic cyanobacteria," in *Ecology of cyanobacteria II*. Editor B. A. Whitton (Dordrecht, Netherlands: Springer), 155–194. doi:10.1007/978-94-007-3855-3_6

Ortiz, J. D., Avouris, D. M., Schiller, S. J., Luvall, J. C., Lekki, J. D., Tokars, R. P., et al. (2019). Evaluating visible derivative spectroscopy by varimax-rotated, principal component analysis of aerial hyperspectral images from the western basin of Lake Erie. *J. Great Lakes Res.* 45 (3), 522–535. doi:10.1016/j.jglr.2019.03.005

Paerl, H. W., Gardner, W. S., Havens, K. E., Joyner, A. R., McCarthy, M. J., Newell, S. E., et al. (2016). Mitigating cyanobacterial harmful algal blooms in aquatic ecosystems impacted by climate change and anthropogenic nutrients. *Harmful Algae* 54, 213–222. doi:10.1016/j.hal.2015.09.009

Paerl, H. W., Hall, N. S., and Calandrino, E. S. (2011). Controlling harmful cyanobacterial blooms in a world experiencing anthropogenic and climatic-induced change. *Sci. Total Environ.* 409 (10), 1739–1745. doi:10.1016/j.scitotenv.2011.02.001

Paerl, H. W., and Huisman, J. (2009). Climate change: a catalyst for global expansion of harmful cyanobacterial blooms. *Environ. Microbiol. Rep.* 1, 27–37. doi:10.1111/j.1758-2229.2008.00004.x

Paerl, H. W., and Huisman, J. (2008). Climate. Blooms like it hot. *Science* 320, 57–58. doi:10.1126/science.1155398

Richerson, P. J., Suchanek, T. H., and Why, S. J. (1994). The causes and control of algal blooms in Clear Lake. Final report, 1–182.

Robbins, I. C., Kirkpatrick, G. J., Blackwell, S. M., Hillier, J., Knight, C. A., and Moline, M. A. (2006). Improved monitoring of HABs using autonomous underwater vehicles (AUV). *Harmful Algae* 5 (6), 749–761. doi:10.1016/j.hal.2006.03.005

Rueda, F. J., and Schladow, S. G. (2003). Dynamics of large polymictic lake. II: numerical simulations. *J. Hydraul. Eng.* 129 (2), 92–101. doi:10.1061/(ASCE)0733-942910.1061/(asce)0733-9429(2003)129:2(92)

Ruiz-Verdú, A., Simis, S. G. H., de Hoyos, C., Gons, H. J., and Peña-Martínez, R. (2008). An evaluation of algorithms for the remote sensing of cyanobacterial biomass. *Remote Sensing Environ.* 112 (11), 3996–4008. doi:10.1016/j.rse.2007.11.019

Siegelman, H. W., and Kycia, H. H. (1978). "Algal biliproteins," in *Handbook of phycological methods: Physiological and biochemical methods*. Editors J. A. Hellebust and J. S. Craigie (Cambridge, United Kingdom: Cambridge University Press), 71–80.

Stroming, S., Robertson, M., Mabee, B., Kuwayama, Y., and Schaeffer, B. (2020). Quantifying the human health benefits of using satellite information to detect cyanobacterial harmful algal blooms and manage recreational advisories in United States lakes. *GeoHealth* 4, e2020GH000254. doi:10.1029/2020GH000254

Stumpf, R. P., Davis, T. W., Wynne, T. T., Graham, J. L., Loftin, K. A., Johengen, T. H., et al. (2016). Challenges for mapping cyanotoxin patterns from remote sensing of cyanobacteria. *Harmful Algae* 54, 160–173. doi:10.1016/j.hal.2016.01.005

Stumpf, R. P., Tomlinson, M. C., Meredith, A., Briggs, T., and Wynne, T. T. (2015). Application of MERIS satellite data to cyanobacterial blooms in California. Report to the San Francisco Estuary Institute from the National Oceanic and Atmospheric Administration National Centers for Coastal Ocean Science.

Taranu, Z. E., Gregory-Eaves, I., Leavitt, P. R., Bunting, L., Buchaca, T., Catalan, J., et al. (2015). Acceleration of cyanobacterial dominance in north temperate-subarctic lakes during the Anthropocene. *Ecol. Lett.* 18 (4), 375–384. doi:10.1111/ele.12420

Tomlinson, M. C., Stumpf, R. P., Wynne, T. T., Dupuy, D., Burks, R., Hendrickson, J., et al. (2016). Relating chlorophyll from cyanobacteria-dominated inland waters to a MERIS bloom index. *Remote Sensing Lett.* 7 (2), 141–149. doi:10.1080/2150704X.2015.1117155

UC Davis Tahoe Environmental Research Center (2020). Data Archive *TERC Clear Lake Research.* Available at: https://terc-clearlake.wixsite.com/cldashboard/dataarchive

Urquhart, E. A., Schaeffer, B. A., Stumpf, R. P., Loftin, K. A., and Werdell, P. J. (2017). A method for examining temporal changes in cyanobacterial harmful algal bloom spatial extent using satellite remote sensing. *Harmful Algae* 67, 144–152. doi:10.1016/j.hal.2017.06.001

Vander Woude, A., Ruberg, S., Johengen, T., Miller, R., and Stuart, D. (2019). Spatial and temporal scales of variability of cyanobacteria harmful algal blooms from NOAA GLERL airborne hyperspectral imagery. *J. Great Lakes Res.* 45 (3), 536–546. doi:10.1016/j.jglr.2019.02.006

Visser, P. M., Ibelings, B. W., Bormans, M., and Huisman, J. (2016). Artificial mixing to control cyanobacterial blooms: a review. *Aquat. Ecol.* 50 (3), 423–441. doi:10.1007/s10452-015-9537-0

Winder, M., Reuter, J., and Schladow, G. (2010). Clear Lake historical data analysis. Clear Lake final report for Lake County. Davis, CA, United States: University of California, 1–51.

Wrigley, R. C., and Horne, A. J. (1974). Remote sensing and lake eutrophication. *Nature* 250 (5463), 213–214. doi:10.1038/250213a0

Wynne, T. T., Meredith, A., Briggs, T., Litaker, W., and Stumpf, R. P. (2018). Harmful algal bloom forecasting branch ocean color satellite imagery processing guidelines. *NOAA Tech. Memorandum NOS NCCOS* 252, 48. doi:10.25923/twc0-f025

Wynne, T. T., Stumpf, R. P., Tomlinson, M. C., and Dyble, J. (2010). Characterizing a cyanobacterial bloom in western Lake Erie using satellite imagery and meteorological data. *Limnol. Oceanogr.* 55 (5), 2025–2036. doi:10.4319/lo.2010.55.5.2025

Wynne, T. T., Stumpf, R. P., Tomlinson, M. C., Warner, R. A., Tester, P. A., Dyble, J., et al. (2008). Relating spectral shape to cyanobacterial blooms in the Laurentian Great Lakes. *Int. J. Remote Sensing* 29 (12), 3665–3672. doi:10.1080/01431160802007640

Xu, M., Liu, H., Beck, R., Lekki, J., Yang, B., Shu, S., et al. (2019). Regionally and locally adaptive models for retrieving chlorophyll-a concentration in inland waters from remotely sensed multispectral and hyperspectral imagery. *IEEE Trans. Geosci. Remote Sensing* 57 (7), 4758–4774. doi:10.1109/TGRS.2019.2892899

Yu, X., Dickey, T., Bellingham, J., Manov, D., and Streitlien, K. (2002). The application of autonomous underwater vehicles for interdisciplinary measurements in Massachusetts and Cape Cod Bays. *Continental Shelf Res.* 22 (15), 2225–2245. doi:10.1016/S0278-4343(02)00070-5

Conflict of Interest: The authors declare that the research was conducted in the absence of any commercial or financial relationships that could be construed as a potential conflict of interest.

Copyright © 2021 Sharp, Forrest, Bouma-Gregson, Jin, Cortés and Schladow. This is an open-access article distributed under the terms of the Creative Commons Attribution License (CC BY). The use, distribution or reproduction in other forums is permitted, provided the original author(s) and the copyright owner(s) are credited and that the original publication in this journal is cited, in accordance with accepted academic practice. No use, distribution or reproduction is permitted which does not comply with these terms.

frontiers in Environmental Science

ORIGINAL RESEARCH
published: 26 May 2021
doi: 10.3389/fenvs.2021.674247

Evaluation of Unoccupied Aircraft System (UAS) Remote Sensing Reflectance Retrievals for Water Quality Monitoring in Coastal Waters

Anna E. Windle and Greg M. Silsbe*

Horn Point Laboratory, University of Maryland Center for Environmental Science, Cambridge, MD, United States

Unoccupied aircraft systems (UAS, or drones) equipped with off-the-shelf multispectral sensors originally designed for terrestrial applications can also be used to derive water quality properties in coastal waters. The at-sensor total radiance a UAS measured constitutes the sum of water-leaving radiance (L_W) and incident radiance reflected off the sea surface into the detector's field of view (L_{SR}). L_W is radiance that emanates from the water and contains a spectral shape and magnitude governed by optically active water constituents interacting with downwelling irradiance while L_{SR} is independent of water constituents and is instead governed by a given sea-state surface reflecting light; a familiar example is sun glint. Failure to accurately account for L_{SR} can significantly influence Rrs, resulting in inaccurate water quality estimates once algorithms are applied. The objective of this paper is to evaluate the efficacy of methods that remove L_{SR} from total UAS radiance measurements in order to derive more accurate remotely sensed retrievals of scientifically valuable in-water constituents. UAS derived radiometric measurements are evaluated against *in situ* hyperspectral Rrs measurements to determine the best performing method of estimating and removing surface reflected light and derived water quality estimates. It is recommended to use a pixel-based approach that exploits the high absorption of water at NIR wavelengths to estimate and remove L_{SR}. Multiple linear regressions applied to UAS derived Rrs measurements and *in situ* chlorophyll *a* and total suspended solid concentrations resulted in 37 and 9% relative error, respectively, which is comparable to coastal water quality algorithms found in the literature. Future research could account for the high resolution and multi-angular aspect of L_{SR} by using a combination of photogrammetry and radiometry techniques. Management implications from this research include improved water quality monitoring of coastal and inland water bodies in order to effectively track trends, identify and mitigate pollution sources, and discern potential human health risks.

Keywords: multispectral, water quality, chlorophyll a, total suspended solids, unoccupied aircraft system, drones, coastal

OPEN ACCESS

Edited by:
Wesley Moses, United States Naval Research Laboratory, United States

Reviewed by:
Amir Ibrahim, National Aeronautics and Space Administration, United States
Jian Xu, Helmholtz Association of German Research Centers (HZ), Germany

****Correspondence:***
Anna E. Windle
awindle110@gmail.com

Specialty section:
This article was submitted to Environmental Informatics and Remote Sensing, a section of the journal Frontiers in Environmental Science

Received: *01 March 2021*
Accepted: *14 May 2021*
Published: *26 May 2021*

Citation:
Windle AE and Silsbe GM (2021) Evaluation of Unoccupied Aircraft System (UAS) Remote Sensing Reflectance Retrievals for Water Quality Monitoring in Coastal Waters. Front. Environ. Sci. 9:674247. doi: 10.3389/fenvs.2021.674247

Abbreviations: DLS, downwelling light sensor; E_d, downwelling irradiance; L, spectral radiance; L_{SR}, surface-reflected radiance; L_{sky}, sky radiance; LUT, lookup table; L_T, total radiance; L_W, water leaving radiance; NIR, near infrared; R_{rs}, remote sensing reflectance; R_{UAS}, UAS total reflectance; UAS, unoccupied aircraft system; ρ, effective sea-surface reflectance of wave facet

INTRODUCTION

Unoccupied aircraft systems (UAS, drones) provide on-demand remote sensing capabilities at ultra-high resolution (<5 cm) without the challenges of cloud cover, land adjacency, and atmospheric effects associated with satellite and airborne remote sensing (Anderson and Gaston, 2013). UAS are becoming an integral tool in studying and managing coastal ecosystems (Johnston, 2019), with applications ranging from thermal remote sensing (Lee et al., 2016; Dugdale et al., 2019) and pollutant tracking (Arango and Nairn, 2019; Morgan et al., 2020), to habitat and population assessments (Gray et al., 2018; Windle et al., 2019). The increased spatial and temporal resolution provided by UAS remote sensing can enhance ecological and biogeochemical research of aquatic ecosystems. UAS have the potential to characterize the degree of eutrophication, identify the extent and movement of harmful algal blooms, and resolve fine-scale coupled biophysical processes in coastal and inland water bodies.

A number of recent studies have derived optical water quality parameters using UAS imagery and are listed in **Table 1**. In these studies, UAS are equipped with a variety of either multispectral or hyperspectral imagers that measure light at discrete wavebands in the visible and near-infrared (NIR) spectrum. Following the large body of research borne from earth observing satellites (Werdell and McClain, 2019), many of these studies use a combination of UAS optical payloads, calibrations, and numerical methods to determine remote sensing reflectance (R_{rs}) defined as:

$$R_{rs}(\theta, \Phi, \lambda) = \frac{L_W(\theta, \Phi, \lambda)}{E_d(\lambda)} \quad (1)$$

where L_W (W m^{-2} nm^{-1} sr^{-1}) is water-leaving radiance, E_d (W m^{-2} nm^{-1}) is downwelling irradiance, θ represents the sensor viewing angle between the sun and the vertical (zenith), ϕ represents the angular direction relative to the sun (azimuth), and λ represents wavelength.

Like all above-water optical measurements, UAS do not measure R_{rs} directly as the at-sensor total radiance (L_T, W m^{-2} nm^{-1} sr^{-1}) constitutes the sum of L_W and incident radiance reflected off the sea surface into the detector's field of view, herein referred to as surface-reflected radiance (L_{SR}). L_W is radiance that emanates from the water and contains a spectral shape and magnitude governed by optically active water constituents interacting with downwelling irradiance, while L_{SR} is independent of water constituents and is instead governed by a given sea-state surface reflecting light; a familiar example is sun glint. Here we define UAS total reflectance (R_{UAS}) as:

$$R_{UAS}(\theta, \Phi, \lambda) = \frac{L_T(\theta, \Phi, \lambda)}{E_d(\lambda)} \quad (2)$$

where

$$L_T(\theta, \Phi, \lambda) = L_W(\theta, \Phi, \lambda) + L_{SR}(\theta, \Phi, \lambda) \quad (3)$$

As UAS measurements are typically performed close to the surface (e.g. United States Federal Aviation Administration's maximum allowable altitude of 122 m), atmospheric measurement effects are routinely assumed to be negligible and ignored (Zeng et al., 2017; Schneider-Zapp et al., 2019). Indeed, this is a key advantage of UAS imagery as atmospheric effects over coastal environments can introduce significant uncertainty in satellite-based measurements (Gordon and Clark, 1980). However, failure to accurately account for L_{SR} can significantly influence R_{rs}, resulting in inaccurate water quality estimates once algorithms are applied (Su, 2017; Zeng et al., 2017).

The objective of this paper is to evaluate the efficacy of methods that remove L_{SR} from total UAS radiance measurements in order to derive more accurate remotely sensed retrievals of scientifically valuable in-water constituents. UAS derived radiometric measurements are evaluated against *in situ* hyperspectral R_{rs} measurements to determine the best performing method of estimating and removing surface reflected light and derived water quality estimates.

TABLE 1 | Summary of existing UAS aquatic remote sensing literature including the UAS sensor(s) used, radiometric quantity studied (where R_{rs} represents UAS derived remote sensing reflectance and R_{UAS} represents UAS derived total reflectance), whether the study accounted for surface reflected radiance (L_{SR}), and the water quality parameter(s) derived.

Reference	UAS sensor(s)	Radiometric quantity	Removal of L_{SR}?	WQ parameter(s)
Zeng et al. (2017)	Ocean optics STS-VIS spectrometers (hyperspectral)	R_{UAS}	No	Chl *a*, CDOM, turbidity
Shang Z. et al. (2017)	AvaSpec-dual spectroradiometers (hyperspectral)	R_{rs}	Yes	Chl *a*
Su, (2017)	Canon powershot S110 RGB and NIR sensors	R_{UAS}	Yes	Chl *a*, secchi disk depth, turbidity
Choo et al. (2018)	MicaSense RedEdge and DLS (multispectral)	R_{UAS}	No	Chl *a*
Baek et al. (2019)	MicaSense RedEdge and DLS (multispectral)	R_{rs}	Yes	Chl *a*
Becker et al. (2019)	Ocean optics STS-VIS spectrometers (hyperspectral)	R_{UAS}	No	Cyanobacteria index, chl *a* TSS
Arango and Nairn. (2019)	MicaSense RedEdge and DLS (multispectral)	R_{UAS}	No	Secchi disk depth, chl *a*, TSS, TN, TP
Olivetti et al. (2020)	Parrot sequoia (multispectral)	R_{UAS}	No	TSS
McEliece et al. (2020)	Sentera multispectral sensor (4 visible bands)	R_{UAS}	No	Chl *a*, turbidity
Kim et al. (2020)	MicaSense RedEdge-M and DLS (multispectral)	R_{rs}	Yes	Chl *a* (but not focus of paper)
Castro et al. (2020)	MicaSense RedEdge and DLS (multispectral)	R_{rs}	No	Chl *a*
O'Shea et al. (2020)	Resonon Pika L spectrometer (hyperspectral) *deployed on a tower, not UAS	R_{rs}	Yes	Chl *a*

Background/Theory

If a water surface was perfectly flat, incident light would reflect specularly and could be measured with known viewing geometries. This specular reflection of a level surface is known as the Fresnel reflection; however, most water bodies are not flat as winds and currents create tilting surface wave facets. Due to differing orientation of wave facets reflecting radiance from different parts of the sky, L_{SR} can vary widely within a single image. A common approach to model L_{SR} is to express it as the product of sky radiance (L_{sky}, W m^{-2} nm^{-1} sr^{-1}) and ρ, the effective sea-surface reflectance of the wave facet (Mobley, 1999 ; Lee et al., 2010):

$$L_{SR}(\theta, \Phi, \lambda) = \rho(\theta, \Phi, \lambda) * L_{sky}(\theta, \Phi, \lambda) \quad (4)$$

Rearranging **Eqs. 3 Eqs. 4**, ρ can be derived by:

$$\rho(\theta, \Phi, \lambda) = \frac{L_T(\theta, \Phi, \lambda) - L_w(\theta, \Phi, \lambda)}{L_{sky}(\theta, \Phi, \lambda)} \quad (5)$$

Given measurements of L_{sky}, an accurate determination of ρ is critical to derive R_{rs} by:

$$R_{rs}(\theta, \Phi, \lambda) = R_{UAS}(\theta, \Phi, \lambda) - \frac{L_{sky}(\theta, \Phi, \lambda) * \rho(\theta, \Phi, \lambda)}{E_d(\lambda)} \quad (6)$$

Methods using the statistics of the sea surface, for a given wind vector, can be used to predict ρ; tabulated values have been derived from numerical simulations with modelled sea surfaces, Cox and Munk wave states (wind), and viewing geometries (Cox and Munk, 1954; Mobley, 1999; Mobley, 2015). Mobley (1999) provides the recommendation of collecting radiance measurements at viewing directions of θ = 40° from nadir and ϕ = 135° from the sun to minimize the effects of sun glint and nonuniform sky radiance with a ρ value of 0.028. The suggested viewing geometries and ρ value from Mobley (1999) have been used to estimate and remove L_{SR} in UAS remote sensing studies (Ruddick et al., 2006; Shang S. et al., 2017; Baek et al., 2019; Kim et al., 2020). However, more recent studies have shown that ρ can be spectrally dependent due to the degree of sky polarization and the ratio of diffuse to direct light; assuming a spectally constant ρ in a roughened sea surface with multi-angular wave facets can lead to erroneous estimates of L_{SR} (Lee et al., 2010; Mobley, 2015). Lee et al. (2010) proposed a spectral optimization approach using spectral inherent optical properties to model R_{rs}, which has been applied in UAS remote sensing studies (O'Shea et al., 2020).

An alternative method to remove L_{SR} relies on the so-called dark pixel assumption that assumes L_W in the NIR is negligible due to strong absorption of water. Where this assumption holds, at-sensor radiance measured in the NIR is solely L_{SR} (Gordon and Wang, 1994; Siegel et al., 2000) and allows ρ to be calculated if L_{sky} is known. Studies have used this assumption to estimate and remove L_{SR}; however, the assumption tends to fail in more turbid waters where high concentrations of particles enhance backscattering and L_W in the NIR (Siegel et al., 2000; Lavender et al., 2005). Other novel image-processing techniques such as nonlocal mean filtering and a matching pixel by pixel algorithm have been proposed to reduce the effects of L_{SR} variation from UAS imagery; however, these region-specific methods exhibit some limitations for applications in other water bodies (Su, 2017; Totsuka et al., 2019).

METHODS

Study Area

This study was conducted in the Choptank River, a major tributary of the Chesapeake Bay (United States). The 1,756 km^2 coastal plain watershed is dominated by agriculture and forest with a relatively low population density, transitions from non-tidal, freshwater reaches to a brackish, tidal mouth, and is eutrophic (Fisher et al., 2021). Data from eight stations located downriver and extending from the mouth of the Choptank River were collected on September 16, 2020 with a relatively clear sky, data from eight stations located up river were collected on October 1, 2020 with varying cloud cover, and data from thirteen stations located in between the downriver and upriver stations were collected on October 22, 2020 with a clear sky (**Figure 1**).

In situ R_{rs}

At each station, a set of hyperspectral radiometers (TriOS RAMSES; Rastede DE) deployed on a float provided *in situ* R_{rs} measurements at every station. The float held a downwelling irradiance sensor (E_d) and an inverted radiance sensor (L_w) positioned above the surface water and with a small black plastic cone that extended just below the surface to block L_{SR} (i.e. light blocking technique, Ahn et al., 1999; Lee et al., 2019). The TriOS radiometers collect 256 wavelength bands at 3.3 nm intervals within the 320–950 nm range. All *in situ* hyperspectral measurements were interpolated at 1 nm intervals. In order to compare these measurements to the UAS, spectral response functions (SRFs) of the five MicaSense wavebands were applied to the *in situ* hyperspectral R_{rs} data (**Figure 2**).

In situ Water Quality Data

At each station, surface water grab samples were collected to measure chlorophyll *a* and total suspended solids (TSS) concentrations. Chlorophyll *a* concentration was measured in duplicate following EPA method 445.0 (Arar and Collins, 1997). Briefly, 100 ml of water from each station was filtered on 47 mm GF/F filters, immersed in 20 ml of 90% acetone and placed in a dark freezer for 24 h. Chlorophyll *a* fluorescence was measured on 5 ml of extract using a fluorometer (Turner 10 AU Fluorometer, San Jose CA) calibrated against chlorophyll *a* pigment standards (DHI, Horsholm DK) before and after acidification with 0.1 ml of 6 N hydrochloric acid. TSS was measured using a gravimetric analysis (American Public Health Association (APHA), 1995). 350 ml of water from each station was filtered using pre-weighed and combusted (450°C) GF/F filters and placed into a 105°C drying oven for at least 2 h. Filters were reweighed and the concentration was calculated by TSS (mg/L) = $W_{post(g)}$ - $W_{combust(g)}$ x 1,000/V(L).

Multispectral Sensor: MicaSense RedEdge-MX Sensor

The MicaSense RedEdge-MX sensor (MicaSense, Seattle, Washington, United States) is a 8.7 × 5.9 × 4.5 cm multispectral camera capable of capturing five simultaneous bands on the electromagnetic spectrum in 12 bit radiometric

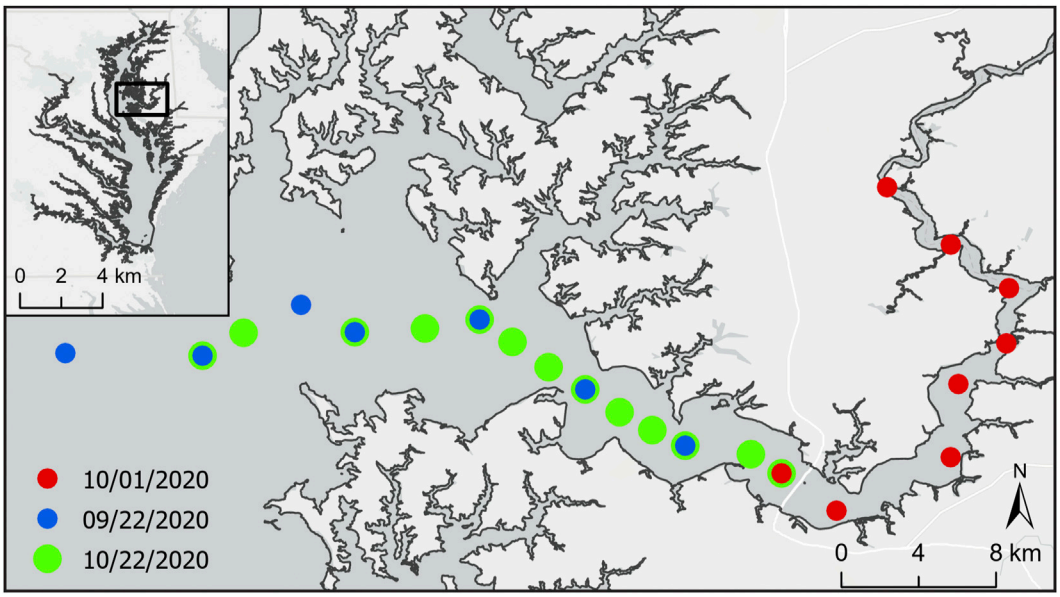

FIGURE 1 | Location of Choptank River (38.63 N, −76.33 W) in Chesapeake Bay, Maryland, United States and locations of stations where data was collected.

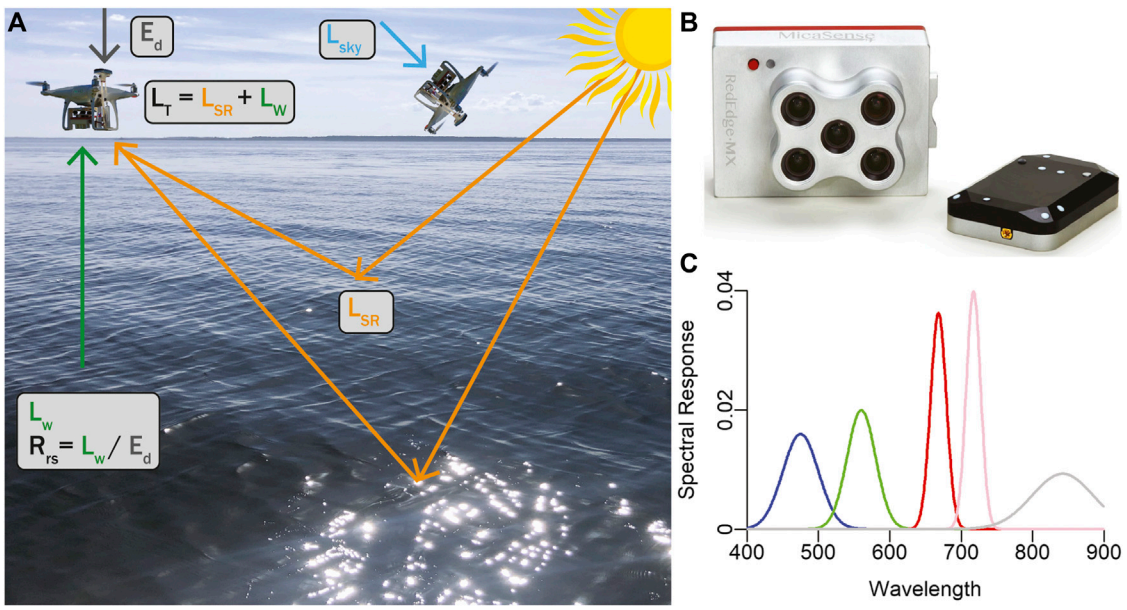

FIGURE 2 | (A) MicaSense RedEdge-MX multispectral sensor and downwelling light sensor (DLS) collects total radiance (L_T) (sum of water-leaving radiance, L_w and surface reflected radiance, L_{SR}) and downwelling irradiance (E_d) measurements while in a low altitude flight. Sky radiance (L_{sky}) is collected by positioning the sensor at 40° angle from zenith away from sun. **(B)** MicaSense RedEdge-MX multispectral sensor and DLS collects L_T and E_d in five wavebands: red, green, blue, red-edge, near-infrared. **(C)** Approximate spectral response functions of MicaSense RedEdge-MX sensor.

resolution: blue (475 nm center, 32 nm bandwidth), green (560 nm center, 27 nm bandwidth), red (668 nm center, 14 nm bandwidth), red edge (717 nm center, 12 nm bandwidth), and NIR (842 nm center, 57 nm bandwidth). The sensor has up to one capture per second, a 47.2° field of view with a spatial resolution of 8 cm per pixel at 120 m altitude. The sensor was mounted on a DJI Phantom four Pro UAS using a 10° 3D-printed mount which resulted in a direct nadir viewing angle while in flight (**Figure 2**). The sensor also includes a downwelling light sensor (DLS) which measures E_d in the same spectral wavebands during in-flight image captures. The DLS measures light incident on a diffuser, providing a downwelling hemispherical irradiance measurement

(Mamaghani and Salvaggio, 2019). The DLS was mounted above the UAS to eliminate shading and collected incident light at a 0° zenith angle. Images were collected at an average flight altitude of 70 m which resulted in 0.02 m pixel resolution (923 × 1219).

At each station, measurements of L_T, L_{sky}, and E_d were collected by the MicaSense RedEdge-MX multispectral sensor and DLS. First, measurements of L_{sky} were collected by positioning the camera 40° from zenith with an approximate azimuthal viewing direction of 135° and taking several image captures (**Figure 2**). L_{sky} at each waveband was computed as the grand mean of all station-specific measurements. Next, the UAS was manually flown and images were automatically captured every 2 s. The MicaSense multispectral sensor has a built-in global positioning system (GPS) and inertial measurement unit (IMU) which recorded the positioning (latitude, longitude, altitude) and orientation (yaw, pitch, roll) of each image capture. Thirty image captures taken at the highest altitude from each station were used in subsequent analyses. This information along with solar elevation, image size, and coordinated universal time (UTC) time, were recorded in the metadata of each image capture.

Pre-Processing

Data collected by the multispectral sensor were radiometrically calibrated using a Python workflow provided by MicaSense[1]. The process of converting raw pixel values (digital number, DN) into total spectral radiance (L_T) values with units of W/m/sr/nm is given in **Eq 7**:

$$L_T = V(x,y) * \frac{a_1}{g} * \frac{DN - DN_{BL}}{t_e + a_2 y - a_3 t_e y} \quad (7)$$

The radiometric calibration compensates for dark pixel subtraction (DN_{BL}), sensor gain (g), exposure settings (t_e), and lens vignette effects (V(x,y)). Coefficients a_1, a_2, and a_3 are radiometric calibration coefficients and x,y is the pixel column and row number, respectively. Lens distortion effects, such as band-to-band image alignment, were removed from image captures by an unwarping procedure and wavebands were aligned to form a stacked TIFF for each image set.

A filtering procedure was applied to all images to remove specular sun glint and instances of the boat when it was present in the image. Studies have suggested filtering out high total radiance values, or instances of specular sun glint, before removing L_{SR} from L_T (Hooker et al., 2002). Specular sun glint arises when direct sunlight reflects off of a wave facet or surface at the viewing angle of the sensor. Sun glint pixels were masked using an empirical upper limit of R_{UAS} measurements in the NIR, and this mask was then propagated to pixels at all other wavebands. Specifically, *in situ* measurements and values from radiative transfer model simulations (see methods below) were used in **Eq. 8** to solve for an upper limit of R_{UAS}(NIR) and pixels with values greater than this upper limit were masked in each waveband.

[1]MicaSense RedEdge Image Processing Tutorials. Retrieved online at https://github.com/micasense/imageprocessing.

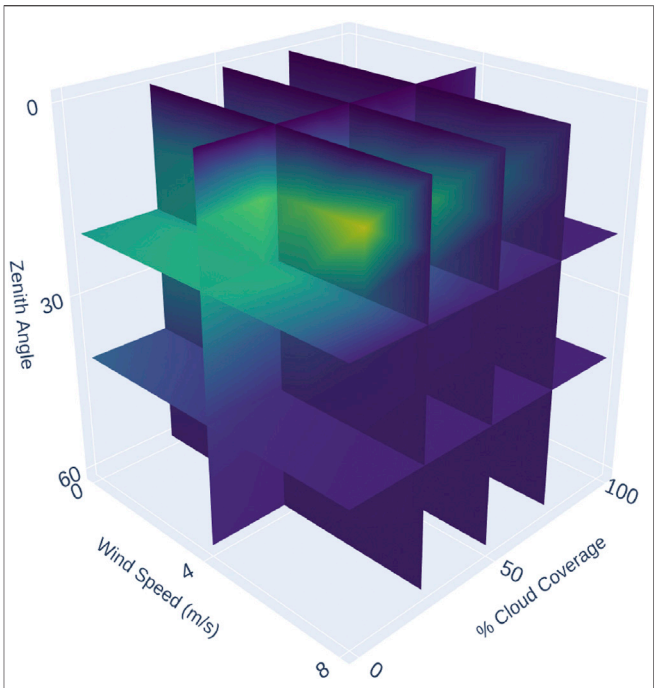

FIGURE 3 | Visualization of the three-dimensional ρ look-up table derived from HydroLight simulations with varying solar zenith angles, wind speed (m/s), and cloud cover (%) corresponding to a nadir viewing angle.

$$R_{UAS}(NIR) = R_{rs}(NIR) + \rho(\mathrm{NIR}) * \frac{L_{sky}}{E_d} \quad (8)$$

Where R_{rs}(NIR) = 0.005 is based on *in situ* measurements in this study and consistent with other turbid waters (Tzortziou et al., 2006), ρ(NIR) varied depending on station, and L_{sky}/E_d = 0.39 is derived from radiative transfer model simulations (HydroLight v6.0, Numerical Optics Ltd., United Kingdom). A lower limit of R_{UAS}(green) = 0.007 was used to mask out the dark canopy of the boat when present in images.

Removal of Surface Reflected Light (L_{SR})

At each station, L_{SR} was estimated using one of four different methods to ultimately derive R_{rs} following **Eq. 6**. These methods are provided below, and herein referred to as "ρ_{LUT}," "NIR = 0," "NIR > 0" and "Deglinting." Resultant UAS R_{rs} estimates were then compared to paired *in situ* R_{rs} data across stations and wavebands. Statistical evaluations to assess the relationship included root mean square error (RMSE), relative root mean squared error (RRMSE), coefficient of determination (R^2), and *p*-values.

ρ_{LUT}. The ρ_{LUT} method follows from Mobley (1999) and involved developing a look-up table (LUT) of ρ values using HydroLight simulations. HydroLight is a numerical model that solves the radiative transfer equation to compute the radiance distribution within and at the surface of a water body. Inputs include absorbing and scattering properties of a water body, the nature of the wind-blown sea surface (Cox-Munk sea surface slopes), and the sun and sky radiance incident on the sea surface (Mobley, 1999). Outputs include the full radiance distribution,

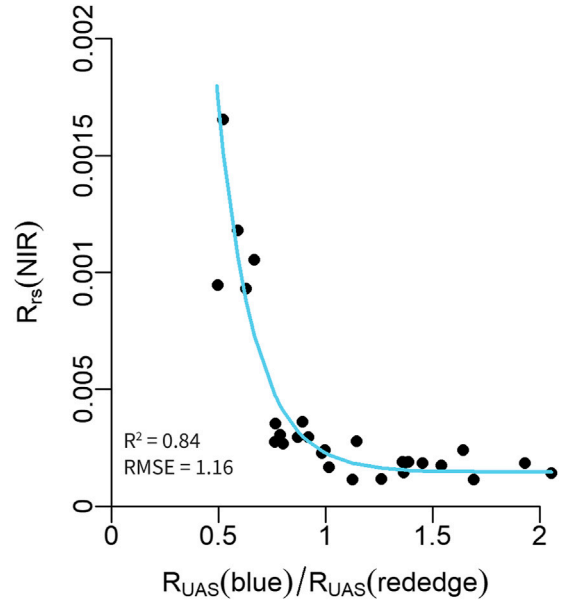

FIGURE 4 | Nonlinear relationship between a blue (475 nm) to red edge (717 nm) ratio of total UAS reflectance to *in situ* R_{rs} in the NIR band (842 nm). An exponential model was used to estimate UAS derived R_{rs}(NIR) baseline in order to estimate L_{SR}.

including an effective ρ value for a range of geometries and wavelengths. Batch HydroLight runs incorporating varying solar zenith angles (0, 10, 20, 30, 40, 50, 60°), wind speeds (0, 2, 4, 6, 8 m/s), and fractional cloud cover (0, 0.2, 0.4, 0.6, 0.8, 1%) were used to develop a multidimensional look-up table of ρ values that correspond to a nadir viewing angle (**Figure 3**). HydroLight returned spectrally explicit $\rho(\theta, \phi, \lambda)$ values and MicaSense SRFs were applied to $\rho(\theta, \phi, \lambda)$ for each waveband. $\rho(\theta, \phi, \lambda)$ values were obtained for each station according to the solar zenith angles obtained from MicaSense metadata, wind speed was collected from the Global Forecast System[2], and cloud cover was determined by the L_{sky} images. Data in this study were collected at solar zenith angles ranging from 36.5 to 58.6°, wind speeds ranged from 1.1 to 3.1 m/s and cloud cover ranged from 0 to 60%.

NIR = 0. L_{SR} was also estimated using a pixel based dark pixel assumption to derive ρ. Assuming R_{rs}(NIR) equals 0, **Eq. 6** can be rearranged to solve for ρ (**Eqs. 9** and **10**). This ρ value is used to calculate R_{rs} across all wavebands (**Eq. 11**).

$$0 = L_T(NIR) - L_{sky}(NIR) * \rho \quad (9)$$

$$\rho = L_T(NIR) \big/ L_{sky}(NIR) \quad (10)$$

$$R_{rs}(\theta, \Phi, \lambda) = R_{UAS}(\theta, \Phi, \lambda) - \frac{L_{sky}(\theta, \Phi, \lambda) * \left(L_T(NIR) \big/ L_{sky}(NIR)\right)}{E_d(\lambda)} \quad (11)$$

[2]Wind speed data was retrieved from https://earth.nullschool.net/about.html.

NIR > 0. Since the dark pixel assumption is invalid in turbid waters including the Chesapeake Bay (Siegel et al., 2000) an alternative pixel based approach was developed to instead estimate a baseline R_{rs}(NIR). Specifically, R_{rs}(NIR) was estimated empirically by a nonlinear regression using *in situ* R_{rs}(NIR) and R_{UAS} data (**Figure 4**). The ratio of R_{UAS}(blue)/R_{UAS}(rededge) led to the most robust predictions of R_{rs}(NIR) using **Eq 12**:

$$R_{rs}(\theta, \Phi, \lambda) = 0.025e^{-5.469 * R_{UAS}(blue) \big/ R_{UAS}(red\ edge)} + 0.00013 \quad (12)$$

Conceptually, this relationship makes sense because with increasing particle concentrations, water becomes less blue and R_{rs}(NIR) increases.

"Deglinting." L_{SR} was also estimated following the "deglinting" methods of Hochberg et al. (2003) and Hedley et al. (2005). For each station, a minimum NIR value was determined by finding the lowest 10% of R_{UAS}(NIR) across all images. For each band, a linear regression was made between all R_{UAS}(NIR) and R_{UAS}(visible) values and the slope (b_i) was determined. Each pixel was corrected by subtracting the product of b_i and the NIR brightness of the pixel (Hedley et al., 2005):

$$R_{rs}(i) = R_{UAS}(i) - b_i(R_{UAS}(NIR) - \min(R_{UAS}(NIR))) \quad (13)$$

Water Quality Retrievals

R_{rs} values from each L_{SR} removal method were compared against *in situ* chlorophyll *a* and TSS data (n = 28) using multiple linear regressions. The best performing model (highest R^2 and lowest RMSE, RRMSE, *p*-values) was used in a stepwise model selection by Akaike information criterion (AIC, "stepAIC" in R). The AIC stepwise regression iteratively added and removed wavelengths in order to determine the combination of data that resulted in the best performing model with low prediction error, while taking into account model simplicity. R_{rs} values were used as input into optical algorithms derived from the best performing multiple linear regressions and mean chlorophyll *a* and TSS concentration at each station was obtained by averaging values across all images. The resulting arrays were georeferenced using the Python libraries "CameraTransform" (Gerum et al., 2019) and "Rasterio" using archived metadata including latitude, longitude, image width, image height to position the images accurately in a known coordinate system (WGS84). Georeferenced arrays were exported as individual TIFFs and mapped using ArcGIS Pro (ESRI Inc. Redlands, CA, United States).

RESULTS

In situ Data

Chlorophyll *a* concentration ranged from 5.19 to 53.30 ug/L with an average of 17.13 ± 10.96 ug/L. TSS concentration ranged from 19.94 mg/L to 39.69 mg/L with an average of 28.25 ± 5.21 mg/L. In general, *in situ* R_{rs} spectra were representative of a eutrophic system (**Figure 5**, Gitelson et al., 2007; Spyrakos et al., 2018). Due to absorption of chromophoric dissolved organic matter (CDOM) and chlorophyll *a* in lower wavelengths, R_{rs} is low in the blue region with a distinct peak in the green region

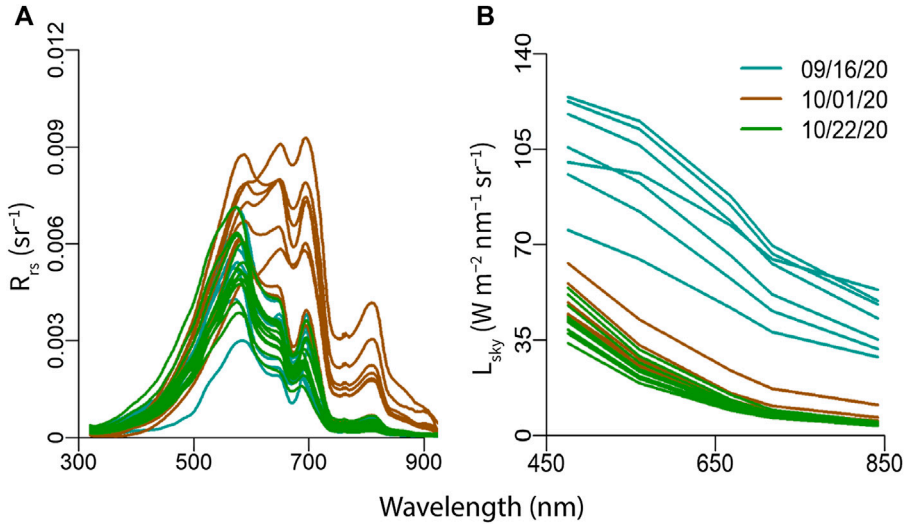

FIGURE 5 | (A) *In situ* remote sensing reflectance (R_{rs}) spectra collected with hyperspectral TriOS radiometers and **(B)** Sky radiance (L_{sky}) spectra collected with MicaSense RedEdge-MX multispectral camera at stations along the Choptank River on 9/16/20 (blue), 10/01/20 (brown), and 10/22/20 (green).

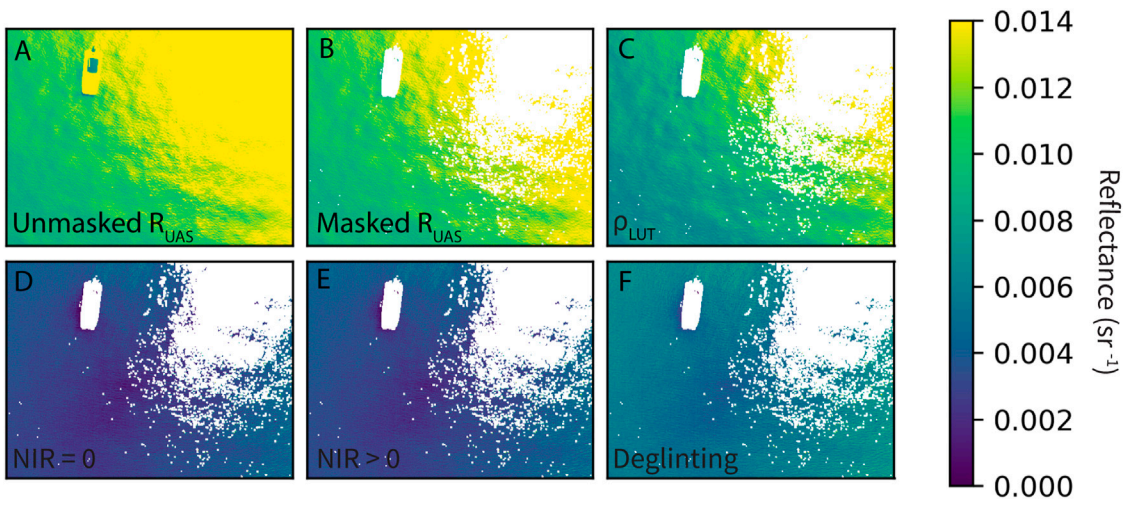

FIGURE 6 | Example of an individual UAS image (green band) with different radiometric values: **(A)** R_{UAS}, **(B)** R_{UAS} with initial sun glint masking and **(C–F)** remote sensing reflectance (R_{rs}) using various methods to remove surface reflected light: **(C)** ρ look-up table (LUT) from HydroLight simulations, **(D)** Dark pixel assumption with NIR = 0, **(E)** Dark pixel assumption with NIR >0, **(F)** Deglingting methods following Hochberg et al. (2003).

(~550 nm). A secondary peak in the red region (~700 nm) corresponds to chlorophyll fluorescence emission (Spyrakos et al., 2018). Overall, spectra collected from upriver stations on 10/01/20 were larger in magnitude and contained a tertiary peak in the NIR region (~800 nm).

Removal of Surface Reflected Light (L_{SR})

UAS measurements of L_{sky} were approximately proportional to the fourth power of the wavelength ($L_{sky} \approx \lambda^{-4}$, **Figure 5**) and were used with estimations of ρ to calculate and remove L_{SR} from R_{UAS} measurements at each station. **Figure 6** illustrates the initial masking and methods to remove L_{SR} using an individual UAS image taken in the green band. When L_{SR} was estimated using the ρ look-up table (ρ_{LUT}), R_{rs} values did not change much from R_{UAS} values; however, R_{rs} values using the pixel-based dark pixel assumptions (NIR = 0, NIR>0) and "deglinting" approach declined and became more homogenous across pixels (**Figure 6**).

UAS derived reflectance measurements from each L_{SR} removal method were plotted as spectra (**Figure 7**) and compared against *in situ* R_{rs} values (**Figure 8**). UAS reflectance spectra are similar in shape to *in situ* R_{rs} spectra and display a distinct peak in the green band (560 nm) and often a secondary peak in the red band (668 nm) corresponding to chlorophyll *a* reflectance and fluorescence,

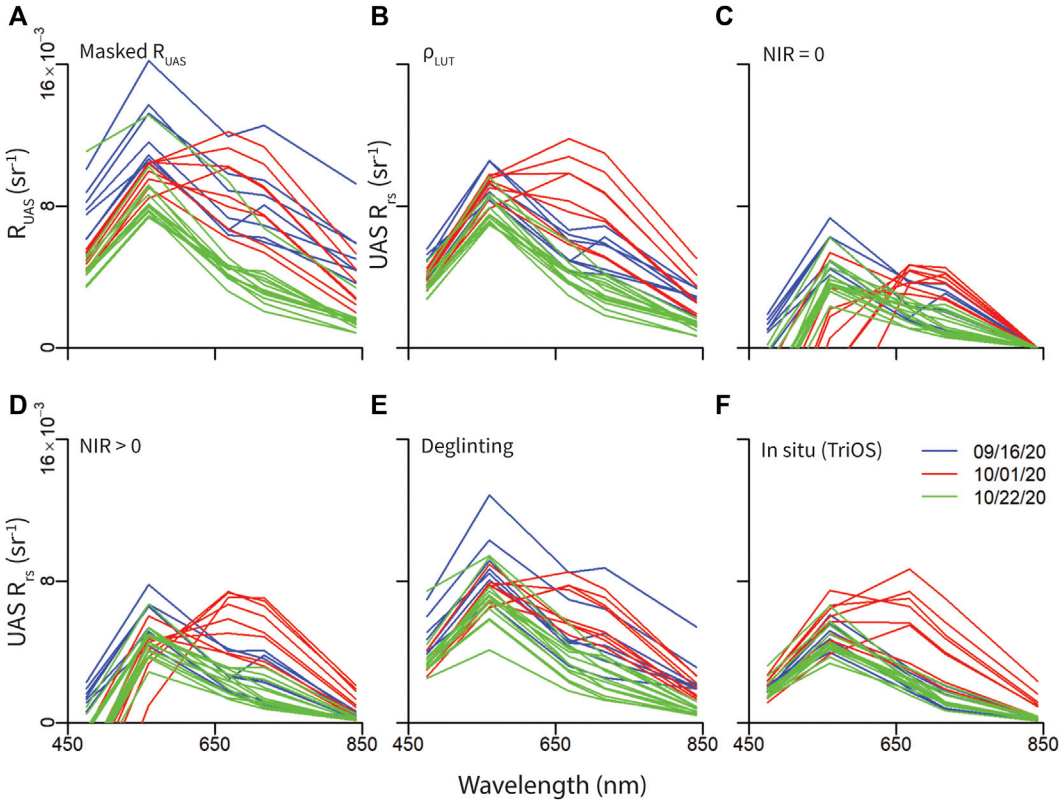

FIGURE 7 | Total UAS reflectance (R_{UAS}) **(A)** and remote sensing reflectance (R_{rs}) spectra using various methods to remove surface reflected light: **(B)** ρ look-up table from HydroLight simulations, **(C)** Dark pixel assumption with NIR = 0, **(D)** Dark pixel assumption with NIR >0, **(E)** Deglinting methods following Hochberg et al. (2003), and **(F)** *In situ* R_{rs} spectra from TriOS sensors with MicaSense SRFs applied. Negative values are not shown in plots.

respectively (**Figure 7**). Spectra collected on the second sampling day (upriver sites) shift to longer wavelengths likely due to scattering of inorganic particles (**Figure 7**). R_{UAS} spectra are higher in magnitude and are overestimated when compared to *in situ* R_{rs} due to the inclusion of L_{SR} (R^2 = 0.55, RMSE = 0.004, $p < 0.05$). When L_{SR} is estimated using the ρ_{LUT}, spectra are similar in shape to *in situ* spectra, but are higher in magnitude and overestimated compared to *in situ* measurements (R^2 = 0.85, RMSE = 0.003, $p < 0.05$). When L_{SR} is estimated with the dark pixel assumption (NIR = 0), R_{rs} spectra are lowest in magnitude, had the poorest fit to *in situ* data (R^2 = 0.18, RMSE = 0.004, $p < 0.05$), and produced negative R_{rs} values in the lower wavelengths. This is not surprising given that the *in situ* measurements in the NIR (**Figure 5A**) are not negligible which leads to an overestimation in L_{SR}. When L_{SR} is estimated using a basline NIR value (NIR>0), R_{rs} spectra are higher in magnitude with a lower error but still indicate negative values in the lower wavelengths, indicating L_{SR} was still slightly overestimated (R^2 = 0.50, RMSE = 0.002, $p < 0.05$). R_{rs} spectra with the "Deglinting" approach are similar in shape to *in situ* spectra but are slightly higher in magnitude (**Figure 7**). This approach contained the second highest correlation and lowest RMSE (R^2 = 0.65, RMSE = 0.002, $p < 0.05$), but still tended to overestimate R_{rs} values (**Figure 8**).

Water Quality Retrieval Algorithms

R_{rs} measurements with L_{SR} estimated using a baseline NIR value (NIR>0) performed best when compared to *in situ* chlorophyll *a* data (R^2 = 0.37, RMSE = 5.89, RRMSE = 37%, $p < 0.05$). A stepwise model selection by AIC demonstrated that the green, red edge, and NIR bands were most important in estimating chlorophyll *a* concentration (**Figure 9**, R^2 = 0.42, RMSE = 5.90, RRMSE = 37%, $p < 0.05$) and a remotely sensed chlorophyll *a* algorithm was determined as:

$$\text{Chlorophyll a}\,(\text{ug/L}) = 24.02 + R_{rs}(560) * -4337.88 + R_{rs}(717) * 9639.75 + R_{rs}(842) * -2922.80$$

R_{rs} measurements with the "deglinting" technique performed best when compared to *in situ* TSS data (R^2 = 0.72, RMSE = 2.53, RRMSE = 9%, $p < 0.05$). A stepwise model selection by AIC demonstrated that the blue, red, red edge, and NIR bands were most important in estimating TSS concentration (**Figure 9**, R^2 = 0.73, RMSE = 2.53, RRMSE = 9%, $p < 0.05$) and a remotely sensed TSS algorithm was determined as:

$$\text{TSS}\,(\text{mg/L}) = 30.57 + R_{rs}(475) * 1364.86 + R_{rs}(668) * -5255.88 + R_{rs}(717) * 2548.08 + R_{rs}(842) * 4579.36$$

Algorithms were applied to respective UAS derived R_{rs} values and average chlorophyll *a* and TSS concentrations were mapped, along with mosaiced georeferenced TIFFs of

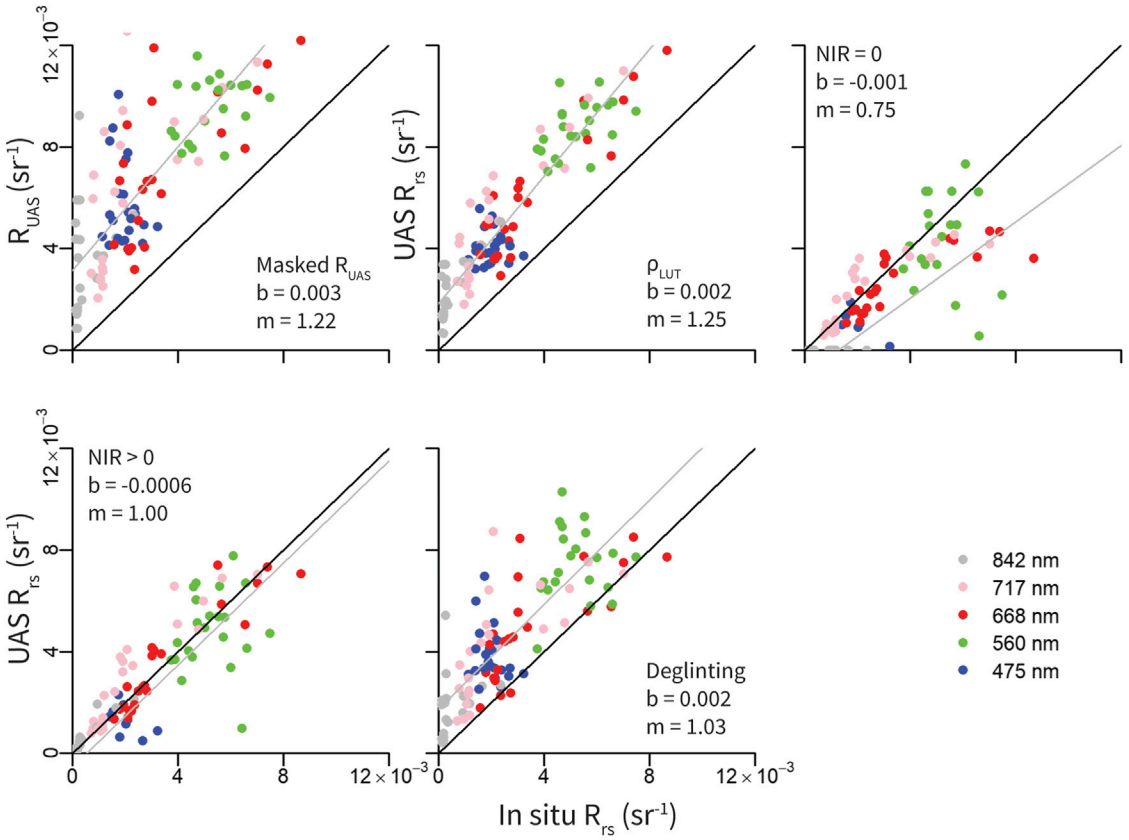

FIGURE 8 | Comparison of UAS radiometry and *in situ* R_{rs} in all bands at each station (n = 28) using different methods to remove surface reflected light after initial sun glint masking. **(A)** Total UAS derived reflectance (R_{UAS}), **(B)** ρ look-up table from HydroLight simulations, **(C)** Dark pixel assumption with NIR = 0, **(D)** Dark pixel assumption with NIR >0, **(E)** Deglinting methods following Hochberg et al. (2003). Negative values are not shown in plots.

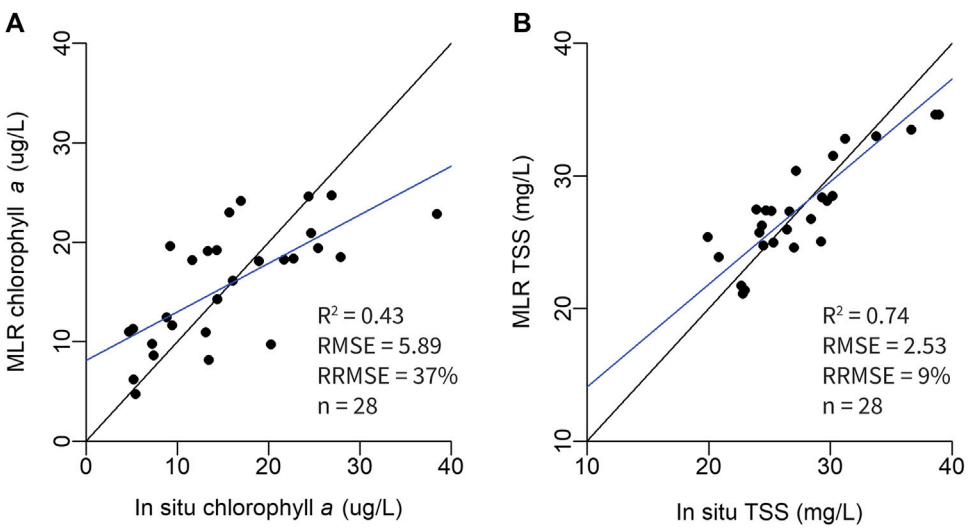

FIGURE 9 | Comparison between *in situ* and modelled **(A)** chlorophyll *a* concentration and **(B)** TSS concentration from multiple linear regressions.

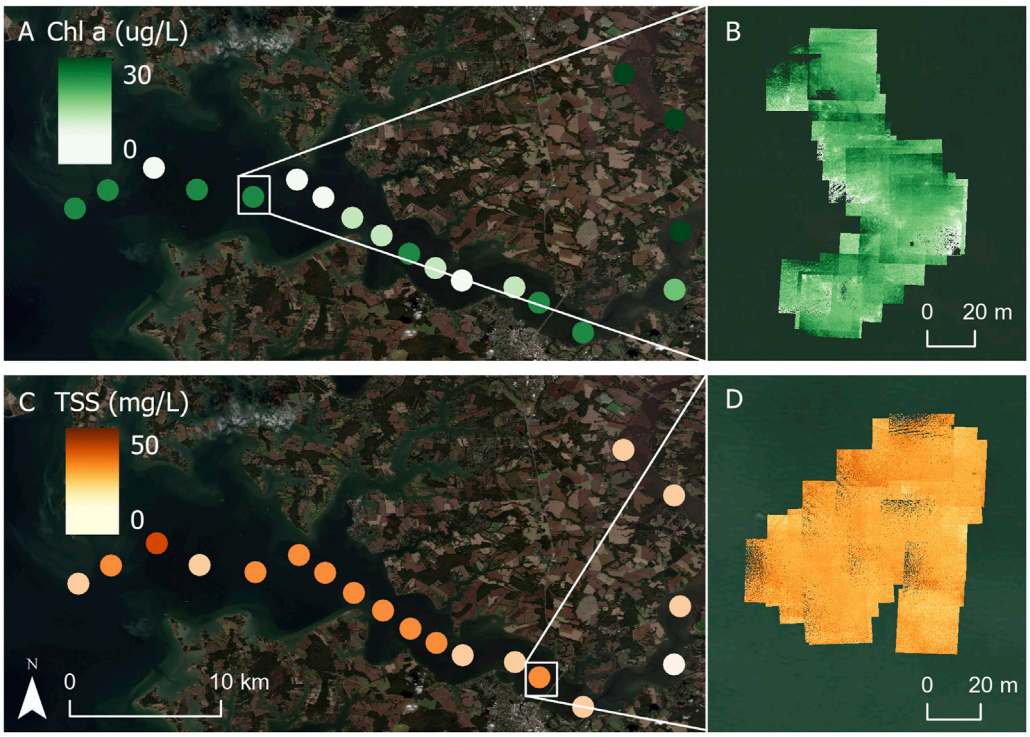

FIGURE 10 | (A) Average chlorophyll *a* concentration across image captures (n = 30) at each station. **(B)** Example of mosaiced georeferenced TIFFs collected at one station with chlorophyll *a* algorithm applied. **(C)** Average TSS concentration across image captures (n = 30) at each station. **(D)** Example of mosaiced georeferenced TIFFs (n = 30) collected at one station with TSS algorithm applied.

individual image captures (**Figure 10**). Average chlorophyll *a* concentration tended to increase at upriver sites while average TSS concentrations were higher at downriver sites (**Figure 10**). This trend was also seen in the *in situ* data. Within the mosaic of individual TIFFs, slight variations in chlorophyll *a* and TSS concentration are visible (**Figure 10**).

DISCUSSION

This study is one of the first to compare methods to remove surface reflected light from high resolution UAS multispectral measurements. An initial filtering procedure and four methods to remove L_{SR} were evaluated against *in situ* R_{rs} measurements. Water quality algorithm performance is compared to those found in the literature. Results have broad implications for improving UAS derived water quality measurements in coastal waters, but several aspects and caveats of this study merit additional discussion.

Performance of Methods to Remove Surface Reflected Light (L_{SR})

Removing surface reflected light from the total radiance measured by a UAS ensures only water-leaving information is used as input into water quality retrievals. Initial filtering techniques successfully masked instances of specular sun glint and non-water objects (i.e. boat) in the UAS imagery using empirical upper and lower R_{rs} limits. This primary step ultimately improved final R_{rs} measurements and derived water quality products. While the magnitude of L_{sky} can impact L_{SR}, the spectral dependence ($\sim\lambda^{-4}$) is constrained and can be measured; therefore, the effective sea-surface reflectance of a wave facet (ρ) needs to be accounted for. Nonetheless, it is important to consider the impact of the varying absolute magnitude of L_{sky} and future work should analyze the effect of L_{sky} variability on UAS R_{rs} measurements.

The ρ_{LUT} method utilized a ρ lookup table approach developed from HydroLight simulations where ρ values were obtained depending on the solar zenith angle, wind speed, and cloud cover at the time of UAS data collection. Mobley (1999) HydroLight simulations led to recommendations of specific sensor viewing angles with a corresponding constant ρ value to reduce effects of L_{SR}; however, most consumer grade UAS sensors and mounts do not have the ability to change viewing angles and are fixed at a nadir viewing angle. Therefore, the ρ values in the look-up table correspond to nadir viewing angles. This method resulted in UAS R_{rs} values that were generally greater than *in situ* R_{rs} values, indicating L_{SR} was underestimated. This can most likely be attributed to a constant ρ value that was used to estimate L_{SR} across all pixels in each image, which averaged out the multifaceted characteristic of a water surface.

The NIR = 0 and NIR >0 methods took advantage of the NIR waveband on the multispectral sensor and incorporated aspects of the dark pixel assumption which allowed L_{SR} to be removed from visible wavelengths by assuming that 1) a NIR signal is composed of L_{SR} and/or a spatially homogeneous NIR component in the water and 2) the amount of L_{SR} in the NIR band is linearly related to the amount of L_{SR} in the visible bands (Mobley, 1999; Siegel et al., 2000). Unlike the ρLUT method that applies a single value to an entire image, the dark pixel assumption approaches estimate L_{SR} on a per pixel basis which decreases resultant R_{rs} variability (**Figures 6**, **8**). When NIR was assumed to be entirely negligible, calculated R_{rs} values were generally lower compared to *in situ* R_{rs} which can be attributed to an enhancement of NIR due to the presence of scattering inorganic particles in turbid waters. Thus, when a baseline NIR value was estimated, the method performed better (higher R^2, lower RMSE and RRMSE); however, negative R_{rs} values in the lower wavelengths indicated L_{SR} was still likely overestimated at some stations.

The "deglinting" method, modelled off a glint removal algorithm introduced by Hochberg et al. (2003), and later Hedley et al. (2005), calculated a constant 'ambient' NIR brightness level which was removed from all pixels in all wavelengths. This approach resulted in UAS R_{rs} measurements slightly overestimated compared to *in situ* values but produced the highest R^2 and lowest RMSE of all methods. This method was applied by averaging pixel values across all thirty images collected at each station and is likely to perform better when applied on individual images.

The ρ_{LUT} method uses ρ values that are based on probability distributions of sea surface slopes which are related to the scale of satellite pixel resolution (100–1000 m) (Cox and Munk, 1954). For images with much higher pixel resolution (>1–10 m), statistical assumptions about the surface of water composed of many reflecting facets are less likely to hold (Kay et al., 2009). Therefore, to collect accurate water-leaving reflectance measurements from high resolution UAS imagery, it is recommended to use a pixel-based approach exploiting the high absorption of water at NIR wavelengths to estimate and remove L_{SR}. If a baseline NIR measurement can be retrieved, the dark pixel assumption should be used to remove L_{SR}. Otherwise, the 'deglinting' methods following Hochberg et al. (2003) and Hedley et al. (2005) are recommended. In open ocean waters without a strong influence of optically active properties, a pixel-based approach assuming NIR is negligible is expected to perform well.

It is important to note a potential caveat to the L_{SR} method evaluation. In this study, *in situ* R_{rs} measurements were provided by hyperspectral radiometers with a skylight blocking approach (Ahn et al., 1999; Lee et al., 2019). This approach consists of attaching an open-ended apparatus, or tube, to the front of a downward looking radiance radiometer and lowering it a few centimeters into the water, blocking surface-reflected light and allowing for a direct measurement of L_W. It is important to note that measurements from this technique are subject to instrument self-shading, which is a function of the water's optical properties, sun elevation, and the size of the skylight-blocking cone (Zhang et al., 2017; Lee et al., 2019). Zhang et al. (2017) estimated that self-shading accounts for approximately 1–20% error under most water properties and solar positions. Methods to correct for this self-shading have been derived (Zhang et al., 2017; Yu et al., 2021) and if applied, have the potential to improve relationships with UAS R_{rs} measurements.

Performance of Water Quality Algorithms

Performance of the multiple linear regressions developed in this study were compared to existing chlorophyll *a* and TSS algorithms designed for coastal waters to determine if UAS measurements can produce accuracy within the range of other water quality algorithms. Performance of the UAS derived chlorophyll *a* multiple linear regression (R^2 = 0.43, RRMSE = 37%) is comparable to other chlorophyll *a* algorithms found in the literature (Ruddick et al., 2001; Gons et al., 2002; Gitelson et al., 2007). A three-band chlorophyll algorithm calibrated using a variety of coastal waters, including the Choptank River, resulted in a RRMSE of 51.9% (Gitelson et al., 2007), a two-band algorithm (red/NIR) with adaptive optimization in the second band calibrated with measurements from the North Sea and Lake Ijless, Netherlands resulted in a RRMSE of 37% (Ruddick et al., 2001), and a two-band algorithm (red/NIR) designed for the Medium Resolution Imaging Spectrometer (MERIS) satellite sensor and calibrated using a variety of coastal and inland waters including Lake IJssel (Netherlands), the Chinese Lake Tau Hu, and the Hudson/Raritan Estuary (New York/New Jersey) resulted in a standard error of 9.2 ug/L (Gons et al., 2002). Performance of the UAS derived TSS multiple linear regression (R^2 = 0.73, RMSE = 2.53, RRMSE = 9%) is also comparable to existing TSS algorithms found in the literature (Nechad et al., 2010; Novoa et al., 2017). Algorithms including a single-band (NIR) second-order polynomial and single-band (red/green) linear models calibrated with measurements from the Gironde Estuary, France resulted in RRMSE values ranging from of 9.11–16.41% (Novoa et al., 2017) and a non-linear regression calibrated with measurements from the Southern North Sea resulted in RRMSE values less than 30% (Nechad et al., 2010). Future work will include improving water quality algorithms.

UAS Sensor Considerations

The innovative use of UAS technology for environmental research is a relatively new field and researchers are only beginning to understand and alleviate the various methodological and sensor performance challenges. Sensors degrade over time from use and environmental conditions which can impact the accuracy of the data being collected. The most recent MicaSense model, the MicaSense RedEdge-MX, is integrated with low-cost, image-frame complementary metal-oxide semiconductor (CMOS) sensors, which compared to typical charged-coupled device (CCD) sensors, tend to generate more noise and have lower sensitivity levels (Mamaghani and Savaggio, 2019). In the present study, raw values were radiometrically calibrated using a workflow[1] provided by Micasense which implements default metadata parameters that remain the same unless a new factory calibration is performed. Due to sensor degradation, these values are likely to gradually

decline over time, lessening the accuracy of the radiometric calibration processing (Mamaghani and Savaggio, 2019). Studies have improved sensor performance by performing vicarious radiometric calibration using ground targets and panels with known radiometric accuracy, calibrating sensors using National Institute of Standards (NIST)-traceable equipment in a laboratory, and developing look-up tables for correction factors to update calibration parameters (Del Pozo et al., 2014; Mamaghani and Salvaggio, 2019; Cao et al., 2020). Baek et al. (2020) conducted an assessment on radiometric accuracy for the MicaSense RedEdge-MX sensor by comparing data to hyperspectral sensors with NIST-traceable calibration (TriOS RAMSES) and showed that MicaSense RedEdge-MX radiance is approximately 5–16% lower, and irradiance is approximately 1–20% lower, depending on wavelength (Baek et al., 2020). The radiometric accuracy of a new or recently/vicariously calibrated UAS sensor should meet the required radiometric accuracy of 5% that is expected with ocean color satellites (McClain et al., 1992).

Precise registration of multispectral bands within a UAS image capture is also important to derive accurate spectral radiometric values across pixels. Sources of misregistration include a difference in the lens location for each band, image acquisition times, and exposure times which can all influence R_{rs} and resulting water quality variables (Kim et al., 2020). In the present study, images collected in each band were registered using MicaSense's default alignment function[1]. This three step process unwarps images using built-in lens calibration, determines a transformation to align each band to a common band, and crops pixels which do not overlap in all bands. Although this method seemed to perform well in this study; it is acknowledged that this type of band registration can perform poorly with images of locational errors, such as moving water, and can produce noise even after removing surface reflected light (Kim et al., 2020). Kim et al. (2020) developed a novel morphological band registration technique designed for high resolution water quality analysis which effectively removes misregistration noise and improves the accuracy of R_{rs}. Future aquatic UAS remote sensing work should consider adapting this technique to improve UAS remotely sensed retrievals over water.

Caveats and Considerations

Many UAS aquatic remote sensing studies use Structure-from-Motion (SfM) photogrammetric techniques to stitch individual UAS images into ortho- and georectified mosaics (Arango and Nairn, 2019; Castro et al., 2020; McEliece et al., 2020; Olivetti et al., 2020). This approach applies matching key points from overlapping UAS imagery in camera pose estimation algorithms to resolve 3D camera location and scene geometry (Westoby et al., 2012; Arango et al., 2020). Commonly used software (e.g. Pix4D) provide workflows that radiometrically calibrate, georeference, and stitch individual UAS images using a weighted average approach to create at-sensor reflectance 2D orthomosaics (Olivetti et al., 2020). L_{SR} removal methods and water quality algorithms can be directly applied to reflectance orthomosaics to effectively derive water quality products of an entire water body. However, current photogrammetry techniques are not capable of stitching UAS images captured over large bodies of water due to a lack of key points in images of homogenous water surfaces (Arango et al., 2020). Orthomosaics of smaller water bodies or rivers can be created if UAS images contain enough surrounding land features containing keypoints that the photogrammetry software can use to successfully stitch the images containing water. This can be accomplished by increasing flight altitude, with the trade-off of lower spatial resolution. Alternative methods include a statistical interpolation method; however interpolated reflectance values can be imprecise when compared to true reflectance values (Arango et al., 2020).

Management Implications and Future Research

Water quality monitoring is important for tracking water quality trends, identifying and mitigating pollution sources, and discerning potential human health risks. Traditional *in situ* based methods of sampling at discrete stations can be expensive due to high costs for boat time and analysis and can also potentially omit important water quality phenomena. Traditional satellite remote sensing can capture variability throughout time and space; however, limitations including the presence of clouds, atmospheric effects, land adjacency effects, and spatial resolution can hinder periodic monitoring (Shi and Wang, 2009; Becker et al., 2019). UAS fill an operational gap between *in situ* and satellite remote sensing methods. While the current available commercial multispectral UAS sensor technology is geared toward terrestrial applications, mostly precision agriculture, the spectral bands have been useful in retrieving water quality parameters in aquatic water bodies (Choo et al., 2018; Arango and Nairn, 2019; Baek et al., 2019; Castro et al., 2020; Olivetti et al., 2020). A UAS sensor package designed for aquatic environments would undoubtedly improve remotely sensed retrievals and water quality measurements.

Since UAS are deployed at a low altitude, atmospheric corrections and remedies to the land adjacency effect are eliminated. UAS are rapidly deployable and can provide the spatial and temporal variability required for useful water quality monitoring in a dynamic and rapidly evolving environment. UAS can enhance fine-scale physical oceanography research by resolving small-scale phenomena and physical processes such as patchy algal blooms, frontal structures, and turbulence characteristics (**Figure 11**, Shang Z. et al., 2017; Osadchiev et al., 2020). UAS remotely sensed water quality retrievals will also likely improve with the development of lightweight, off-the-shelf hyperspectral sensors, allowing for higher spatial and spectral resolution to better distinguish optical properties of the water (Shang S. et al., 2017; O'Shea et al., 2020).

Future research in turbid coastal waters may benefit from sensor packages that use longer wavelengths (e.g. shortwave infrared, SWIR). SWIR wavelengths have shown to be more effective in satellite atmospheric correction techniques in turbid waters due to the stronger water absorption relative to NIR (Shi and Wang, 2009). This will be advantageous for removing L_{SR} and will improve R_{rs} retrievals in coastal, turbid waters. Future research could also consider combining UAS radiometry with photogrammetry

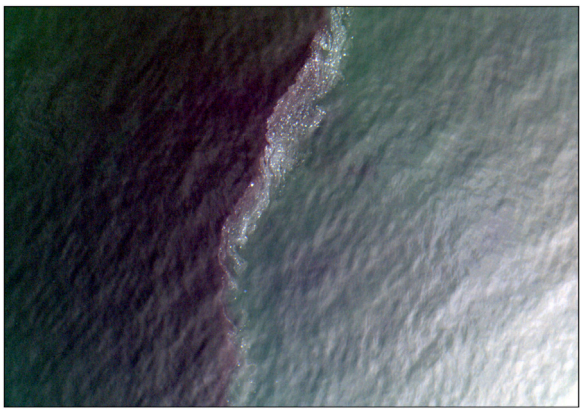

FIGURE 11 | Frontal process observed in UAS RGB imagery collected in the Choptank River, Maryland, United States with MicaSense RedEdge-MX multispectral camera.

computer vision to estimate L_{SR}. Schneider-Zapp et al. (2019) developed a method to estimate a hemispherical-directional reflectance factor (HDRF) from multi-angular UAS measurements. From a combination of photogrammetry and radiometry, a precise estimation of the downwelling light sensor position and orientation can be used to derive a multi-angular reflectance factor, which has the potential to significantly improve estimates of the multifaceted aspect of L_{SR}. An alternative approach to reduce L_{SR} is installing additional hardware to a UAS sensor. O'Shea et al. (2020) tested a hardware-based vertical polarizer on a hyperspectral spectrometer which effectively blocked horizontally polarized reflected skylight. This relatively simple approach could be an attractive solution to researchers and managers who are interested in applying a single algorithm to R_{rs} values to derive water quality parameters and should be further investigated.

CONCLUSION

UAS-based applications of multispectral or hyperspectral remote sensing in aquatic remote sensing have the potential to effectively fill current observation gaps in aquatic remote sensing and provide critical information needed for water quality forecasting, ecosystem monitoring, and ultimately climate change research. While atmospheric effects can usually be ignored in low altitude UAS flights, the effect of sun glint and surface reflected light should be accounted for in order to obtain the highest accuracy of water quality data. The inclusion of surface reflected light can lead to an overestimation of R_{rs} and remotely sensed water quality retrievals. This study presents a comparison of four approaches to remove sun glint and surface reflected light that can be applied to UAS remote sensing to derive water quality parameters such as chlorophyll *a* and TSS concentration. Overall, the performance of the MicaSense RedEdge-MX multispectral sensor appears sufficient for providing high resolution water quality estimates of coastal water bodies when surface reflected light is removed. Of the four approaches examined, a pixel-based deglinting procedure utilizing the brightness of the NIR band performed best when compared to *in situ* R_{rs} measurements. This method also led to the best estimates of TSS while a pixel-based approach utilizing an ambient NIR signal to estimate and remove surface reflected light led to the best estimates of chlorophyll *a* concentration. Future work will include improving algorithms for water quality parameters. Future research should also consider the effects of sensor calibration and the residual misregistration between bands of a UAS multispectral camera.

DATA AVAILABILITY STATEMENT

The raw data supporting the conclusions of this article will be made available by the authors, without undue reservation.

AUTHOR CONTRIBUTIONS

Both AW and GS contributed to the development, planning, and data collection of the study as well as the data analysis, interpretation, and writing of the manuscript.

FUNDING

AW received support from Maryland Sea Grant under award NA18OAR4170070, SA75281900-J from the National Oceanic and Atmospheric Administration, U.S. Department of Commerce and from the Mid-Shore Chapter of the Izaak Walton League. Equipment and parts were funded by Horn Point Laboratory.

ACKNOWLEDGMENTS

We thank the Choptank RiverKeeper, Matt Pluta from ShoreRivers for boat time during his routine water quality monitoring. Thank you to Ph.D. candidate Patrick Gray from the Duke Marine Robotics and Remote Sensing Lab for guidance and supportive conversations throughout this study.

REFERENCES

Ahn, Y. H., Ryu, J. H., and Moon, J. E. (1999). *Development of Redtide & Water Turbidity Algorithms Using Ocean Color Satellite*. KORDI Report No. BSPE 98721-00-1224-01. Seoul, Korea: KORDI.

American Public Health Association (Apha) (1995). "Standard Methods for the Examination of Water and Wastewater," in *Topic 2540 Solids*. 19th Ed. (Washington D.C: APHA).

Anderson, K., and Gaston, K. J. (2013). Lightweight Unmanned Aerial Vehicles Will Revolutionize Spatial Ecology. *Front. Ecol. Environ.* 11 (3), 138–146. doi:10.1890/120150

Arango, J. G., and Nairn, R. W. (2019). Prediction of Optical and Non-optical Water Quality Parameters in Oligotrophic and Eutrophic Aquatic Systems Using a Small Unmanned Aerial System. *Drones* 4 (1), 1. doi:10.3390/drones4010001

Arango, J. G., Holzbauer-Schweitzer, B. K., Nairn, R. W., and Knox, R. C. (2020). Generation of Geolocated and Radiometrically Corrected True Reflectance Surfaces in the Visible Portion of the Electromagnetic Spectrum over Large Bodies of Water Using Images from a sUAS. *J. Unmanned Veh. Sys.* 8 (3), 172–185. doi:10.1139/juvs-2019-0020

Arar, E. J., and Collins, G. B. (1997). *Method 445.0* in Vitro *Determination of Chlorophyll a and Pheophytin Ain Marine and Freshwater Algae by Fluorescence*. Washington, DC: U.S. Environmental Protection Agency.

Baek, J.-Y., Jo, Y.-H., Kim, W., Lee, J.-S., Jung, D., Kim, D.-W., et al. (2019). A New Algorithm to Estimate Chlorophyll-A Concentrations in Turbid Yellow Sea Water Using a Multispectral Sensor in a Low-Altitude Remote Sensing System. *Remote Sensing* 11 (19), 2257. doi:10.3390/rs11192257

Baek, S., Koh, S., and Kim, W. (2020). Calculation of Correction Coefficients for the RedEdge-MX Multispectral Camera through Intercalibration with a Hyperspectral Sensor. *J. Korean Soc. Surv. Geodesy, Photogramm. Cartography* 38 (6), 707–716. doi:10.7848/KSGPC.2020.38.6.707

Becker, R. H., Sayers, M., Dehm, D., Shuchman, R., Quintero, K., Bosse, K., et al. (2019). Unmanned Aerial System Based Spectroradiometer for Monitoring Harmful Algal Blooms: A New Paradigm in Water Quality Monitoring. *J. Great Lakes Res.* 45 (3), 444–453. doi:10.1016/j.jglr.2019.03.006

Cao, H., Gu, X., Wei, X., Yu, T., and Zhang, H. (2020). Lookup Table Approach for Radiometric Calibration of Miniaturized Multispectral Camera Mounted on an Unmanned Aerial Vehicle. *Remote Sensing* 12 (24), 4012. doi:10.3390/rs12244012

Castro, C. C., Domínguez Gómez, J. A., Delgado Martín, J., Hinojo Sánchez, B. A., Cereijo Arango, J. L., Cheda Tuya, F. A., et al. (2020). An UAV and Satellite Multispectral Data Approach to Monitor Water Quality in Small Reservoirs. *Remote Sensing* 12 (9), 1514. doi:10.3390/rs12091514

Choo, Y., Kang, G., Kim, D., and Lee, S. (2018). A Study on the Evaluation of Water-Bloom Using Image Processing. *Environ. Sci. Pollut. Res.* 25 (36), 36775–36780. doi:10.1007/s11356-018-3578-6

Cox, C., and Munk, W. (1954). Measurement of the Roughness of the Sea Surface from Photographs of the Sun's Glitter. *J. Opt. Soc. Am.* 44 (11), 838–850. doi:10.1364/josa.44.000838

Del Pozo, S., Rodríguez-Gonzálvez, P., Hernández-López, D., and Felipe-García, B. (2014). Vicarious Radiometric Calibration of a Multispectral Camera on Board an Unmanned Aerial System. *Remote Sens.* 6 (3), 1918–1937. doi:10.3390/rs6031918

Dugdale, S. J., Kelleher, C. A., Malcolm, I. A., Caldwell, S., and Hannah, D. M. (2019). Assessing the Potential of Drone-based thermal Infrared Imagery for Quantifying River Temperature Heterogeneity. *Hydrol. Process.* 33 (7), 1152–1163. doi:10.1002/hyp.13395

Fisher, T. R., Fox, R. J., Gustafson, A. B., Koontz, E., Lepori-Bui, M., and Lewis, J. (2021). Localized Water Quality Improvement in the Choptank Estuary, a Tributary of Chesapeake Bay. *Estuaries Coasts*, 1–20. doi:10.1007/s12237-020-00872-4

Gerum, R. C., Richter, S., Winterl, A., Mark, C., Fabry, B., Le Bohec, C., et al. (2019). CameraTransform: A Python Package for Perspective Corrections and Image Mapping. *SoftwareX* 10, 100333. doi:10.1016/j.softx.2019.100333

Gitelson, A. A., Schalles, J. F., and Hladik, C. M. (2007). Remote Chlorophyll-A Retrieval in Turbid, Productive Estuaries: Chesapeake Bay Case Study. *Remote Sens. Environ.* 109 (4), 464–472. doi:10.1016/j.rse.2007.01.016

Gons, H. J., Rijkeboer, M., and Ruddick, K. G. (2002). A Chlorophyll-Retrieval Algorithm for Satellite Imagery (Medium Resolution Imaging Spectrometer) of Inland and Coastal Waters. *J. Plankton Res.* 24 (9), 947–951. doi:10.1093/plankt/24.9.947

Gordon, H. R., and Clark, D. K. (1980). Atmospheric Effects in the Remote Sensing of Phytoplankton Pigments. *Boundary-layer Meteorol.* 18 (3), 299–313. doi:10.1007/bf00122026

Gordon, H. R., and Wang, M. (1994). Retrieval of Water-Leaving Radiance and Aerosol Optical Thickness over the Oceans with SeaWiFS: a Preliminary Algorithm. *Appl. Opt.* 33 (3), 443–452. doi:10.1364/ao.33.000443

Gray, P., Ridge, J., Poulin, S., Seymour, A., Schwantes, A., Swenson, J., et al. (2018). Integrating Drone Imagery into High Resolution Satellite Remote Sensing Assessments of Estuarine Environments. *Remote Sens.* 10 (8), 1257. doi:10.3390/rs10081257

Hedley, J. D., Harborne, A. R., and Mumby, P. J. (2005). Technical Note: Simple and Robust Removal of Sun Glint for Mapping Shallow-water Benthos. *Int. J. Remote Sens.* 26 (10), 2107–2112. doi:10.1080/01431160500034086

Hochberg, E. J., Andréfouët, S., and Tyler, M. R. (2003). Sea Surface Correction of High Spatial Resolution Ikonos Images to Improve Bottom Mapping in Near-Shore Environments. *IEEE Trans. Geosci. Remote Sensing* 41 (7), 1724–1729. doi:10.1109/tgrs.2003.815408

Hooker, S. B., Lazin, G., Zibordi, G., and McLean, S. (2002). An Evaluation of above- and In-Water Methods for Determining Water-Leaving Radiances. *J. Atmos. Oceanic Technol.* 19 (4), 486–515. doi:10.1175/1520-0426(2002)019<0486:aeoaai>2.0.co;2

Johnston, D. W. (2019). Unoccupied Aircraft Systems in marine Science and Conservation. *Annu. Rev. Mar. Sci.* 11, 439–463. doi:10.1146/annurev-marine-010318-095323

Kay, S., Hedley, J., and Lavender, S. (2009). Sun Glint Correction of High and Low Spatial Resolution Images of Aquatic Scenes: a Review of Methods for Visible and Near-Infrared Wavelengths. *Remote sensing* 1 (4), 697–730. doi:10.3390/rs1040697

Kim, W., Jung, S., Moon, Y., and Mangum, S. C. (2020). Morphological Band Registration of Multispectral Cameras for Water Quality Analysis with Unmanned Aerial Vehicle. *Remote Sensing* 12 (12), 2024. doi:10.3390/rs12122024

Lavender, S. J., Pinkerton, M. H., Moore, G. F., Aiken, J., and Blondeau-Patissier, D. (2005). Modification to the Atmospheric Correction of SeaWiFS Ocean Colour Images over Turbid Waters. *Cont. Shelf Res.* 25 (4), 539–555. doi:10.1016/j.csr.2004.10.007

Lee, Z., Ahn, Y.-H., Mobley, C., and Arnone, R. (2010). Removal of Surface-Reflected Light for the Measurement of Remote-Sensing Reflectance from an Above-Surface Platform. *Opt. Express* 18 (25), 26313–26324. doi:10.1364/oe.18.026313

Lee, E., Yoon, H., Hyun, S. P., Burnett, W. C., Koh, D. C., Ha, K., et al. (2016). Unmanned Aerial Vehicles (UAVs)-based thermal Infrared (TIR) Mapping, a Novel Approach to Assess Groundwater Discharge into the Coastal Zone. *Limnol. Oceanogr. Methods* 14 (11), 725–735. doi:10.1002/lom3.10132

Lee, Z. P., Wei, J., Shang, Z., Garcia, R., Dierssen, H. M., Ishizaka, J., et al. (2019). "On-water Radiometry Measurements: Skylight-Blocked Approach and Data Processing," in *Appendix to Protocols for Satellite Ocean Colour Data Validation: In Situ Optical Radiometry. IOCCG Ocean Optics and Biogeochemistry Protocols for Satellite Ocean Colour Sensor Validation*. Editors G. Zibordi, K. J. Voss, B. C. Johnson, and J. L. Mueller (Dartmouth, Nova Scotia, Canada), Vol. 3.0, 7.

Mamaghani, B., and Salvaggio, C. (2019). Multispectral Sensor Calibration and Characterization for sUAS Remote Sensing. *Sensors* 19 (20), 4453. doi:10.3390/s19204453

McClain, C., Esaias, W. E., Barnes, W., Guenther, B., Endres, D., Hooker, S. B., et al. (1992). SeaWiFS Calibration and Validation Plan. In: *NASA Technical Memorandum 104566*, ed. by S. Hooker and E. Firestone. Vol. 3. *Prelaunch Technical Report Series. NASA Goddard Space Flight Center*, Greenbelt, MD, 41 pp.

McEliece, R., Hinz, S., Guarini, J.-M., and Coston-Guarini, J. (2020). Evaluation of Nearshore and Offshore Water Quality Assessment Using UAV Multispectral Imagery. *Remote Sens.* 12 (14), 2258. doi:10.3390/rs12142258

Mobley, C. D. (1999). Estimation of the Remote-Sensing Reflectance from Above-Surface Measurements. *Appl. Opt.* 38 (36), 7442–7455. doi:10.1364/ao.38.007442

Mobley, C. D. (2015). Polarized Reflectance and Transmittance Properties of Windblown Sea Surfaces. *Appl. Opt.* 54 (15), 4828–4849. doi:10.1364/ao.54.004828

Morgan, B. J., Stocker, M. D., Valdes-Abellan, J., Kim, M. S., and Pachepsky, Y. (2020). Drone-based Imaging to Assess the Microbial Water Quality in an Irrigation Pond: A Pilot Study. *Sci. Total Environ.* 716, 135757. doi:10.1016/j.scitotenv.2019.135757

Nechad, B., Ruddick, K. G., and Park, Y. (2010). Calibration and Validation of a Generic Multisensor Algorithm for Mapping of Total Suspended Matter in Turbid Waters. *Remote Sens. Environ.* 114 (4), 854–866. doi:10.1016/j.rse.2009.11.022

Novoa, S., Doxaran, D., Ody, A., Vanhellemont, Q., Lafon, V., Lubac, B., et al. (2017). Atmospheric Corrections and Multi-Conditional Algorithm for Multi-

Sensor Remote Sensing of Suspended Particulate Matter in Low-To-High Turbidity Levels Coastal Waters. *Remote Sens.* 9 (1), 61. doi:10.3390/rs9010061

O'Shea, R. E., Laney, S. R., and Lee, Z. (2020). Evaluation of Glint Correction Approaches for fine-scale Ocean Color Measurements by Lightweight Hyperspectral Imaging Spectrometers. *Appl. Opt.* 59 (7), B18–B34. doi:10.1364/AO.377059

Olivetti, D., Roig, H., Martinez, J.-M., Borges, H., Ferreira, A., Casari, R., et al. (2020). Low-Cost Unmanned Aerial Multispectral Imagery for Siltation Monitoring in Reservoirs. *Remote Sens.* 12 (11), 1855. doi:10.3390/rs12111855

Osadchiev, A., Barymova, A., Sedakov, R., Zhiba, R., and Dbar, R. (2020). Spatial Structure, Short-Temporal Variability, and Dynamical Features of Small River Plumes as Observed by Aerial Drones: Case Study of the Kodor and Bzyp River Plumes. *Remote Sens.* 12 (18), 3079. doi:10.3390/rs12183079

Ruddick, K. G., Gons, H. J., Rijkeboer, M., and Tilstone, G. (2001). Optical Remote Sensing of Chlorophyll a in Case 2 Waters by Use of an Adaptive Two-Band Algorithm with Optimal Error Properties. *Appl. Opt.* 40 (21), 3575–3585. doi:10.1364/ao.40.003575

Ruddick, K. G., De Cauwer, V., Park, Y.-J., and Moore, G. (2006). Seaborne Measurements of Near Infrared Water-Leaving Reflectance: The Similarity Spectrum for Turbid Waters. *Limnol. Oceanogr.* 51 (2), 1167–1179. doi:10.4319/lo.2006.51.2.1167

Schneider-Zapp, K., Cubero-Castan, M., Shi, D., and Strecha, C. (2019). A New Method to Determine Multi-Angular Reflectance Factor from Lightweight Multispectral Cameras with Sky Sensor in a Target-Less Workflow Applicable to UAV. *Remote Sens. Environ.* 229, 60–68. doi:10.1016/j.rse.2019.04.007

Shang, S., Lee, Z., Lin, G., Hu, C., Shi, L., Zhang, Y., et al. (2017). Sensing an Intense Phytoplankton Bloom in the Western Taiwan Strait from Radiometric Measurements on a UAV. *Remote Sens. Environ.* 198, 85–94. doi:10.1016/j.rse.2017.05.036

Shang, Z., Lee, Z., Dong, Q., and Wei, J. (2017). Self-shading Associated with a Skylight-Blocked Approach System for the Measurement of Water-Leaving Radiance and its Correction. *Appl. Opt.* 56 (25), 7033–7040. doi:10.1364/ao.56.007033

Shi, W., and Wang, M. (2009). An Assessment of the Black Ocean Pixel assumption for MODIS SWIR Bands. *Remote Sens. Environ.* 113 (8), 1587–1597. doi:10.1016/j.rse.2009.03.011

Siegel, D. A., Wang, M., Maritorena, S., and Robinson, W. (2000). Atmospheric Correction of Satellite Ocean Color Imagery: the Black Pixel assumption. *Appl. Opt.* 39 (21), 3582–3591. doi:10.1364/ao.39.003582

Spyrakos, E., O'Donnell, R., Hunter, P. D., Miller, C., Scott, M., Simis, S. G. H., et al. (2018). Optical Types of Inland and Coastal Waters. *Limnol. Oceanogr.* 63 (2), 846–870. doi:10.1002/lno.10674

Su, T.-C. (2017). A Study of a Matching Pixel by Pixel (MPP) Algorithm to Establish an Empirical Model of Water Quality Mapping, as Based on Unmanned Aerial Vehicle (UAV) Images. *Int. J. Appl. earth obs. geoinformation* 58, 213–224. doi:10.1016/j.jag.2017.02.011

Totsuka, S., Kageyama, Y., Ishikawa, M., Kobori, B., and Nagamoto, D. (2019). Noise Removal Method for Unmanned Aerial Vehicle Data to Estimate Water Quality of Miharu Dam Reservoir, Japan. *Jaciii* 23 (1), 34–41. doi:10.20965/jaciii.2019.p0034

Tzortziou, M., Herman, J. R., Gallegos, C. L., Neale, P. J., Subramaniam, A., Harding, L. W., Jr, et al. (2006). Bio-optics of the Chesapeake Bay from Measurements and Radiative Transfer Closure. *Estuarine, Coastal Shelf Sci.* 68 (1-2), 348–362. doi:10.1016/j.ecss.2006.02.016

Werdell, P. J., and McClain, C. R. (2019). Satellite Remote Sensing: Ocean Color. *Encycl. Ocean Sci.* 3, 443–455. doi:10.1016/B978-0-12-409548-9.10817-6

Westoby, M. J., Brasington, J., Glasser, N. F., Hambrey, M. J., and Reynolds, J. M. (2012). 'Structure-from-Motion' Photogrammetry: A Low-Cost, Effective Tool for Geoscience Applications. *Geomorphol.* 179, 300–314. doi:10.1016/j.geomorph.2012.08.021

Windle, A., Poulin, S., Johnston, D., and Ridge, J. (2019). Rapid and Accurate Monitoring of Intertidal Oyster Reef Habitat Using Unoccupied Aircraft Systems and Structure from Motion. *Remote Sens.* 11 (20), 2394. doi:10.3390/rs11202394

Yu, X., Lee, Z., Shang, Z., Lin, H., and Lin, G. (2021). A Simple and Robust Shade Correction Scheme for Remote Sensing Reflectance Obtained by the Skylight-Blocked Approach. *Opt. Express* 29 (1), 470–486. doi:10.1364/oe.412887

Zeng, C., Richardson, M., and King, D. J. (2017). The Impacts of Environmental Variables on Water Reflectance Measured Using a Lightweight Unmanned Aerial Vehicle (UAV)-based Spectrometer System. *ISPRS J. Photogramm. Remote Sens.* 130, 217–230. doi:10.1016/j.isprsjprs.2017.06.004

Conflict of Interest: The authors declare that the research was conducted in the absence of any commercial or financial relationships that could be construed as a potential conflict of interest.

Copyright © 2021 Windle and Silsbe. This is an open-access article distributed under the terms of the Creative Commons Attribution License (CC BY). The use, distribution or reproduction in other forums is permitted, provided the original author(s) and the copyright owner(s) are credited and that the original publication in this journal is cited, in accordance with accepted academic practice. No use, distribution or reproduction is permitted which does not comply with these terms.

frontiers in Environmental Science

REVIEW
published: 07 June 2021
doi: 10.3389/fenvs.2021.649528

Living up to the Hype of Hyperspectral Aquatic Remote Sensing: Science, Resources and Outlook

Heidi M. Dierssen[1], Steven G. Ackleson[2], Karen E. Joyce[3], Erin L. Hestir[4], Alexandre Castagna[5], Samantha Lavender[6] and Margaret A. McManus[7]*

[1]Department of Marine Sciences, University of Connecticut, Groton, CT, United States, [2]Naval Research Laboratory, Washington, DC, United States, [3]College of Science and Engineering / TropWATER, James Cook University Nguma-bada Campus, Cairns, QLD, Australia, [4]Civil & Environmental Engineering, University of California Merced, Merced, CA, United States, [5]Protistology and Aquatic Ecology, Ghent University, Ghent, Belgium, [6]Pixalytics Ltd., Plymouth, United Kingdom, [7]Department of Oceanography, University of Hawai'i at Mānoa, Honolulu, HI, United States

Intensifying pressure on global aquatic resources and services due to population growth and climate change is inspiring new surveying technologies to provide science-based information in support of management and policy strategies. One area of rapid development is hyperspectral remote sensing: imaging across the full spectrum of visible and infrared light. Hyperspectral imagery contains more environmentally meaningful information than panchromatic or multispectral imagery and is poised to provide new applications relevant to society, including assessments of aquatic biodiversity, habitats, water quality, and natural and anthropogenic hazards. To aid in these advances, we provide resources relevant to hyperspectral remote sensing in terms of providing the latest reviews, databases, and software available for practitioners in the field. We highlight recent advances in sensor design, modes of deployment, and image analysis techniques that are becoming more widely available to environmental researchers and resource managers alike. Systems recently deployed on space- and airborne platforms are presented, as well as future missions and advances in unoccupied aerial systems (UAS) and autonomous in-water survey methods. These systems will greatly enhance the ability to collect interdisciplinary observations on-demand and in previously inaccessible environments. Looking forward, advances in sensor miniaturization are discussed alongside the incorporation of citizen science, moving toward open and FAIR (findable, accessible, interoperable, and reusable) data. Advances in machine learning and cloud computing allow for exploitation of the full electromagnetic spectrum, and better bridging across the larger scientific community that also includes biogeochemical modelers and climate scientists. These advances will place sophisticated remote sensing capabilities into the hands of individual users and provide on-demand imagery tailored to research and management requirements, as well as provide critical input to marine and climate forecasting systems. The next decade of hyperspectral aquatic remote sensing is on the cusp of revolutionizing the way we assess and monitor aquatic environments and detect changes relevant to global communities.

Keywords: imaging spectroscopy, aquatic optics, surface biology and geology (SBG), plankton aerosol cloud and ocean ecosystem (PACE), Unoccupied Aerial Vehicles (UAV)

OPEN ACCESS

Edited by:
Xuan Zhu,
Monash University, Australia

Reviewed by:
Dimitris Poursanidis,
Foundation for Research and Technology Hellas (FORTH), Greece
Cédric Jamet,
UMR8187 Laboratoire d'océanologie et de géosciences (LOG), France

****Correspondence:***
Heidi M. Dierssen
heidi.dierssen@uconn.edu

Specialty section:
This article was submitted to Environmental Informatics and Remote Sensing, a section of the journal Frontiers in Environmental Science

Received: *04 January 2021*
Accepted: *14 April 2021*
Published: *07 June 2021*

Citation:
Dierssen HM, Ackleson SG, Joyce KE, Hestir EL, Castagna A, Lavender S and McManus MA (2021) Living up to the Hype of Hyperspectral Aquatic Remote Sensing: Science, Resources and Outlook. Front. Environ. Sci. 9:649528. doi: 10.3389/fenvs.2021.649528

INTRODUCTION

In response to mounting ecological stressors, natural resource managers look to remote sensing as a means of providing timely and spatially coherent environmental information that can inform decision making. However, current products provided by the ocean color community do not satisfy the needs required for management of aquatic ecosystems spanning the open ocean to inland waters. As water surfaces are much darker than terrestrial surfaces, the signal emerging from the water is obscured by the atmosphere, when viewed from high altitude or space, and dedicated sensors with large dynamic ranges and longer integration times are often required to achieve the measurement sensitivity needed (Mouroulis et al., 2008). For many applications, the spatial footprint of space-based ocean color sensors can be too large (typically 0.5–1 km) and the revisit time of land-imaging sensors, which have the capability to resolve coasts and inland waters, is often too infrequent (weekly to monthly). Further, increases in spatial resolution typically go hand-in-hand with decreases in spectral resolution, and the products afforded by limited spectral imagery are high in uncertainty and low in specificity (Dekker and et al., 2018). The tradeoffs between spectral, spatial, and temporal sampling often mean that no single sensor or platform can provide all of the needs for any single user community or application (Muller-Karger et al., 2018). As a result, current capabilities for monitoring water quality and biodiversity across diverse habitats, from lakes and wetlands to coastal pelagic and benthic communities, have only been demonstrated on limited scales and have yet to achieve routine operational use by environmental managers.

Traditional ocean color remote sensing involves multi-spectral sensors that have a small number of broad discontiguous spectral bands measuring portions of the visible and infrared electromagnetic spectrum. These bands were placed at key wavelength regions mainly designed to detect the concentration of the primary pigment in phytoplankton, chlorophyll *a* (Gordon and Morel, 1983). Airborne and spaceborne sensor technology has advanced rapidly in the last few decades to include imaging spectrometers with continuous spectral coverage throughout the visible and near-infrared spectrum (VNIR), typically between 400 and 1,000 nm, and sometimes extending to the shortwave infrared regions as well (up to 2,500 nm). To differentiate from multi-spectral sensors with discrete, often broad wavebands, such imaging spectrometers are commonly referred to as "hyperspectral" imaging systems. The terms "hyperspectral imaging" and "imaging spectrometry" are interoperable. No standard definitions have been adopted as to the number of bands and associated bandwidths required for a sensor to be considered "hyperspectral." Still, generally, hyperspectral sensors for coastal applications have bandwidths less than 15 nm and >20 bands in visible wavelengths. However, sensitivity studies spanning a range of diverse aquatic water bodies recommend hyperspectral sensors bandwidths of 5 nm (Wolanin et al., 2016; Vandermeulen et al., 2017; Dekker et al., 2018). Consequently, the majority of the present and future hyperspectral sensors have at least 60 bands within the VNIR spectral range (**Figure 1**).

The field of aquatic hyperspectral remote sensing is advancing rapidly, and new products are informing water quality monitoring, as well as the biodiversity of organisms swimming and floating in pelagic habitats and dwelling on and near the bottom in benthic habitats (reviewed in Tyler et al., 2016; Giardino et al., 2019; Kutser et al., 2020). The continuous spectrum can always be sub-sampled to yield any multispectral band combination to take advantage of legacy algorithms or to amplify the signal to noise ratio. However, hyperspectral data provides potential new applications that are not limited by gaps in the spectrum based on historic notions of utility in open ocean ecosystems. Indeed, several multispectral ocean color sensors are programmable spectrometers resampled onboard to specific wavebands (e.g., Sentinel-3 OLCI). Utilizing the full spectrum, even simple approaches that characterize the spectral dimensionality and variability can be used to identify and track subtle differences between water masses and over time that could not be tracked by bulk chlorophyll *a* estimates (Vandermeulen et al., 2020). Full-spectrum estimates of the diffuse attenuation coefficient (K_d) may lead to new insights about aquatic ecosystems and biodiversity processes like spectral niche partitioning and complementarity (Striebel et al., 2009), or behavior and evolutionary traits of aquatic invertebrates and vertebrates (Russell and Dierssen, 2015; Cummings and Endler, 2018). Thus, imaging spectrometry can inspire and support new algorithm concepts that require continuous and dense spectral sampling. The benefits of merging hyperspectral imagery with other types of remote sensing imagery and environmental parameters through modeling (IOCCG, 2020) will also be an avenue for the future

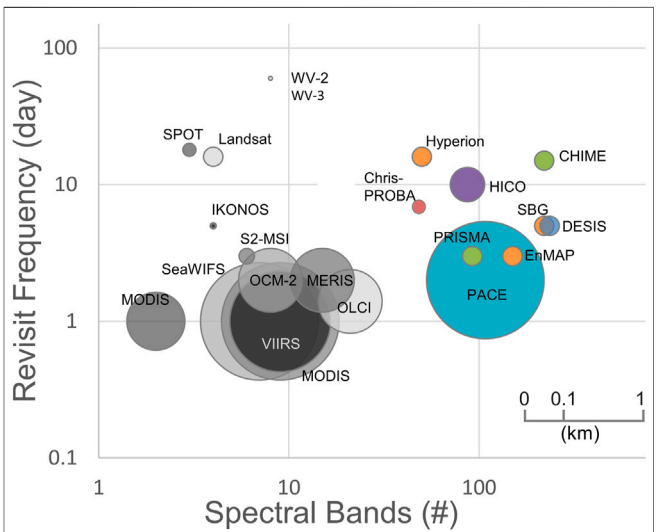

FIGURE 1 | Architecture of various international missions showing the tradeoff between number of spectral bands, revisit frequency (*X* and *Y* axes, respectively) and the spatial footprint (approximated as the size of circle). Gray represent multi-spectral missions and colors represent the hyperspectral missions. Modified from Hestir et al. (2015a).

TABLE 1 | Recent reviews including hyperspectral aquatic remote sensing.

Primary author (# Coauthors)	Title	Publisher	Year	Subjects covered (relevant to hyperspectral)
Gege and Dekker (2020) (1)	Spectral and radiometric measurement requirements for inland, coastal and reef waters	Rem. Sens.	2020	Sensitivity study of measurement needs for inland and coastal water
Kutser, et al. (2020) (4)	Remote sensing of shallow waters–A 50 years retrospective and future directions	Rem. Sens. Environ.	2020	History, sensors, algorithms, satellite systems, future directions
Dierssen et al. (2020) (4)	Data needs for hyperspectral detection of algal diversity across the globe	Oceanography	2020	Data recommendations, phytoplankton composition, future needs
Banks et al. (2020) (10)	Fiducial reference measurements for satellite ocean color	Rem. Sens.	2020	Framework, standards, and protocols for validation efforts
Jeziorska (2019) (0)	UAS for wetland mapping and hydrological modeling	Rem. Sens.	2019	Hardware, software, regulations, applications, data collection and processing
Wu et al. (2019) (3)	A review of drone-based harmful algae blooms monitoring	Environ. Monit. Assess.	2019	UAVs, sensors, work-flow, algorithms, challenges and opportunities
Giardino et al. (2019) (12)	Imaging spectrometry of inland and coastal waters: State of the art, achievements and perspectives	Surv. Geophys.	2019	Theory, algorithms, uncertainties, applications, future directions, *in situ* observations
IOCCG (2019) (23)	Synergy between ocean color and biogeochemical/ ecosystem models	IOCCG Report 19	2019	Assimilation, forecast, and hindcast modeling relevant to ocean color imagery
CEOS, Dekker et al. (2018) (15)	Feasibility study for an aquatic ecosystem earth observing system	Comm. on Earth obs. Sat. (CEOS)	2018	Spectral, spatial and temporal requirements for coastal and inland aquatic applications
Lodhi et al. (2018) (2)	Hyperspectral imaging of earth observation: Platforms and instruments	J. Indian Inst. Sci	2018	Sensors, platforms, applications (above water, in-water, underwater)
IOCCG, Greb et al. (2018) (23)	Earth observations in support of global water quality monitoring	IOCCG Report 17	2018	Theory, sensors, approaches and limitations to water quality
Manfreda et al. (2018) (22)	On the use of unmanned erial systems for environmental monitoring	Rem. Sens.	2018	Number of articles per year, sensors, software, mission planning, inland waters
Khan et al. (2018). (4)	Modern trends in hyperspectral image analysis: A review	IEEE access	2018	HIS analysis approach including deep learning and artifical intellagence
Muller-Karger et al. (2018) (52)	Satellite sensor requirements for monitoring essential biodiversity variables of coastal ecosystems	Ecol. Appl	2018	Societal needs, remote sensing approaches, HIS, recommendations
Thamaga and Dube (2018) (1)	Remote sensing of invasive water hyacinth (Eichhornia crassipes): A review on applications and challenges	Rem. Sens. Appl. Soc. Environ	2018	History, pubs/year, satellite systems, future directions
Werdell et al. (2018) (14)	An overview of approaches and challenges for retrieving marine inherent optical properties from ocean color remote sensing	Prog. Oceanogr	2018	Theory, algorithms, uncertainties, future directions
Mishra et al. (2017) (24)	Bio-optical modeling and remote sensing of inland waters	Elsevier	2017	Book with 9 Chapters covering applications of bio-optics to inland aquatic environments
Gege (2017) (0)	Radiative transfer theory for inland waters	Elsevier	2017	Radiometry, inherent and apparent optical properties, bio-optical models
Szabo et al. (2018) (5)	Zoomin on aerial surveys	Springer	2017	Basic system elements, mapping procedures, sensors, platforms
Pu et al. (2017) (3)	Applications of imaging spectrometry in inland water quality monitoring - a review of recent developments	Water Air Soil Pollut.	2017	Review of airborne and satellite systems, theory, algorithms, *in situ* spectrometers for ground truth, future outlook
Bracher et al. 2017a (21)	Obtaining phytoplankton diversity from ocean color: A scientific roadmap for future development	Front. Mar. Sci.	2017	State of science, user needs, data gaps and future directions
Gholizdeh et al. (2016) (2)	A comprehensive review on water quality parameters estimation using remote sensing techniques	Sensors	2016	Hyperspectral systems, airborne and satellite systems, history, theory, algorithms, etc
Hedley et al. (2016a) (12)	Remote sensing of coral reefs for monitoring and management: A review	Rem. Sens.	2016	Satellite and airborne hyperspectral systems, applications, products, societal value
Johnsen et al. (2013) (3)	The use of hyperspectral imaging deployed on remotely operated vehicles -- methods and applications	Woodhead Publ.	2016	Underwater deep imaging with light sources, corrections for platform dynamics, methods to ground-truth images
Tyler et al. (2016) (5)	Development in earth observation for the assessment and monitoring of inland, terrestrial, coastal and shelf-sea waters	Sci. Total Environ.	2016	Satellite sensors, theory, algorithmic approaches, examples
Hestir et al. (2015) (6)	Measuring freshwater aquatic ecosystems: The need for a hyperspectral global mapping satellite system	Rem. Sens. Environ.	2015	Application and product case studies, sensor resolution needs, publications/year since 2000
Mouw et al. (2015) (11)	Aquatic color radiometry remote sensing of coastal and inland waters: Challenges and recommendations for future satellite systems	Rem. Sens. Environ.	2015	Theory, algorithms, satellite systems, *in situ* measurements, future recommendations
Palmer et al. (2015) (2)	Remote sensing of inland waters: Challenges, progress, and future directions	Rem. Sens. Environ.	2015	Hyperspectral systems, historical review, future outlook

(Continued on following page)

TABLE 1 | (*Continued*) Recent reviews including hyperspectral aquatic remote sensing.

Primary author (# Coauthors)	Title	Publisher	Year	Subjects covered (relevant to hyperspectral)
Blondeau-Patissier et al. (2014) (4)	A review of ocean color remote sensing methods and statistical techniques for the detection, mapping and analysis of phytoplankton blooms in coastal and open oceans	Prog. Oceanogr.	2014	Ocean color algorithms, References to hyperspectral

to address a wide range in societal problems including the response of coastal ocean ecosystems to population growth and climate change (Muller-Karger et al., 2018).

The motivation for this review emerged from a recent workshop focused on the advances and challenges of hyperspectral remote sensing technology applied to coastal aquatic environments. The workshop, conducted at the University of Hawai'i at Mānoa on 15 and 16 May 2018, was convened by the Alliance for Coastal Technologies (ACT) and sponsored by the National Oceanic and Atmospheric Administration (NOAA)/U.S. Integrated Observing System (US.IOOS) (workshop report available at http://www.act-us.info/workshops.php). The overarching goal of this article is to present advances and resources relevant to hyperspectral remote sensing in aquatic ecosystems for those newly diving into the field, as well as for those already deeply submerged within remote sensing and aquatic optics. With the advent of new sensor capabilities across all platforms from orbiting in space, to flying autonomously over reefs (Joyce et al., 2019), to cruising along the dark, cold ocean floor (Johnsen et al., 2013), hyperspectral remote sensing is rapidly growing its user base. Many resources are already available for algorithm developers, and users of the data depending on the specific user need. Here, we have compiled lists of reviews, software, and databases relevant to developing and implementing aquatic hyperspectral remote sensing approaches. Finally, we discuss how remote sensing of coastal aquatic systems might advance in the coming decade.

A BLAST FROM THE PAST: A BRIEF HISTORY OF HYPERSPECTRAL IMAGING

Many excellent reviews have been written in the last five years alone about the history and requirements for aquatic remote sensing that relate to hyperspectral imaging spectroscopy (**Table 1**). Some reviews focus on specific habitats from open ocean to coastal and inland waters; some review techniques relevant for data collection or modeling; and, others focus on applications including water quality assessment, phytoplankton composition, bathymetry and benthic cover in optically shallow waters. Here, we build on those studies to provide a summary of advances made specifically in imaging spectroscopy for aquatic applications. This overview is meant to show the breadth of the field and theoretical studies from the vast oligotrophic ocean to coral reefs to lakes and rivers.

The origins of the discipline are challenging to pinpoint, as it arose from a merging of technology and research coming from limnology and oceanography, as well as building from advances made in terrestrial, atmospheric, and cryospheric remote sensing. Wernand (2011) provides a comprehensive overview of the scientists, their hypothesis and experiments in the historical development of hydrologic optics since the seventeenth century that culminated in the theoretical foundations provided by Raman (Raman, 1922) and Shoulejkin (Shoulejkin, 1923). Field experiments were also conducted at that time, such as those done by the limnologist Edison Pettit who conducted spectroscopic investigations into the volume scattering and absorption processes underlying the color of Crater Lake, OR, USA (Pettit, 1936). Modern optical oceanography is considered to have originated around the 1950s, with the pioneering research by the Danish oceanographer Nils Jerlov who established a continuum of optical water types from the clear pelagic ocean to the turbid coast (Jerlov, 1951, 1963). However, as noted below, aquatic remote sensing really began in earnest in the late 1960s and 1970s with theoretical and experimental research spanning inland, coastal and open ocean environments (reviewed in Acker, 2015; Kutser et al., 2020).

In the late 1960s, Clarke et al. (1970) detail an airborne spectroradiometer flown in North Atlantic waters that demonstrated how increasing amounts of chlorophyll were found to be associated with a relative decrease in the blue portion of the spectra and an increase in the green in backscattered light (Clarke et al., 1970). Concomitantly in 1970, international collaboration on the development of spectrometers culminated in a sea trial as part of Scientific Committee on Oceanographic Research (SCOR) Working Group 15 that included optical measurements in combination with phytoplankton species composition and sizes, primary productivity, chlorophyll and nutrients with researchers from Australia, Denmark, France, Japan, Norway, Russia, Scotland, and the United States (Tyler, 1970). Collectively, such international partnerships provided proof-of-concept evidence for satellite-based ocean color remote sensing. This underpinning work led to the first ocean color mission, the Coastal Zone Color Scanner (CZCS), and continues today with the International Ocean Color Coordinating Group (IOCCG).

In addition to these oceanic studies, many other parallel lines of research were occurring in the 1970s in the broader field of experimental and theoretical aquatic optics. Investigations were beginning in shallow water optics with the mapping of the Great Barrier Reef using Landsat data (Smith et al., 1975) and the seminal work of Polcyn et al. (1970) and Lyzenga (1978), which

provided methods to retrieve bathymetry and benthic composition of sand, mud and vegetation from passive remote sensing imagery (Polcyn et al., 1970; Lyzenga, 1978). Some of the first laboratory reflectance measurements of phytoplankton cultures were summarized in a 1977 report entitled "Assessment of Aquatic Environments by Remote Sensing" demonstrating that blue-green algae, green algae and diatoms could be differentiated from "laboratory reflectance fingerprints" (Adams et al., 1977). Multi-spectral and thermal airborne remote sensing of algal blooms was initiated in the Great Lakes (Strong, 1974). Goldman et al. (1974) used color and multispectral aerial photography to delineate sediment plumes into Lake Tahoe, California and correlate them with suspended sediment, inorganic carbon, light penetration and primary productivity (Goldman et al., 1974). Concurrently, radiative transfer simulations studies helped to provide a qualitative and quantitative interpretation of the water leaving signal (Gordon et al., 1975; Gordon and McCluney, 1975). Further theoretical and mathematical developments were established when Preisendorfer culminated his research on radiative transfer theory in 1976 with a six-volume treatize entitled *Hydrologic Optics* (Preisendorfer, 1976). Preisendorfer's method for radiative transfer solution is implemented in the Hydrolight software, that became the community standard for the simulation of scalar aquatic spectral reflectance (Mobley, 1994). This decade of independent and parallel research provided the foundations for many of the techniques and applications for the broader field of aquatic hyperspectral remote sensing today.

Over the past three decades, the emergence of imaging spectroscopy with the ability to produce a spectrally resolved image of a scene has advanced rapidly in sensor technology, calibration, deployment modes, and applications as briefly outlined below. With the limited availability of satellite data, the period between the early 1980s and 1999 ushered in the age of operational aircraft-based hyperspectral from AVIRIS to CASI (reviewed in Giardino et al., 2019). Other relevant airborne hyperspectral sensors were the Operational Modular Imaging Spectrometer (OMIS) and the Pushbroom Hyperspectral Imaging (PHI) developed in China (Tong et al., 2001). These airborne imagers were designed primarily for terrestrial applications but were nonetheless successfully used to identify brighter aquatic targets such as identifying sediment plumes (e.g. Moore et al. (1999) that became the basis for the MERIS bright pixel atmospheric correction) and bathymetry and benthic composition in shallow water. Collins and Pattiaratchi (1984) used the Daedalus Airborne Thematic Mapper, which was operated alongside CASI by the Natural Environment Research Council Airborne Research Facility for its thermal capabilities, noting that both relative and absolute increases in suspended sediment produced a shift toward longer (red) wavelengths.

However, these initial aquatic applications had limited success due to the airborne sensors having a relatively low signal-to-noise ratio (SNR) and a limited dynamic range (reviewed in Kutser 2020). The operators needed to set the appropriate integration time for the low aquatic signal and develop robust procedures for instrument calibration. Therefore, data from these sensors were often aggregated spectrally and spatially to obtain higher signal or smoothed considerably in post-processing to reduce spectral noise (Carder et al., 1993) and provided only multispectral data over aquatic targets (Mumby et al., 1997; Sathyendranath et al., 1997). As a result, little was gained from the hyperspectral signal.

The 2000s were a time for targeting new sensors and programs designed to facilitate aquatic applications. Even though the potential for imaging spectrometry was recognized early on (Dekker and Donze, 1994), inland and coastal waters provide critical challenges to spectrometer system design including reflectance of targets varying from <1% for dark water to over 90% for bright sand. The Ocean Portable Hyperspectral Imager for Low-Light Spectroscopy (PHILLS) was a pushbroom-scanning instrument designed specifically for aquatic applications (Davis et al., 2002). Early deployments of Ocean PHILLS include those as part of the Coastal Benthic Optical Properties (CoBOP) program at Lee Stocking Island, Bahamas (May/June 1999 and May 2000), the Hyperspectral Coupled Ocean Dynamics Experiments (HyCODE) program on the West Florida Shelf (2000 and 2001) and at the LEO-15 site in New Jersey (July 2000 and July 2001). The field and airborne efforts from those projects provided some of the foundational hyperspectral algorithms for evaluating optically important constituents, estimating vertical structure in the near-surface ocean, developing benthic cover and bathymetry algorithms, and refining treatment of optical properties in coupled ocean-atmosphere models (Davis, 2001; Mazel, 2002; Chang et al., 2004; Wang, 2004).

More technological advances were also brought about by the National Aeronautics and Space Administration (NASA) Jet Propulsion Laboratory (JPL) Portable Hyperspectral Imaging SpectroMeter (PRISM) developed in 2008 designed to handle the dynamic range of aquatic surfaces, with an improved spectral resolution, polarization sensitivity, response uniformity, and minimal spectrometer distortions (Mouroulis et al., 2008). First flight results over calibration sites in Elkhorn Slough, California, demonstrated good agreement between *in situ* and remotely sensed data (Heupel et al., 2013; Mouroulis et al., 2014) and the sensor has found modern use in applications from differentiating floating vegetation, water contaminants, chlorophyll fluorescence, and coral reef assessments (Dierssen et al., 2015; Fichot et al., 2016; Garcia et al., 2018; Erickson et al., 2019). Similar high-quality imagery is now available in sensors like Airborne Prism Experiment (APEX) and from commercial vendors (reviewed in Giardino et al., 2019).

Moving from suborbital to orbital platforms, the first decade of the 21st Century also involved the launch of several hyperspectral imagers with applications to aquatic ecosystems including: Hyperion launched aboard the EO-1 spacecraft in 2000 (Dekker et al., 2001), the Compact High Resolution Imaging Spectrometer (CHRIS) launched on PROBA-1 in 2001 (Cutter et al., 2004), the Scanning Imaging Absorption Spectrometer for Atmospheric Chartography (SCIAMACHY) launched on ENVISAT in 2002 (Bracher et al., 2009) and the Hyperspectral Imager for the Coastal Ocean (HICO) installed on the International Space Station in 2009 (Ryan et al., 2014). Except

for SCIAMCHY, these sensors had smaller footprints optimized for coastal applications (20–90 m) and were targeted mappers acquiring data over particular areas based on data acquisition requests with limited collections per day (**Figure 1**). Similar to the early airborne instruments, the data exhibited low signals over many aquatic targets and were often binned spatially and spectrally for aquatic applications (Hestir et al., 2015). SCIAMACHY provided global mapping capabilities at much finer spectral resolution (<0.5 nm bands), but at much larger spatial resolutions of 30 km pixels. Such applications demonstrated that hyperspectral signals could move beyond typical remote sensing methods and be used to assess bathymetry, benthic cover, and phytoplankton composition. These applications are summarized in many different reviews of hyperspectral and aquatic remote sensing provided in **Table 1**.

LAUNCHING THE FUTURE OF HYPERSPECTRAL IMAGING

Here we discuss both the orbital and suborbital systems proposed for hyperspectral imaging of aquatic ecosystems including advances in sensor miniaturization and autonomous sampling platforms.

Satellite Systems

Building on these past successes, we now find ourselves on the verge of significant global advances in hyperspectral remote sensing with the recent and pending launch of an array of hyperspectral satellites poised to sense the Earth from different platforms and orbits (**Figure 1**). Most recently, several targeted mappers have been launched, of which we highlight a few missions with publicly available imagery such as Deutsches Zentrum fur Luft–und Raumfahrt German Aerospace Center (DLR) Earth Sensing Imaging Spectrometer (DESIS) (Müller et al., 2016) installed on the International Space Station and the launch of China's Advanced Hyperspectral Imager (AHSI) onboard the GaoFeng-5 satelite (Liu et al., 2019) in 2018, followed by the launch of the PRecursore IperSpettrale della Missione Applicativa (PRISMA) sensor by the Italian Space Agency in 2019 (Giardino et al., 2020) and HyperScout instruments launched on nanosatellites (Esposito and Zuccaro Marchi (2019). On the future horizon are low-Earth orbiting global mapping hyperspectral missions including NASA's Plankton Erosol Cloud and ocean Ecosystem (PACE) and Surface Biology and Geology (SBG) missions, and the European Space Agency's Copernicus Hyperspectral Imaging Mission for the Environment (CHIME), as well as geostationary missions like NASA's Geosynchronous Littoral Imaging and Monitoring Radiometer (GLIMR). Recognizing that no single mission can satisfy all applications, concepts have started to formulate among space agencies, researchers, resource managers, and policy experts for combining multiple instruments into a virtual constellation that meets many observation needs, as well as combining hyperspectral imagery with other sources of remote, *in situ*, and modeled data to better assess ecosystem health and biodiversity (Duffy et al., 2013; Greb et al., 2018; Muller-Karger et al., 2018).

Suborbital Systems

It is exciting that sensor design has also moved toward smaller, solid state systems requiring less power for deployment on small satellites (Doubleday et al., 2015; Bender et al., 2018), aircraft, autonomous unoccupied aerial systems (UAS) (Wu et al., 2019), or small watercraft dedicated to specific problems (Klemas, 2015; Ackleson et al., 2017). This represents an emerging dimension to how modern remote sensing data are acquired. Traditional sources of coverage by orbiting sensors are inherently limited by cloud cover and orbital dynamics, and engineering trades made in sensor design between spatial, spectral and radiometric resolution. Portable sensors flown on aircraft or drones provide a critical sampling niche distinct from satellite-borne sensors that are particularly well suited for coastal and inland water applications Such sensors can sample at fine spatial scales, can operate under clouds and with nearly unlimited repeat coverage, and are effective platforms for high resolution active sensors (e.g., lidar). Aircraft overflights are also subject to limitations of transporting gear, aircraft and personnel to the study area, as well as being subject to local weather conditions and flight restrictions. Autonomous systems are more portable and completely controlled by the individual research team, permitting imaging schedule and geometry, e.g., relative to the Sun location, to be adjusted in real time.

Unoccupied Aerial Systems

Perhaps some of the greatest future advances will come with the rapid advances in UAS technology. The term UAS is used to include both the unoccupied aerial vehicle (UAV) or drone, as well as the ground-based control system. UAS for civilian applications started in the early 1980s using remote controlled aircraft equipped with aerial mapping cameras (Wester-Ebbinghaus, 1980). Since that time, both sensor and drone technology have advanced significantly (Colomina and Molina, 2014; Aasen et al., 2018) with decreasing expense and mission planning, and navigation software requiring less experience from the remote operator. Users can readily create custom UAS systems or purchase complete systems, including sensors, aircraft, and mission planning and data analysis software, tailored to applications. A recent review of UAS remote sensing systems in environmental biology found that publication rates from studies using this technology increased 10 fold between 2000 and 2018 with most of the increase occurring since 2011 (Nowak et al., 2018).

Compact hyperspectral imaging sensors appropriate for small UAV operations are a fairly recent development, starting in the 2010 time frame based on published reports. Advances in gimbaling systems have allowed for better image quality to minimize artifacts from pitch and roll of the drone and vibrations (Wu et al., 2019). UAV flight lines and scanning geometries can also be oriented to optimize retrievals (e.g., avoid Sun glint) and their range can be greatly expanded by launching from ships. Because of cloud cover and orbital constraints, the temporal resolution from satellites is often not

sufficient to track episodic events like harmful algal blooms (HABs) compared to a drone that can be deployed in a rapid response during an outbreak. Imagery from UAS can provide details at the centimeter scale and temporal frequencies at the hourly scale with relatively low costs. Moreover, the technology can be closely synchronized with water sampling in order to characterize phytoplankton types and quantify the concentrations of cells and toxins (Wu et al., 2019).

Much of the excellent work undertaken in the early 2000s with autonomous field spectrometers can now be expanded using spectrometers from UAS. Where early work focused on spectral characteristics of marine and aquatic features at very high temporal scales at a single point scale from moorings (Dickey and Chang, 2002) it is possible to now include similar spectrometers on a UAS payload, rapidly capturing thousands of point-based spectroscopic measurements traversing large areas at very low cost from small off the shelf platforms (Cornet and Joyce, in review). For more advanced solutions, imaging technology over broader scales allows researchers to explore spatial and temporal dynamics in even greater detail. UAS have become a popular tool for monitoring the emergence and extent of intense phytoplankton blooms, particularly those that are considered HABs (Becker et al., 2019; Wu et al., 2019). For example, drone imagery, coupled with satellite technology, was used to effectively detect, forecast, and manage the green tides in South Yellow Sea, China (Xu et al., 2017). Researchers also used a drone to track and quantify an intense phytoplankton bloom in Weitou Bay in the western Taiwan Strait (Shang et al., 2017). Similarly, several studies have used RGB imagery from drones to map intertidal coral reefs (Murfitt et al., 2017; Muslim et al., 2019). Application of hyperspectral UAS for aquatic environments, including water quality (Zeng et al., 2017), HABs (Becker et al., 2019), shallow water benthic mapping (Parsons et al., 2018), and marine fauna surveys (Colefax et al., 2018).

Deriving quantitative estimates of reflectance can be particularly challenging from UAVs, particularly under glint or variable cloud cover when the downwelling irradiance at the sea surface can be quite different from that measured at the drone. Shang et al. (2017) provide an innovative method to calibrate the signal and derive hyperspectral water-leaving reflectance from drones. Joyce et al. (2019) provide data collection workflows for planning UAS campaigns to ensure that necessary pre-planning and safety steps are considered, as well as requirements including licensing, data processing and logistical considerations. As noted further in **Section 8**, we are on the cusp of achieving significant advances in hyperspectral remote sensing across the aquatic landscape or "aquascape".

Autonomous Floating and Underwater Sampling

The availability of high quality *in situ* observations suitable for remote sensing algorithm development and product validation is key to any quantitative remote sensing activity. Unfortunately, coastal and inland aquatic systems are notoriously difficult to sample, especially in coordination with airborne or spaceborne remote sensing. Water constituent concentration and bottom depth vary across a wide range in temporal and spatial scale. Correlation scales of water and benthic properties are typically <10 m and often less than 1 m and traditional ship-based operations are limited and often prohibited by shallow bathymetry. Thus, there are significant challenges resulting from inadequate *in situ* knowledge that currently limits progress in any application of remote sensing to coastal and inland aquatic problems, regardless of sensor configuration. To address these issues, researchers have begun exploring autonomous methods of collecting *in situ* observations. Autonomous platforms, primarily underwater versions, have been in development for several decades and have focused on bathymetry, chlorophyll, and water physical properties associated with optically deep water (Moline et al., 2005; Ryan et al., 2010; Johnsen et al., 2013). More recently, attention has turned to instrumented surface systems designed to support interdisciplinary applications of hyperspectral remote sensing operations in shallow coastal environments (Ackleson et al., 2017).

LOOKING UNDER THE HOOD

Hyperspectral imagery is generated in a "Datacube" with spatial dimensions in the *X* and *Y* axis and wavelength as the *Z* axis. With >100 bands, hyperspectral images are notoriously large files that can be challenging to download and process with some of the traditional software tools employed in multi-spectral remote sensing. For example, 12 flight lines from the PRISM airborne sensor covering 100 km^2 of Elkhorn Slough, California and two long flight lines out 40 km into Monterey Bay, California provided over 400 GB of raw imagery (Heupel et al., 2013). Similarly, 16 flightlines covering 250 km^2 of a wetland near Sacramento, California collected by a UAS-mounted Headwall Nano-Hyperspec pushbroom sensor provided roughly 40 GB of raw imagery (Bolch et al., 2020). An entire image cannot be fully loaded into a typical computer memory and the image must be treated as data tiles, either spectrally or spatially, such that only a subset of bands or pixels are loaded into memory at one time. For rendering, an RGB representation of the image is often shown where a single red, green and blue wavelength is selected to mimic the human eye as a pseudo-true color. For image processing, spatial subsets are processed sequentially with some overlap typically required for certain functions. Software has been developed and optimized for processing such large imagery and automatically conducting data tiling spatially or spectrally as needed for the user (**Table 2**).

Computational power, data storage and I/O bottlenecks have been frequent limitations of using hyperspectral data given the large volume of data. Hence, many of the early studies reduce the dimensionality of hyperspectral imagery to a few multi-spectral bands for simple estimates of chlorophyll *a* and suspended particulate matter. As high-performance computing and easy-to-implement parallel processing workflows have proliferated, increasing data volumes with increasing hyperspectral datasets and the associated challenges remain lock-step with computing advances. Data reduction is also common because of the limited amount of hyperspectral datasets coupled with biogeochemical

TABLE 2 | Software available for hyperspectral data processing.

Name	Website and Description	Interface	Publication
Free			
ASFit	https://github.com/darioomanovic/ASFit An all-inclusive tool for analysis of UV–Visible spectra of colored dissolved organic matter (CDOM)	Standalone (GUI)	Omanovic et al. (2019)
EnMAP-Box	https://enmap-box.readthedocs.io/en/latest/# Developed for viewing and processing hyperspectral remote sensing imagery	Plugin for QGIS, GUI and CLI (python)	
Hylatis	https://github.com/lasp/hylatis Cloud-based hyperspectral image analysis toolkit	Cloud-based	Wilson et al. (2018)
HyTools	https://github.com/EnSpec/HyTools-sandbox Contribution of files used to load and process hyperspectral imagery	Python library	
Hyperspectral Image Analysis Toolbox (HIAT)	http://www.censsis.neu.edu/software/hyperspectral/hyperspectral.html Collection of files for processing hyperspectral data	Matlab library	Velez-Reyes (2015)
Multi Endmember Spectral Mixture Analysis (MESMA)	https://mesma.readthedocs.io/en/latest/ Processing, post-processing and visualization of MESMA results.	Python library and plugin for QGIS	Crabbé et al. (2020)
R packages for raster data (e.g., *stars* and *raster*)	https://github.com/r-spatial/stars https://github.com/rspatial/raster Representation classes for raster data in R, vizualization and analysis tools	R Libraries	
SCIATRAN	https://www.iup.uni-bremen.de/sciatran/ Coupled ocean atmosphere radiative transfer model.	Standalone (CLI)	Rozanov et al. (2014), Rozanov et al. (2017)
Spectral Library Tool	https://spectral-libraries.readthedocs.io Creates spectral libraries interactively from an image and manages the metadata	Python library and plugin for QGIS	
Spectral Python	http://www.spectralpython.net/	Python library	
Water Color Simulator and WASI-2D	https://c.1und1.de/@519891561215951357/6PlmFxS0RAyf4FLNjVot4A Radiative transfer and semi-analytical inversion software for aquatic applications	Standalone (GUI)	Gege (2015)
BigDataViewer	https://imagej.net/BigDataViewer Visualization and processing for large image data sets	Plugin for Fiji	Pietzsch et al. (2015)
For purchase			
ENVI Image Analysis	https://www.harris.com/solution/envi	Standalone (GUI)	
Hydrolight Radiative Transfer	https://www.sequoiasci.com/product/hydrolight/ Evaluate how different absorbers and scatterers influence light fields in the water column	Standalone (GUI and CLI)	Mobley (1994)
EPINA Image Lab	http://www.imagelab.at/en_home.html	Standalone (GUI)	
Trimble eCognition	https://geospatial.trimble.com/products-and-solutions/ecognition Image segmentation and feature extraction	Standalone (GUI)	
Other resources			
IOCCG	https://ioccg.org/resources/software/	Several	

CLI = Command Line Interface; GUI = Graphical User Interface.

information for algorithm development and validation (Dierssen et al., 2020). In addition, many approaches are not repeatable because the imagery has not been adequately corrected for atmospheric absorption and scattering and sea surface reflections. In the following sections, we discuss some of the approaches that have been used for atmospheric correction and processing hyperspectral imagery.

FINDING THE OCEAN NEEDLE IN THE ATMOSPHERIC HAYSTACK

Water bodies are typically much darker than the land or atmosphere above and pulling out the signal that represents the color of the water is extremely challenging. Except in highly turbid waters, the water signal is only a few percent in the pool of photons that reaches a spaceborne sensor. The term "Atmospheric correction" refers to the techniques used to adjust at-sensor radiance on airborne and spaceborne platforms for atmospheric effects, though typically includes compensation for solar irradiance, water surface effects and directional dependency of the water leaving signal (Mobley et al., 2016; Frouin et al., 2019). Particular challenges for atmospheric correction include absorbing aerosols, clouds, adjacency effects and identifying when there is interference from bottom reflection (Brando et al., 2009). Atmospheric correction routines consider the absorption properties of atmospheric gases, as well as light scattered within the atmosphere and reflected from the water surface and/or whitecaps. Such approaches can be extra challenging for hyperspectral imagery that includes spectral regions where atmospheric gases absorb and aquatic ecosystems with high particle loads that scatter light in the near infrared parts of the spectrum. Hyperspectral imagery from the ultraviolet to near infrared also holds the promise of improving upon atmospheric correction, particularly for estimating absorbing aerosols (Frouin et al., 2019).

Because contributions of diffuse and direct sunlight are variable and sea surfaces are not flat, removal of reflected light

TABLE 3 | Atmospheric correction approaches for aquatic applications.

Name	Website	Citations
ACOLITE	Standalone multi-spectral imagery but with prototype support for hyperspectral sensors https://github.com/acolite/acolite	Vanhellemont (2019)
ACORN	Commercially software that uses MODTRAN4	Gao et al. (2009)
ATREM	Used for airborne imagery. https://www.researchgate.net/publication/268979253_Atmospheric_Removal_Program_ATREM_Users_Guide_Version_30	Thompson et al. (2015)
CASIDAS	Initially developed for CASI and then applied to various hyperspectral and multispectral sensors	Lavender and Nagur (2002) Lavender (2014)
COCHISE	Hyperspectral data in the VNIR-SWIR (shortwave infrared) wavelengths	Boucher et al. (2002)
FLAASH	Plugin to ENVI processing software https://www.harrisgeospatial.com/docs/FLAASH.html	Cooley et al. (2002)
HATCH	Hyperspectral data in the visible and SWIR wavelengths	Qu et al. (2003)
iCOR	Plugin available in the SNAP toolbox https://remotesensing.vito.be/case/icor	De Keukelaere (2018)
ISOFIT	Python. Simultaneous fitting of surface, atmosphere and instrument models to imaging spectrometer data https://github.com/isofit/isofit	Thompson et al. (2019)
POLYMER	Standalone used to process multi-sensor multi-spectral ocean color imagery http://hygeos.com/polymer	Steinmetz et al. (2011)
SCAPE-M	Plugin for SNAP designed for inland water bodies surrounded by land https://github.com/senbox-org/s3tbx-scape-m	Guanter et al. (2010)
SeaDAS-hyperspectral	Plugin for NASA SeaDAS to process HICO and future PACE imagery https://seadas.gsfc.nasa.gov/	Ibrahim et al. (2018)

off the sea surface is challenging for both field and remotely sensed measurements. Ideally, missions tend to minimize Sun glint by optimizing viewing geometry and mission scheduling, which may involve designing spaceborne sensors with pre-defined oblique viewing angles and orbital dynamics that result in mid-morning or mid-afternoon overpasses (Hovis et al., 1980). For aircraft operations, flight planning may include avoidance of observations made close to local noon and flight paths that are oriented into or out of the solar direction to avoid cross-track illumination. There is also a need to account for glitter that exists as whole pixels (Lavender and Nagur, 2002). Regardless of sensor design, Sun glint, adjacency effects, and whitecaps can limit the utility of data even with the most advanced correction routines.

Some of the more common approaches applied to multi-spectral and hyperspectral imagery over aquatic water bodies are provided as a resource (**Table 3**), in addition to a review of hyperspectral atmospheric correction approaches (Gao et al., 2009). However, we also note that historically the atmosphere has been treated as a prior step to ocean techniques, but advanced methods for coupled ocean-atmosphere retrievals are an area of growth in the future (Stamnes, 2003; Jamet et al., 2005; Kuchinke et al., 2009; Steinmetz et al., 2011; Stamnes et al., 2018). Hyperspectral atmospheric correction routines include those that use simulated water leaving reflectance shapes and retrieve spectra based on some type of *a priori* spectral library (Steinmetz et al., 2011; Thompson et al., 2019). Others attempt to independently retrieve the water and atmospheric properties and only "lightly constrain" the water-leaving spectral reflectance (Lavender and Nagur, 2002; Ibrahim et al., 2018; Vanhellemont, 2019). Most approaches retrieve all components on a pixel-by-pixel basis, but some are optimized to use features in the imagery to help constrain one or more parameter in the solution for the entire scene under investigation (Guanter et al., 2010; Vanhellemont, 2019). Hence, different techniques can be used for imagery collected close to land or within land compared to open ocean. Another problem is the influence of reflectance from adjacent land/ice pixels that can be scattered into the field of view of the sensor and "contaminate" the water signal with often brighter and spectrally disparate material. This adjacency is particularly problematic for water near bright ice surfaces and inland waters surrounded by bright land and vegetation, and can interfere with techniques to atmospherically correct for aerosols and other imagery. Various techniques have been proposed for addressing adjacency (Reinersman and Carder, 1995; Santer and Schmechtig, 2000; Sterckx et al., 2011; Bulgarelli and Zibordi, 2018), but challenges occur in making the approach applicable across all diverse landscapes. New approaches have also been proposed for dealing with pixels containing whitecaps and foam (Dierssen, 2019). Finally, as further highlighted below, inverse methods that simultaneously retrieve parameters from a coupled ocean and atmosphere system without individual atmospheric correction routines are becoming more common (Chomko et al., 2003; Stamnes, 2003).

COOKING UP AN ALGORITHM STORM

The number of unknown parameters that can be retrieved from hyperspectral data will be much less than the number of spectral bands because of the correlated information between wavebands (Dekker et al., 2018). Therefore, hyperspectral data may be most diagnostic for environmental conditions that result in independent variation of the different optically active constituents, or to collections of environments (regional or global scope) each with its own correlation structure. Those can include systems with surface blooms of different algal

TABLE 4 | Hyperspectral aquatic optical and biodiversity databases.

Dataset	Source	Description
Field and culture data		
Casey et al. (2020). Earth System Science Data, 12 (2), 1,123–1,139. https://doi.org/10.5194/essd-12-1123-2020. https://doi.pangaea.de/10.1594/PANGAEA.902230	Field, Global	A global compilation of *in situ* aquatic high spectral resolution inherent and apparent optical property data for remote sensing applications
LIMNADES https://limnades.stir.ac.uk	Field, Global	Lake bio-optical measurements and matchup data for remote sensing
Carpenter, Dierssen, Hochberg, Lee. 2014–2017. The Coral Reef Airborne Laboratory (CORAL) database. https://doi.org/10.5067/SeaBASS/CORAL/DATA001 https://airbornescience.jpl.nasa.gov/campaign/coral	Field, Pacific Reefs	*In situ* IOP and AOP data collected over Pacific coral reefs in conjunction with PRISM hyperspectral imagery
Knaeps et al. (2018). The SeaSWIR dataset. https://doi.org/10.1594/PANGAEA.886287	Field, Regional	Hyperspectral marine reflectances, total suspended matter, and turbidity measurements gathered at three turbid estuarine sites
Behrenfeld et al., 2014–2017. North American Aerosol and Marine Ecosystem Study (NAAMES). https://doi.org/10.5067/SeaBASS/NAAMES/DATA001	Field, North Atlantic	Four cruises in North Atlantic with AOPs, IOPs, associated with phytoplankton and aerosol data
Siegel et al. 2018–2020. Ocean EXPORTS https://doi.org/10.5067/SeaBASS/EXPORTS/DATA001	Field, Pacific and Atlantic	Data on export and fate of upper ocean net primary production coupled to IOP and AOP measurements
Marine Biodiversity Observation Network (MBON) data portal. https://mbon.ioos.us/	Field, Regional	Biodiversity time series of flora and fauna along coastal zones with ancillary data
Mortelmans et al. (2019). Lifewatch Flanders Marine Institute observatory data. In prep for reflectance https://doi.org/10.14284/393	Field, Coastal North Sea	Monthly phytoplankton pigment, suspended matter, turbidity, and recently hyperspectral radiometry
Vanderwoude et al. (2020). NOAA GLERL Great Lakes Harmful Algal Bloom database. In prep. remove link	Field, Great Lakes	Monthly sampling of Great Lakes phytoplankton composition and hyperspectral optics
Bracher et al. (2020). Coupled phytoplankton composition and radiometry from Atlantic Ocean. https://doi.org/10.1594/PANGAEA.913536	Field, Atlantic	Phytoplankton pigment concentration, groups, and radiometric measurements in the Atlantic Ocean
Bagniewski, W. et al. (2011). North Atlantic Bloom Experiment 2008. https://www.bco-dmo.org/project/2098	Field, Atlantic	Phytoplankton dynamics, profiled hyperspectral reflectance with autonomous optical backscatter, attenuation, radiance
Dekker, Anstee, in prep. Digital Earth Australia. Australian shallow waters spectral library https://ozcoasts.org.au/management/library/	Field, Australia	Spectral library repository for aquatic ecosystem substratum and substratum cover types
Clementson and Wojtasiewicz (2019a) Australian national algae culture collection https://doi.org/10.1016/j.dib.2019.103875	Standards	Dataset on the absorption characteristics of extracted phytoplankton pigments
Clementson and Wojtasiewicz (2019b) Australian national algae culture collection https://doi.org/10.1016/j.dib.2019.104020	Culture	Dataset on the *in vivo* absorption characteristics and pigment composition of various phytoplankton species
Voss et al. (2017) NOAA marine optical buoy (MOBY) https://www.star.nesdis.noaa.gov/socd/moby/filtered_spec/	Field, Hawaii	Hyperspectral water-leaving reflectance in clear waters
Joyce, K. 2020. Shared drone spectroscopy https://www.geonadir.com/	Field, Global	Public repository for drone data including hyperspectral datasets
Simulated and derived data		
Craig et al. (2020). National Aeronautics and Space Administration, PANGAEA, https://doi.org/10.1594/PANGAEA.915747	Simulated, Global	Top of atmosphere, hyperspectral synthetic dataset for PACE ocean color algorithm development
Gregg and Rousseaux (2017). Simulating PACE global ocean radiances. Frontiers in Marine Science, 4. https://doi.org/10.3389/fmars.2017.00060	Simulated, Global	Dynamic simulation of global water-leaving radiances at 1 nm spectral resolution using an ocean model containing multiple ocean phytoplankton groupsetc.
Bracher et al. (2017). Phytoplankton composition from 2002–2012 in world ocean https://doi.org/10.1594/PANGAEA.870486	Derived, Global	Global monthly mean surface chlorophyll *a* for diatoms, coccolithophores and cyanobacteria from SCIAMACHY data

(Continued on following page)

TABLE 4 | (*Continued*) Hyperspectral aquatic optical and biodiversity databases.

Dataset	Source	Description
General searchable databases		
OBIS: https://obis.org/ SPECCHIO: https://specchio.ch/ PANGAEA: https://www.pangaea.de/ SEABASS: https://seabass.gsfc.nasa.gov/ BCO-DMO: https://www.bco-dmo.org/ SPECLIB: https://speclib.jpl.nasa.gov/	Field, Global	

communities that present unique absorption and scattering properties, and water masses that are potentially influenced by land processes (e.g., erosion, organic leaching), benthic-pelagic coupling (e.g., tidal and/or wind driven resuspension of sediments), and flocculation driven by time-space dependent turbulence and chemistry (estuaries). Much of the information content studies have been done with simulated data that may not fully represent the inherent optical properties of natural systems and do not typically model inelastic processes such as Raman scattering and fluorescence (Lee et al., 2007; Wolanin et al., 2016), polarization (Harmel, 2016) and directional dependency, particularly for three-dimensional benthic structures (Hedley et al., 2017, 2018). Presently, there is a lack of hyperspectral backscattering data for different types of aquatic particles for use in simulations. Therefore, optical closure between models (Werdell et al., 2018) and measurement techniques is challenging in bloom conditions and complex water types. To aid in algorithm development, we have compiled a list of hyperspectral datasets that may be useful for evaluating different approaches for estimating aquatic parameters, including phytoplankton and benthic community composition (**Table 4**). With more hyperspectral field data across a wide variety of conditions (Dierssen et al., 2020), particularly for applications for inland and coastal waters, we may find potentially new information in parts of the spectrum previously overlooked. Even without this further information, hyperspectral data will help reduce the uncertainty in the retrieved parameters (Werdell et al., 2018).

Blondeau-Patissier et al. (2014) provide a detailed description of many common indices and numerical techniques used in multi-spectral ocean color remote sensing. A more recent review of ocean color methods for quantifying the inherent optical properties (IOPs) grouped algorithmic approaches into three broad categories; empirical, semi-analytical (also referred to as quasi-analytical), and spectral libraries (also referred to as look-up tables) (Werdell et al., 2018). However, we believe that a more general framework is possible to unify approaches and reduce community-specific jargon with modern terminology of computer and data science. Empirical relations are inevitably introduced in our methods because purely analytical approaches are not possible from remote sensing above the water surface due to complete internal reflection which limits the angular distribution of light crossing the air-sea interface and lack of information on the vertical distribution of particles (Zaneveld, 1995). More information is available from sensors simultaneously measuring at multiple angles from a sea surface. Still, such signals can be challenging to interpret given variable path lengths through the atmosphere and the ever-changing nature of sea surfaces with non-random distributions of waves and swells. Ocean color sensors typically have a small solid angle of detection and measure light fields that originated from near-nadir directions (upwards) within the water (McClain, 2009).

Rather than merely list algorithms, we step back and consider the fundamentals of developing an algorithm with independent steps of "Data Transformations" and "Retrieval Algorithms." This grouping is done because many of the techniques are often identified with the name of the numerical transformation (e.g., derivatives, principal components). Still, the parameters of interest are identified through statistical techniques like multiple linear regression. Many of the so-called "Semi-analytical" algorithms fall within the broader category of "Spectra as References," where the remote sensed spectrum is used as a reference that is matched to spectra modeled using approximations of the forward radiative transfer equations and spectral shape functions. Some algorithms are less sensitive to uncertainties in atmospheric correction such as those focused on narrowband features, and others may require highly calibrated data across the spectrum. While uncertainties can be quantified directly with some techniques, like so-called Optimal Estimation (Rodgers, 1998), techniques have been proposed for propagating uncertainties through other types of algorithms (McKinna et al., 2019).

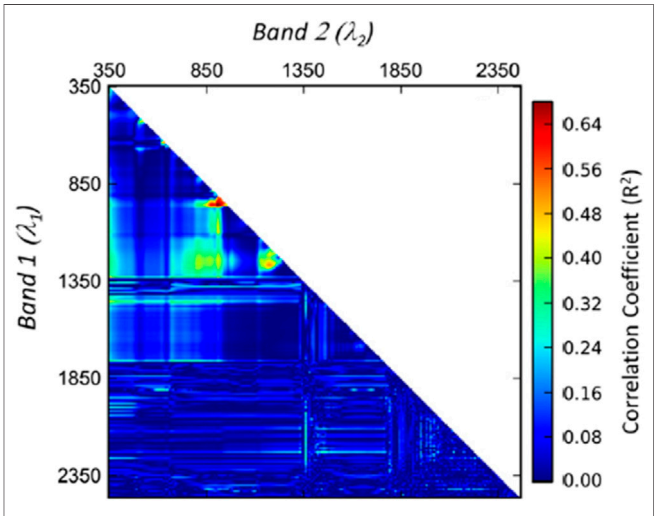

FIGURE 2 | A pairwise correlation analysis can provide information on narrowband features that may be related to a parameter of interest. (Modified from Dierssen et al. (2015)).

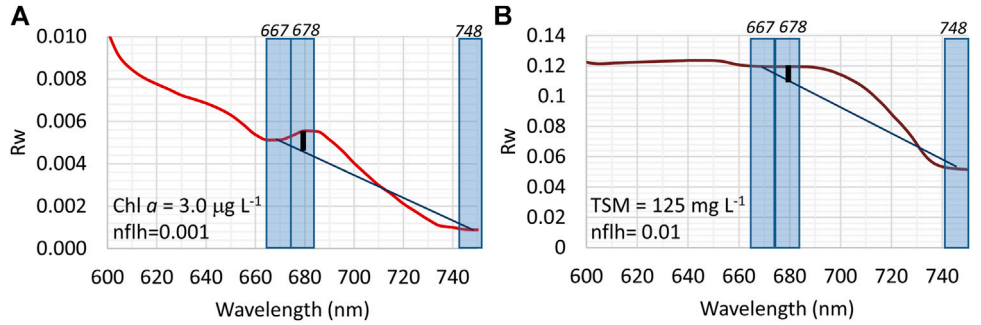

FIGURE 3 | Narrowband features like chlorophyll fluorescence can be inaccurately estimated when using multi-spectral bands that are distant from the feature, such as the blue bands used in the normalized fluorescence line height (nflh). Examples of **(A)** water-leaving Reflectance (Rw) spectrum with a typical chlorophyll fluorescence feature and **(B)** a spectrum representative of high sediment water with no observable chlorophyll fluorescence leads to an erroneously high nflh.

Data Transformations

Data transformations are performed to amplify spectral signals that are related to the specific components to be retrieved. Sometimes the transformed data becomes the parameter of interest, such as the normalized fluorescence line height or normalized difference vegetation index (NDVI). Still, often the transformed data is then related to a parameter of interest via other solution methods as outlined in *Retrieval Algorithms* below. In the latter case, transformations are conducted prior to retrieval of the parameter of interest. The most fundamental transformation applied in remote sensing is the normalization of the measured radiance by the estimated downwelling irradiance to remove variations induced by the quantity and quality of the incident light field, increasing the correlation of the measured signal across multiple conditions with the system properties of interest. After this transformation to reflectance, several methods are applied to amplify the signal further. Listed below are some of the most common transformations, such as normalization of the signal magnitude, reflectance line heights, spectral derivatives, and coordinate system transformation.

Band Math

The simplest transformations are conducted by applying a common mathematical operation or function to the reflectance spectrum. One classical example typically used in multispectral algorithms is to conduct a ratio of two different bands to evaluate relative differences rather than the absolute magnitude (Dierssen, 2010). Similarly, the normalized difference index (NDI), a generalized version of the NDVI, is calculated as the difference between two bands normalized by the sum of the two bands (Hu and Feng, 2016). A common transformation conducted in hyperspectral analyses is to normalize all bands to a given band, approximately removing the dominance of magnitude differences over the signal, enhancing the relative spectral differences. A similar effect can be achieved by normalizing the spectra to its spectral integral (Spyrakos et al., 2018).

Hyperspectral data are particularly suited for investigating absorption and fluorescence features that appear as local minima and maxima in the reflectance spectrum. Such feature-centric algorithms are mathematically simple and work well when the feature of interest covers a narrow spectral range and dominates the reflectance spectrum. Narrow-band analyses are generally less sensitive to uncertainties in the atmospheric correction. A common method for finding such narrowband features is to produce a correlation matrix quantifying the relationships between the feature of interest and all pairs of wavebands across the spectrum. For example, such an approach was used to assess the age of floating seagrass wrack using a narrowband water absorption feature at 750 nm (**Figure 2**) (Dierssen et al., 2015).

Line heights (LH) can be calculated following from a continuum formed by the line between bands (B1 and B3) surrounding the spectral feature of interest (B2) following:

$$LH = \left| \frac{(\lambda_{B2} - \lambda_{B1})(R_{B3} - R_{B1})}{(\lambda_{B3} - \lambda_{B1})} + R_{B1} - R_{B2} \right|.$$

Using widely spaced multispectral data for line heights, such as in the NASA normalized fluorescence line height algorithm (nflh) (Behrenfeld et al., 2009), can be problematic because the selected bands may not be isolated around the feature of interest. The nflh algorithm, for example, uses 748 nm for Band 3, which is over 60 nm away from the fluorescence peak. Such a distant anchor point works reasonably well for average Chlorophyll waters (**Figure 3A**), but produces an order of magnitude higher nflh under high suspended sediment load with no fluorescence peak (**Figure 3B**) (e.g., Zhao and Ghedira, 2014; Amin and Shulman, 2015).

Hyperspectral line heights have been used to detect specific accessory pigments like Chlorophyll-*c3* at 467 nm (Astoreca et al., 2008). Variations on line heights and shifting peak wavelengths can also untangle the complexities of fluorescence in coastal waters where scattered light (elastic reflectance) significantly influences the fluorescence band (Gilerson et al., 2007) and for some types of bloom or seasons when fluorescence is not as prevalent as scattering enhancements observed in the far red wavelengths, also referred to as the "red edge" (Gower et al., 2008; Matthews et al., 2012; Freitas and Dierssen, 2019). Additionally, hyperspectral data can also reveal different fluorescence peaks such as the yellow fluorescence observed from phycoerythrin pigment in the ciliate *Mesodinium rubrum* (Dierssen et al., 2015).

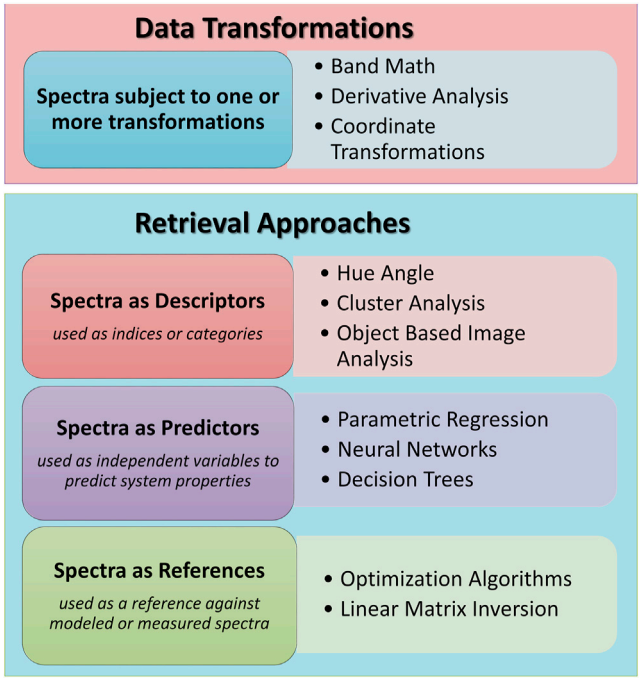

FIGURE 4 | Approaches for building a hyperspectral algorithm with selected examples.

Derivative Analysis

Spectral derivatives solved as finite difference derivative approximations (e.g., Torrecilla et al., 2011) can reduce relative magnitudes variation in the spectrum, enhancing the signal of the presence of local minima and maxima. Spectral derivatives have long been used to evaluate phytoplankton pigments such that a trough in reflectance is related to absorption and a peak in reflectance associated with reduced of absorption or pigment fluorescence. Since the second derivative is a measure of curvature, it amplifies high-frequency features of interest that are otherwise quite subtle within the spectrum and depresses low-frequency changes, such as the gradual decrease in absorption due to colored dissolved and detrital matter. However, this also means that very high-frequency features, such as band-to-band differences due to sensor noise and relative calibration errors, will also be amplified within the derivative spectrum. For this reason, spectral smoothing is often conducted before the application of derivative analysis, and various techniques have been recommended for how to smooth data for effective derivative analysis. Often, a statistical approach like multiple linear regression or optimization is then used to link the derivative spectrum to the parameters of interest, but decision trees based on arguments of the maxima and minima (argmax and argmin) have also been used (Lubac et al., 2008). Application of derivative analysis to aquatic remote sensing data has been useful for detecting the presence of pigments associated with phytoplankton including harmful species (Bidigare et al., 1989; Craig et al., 2006; Lubac et al., 2008; Cheng et al., 2013) and benthic organisms associated with shallow coral reef habitats (Hochberg and Atkinson, 2000; Louchard et al., 2003).

Coordinate Transformations

Transformations of the coordinate system are typically used to produce a set of orthogonal variables with uneven distribution of the total variance, as in classical Principal Components Analysis (a.k.a., Empirical Orthogonal Functions). The new variables can be used as a descriptive multivariate method of the optical data, in which case further transformations of the variables might be relevant for interpretation (e.g., varimax PCA). They can also be used for prediction in methods that condition the rotation in the optical data matrix to achieve an improved classification of (e.g., Linear Discriminant Analysis) or correlation with the dependent variable (e.g., Partial Least Squares Regression). In its simplest application for retrievals, the coordinate transformation with PCA is an isolated step after which the new variables are included in multilinear regression. Preisendorfer also provided a fundamental text on PCA (Preisendorfer, 1988). These approaches are increasingly being used to identify different groups of phytoplankton and suspended mineral composition (Catlett and Siegel, 2018; Ortiz et al., 2019; Bracher et al., 2020a; Smith and Bernard, 2020). A related concept is the transformation of the hyperspectral information to chromaticity coordinates (hue angle and saturation).

Retrieval Algorithms

A wide variety of hyperspectral methodologies rely on machine learning techniques across the broad field of environmental science, as detailed in extensive reviews over the last decade (reviewed in Paoletti et al., 2019). The basis of most algorithms is considered within the framework of machine learning, where statistics theory is used to find patterns in data or to estimate the process that generates the data. In the first case, methods fall in the class of unsupervized machine learning with cluster analysis and other methods that also take in consideration the spatial context, as in object based image analysis. In the latter case, methods are either in the context of supervised machine learning, spectral matching or linear matrix inversion. Within this group, a variety of approaches are used to related a spectrum, either measured at-sensor, atmospherically corrected (*Finding the Ocean Needle in the Atmospheric Haystack*), or subject to one or more transformations (*Data Transformations*), to a parameter or set of parameters of interest. Parameters can include classes of optical water types, optical properties including absorption and backscattering, and biogeochemical quantities of interest like pigment or sediment concentrations. Clearly, the more representative the training data available across space and time, the better the models will perform across the domain. The field of machine learning is advancing rapidly and influencing the way nearly all algorithms are developed, tested, and implemented. Some approaches are focused more on prediction rather than understanding or description of processes, and many final algorithms involve multiple steps including data transformations and statistical analyses. Here, we group the retrieval approaches by the way the spectra are used in the algorithm (**Figure 4**).

Spectra as Descriptors

The following section highlights some of the common methods where spectra are used to estimate indices or categories.

Optical Indices

In addition to various band math indices like normalized fluorescence line height discussed above in *Data Transformations*, many different other types of indices have been proposed to detect differences between floating *Sargassum* and seagrass wrack (Dierssen et al., 2015) or to detect different harmful algal bloom formers (Smith and Bernard, 2020). A spectral classification index was recently developed by Vandermuelen et al. (2020) to quantitatively describe the shape of a hyperspectral dataset using a weighted harmonic mean. Similar to transformations of hyperspectral data to chromaticity coordinates that relate to colors observed by the human eye (Dierssen et al., 2006; Wernand et al., 2013), the Apparent Visible Wavelength (AVW) represents a one-dimensional geophysical metric of "color" that is correlated to spectral shape. Such simple metrics correspond to conceptual changes that can easily be explained to a broad audience (e.g., the water is "greener" or "bluer") and can be diagnostic of slight optical changes that are masked in chlorophyll retrievals.

Cluster Analysis

Many different indices have been developed to classify water types broadly from clear to turbid similar to the original water classes of Jerlov (1963) or to identify specific types of algal blooms or properties of interest. Clustering methods are frequently used to partition out different types of spectra locally or globally and track water mass movement and change over time (Lubac and Loisel, 2007; Aurin et al., 2010; Uitz et al., 2015; Ye et al., 2016). Clustering methods can include K-means, fuzzy C-means, hierarchical clustering (e.g., Euclidean distance, Ward linkage), and hybrid methods. Classification approaches in the pelagic ocean (i.e., "Seascapes") have been used to identify water masses with particular biogeochemical features that can be linked to biomes and biophysical provinces and provide rapid information to decision-makers about the changing environmental conditions (Kavanaugh et al., 2016). Seascapes are classified using a suite of synoptic time-series observations from satellites (Montes et al., 2020).

Object Based Image Analysis

Traditional pixel-based image classification considers all pixels similarly without the context of neighboring pixels or the image as a whole. However, OBIA segments an image and groups pixels together into vector objects (Blaschke, 2010). Such approaches are not common to ocean optics given the relative homogeneity of ocean surfaces and the lack of structures like rectangular buildings and long and narrow roads. However, these techniques are gaining popularity in optically shallow water remote sensing where bottom features may have spatial patterns and features (Phinn et al., 2012; Roelfsema et al., 2018). A variety of methods are available to segment an image based on the shape and spectral information prior to classification (**Table 2**). This can also prevent unwanted salt and pepper retrievals where classes vary unrealistically within an aquascape.

Spectra as Predictors

The following section presents example techniques where the spectra or the transformed spectra are used as independent variables to predict parameters of the system. Prediction requires the supervised approach to machine learning and comprises methods of classification and regression analysis. The term "classification" is used when the dependent variable is categorical and the term "regression" is used when the it is continuous. Most familiar methods are those of parametric regression using linear or non-linear models, but nonparametric models such as artificial neural networks are gaining popularity. Below we present an overview of some common methods.

Parametric Regression

Parametric regression imposes a structure to the modeled relationship between spectral data and a continuous target parameter. This requires specifying the relationship structure *a priori*, from dedicated exploratory data analysis. For complex data relations, it demands sophistication in terms of mathematical functions and orthogonal basis expansions. A benefit of this approach is that it is data-efficient and can be applied to sparsely populated sample space. As a contrast, nonparametric regression does not impose a model structure and often requires a more densely populated sample space. As discussed above, data is often transformed first and then linked to a parameter of interest using linear or nonlinear regression techniques. This type of approach has been used for the current band ratio chlorophyll *a* algorithms and for other parameters like ancillary pigments, phytoplankton groups, and total suspended matter (Catlett and Siegel, 2018; Ortiz et al., 2019; Bracher et al., 2020; Smith and Bernard, 2020). For many aquatic parameters, the regression analysis is conducted on log-transformed data to cover the full range of environmental conditions.

Neural Networks

Recently, Artificial Neural Networks have gained much popularity due to their flexibility in addressing different applications and can be used with raw data or applied after data transformations. Training data sets may consist of field measurements or model simulations representing the wide range of conditions found in the natural world. Researchers "train" a neural network over time by analyzing its outputs on different problems and comparing them with the correct answers. As in any regression, model development must consider trade-offs between adding complexity to improve prediction and increasing the risk of overfitting the solution to the training data. Accumulation of global datasets covering a wide range of conditions and advances in computer processing power have enabled machine learning researchers to vastly expand the size and complexity of the models, simulate larger datasets for training, train the models faster, and overall achieve better results. Neural networks have been gaining popularity in the aquatic remote sensing and used to derive the diffuse attenuation coefficient (Jamet et al., 2012; Chen et al., 2014), uncouple constituents in optically complex waters (Doerffer and Helmut, 2000; Ioannou et al., 2013), map shallow-water

benthic features (Sandidge and Holyer, 1998; Filippi, 2007; Liu et al., 2015), and to evaluate features across different scales (e.g., Hieronymi et al., 2017; Pahlevan et al., 2020). Salcedo-Sanz and colleagues, for example, implemented a neural network to map shallow benthic coral reef features and concluded that neural network approaches generally out perform traditional empirical approaches to the problem such as supervised and unsupervized classification and regression analysis (Salcedo-Sanz et al., 2016).

Decision Trees

In a decision tree, the analysis begins at the top of the tree where a single feature of the data is considered and analysis proceeds downwards based on the decisions made in previous levels of the tree. At each level of the tree, the computation splits off into two or more children nodes based on features of the data. The computation ends when you reach a terminal node at the bottom of the tree. Even in the simplest algorithms, many decisions are required to assess whether reflectance in a pixel is appropriate for subsequent analysis. Some of these decisions may be considered as part of the "Atmospheric Correction" decisions such as "*Is this a water pixel?*" or "*Is there a cloud or cloud shadow obscuring the pixel?*" or "*Is this optically deep water?*" Many common algorithms in ocean color are decision trees that use different approaches depending on criteria established from the spectrum, such as NASA's current Chlorophyll *a* algorithm which uses two different algebraic approaches depending on whether the pixel is considered a high or low chlorophyll pixel. Such decisions often involve subjective or fitted thresholds which determine which approach will be used. Setting thresholds can be challenging, and such delineation often does not apply widely across different images collected in space and time and require tuning for each application. Decision Trees are common for differentiating water types, benthic flora and floating vegetation (Hill et al., 2014; Ye et al., 2016; Castagna et al., 2020).

The supervised Random Forest (RF) classifier belongs to the group of classifiers that use decision trees and independent random vectors, with the approach driven by the relationship between the training and the response dataset rather than starting with a data model (Breiman, 2001). It provides several benefits over other supervised classification algorithms, including the ability to calculate internal error estimates and variable importance, as well as the capacity to handle weak explanatory variables (Gislason et al., 2006). The approach has received attention within the remote sensing community due to both the classification accuracy and processing speed. Applications include the classification of submerged vegetation (Espel et al., 2020) and estimation of bathymetric depth (Yunus et al., 2019).

Spectra as References

A different approach to estimation of a continous variable occurs when the measured spectrum is taken as a reference and the methods involve calculating the mixing of endmembers or the system composition that would result in the observed spectrum. This approach is typically solved numerically with optimization, where the measured spectra is taken as a reference to be matched against by spectra in a spectral library. The parameter values of

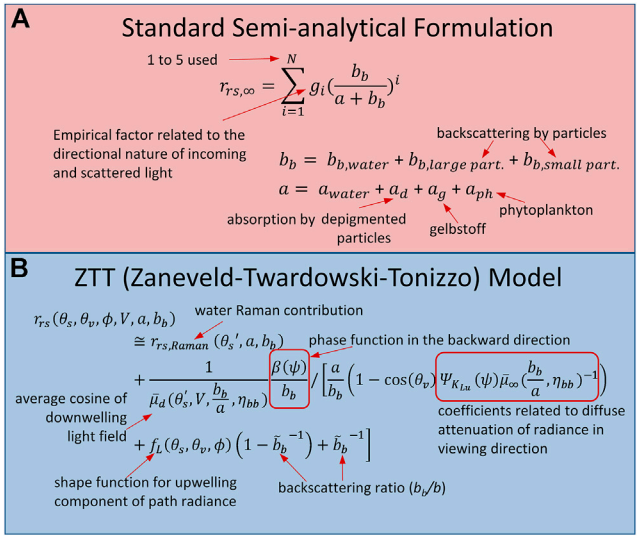

FIGURE 5 | Physical models link the water column optical properties to the light field measured by a satellite. **(A)** Most semi-analytical algorithms use a simplification where the directional nature of light is approximated with empirical constants (Werdell et al., 2018). **(B)** A newly posed ZTT model parameterizes the shape of light in the backward direction (phase function), the shape of the upwelling component of path radiance and the average cosine of downwelling light Twardowski and Tonizzo (2018).

the best matching spectra are taken as estimates for the measurement. An analytical solution via linear matrix inversion is possible in linear problems, such as linear mixing of endmembers or when using a linear approximation to the radiative transfer equation. In the latter, the analysis calculates the magnitudes (eigenvalues) associated with predefined relative spectral shapes (eigenvectors) of system components that would result in the observed spectrum.

The spectral library can contain previous measurements in which the parameters of interest are known, or can be built from simulation with a physical model. In the case of simulations, the library can be generated dynamically at each iteration step or through the use of a static library or "look-up table" of measurements or pre-computed simulations. Iterative approaches can be computationally expensive when applied to each pixel in a remote sensing image. The computational time involved in searching the library for the best matching spectrum, however, may also be high given the number of properties that must be considered, the number of spectral bands, and how each parameter varies across the expected range. Library size can be decreased to an extent by limiting the dimensionality of the hyperspectral signal to regions of the spectrum containing most of the information pertaining to the properties of interest. Spectral libraries have been developed and applied to differentiating phytoplankton groups or biodiversity (Palacios et al., 2015) and in optically shallow water to retrieve bottom depth and benthic cover (Louchard et al., 2003; Mobley et al., 2005).

Many of the so-called "Semi-analytical Models" fall within the broader category of optimization using a physical model

representative of the system. Such techniques involve: 1) Formulation of the problem in a forward model; 2) Iterating or inverting the forward model algebraically or numerically; and 3) Finding the best solution in terms of uniqueness, accuracy and efficiency of the model. The formulation of the forward model in aquatic models often relate inherent optical properties of the water column (typically the absorption and backscattering properties of the water constituents) through radiative transfer theory (Gege, 2017). To-date, most of the aquatic models have used an approximation of the radiative transfer equation relating the ratio of backscattering to absorption with an empirical parameter, g_i, that accounts for the angular distribution of incoming and scattered light (**Figure 5A**) (Gordon and Brown, 1988). A more detailed formulation of the forward model was recently proposed, the Zaneveld-Twardowski-Tonizzo (ZTT) Model, that parameterizes the angular distribution of both incoming and upwelled light in the water column (**Figure 5B**) (Twardowski and Tonizzo, 2018). Angular considerations become more critical when retrieving optical properties in more complex coastal and inland waters.

Many different numerical solutions have been used from non-linear spectral optimization to adaptive linear matrix inversion (e.g., see Table 4 of Werdell et al., 2018). Some form of empirically determined spectral shape functions are required to retrieve the inherent optical properties of different constituents, including particulate backscattering and absorption by phytoplankton, gelbstoff, and depigmented particles. The term "depigmented particles" is used rather than tripton, detritus or non-algal particles because the measurement includes all types of depigmented particles, including algal cells (Neeley et al., 2018). The solution involves varying the quantities of each parameter until the difference between the derived and the measured spectrum is sufficiently minimized. Many solution methods include techniques to avoid local minima and maxima and sample the whole parameters space (e.g., Dierssen et al., 2019).

Derived inherent optical properties can then be related to other parameters of interest such as concentrations of chlorophyll *a*, total suspended matter, and potentially estimates of phytoplankton community composition via supervised regression techniques discussed above. In addition to the optical properties regularly produced from ocean color imagery (Lee et al., 2002; Werdell et al., 2013), similar approaches have also been successfully used in simultaneously retrieving water column depth, inherent optical properties and benthic diversity from hyperspectral imagery (Hedley et al., 2016b; Garcia et al., 2018; Dierssen et al., 2019). A significant advantage of optimization approaches is that uncertainties due to instrumental and environmental noise can be estimated numerically via the addition of spectral noise before inversion (Garcia et al., 2014).

A class of optimization techniques well suited for hyperspectral imagery are referred to as "Optimal Estimation" using Bayes' theorem (Rodgers, 1998). It entails specifying probability distributions for the natural variability of the hidden physical processes ("priors"), a distribution for the spectral measurement errors, and an explicit forward model. Assuming all distributional parameters are known, the retrieved state is then the maximum a posteriori (MAP) estimate of the state given the observed, noisy radiances. Specifying the sources of variability within a Bayesian framework allows for the parameterization of the sources of error and the ability to propagate them into estimates of retrieval uncertainty (Nguyen et al., 2019).

UNLOCKING BIODIVERSITY: NEITHER FISH NOR FOWL

Biodiversity, the diversity within species, between species, and of ecosystems, is a fundamental characteristic of Earth, and underpins the structure and functioning of Earth's ecosystems, as well as human health, nutrition, and economic livelihoods (Secretariat of the Convention on Biological Diversity, 2020). Many of the benefits that we gain from aquatic ecosystems depend on the number and abundance of species, the interactions between the organisms and the environment, and the number of different habitats (Malone et al., 2014). In recognition of the global threats to biodiversity, the Convention on Biological Diversity (CBD) has listed several targets for preserving aquatic biodiversity including: sustainable management of fisheries and aquaculture, prevention of nutrient pollution, as well as minimization of anthropogenic pressures on coral reefs and other vulnerable ecosystems. Measures for biodiversity referred to as Essential Biodiversity Variables (EBVs) are commonly grouped into six classes: genetic composition, species populations species traits, community composition, ecosystem structure, and ecosystem function. Since Muller-Karger et al. (2018), more biodiversity variables for phytoplankton are routinely produced from satellites like Sentinel-2 OLCI, including pigments (chlorophyll *a* and phycocyanin) and certain taxonomic groups like cyanobacteria are routinely produced from aquatic remote sensing platforms) (**Figure 6**).

Measurements of distribution, abundance, and phenology of bulk phytoplankton in the open ocean (i.e., derived chlorophyll-a) are regularly produced from satellite remote sensing. Parameters that Muller-Karger et al. (2018) classified as "demonstrated limited cases" could become operational with regular, hyperspectral observations. In particular, high spatial and radiometric resolution hyperspectral data is required with a high repeat frequency would enable measurements of primary producers such as phytoplankton, wetland and submersed plant and macroalgae species and distribution (including vertical), pigments and other traits, taxonomic diversity and functional types (Santos et al., 2012; Anderson et al., 2016; Santos et al., 2016; Bracher et al., 2017a; Hedley et al., 2017). Where species cannot be measured directly, hyperspectral remote sensing can be used to monitor drivers and proxies of biodiversity. For example, hyperspectral remote sensing can be used to discriminate the water quality constituents and the spectral underwater light field of the aquatic environment, which forms the niche for many fish species. Spectral diversity of the primary producers in aquatic and wetland ecosystems can be used to make inferences about biodiversity and ecosystem function (Muller-Karger et al., 2018; Rebelo et al., 2018). Indeed, monitoring of biodiversity of benthic and pelagic organisms in aquatic ecosystems will advance remote sensing capabilities with diverse applications that serve both the research and management communities (**Figure 7**).

Spectral "fingerprints" can be used to elucidate different light absorbing, scattering, and fluorescence properties that are related to the biodiversity of photosynthesizing flora and fauna in the water column (pelagic), on the seafloor (benthos), and floating on the sea

Class	Essential Biodiversity Variable (EBV)	Wetlands	Benthic communities		Pelagic		
		Mangrove/ Salt marsh	Macro-phytes & Macroalgae	Coral	Phyto-plankton	Fish, Zoo-plankton	Apex Predator
Genetic Composition	Population genetic diversity						
Species Populations	Distribution						
	Abundance						
	Size/vertical distribution					**	
Species Traits	Pigments*					NA	NA
	Phenology						
Community Composition	Taxonomic diversity*						
Ecosystem Structure	Functional type*						
	Fragmentation/ heterogeneity						
Ecosystem Function	Net primary production					NA	NA
	Net ecosystem production					NA	NA

*Select types may be differentiated. ** using lidar techniques

Routine	Demon-strated	Unproven	Ecosystem Model

FIGURE 6 | Current capabilities of remotely sensed data for measuring Essential Biodiversity Variables modified from Muller-Karger et al. (2018). "Unproven" indicates that methods have not yet been developed to collect these measurements from remote sensing imagery. "Demonstrated" are methods that have been demonstrated and could potentially be produced with hyperspectral imagery. "Routine" indicates measurements that are produced regularly. "Ecosystem model" indicates EBVs that can be predicted on the basis of ecosystem models that may incorporate remote sensing imagery. "NA" indicates that the observation is not applicable.

surface. Photosynthesizing flora includes different assemblages of phytoplankton which provide the bulk of the photosynthesis in the world ocean, and photosynthesizing fauna includes tropical coral reefs and select mixotrophic plankton like ciliates. Algorithms for estimating pigment concentration are usually associated with large uncertainty when applied globally because of the variability in size and shape of phytoplankton and cellular levels of pigment related to environmental conditions (Dierssen et al., 2020). Increasingly studies show that only a limited number of phytoplankton groups (~5) may be differentiated globally using hyperspectral absorption spectra in visible wavelengths (Kramer and Siegel, 2019). The spectral signatures of the different phytoplankton groups of interest are similar within the uncertainty of the measurement largely because of the considerable overlap in pigment composition between different groups (Cael et al., 2020). Recent analyses of the oligotrophic ocean from the Tara Oceans expedition, for example, suggests that only around five different phytoplankton groups can be reliably differentiated from their spectral signatures (Cael et al., 2020). Data from the Santa Barbara Channel, California revealed that around five phytoplankton pigment communities, which are covarying assemblages of phytoplankton groups, could be differentiated based on their spectral properties (Catlett and Siegel, 2018). Similarly, data from the upwelling waters around South Africa also was used to retrieve five different phytoplankton communities relevant to the aquaculture industry (Smith and Bernard, 2020). However, remote sensing algorithms and biogeochemical models can be derived and tuned for the regional or local phytoplankton groups down to specific taxa, if they are known to occur in an area. And, we have only begun to assess the hyperspectral scattering and fluorescence properties that may also aid in differentiating different types and stages of blooms, as well as relationships to seasonal trends and other remotely sensed parameters including polarization parameters, temperature, photosynthetically available radiation, and salinity.

PEERING INTO THE ABYSS

As the pressures of human population and climate change on coastal and inland aquatic environments rise, the need will increase for more accurate and timely environmental information to support research and resource management. With an economic value to the Asia Pacific region alone currently estimated at U.S. $372 billion, jumping to U.S. $1.35 trillion by 2030 (Commonwealth of Australia, 2019) Earth and marine observing is emerging as a significant business in its

FIGURE 7 | A host of new applications will be available with better discrimination of pelagic and benthic biodiversity promised by hyperspectral imagery. Modified from Dierssen et al. (2020).

own right. Hyperspectral remote sensing, in particular, is becoming a powerful mapping and survey tool that is well suited for optically complicated coastal and inland aquatic environments, as well as a host of other applications of societal importance, such as in areas of agriculture, mineral exploration, forestry, and urban planning. This broad scope of application will ensure that hyperspectral technology and access will continue to improve with time. It is, therefore, reasonable to speculate how future technological advances may improve how we sense and understand aquatic environments and to point out key challenges to overcome in order to capitalize on future technology (**Figures 7**).

As noted in *Suborbital Systems*, sensor miniaturization is one of the most exciting recent advances in hyperspectral technology for observing highly heterogeneous benthic environments. We can now mount small and lightweight imaging spectrometers on drone platforms to fly at low altitude (Parsons et al., 2018), or within submersible housings to acquire data with an unparalleled spatial resolution (Chennu et al., 2017; Mogstad and Johnsen, 2017; Bongiorno et al., 2018). The combined hyperspectral hyperspatial data will allow us to revisit the research findings in aquatic and marine applications using point-based spectrometers of the early 2000s and apply it in a new spatially explicit manner, while including context, shape, size, and textural measures for more detailed classifications. Further, with the availability of sensors of the caliber that were previously limited to military or high-end commercial consulting, data capture is rapidly decentralizing and distributing within an expanding user community. This expansion of platforms results in potentially many more data sets available to be analyzed and exploited.

The shift in imaging system access and control from external organizations and large satellites to the individual researcher with UAS is analogous to transferring computing power from mainframes to personal computers in the 1980s. By embedding the technology within research activities, users have more flexibility in deciding when, where, and how frequently to collect observations, thus increasing data value and, therefore, project efficiency. Users can readily create custom UAS-based systems, or purchase complete systems including sensors, aircraft, and mission planning and data analysis software, tailored to applications (Adão et al., 2017). This is a careful balance though, as the adoption of UAS systems often comes at the expense of loss of coverage across large areas without great investment in personnel time and extremely large data volumes still not manageable for many individual research groups or investigators (Bolch et al., 2021).

TABLE 5 | Relevant outreach programs.

Name	Citation/Link	Description
Geo Aquawatch	https://www.geoaquawatch.org/	Develop and build the global capacity and utility of earth observation-derived water quality data, products and information to support water resources management and decision making
HYPERedu	https://www.enmap.org/events_education/hyperedu	An online learning platform for hyperspectral remote sensing as part of the education initiative within the EnMAP mission
IOCCG	https://ioccg.org/	Promotes the application of remotely sensed ocean color and inland water radiometry data across all aquatic environments, through coordination, training, advocacy and provision of expert advice
PACE Early Adopters	https://pace.oceansciences.org/app_adopters.htm	Promotes applied science and applications research designed to scale and integrate PACE data into policy, business, and management activities that benefit society and inform decision making
Remote Sensing Toolkit	https://www.rsrc.org.au/rstoolkit	Designed for managers to understand how images collected from different satellites and aircraft can be used to map and monitor changes over time

However, more data is not always synonymous with better data. Further, neither necessarily leads to better decisions. Decentralized data capture can lead to inconsistencies in quality, making comparisons between studies difficult. By popularizing the collection of remote sensing data, standardized community best practices in data capture and quality control are needed to avoid 'garbage in, garbage out' scenarios (Joyce et al., 2019). Development of standardized instrument calibration procedures and data capture protocols, including thorough accompanying metadata (Janssen et al., 2012; Kalinauskaitė, 2017), should be a future priority of the user community. For example, no accepted protocols are currently available on how to best calibrate commercial off-the-shelf hyperspectral imaging spectrometers for aquatic applications. Such standardization will be particularly important when conducting multi-temporal analyses and when sharing datasets between users.

Data sharing is widely recognized for promoting innovation and growth. Recent moves toward creating open and FAIR (findable, accessible, interoperable, and reusable) data archives have largely contributed to an acceleration of new remote sensing applications. One only needs to look to the vast number of new and exciting applications of Landsat data that followed open access to the 30 + year archives to realize the value in this approach (Wulder et al., 2016; Zhu et al., 2019). This challenges the assumption that we only obtain value through a financial transaction when the data collector sells its raw data. Instead, FAIR data policies place value on the benefits of derived products. We expect that continued FAIR data practices will continue to remove barriers to remote sensing technology, including the availability of hyperspectral imagery, and result in a greater diversity of people engaging with the data to address the many environmental challenges facing society.

To allow users to truly exploit raw data, derive products, and create new knowledge, it is essential to support FAIR data with the appropriate infrastructure and systems architecture on similarly accessible platforms (Janssen et al., 2012; Kalinauskaitė, 2017). Supporting open-source software options such as QGIS (see **Table 2**) are critical in continuing to grow relevant applications through open-minded community collaboration. Yet, locally hosted software options are unlikely to be the future for hyperspectral data processing. Hyperspectral data fits within the category of "big geo data" (Krämer and Senner, 2015) and is, therefore, better suited to scalable and distributed cloud processing rather than local computing capabilities (Wilson et al., 2018; Haut et al., 2019). Although cloud-based high-performance computing (HPC) is not a new concept (e.g., Plaza et al., 2011), its intersection with hyperspectral data for environmental analyses–particularly in aquatic environments–is in its infancy and remains an area for considerable future growth.

Technological advances in computing technology, data storage, and processing combined with the potential for increased data availability due to decentralized data capture presents exciting challenges and opportunities for hyperspectral aquatic remote sensing in the future. The inherent high dimensionality, noise, and intra-class variability plague the deep learning models that are otherwise becoming a favored means for analyzing remotely sensed data (Paoletti et al., 2019). However, with distributed analyses, opportunities for community collaboration and crowdsourcing emerge. Examples of this dynamic abound within the rapidly developing field of machine learning and artificial intelligence (Chirayath and Li, 2019).

Similarly, global initiatives such as AquaWatch and IOCCG connect global networks of people, sensors, and platforms to provide an integrated approach to aquatic ecosystem analyses (**Table 5**). Such international groups can also provide a framework for broad data access spanning nations and individual satellite missions. In addition, the ocean optics community should be engaged closely with the broader scientific community involved with biogeochemical and ecosystem modeling (IOCCG, 2020). Going forward, better quantification of parameter uncertainties will provide ocean modelers with the metrics needed for assessing model performance. Finally, merging of hyperspectral imagery with other types of remote sensing, such as polarimetry (Chowdhary et al., 2019), provides exciting new avenues for growth in what can be retrieved across Earth's diverse aquascape. There will continue to be a mutual benefit for the hyperspectral community to continue to engage more broadly with Earth and marine observations.

In conclusion, the field of hyperspectral aquatic remote sensing is on the cusp of providing novel ways to sense aquatic ecosystems and new parameters that can be better used by decision-makers and scientists alike. The lists of resources and tools provided here are only a starting point and will expand over time as more hyperspectral data from satellites, drones and other platforms becomes accessible to the larger community of scientists and practitioners. To aid in this effort, we recommend posting resource information on public forums and

updating resource lists and tools regularly. While the foundations for algorithm development and data processing are becoming well established, a significant gap is the availability of field data for both algorithm training and validation across the global ocean and inland waterways including common and episodic environmental conditions. This includes not just the collection of well-calibrated hyperspectral imagery but merged datasets coupling hyperspectral reflectance with ancillary biodiversity and biogeochemical properties obtained with consistent methodology and metadata. Such efforts will require global cooperation and data sharing. Indeed, interdisciplinary, international, commercial, and citizen collaborations will drive us forward as a community to realize the hype of hyperspectral remote sensing and provide important new insights into the blue marble Earth.

AUTHOR CONTRIBUTIONS

HD was the lead author of the manuscript. All of the coauthors contributed to conceptual discussions about paper content and writing and editing of the manuscript.

FUNDING

Funding was provided by the Alliance for Coastal Technologies program sponsored by the National Oceanic and Atmospheric Administration/US Integrated Observing System (US.IOOS Award number: NA16NOS012OO). Additional funding was provided to HD from NASA Ocean Biology and Biogeochemistry (80NSSC20M0206). AC was funded by the Belgian Science Policy Office (BELSPO) project HYPERMAQ (SR/00/335). Support for SA was provided through the Naval Research Laboratory base funding program.

ACKNOWLEDGMENTS

We would like to acknowledge the organizers of the 2018 Alliance for Coastal Technologies (ACT) Hyperspectral Imaging of Coastal Waters Workshop, Mario Tamburri the director of ACT, and all workshop participants. We would also like to acknowledge Astrid Bracher who provided additional resource information.

REFERENCES

Aasen, H., Honkavaara, E., Lucieer, A., and Zarco-Tejada, P. (2018). Quantitative Remote Sensing at Ultra-high Resolution with UAV Spectroscopy: a Review of Sensor Technology, Measurement Procedures, and Data Correction Workflows. *Remote Sensing* 10, 1091. doi:10.3390/rs10071091

Acker, J. G. (2015). *The Color of the Atmosphere with the Ocean below: A History of NASA's Ocean Color Missions*. Scotts Valley, CA: CreateSpace Independent Publishing Platform.

Ackleson, S. G., Smith, J. P., Rodriguez, L. M., Moses, W. J., and Russell, B. J. (2017). Autonomous Coral Reef Survey in Support of Remote Sensing. *Front. Mar. Sci.* 4, 325. doi:10.3389/fmars.2017.00325

Adams, M. S., Scarpace, F. L., Scherz, J. P., and Woelkerling, W. J. (1977). *Assessment Of Aquatic Environments By Remote Sensing*. IES Report 84. Madison, WI: University of Wisconsin-Madison.

Adão, T., Hruška, J., Pádua, L., Bessa, J., Peres, E., Morais, R., et al. (2017). Hyperspectral Imaging: A Review on UAV-Based Sensors, Data Processing and Applications for Agriculture and Forestry. *Remote Sensing* 9, 1110. doi:10.3390/rs9111110

Amin, R., and Shulman, I. (2015). Hourly Turbidity Monitoring Using Geostationary Ocean Color Imager Fluorescence Bands. *J. Appl. Remote Sens* 9, 096024. doi:10.1117/1.JRS.9.096024

Anderson, F. E., Bergamaschi, B., Sturtevant, C., Knox, S., Hastings, L., Windham-Myers, L., et al. (2016). Variation of Energy and Carbon Fluxes from a Restored Temperate Freshwater Wetland and Implications for Carbon Market Verification Protocols. *J. Geophys. Res. Biogeosci.* 121, 777–795. doi:10.1002/2015JG003083

Astoreca, R., Rousseau, V., Ruddick, K., Knechciak, C., Van Mol, B., Parent, J.-Y., et al. (2008). Development and Application of an Algorithm for Detecting Phaeocystis Globosa Blooms in the Case 2 Southern North Sea Waters. *J. plankton Res.* 31, 287–300. doi:10.1093/plankt/fbn116

Aurin, D. A., Dierssen, H. M., Twardowski, M. S., and Roesler, C. S. (2010). Optical Complexity in Long Island Sound and Implications for Coastal Ocean Color Remote Sensing. *J. Geophys. Res.* 115, 1–11. doi:10.1029/2009JC005837

Bagniewski, W., Fennel, K., Perry, M. J., and D'Asaro, E. A. (2011). Optimizing Models of the North Atlantic Spring Bloom Using Physical, Chemical and Bio-Optical Observations from a Lagrangian Float. *Biogeosciences* 8, 1291–1307. doi:10.5194/bg-8-1291-2011

Banks, A. C., Vendt, R., Alikas, K., Bialek, A., Kuusk, J., Lerebourg, C., et al. (2020). Fiducial Reference Measurements for Satellite Ocean Colour (FRM4SOC). *Remote Sensing* 12, 1322. doi:10.3390/rs12081322

Becker, R. H., Sayers, M., Dehm, D., Shuchman, R., Quintero, K., Bosse, K., et al. (2019). Unmanned Aerial System Based Spectroradiometer for Monitoring Harmful Algal Blooms: A New Paradigm in Water Quality Monitoring. *J. Great Lakes Res.* 45, 444–453. doi:10.1016/j.jglr.2019.03.006

Behrenfeld, M. J., Westberry, T. K., Boss, E. S., O'Malley, R. T., Siegel, D. A., Wiggert, J. D., et al. (2009). Satellite-detected Fluorescence Reveals Global Physiology of Ocean Phytoplankton. *Biogeosciences* 6, 779–794. doi:10.5194/bg-6-779-2009

Bender, H. A., Mouroulis, P., Dierssen, H. M., Painter, T. H., Thompson, D. R., Smith, C. D., et al. (2018). Snow and Water Imaging Spectrometer: Mission and Instrument Concepts for Earth-Orbiting CubeSats. 12, 044001, 12–21. doi:10.1117/1.jrs.12.044001

Bidigare, R. R., Morrow, J. H., and Kiefer, D. A. (1989). Derivative Analysis of Spectral Absorption by Photosynthetic Pigments in the Western Sargasso Sea. *J. Mar. Res.* 47, 323–341. doi:10.1357/002224089785076325

Blaschke, T. (2010). Object Based Image Analysis for Remote Sensing. *ISPRS J. Photogrammetry Remote Sensing* 65, 2–16. doi:10.1016/j.isprsjprs.2009.06.004

Blondeau-Patissier, D., Gower, J. F. R., Dekker, A. G., Phinn, S. R., and Brando, V. E. (2014). A Review of Ocean Color Remote Sensing Methods and Statistical Techniques for the Detection, Mapping and Analysis of Phytoplankton Blooms in Coastal and Open Oceans. *Prog. oceanography* 123, 123–144. doi:10.1016/j.pocean.2013.12.008

Bolch, E. A., Hestir, E. L., and Khanna, S. (2021). Performance and Feasibility of Drone-Mounted Imaging Spectroscopy for Invasive Aquatic Vegetation Detection. in *Remote Sens.* 13, 582. doi:10.3390/rs13040582

Bolch, E. A., Santos, M. J., Ade, C., Khanna, S., Basinger, N. T., Reader, M. O., et al. (2020). "Remote Detection of Invasive Alien Species," in *Remote Sensing Of Plant Biodiversity* (Cham, Switzerland: Springer), 267–307. doi:10.1007/978-3-030-33157-3_12

Bongiorno, D. L., Bryson, M., Bridge, T. C. L., Dansereau, D. G., and Williams, S. B. (2018). Coregistered Hyperspectral and Stereo Image Seafloor Mapping from an Autonomous Underwater Vehicle. *J. Field Robotics* 35, 312–329. doi:10.1002/rob.21713

Boucher, Y., Poutier, L., Achard, V., Lenot, X., and Miesch, C. (2002). "Validation and Robustness of an Atmospheric Correction Algorithm for Hyperspectral Images," in *Algorithms and Technologies for Multispectral, Hyperspectral, and Ultraspectral Imagery VIII* (Washington, DC: International Society for Optics and Photonics), 459–470.

Bracher, A., Bouman, H. A., Brewin, R. J. W., Bricaud, A., Brotas, V., Ciotti, A. M., et al. (2017a). Obtaining Phytoplankton Diversity from Ocean Color: A Scientific Roadmap for Future Development. *Front. Mar. Sci.* 4, 55. doi:10.3389/fmars.2017.00055

Bracher, A., Dinter, T., Wolanin, A., Rozanov, V. V., Losa, S. N., Soppa, M. A., et al. (2017b). "Global Monthly Mean Chlorophyll a Surface Concentrations from August 2002 to April 2012 for Diatoms, Coccolithophores and Cyanobacteria from PhytoDOAS Algorithm Version 3.3 Applied to SCIAMACHY Data, Link to NetCDF Files in ZIP Archive," PANGEA. doi:10.1594/PANGAEA.870486

Bracher, A., Vountas, M., Dinter, T., Burrows, J. P., Röttgers, R., and Peeken, I. (2009). Quantitative Observation of Cyanobacteria and Diatoms from Space Using PhytoDOAS on SCIAMACHY Data. *Biogeosciences* 6, 751–764. doi:10.5194/bg-6-751-2009

Bracher, A., Xi, H., Dinter, T., Mangin, A., Strass, V., Von Appen, W.-J., et al. (2020a). High Resolution Water Column Phytoplankton Composition across the Atlantic Ocean from Ship-Towed Vertical Undulating Radiometry. *Front. Mar. Sci.* 7, 235. doi:10.3389/fmars.2020.00235

Bracher, A., Xi, H., Dinter, T., and Wiegmann, S. (2020b). Phytoplankton Pigment Concentration and Phytoplankton Groups Measured on Water Samples and from Radiometric Measurements Obtained during POLARSTERN Cruise PS113 in the Atlantic Ocean. doi:10.1594/PANGAEA.913536

Brando, V. E., Anstee, J. M., Wettle, M., Dekker, A. G., Phinn, S. R., and Roelfsema, C. (2009). A Physics Based Retrieval and Quality Assessment of Bathymetry from Suboptimal Hyperspectral Data. *Remote Sensing Environ.* 113, 755–770. doi:10.1016/j.rse.2008.12.003

Breiman, L. (2001). Random Forests. *Machine Learn.* 45, 5–32. doi:10.1023/a:1010933404324

Bulgarelli, B., and Zibordi, G. (2018). On the Detectability of Adjacency Effects in Ocean Color Remote Sensing of Mid-latitude Coastal Environments by SeaWiFS, MODIS-A, MERIS, OLCI, OLI and MSI. *Remote sensing Environ.* 209, 423–438. doi:10.1016/j.rse.2017.12.021

Cael, B. B., Chase, A., and Boss, E. (2020). Information Content of Absorption Spectra and Implications for Ocean Color Inversion. *Appl. Opt.* 59, 3971–3984. doi:10.1364/ao.389189

Carder, K. L., Reinersman, P., Chen, R. F., Muller-Karger, F., Davis, C. O., and Hamilton, M. (1993). AVIRIS Calibration and Application in Coastal Oceanic Environments. *Remote Sensing Environ.* 44, 205–216. doi:10.1016/0034-4257(93)90016-q

Casey, K. A., Rousseaux, C. S., Gregg, W. W., Boss, E., Chase, A. P., Craig, S. E., et al. (2020). A Global Compilation of In Situ Aquatic High Spectral Resolution Inherent and Apparent Optical Property Data for Remote Sensing Applications. *Earth Syst. Sci. Data* 12, 1123–1139. doi:10.5194/essd-12-1123-2020

Castagna, A., Simis, S., Dierssen, H., Vanhellemont, Q., Sabbe, K., and Vyverman, W. (2020). Extending Landsat 8: Retrieval of an Orange Contra-band for Inland Water Quality Applications. *Remote Sensing* 12, 637. doi:10.3390/rs12040637

Catlett, D., and Siegel, D. A. (2018). Phytoplankton Pigment Communities Can Be Modeled Using Unique Relationships with Spectral Absorption Signatures in a Dynamic Coastal Environment. *J. Geophys. Res. Oceans* 123, 246–264. doi:10.1002/2017jc013195

Chang, G., Mahoney, K., Briggs-Whitmire, A., Kohler, D., Mobley, C., Lewis, M., et al. (2004). The New Age of Hyperspectral Oceanography. *oceanog* 17, 16–23. doi:10.5670/oceanog.2004.43

Chen, J., Cui, T., Ishizaka, J., and Lin, C. (2014). A Neural Network Model for Remote Sensing of Diffuse Attenuation Coefficient in Global Oceanic and Coastal Waters: Exemplifying the Applicability of the Model to the Coastal Regions in Eastern China Seas. *Remote Sensing Environ.* 148, 168–177. doi:10.1016/j.rse.2014.02.019

Cheng, C., Wei, Y., Sun, X., and Zhou, Y. (2013). Estimation of Chlorophyll-A Concentration in Turbid Lake Using Spectral Smoothing and Derivative Analysis. *Ijerph* 10, 2979–2994. doi:10.3390/ijerph10072979

Chennu, A., Färber, P., De'ath, G., de Beer, D., and Fabricius, K. E. (2017). A Diver-Operated Hyperspectral Imaging and Topographic Surveying System for Automated Mapping of Benthic Habitats. *Sci. Rep.* 7, 7122. doi:10.1038/s41598-017-07337-y

Chirayath, V., and Li, A. (2019). Next-Generation Optical Sensing Technologies for Exploring Ocean Worlds-NASA FluidCam, MiDAR, and NeMO-Net. *Front. Mar. Sci.* 6. doi:10.3389/fmars.2019.00521

Chomko, R. M., Gordon, H. R., Maritorena, S., and Siegel, D. A. (2003). Simultaneous Retrieval of Oceanic and Atmospheric Parameters for Ocean Color Imagery by Spectral Optimization: a Validation. *Remote Sensing Environ.* 84, 208–220. doi:10.1016/S0034-4257(02)00108-6

Chowdhary, J., Zhai, P., Boss, E., Dierssen, H. M., Frouin, R. J., Ibrahim, A. I., et al. (2019). Modeling Atmosphere-Ocean Radiative Transfer: A PACE Mission Perspective. *Front. Earth Sci.* 7, 100. doi:10.3389/feart.2019.00100

Clarke, G. L., Ewing, G. C., and Lorenzen, C. J. (1970). Spectra of Backscattered Light from the Sea Obtained from Aircraft as a Measure of Chlorophyll Concentration. *Science* 167, 1119–1121. doi:10.1126/science.167.3921.1119

Clementson, L. A., and Wojtasiewicz, B. (2019a). Dataset on the Absorption Characteristics of Extracted Phytoplankton Pigments. *Data in Brief* 24, 103875. doi:10.1016/j.dib.2019.103875

Clementson, L. A., and Wojtasiewicz, B. (2019b). Dataset on the In Vivo Absorption Characteristics and Pigment Composition of Various Phytoplankton Species. *Data in Brief* 25, 104020. doi:10.1016/j.dib.2019.104020

Cooley, T., Anderson, G. P., Felde, G. W., Hoke, M. L., Ratkowski, A. J., Chetwynd, J. H., et al. (2002). FLAASH, a MODTRAN4-based atmospheric correction algorithm, its application and validation. *IEEE Intern. Geosci. Remote Sensing Sympo.* 3, 1414–1418. doi:10.1109/IGARSS.2002.1026134

Colefax, A. P., Butcher, P. A., and Kelaher, B. P. (2018). The Potential for Unmanned Aerial Vehicles (UAVs) to Conduct Marine Fauna Surveys in Place of Manned Aircraft. *ICES J. Mar. Sci.* 75, 1–8. doi:10.1093/icesjms/fsx100

Collins, M., and Pattiaratchi, C. (1984). Identification of Suspended Sediment in Coastal Waters Using Airborne Thematic Mapper Data. *Int. J. Remote Sensing* 5, 635–657. doi:10.1080/01431168408948848

Colomina, I., and Molina, P. (2014). Unmanned Aerial Systems for Photogrammetry and Remote Sensing: A Review. *ISPRS J. photogrammetry remote sensing* 92, 79–97. doi:10.1016/j.isprsjprs.2014.02.013

Commonwealth of Australia (2019). Current and Future Value of Earth and Marine Observing to the Asia-Pacific Region. G. A. P. E. Corporation. Available at: https://www.industry.gov.au/sites/default/files/2019-11/current-and-future-value-of-earth-and-marine-observing-to-asia-pacific-region.pdf.A.

Cornet, V. J., and Joyce, K. E.. (in review) Assessing the Potential of Remotely-Sensed Drone Spectroscopy to Determine Live Coral Cover on Heron Reef. *Drones*.

Crabbé, A. H., Somers, B., Roberts, D. A., Halligan, K., Dennison, P., and Dudley, K. (2020). MESMA QGIS Plugin.

Craig, S. E., Lee, Z., and Du, K. (2020). *Top of Atmosphere, Hyperspectral Synthetic Dataset for PACE (Phytoplankton, Aerosol, and Ocean Ecosystem) Ocean Color Algorithm Development*. Washington, DC: National Aeronautics and Space Administration. doi:10.1594/PANGAEA.915747

Craig, S. E., Lohrenz, S. E., Lee, Z., Mahoney, K. L., Kirkpatrick, G. J., Schofield, O. M., et al. (2006). Use of Hyperspectral Remote Sensing Reflectance for Detection and Assessment of the Harmful Alga, Karenia Brevis. *Appl. Opt.* 45, 5414–5425. doi:10.1364/AO.45.005414

Cummings, M. E., and Endler, J. A. (2018). 25 Years of Sensory Drive: the Evidence and its Watery Bias. *Curr. Zool* 64, 471–484. doi:10.1093/cz/zoy043

Cutter, M. A., Johns, L. S., Lobb, D. R., Williams, T. L., and Settle, J. J. (2004). "Flight Experience of the Compact High-Resolution Imaging Spectrometer (CHRIS)," in *Imaging Spectrometry IX* (Washington, DC: International Society for Optics and Photonics), 392–405.

Davis, C., Bowles, J., Leathers, R., Korwan, D., Downes, T. V., Snyder, W., et al. (2002). Ocean PHILLS Hyperspectral Imager: Design, Characterization, and Calibration. *Opt. Express* 10, 210–221. doi:10.1364/oe.10.000210

Davis, C. O. (2001). *Airborne Hyperspectral Remote Sensing*. Washington, DC: Naval Research Lab. . Available at: https://apps.dtic.mil/sti/citations/ADA625021 (Accessed November 10, 2020) doi:10.21236/ada625021

De Keukelaere, L., Sterckx, S., Adriaensen, S., Knaeps, E., Reusen, I., Giardino, C., et al. (2018). Atmospheric Correction of Landsat-8/OLI and Sentinel-2/MSI Data Using iCOR Algorithm: Validation for Coastal and Inland Waters. *Eur. J. Remote Sensing* 51, 525–542. doi:10.1080/22797254.2018.1457937

Dekker, A., (2018). Feasibility Study for an Aquatic Ecosystem Earth Observing System. Available at: www.ceos.org (Committee on Earth Observation Satellites (CEOS).

Dekker, A. G., Brando, V. E., Anstee, J., Pinnel, N., and Held, A. (2001). "Preliminary Assessment of the Performance of Hyperion in Coastal Waters. Cal/Val Activities in Moreton Bay, Queensland, Australia," in *IGARSS 2001. Scanning the Present and Resolving the Future. Proceedings.*

IEEE 2001 International Geoscience and Remote Sensing Symposium (Cat. No. 01CH37217) (New York, NY: IEEE), 2665–2667.

Dekker, A. G., and Donze, M. (1994). "Imaging Spectrometry as a Research Tool for Inland Water Resources Analysis," in *Imaging Spectrometry—a Tool for Environmental Observations* (Springer), 295–317.

Dickey, T. D., and Chang, G. C. (2002). *Recent Advances and Future Visions: Temporal Variability of Optical and Bio-Optical Properties of the Ocean*, 14. Washington, Dc: Oceanography Society, 15–29.

Dierssen, H., Bracher, A., Brando, V., Loisel, H., and Ruddick, K. (2020). Data Needs for Hyperspectral Detection of Algal Diversity across the Globe. *Oceanog* 33, 74–79. doi:10.5670/oceanog.2020.111

Dierssen, H. M., Bostrom, K. J., Chlus, A., Hammerstrom, K., Thompson, D. R., and Lee, Z. (2019). Pushing the Limits of Seagrass Remote Sensing in the Turbid Waters of Elkhorn Slough, California. *Remote Sensing* 11, 1664. doi:10.3390/rs11141664

Dierssen, H. M., Chlus, A., and Russell, B. (2015). Hyperspectral Discrimination of Floating Mats of Seagrass Wrack and the Macroalgae Sargassum in Coastal Waters of Greater Florida Bay Using Airborne Remote Sensing. *Remote Sensing Environ.* 167, 247–258. doi:10.1016/j.rse.2015.01.027

Dierssen, H., McManus, G. B., Chlus, A., Qiu, D., Gao, B.-C., and Lin, S. (2015b). Space Station Image Captures a Red Tide Ciliate Bloom at High Spectral and Spatial Resolution. *Proc. Natl. Acad. Sci. USA* 112, 14783–14787. doi:10.1073/pnas.1512538112

Dierssen, H. M. (2019). Hyperspectral Measurements, Parameterizations, and Atmospheric Correction of Whitecaps and Foam from Visible to Shortwave Infrared for Ocean Color Remote Sensing. *Front. Earth Sci.* 7, 14. doi:10.3389/feart.2019.00014

Dierssen, H. M., Kudela, R. M., Ryan, J. P., and Zimmerman, R. C. (2006). Red and Black Tides: Quantitative Analysis of Water-Leaving Radiance and Perceived Color for Phytoplankton, Colored Dissolved Organic Matter, and Suspended Sediments. *Limnol. Oceanogr.* 51, 2646–2659. doi:10.4319/lo.2006.51.6.2646

Dierssen, H. M. (2010). Perspectives on Empirical Approaches for Ocean Color Remote Sensing of Chlorophyll in a Changing Climate. *Proc. Natl. Acad. Sci.* 107, 17073–17078. doi:10.1073/pnas.0913800107

Doerffer, R., and Helmut, S. (2000). "Neural Network for Retrieval of Concentrations of Water Constituents with the Possibility of Detecting Exceptional Out of Scope Spectra," in *IGARSS 2000. IEEE 2000 International Geoscience and Remote Sensing Symposium. Taking the Pulse of the Planet: The Role of Remote Sensing in Managing the Environment. Proceedings (Cat. No.00CH37120)*, Berlin, Germany: Springer. 2, 714–717. doi:10.1109/IGARSS.2000.861680

Doubleday, J., Chien, S., Norton, C., Wagstaff, K., Thompson, D. R., Bellardo, J., et al. (2015). "Autonomy for Remote Sensing—Experiences from the IPEX CubeSat," in Proceedings of the 2015 IEEE International Geoscience and Remote Sensing Symposium (IGARSS), Milan, Italy, July 26–31, 2015. 5308–5311.

Duffy, J. E., Amaral-Zettler, L. A., Fautin, D. G., Paulay, G., Rynearson, T. A., Sosik, H. M., et al. (2013). Envisioning a Marine Biodiversity Observation Network. *Bioscience* 63, 350–361. doi:10.1525/bio.2013.63.5.8

IOCCG (2019). "Synergy between Ocean Colour and Biogeochemical/Ecosystem Models," in *IOCCG Report 19*. Editor S. Dutkiewicz, 184.

Erickson, Z. K., Frankenberg, C., Thompson, D. R., Thompson, A. F., and Gierach, M. (2019). Remote Sensing of Chlorophyll Fluorescence in the Ocean Using Imaging Spectrometry: Toward a Vertical Profile of Fluorescence. *Geophys. Res. Lett.* 46, 1571–1579. doi:10.1029/2018gl081273

Espel, D., Courty, S., Auda, Y., Sheeren, D., and Elger, A. (2020). Submerged Macrophyte Assessment in Rivers: An Automatic Mapping Method Using Pléiades Imagery. *Water Res.* 186, 116353. doi:10.1016/j.watres.2020.116353

Fichot, C. G., Downing, B. D., Bergamaschi, B. A., Windham-Myers, L., Marvin-DiPasquale, M., Thompson, D. R., et al. (2016). High-Resolution Remote Sensing of Water Quality in the San Francisco Bay-Delta Estuary. *Environ. Sci. Technol.* 50, 573–583. doi:10.1021/acs.est.5b03518

Filippi, A. M. (2007). Derivative-Neural Spectroscopy for Hyperspectral Bathymetric Inversion. *The Prof. Geographer* 59, 236–255. doi:10.1111/j.1467-9272.2007.00610.x

Freitas, F. H., and Dierssen, H. M. (2019). Evaluating the Seasonal and Decadal Performance of Red Band Difference Algorithms for Chlorophyll in an Optically Complex Estuary with Winter and Summer Blooms. *Remote Sensing Environ.* 231, 111228.

Frouin, R. J., Franz, B. A., Ibrahim, A., Knobelspiesse, K., Ahmad, Z., Cairns, B., et al. (2019). Atmospheric Correction of Satellite Ocean-Color Imagery during the PACE Era. *Front. Earth Sci.* 7, 145. doi:10.3389/feart.2019.00145

Gao, B.-C., Montes, M. J., Davis, C. O., and Goetz, A. F. H. (2009). Atmospheric Correction Algorithms for Hyperspectral Remote Sensing Data of Land and Ocean. *Remote sensing Environ.* 113, S17–S24. doi:10.1016/j.rse.2007.12.015

Garcia, R. A., McKinna, L. I. W., Hedley, J. D., and Fearns, P. R. C. S. (2014). Improving the Optimization Solution for a Semi-analytical Shallow Water Inversion Model in the Presence of Spectrally Correlated Noise. *Limnol. Oceanogr.* 12, 651–669. doi:10.4319/lom.2014.12.651

Garcia, R., Lee, Z., and Hochberg, E. (2018). Hyperspectral Shallow-Water Remote Sensing with an Enhanced Benthic Classifier. *Remote Sensing* 10, 147. doi:10.3390/rs10010147

Gege, P., and Dekker, A. G. (2020). Spectral and Radiometric Measurement Requirements for Inland, Coastal and Reef Waters. *Remote Sensing* 12, 2247. doi:10.3390/rs12142247

Gege, P. (2017). "Radiative Transfer Theory for Inland Waters," in *Bio-optical Modeling And Remote Sensing Of Inland Waters* (Amsterdam, Netherlands: Elsevier), 25–67. doi:10.1016/b978-0-12-804644-9.00002-1

Gege, P. (2015). "WASI-2D: A Software for the Analysis of Remote Sensing Images from Deep and Shallow Waters," in EOS Topical Meeting on Blue Photonics, Barcelona, Spain, May 11–13, 2015.

Gholizadeh, M., Melesse, A., and Reddi, L. (2016). A Comprehensive Review on Water Quality Parameters Estimation Using Remote Sensing Techniques. *Sensors* 16, 1298. doi:10.3390/s16081298

Giardino, C., Brando, V. E., Gege, P., Pinnel, N., Hochberg, E., Knaeps, E., et al. (2019). Imaging Spectrometry of Inland and Coastal Waters: State of the Art, Achievements and Perspectives. *Surv. Geophys.* 40, 401–429. doi:10.1007/s10712-018-9476-0

Giardino, C., Bresciani, M., Braga, F., Fabbretto, A., Ghirardi, N., Pepe, M., et al. (2020). First Evaluation of PRISMA Level 1 Data for Water Applications. *Sensors* 20, 4553. doi:10.3390/s20164553

Gilerson, A., Zhou, J., Hlaing, S., Ioannou, I., Schalles, J., Gross, B., et al. (2007). Fluorescence Component in the Reflectance Spectra from Coastal Waters. Dependence on Water Composition. *Opt. Express* 15, 15702–15721. doi:10.1364/oe.15.015702

Gislason, P. O., Benediktsson, J. A., and Sveinsson, J. R. (2006). Random Forests for Land Cover Classification. *Pattern Recognition Lett.* 27, 294–300. doi:10.1016/j.patrec.2005.08.011

Goldman, C. R., Richards, R. C., Paerl, H. W., Wrigley, R. C., Oberbeck, V. R., and Quaide, W. L. (1974). Limnological Studies and Remote Sensing of the Upper Truckee River Sediment Plume in Lake Tahoe, California-Nevada. *Remote Sensing Environ.* 3, 49–67. doi:10.1016/0034-4257(74)90038-8

Gordon, H. R., and Brown, O. B. (1988). A Semianalytic Radiance Model of Ocean Color. *J. Geophys. Res.* 93, 10909–10924. doi:10.1029/jd093id09p10909

Gordon, H. R., Brown, O. B., and Jacobs, M. M. (1975). Computed Relationships between the Inherent and Apparent Optical Properties of a Flat Homogeneous Ocean. *Appl. Opt.* 14, 417–427. doi:10.1364/AO.14.000417

Gordon, H. R., and McCluney, W. R. (1975). Estimation of the Depth of Sunlight Penetration in the Sea for Remote Sensing. *Appl. Opt.* 14, 413–416. doi:10.1364/AO.14.000413

Gordon, H. R., and Morel, A. Y. (1983). *Remote Assessment of Ocean Color for Interpretation of Satellite Visible Imagery: A Review*. New York, NY: Springer-Verlag.

Gower, J., King, S., Borstad, G., and Brown, L. (2008). The Importance of a Band at 709 Nm for Interpreting Water-Leaving Spectral Radiance. *Can. J. Remote Sensing* 34, 287–295.

Greb, S., Dekker, A., and Binding, C. (2018). *Earth Observations in Support of Global Water Quality Monitoring*. IOCCG Report Series, No. 17. Dartmouth, Canada: International Ocean Colour Coordinating Group.

Gregg, W. W., and Rousseaux, C. S. (2017). Simulating PACE Global Ocean Radiances. *Front. Mar. Sci.* 4. doi:10.3389/fmars.2017.00060

Guanter, L., Ruiz-Verdú, A., Odermatt, D., Giardino, C., Simis, S., Estellés, V., et al. (2010). Atmospheric Correction of ENVISAT/MERIS Data over Inland Waters:

Validation for European Lakes. *Remote Sensing Environ.* 114, 467–480. doi:10.1016/j.rse.2009.10.004

Harmel, T. (2016). "Recent Developments in the Use of Light Polarization for Marine Environment Monitoring from Space," in *Light Scattering Reviews 10: Light Scattering And Radiative Transfer Springer Praxis Books*. Editor A. A. Kokhanovsky (Berlin, Heidelberg: Springer), 41–84. doi:10.1007/978-3-662-46762-6_2

Haut, J. M., Gallardo, J. A., Paoletti, M. E., Cavallaro, G., Plaza, J., Plaza, A., et al. (2019). Cloud Deep Networks for Hyperspectral Image Analysis. *IEEE Trans. Geosci. Remote Sensing* 57, 9832–9848. doi:10.1109/TGRS.2019.2929731

Hedley, J. D., Russell, B. J., Randolph, K., Pérez-Castro, M. Á., Vásquez-Elizondo, R. M., Enríquez, S., et al. (2017). Remote Sensing of Seagrass Leaf Area Index and Species: The Capability of a Model Inversion Method Assessed by Sensitivity Analysis and Hyperspectral Data of Florida Bay. *Front. Mar. Sci.* 4, 362. doi:10.3389/fmars.2017.00362

Hedley, J., Mirhakak, M., Wentworth, A., and Dierssen, H. (2018). Influence of Three-Dimensional Coral Structures on Hyperspectral Benthic Reflectance and Water-Leaving Reflectance. *Appl. Sci.* 8, 2688. doi:10.3390/app8122688

Hedley, J., Roelfsema, C., Chollett, I., Harborne, A., Heron, S., Weeks, S., et al. (2016a). Remote Sensing of Coral Reefs for Monitoring and Management: A Review. *Remote Sensing* 8, 118. doi:10.3390/rs8020118

Hedley, J., Russell, B., Randolph, K., and Dierssen, H. (2016b). A Physics-Based Method for the Remote Sensing of Seagrasses. *Remote Sensing Environ.* 174, 134–147. doi:10.1016/j.rse.2015.12.001

Hestir, E. L., Brando, V. E., Bresciani, M., Giardino, C., Matta, E., Villa, P., et al. (2015). Measuring Freshwater Aquatic Ecosystems: The Need for a Hyperspectral Global Mapping Satellite Mission. *Remote Sensing Environ.* 167, 181–195. doi:10.1016/j.rse.2015.05.023

Heupel, E. E., Dierssen, H. M., Gao, B., Green, R. O., and Mouroulis, P. (2013). Hyperspectral Remote Sensing in Coastal Regions: Prism Field Validation in Elkhorn Slough. in Proceedings of the 2013 5th Workshop on Hyperspectral Image and Signal Processing: Evolution in Remote Sensing, Gainesville, FL, June 26–28, 2013. 1–4.

Hieronymi, M., Müller, D., and Doerffer, R. (2017). The OLCI Neural Network Swarm (ONNS): A Bio-Geo-Optical Algorithm for Open Ocean and Coastal Waters. *Front. Mar. Sci.* 4. doi:10.3389/fmars.2017.00140

Hill, V. J., Zimmerman, R. C., Bissett, W. P., Dierssen, H., and Kohler, D. D. (2014). Evaluating Light Availability, Seagrass Biomass, and Productivity Using Hyperspectral Airborne Remote Sensing in Saint Joseph's Bay, Florida. *Estuaries and Coasts*, 1–23.

Hochberg, E. J., and Atkinson, M. J. (2000). Spectral Discrimination of Coral Reef Benthic Communities. *Coral Reefs* 19, 164–171. doi:10.1007/s003380000087

Hovis, W. A., Clark, D. K., Anderson, F., Austin, R. W., Wilson, W. H., Baker, E. T., et al. (1980). Nimbus-7 Coastal Zone Color Scanner: System Description and Initial Imagery. *Science* 210, 60–63. doi:10.1126/science.210.4465.60

Hu, C., and Feng, L. (2016). Modified MODIS Fluorescence Line Height Data Product to Improve Image Interpretation for Red Tide Monitoring in the Eastern Gulf of Mexico. *J. Appl. Remote Sensing* 11. doi:10.1117/1.jrs.11.012003

Ibrahim, A., Franz, B., Ahmad, Z., Healy, R., Knobelspiesse, K., Gao, B.-C., et al. (2018). Atmospheric Correction for Hyperspectral Ocean Color Retrieval with Application to the Hyperspectral Imager for the Coastal Ocean (HICO). *Remote Sensing Environ.* 204, 60–75. doi:10.1016/j.rse.2017.10.041

Ioannou, I., Gilerson, A., Gross, B., Moshary, F., and Ahmed, S. (2013). Deriving Ocean Color Products Using Neural Networks. *Remote Sensing Environ.* 134, 78–91. doi:10.1016/j.rse.2013.02.015

Jamet, C., Loisel, H., and Dessailly, D. (2012). Retrieval of the Spectral Diffuse Attenuation Coefficient Kd (λ) in Open and Coastal Ocean Waters Using a Neural Network Inversion. *J. Geophys. Res. Oceans* 117. doi:10.1029/2012jc008076

Jamet, C., Thiria, S., Moulin, C., and Crépon, M. (2005). Use of a Neurovariational Inversion for Retrieving Oceanic and Atmospheric Constituents from Ocean Color Imagery: A Feasibility Study. *J. Atmos. Oceanic Tech.* 22, 460–475. doi:10.1175/jtech1688.1

Janssen, M., Charalabidis, Y., and Zuiderwijk, A. (2012). Benefits, Adoption Barriers and Myths of Open Data and Open Government. *Inf. Syst. Manage.* 29, 258–268. doi:10.1080/10580530.2012.716740

Jerlov, N. G. (1951). Optical Measurement of Particle Distribution in the Sea. *Tellus* 3, 122–128. doi:10.3402/tellusa.v3i3.8637

Jerlov, N. G. (1963). Optical Oceanography. *Oceanogr. Mar. Biol. Ann. Rev.* 1, 89–114.

Jeziorska, J. (2019). UAS for Wetland Mapping and Hydrological Modeling. *Remote Sensing* 11, 1997. doi:10.3390/rs11171997

Johnsen, G., Volent, Z., Dierssen, H. M., Pettersen, R., Van Aredelan, M., Søreide, F., et al. (2013). "Underwater Hyperspectral Imagery to Create Biogeochemical Maps of Seafloor Properties," In *Subsea Optics And Imaging* (Cambridge, United Kingdom: Woodhead Publishing).

Joyce, K. E., Duce, S., Leahy, S. M., Leon, J., and Maier, S. W. (2019). Principles and Practice of Acquiring Drone-Based Image Data in Marine Environments. *Mar. Freshw. Res.* 70, 952–963. doi:10.1071/mf17380

Kalinauskaitė, D. (2017). To Be Findable, Accessible, Interoperable and Reusable: Language Data and Technology Infrastructure for Supporting the FAIR Data Approach. Available at: https://www.vdu.lt/cris/handle/20.500.12259/35989 (Accessed November 10, 2020).

Kavanaugh, M. T., Oliver, M. J., Chavez, F. P., Letelier, R. M., Muller-Karger, F. E., and Doney, S. C. (2016). Seascapes as a New Vernacular for Pelagic Ocean Monitoring, Management and Conservation. *ICES J. Mar. Sci.* 73, 1839–1850. doi:10.1093/icesjms/fsw086

Khan, M. J., Khan, H. S., Yousaf, A., Khurshid, K., and Abbas, A. (2018). Modern Trends in Hyperspectral Image Analysis: a Review. *IEEE Access* 6, 14118–14129. doi:10.1109/access.2018.2812999

Klemas, V. V. (2015). Coastal and Environmental Remote Sensing from Unmanned Aerial Vehicles: An Overview. *J. coastal Res.* 315, 1260–1267. doi:10.2112/jcoastres-d-15-00005.1

Knaeps, E., Doxaran, D., Dogliotti, A., Nechad, B., Ruddick, K., Raymaekers, D., et al. (2018). The SeaSWIR Dataset. *Earth Syst. Sci. Data* 10, 1439–1449. doi:10.5194/essd-10-1439-2018

Krämer, M., and Senner, I. (2015). A Modular Software Architecture for Processing of Big Geospatial Data in the Cloud. *Comput. Graphics* 49, 69–81. doi:10.1016/j.cag.2015.02.005

Kramer, S. J., and Siegel, D. A. (2019). How Can Phytoplankton Pigments Be Best Used to Characterize Surface Ocean Phytoplankton Groups for Ocean Color Remote Sensing Algorithms?. *J. Geophys. Res. Oceans* 124, 7557–7574. doi:10.1029/2019jc015604

Kuchinke, C. P., Gordon, H. R., and Franz, B. A. (2009). Spectral Optimization for Constituent Retrieval in Case 2 Waters I: Implementation and Performance. *Remote Sensing Environ.* 113, 571–587. doi:10.1016/j.rse.2008.11.001

Kutser, T., Hedley, J., Giardino, C., Roelfsema, C., and Brando, V. E. (2020). Remote Sensing of Shallow Waters - A 50 Year Retrospective and Future Directions. *Remote Sensing Environ.* 240, 111619. doi:10.1016/j.rse.2019.111619

Lavender, S. (2014). Multi-sensor Ocean Colour Atmospheric Correction for Time-Series Data: Application to LANDSAT ETM+ and OLI Data. *EARSeL eProceedings* 13, 58–66.

Lavender, S. J., and Nagur, C. R. C. (2002). Mapping Coastal Waters with High Resolution Imagery: Atmospheric Correction of Multi-Height Airborne Imagery. *J. Opt. A: Pure Appl. Opt.* 4, S50–S55. doi:10.1088/1464-4258/4/4/363

Lee, Z., Carder, K., Arnone, R., and He, M. (2007). Determination of Primary Spectral Bands for Remote Sensing of Aquatic Environments. *Sensors* 7, 3428–3441. doi:10.3390/s7123428

Lee, Z., Carder, K. L., and Arnone, R. A. (2002). Deriving Inherent Optical Properties from Water Color: a Multiband Quasi-Analytical Algorithm for Optically Deep Waters. *Appl. Opt.* 41, 5755–5772. doi:10.1364/ao.41.005755

Liu, S., Gao, Y., Zheng, W., and Li, X. (2015). Performance of Two Neural Network Models in Bathymetry. *Remote sensing Lett.* 6, 321–330. doi:10.1080/2150704x.2015.1034885

Liu, Y.-N., Zhang, J., Zhang, Y., Sun, W.-W., Jiao, L.-L., Sun, D.-X., et al. (2019). The Advanced Hyperspectral Imager: Aboard China's GaoFen-5 Satellite. *IEEE Geosci. Remote Sens. Mag.* 7, 23–32. doi:10.1109/mgrs.2019.2927687

Lodhi, V., Chakravarty, D., and Mitra, P. (2018). Hyperspectral Imaging for Earth Observation: Platforms and Instruments. *J. Indian Inst. Sci.* 98, 429–443. doi:10.1007/s41745-018-0070-8

Louchard, E. M., Reid, R. P., Stephens, F. C., Davis, C. O., Leathers, R. A., and T. Valerie, D. (2003). Optical Remote Sensing of Benthic Habitats and Bathymetry in Coastal Environments at Lee Stocking Island, Bahamas: A Comparative Spectral Classification Approach. *Limnol. Oceanogr.* 48, 511–521. doi:10.4319/lo.2003.48.1_part_2.0511

Lubac, B., Loisel, H., Guiselin, N., Astoreca, R., Felipe Artigas, L., and Mériaux, X. (2008). Hyperspectral and Multispectral Ocean Color Inversions to Detect Phaeocystis Globosa Blooms in Coastal Waters. *J. Geophys. Res. Oceans* 113, 2008 Available at: http://onlinelibrary.wiley.com/doi/10.1029/2007JC004451/full (Accessed July 10, 2017). doi:10.1029/2007jc004451

Lubac, B., and Loisel, H. (2007). Variability and Classification of Remote Sensing Reflectance Spectra in the Eastern English Channel and Southern North Sea. *Remote Sensing Environ.* 110, 45–58. doi:10.1016/j.rse.2007.02.012

Lyzenga, D. R. (1978). Passive Remote Sensing Techniques for Mapping Water Depth and Bottom Features. *Appl. Opt.* 17, 379–383. doi:10.1364/ao.17.000379

Malone, T. C., DiGiacomo, P. M., Gonçalves, E., Knap, A. H., Talaue-McManus, L., and de Mora, S. (2014). A Global Ocean Observing System Framework for Sustainable Development. *Mar. Pol.* 43, 262–272. doi:10.1016/j.marpol.2013.06.008

Manfreda, S., McCabe, M., Miller, P., Lucas, R., Pajuelo Madrigal, V., Mallinis, G., et al. (2018). On the Use of Unmanned Aerial Systems for Environmental Monitoring. *Remote sensing* 10, 641. doi:10.3390/rs10040641

Matthews, M. W., Bernard, S., and Robertson, L. (2012). An Algorithm for Detecting Trophic Status (Chlorophyll-a), Cyanobacterial-Dominance, Surface Scums and Floating Vegetation in Inland and Coastal Waters. *Remote Sensing Environ.* 124, 637–652. doi:10.1016/j.rse.2012.05.032

Mazel, C. H. (2002). *Coastal Benthic Optical Properties (CoBOP): Optical Properties of Benthic Marine Organisms and Substrates*. Andover, MA: Physical Sciences Inc..

McClain, C. R. (2009). A Decade of Satellite Ocean Color Observations. *Annu. Rev. Mar. Sci.* 1, 19–42. doi:10.1146/annurev.marine.010908.163650

McKinna, L. I. W., Cetinić, I., Chase, A. P., and Werdell, P. J. (2019). Approach for Propagating Radiometric Data Uncertainties through NASA Ocean Color Algorithms. *Front. Earth Sci.* 7. doi:10.3389/feart.2019.00176

Mishra, D. R., Ogashawara, I., and Gitelson, A. A. (2017). *Bio-optical Modeling and Remote Sensing of Inland Waters*. Amsterdam, Netherlands: Elsevier.

Mobley, C. D. (1994). *Light and Water: Radiative Transfer in Natural Waters*. San Diego, CA: Academic Press.

Mobley, C. D., Sundman, L. K., Davis, C. O., Bowles, J. H., Downes, T. V., Leathers, R. A., et al. (2005). Interpretation of Hyperspectral Remote-Sensing Imagery by Spectrum Matching and Look-Up Tables. *Appl. Opt.* 44, 3576–3592. doi:10.1364/ao.44.003576

Mobley, C. D., Werdell, J., Franz, B., Ahmad, Z., and Bailey, S. (2016). *Atmospheric Correction for Satellite Ocean Color Radiometry*.

Mogstad, A. A., and Johnsen, G. (2017). Spectral Characteristics of Coralline Algae: a Multi-Instrumental Approach, with Emphasis on Underwater Hyperspectral Imaging. *Appl. Opt.* 56, 9957–9975. doi:10.1364/AO.56.009957

Moline, M. A., Blackwell, S. M., von Alt, C., Allen, B., Austin, T., Case, J., et al. (2005). Remote Environmental Monitoring Units: An Autonomous Vehicle for Characterizing Coastal Environments. *J. Atmos. Oceanic Tech.* 22, 1797–1808. doi:10.1175/JTECH1809.1

Montes, E., Djurhuus, A., Muller-Karger, F. E., Otis, D., Kelble, C. R., and Kavanaugh, M. T. (2020). Dynamic Satellite Seascapes as a Biogeographic Framework for Understanding Phytoplankton Assemblages in the Florida Keys National Marine Sanctuary, United States. *Front. Mar. Sci.* 7, 575. doi:10.3389/fmars.2020.00575

Moore, G. F., Aiken, J., and Lavender, S. J. (1999). The Atmospheric Correction of Water Colour and the Quantitative Retrieval of Suspended Particulate Matter in Case II Waters: Application to MERIS. *Int. J. Remote Sensing* 20, 1713–1733. doi:10.1080/014311699212434

Mortelmans, J., Deneudt, K., Cattrijsse, A., Beauchard, O., Daveloose, I., Vyverman, W., et al. (2019). Nutrient, Pigment, Suspended Matter and Turbidity Measurements in the Belgian Part of the North Sea. *Scientific data* 6, 1–8. doi:10.1038/s41597-019-0032-7

Mouw, C. B., Greb, S., Aurin, D., DiGiacomo, P. M., Lee, Z., and Twardowski, M. (2015). Aquatic color radiometry remote sensing of coastal and inland waters: Challenges and recommendations for future satellite missions. *Rem. Sens. Environ.* 160, 15–30. doi:10.1016/j.rse.2015.02.001

Mouroulis, P., Green, R. O., and Wilson, D. W. (2008). Optical Design of a Coastal Ocean Imaging Spectrometer. *Opt. Express* 16, 9087–9096. doi:10.1364/oe.16.009087

Mouroulis, P., Van Gorp, B., Green, R. O., Dierssen, H., Wilson, D. W., Eastwood, M., et al. (2014). Portable Remote Imaging Spectrometer Coastal Ocean Sensor: Design, Characteristics, and First Flight Results. *Appl. Opt.* 53, 1363–1380. doi:10.1364/ao.53.001363

Müller, R., Avbelj, J., Carmona, E., Eckardt, A., Gerasch, B., Graham, L., et al. (2016). The New Hyperspectral Sensor Desis on the Multi-Payload Platform Muses Installed on the Iss. *Int. Arch. Photogramm. Remote Sens. Spat. Inf. Sci.* XLI-B1, 461–467. doi:10.5194/isprsarchives-xli-b1-461-2016

Muller-Karger, F. E., Hestir, E., Ade, C., Turpie, K., Roberts, D. A., Siegel, D., et al. (2018). Satellite Sensor Requirements for Monitoring Essential Biodiversity Variables of Coastal Ecosystems. *Ecol. Appl.* 28, 749–760. doi:10.1002/eap.1682

Mumby, P., Green, E., Edwards, A., and Clark, C. (1997). Measurement of Seagrass Standing Crop Using Satellite and Digital Airborne Remote Sensing. *Mar. Ecol. Prog. Ser.* 159, 51–60. doi:10.3354/meps159051

Murfitt, S. L., Allan, B. M., Bellgrove, A., Rattray, A., Young, M. A., and Ierodiaconou, D. (2017). Applications of Unmanned Aerial Vehicles in Intertidal Reef Monitoring. *Scientific Rep.* 7, 1–11. doi:10.1038/s41598-017-10818-9

Muslim, A. M., Chong, W. S., Safuan, C. D. M., Khalil, I., and Hossain, M. S. (2019). Coral Reef Mapping of UAV: a Comparison of Sun Glint Correction Methods. *Remote Sensing* 11, 2422. doi:10.3390/rs11202422

Neeley, A. R., and Mannino, A.IOCCG (2018). Ocean Optics and Biogeochemistry Protocols for Satellite Ocean Colour Sensor Validation; Volume 1.0. Inherent Optical Property Measurements and Protocols: Absorption Coefficient. *Int. Ocean Colour Coordinating Group (Ioccg)*. doi:10.25607/OBP-119

Nguyen, H., Cressie, N., and Hobbs, J. (2019). Sensitivity of Optimal Estimation Satellite Retrievals to Misspecification of the Prior Mean and Covariance, with Application to OCO-2 Retrievals. *Remote Sensing* 11, 2770. doi:10.3390/rs11232770

Nowak, M. M., Dziób, K., and Bogawski, P. (2018). Unmanned Aerial Vehicles (UAVs) in Environmental Biology: A Review. *Eur. J. Ecol.* 4, 56–74.

Omanović, D., Santinelli, C., Marcinek, S., and Gonnelli, M. (2019). ASFit - an All-Inclusive Tool for Analysis of UV–Vis Spectra of Colored Dissolved Organic Matter (CDOM). *Comput. Geosciences* 133, 104334. doi:10.1016/j.cageo.2019.104334

Ortiz, J. D., Avouris, D. M., Schiller, S. J., Luvall, J. C., Lekki, J. D., Tokars, R. P., et al. (2019). Evaluating Visible Derivative Spectroscopy by Varimax-Rotated, Principal Component Analysis of Aerial Hyperspectral Images from the Western Basin of Lake Erie. *J. Great Lakes Res.* 45, 522–535. doi:10.1016/j.jglr.2019.03.005

Pahlevan, N., Smith, B., Schalles, J., Binding, C., Cao, Z., Ma, R., et al. (2020). Seamless Retrievals of Chlorophyll-A from Sentinel-2 (MSI) and Sentinel-3 (OLCI) in Inland and Coastal Waters: A Machine-Learning Approach. *Remote Sensing Environ.* 240, 111604. doi:10.1016/j.rse.2019.111604

Palacios, S. L., Kudela, R. M., Guild, L. S., Negrey, K. H., Torres-Perez, J., and Broughton, J. (2015). Remote Sensing of Phytoplankton Functional Types in the Coastal Ocean from the HyspIRI Preparatory Flight Campaign. *Remote Sensing Environ.* 167, 269–280. doi:10.1016/j.rse.2015.05.014

Palmer, S. C., Kutser, T., and Hunter, P. D. (2015). *Remote Sensing of Inland Waters: Challenges, Progress and Future Directions. Rem. Sens. Environ.* 157, 1–8. doi:10.1016/j.rse.2014.09.021

Paoletti, M. E., Haut, J. M., Plaza, J., and Plaza, A. (2019). Deep Learning Classifiers for Hyperspectral Imaging: A Review. *ISPRS J. Photogrammetry Remote Sensing* 158, 279–317. doi:10.1016/j.isprsjprs.2019.09.006

Parsons, M., Bratanov, D., Gaston, K., and Gonzalez, F. (2018). UAVs, Hyperspectral Remote Sensing, and Machine Learning Revolutionizing Reef Monitoring. *Sensors* 18, 2026. doi:10.3390/s18072026

Pettit, E. (1936). On the Color of Crater Lake Water. *Proc. Natl. Acad. Sci.* 22, 139–146. doi:10.1073/pnas.22.2.139

Phinn, S. R., Roelfsema, C. M., and Mumby, P. J. (2012). Multi-scale, Object-Based Image Analysis for Mapping Geomorphic and Ecological Zones on Coral Reefs. *Int. J. Remote Sensing* 33, 3768–3797. doi:10.1080/01431161.2011.633122

Pietzsch, T., Saalfeld, S., Preibisch, S., and Tomancak, P. (2015). BigDataViewer: Visualization and Processing for Large Image Data Sets. *Nat. Methods* 12, 481–483. doi:10.1038/nmeth.3392

Plaza, A., Du, Q., Chang, Y.-L., and King, R. L. (2011). High Performance Computing for Hyperspectral Remote Sensing. *IEEE J. Sel. Top. Appl. Earth Observations Remote Sensing* 4, 528–544. doi:10.1109/JSTARS.2010.2095495

Polcyn, F. C., Brown, W. L., and Sattinger, I. J. (1970). *The Measurement of Water Depth by Remote Sensing Techniques*. Report 8973-26F. Ann Arbor, MI: Willow Run Laboratories, The University of Michigan.

Preisendorfer, R. W. (1976). *Hydrologic Optics*. Honolulu, Hawaii: U.S. Dept. of Commerce, National Oceanic and Atmospheric Administration.

Preisendorfer, R. W., and Mobley, C. D. (1988). Principal Component Analysis in Meteorology and Oceanography. *Dev. Atmos. Sci.* 17.

Pu, H., Liu, D., Qu, J.-H., and Sun, D.-W. (2017). Applications of Imaging Spectrometry in Inland Water Quality Monitoring—A Review of Recent Developments. *Water Air Soil Pollut.* 228, 131. doi:10.1007/s11270-017-3294-8

Qu, Z., Kindel, B. C., and Goetz, A. F. (2003). The High Accuracy Atmospheric Correction for Hyperspectral Data (HATCH) Model. *IEEE Trans. Geosci. Remote Sensing* 41, 1223–1231.

Raman, C. V. (1922). On the Molecular Scattering of Light in Water and the Colour of the Sea. *Proc. R. Soc. Lond. Ser. A, Containing Pap. a Math. Phys. Character* 101, 64–80. doi:10.1098/rspa.1922.0025

Rebelo, A. J., Somers, B., Esler, K. J., and Meire, P. (2018). Can Wetland Plant Functional Groups Be Spectrally Discriminated?. *Remote Sensing Environ.* 210, 25–34. doi:10.1016/j.rse.2018.02.031

Reinersman, P. N., and Carder, K. L. (1995). Monte Carlo Simulation of the Atmospheric Point-Spread Function with an Application to Correction for the Adjacency Effect. *Appl. Opt.* 34, 4453–4471. doi:10.1364/ao.34.004453

Rodgers, C. D. (1998). Information Content and Optimisation of High Spectral Resolution Remote Measurements. *Adv. Space Res.* 21, 361–367. doi:10.1016/s0273-1177(97)00915-0

Roelfsema, C., Kovacs, E., Roos, P., Terzano, D., Lyons, M., and Phinn, S. (2018). Use of a Semi-automated Object Based Analysis to Map Benthic Composition, Heron Reef, Southern Great Barrier Reef. *Remote Sensing Lett.* 9, 324–333. doi:10.1080/2150704x.2017.1420927

Rozanov, V.V., Dinter, T., Rozanov, A.V., Wolanin, A., Bracher, A., and Burrows, J. P. (2017). Radiative transfer modeling through terrestrial atmosphere and ocean accounting for inelastic processes: Software package SCIATRAN. *J. Quant Spectrosc. Radiat. Transf.* 194, 65–85. doi:10.1016/j.jqsrt.2017.03.009

Rozanov, V. V., Rozanov, A. V., Kokhanovsky, A. A., and Burrows, J. P. (2014). Radiative Transfer through Terrestrial Atmosphere and Ocean: Software Package SCIATRAN. *J. Quantitative Spectrosc. Radiative Transfer* 133, 13–71. doi:10.1016/j.jqsrt.2013.07.004

Russell, B. J., and Dierssen, H. M. (2015). Use of Hyperspectral Imagery to Assess Cryptic Color Matching in Sargassum Associated Crabs. *PloS one* 10. doi:10.1371/journal.pone.0136260

Ryan, J., Davis, C., Tufillaro, N., Kudela, R., and Gao, B.-C. (2014). Application of the Hyperspectral Imager for the Coastal Ocean to Phytoplankton Ecology Studies in Monterey Bay, CA, USA. *Remote Sensing* 6, 1007–1025. doi:10.3390/rs6021007

Ryan, J. P., Johnson, S. B., Sherman, A., Rajan, K., Py, F., Thomas, H., et al. (2010). Mobile Autonomous Process Sampling within Coastal Ocean Observing Systems. *Limnol. Oceanogr. Methods* 8, 394–402. doi:10.4319/lom.2010.8.394

Salcedo-Sanz, S., Cuadra, L., and Vermeij, M. J. A. (2016). A Review of Computational Intelligence Techniques in Coral Reef-Related Applications. *Ecol. Inform.* 32, 107–123. doi:10.1016/j.ecoinf.2016.01.008

Sandidge, J. C., and Holyer, R. J. (1998). Coastal Bathymetry from Hyperspectral Observations of Water Radiance. *Remote Sensing Environ.* 65, 341–352. doi:10.1016/s0034-4257(98)00043-1

Santer, R., and Schmechtig, C. (2000). Adjacency Effects on Water Surfaces: Primary Scattering Approximation and Sensitivity Study. *Appl. Opt.* 39, 361–375. doi:10.1364/AO.39.000361

Santos, M. J., Hestir, E. L., Khanna, S., and Ustin, S. L. (2012). Image Spectroscopy and Stable Isotopes Elucidate Functional Dissimilarity between Native and Nonnative Plant Species in the Aquatic Environment. *New Phytol.* 193, 683–695. doi:10.1111/j.1469-8137.2011.03955.x

Santos, M. J., Khanna, S., Hestir, E. L., Greenberg, J. A., and Ustin, S. L. (2016). Measuring Landscape-Scale Spread and Persistence of an Invaded Submerged Plant Community from Airborne Remote Sensing. *Ecol. Appl.* 26, 1733–1744. doi:10.1890/15-0615

Sathyendranath, S., Rao, D. V. S., Chen, Z., Stuart, V., Platt, T., Bugden, G. L., et al. (1997). Aircraft Remote Sensing of Toxic Phytoplankton Blooms: a Case Study from Cardigan River, Prince Edward Island. *Can. J. remote sensing* 23, 15–23. doi:10.1080/07038992.1997.10874674

Secretariat of the Convention on Biological Diversity (2020). Administrator of Global Biodiversity: SpringerLink. Available at: https://link.springer.com/article/10.1007/s10531-006-9043-8 (Accessed November 9, 2020).

Shang, S., Lee, Z., Lin, G., Hu, C., Shi, L., Zhang, Y., et al. (2017). Sensing an Intense Phytoplankton Bloom in the Western Taiwan Strait from Radiometric Measurements on a UAV. *Remote Sensing Environ.* 198, 85–94. doi:10.1016/j.rse.2017.05.036

Shoulejkin, W. (1923). On the Color of the Sea. *Phys. Rev.* 22, 85–100. doi:10.1103/PhysRev.22.85

Smith, M. E., and Bernard, S. (2020). Satellite Ocean Color Based Harmful Algal Bloom Indicators for Aquaculture Decision Support in the Southern Benguela. *Front. Mar. Sci.* 7, 61. doi:10.3389/fmars.2020.00061

Smith, V., Rogers, R., and Reed, L. (1975). Automated Mapping and Inventory of Great Barrier Reef Zonation with LANDSAT Data. OCEAN 75 Conference (New York, NY: IEEE), 775–780.

Spyrakos, E., O'Donnell, R., Hunter, P. D., Miller, C., Scott, M., Simis, S. G. H., et al. (2018). Optical Types of Inland and Coastal Waters. *Limnol. Oceanogr.* 63, 846–870. doi:10.1002/lno.10674

Stamnes, K., Li, W., Yan, B., Eide, H., Barnard, A., Pegau, W. S., et al. (2003). Accurate and Self-Consistent Ocean Color Algorithm: Simultaneous Retrieval of Aerosol Optical Properties and Chlorophyll Concentrations. *Appl. Opt.* 42, 939–951. doi:10.1364/ao.42.000939

Stamnes, S., Hostetler, C., Ferrare, R., Burton, S., Liu, X., Hair, J., et al. (2018). Simultaneous Polarimeter Retrievals of Microphysical Aerosol and Ocean Color Parameters from the "MAPP" Algorithm with Comparison to High-Spectral-Resolution Lidar Aerosol and Ocean Products. *Appl. Opt.* 57, 2394–2413. doi:10.1364/ao.57.002394

Steinmetz, F., Deschamps, P.-Y., and Ramon, D. (2011). Atmospheric Correction in Presence of Sun Glint: Application to MERIS. *Opt. Express* 19, 9783–9800. doi:10.1364/OE.19.009783

Sterckx, S., Knaeps, E., and Ruddick, K. (2011). Detection and Correction of Adjacency Effects in Hyperspectral Airborne Data of Coastal and Inland Waters: the Use of the Near Infrared Similarity Spectrum. *Int. J. Remote Sensing* 32, 6479–6505. doi:10.1080/01431161.2010.512930

Striebel, M., Behl, S., Diehl, S., and Stibor, H. (2009). Spectral Niche Complementarity and Carbon Dynamics in Pelagic Ecosystems. *The Am. Naturalist* 174, 141–147. doi:10.1086/599294

Strong, A. E. (1974). Remote Sensing of Algal Blooms by Aircraft and Satellite in Lake Erie and Utah Lake. *Remote sensing Environ.* 3, 99–107. doi:10.1016/0034-4257(74)90052-2

Szabó, G., Bertalan, L., Barkóczi, N., Kovács, Z., Burai, P., and Lénárt, C. (2018). "Zooming on Aerial Survey," in *Small Flying Drones* (Berlin, Germany: Springer), 91–126. doi:10.1007/978-3-319-66577-1_4

Thamaga, K. H., and Dube, T. (2018). Remote Sensing of Invasive Water Hyacinth (Eichhornia crassipes): A Review on Applications and Challenges. *Remote Sensing Appl. Soc. Environ.* 10, 36–46. doi:10.1016/j.rsase.2018.02.005

Thompson, D. R., Cawse-Nicholson, K., Erickson, Z., Fichot, C. G., Frankenberg, C., Gao, B.-C., et al. (2019). A Unified Approach to Estimate Land and Water Reflectances with Uncertainties for Coastal Imaging Spectroscopy. *Remote Sensing Environ.* 231, 111198. doi:10.1016/j.rse.2019.05.017

Thompson, D. R., Gao, B.-C., Green, R. O., Roberts, D. A., Dennison, P. E., and Lundeen, S. R. (2015). Atmospheric Correction for Global Mapping Spectroscopy: ATREM Advances for the HyspIRI Preparatory Campaign. *Remote Sensing Environ.* 167, 64–77. doi:10.1016/j.rse.2015.02.010

Tong, Q., Zheng, L., Xue, Y., Zhang, B., Zhao, Y., and Liu, L. (2001). "Hyperspectral Remote Sensing in China," in *Multispectral and Hyperspectral Image Acquisition and Processing* (Washington, DC: International Society for Optics and Photonics), 1–9.

Torrecilla, E., Stramski, D., Reynolds, R. A., Millán-Núñez, E., and Piera, J. (2011). Cluster Analysis of Hyperspectral Optical Data for Discriminating Phytoplankton Pigment Assemblages in the Open Ocean. *Remote Sensing Environ.* 115, 2578–2593. doi:10.1016/j.rse.2011.05.014

Twardowski, M., and Tonizzo, A. (2018). Ocean Color Analytical Model Explicitly Dependent on the Volume Scattering Function. *Appl. Sci.* 8, 2684. doi:10.3390/app8122684

Tyler, A. N., Hunter, P. D., Spyrakos, E., Groom, S., Constantinescu, A. M., and Kitchen, J. (2016). Developments in Earth Observation for the Assessment and Monitoring of Inland, Transitional, Coastal and Shelf-Sea Waters. *Sci. Total Environ.* 572, 1307–1321. doi:10.1016/j.scitotenv.2016.01.020

Tyler, J. E. (1970). *Expedition Report, SCOR Working Group 15, Discoverer Expedition*. San Diego, CA: Scripps Institution of Oceanography.

Uitz, J., Stramski, D., Reynolds, R. A., and Dubranna, J. (2015). Assessing Phytoplankton Community Composition from Hyperspectral Measurements of Phytoplankton Absorption Coefficient and Remote-Sensing Reflectance in Open-Ocean Environments. *Remote Sensing Environ.* 171, 58–74. doi:10.1016/j.rse.2015.09.027

Vandermeulen, R. A., Mannino, A., Craig, S. E., and Werdell, P. J. (2020). 150 Shades of Green: Using the Full Spectrum of Remote Sensing Reflectance to Elucidate Color Shifts in the Ocean. *Remote Sensing Environ.* 247, 111900. doi:10.1016/j.rse.2020.111900

Vandermeulen, R. A., Mannino, A., Neeley, A., Werdell, J., and Arnone, R. (2017). Determining the Optimal Spectral Sampling Frequency and Uncertainty Thresholds for Hyperspectral Remote Sensing of Ocean Color. *Opt. Express* 25, A785–A797. doi:10.1364/oe.25.00a785

Vanhellemont, Q. (2019). Adaptation of the Dark Spectrum Fitting Atmospheric Correction for Aquatic Applications of the Landsat and Sentinel-2 Archives. *Remote Sensing Environ.* 225, 175–192. doi:10.1016/j.rse.2019.03.010

Velez-Reyes, M., rosario-torres, S., and Jimenez-Rodriguez, L. (2015). The MATLAB Hyperspectral Image Analysis Toolbox. doi:10.13140/RG.2.1.1220.7203

Voss, K. J., Johnson, C. B., Yarbrough, M. A., Gleason, A., Flora, S. J., Feinholz, M. E., et al. (2017). An Overview of the Marine Optical Buoy (MOBY): Past, Present and Future. Proceedings of the D-240 FRM4SOC-PROC1 Proceedings of WKP-1 (PROC-1) Fiducial Reference Measurements for Satellite Ocean Colour (FRM4SOC). *Tartu, Estonia*, 8–13.

Wang, P. (2004). A Method to Quantify the Uncertainties Associated with Semi-analytic Algorithm for Inversion of Ocean Color. Available at: https://digitalcommons.library.umaine.edu/etd/1560 (Accessed November 10, 2020).

Werdell, P. J., Franz, B. A., Bailey, S. W., Feldman, G. C., Boss, E., Brando, V. E., et al. (2013). Generalized Ocean Color Inversion Model for Retrieving Marine Inherent Optical Properties. *Appl. Opt.* 52, 2019. doi:10.1364/AO.52.002019

Werdell, P. J., McKinna, L. I. W., Boss, E., Ackleson, S. G., Craig, S. E., Gregg, W. W., et al. (2018). An Overview of Approaches and Challenges for Retrieving Marine Inherent Optical Properties from Ocean Color Remote Sensing. *Prog. oceanography* 160, 186–212. doi:10.1016/j.pocean.2018.01.001

Wernand, M. R. (2011). Poseidon's Paintbox: Historical Archives of Ocean Colour in Global-Change Perspective. PhDT.

Wernand, M. R., van der Woerd, H. J., and Gieskes, W. W. (2013). Trends in Ocean Colour and Chlorophyll Concentration from 1889 to 2000, Worldwide. Available at: http://dx.plos.org/10.1371/journal.pone.0063766 (Accessed December 7, 2015).

Wester-Ebbinghaus, W. (1980). Aerial Photography by Radio Controlled Model Helicopter. *Photogrammetric Rec.* 10, 85–92.

Wilson, A., Lindholm, D. M., Coddington, O., Pilewskie, P., and Kent, J. (2018). Hylatis, a Cloud-Based Hyperspectral Image Analysis Toolkit, 51. AGU Fall Meeting Abstracts. Available at: http://adsabs.harvard.edu/abs/2018AGUFMIN51B0579W (Accessed December 10, 2020).

Wolanin, A., Soppa, M., and Bracher, A. (2016). Investigation of Spectral Band Requirements for Improving Retrievals of Phytoplankton Functional Types. *Remote Sensing* 8, 871. doi:10.3390/rs8100871

Wu, D., Li, R., Zhang, F., and Liu, J. (2019). A Review on Drone-Based Harmful Algae Blooms Monitoring. *Environ. Monit. Assess.* 191, 211. doi:10.1007/s10661-019-7365-8

Wulder, M. A., White, J. C., Loveland, T. R., Woodcock, C. E., Belward, A. S., Cohen, W. B., et al. (2016). The Global Landsat Archive: Status, Consolidation, and Direction. *Remote Sensing Environ.* 185, 271–283. doi:10.1016/j.rse.2015.11.032

Xu, F., Gao, Z., Jiang, X., Ning, J., Zheng, X., Song, D., et al. (2017). "Mapping of Green Tide Using True Color Aerial Photographs Taken from a Unmanned Aerial Vehicle," in *Remote Sensing and Modeling of Ecosystems for Sustainability XIV* (Washington, DC: International Society for Optics and Photonics). doi:10.1117/12.2271732

Ye, H., Li, J., Li, T., Shen, Q., Zhu, J., Wang, X., et al. (2016). Spectral Classification of the Yellow Sea and Implications for Coastal Ocean Color Remote Sensing. *Remote Sensing* 8, 321. doi:10.3390/rs8040321

Yunus, A. P., Dou, J., Song, X., and Avtar, R. (2019). Improved Bathymetric Mapping of Coastal and Lake Environments Using Sentinel-2 and Landsat-8 Images. *Sensors* 19, 2788. doi:10.3390/s19122788

Zaneveld, J. R. V. (1995). A Theoretical Derivation of the Dependence of the Remotely Sensed Reflectance of the Ocean on the Inherent Optical Properties. *J. Geophys. Res.* 100 (13), 135–213. doi:10.1029/95jc00453

Zeng, C., Richardson, M., and King, D. J. (2017). The Impacts of Environmental Variables on Water Reflectance Measured Using a Lightweight Unmanned Aerial Vehicle (UAV)-based Spectrometer System. *ISPRS J. Photogrammetry Remote Sensing* 130, 217–230. doi:10.1016/j.isprsjprs.2017.06.004

Zhao, J., and Ghedira, H. (2014). Monitoring Red Tide with Satellite Imagery and Numerical Models: A Case Study in the Arabian Gulf. *Mar. Pollut. Bull.* 79, 305–313. doi:10.1016/j.marpolbul.2013.10.057

Zhu, Z., Wulder, M. A., Roy, D. P., Woodcock, C. E., Hansen, M. C., Radeloff, V. C., et al. (2019). Benefits of the Free and Open Landsat Data Policy. *Remote Sensing Environ.* 224, 382–385. doi:10.1016/j.rse.2019.02.016

Conflict of Interest: SL was employed by Pixalytics Ltd.

The remaining authors declare that the research was conducted in the absence of any commercial or financial relationships that could be construed as a potential conflict of interest.

Copyright © 2021 Dierssen, Ackleson, Joyce, Hestir, Castagna, Lavender and McManus. This is an open-access article distributed under the terms of the Creative Commons Attribution License (CC BY). The use, distribution or reproduction in other forums is permitted, provided the original author(s) and the copyright owner(s) are credited and that the original publication in this journal is cited, in accordance with accepted academic practice. No use, distribution or reproduction is permitted which does not comply with these terms.

frontiers in Environmental Science

ORIGINAL RESEARCH
published: 17 June 2021
doi: 10.3389/fenvs.2021.647966

Detection and Sourcing of CDOM in Urban Coastal Waters With UV-Visible Imaging Spectroscopy

Joshua P. Harringmeyer[1], Karl Kaiser[2,3†], David R. Thompson[4], Michelle M. Gierach[4], Curtis L. Cash[5] and Cédric G. Fichot[1]**

[1]Department of Earth and Environment, Boston University, Boston, MA, United States, [2]Department of Marine and Coastal Environmental Science, Texas A&M University Galveston Campus, Galveston, TX, United States, [3]Department of Oceanography, Texas A&M, College Station, TX, United States, [4]Jet Propulsion Laboratory, California Institute of Technology, Pasadena, CA, United States, [5]Environmental Monitoring Division, LA Sanitation and Environment, City of Los Angeles, Los Angeles, CA, United States

OPEN ACCESS

Edited by:
Sherry L. Palacios, California State University, Monterey Bay, United States

Reviewed by:
Ana B. Ruescas, University of Valencia, Spain
Shuisen Chen, Guangzhou Institute of Geography, China

***Correspondence:**
Joshua P. Harringmeyer
joshuaph@bu.edu
Cédric G. Fichot
cgfichot@bu.edu

†ORCID:
Karl Kaiser
orcid.org/0000-0002-4951-4665

Specialty section:
This article was submitted to Environmental Informatics and Remote Sensing, a section of the journal Frontiers in Environmental Science

Received: 30 December 2020
Accepted: 25 May 2021
Published: 17 June 2021

Citation:
Harringmeyer JP, Kaiser K, Thompson DR, Gierach MM, Cash CL and Fichot CG (2021) Detection and Sourcing of CDOM in Urban Coastal Waters With UV-Visible Imaging Spectroscopy. Front. Environ. Sci. 9:647966. doi: 10.3389/fenvs.2021.647966

Ultraviolet (UV)-visible imaging spectroscopy is an emerging and highly anticipated technology, expected to improve the remote sensing of coastal waters and expand its range of applications. Upcoming NASA satellite missions including PACE and GLIMR will feature imaging spectrometers capable of measuring hyperspectral remote-sensing reflectance (R_{rs}) across the visible range and well into the near-infrared and ultraviolet domains. The availability of UV reflectance is expected to facilitate the remote sensing of chromophoric dissolved organic matter (CDOM) in optically complex waters, thereby improving coastal water-quality monitoring. Although this argument is well supported by the dominance of CDOM absorption in the UV domain, few studies have directly evaluated the potential advantages conferred by UV reflectance for monitoring CDOM-related coastal water quality. Here, we took advantage of a 6-week wastewater diversion event in Santa Monica Bay, California in 2015 and the availability of Portable Remote Imaging SpectroMeter (PRISM) imagery acquired during the diversion to assess if UV-visible imaging spectroscopy could facilitate the detection of CDOM and help differentiate wastewater effluent-derived CDOM from other sources. A comparison of local empirical algorithms with varying amounts of spectral information implemented on PRISM data showed that incorporating UV R_{rs} as a predictor significantly improved retrieval of CDOM absorption coefficients (a_g). Optimal performance was reached when combining R_{rs}(365), R_{rs}(400), and R_{rs}(700) as predictors of a_g in a multiple linear regression. The use of the entire UV-visible spectrum (365–700 nm) in a partial-least-squares regression (PLSR) did not improve retrievals, indicating that a few carefully chosen predictors in the UV-visible domain were sufficient to empirically differentiate CDOM from phytoplankton in coastal waters minimally influenced by sediments or bottom reflectance. Finally, the development of a new fluorescence-based indicator of effluent-derived CDOM (effluent fluorescence ratio, *EFR*) helped demonstrate the feasibility of remotely detecting CDOM from wastewater. A PLSR-based algorithm using R_{rs}(365–700) provided reasonable *EFR* retrievals and successfully identified effluent-derived CDOM at the wastewater outfall when implemented on PRISM imagery. Although further work should investigate the influence of effluent-CDOM fluorescence on R_{rs} more mechanistically, these results

confirmed that UV-visible imaging spectrometers can facilitate coastal CDOM-related water quality monitoring and expand its range of applications.

Keywords: imaging spectroscopy, hyperspectral, UV reflectance, water quality, CDOM, fluorescence, wastewater, coastal

INTRODUCTION

Urban coastal waters are productive environments that provide important ecosystem services to humans, including the dilution of terrestrial inputs (IOCCG, 2008; Rabalais et al., 2009; McLaughlin et al., 2017), fisheries and aquaculture, and various recreational and transportation services (Halpern et al., 2012; Caron et al., 2017; Gierach et al., 2017). The rapid expansion of urban centers around the world has dramatically increased the impact of human activities on land use, runoff, hydrodynamics, atmospheric deposition, and local climate at the land-ocean interface, and these can influence the water quality of the adjacent coastal waters (McKinney, 2002; Halpern et al., 2008; Halpern et al., 2012). Increased runoff from impervious surfaces (Ackerman and Weisberg, 2003; Bay et al., 2003; Dojiri et al., 2003) and pollution point sources (e.g., wastewater effluent) can lead to elevated concentrations of nutrients, organic matter, and contaminants in urban coastal waters and negatively impact water quality in this environment. These water quality impacts have serious consequences for the services these ecosystems provide and for human health in these densely populated areas.

Chromophoric dissolved organic matter (CDOM) is a major optical water-quality indicator that can be diagnostic of runoff and point sources of pollution in urban coastal waters (IOCCG, 2015; Fichot et al., 2016; Cao et al., 2018). CDOM is ubiquitous and naturally present in coastal waters, where it is not only produced *in situ* by biological processes, but is also strongly influenced by terrestrial sources (e.g., soils) through runoff (Hansell and Carlson, 2014). The spectral optical properties of CDOM (absorption and fluorescence) have therefore been used in various proxies of terrestrial runoff and/or as indicators of dissolved organic matter (DOM) source and degradation state in coastal waters (Vodacek et al., 1997; Hernes and Benner, 2003; Stedmon and Markager, 2003; Boyd and Osburn, 2004; Chen et al., 2004; Helms et al., 2008; Tzortziou et al., 2008; Fichot and Benner, 2012; Murphy et al., 2013; Yamashita et al., 2013). In urban waters, wastewater effluent represents another potentially significant source of CDOM with characteristic optical properties (Goldman et al., 2012; Devlin et al., 2015), which can be leveraged and used in optical proxies indicative of CDOM-related pollution.

CDOM is optically active and therefore has the advantage of being amenable to ocean-color remote sensing (Siegel et al., 2002; Mannino et al., 2008; Swan et al., 2013; Cao et al., 2018; Werdell et al., 2018). Ocean-color remote sensing can facilitate the monitoring of several optical water quality indicators (e.g., phytoplankton, turbidity, CDOM) over large areas and could enable the detection of CDOM-related pollution in urban coastal waters (IOCCG, 2015). However, it faces major challenges in these types of waters, where a combination of difficult atmospheric corrections and optical complexity of the waters can lead to large uncertainties and errors in the derived water-quality products (Aurin and Dierssen, 2012; Werdell et al., 2018). Coastal waters are generally optically complex, (IOCCG, 2000) because they are influenced by a combination of riverine and coastal-wetland inputs, upwelling of deep water, phytoplankton blooms, and in some cases urban wastewater effluent. This optical complexity often cannot be accurately resolved using existing multispectral sensors, which have constrained spectral ranges and resolutions (Aurin and Dierssen, 2012; Dekker et al., 2018). Considering that CDOM optical properties are most prominent in the ultraviolet (UV) and blue regions, these spectral limitations are particularly restrictive for detecting CDOM and distinguishing among different CDOM sources. UV observations are beyond the spectral ranges of many current ocean color sensors, and phytoplankton can interfere with or even dominate optical variability at blue wavelengths in more phytoplankton-dominated waters (Mobley et al., 2005; Zhu et al., 2011; Fichot et al., 2016; Werdell et al., 2018).

Recent advances in imaging spectroscopy (hyperspectral imagery) with broader and finer spectral capabilities than multispectral ocean-color sensors are expected to improve retrieval accuracy for in-water constituents in complex coastal waters from remote-sensing reflectance, $R_{rs}(\lambda)$ (Mouw et al., 2015; Werdell et al., 2018). UV reflectance, in particular, is expected to facilitate the separation of chlorophyll-a and CDOM in optically complex waters. The upcoming NASA Plankton, Aerosol, Cloud, ocean Ecosystems (PACE) and Geosynchronous Littoral Imaging and Monitoring Radiometer (GLIMR) missions will provide UV-visible observations of the coastal ocean at high spectral resolution. These new spectral capabilities offer the potential to improve CDOM retrievals in optically complex coastal waters and to retrieve more specific optical properties of CDOM that are indicative of its source. However, few studies have directly assessed the utility of these new spectral capabilities for retrieving CDOM and differentiating its sources in coastal waters.

In this study, we evaluated the utility of UV-visible imaging spectroscopy for detecting CDOM accurately in urban coastal waters. We also tested the feasibility of remotely differentiating effluent-derived CDOM from other sources (e.g. terrestrial runoff). We specifically assessed the value of UV reflectance and of enhanced spectral resolution. This study took advantage of a 6-week wastewater diversion event and a related water-quality monitoring effort that took place in the urban waters of Santa Monica Bay (Southern California) in fall 2015 (City of Los Angeles, Environmental Monitoring Division, 2017; Trinh et al., 2017), and leveraged imagery from the NASA/JPL Portable Remote Imaging SpectroMeter (PRISM) airborne instrument (Mouroulis et al., 2014; Thompson et al., 2019). We

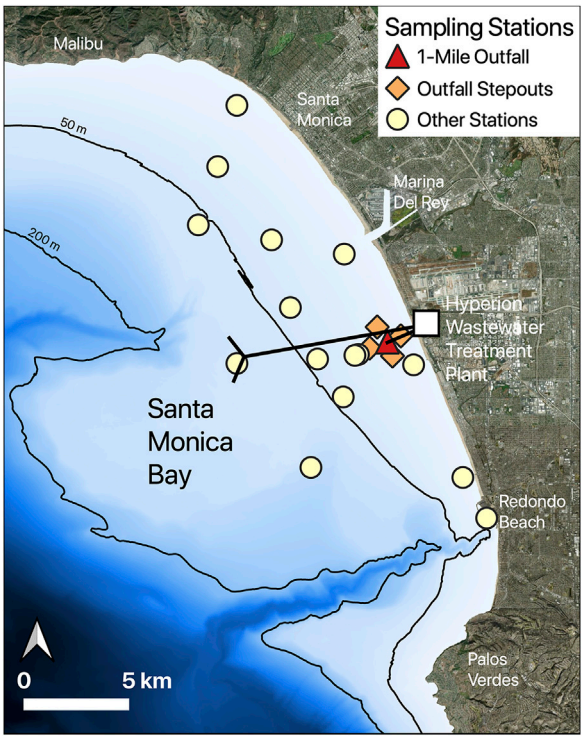

FIGURE 1 | Map of Santa Monica Bay with the sampling stations including the 1-mile outfall station (D9W, red triangle), the stepout stations surrounding the outfall (orange diamonds), and the other stations (yellow circles). The 1-mile and 5-mile outfall pipes extending from the Hyperion Wastewater Treatment Plant are represented by black lines.

used the PRISM data, as well as *in-situ* hyperspectral measurements of $R_{rs}(\lambda)$ and coincident laboratory measurements of CDOM spectral absorption and excitation-emission matrix (EEM) fluorescence, to compare the performance of several algorithms with varying levels of UV-visible spectral information. The data were also used to develop a fluorescence-based indicator of wastewater effluent and evaluate the amenability of this indicator to UV-visible imaging spectroscopy to detect point-source effluent. To the extent of our knowledge, this is the first attempt to use imaging spectroscopy in the UV range to facilitate water quality monitoring in coastal waters.

Study Area and Wastewater Effluent Diversion

Santa Monica Bay is a semi-enclosed coastal bay in the Southern California Bight that ranges from Malibu in the north to the Palos Verdes peninsula in the south (**Figure 1**). Santa Monica Bay is directly adjacent to the heavily urbanized greater Los Angeles area, which includes many densely populated coastal communities such as Santa Monica and Venice as well as the heavily trafficked Marina del Rey and Los Angeles International Airport. The bay provides valuable resources in the form of recreation, fisheries, transportation, wastewater disposal, water for industrial processes, and various other ecosystem services (Ackerman and Weisberg, 2003; Bay et al., 2003; Dojiri et al., 2003). The northern margin of Santa Monica Bay is dominated by the Santa Monica Mountains National Recreation Area, and has higher topographic relief and a sparser population (Bay et al., 2003) than the rest of the bay. Across much of the bay, water depth is less than 50 m but can reach depths greater than 500 m in submarine canyons that chisel through the bay (**Figure 1**).

This urban coastal-water system consists of heterogeneous, dynamic and optically complex waters influenced by marine currents, precipitation, and point sources of nutrients (Howard et al., 2014; Howard et al., 2017) or pollution (Trinh et al., 2017). Relative to the nearby open ocean, productivity in Santa Monica Bay is high, stimulated by nutrient inputs from spring upwelling events, as well as point sources of nutrients within the bay (Bray et al., 1999). Nutrient availability and currents in the bay are also influenced by the introduction of cold waters from the California Current System, intensified by seasonal coastal upwelling (Caron et al., 2017; Trinh et al., 2017). Local currents within Santa Monica Bay are highly variable, influenced by interactions of wind and strong temperature gradients with regional currents in the Southern California Bight (Washburn et al., 2003; Caron et al., 2017; City of Los Angeles, Environmental Monitoring Division, 2017).

Santa Monica Bay receives less runoff than most river-influenced coastal margins due to the dry local climate of Southern California, with salinity in the bay typically varying over a relatively narrow range (33 ± 2 PSU) outside of terrigenous freshwater plumes (Tiefenthaler et al., 2000). Santa Monica Bay receives low riverine inputs relative to other coastal areas. Low precipitation conditions are punctuated by intermittent, although often intense, rain events (Bay et al., 2003; Dojiri et al., 2003). Runoff reaches the bay through several highly engineered, concrete-hardened urban creeks in greater Los Angeles (Ballona Creek and Santa Monica Creek) and through the more natural creek and river systems that drain the Santa Monica Mountains to the north of the bay (including Malibu Creek and Topanga Creek (Ackerman and Weisberg, 2003; Bay et al., 2003; Dojiri et al., 2003). These intermittent runoff events have been shown to substantially influence coastal water quality and biogeochemistry in the bay (City of Los Angeles, Environmental Monitoring Division, 2017).

The Hyperion Wastewater Reclamation Plant is the largest wastewater treatment facility in Los Angeles. It released approximately 230 million gallons of secondary-treated wastewater effluent into Santa Monica Bay daily in 2015 (City of Los Angeles, Environmental Monitoring Division, 2017). This effluent is treated with physically, chemically, and bacterially mediated processes to remove sediments and organo-solids. During normal operations, effluent is released through a 5-mile offshore outfall in waters that are more than 60 m deep (Lyon and Sutula, 2011; City of Los Angeles, Environmental Monitoring Division, 2017; Gierach et al., 2017; Trinh et al., 2017). In fall 2015, during scheduled maintenance lasting 6 weeks (September 21, 2015-November 2, 2015), secondary-treated effluent from Hyperion was released at an older 1-mile offshore outfall in waters less than 20 m deep (City of Los

TABLE 1 | Summary of *in-situ* variables. Ranges of observed environmental parameters are reported for each sampling day. Gray rows denote sampling conducted during the wastewater effluent diversion.

Sampling date	Salinity [PSU]	$a_g(365)$ [m^{-1}]	$a_g(443)$ [m^{-1}]	EEM mean effluent peak F_E [RU]	EEM mean runoff peak F_R [RU]	Chlorophyll-a Fluorescence [FU]	[DOC] [$\mu mol\ L^{-1}$]
September 16, 2015	32.64–33.24	0.10–0.57	0.027–0.18	0.0071–0.033	0.012–0.067	0.013–0.15	159–214
September 24, 2015	32.21–33.31	0.17–0.60	0.050–0.20	—	—	—	—
September 30, 2015	31.80–33.44	0.07–0.92	0.017–0.32	0.0036–0.18	0.0089–0.11	0.0–3.6	155–350
October 14, 2015	31.75–33.48	0.06–0.75	0.015–0.26	0.0039–0.14	0.010–0.092	0.0079–1.2	147–284
October 21, 2015	32.11–33.45	0.08–0.66	0.021–0.22	0.0049–0.092	0.0085–0.073	0.018–3.5	146–230
October 26, 2015	33.64–32.40	0.07–0.33	0.019–0.10	0.0076–0.070	0.026–0.068	—	168–226
November 5, 2015	33.30–33.38	0.11–0.20	0.030–0.063	0.0060–0.014	0.011–0.021	0.050–1.3	155–167
November 11, 2015	33.35–33.44	0.10–0.21	0.028–0.064	0.0055–0.013	0.0091–0.020	0.047–0.32	139–155

Angeles, Environmental Monitoring Division, 2017). High surface concentrations of organic matter, coliform bacteria, and algal blooms were associated with the effluent plume and impacted surface water quality. Preemptive closure of nearby beaches was therefore necessary at times during the diversion (City of Los Angeles, Environmental Monitoring Division, 2017). The water quality monitoring efforts described in this paper, including *in-situ* sampling, were led by the City of Los Angeles Environmental Monitoring Division (CLAEMD). Field measurements during the water quality monitoring efforts were aided by the collection of PRISM airborne imagery.

DATA AND METHODS

In-situ Sample Collection and Measurements

Eighty-three surface water samples were collected before, during, and after the wastewater diversion (sampling from September 16-November 11, 2015) aboard the R/V *La Mer* and R/V *Marine Surveyor* along a zig-zagging pattern of stations oriented northwest-southeast in Santa Monica Bay (**Figure 1** and **Table 1**). One station was located directly above the 1-mile Hyperion effluent outfall (Station D9W), and four more stations were positioned at "stepout" locations approximately 750 m north, south, east, and west of the outfall (**Figure 1**). The dispersion of the effluent from the outfall during the diversion was driven by complex and variable current patterns in Santa Monica Bay during the diversion (City of Los Angeles, Environmental Monitoring Division, 2017). As a result, some stepout stations were heavily influenced by effluent whereas others were minimally impacted. Salinity was measured at 1-m depth using an SBE 19-plus Conductivity-Temperature-Depth (CTD) rosette (Seabird Scientific®) equipped with 1.7 L Niskin bottles. Two WETLabs® WETStar single-channel fluorescence sensors were also mounted in the CTD rosette and provided simultaneous measurements of chlorophyll-a fluorescence (460 nm excitation and 695 nm emission) and DOM fluorescence (370 nm excitation and 460 nm emission). Surface water samples were collected at 1 m depth using the Niskin bottles of the CTD rosette. Samples were gravity filtered through 0.7 μm filters (*GF/F* glass-fiber filters) directly from the Niskin bottles into clean borosilicate EPA clear glass vials (acid washed with 10%-HCl and furnaced at 450°C for 4 h) and placed immediately at 4°C in the dark until analysis in the laboratory. Glass-fiber filters with a 0.7 μm effective pore size were used in this study as a clean filtration method that allowed samples to be rapidly filtered between sample collections. Differences between filtration through 0.7 and 0.2 μm filters are likely to be small for the relatively low particle concentrations measured in Santa Monica Bay (Laanen et al., 2011). Scattering effects from any remaining sub-micron-scale particles after 0.7 μm filtration are expected to be further mitigated by the spectral fitting routine applied during laboratory analysis for CDOM absorption (Zhu et al., 2020; described below).

In-situ Radiometry

In-situ radiometric measurements were collected nearly simultaneously with sample collection at 45 stations using a Satlantic Inc. HyperPro free-falling optical profiling system (Seabird Scientific). The HyperPro system is composed of three, hyperspectral Satlantic Hyper Ocean Color Radiometers (HyperOCR): two HyperOCR mounted on the profiler to measure underwater downwelling irradiance $E_d(\lambda)$ and upwelling radiance $L_u(\lambda)$ and a third radiometer that measures downwelling surface irradiance above the air-water interface $E_s(\lambda)$. The HyperPro was used in two deployment methods during field sampling: tethered surface reflectance buoy mode and profiling mode. These methods are described in further detail for these data in a previous publication (Trinh et al., 2017). Briefly, in both modes, the water-leaving radiance $L_w(\lambda)$ is calculated by extrapolating below-surface upwelling radiance and downwelling irradiance measurements across the air-water interface. Water-leaving radiance is then divided by $E_s(\lambda)$, measured by the above-water reference sensor, to calculate remote sensing reflectance $R_{rs}(\lambda) = L_w(\lambda)/E_s(\lambda)$. Care was taken during both surface reflectance buoy-mode and profiler-mode deployments to keep the profiler at least 30 m away on the sunward side of the ship to minimize instrument shading. In profiler mode, observations from multiple freefall casts were combined to collect repeatable, representative R_{rs} measurements. Spectral $R_{rs}(\lambda)$

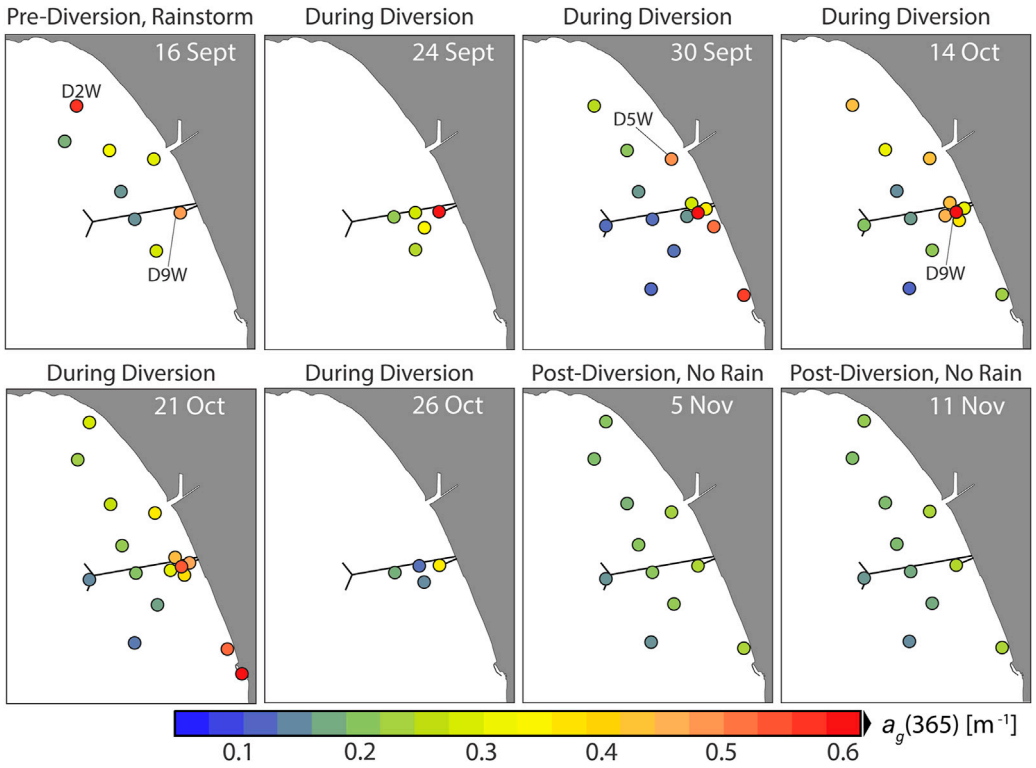

FIGURE 2 | Map of *in-situ* $a_g(365)$ measured during the field campaign in the fall 2015. Pre-diversion samples were measured on September 16 after a heavy precipitation event on September 15 (>6 cm of rain) and exhibited higher CDOM content at the north end of the bay. During the wastewater diversion, the highest $a_g(365)$ were observed near the 1-mile outfall. After the end of the wastewater diversion, there was little precipitation, and $a_g(365)$ was low at all sampling stations across Santa Monica Bay.

measurements from the HyperPro, covered a range from 350 to 700 nm in 3–4 nm increments, but were interpolated to 1 nm spectral resolution. *In-situ* $R_{rs}(\lambda)$ data were smoothed using a Savitzky-Golay filter (Savitzky and Golay, 1964) with frame size of 13 nm and polynomial of order 4 (Vandermeulen et al., 2017) implemented using the *sgolayfilt* function in Matlab. This smoothing was selected for its preservation of spectral shape and with a window chosen to smooth spectra without eliminating narrow features (Vandermeulen et al., 2017). *In-situ* $R_{rs}(\lambda)$ data were used to validate PRISM $R_{rs}(\lambda)$ and to calibrate empirical algorithms. For inter-comparability with PRISM data described below, $R_{rs}(\lambda)$ analyses were limited to the 365–700 nm spectral range. $R_{rs}(\lambda)$ spectra collected at *in-situ* stations are shown in **Supplementary Figure S1**.

Chromophoric Dissolved Organic Matter Absorption Coefficient Spectra

Absorption-coefficient spectra of CDOM, $a_g(\lambda)$, were determined for the 83 surface-water samples (**Figure 2**) and five effluent-dilution samples (see below) using a Shimadzu UV-1830 dual-beam spectrophotometer. As described above, samples were gravity filtered using pre-combusted glass fiber filters (0.7 µm pore size) and stored at 4°C in borosilicate glass bottles prior to measurement. The absorbance (optical density) of each filtered sample was measured in 1-nm increments from 250 to 700 nm. Samples were placed in 5 cm-pathlength quartz cells, and measurements were compared to simultaneous blank measurements of pure water (Millipore Milli-Q Direct 16). Samples were allowed to equilibrate to room temperature to avoid artifacts in pure-water absorption at longer wavelengths caused by temperature differences (Sullivan et al., 2006).

An exponential fit of the absorbance spectrum from 500 to 700-nm was used to compute an offset value that was subtracted from the entire absorbance spectrum (Fichot and Benner, 2011; Zhu et al., 2020). Offset-corrected spectral absorbances were converted to Napierian CDOM absorption coefficients, [m^{-1}]. This offset correction is well suited to coastal waters, because it does not assume that absorption coefficients in the 680–700 nm are negligible as is often done in procedures used to correct CDOM absorbance for open ocean waters (Johannessen et al., 2003).

Chromophoric Dissolved Organic Matter Fluorescence Excitation-Emission Matrices

Seventy-six filtered (0.7 µm) surface water samples and the five effluent-dilution samples were analyzed for excitation and

emission matrix (EEM) fluorescence using a Photon Technology International PTI 814 spectrofluorometer with a 1 cm quartz cuvette (Walker et al., 2009). Excitation was performed in 5 nm increments from 240 to 450 nm, and emission was measured in 2 nm increments from 300 to 600 nm. During the measurement, the emission signal was normalized to a reference detector to remove fluctuations of the light source. The raw EEM spectra were exported to MATLAB and processed with the drEEM toolbox (Murphy et al., 2013) to correct for the inner filter effect and to apply a Raman calibration. Finally, a Raman-normalized excitation and emission spectrum of Milli-Q water (18.2 MΩ cm) was subtracted from sample EEM spectra to remove the Raman signal. EEM fluorescence was not measured on September 24 and at two stations on October 21 because of low sample volume.

Dissolved Organic Carbon Concentration

Dissolved organic carbon (DOC) was measured by high-temperature combustion using a Shimadzu TOC-V analyzer equipped with an autosampler (Fichot and Benner, 2011). Samples were gravity filtered using pre-combusted glass fiber filters (0.7 μm pore size), acidified with 2 mol L^{-1} HCl, and stored at 4°C in borosilicate glass bottles until analysis within a few days of sampling. DOC concentration in the blanks were negligible, and accuracy and consistency of measured DOC concentrations was checked by measuring a deep seawater reference standard (University of Miami) every sixth sample.

Effluent Dilution Experiment

A sample of undiluted wastewater effluent was provided by the Hyperion Wastewater Reclamation Plant for our use in a dilution experiment. In order to simulate the effects of effluent-derived DOM on the absorption and fluorescence characteristics of the water, the effluent sample was diluted in a surface seawater sample obtained in offshore Santa Monica Bay after the diversion. Specifically, the pure effluent sample (100%) was diluted to generate seawater solutions containing 5, 1, 0.2, and 0% (no addition) of effluent by volume. Each sample was then analyzed for CDOM absorption spectra and EEM fluorescence as described above.

Algorithm Development

We developed local empirical algorithms for the remote retrieval of CDOM absorption coefficient from UV-visible $R_{rs}(\lambda)$ measurements. These algorithms were tested against two standard methods: a local empirical blue-red band ratio algorithm, and the Quasi-Analytical Algorithm version 6, updated in 2014 (QAA_V6) (Lee et al., 2007; Lee et al., 2009; Lee et al., 2014). Absorption at 365 and 443 nm were selected as representative scalar measures of CDOM to be inferred by the algorithms. The $a_g(365)$ was selected because it directly influences $R_{rs}(365)$, the shortest UV wavelength for which we have $R_{rs}(\lambda)$. The $R_{rs}(\lambda)$ in this wavelength range is expected to be less influenced by other in-water constituents. Algorithms were also developed for $a_g(443)$, to facilitate comparison with the QAA. Absorption coefficients of CDOM at 365 and 443 nm were highly correlated, and the accuracy of their retrieval by empirical algorithms was comparable, allowing for fair comparison of local empirical algorithms that utilize UV reflectance with other methods.

Empirical Algorithms for $a_g(\lambda)$

UV-red and blue-red band-ratio algorithms were compared to assess the utility of including UV reflectance in simple empirical algorithms to facilitate the retrieval of accurate $a_g(365)$ and $a_g(443)$ in a coastal environment where optical variability is largely driven by phytoplankton (Trinh et al., 2017). We also assessed the value of additional spectral information for the development of such empirical algorithms. Algorithms based on multiple linear regression (MLR) utilizing three bands and a full-spectrum partial least squares regression (PLSR) algorithm were compared to explore the improvements in CDOM retrieval offered by increasing spectral resolution. Specifically, to assess the utility of UV measurements and high spectral resolution data for the retrieval of $a_g(443)$, five strategies were tested:

1) univariate regression on a blue-red reflectance band ratio $R_{rs}(443)/R_{rs}(665)$;
2) univariate regression on a UV-red reflectance band ratio $R_{rs}(365)/R_{rs}(665)$;
3) visible multiple linear regression on $R_{rs}(412)$, $R_{rs}(443)$, and $R_{rs}(700)$;
4) UV-visible multiple linear regression on $R_{rs}(365)$, $R_{rs}(400)$, and $R_{rs}(700)$;
5) UV-visible partial least squares regression on full-spectrum $R_{rs}(365–700)$.

Empirical algorithms for deriving bio-optical properties from $R_{rs}(\lambda)$ were calibrated using *in-situ* data including stations where $R_{rs}(\lambda)$ was measured along with CDOM absorption (n =41). Empirical fits for $a_g(\lambda)$ were conducted by first taking the log-log transform of $a_g(443)$ and the R_{rs} predictor variables and then performing linear regression (equivalent to fitting a power-law). For all multiple linear regression algorithms, initial wavelength selection was conducted by performing forward and backward variable selection, conducted using the MATLAB *stepwiselm* function to select variables based on local minimization of the Bayes Information Criterion (BIC). As stepwise variable selection is sensitive to initial selection of predictors, it was performed using reflectance observations at 5 nm intervals across the entire measured wavelength range (or from 412 to 700 for the visible-only MLR) as the initial predictor variable. The wavelengths most frequently selected by stepwise variable selection were then tested together in different combinations of wavebands, based on understanding of bio-optical signatures and chosen to reduce correlation between variables by not choosing $R_{rs}(\lambda)$ observations from wavelengths <10 nm apart. Finally, forward and backward variable selection was again conducted using the MATLAB *stepwiselm* function to identify a best-performing MLR model.

We also tested empirical algorithms for inferring CDOM using partial least squares regression. PLSR is a statistical technique for collapsing many highly correlated explanatory

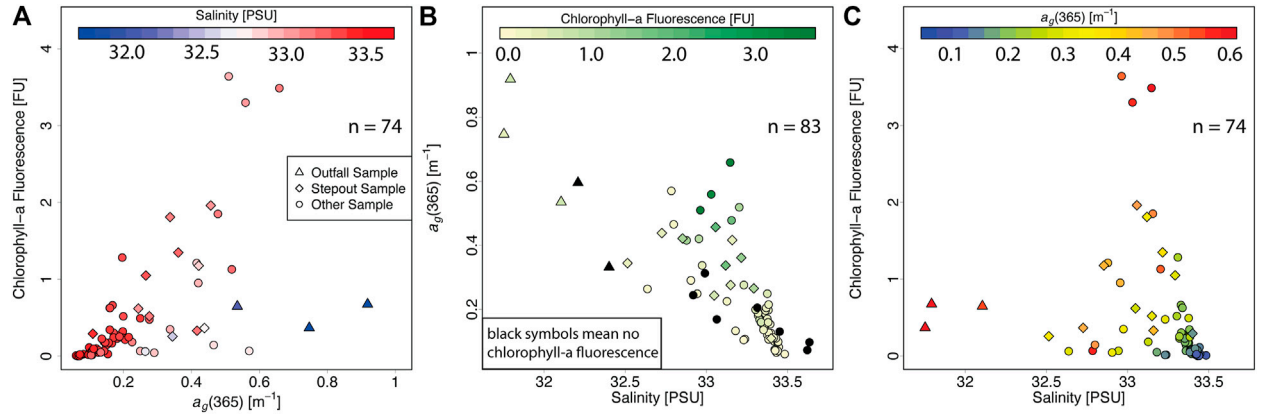

FIGURE 3 | Comparison of *in-situ* environmental parameters measured during the field campaign: **(A)** a_g(365) versus chlorophyll-a fluorescence with color scale indicative of salinity, **(B)** salinity versus a_g(365) with color scale indicative of chlorophyll-a fluorescence, and **(C)** salinity versus chlorophyll-a fluorescence with color scale indicative of a_g(365). *In situ* chlorophyll-a fluorescence was not measured at all stations (black symbols in panel **B** do not have chlorophyll-a data).

variables into a smaller number of uncorrelated predictors ranked in order of explanatory power (Mevik and Wehrens, 2007). Linear combinations of predictors are used to create components that have maximized correlation with the response variable. To predict bio-optical parameters, PLSR was implemented using the MATLAB *plsregress* function from the Statistics and Machine Learning Toolbox™. PLSR models were tested for both log-transformed and linear R_{rs} and log-transformed and linear bio-optical properties.

PLSR was tested for overfitting using a "leave-*p*-out" cross-validation routine with $p = 4$. Four data points, representing approximately 10% of the available data, was selected as an appropriate subset for validation in order to balance bias and variance in cross-validation (Arlot and Celisse, 2010). During "leave-four-out" cross-validation, PLSR coefficients were calibrated using the remaining n–4 data points, and the resulting empirical algorithm was validated using the four points that had been held out. Error statistics (root mean squared error (RMSE), mean absolute error (MAE), mean absolute percent error (MAPE), and R^2) were calculated between the fitted and measured parameter of interest on the four points that were held out. This process was repeated for all possible subsets of four stations (40 choose four combinations for predicting EEM fluorescence peak ratio and 45 choose four combinations for fits on a_g), and averaged error statistics across all leave-four-out combinations were calculated. The averaged leave-four-out error statistics were used to select an appropriate number of PLSR components.

Full error statistics for empirical algorithm calibration are presented in **Table 2**. The performance of these empirical algorithms was also compared to QAA retrievals to assess the performance of locally calibrated empirical algorithms against a well-established semi-analytical approach. The same procedure was used to calibrate empirical algorithms for a_g(365), but in this case no direct comparison with the QAA was possible.

Effluent Fluorescence Peak Ratio Empirical Algorithm Development

We also assessed the feasibility of remotely detecting CDOM source information, specifically inferring a fluorescence proxy for the degree of effluent impact. From *in-situ* stations where both $R_{rs}(\lambda)$ and EEM fluorescence were measured ($n = 40$), we developed empirical algorithms for inferring the ratio between the mean intensity of an EEM fluorescence peak associated with effluent, F_E, (340–360 nm excitation and 426–454 nm emission), and one that was indicative of runoff-influenced CDOM, F_R, (255–265 nm excitation and 382–398 nm emission) from remote sensing reflectance (see *Results*). The effluent fluorescence ratio (*EFR*, mean intensity of the effluent-associated peak/mean intensity of the runoff-associated peak) was used as an optical proxy for the degree of effluent impact in a sample (see below for full definition of *EFR*). Unlike F_E, which increased with increasing CDOM regardless of source (although the increase in F_E was greater for effluent-derived CDOM), *EFR* compared the relative intensity of fluorescence in different ranges of the spectrum. Therefore, *EFR* was a specific indicator of effluent, because it increased only when the amount of effluent-derived CDOM increased and was decreased by the addition of runoff-derived CDOM. Empirical algorithms utilizing MLR on $R_{rs}(400)$, $R_{rs}(425)$, and $R_{rs}(400)/R_{rs}(425)$ and a full-spectrum, R_{rs}(365–700), PLSR were fitted to data from 36 calibration stations with *in-situ* R_{rs} and EEM fluorescence data.

Portable Remote Imaging SpectroMeter Imagery

PRISM imagery was collected during a flyover on October 26, 2015. The instrument, mounted on an ER-2 aircraft flying at an approximate altitude of 20 km, captured a swath from northwest to southeast along the coastline of Santa Monica Bay. Atmospheric correction was conducted using an Optimal Estimation formulation that simultaneously models surface and atmospheric reflectance contributions from statistical

TABLE 2 | Summary statistics associated with the performance comparison of the six $a_g(443)$ algorithms (see also **Figure 8**). Statistics include root mean squared error (RMSE), mean average percent error (MAPE), mean absolute error (MAE), and R-squared for each algorithm.

Algorithm	RMSE	MAPE	MAE	R^2
Blue-red band ratio				
$\log(a_g(443))$ on $\log(R_{rs}(443)/R_{rs}(665))$	0.051	29.364	0.028	0.378
UV-red band ratio				
$\log(a_g(443))$ on $\log(R_{rs}(365)/R_{rs}(665))$	0.037	23.108	0.021	0.671
QAA v.6				
(Not including major outlier[a])	0.038	23.969	0.022	0.637
Visible-only multiple linear regression (MLR)				
$\log(a_g(443))$ on $\log(R_{rs}(412)) + \log(R_{rs}(443)) + \log(R_{rs}(700))$	0.030	20.140	0.016	0.765
UV-Visible multiple linear regression (MLR)				
$\log(a_g(443))$ on $\log(R_{rs}(365)) + \log(R_{rs}(400)) + \log(R_{rs}(700))$	0.026	13.782	0.012	0.831
Partial-least-square regression (PLSR)				
$\log(a_g(443))$ on $\log(R_{rs}(365{:}700))$; 5 components	0.026	13.896	0.012	0.830

[a]*Major outlier of the QAA algorithm was sample D5W collected on September 30, 2015 (See **Figure 2**).*

priors (Thompson et al., 2018). The atmospheric correction approach, including the calibration and orthorectification of the PRISM imagery were described at length in a recent manuscript (Thompson et al., 2019). The spatial resolution of the image is approximately 20 m, and includes spectral measurements made approximately every 3 nm from 350 to 1,050 nm. This high spatial resolution provides opportunities for detecting patterns in water quality at small scales, but also introduces additional challenges for interpreting data in some areas. For example, several boats are visible in maps of $R_{rs}(\lambda)$ and derived products. Reflectance measurements at wavelengths shorter than 365 nm were not available for this analysis because they were excluded during the Level-1-to-Level-2 processing of the PRISM data in order to include only spectral regions of reliable instrument calibration and atmospheric correction. PRISM swaths were trimmed to remove sensor artifacts at the edges of the swath and to remove waters with depth <10 m due to suspected influence of wave action and bottom effects in shallower waters (**Supplementary Figure S2**).

Statistical Analysis

Statistical analyses were conducted in R (R Core Team, 2018) and MATLAB version R2018b. Figures were produced in R using the fields package, and in MATLAB. Multiple linear regression and partial least squares regression were implemented using MATLAB version R2018b.

RESULTS

Chromophoric Dissolved Organic Matter Variability in Santa Monica Bay

The spatial distribution of CDOM absorption in Santa Monica Bay was very variable over the course of the fall sampling, as local inputs from riverine and wastewater effluent sources were added to the bay (**Figure 2**). On September 16, following a major rain event before the diversion (>6 cm of rain fell on September 15 in the wettest September storm in more than 100 years), higher $a_g(365)$ values were observed nearshore and in the northern end of the bay (**Figure 2**), where several rivers and creeks from the Santa Monica Mountains drain to the bay. Later, during the Hyperion wastewater diversion (sampling from September 16-November 11, 2015), the highest $a_g(365)$ values (up to 0.92 m^{-1} on September 30) were typically observed at or near the diverted 1-mile outfall (**Figure 2** and **Supplementary Figure S3**). After the diversion, precipitation was low and $a_g(365)$ values remained low across the entire bay, with a small offshore-inshore gradient (**Figure 2**). This change in CDOM distribution during the sampling window illustrated several of the dominant CDOM regimes in Santa Monica Bay: 1) runoff-dominated before the diversion, 2) influenced by wastewater effluent during the diversion, and 3) low-CDOM conditions after the diversion.

The relationships between CDOM, chlorophyll-a, and salinity in this data set were complex and variable, and were consistent with variable sourcing of in-water constituents (**Figure 3**). Overall, these urban coastal waters exhibited general correlations between chlorophyll-a, $a_g(365)$, and salinity that were consistent with terrigenous inputs driving most of the optical variability (Bowers and Brett, 2008). However, upon close inspection, the relationships between $a_g(365)$, chlorophyll-a, and salinity clearly separated into two distinguishable trends. The first, where lower salinities were accompanied by elevated levels of chlorophyll-a and CDOM, was consistent with the influence of terrigenous inputs. The second, where lower salinities were accompanied by elevated CDOM but much more moderate levels of chlorophyll-a, corresponded to the wastewater-influenced waters of the diversion.

Attempting to Differentiate Chromophoric Dissolved Organic Matter Sources Using Absorption

Overall, the variability of the CDOM absorption coefficient spectra adhered to expected relationships, but did not enable the identification of different CDOM sources. The absorption spectra followed the typical exponential spectral shape for CDOM (**Supplementary Figure S3**), and $a_g(\lambda)$ was well correlated across wavelengths. In particular, the two wavelengths explored in this

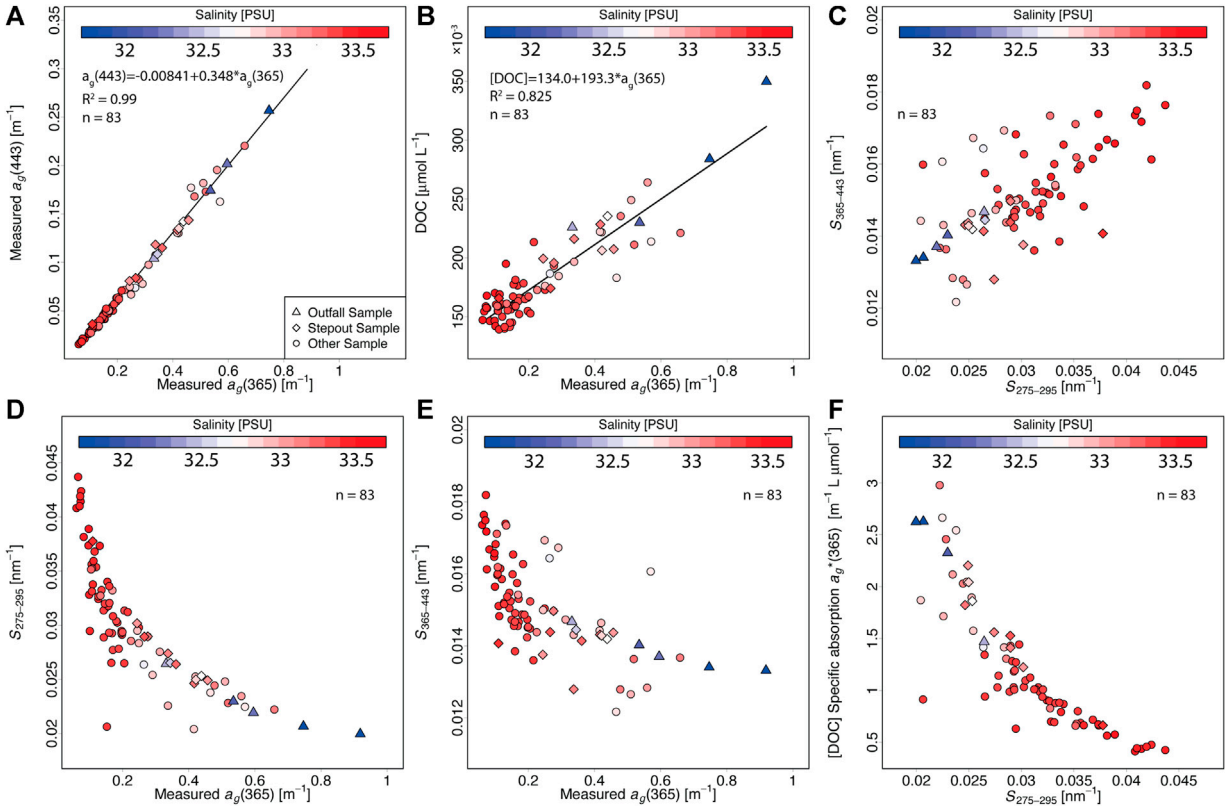

FIGURE 4 | Plots of CDOM absorption characteristics: **(A)** relationship between absorption coefficients of CDOM at 365 and 443 nm, **(B)** relationship between $a_g(365)$ and [DOC], **(C)** spectral slope in the UV-B ($S_{275–295}$) versus UV-A to visible ($S_{365–443}$) domain, **(D)** relationship between $a_g(365)$ and $S_{275–295}$, **(E)** relationship between $a_g(365)$ and $S_{365–443}$, and **(F)** relationship between $S_{275–295}$ and [DOC]-specific absorption by CDOM (a_g^*). Organic matter in effluent impacted samples, collected at the 1-mile outfall during the diversion, occurs in relatively high abundance, but does not differ in absorption characteristics from other CDOM sources.

study, a_g (365) and a_g (443), were strongly and linearly correlated with an R^2 = 0.99 (**Figure 4A**), indicating a limited range of CDOM spectral slope coefficient values in the 365–443 nm range and no obvious differences between CDOM from different sources (e.g., terrestrial runoff versus wastewater effluent). In a few cases, some $a_g(\lambda)$ spectra exhibited broad features at $\lambda <$ 360 nm that were suggestive of the presence of dissolved mycosporine-like amino acids (MAAs) exuded from phytoplankton (Morrison and Nelson, 2004; Tilstone et al., 2010). As in most coastal environments, CDOM absorption was also strongly correlated with DOC concentration (**Figure 4B**; (Mannino et al., 2008; Fichot and Benner, 2011)). Although this relationship remained consistent during the sampling window and enabled estimation of [DOC] from CDOM with reasonable accuracy, it did not help discriminate between different sources of CDOM.

Spectral slopes of CDOM absorption coefficient also did not offer opportunities to differentiate effluent-derived CDOM from other sources. Absorption spectral slopes between 275 and 295 nm ($S_{275–295}$) were correlated with UV-visible spectral slope ($S_{365–443}$), with no difference in behavior for effluent-derived CDOM (**Figure 4C**) from other sources. The spectral slope coefficient between 275 and 295 nm ($S_{275–295}$), a now well-established tracer of terrigenous inputs in coastal waters (Helms et al., 2008; Fichot and Benner, 2012), generally adhered to an expected power-law relationship with a_g (365) and did not facilitate the discrimination of effluent-derived CDOM from other sources (**Figure 4D**). The UV-visible spectral slope, $S_{365–443}$, followed a similar yet less well-defined pattern, decreasing with increasing a_g (365) (**Figure 4E**). Effluent samples did not differ in DOC-specific CDOM absorption from other CDOM sources either. The DOC-specific CDOM absorption coefficient, $a_g^*(365) = a_g(365)/[DOC]$, followed previously described relationships with $S_{275–295}$ for coastal areas (Fichot and Benner, 2012; Cao et al., 2018), and almost all samples plotted along the same general relationship (**Figure 4F**).

Samples collected near the effluent outfall during the diversion exhibited high a_g (365), but that criterion alone was not sufficient to identify wastewater effluent, as runoff and phytoplankton blooms are also associated with elevated CDOM. Furthermore, the effluent-derived CDOM also exhibited low $S_{275–295}$ and $S_{365–443}$ values similar to those of terrigenous CDOM. The spectral shape of CDOM absorption did not differ significantly enough to facilitate the distinction of effluent-derived CDOM. Therefore, while effluent-impacted samples had relatively high

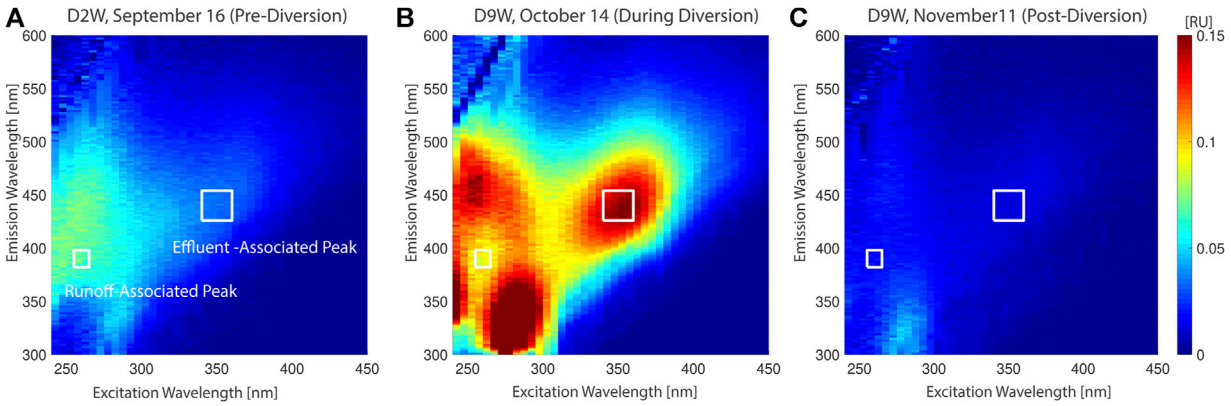

FIGURE 5 | CDOM fluorescence excitation emission matrices (EEMs): **(A)** EEM of a pre-diversion sample with high $a_g(365)$ associated with terrigenous runoff that fluoresces strongly at the runoff-associated peak F_R (255–265 nm excitation and 382–398 nm emission), **(B)** EEM of an effluent-impacted sample, collected at the 1-mile outfall during the diversion, which exhibits a strong effluent-associated fluorescence peak F_E (340–360 nm excitation and 426–454 nm emission) that is much less prominent in samples not influenced by effluent, **(C)** EEM of a low $a_g(365)$ sample collected at the 1-mile outfall after the diversion.

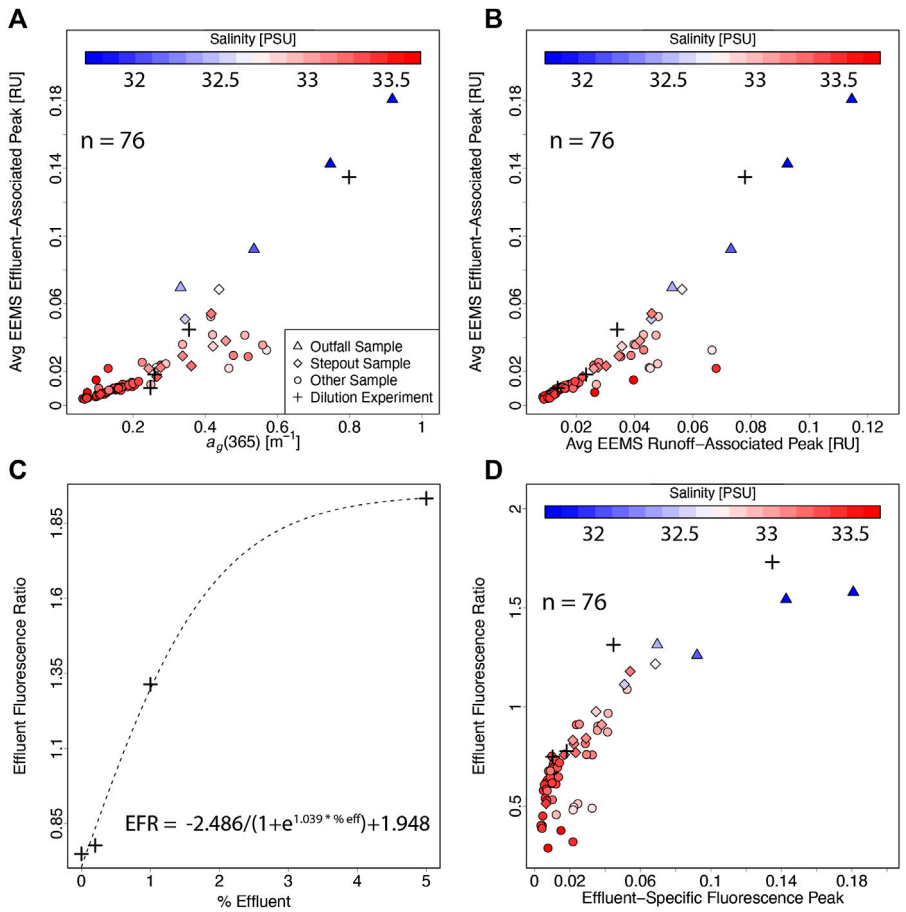

FIGURE 6 | Relationships between: **(A)** intensity of the effluent-associated fluorescence peak F_E and $a_g(365)$, **(B)** intensity of effluent-associated fluorescence peak F_E and intensity of the runoff-associated fluorescence peak F_R, **(C)** the effluent fluorescence ratio $EFR = F_E/F_R$ and the % effluent by volume from the dilution experiment samples, and **(D)** the *EFR* and $a_g(365)$.

CDOM, absorption alone did not offer prescriptive characteristics for separating wastewater effluent-impacted waters from riverine and autochthonous CDOM in Santa Monica Bay.

Differentiating Chromophoric Dissolved Organic Matter Sources Using Fluorescence

In contrast to CDOM absorption, EEM fluorescence proved useful for separating effluent-derived CDOM from other sources. Samples collected around the 1-mile outfall during the diversion exhibited a distinct fluorescence peak (F_E) often associated with wastewater effluent (sometimes described in previous literature as Peak C) (Goldman et al., 2012; Carstea et al., 2016), centered around 340–360 nm excitation and 426–454 nm emission (**Figure 5**). Other regions of the fluorescence EEM, such as the F_R peak centered at 255–265 nm excitation and 382–398 nm emission (**Figure 5**), were less sensitive to effluent and more sensitive to other sources of CDOM such as runoff. These fluorescence features associated with different origins of CDOM provided an opportunity to discriminate between CDOM sources based on fluorescence.

Samples collected at or near the wastewater effluent outfall during the diversion fluoresced more intensely at the effluent peak (higher F_E values) than other samples with similar $a_g(365)$ values. This was evident in the observed relationship between $a_g(365)$ and F_E for all samples (**Figure 6A**), in which samples near the outfall clearly had enhanced F_E for the same level of $a_g(365)$. Furthermore, the samples from the effluent dilution experiment (created by diluting a sample of pure effluent provided by the Hyperion wastewater treatment plant with deep-ocean seawater) also exhibited a very similar relationship between F_E with $a_g(365)$ as the bay samples. The relationship between F_E and F_R (**Figure 6B**) was generally similar to the relationship between F_E and $a_g(365)$, with samples collected near the outfall exhibiting higher F_E and F_R than samples collected at other locations in Santa Monica Bay. However, samples that were solely influenced by runoff (samples collected at other locations in Santa Monica bay with relatively high $a_g(365)$ and low salinity) exhibited much lower F_E values for the same F_R. A ratio of the two peaks captures this effluent-influenced fluorescence pattern, while limiting the influence of total CDOM content.

The dependence of F_E and F_R on CDOM source provided an opportunity to distinguish CDOM from effluent-influenced samples. Here, we propose *EFR*,

$$EFR = \frac{F_E}{F_R} \quad (1)$$

as an optical indicator of effluent-impacted waters, where F_E is the mean fluorescence intensity in Raman Units (RU) of the effluent peak (340–360 nm excitation and 426–454 nm emission), and F_R is the mean fluorescence intensity in RU for the runoff peak (255–265 nm excitation and 382–398 nm emission). *EFR* was selected as a specific indicator of effluent impact, because it was increased by increasing effluent-derived CDOM, but not by increasing runoff-derived CDOM. F_E alone was not a specific indicator of effluent, since some samples with increased F_E (>0.02 RU) were collected from both effluent-impacted and runoff-impacted waters. However, by including a ratio of F_E/F_R, *EFR* leveraged the fact that effluent-impacted CDOM had higher F_E relative to other fluorescence peaks, thereby facilitating effluent detection.

The effluent dilution experiment clearly revealed the dependence of the *EFR* on the fraction of wastewater effluent diluted in a local seawater sample (**Figure 6C**). *EFR* values increased asymptotically with the fraction of effluent from a value of approximately 0.75 for 0% effluent to almost 2 for 5% effluent. The increased utility of *EFR* over F_E for distinguishing samples impacted by wastewater effluent was further demonstrated by the relationship between F_E and *EFR* for the samples collected in the bay (**Figure 6D**). In particular, a few runoff-impacted samples had increased F_E values (~0.2), but exhibited no such increase in *EFR*. Samples from the outfall during the diversion and from the effluent dilution have higher *EFR* than those collected at other stations, and this behavior allowed for the differentiation of effluent-derived CDOM from runoff-derived CDOM.

The spatial distribution of *EFR* values in Santa Monica Bay during the sampling window (**Figure 7**) was very consistent with the modeled dispersion of the effluent (**Supplementary Figure S4**). No *EFR* higher than 0.8 were detected before or after the diversion, and the highest *EFR* values detected during the diversion (>1.5) were at the wastewater outfall. Higher *EFR* values (>1.0) also occurred in the area surrounding the outfall (stepout stations). Samples with increased *EFR* generally occurred near the path of effluent plume, as inferred in particle trajectory modeling (**Supplementary Figure S4**) conducted by the Southern California Coastal Observatory System based high frequency radar observations of local currents in Santa Monica Bay (City of Los Angeles, Environmental Monitoring Division, 2017).

The effluent fluorescent peak F_E is a well-positioned fluorescence feature in CDOM because it has the potential to influence remote-sensing reflectance. This fluorescence is particularly intense, meaning it can produce a significant radiance. Furthermore, unlike most other CDOM fluorescence peaks which require excitation at wavelengths shorter than 300 nm, the F_E peak is excited by UV radiation (~350 nm) that is naturally present in underwater solar irradiance (Fichot and Miller, 2010). It also emits broadly in the blue part of the spectrum (~440 nm). Phytoplankton also absorb strongly in this wavelength range creating potential for fluorescence reabsorption and possibly introducing further challenges for remote detection. However, past studies (Hoge et al., 1993; Green and Blough, 1994; Lee et al., 1994), have included remote detection of CDOM fluorescence features despite interference from phytoplankton absorption, indicating that some changes in CDOM fluorescence are remotely detectable. Therefore, we expect that the sun-induced fluorescence of effluent-derived CDOM could drive detectable changes in remote-sensing reflectance, allowing for the fully remote detection of wastewater effluent based on its optical characteristics. As an optical proxy based in part on F_E, *EFR* offers utility for differentiating effluent-derived CDOM from other sources. It also offers a potential mechanism for inferring

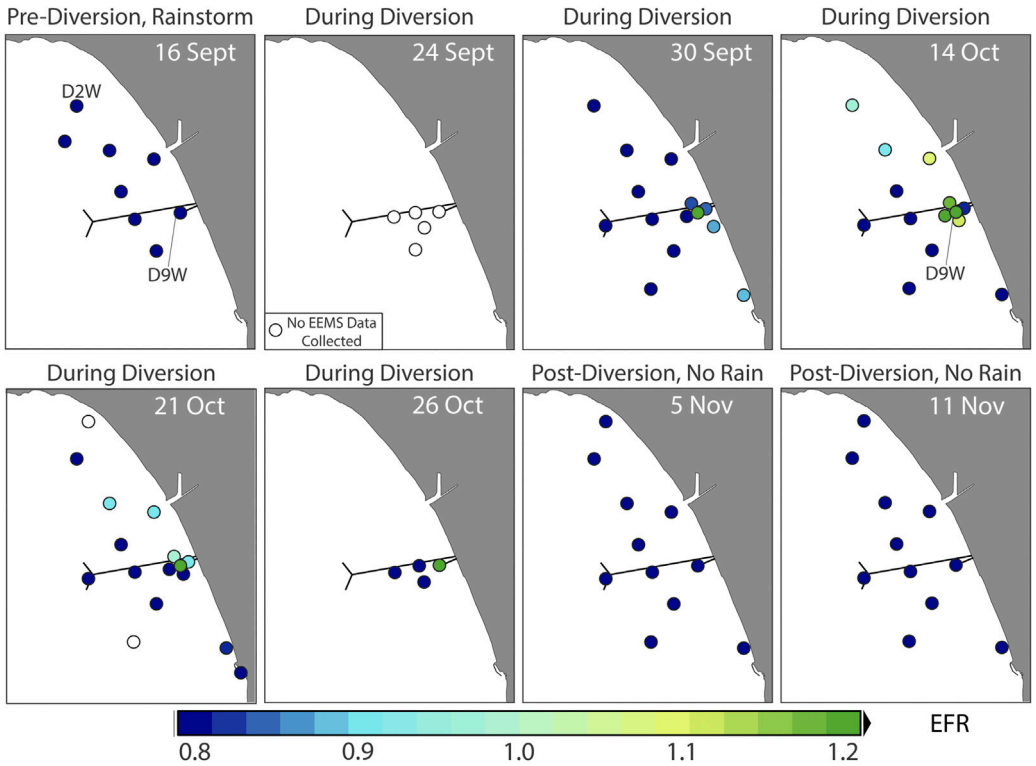

FIGURE 7 | Distribution of *in-situ EFR* in Santa Monica Bay during the sampling window. No EEM analysis was conducted for September 24. *EFR* values >1.0 were only detected near the outfall during the diversion. Data from September 16 (after major rain event) show that the *EFR* is largely insensitive to runoff.

effluent influence from ocean color remote sensing. The potential applications and challenges remote *EFR* detection are further explored in the Discussion section in the context of the results of this work.

Algorithm Performance Comparison

We compared the performance of empirical algorithms developed for a_g (443) to specifically assess the utility of: 1) R_{rs} in the UV range, and 2) R_{rs} at high spectral resolution (**Figure 8**). Our results indicated that the MLR algorithm utilizing R_{rs} (365), R_{rs} (400), and R_{rs} (700) inferred a_g (443) with the highest accuracy (full summary statistics in **Table 2**) between fitted and measured values (RMSE = 0.026). Despite including much more spectral information, the five-component PLSR algorithm performed similarly (RMSE = 0.026) to the MLR, suggesting that a large number of spectral bands was not necessary for retrieving CDOM accurately with empirical approaches. The MLR coefficients for all algorithms are listed in **Supplementary Table S2**, the PLSR component loading plots are presented in **Supplementary Figure S5**, and summaries of leave-four-out error for selecting number of components are presented in **Supplementary Table S1**. The two band ratio algorithms performed substantially worse than the empirical algorithms utilizing more predictors. The UV-red algorithm (RMSE = 0.037) performed better than the standard blue-red method (RMSE = 0.051). As expected, the UV-visible MLR (RMSE = 0.026) also outperformed the visible MLR (RMSE = 0.030). From the performance of the five empirical algorithms, we found that adding UV bands, in addition to red and blue, improved CDOM retrieval in complex coastal waters (in both the band ratio and MLR algorithms), but that increasing the number of bands (as in the PLSR algorithm) beyond three bands used in the UV-visible MLR algorithm offered minimal improvement to a_g (443) retrieval accuracy.

To compare empirical CDOM absorption retrieval to an established semi-analytical method, we included a_g (443) retrieved by the QAA in our analysis. While the QAA returns spectrally-resolved water inherent optical properties (IOPs), it pools absorption by detritus (a_d) and a_g into a combined a_{dg} (λ) spectrum, only inferring a_g independently from a_d at 443 nm (Lee et al., 2014). Due to the semi-analytical, more mechanistic nature of the QAA, no calibration was conducted. The best-performing empirical algorithms for a_g (443), MLR and PLSR, outperformed the QAA (RMSE = 0.038) in the complex, coastal waters of Santa Monica Bay. However, QAA retrieval of a_g (443) outperformed the red-blue band ratio and had comparable accuracy to the UV-red band ratio algorithm.

Across all of the algorithms tested, the sample collected at D9W (wastewater outfall) on October 14 was an outlier, with inferred a_g (443) anomalously low relative to measured a_g (443) (**Figure 8**). This mismatch may have been caused by boat drift between radiometry and sample collection, particularly as conditions changed rapidly over steep spatial gradients around the outfall, or potential contamination of the sample. However,

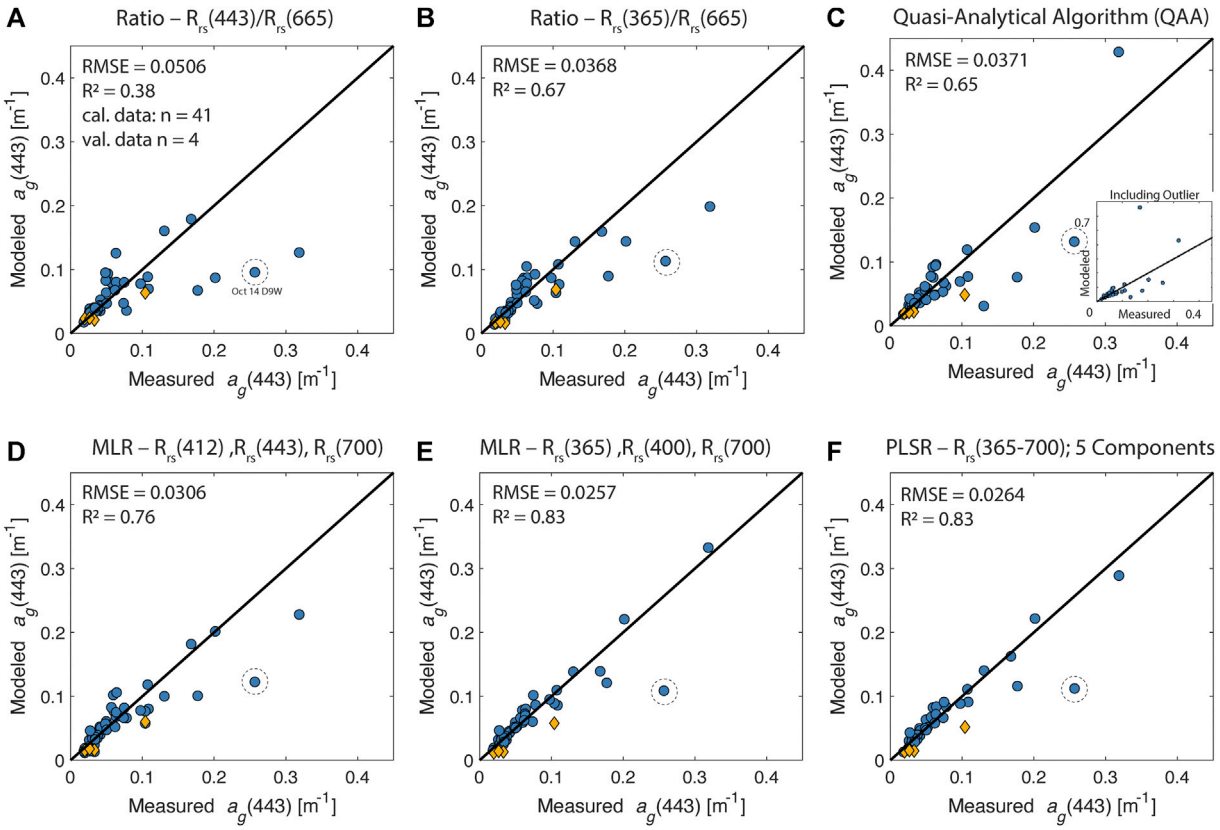

FIGURE 8 | Performance comparison of six different $a_g(443)$ algorithms. *In-situ* data used for calibration (n = 41) are displayed as blue circles, and end-to-end validation points comparing measured $a_g(443)$ to inferred $a_g(443)$ from nearest neighbor PRISM pixels (n = 4) are displayed as orange diamonds. Most of the $a_g(443)$ algorithms presented here, with the exception of the QAA, are empirical and were developed using coincident *in-situ* measurements of R_{rs} and $a_g(443)$: **(A)** log-log fit on blue-red band ratio $R_{rs}(443)/R_{rs}(665)$, **(B)** log-log fit on UV-red band ratio $R_{rs}(365)/R_{rs}(665)$, **(C)** the QAA algorithm v.6, which exhibited one major outlier and is plotted without it to facilitate comparison (inset plot includes outlier), **(D)** log-log visible-only multiple linear regression (MLR) on $R_{rs}(412)$, $R_{rs}(443)$, $R_{rs}(700)$; **(E)** log-log UV-visible MLR on $R_{rs}(365)$, $R_{rs}(400)$, $R_{rs}(700)$, and **(F)** a log-log partial-least-square regression (PLSR) on the full spectrum $R_{rs}(365–700)$, using the first five components. The sample collected at station D9W on October 14 was an outlier, with low inferred $a_g(443)$ relative to measured $a_g(443)$ for all algorithms. This sample is indicated with a dashed circle.

we did not have a definitive basis on which to exclude that data point, and therefore included it in our analyses.

Implementation of Chromophoric Dissolved Organic Matter Algorithms on Portable Remote Imaging SpectroMeter Imagery

The CDOM algorithms were implemented on the PRISM remote-sensing reflectance (**Figure 9**) to produce maps of CDOM at 20 m resolution in Santa Monica Bay for October 26. Mapped $R_{rs}(\lambda)$ from PRISM imagery followed reasonable distributions in Santa Monica Bay, with variability tracking different water masses. $R_{rs}(665)$ and $R_{rs}(555)$ increased in nearshore coastal areas and at the wastewater effluent outfall, highlighting areas with higher backscattering from suspended particles or phytoplankton. Distributions of $R_{rs}(443)$ and $R_{rs}(365)$ showed some similarities, with decreased reflectance in these nearshore and outfall areas, likely driven by increased CDOM and phytoplankton absorption at short wavelengths. A plume of water with decreased reflectance at $R_{rs}(443)$ and, especially, $R_{rs}(365)$ delineated a counterclockwise swirling, current-driven entrainment of material at the northern end of the bay. Overall, the observed spatial patterns of all $R_{rs}(\lambda)$, even for $R_{rs}(\lambda)$ in the UV domain, were very realistic and consistent with expectations for this coastal environment. To the extent of our knowledge, this represents one of the first high-resolution images of UV remote-sensing reflectance at wavelengths shorter than 380 nm collected over coastal waters.

The spatial distributions and inferred ranges of $a_g(443)$ from the different algorithms showed expected similarities but also some important differences (**Figure 10**). All approaches identified a point source of high CDOM at the diverted wastewater outfall as well as plumes of CDOM swirling in Santa Monica Bay north of Marina del Rey, and smaller plumes of higher $a_g(443)$ at the north end of the bay. The

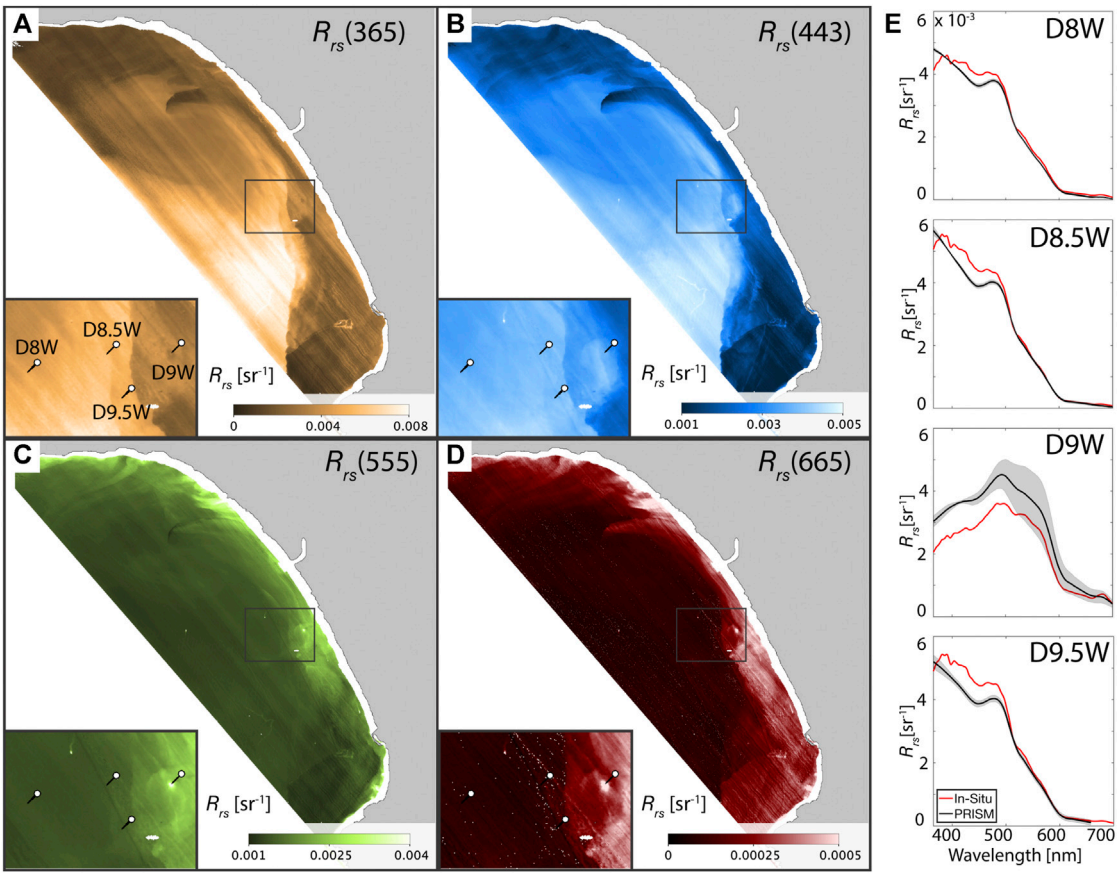

FIGURE 9 | Remote-sensing reflectance spectra, $R_{rs}(\lambda)$, measured by the airborne Portable Remote Imaging SpectroMeter (PRISM) after atmospheric correction (Thompson et al., 2019) during a flyover of Santa Monica Bay, CA on October 26, 2015: **(A)** R_{rs} (365) map, **(B)** R_{rs} (443) map, **(C)** R_{rs} (555) map, **(D)** R_{rs} (665) map, and **(E)** comparison of PRISM-derived $R_{rs}(\lambda)$ spectra with coincident $R_{rs}(\lambda)$ spectra measured *in situ* with a Satlantic HyperPro at four matchup stations: D8W, D8.5W, D9W (outfall), and D9.5W.

location of this high a_g(443) plumes in northern Santa Monica Bay is consistent with the presence of rivers and creeks draining the Santa Monica Mountains. The band ratio algorithms (**Figures 10A,B**) appear to overestimate a_g(443) in areas with intermediate CDOM content ($0.05 < a_g(443) < 0.1$), relative to other strategies. Overestimation of a_g(443) relative to measured data was also visible in band ratio fits of the *in-situ* data. Perhaps surprisingly, the maps derived from the UV-red band ratio and the blue-red band ratio exhibited similar patterns, suggesting that UV reflectance alone used in a band ratio was not sufficient to retrieve CDOM in this phytoplankton-dominated system. Similar algorithms were developed for a_g(365) and these were applied to PRISM Imagery (**Supplementary Table S3**). Summaries of a_g(365) algorithm performance and maps of a_g(365) are presented in **Supplementary Figures S6, S7**.

We also conducted an end-to-end validation (**Figure 8** and **Supplementary Figure S8**) for which a_g(443) retrieved from PRISM $R_{rs}(\lambda)$ were compared to a_g(443) measured at collocated matchup stations on October 26. However, only a very small number of data points from closely located validation stations ($n = 4$) were available for this validation, and these data did not provide sufficient information for reliable validation and meaningful comparison of the algorithms.

Effluent-Chromophoric Dissolved Organic Matter Detection Algorithm and Implementation on Portable Remote Imaging SpectroMeter

Algorithms for retrieving *EFR* were developed using a five-component PLSR on R_{rs}(365–700) (**Figure 11**). The component loading plots for the PLSR is presented in **Supplementary Figure S9**. The performance of this fully spectral algorithm was compared to that of a simpler algorithm based on the MLR of *EFR* on R_{rs}(400), R_{rs}(425), and $R_{rs}(400)/R_{rs}(425)$. Based on *in-situ* data alone, the PLSR algorithm retrieved *EFR* with a slightly higher accuracy (RMSE = 0.156, $R^2 = 0.608$) than the MLR algorithm (RMSE = 0.160, $R^2 = 0.589$). However, for error metrics that were comparable across

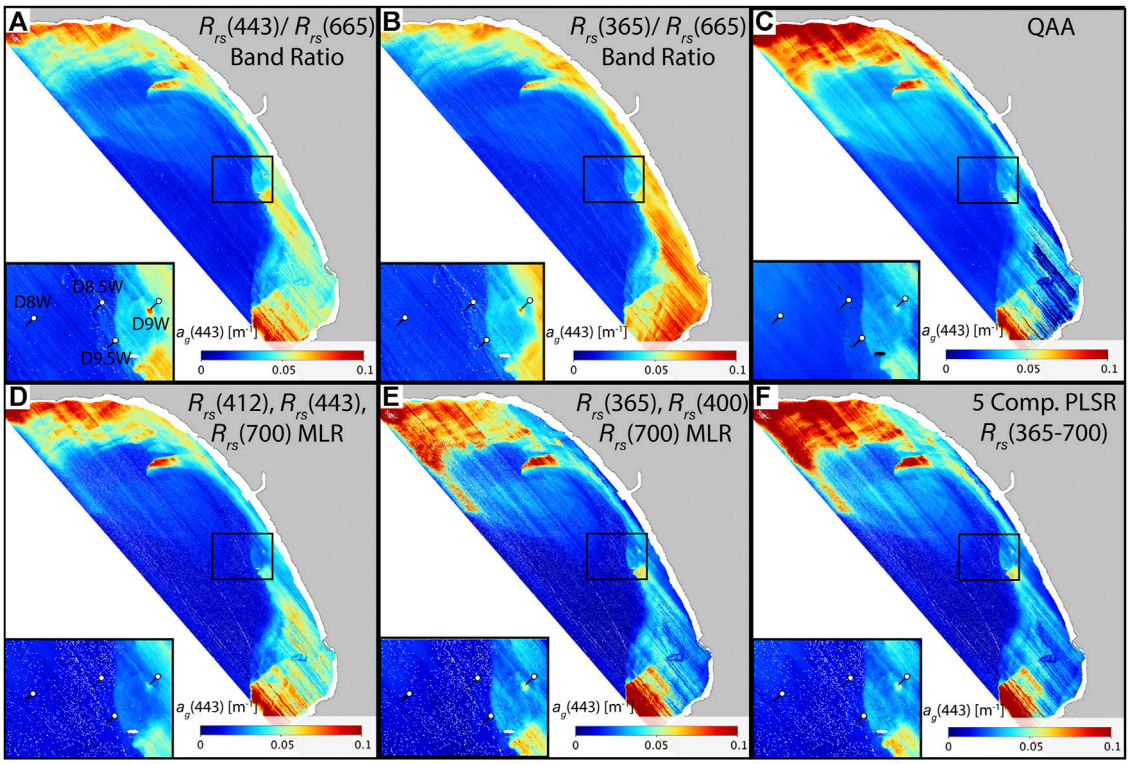

FIGURE 10 | Maps of a_g (443) retrieved from the PRISM R_{rs} (λ) using the QAA and the empirical algorithms developed in this study. The a_g (443) retrievals were made using the following algorithms: **(A)** blue-red band ratio R_{rs}(443)/R_{rs}(665), **(B)** UV-red band ratio R_{rs}(365)/R_{rs}(665), **(C)** QAA algorithm v.6, **(D)** visible-only multiple linear regression (MLR) on R_{rs}(412), R_{rs}(443), R_{rs}(700); **(E)** UV-visible MLR on R_{rs}(365), R_{rs}(400), R_{rs}(700), and **(F)** partial-least-square regression (PLSR) on the full spectrum R_{rs}(365–700) using the first five components.

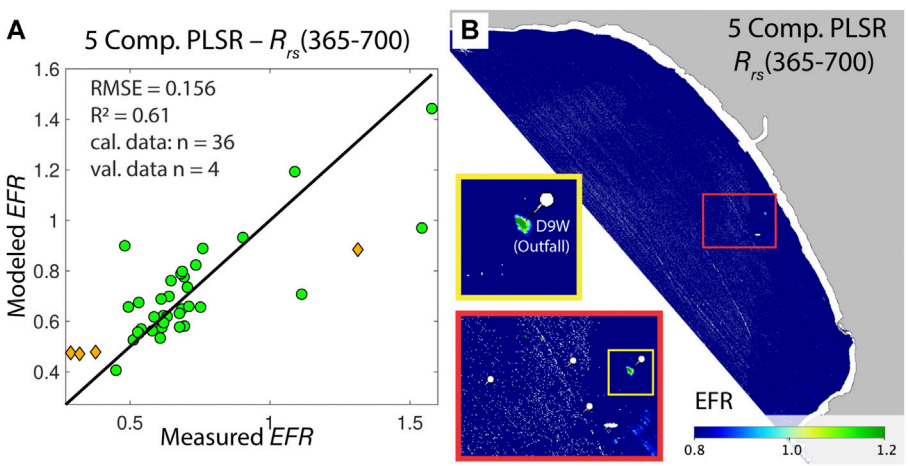

FIGURE 11 | Performance of an empirical PLSR-based algorithm for Effluent Fluorescence Ratio (*EFR*) and its implementation on the PRISM R_{rs} (λ) data: **(A)** *EFR* values modeled from the *in-situ* measured R_{rs} (λ) using the PLSR-based algorithm, versus *EFR* values measured on the samples' fluorescence EEM spectra. *In-situ* data used for calibration (n = 36) are displayed as green circles, and end-to-end validation points comparing measured *EFR* to inferred *EFR* from nearest neighbor PRISM pixels (n = 4) are displayed as orange diamonds. **(B)** Implementation of the PLSR-based algorithm on the PRISM R_{rs} (λ) data.

parameters, (MAPE and R^2), retrieval accuracies for both *EFR* algorithms were lower than for their corresponding a_g (443) algorithms (Compare **Tables 2**, **3**).

The *EFR* algorithm was applied to the PRISM imagery and generated maps of *EFR* at 20 m resolution across Santa Monica Bay. The range of remotely sensed *EFR* values matched that of the

TABLE 3 | Summary statistics associated with the performance comparison of the two *EFR* algorithms (see also **Figure 11** and **Supplementary Figure S10**). Statistics include root mean squared error (RMSE), mean average percent error (MAPE), mean absolute error (MAE), and *R*-squared for each algorithm.

Algorithm	RMSE	MAPE	MAE	R^2
Multiple linear regression (MLR)				
EFR on $R_{rs}(400) + R_{rs}(425) + R_{rs}(400)/R_{rs}(425)$	0.160	16.934	0.119	0.589
Partial-least-square regression (PLSR)				
EFR on $R_{rs}(365–700)$; 5 components	0.156	13.490	0.100	0.608

in-situ data. The map of *EFR* derived from the PLSR algorithm correctly detected the highest *EFR* at the wastewater effluent outfall (*EFR* between 0.85 and 1.25) and low *EFR* (<0.85) across the rest of Santa Monica Bay. In this respect, the PLSR algorithm appeared to successfully infer the wastewater effluent-influenced plume of DOM at the outfall, while minimizing sensitivity to CDOM from runoff and other sources. The MLR algorithm did not detect a similar maximum at the outfall (**Supplementary Figure S10**), and retrieved high EFR at other locations with high CDOM. Fitting and mapping of the MLR algorithm suggested that the small number of spectral R_{rs} bands may not have provided sufficient information to resolve *EFR* independently from CDOM concentration.

DISCUSSION

Ultraviolet Reflectance Improved Chromophoric Dissolved Organic Matter Retrievals in Urban Coastal Waters

Incorporating UV reflectance in empirical band-ratio algorithms offered only minor improvements to the accuracy of CDOM retrievals in Santa Monica Bay. A single blue-red band-ratio algorithm did not perform well in these waters and produced a spatial distribution of CDOM that closely resembled the distribution of chlorophyll-a (Trinh et al., 2017). Surprisingly, replacing the blue band (443 nm) with a UV band (365 nm), a domain where CDOM has a stronger influence, only slightly improved the accuracy of CDOM retrievals. The average percent error of $a_g(443)$ estimates decreased from approximately 30% for the red-blue ratio, to about 23% for the UV-red algorithm. This limited improvement is likely due to other in-water constituents also exerting a significant influence on UV reflectance in these waters. The dry climate of Southern California introduces less terrigenous CDOM to Santa Monica Bay compared to the more river-influenced waters typically found along the US coastline. As a result, the optical variability of the Santa Monica Bay waters tends to be strongly influenced by phytoplankton dynamics (Kahru et al., 2012; Caron et al., 2017; Trinh et al., 2017), making it more challenging to retrieve CDOM in these waters. The similarities between the mapped distribution of $a_g(443)$ inferred using the UV-red band ratio and the distribution inferred by the blue-red band ratio indicated that simply replacing a blue band by a UV one was not sufficient to remove the interference of other constituents in coastal waters strongly influenced by phytoplankton dynamics.

However, the inclusion of both UV and blue reflectance in a simple multi-band regression algorithm (MLR-based) significantly improved $a_g(443)$ retrievals. The UV-visible MLR-based algorithm combined UV, blue, and red R_{rs} and performed substantially better than the simpler UV-red band ratio algorithm, producing an average percent error of <14% for $a_g(443)$. The combined use of UV and blue R_{rs} in this algorithm likely facilitated the empirical differentiation between phytoplankton and CDOM. The benefit of using UV reflectance in the UV-visible MLR-based algorithm was also evident when comparing its performance to that of a similar MLR-based algorithm that used only visible bands (i.e., 412, 443, and 700 nm). The visible-only MLR-based algorithm produced slightly better results than the two band-ratio algorithms, but was outperformed by the UV-visible MLR-based algorithm, and its corresponding $a_g(443)$ map still included features influenced by phytoplankton. In contrast, the UV-visible MLR algorithm and the QAA both produced a similar $a_g(443)$ distribution that was distinct from that of phytoplankton. From the *in-situ* data alone, the UV-visible MLR algorithm actually outperformed the QAA. However, the QAA is not specifically optimized for the waters in Santa Monica Bay and the inclusion of UV spectral information likely offered an advantage to the UV-visible MLR-based algorithm. Overall, this analysis revealed that a simple combination of three UV, blue and red bands in a local empirical algorithm was able to retrieve $a_g(443)$ accurately and produced realistic CDOM maps in these phytoplankton-dominated waters.

The inclusion of additional spectral bands did not improve the performance of the empirical $a_g(443)$ algorithms. The PLSR algorithm leveraged all the spectral information available, but had comparable accuracy to the much simpler UV-visible MLR-based algorithm. This finding is consistent with CDOM absorption not having narrow characteristic absorption peaks like phytoplankton pigments (Rowan, 1989; Bricaud et al., 1995; Kutser et al., 2006). Instead, CDOM has a broad, featureless exponential shape, where the $a_g$variation at a single wavelength is highly predictive of that at other wavelengths. It is therefore not surprising that $a_g(443)$ was inferred with optimal accuracy from a small number of carefully chosen bands. In some cases, redundant spectral information in empirical approaches can be detrimental due to the potential of overfitting if precautions are not taken to avoid it (e.g., cross-validation as used in this study).

Although the three-band approach optimally retrieved $a_g(443)$ in Santa Monica Bay, a larger number of bands would likely prove useful or essential to retrieve CDOM accurately in more optically complex waters. The strong influence of

phytoplankton in Santa Monica Bay presented some challenges for differentiating CDOM from phytoplankton. However, these waters have only moderate concentrations of in-water constituents and relatively low concentrations of non-algal particles relative to many other coastal environments, thereby avoiding challenges associated with highly absorbing and/or turbid waters (Brezonik et al., 2015; Zheng et al., 2015; Fichot et al., 2016). Accounting for the influence of non-algal particles is expected to be feasible for these applications, but might require the use of more bands. Waters in Santa Monica Bay are also mostly optically deep, so complex optical influences from bottom reflectance did not impede retrieval of water-column optical properties. Other studies have leveraged hyperspectral $R_{rs}(\lambda)$ to improve the retrieval of IOPs in waters also influenced by or bottom reflectance (Lee et al., 1994; Mobley et al., 2005; Dekker et al., 2011). Increasing the amount of spectral information, and utilizing more complex, radiative-transfer-informed approaches may be necessary to retrieve CDOM accurately in optically shallow waters.

On the Specific Detection of Effluent-Derived Chromophoric Dissolved Organic Matter

The *EFR*, a new fluorescence-based water quality indicator that we introduced in this study, facilitated the differentiation of effluent-derived CDOM from other sources of CDOM in coastal waters. The fact that all effluent-impacted waters in Santa Monica Bay had high CDOM, but not all high-CDOM waters were effluent-impacted presented challenges for prescriptively identifying effluent. Here, the *EFR* leveraged the enhanced fluorescence of effluent-impacted samples at the F_E peak relative to the fluorescence at the F_R peak in order to overcome this challenge. The ratio of two fluorescence peaks associated with different CDOM sources (F_E being more sensitive to effluent, and F_R being more sensitive to runoff) provided the means to differentiate between two sources of CDOM independently of the level of CDOM absorption observed. As a result, the *EFR* represents a simple but reliable potential indicator of the degree of effluent influence in these waters.

Here, we tested the feasibility of retrieving *EFR* empirically from remote sensing. In contrast to other CDOM fluorescence peaks in EEM spectra, the F_E peak that is characteristic of the effluent CDOM (340–360 nm excitation and 426–454 nm emission) is theoretically amenable to remote sensing. The fluorescence of peak F_E is stimulated *in situ* by UV radiation that is naturally abundant in incident solar irradiance and emits fluorescence in the blue region, thereby producing a sun-induced fluorescence signal that can influence $R_{rs}(\lambda)$. Here, the empirical algorithms developed from the *in-situ* data set retrieved *EFR* with enough accuracy (*EFR* error of ~0.1) to separate samples heavily influenced by effluent. A PLSR-based algorithm retrieved *EFR* more accurately than the best 3-band MLR algorithm we were able to produce. When applied to PRISM data, the PLSR algorithm produced an *EFR* map with high values (>1.0) found only in the vicinity of the wastewater outfall. This algorithm specifically identified waters containing significant wastewater effluent, without being sensitive to CDOM from runoff or planktonic sources. In contrast, the MLR-based algorithm proved ineffective at discerning effluent-impacted *EFR* from the other CDOM sources, thereby suggesting the crucial importance of high spectral resolution for this purpose. While other strategies have leveraged EEMs to detect wastewater effluent (Goldman et al., 2012; Carstea et al., 2016), this is, to the extent of our knowledge, the first successful attempt at sourcing effluent-derived CDOM with remote sensing.

The presence of effluent in surface waters was only detected at relatively high concentrations of effluent. CDOM fluorescence is a relatively weak IOP, and its small influence relative to backscattering or absorption is likely responsible for the challenge of detecting effluent at low concentrations. The re-absorption of emitted fluorescence by effluent-CDOM and other absorbing constituents further decreased the influence of fluorescence signatures on ocean color. Due to the resulting small impact of fluorescence on $R_{rs}(\lambda)$, minor errors in atmospheric correction, temporal or spatial mismatch between stations and remote sensing, and measurement differences between *in-situ* and airborne reflectance measurements can have a disproportionate effect on retrieval accuracy. At low effluent concentrations, the optical signature of effluent-derived CDOM fluorescence is therefore expected to rapidly decrease below the detection threshold set by these practical limitations.

This feasibility study identified purely empirical relationships and did not explore the mechanistic relationship between effluent-impacted CDOM fluorescence and $R_{rs}(\lambda)$. Radiative transfer modeling of the effects of wastewater effluent fluorescence on surface $R_{rs}(\lambda)$ would help further refine the detection limits of effluent-derived CDOM. For example, the HydroLight radiative transfer numerical model (Mobley, 1989; Mobley et al., 1993; Mobley et al., 2020) already allows for the inclusion of a standard CDOM fluorescence when modeling $R_{rs}(\lambda)$, but would need to be modified to facilitate the incorporation of different types of CDOM fluorescence to help specifically assess the effects effluent-CDOM fluorescence on $R_{rs}(\lambda)$. Future avenues for this work could also include developing *in-situ* optical instruments leveraging the effluent-associated fluorescence peak. Prior studies have also sought to detect CDOM remotely using its fluorescence (Green and Blough, 1994; Lee et al., 1994) through stimulated fluorescence with a UV laser (Hoge et al., 1993; Vodacek et al., 1995). An active sensor providing appropriate light for fluorescence excitation could stimulate the F_E peak (e.g. an 350 nm excitation and 440 nm emission) and would yield a stronger fluorescence signal in effluent impacted waters. Work also remains for generalizing this approach beyond a single effluent release scenario. A broader survey of wastewater optical characteristics across a wide range of scenarios could allow for the remote detection of source-specific optical properties different environmental settings.

Relevance to Coastal Water-Quality Monitoring With Future Ocean Color Missions

This study revealed that some improvements to CDOM-related coastal water quality monitoring can be made possible through the use of UV-visible imaging spectroscopy, an area where visible multispectral approaches have had limited success (IOCCG, 2000; Aurin and Dierssen, 2012; IOCCG, 2015; Dekker et al., 2018). The upcoming PACE and GLIMR missions will include UV-visible imaging spectrometers with comparable specifications as PRISM and are therefore expected to provide such improvements in coastal water quality monitoring. Here, the inclusion of UV reflectance (using simple-to-implement empirical algorithms) not only facilitated the accurate detection of CDOM in urban coastal waters, but also enabled its sourcing. This study also showed that high spectral resolution was essential to remotely differentiating effluent-derived CDOM. Stepping beyond the usual retrieval of a_g, the identification of CDOM source presents exciting opportunities for water quality monitoring in complex urban coastal waters. Improved CDOM retrievals will also help improve coastal organic-carbon budgets. The empirical relationships typically observed between $a_g(\lambda)$ and [DOC] in coastal waters (Ferrari et al., 1996; del Vecchio and Blough, 2004; Mannino et al., 2008; Fichot and Benner, 2011) will facilitate the remote quantification of DOC stores and dynamics in ocean margins (Fichot and Benner, 2014; Mannino et al., 2016; Cao et al., 2018). In turn, these will help improve carbon budgets for the coastal ocean which currently have large uncertainties (Cai, 2011; Bauer et al., 2013; Najjar et al., 2018).

The extent to which water-quality monitoring capabilities will be enhanced by UV-visible imaging spectroscopy will be contingent on our ability to apply accurate atmospheric corrections and on the availability of high-quality *in-situ* validation data (IOCCG, 2012). The extended spectral range, enhanced spectral resolution, and improved signal-to-noise ratio of imaging spectrometers in upcoming missions (e.g., PACE and GLIMR) should facilitate the detection of CDOM and its subtler IOPs like effluent-CDOM fluorescence, but can only do so if accurate $R_{rs}(\lambda)$ are retrieved in the UV region. State-of-the-art atmospheric corrections and comprehensive field-validation strategies in coastal environments that include the UV region will therefore be necessary (IOCCG, 2012; Werdell et al., 2018) to achieve these improvements. Fortunately, upcoming missions like PACE will include polarimeters to better account for the contribution of various types of aerosols and are expected to facilitate atmospheric corrections and considerably improve $R_{rs}(\lambda)$ measurements in the UV and blue regions. Furthermore, ambitious field-data collection efforts are also planned in support of the PACE mission and will provide data for vicarious calibration and validation. The consistent collection of high-quality CDOM absorption and fluorescence properties (EEM) in coastal waters should be an integral part of these efforts.

DATA AVAILABILITY STATEMENT

The raw data supporting the conclusion of this article will be made available by the authors, without undue reservation.

AUTHOR CONTRIBUTIONS

JH and CF directed the study. CF led the project planning, conducted field data collection, processed *in-situ* radiometry, and contributed to data analysis and writing. JH led the data analysis and writing of the manuscript. KK conducted the CDOM, EEM, and DOC analyses on the samples. MG provided support for PRISM imagery collection and participated in the field data acquisition. DT conducted the atmospheric correction of the PRISM imagery. CC provided field campaign leadership and support. All authors commented and edited the manuscript.

FUNDING

This research was supported by a NASA Water Quality grant 80NSSC18K0344 to CF, and NASA FINESST grant 80NSSC20K1648 to graduate student JH (PI CF). Part of this research was performed at the Jet Propulsion Laboratory, California Institute of Technology, under a contract with the National Aeronautics and Space Administration (80NM0018D0004). Copyright 2020, All Rights Reserved.

ACKNOWLEDGMENTS

We thank the crew of the R/V *La Mer* and R/V *Marine Surveyor*, as well as the employees of the City of Los Angeles who participated in the sampling. We also thank Rebecca Trinh for her assistance in collecting radiometry data, and Jesus Mariano Duran and Frazier Peluso who helped with the analysis of CDOM samples.

SUPPLEMENTARY MATERIAL

The Supplementary Material for this article can be found online at: https://www.frontiersin.org/articles/10.3389/fenvs.2021.647966/full#supplementary-material

REFERENCES

Ackerman, D., and Weisberg, S. B. (2003). Relationship Between Rainfall and Beach Bacterial Concentrations on Santa Monica Bay Beaches. *J. Water Health* 1, 85–89. doi:10.2166/wh.2003.0010

Arlot, S., and Celisse, A. (2010). A Survey of Cross-Validation Procedures for Model Selection. *Statist. Surv.* 4, 40–79. doi:10.1214/09-SS054

Aurin, D. A., and Dierssen, H. M. (2012). Advantages and Limitations of Ocean Color Remote Sensing in CDOM-Dominated, Mineral-Rich Coastal and Estuarine Waters. *Remote Sens. Environ.* 125, 181–197. doi:10.1016/j.rse.2012.07.001

Bauer, J. E., Cai, W.-J., Raymond, P. A., Bianchi, T. S., Hopkinson, C. S., and Regnier, P. A. G. (2013). The Changing Carbon Cycle of the Coastal Ocean. *Nature* 504, 61–70. doi:10.1038/nature12857

Bay, S., Jones, B. H., Schiff, K., and Washburn, L. (2003). Water Quality Impacts of Stormwater Discharges to Santa Monica Bay. *Mar. Environ. Res.* 56, 205–223. doi:10.1016/S0141-1136(02)00331-8

Bowers, D. G., and Brett, H. L. (2008). The Relationship Between CDOM and Salinity in Estuaries: An Analytical and Graphical Solution. *J. Mar. Syst.* 73, 1–7. doi:10.1016/j.jmarsys.2007.07.001

Bray, N. A., Keyes, A., and Morawitz, W. M. L. (1999). The California Current System in the Southern California Bight and the Santa Barbara Channel. *J. Geophys. Res.* 104, 7695–7714. doi:10.1029/1998jc900038

Brezonik, P. L., Olmanson, L. G., Finlay, J. C., and Bauer, M. E. (2015). Factors Affecting the Measurement of CDOM by Remote Sensing of Optically Complex Inland Waters. *Remote Sens. Environ.* 157, 199–215. doi:10.1016/j.rse.2014.04.033

Bricaud, A., Babin, M., Morel, A., and Claustre, H. (1995). Variability in the Chlorophyll-specific Absorption Coefficients of Natural Phytoplankton: Analysis and Parameterization. *J. Geophys. Res.* 100, 13321–13332. doi:10.1029/95jc00463

Boyd, T. J., and Osburn, C. L. (2004). Changes in CDOM Fluorescence From Allochthonous and Autochthonous Sources During Tidal Mixing and Bacterial Degradation in Two Coastal Estuaries. *Mar. Chem.* 89, 189–210. doi:10.1016/j.marchem.2004.02.012

Cai, W.-J. (2011). Estuarine and Coastal Ocean Carbon Paradox: CO2 Sinks or Sites of Terrestrial Carbon Incineration?. *Annu. Rev. Mar. Sci.* 3, 123–145. doi:10.1146/annurev-marine-120709-142723

Cao, F., Tzortziou, M., Hu, C., Mannino, A., Fichot, C. G., del Vecchio, R., et al. (2018). Remote Sensing Retrievals of Colored Dissolved Organic Matter and Dissolved Organic Carbon Dynamics in North American Estuaries and Their Margins. *Remote Sens. Environ.* 205, 151–165. doi:10.1016/j.rse.2017.11.014

Caron, D. A., Gellene, A. G., Smith, J., Seubert, E. L., Campbell, V., Sukhatme, G. S., et al. (2017). Response of Phytoplankton and Bacterial Biomass During a Wastewater Effluent Diversion Into Nearshore Coastal Waters. *Estuar. Coast. Shelf Sci.* 186, 223–236. doi:10.1016/j.ecss.2015.09.013

Carstea, E. M., Bridgeman, J., Baker, A., and Reynolds, D. M. (2016). Fluorescence Spectroscopy for Wastewater Monitoring: A Review. *Water Res.* 95, 205–219. doi:10.1016/j.watres.2016.03.021

Chen, R. F., Bissett, P., Coble, P., Conmy, R., Gardner, G. B., Moran, M. A., et al. (2004). Chromophoric Dissolved Organic Matter (CDOM) Source Characterization in the Louisiana Bight. *Mar. Chem.* 89, 257–272. doi:10.1016/j.marchem.2004.03.017

City of Los Angeles, Environmental Monitoring Division (2017). *Fall 2015 Hyperion Treatment Plant Effluent Diversion to the 1-Mile Outfall Comprehensive Monitoring Program Final Report*. Los Angeles: Environmental Monitoring Division, Bureau of Sanitation, Department of Public Works, City of Los Angeles.

Dekker, A. G., Phinn, S. R., Anstee, J., Bissett, P., Brando, V. E., Casey, B., et al. (2011). Intercomparison of Shallow Water Bathymetry, Hydro-Optics, and Benthos Mapping Techniques in Australian and Caribbean Coastal Environments. *Limnol. Oceanogr. Methods* 9, 396–425. doi:10.4319/lom.2011.9.396

Dekker, A. G., Pinnel, N., Gege, P., Briottet, X., Court, A., Peters, S., et al. (2018). *Feasibility Study for an Aquatic Ecosystem Earth Observing System*. Committee on Earth Observation Satellites. Available online: hal-02172188. (Accessed December 14, 2020).

del Vecchio, R., and Blough, N. v. (2004). Spatial and Seasonal Distribution of Chromophoric Dissolved Organic Matter and Dissolved Organic Carbon in the Middle Atlantic Bight. *Mar. Chem.* 89, 169–187. doi:10.1016/j.marchem.2004.02.027

Devlin, M., Petus, C., da Silva, E., Tracey, D., Wolff, N., Waterhouse, J., et al. (2015). Water Quality and River Plume Monitoring in the Great Barrier Reef: An Overview of Methods Based on Ocean Colour Satellite Data. *Remote Sens.* 7, 12909–12941. doi:10.3390/rs71012909

Dojiri, M., Yamaguchi, M., Weisberg, S. B., and Lee, H. J. (2003). Changing Anthropogenic Influence on the Santa Monica Bay Watershed. *Mar. Environ. Res.* 56, 1–14. doi:10.1016/S0141-1136(03)00003-5

Ferrari, G. M., Dowell, M. D., Grossi, S., and Targa, C. (1996). Relationship Between the Optical Properties of Chromophoric Dissolved Organic Matter and Total Concentration of Dissolved Organic Carbon in the Southern Baltic Sea Region. *Mar. Chem.* 55, 299–316. doi:10.1016/S0304-4203(96)00061-8

Fichot, C. G., and Benner, R. (2011). A Novel Method to Estimate DOC Concentrations from CDOM Absorption Coefficients in Coastal Waters. *Geophys. Res. Lett.* 38, L03610. doi:10.1029/2010GL046152

Fichot, C. G., and Benner, R. (2014). The Fate of Terrigenous Dissolved Organic Carbon in a River-Influenced Ocean Margin. *Glob. Biogeochem. Cycles* 28, 300–318. doi:10.1002/2013GB004670

Fichot, C. G., and Benner, R. (2012). The Spectral Slope Coefficient of Chromophoric Dissolved Organic Matter (S 275-295) as a Tracer of Terrigenous Dissolved Organic Carbon in River-Influenced Ocean Margins. *Limnol. Oceanogr.* 57, 1453–1466. doi:10.4319/lo.2012.57.5.1453

Fichot, C. G., Downing, B. D., Bergamaschi, B. A., Windham-Myers, L., Marvin-Dipasquale, M., Thompson, D. R., et al. (2016). High-Resolution Remote Sensing of Water Quality in the San Francisco Bay-Delta Estuary. *Environ. Sci. Technol.* 50, 573–583. doi:10.1021/acs.est.5b03518

Fichot, C. G., and Miller, W. L. (2010). An Approach to Quantify Depth-Resolved marine Photochemical Fluxes Using Remote Sensing: Application to Carbon Monoxide (CO) Photoproduction. *Remote Sens. Environ.* 114, 1363–1377. doi:10.1016/j.rse.2010.01.019

Gierach, M. M., Holt, B., Trinh, R., Jack Pan, B., and Rains, C. (2017). Satellite Detection of Wastewater Diversion Plumes in Southern California. *Estuar. Coast. Shelf Sci.* 186, 171–182. doi:10.1016/j.ecss.2016.10.012

Goldman, J. H., Rounds, S. A., and Needoba, J. A. (2012). Applications of Fluorescence Spectroscopy for Predicting Percent Wastewater in an Urban Stream. *Environ. Sci. Technol.* 46, 4374–4381. doi:10.1021/es2041114

Green, S. A., and Blough, N. V. (1994). Optical Absorption and Fluorescence Properties of Chromophoric Dissolved Organic Matter in Natural Waters. *Limnol. Oceanogr.* 39, 1903–1916. doi:10.4319/lo.1994.39.8.1903

Halpern, B. S., Longo, C., Hardy, D., McLeod, K. L., Samhouri, J. F., Katona, S. K., et al. (2012). An index to Assess the Health and Benefits of the Global Ocean. *Nature* 488, 615–620. doi:10.1038/nature11397

Halpern, B. S., Walbridge, S., Selkoe, K. A., Kappel, C. v., Micheli, F., D'Agrosa, C., et al. (2008). A Global Map of Human Impact on marine Ecosystems. *Science* 319, 948–952. doi:10.1126/science.1149345

Hansell, D. A., and Carlson, C. A. (2014). *Biogeochemistry of Marine Dissolved Organic Matter*. 2nd Edn. San Diego, CA: Elsevier.

Helms, J. R., Stubbins, A., Ritchie, J. D., Minor, E. C., Kieber, D. J., and Mopper, K. (2008). Absorption Spectral Slopes and Slope Ratios as Indicators of Molecular Weight, Source, and Photobleaching of Chromophoric Dissolved Organic Matter. *Limnol. Oceanogr.* 53, 955–969. doi:10.4319/lo.2008.53.3.0955

Hernes, P. J., and Benner, R. (2003). Photochemical and Microbial Degradation of Dissolved Lignin Phenols: Implications for the Fate of Terrigenous Dissolved Organic Matter in marine Environments. *J. Geophys. Res.* 108, 7-1–7-9. doi:10.1029/2002jc001421

Hoge, F. E., Vodacek, A., and Blough, N. v. (1993). Inherent Optical Properties of the Ocean: Retrieval of the Absorption Coefficient of Chromophoric Dissolved Organic Matter From Fluorescence Measurements. *Limnol. Oceanogr.* 38, 1394–1402. doi:10.4319/lo.1993.38.7.1394

Howard, M. D. A., Kudela, R. M., and McLaughlin, K. (2017). New Insights Into Impacts of Anthropogenic Nutrients on Urban Ecosystem Processes on the Southern California Coastal Shelf: Introduction and Synthesis. *Estuar. Coast. Shelf Sci.* 186, 163–170. doi:10.1016/j.ecss.2016.06.028

Howard, M. D. A., Sutula, M., Caron, D. A., Chao, Y., Farrara, J. D., Frenzel, H., et al. (2014). Anthropogenic Nutrient Sources Rival Natural Sources on Small Scales in the Coastal Waters of the Southern California Bight. *Limnol. Oceanogr.* 59, 285–297. doi:10.4319/lo.2014.59.1.0285

IOCCG (2000). "Remote Sensing of Ocean Colour in Coastal and Other Optically-Complex Waters," in *Reports of the International Ocean-Colour Coordinating Group, No. 3*. Editor S. Sathyendranath (Dartmouth, Canada: IOCCG). Available at: https://ioccg.org/wp-content/uploads/2015/10/ioccg-report-03.pdf (Accessed December 14, 2020).

IOCCG (2008). "Why Ocean Colour? the Societal Benefits of Ocean-Colour Technology," in *Reports of the International Ocean-Colour Coordinating Group, No. 7*. Editors T. Platt, N. Hoepffner, V. Stuart, and C. Brown (Dartmouth, Canada: IOCCG). Available at: https://ioccg.org/wp-content/uploads/2015/10/ioccg-report-07.pdf (Accessed December 14, 2020).

IOCCG (2012). "Mission Requirements for Future Ocean-Colour Sensors," in *Reports of the International Ocean-Colour Coordinating Group, No. 13*. Editors C. R. McClain and G. Meister (Dartmouth, Canada: IOCCG). Available at: http://www.ioccg.org/reports/IOCCG_Report13.pdf (Accessed December 14, 2020).

IOCCG (2015). "Earth Observations in Support of Global Water Quality Monitoring," in *Reports of the International Ocean-Colour Coordinating Group, No. 17*. Editors A. Dekker and C. Binding (Dartmouth, Canada: International Ocean Colour Coordinating Group). Available at: https://ioccg.org/wp-content/uploads/2018/09/ioccg_report_17-wq-rr.pdf (Accessed December 14, 2020).

Johannessen, S. C., Miller, W. L., and Cullen, J. J. (2003). Calculation of UV Attenuation and Colored Dissolved Organic Matter Absorption Spectra From Measurements of Ocean Color. *J. Geophys. Res.* 108, 17-1–17-13. doi:10.1029/2000jc000514

Kahru, M., di Lorenzo, E., Manzano-Sarabia, M., and Mitchell, B. G. (2012). Spatial and Temporal Statistics of Sea Surface Temperature and Chlorophyll Fronts in the California Current. *J. Plankton Res.* 34, 749–760. doi:10.1093/plankt/fbs010

Kutser, T., Metsamaa, L., Strömbeck, N., and Vahtmäe, E. (2006). Monitoring Cyanobacterial Blooms by Satellite Remote Sensing. *Estuar. Coast. Shelf Sci.* 67, 303–312. doi:10.1016/j.ecss.2005.11.024

Laanen, M. L., Peters, S. W. M., Dekker, A. G., and Woerd, H. J. v. d. (2011). Assessment of the Scattering by Sub-Micron Particles in Inland Waters. *J. Eur. Opt. Soc. Rapid. Publ.* 6, 15. doi:10.2971/jeos.2011.11046

Lee, Z., Carder, K. L., and Arnone, R. A. (2002). Deriving Inherent Optical Properties From Water Color: A Multiband Quasi-Analytical Algorithm for Optically Deep Waters. *Appl. Opt.* 41, 5755. doi:10.1364/ao.41.005755

Lee, Z., Carder, K. L., Hawes, S. K., Steward, R. G., Peacock, T. G., and Davis, C. O. (1994). Model for the Interpretation of Hyperspectral Remote-Sensing Reflectance. *Appl. Opt.* 33, 5721. doi:10.1364/ao.33.005721

Lee, Z., Lubac, B., Werdell, J., and Arnone, R. (2009). An Update of the Quasi-Analytical Algorithm (QAA_v5). Available at: https://www.ioccg.org/groups/Software_OCA/QAA_v5.pdf (Accessed December 6, 2020).

Lee, Z., Lubac, B., and Werdell, J. (2014). Update of the Quasi-Analytical Algorithm (QAA_v6). Available at: http://www.ioccg.org/groups/Software_OCA/QAA_v6_2014209.pdf (Accessed December 6, 2020).

Lyon, G. S., and Sutula, M. A. (2011). "Effluent Discharges to the Southern California Bight From Large Municipal Wastewater Treatment Facilities From 2005 to 2009," in *South California Coastal Watershed Research Project Annual Report 2011*, Editors Weisberg, S. B., and Miller, K.. Costa Mesa, CA, 223–236.

Mannino, A., Russ, M. E., and Hooker, S. B. (2008). Algorithm Development and Validation for Satellite-Derived Distributions of DOC and CDOM in the U.S. Middle Atlantic Bight. *J. Geophys. Res.* 113, 1–19. doi:10.1029/2007JC004493

Mannino, A., Signorini, S. R., Novak, M. G., Wilkin, J., Friedrichs, M. A. M., and Najjar, R. G. (2016). Dissolved Organic Carbon Fluxes in the Middle Atlantic Bight: An Integrated Approach Based on Satellite Data and Ocean Model Products. *J. Geophys. Res. Biogeosci.* 121, 312–336. doi:10.1002/2015JG003031

McKinney, M. L. (2002). Urbanization, Biodiversity, and Conservation. *Bioscience* 52, 583–590. doi:10.1641/0006-3568(2002)052

McLaughlin, K., Nezlin, N. P., Howard, M. D. A., Beck, C. D. A., Kudela, R. M., Mengel, M. J., et al. (2017). Rapid Nitrification of Wastewater Ammonium Near Coastal Ocean Outfalls, Southern California, USA. *Estuar. Coast. Shelf Sci.* 186, 263–275. doi:10.1016/j.ecss.2016.05.013

Mevik, B.-H., and Wehrens, R. (2007). TheplsPackage: Principal Component and Partial Least Squares Regression in R. *J. Stat. Soft.* 18, 1–23. doi:10.18637/jss.v018.i02

Mobley, C. D. (1989). A Numerical Model for the Computation of Radiance Distributions in Natural Waters With Wind-Roughened Surfaces. *Limnol. Oceanogr.* 34, 1473–1483. doi:10.4319/lo.1989.34.8.1473

Mobley, C. D., Boss, E., and Roesler, C. (2020). A Collaborative Web-Based Book on Optical Oceanography. Available at: https://www.oceanopticsbook.info/view/radiative-transfer-theory/level-2/hydrolight (Accessed December 21, 2020).

Mobley, C. D., Gentili, B., Gordon, H. R., Jin, Z., Kattawar, G. W., Morel, A., et al. (1993). Comparison of Numerical Models for Computing Underwater Light fields. *Appl. Opt.* 32, 7484–7504. doi:10.1364/AO.32.007484

Mobley, C. D., Sundman, L. K., Davis, C. O., Bowles, J. H., Downes, T. V., Leathers, R. A., et al. (2005). Interpretation of Hyperspectral Remote-Sensing Imagery by Spectrum Matching and Look-Up Tables. *Appl. Opt.* 44, 3576. doi:10.1364/AO.44.003576

Morrison, J. R., and Nelson, N. B. (2004). Seasonal Cycle of Phytoplankton UV Absorption at the Bermuda Atlantic Time-Series Study (BATS) Site. *Limnol. Oceanogr.* 49, 215–224. doi:10.4319/lo.2004.49.1.0215

Mouroulis, P., van Gorp, B., Green, R. O., Dierssen, H., Wilson, D. W., Eastwood, M., et al. (2014). Portable Remote Imaging Spectrometer Coastal Ocean Sensor: Design, Characteristics, and First Flight Results. *Appl. Opt.* 53, 1363. doi:10.1364/ao.53.001363

Mouw, C. B., Greb, S., Aurin, D., DiGiacomo, P. M., Lee, Z., Twardowski, M., et al. (2015). Aquatic Color Radiometry Remote Sensing of Coastal and Inland Waters: Challenges and Recommendations for Future Satellite Missions. *Remote Sens. Environ.* 160, 15–30. doi:10.1016/j.rse.2015.02.001

Murphy, K. R., Stedmon, C. A., Graeber, D., and Bro, R. (2013). Fluorescence Spectroscopy and Multi-Way Techniques. PARAFAC. *Anal. Methods* 5, 6557–6566. doi:10.1039/c3ay41160e

Najjar, R. G., Herrmann, M., Alexander, R., Boyer, E. W., Burdige, D. J., Butman, D., et al. (2018). Carbon Budget of Tidal Wetlands, Estuaries, and Shelf Waters of Eastern North America. *Glob. Biogeochem. Cycles* 32, 389–416. doi:10.1002/2017GB005790

R Core Team (2018). *R: A Language and Environment for Statistical Computing*. Vienna, Austria: R Foundation for Statistical Computing.

Rabalais, N. N., Turner, R. E., Díaz, R. J., and Justić, D. (2009). Global Change and Eutrophication of Coastal Waters. *ICES J. Mar. Sci.* 66, 1528–1537. doi:10.1093/icesjms/fsp047

Rowan, K. S. (1989). *Photosynthetic Pigments of Algae*. New York, NY: CUP Archive.

Savitzky, A., and Golay, M. J. E. (1964). Smoothing and Differentiation of Data by Simplified Least Squares Procedures. *Anal. Chem.* 36, 1627–1639. doi:10.1021/ac60214a047

Siegel, D. A., Maritorena, S., Nelson, N. B., Hansell, D. A., and Lorenzi-Kayser, M. (2002). Global Distribution and Dynamics of Colored Dissolved and Detrital Organic Materials. *J. Geophys. Res.* 107, 21–1. doi:10.1029/2001jc000965

Stedmon, C. A., and Markager, S. (2003). Behaviour of the Optical Properties of Coloured Dissolved Organic Matter Under Conservative Mixing. *Estuar. Coast. Shelf Sci.* 57, 973–979. doi:10.1016/S0272-7714(03)00003-9

Sullivan, J. M., Twardowski, M. S., Zaneveld, J. R. v., Moore, C. M., Barnard, A. H., Donaghay, P. L., et al. (2006). Hyperspectral Temperature and Salt Dependencies of Absorption by Water and Heavy Water in the 400-750 nm Spectral Range. *Appl. Opt.* 45, 5294. doi:10.1364/AO.45.005294

Swan, C. M., Nelson, N. B., Siegel, D. A., and Fields, E. A. (2013). A Model for Remote Estimation of Ultraviolet Absorption by Chromophoric Dissolved Organic Matter Based on the Global Distribution of Spectral Slope. *Remote Sens. Environ.* 136, 277–285. doi:10.1016/j.rse.2013.05.009

Thompson, D. R., Cawse-Nicholson, K., Erickson, Z., Fichot, C. G., Frankenberg, C., Gao, B.-C., et al. (2019). A Unified Approach to Estimate Land and Water Reflectances with Uncertainties for Coastal Imaging Spectroscopy. *Remote Sens. Environ.* 231, 111198. doi:10.1016/j.rse.2019.05.017

Thompson, D. R., Natraj, V., Green, R. O., Helmlinger, M. C., Gao, B.-C., and Eastwood, M. L. (2018). Optimal Estimation for Imaging Spectrometer Atmospheric Correction. *Remote Sens. Environ.* 216, 355–373. doi:10.1016/j.rse.2018.07.003

Tiefenthaler, L. L., Schiff, K. C., and Leecaster, M. K. (2000). Temporal Variability Patterns of Stormwater Concentrations in Urban Stormwater Runoff," *Southern California Coastal Water Research Project Annual Report*. Westminster, CA, 52–62.

Tilstone, G. H., Airs, R. L., Vicente, V. M., Widdicombe, C., Llewellyn, C., and Stramski, D. (2010). High Concentrations of Mycosporine-Like Amino Acids and Colored Dissolved Organic Matter in the Sea Surface Microlayer off the Iberian Peninsula. *Limnol. Oceanogr.* 55, 1835–1850. doi:10.4319/lo.2010.55.5.1835

Trinh, R. C., Fichot, C. G., Gierach, M. M., Holt, B., Malakar, N. K., Hulley, G., et al. (2017). Application of Landsat 8 for Monitoring Impacts of Wastewater Discharge on Coastal Water Quality. *Front. Mar. Sci.* 4, 329. doi:10.3389/fmars.2017.00329

Tzortziou, M., Neale, P. J., Osburn, C. L., Megonigal, J. P., Maie, N., and JaffÉ, R. (2008). Tidal Marshes as a Source of Optically and Chemically Distinctive Colored Dissolved Organic Matter in the Chesapeake Bay. *Limnol. Oceanogr.* 53, 148–159. doi:10.4319/lo.2008.53.1.0148

Vandermeulen, R. A., Mannino, A., Neeley, A., Werdell, J., and Arnone, R. (2017). Determining the Optimal Spectral Sampling Frequency and Uncertainty Thresholds for Hyperspectral Remote Sensing of Ocean Color. *Opt. Express* 25, A785. doi:10.1364/oe.25.00a785

Vodacek, A., Blough, N. v., DeGrandpre, M. D., DeGrandpre, M. D., and Nelson, R. K. (1997). Seasonal Variation of CDOM and DOC in the Middle Atlantic Bight: Terrestrial Inputs and Photooxidation. *Limnol. Oceanogr.* 42, 674–686. doi:10.4319/lo.1997.42.4.0674

Vodacek, A., Hogel, F. E., Swift, R. N., Yungel, J. K., Peltzer, E. T., and Blough, N. V. (1995). The Use of *In Situ* and Airborne Fluorescence Measurements to Determine UV Absorption Coefficients and DOC Concentrations in Surface Waters. *Limnol. Oceanogr.* 40, 411–415. doi:10.4319/lo.1995.40.2.0411

Walker, S. A., Amon, R. M. W., Stedmon, C., Duan, S., and Louchouarn, P. (2009). The Use of PARAFAC Modeling to Trace Terrestrial Dissolved Organic Matter and Fingerprint Water Masses in Coastal Canadian Arctic Surface Waters. *J. Geophys. Res.* 114, 1–12. doi:10.1029/2009JG000990

Washburn, L., McClure, K. A., Jones, B. H., and Bay, S. M. (2003). Spatial Scales and Evolution of Stormwater Plumes in Santa Monica Bay. *Mar. Environ. Res.* 56, 103–125. doi:10.1016/S0141-1136(02)00327-6

Werdell, P. J., McKinna, L. I. W., Boss, E., Ackleson, S. G., Craig, S. E., Gregg, W. W., et al. (2018). An Overview of Approaches and Challenges for Retrieving marine Inherent Optical Properties from Ocean Color Remote Sensing. *Prog. Oceanogr.* 160, 186–212. doi:10.1016/j.pocean.2018.01.001

Yamashita, Y., Boyer, J. N., and Jaffé, R. (2013). Evaluating the Distribution of Terrestrial Dissolved Organic Matter in a Complex Coastal Ecosystem Using Fluorescence Spectroscopy. *Cont. Shelf Res.* 66, 136–144. doi:10.1016/j.csr.2013.06.010

Zheng, G., Stramski, D., and Digiacomo, P. M. (2015). A Model for Partitioning the Light Absorption Coefficient of Natural Waters Into Phytoplankton, Nonalgal Particulate, and Colored Dissolved Organic Components: A Case Study for the Chesapeake Bay. *J. Geophys. Res. Oceans* 120, 2601–2621. doi:10.1002/2014JC010604

Zhu, W., Yu, Q., Tian, Y. Q., Chen, R. F., and Gardner, G. B. (2011). Estimation of Chromophoric Dissolved Organic Matter in the Mississippi and Atchafalaya River Plume Regions Using Above-Surface Hyperspectral Remote Sensing. *J. Geophys. Res.* 116, 1–22. doi:10.1029/2010JC006523

Zhu, X., Miller, W. L., and Fichot, C. G. (2020). Simple Method to Determine the Apparent Quantum Yield Matrix of CDOM Photobleaching in Natural Waters. *Environ. Sci. Technol.* 54, 14096–14106. doi:10.1021/acs.est.0c03605

Conflict of Interest: The authors declare that the research was conducted in the absence of any commercial or financial relationships that could be construed as a potential conflict of interest.

Copyright © 2021 Harringmeyer, Kaiser, Thompson, Gierach, Cash and Fichot. This is an open-access article distributed under the terms of the Creative Commons Attribution License (CC BY). The use, distribution or reproduction in other forums is permitted, provided the original author(s) and the copyright owner(s) are credited and that the original publication in this journal is cited, in accordance with accepted academic practice. No use, distribution or reproduction is permitted which does not comply with these terms.

frontiers | Frontiers in Environmental Science

ORIGINAL RESEARCH
published: 14 July 2022
doi: 10.3389/fenvs.2022.690963

Kelp Patch-Specific Characteristics Limit Detection Capability of Rapid Survey Method for Determining Canopy Biomass Using an Unmanned Aerial Vehicle

Meredith L. McPherson[1,2]* *and Raphael M. Kudela*[1]

[1]Ocean Sciences Department, University of California, Santa Cruz, Santa Cruz, CA, United States, [2]Department of Biology, University of Massachusetts Boston, Boston, MA, United States

Kelp forests dominate autotrophic biomass and primary productivity of approximately 30,000 to 60,000 km of shallow temperate and Arctic rocky reef coastline globally and contribute significantly to carbon cycling in the coastal ocean. Rapid biomass turnover is driven by very high growth rates and seasonal environmental drivers. As a result, kelp biomass varies greatly with time, space, and by species. In the northeast Pacific region, bull kelp (*Nereocystis leutkeana*) and giant kelp (*Macrocystis pyrifera*) form extensive floating surface canopies with a distinct spectral signature compared to the surrounding water. Studies have shown that remote sensing is advantageous for deriving large-scale estimates of floating surface canopy biomass, which comprises more than 90% of bull and giant kelp standing stock. However, development and validation of remotely derived kelp canopy biomass is lacking because existing approaches are time intensive and costly. This study attempted to close that gap by developing a rapid survey design utilizing diver and unmanned aerial vehicle (UAV) imagery across six sites in northern and central California. Kelp sporophytes were collected and measured for morphometric characteristics and genera-specific allometry to canopy biomass. Kelp density was measured using *in situ* diver surveys and coupled with UAV imagery to quantify kelp canopy biomass at a range of ground sampling distances. We successfully estimated kelp canopy biomass from UAV imagery at 33% (2/6) of the survey sites, but consistently determining canopy biomass via this approach was challenged by both survey design and kelp patch-specific spatial characteristics. The morphologies of bull kelp in Monterey were significantly different than other regions measured, but further work should be conducted to fully characterize differences in canopy biomass at the regional and sub-regional scale. We use this opportunity to suggest survey design strategies that will increase the success of future methodological development of UAV biomass retrieval. We also recommend developing long-term, annual genera-specific monitoring programs across the northeast Pacific region and beyond to validate remote sensing derived biomass estimates beyond the small number of existing well-characterized sites.

Keywords: nereocystis, macrocystis, bull kelp, giant kelp, canopy biomass, semi-variogram, UAV, UAS

OPEN ACCESS

Edited by:
Wesley Moses,
United States Naval Research Laboratory, United States

Reviewed by:
Wiebe Nijland,
Utrecht University, Netherlands
Tianhai Cheng,
Institute of Remote Sensing and Digital Earth (CAS), China

***Correspondence:**
Meredith L. McPherson
Meredith.McPherson@umb.edu

Specialty section:
This article was submitted to Environmental Informatics and Remote Sensing, a section of the journal Frontiers in Environmental Science

Received: *05 April 2021*
Accepted: *06 June 2022*
Published: *14 July 2022*

Citation:
McPherson ML and Kudela RM (2022) Kelp Patch-Specific Characteristics Limit Detection Capability of Rapid Survey Method for Determining Canopy Biomass Using an Unmanned Aerial Vehicle. Front. Environ. Sci. 10:690963. doi: 10.3389/fenvs.2022.690963

INTRODUCTION

Kelp forests are highly productive and diverse nearshore ecosystems that thrive along shallow temperate and Arctic rocky reefs (Steneck et al., 2002) and they dominate autotrophic biomass and primary productivity across approximately 25% of the world's coastlines (Reed and Brzezinski, 2009; Wernberg et al., 2019). As a result, kelp forests are a biogenic habitat that support a range of goods and services of ecological (three-dimensional habitat structure, biodiversity, nutrient cycling, etc.) and economic (coastline defense, recreational and commercial fisheries, harvestable biomass) value (Teagle et al., 2017). Kelps contribute significantly to nutrient and carbon cycling in the coastal ocean (Reed and Brzezinski, 2009), where rapid biomass turnover is driven by very high growth rates and seasonal environmental drivers (Reed et al., 2008). However, deriving large-scale estimates of kelp standing stock is challenging because kelp forests and macroalgal habitats are spatially and temporally dynamic (Dayton et al., 1999). Distribution of biomass is driven by species, environmental conditions, and physical disturbance such as waves and swell (Ebeling et al., 1985), and patch-level biological and physical factors such as grazing, spore dispersal, and substrate type (Dayton et al., 1984). These challenges influence our ability to determine accurate regional and global rates of kelp net primary productivity, carbon cycling, and carbon sequestration. Determining kelp biomass based carbon metrics is imperative as kelp forests are threatened by the influence of anthropogenic factors such as climate change (Wernberg et al., 2016; Rasher et al., 2020), increasing frequency and intensity of marine heatwaves (Oliver et al., 2017; Cavanaugh et al., 2019; Straub et al., 2019; Dexter et al., 2020; McPherson et al., 2021), and overfishing (Ling et al., 2009).

In the northeast Pacific region (Aleutians Islands, Alaska to Baja California, Mexico) giant kelp (*Macrocystis pyrifera*) and bull kelp (*Nereocystis luetkeana*) are the dominant surface canopy forming kelps. Their canopies are easily observed using remote sensing techniques, such as plane-based aerial surveys, spaceborne satellites, and unmanned aerial vehicles (UAVs) because the spectral signature of the surface canopy is distinct from the surrounding water. This is advantageous for determining estimates of standing stock because nearly all (>90%) of bull and giant kelp biomass and, thereby primary production, is contained within the surface canopy. Historically, the most common kelp mapping approaches have evaluated kelp canopy area rather than biomass because 1) many mapping campaigns are conducted by state natural resource departments that have prioritized canopy extent as a metric for kelp as a harvestable and managed natural resource (e.g. California Department of Fish and Wildlife (CDFW), Oregon Department of Fish and Wildlife (ODFW), Washington Department of Natural Resources (WDNR), Alaska Department of Fish and Game, etc.), and 2) species- or region-specific relationships between pixel spectral characteristics and biomass have not been widely developed nor validated. While there is significant value in monitoring kelp canopy area, estimating large-scale rates of primary productivity and carbon sequestration will continue to be limited unless region and genera-specific biomasses can be derived from remote sensing data.

Studies reporting validation of remote sensing derived estimates of kelp canopy biomass are limited, but the general approach is to establish location specific empirical relationships between *in situ* measurements of kelp biomass and image-based kelp classification methods. Allometry is primarily used to derive *in situ* biomass from kelp morphology such as blade length, bulb diameter (Stekoll et al., 2006), or a combination of multiple morphometric features (Rassweiler et al., 2008). Stekoll et al. (2006) created the first remote estimates of kelp canopy biomass for bull kelp and *Allaria fistulosa* in southeast Alaska using high spatial resolution (0.5–2 m) multispectral (4 band) airborne data and ground truthing techniques in 2002 and 2003. Normalized difference $[(\rho_{nir} - \rho_{blue})/(\rho_{nir} + \rho_{blue})]$ was used to generate kelp classification and was converted to biomass using *in situ* density counts in 16 m^2 surface quadrats and an allometric relationship to sub-bulb diameter (defined as 15 cm below the greatest diameter of the bulb). Cavanaugh et al. (2010), Cavanaugh et al. (2011) found a strong correlation between spectral band information and canopy biomass using 10 m (SPOT) and 30 m (Landsat TM) spatial resolutions for giant kelp along the Santa Barbara coast. Image based kelp classification was conducted using both normalized difference vegetation index (NDVI; Cavanaugh et al., 2010) and multiple endmember spectral mixture analysis (MESMA; Cavanaugh et al., 2011). Satellite data were linked to canopy biomass derived from long-term subtidal monitoring of giant kelp by the Santa Barbara Channel Long-term Ecological Research program within permanent approximately 1,600 m^2 plots (Rassweiler et al., 2008). Canopy biomass was derived using diver measurements of frond length and conversion factors derived from sporophytes collected and dissected in the lab monthly for a 2 year period (Rassweiler et al., 2008). Subsequently, the relationship between MESMA derived kelp fraction and Santa Barbara giant kelp canopy biomass has been used to make regional estimates of canopy biomass from Baja California, Mexico to Año Nuevo, California using USGS Landsat imagery across more than 30 years (Bell et al., 2015; Cavanaugh et al., 2019; Bell et al., 2020b). Despite the robust nature of the satellite-derived canopy biomass from the Santa Barbara coastal sites, sub-regional differences in sporophyte morphology and allometry affecting the broader regional validity of this relationship have not previously been considered.

In addition to the applicability of biomass predictions, there is increasing motivation to apply higher spatial resolution (<30 m) imagery to kelp mapping efforts in regions where complex shoreline topography exists (Nijland et al., 2019) and significant kelp canopy declines have occurred (McPherson et al., 2021). To date, a range of platforms with varying spatial resolutions have been applied to kelp mapping efforts (Schroeder et al., 2019). Multispectral USGS Landsat imagery (30 m spatial resolution) has been widely used because of the large temporal and spatial scales at which data are freely available (Cavanaugh et al., 2010; Cavanaugh et al., 2011; Bell et al., 2015; Young et al., 2015; Beas-Luna et al., 2020; Bell et al., 2020b; Friedlander et al., 2020; McPherson et al., 2021; Houskeeper

et al., 2022). Studies comparing the suite of sensors (Landsat TM, ETM+, and OLI) to higher spatial resolution aerial imagery (e.g. CDFW/ODFW) have found that though false positives (water pixels mis-identified as kelp) by Landsat are uncommon, the sensor often misses pixels containing less than 20% kelp (Hamilton et al., 2020; Finger et al., 2021). Furthermore, the difference between relatively high (~2 m) and moderate (30 m) spatial resolution is pronounced when canopy coverage is low (Finger et al., 2021; kelp reflectance signals are lower than Landsat's detection capabilities) or coastline features (large tidal range and complex topography) limit detection of fringing kelp beds within a 30 m buffer to the shore (Nijland et al., 2019). Mora-Soto et al. (2020) and Huovinen et al. (2020) were the first studies to use European Space Agency (ESA) Sentinel-2 (10 m) imagery to map giant kelp. The creation of a global kelp map by Mora-Soto et al. (2020) was validated against previously surveyed or observed beds, but the approach was not effective at detecting bed sizes <1 ha (10,000 m^2) and results were limited to kelp canopy area rather than biomass or productivity.

Increasingly, scientists and managers are using UAV platforms to customize and validate kelp mapping efforts, despite the tradeoffs in the total area covered using UAVs versus other platforms and logistical challenges. UAVs offer flexibility for studying kelp beds at local, and potentially sub-regional, scales and have applicability in offshore aquaculture (Bell et al., 2020a), satellite remote sensing validation (Mora-Soto et al., 2020), physiology (Bell et al., 2020a), and may supplement expensive aerial surveys by resource management/monitoring efforts (Hohman et al., 2019). UAVs are also optimal for observations of local scale kelp bed variability; Cavanaugh et al. (2021) illustrated the significance of tidal height and current velocity on changes in kelp canopy area and the effect across sites.

Given the flexibility of UAV platforms, developing effective field surveys is more accessible than with satellite imagery and the potential for quantifying fine-scale physiological metrics using UAVs mounted with multispectral or hyperspectral sensors is possible given sufficient understanding of biomass. Due to the limited number of validation studies deriving kelp canopy biomass using remote sensing data we designed a rapid sampling approach where morphology measurements and diver surveys were used to estimate *in situ* kelp canopy biomass and a UAV platform was used to map floating kelp canopy. Though the surveys were designed with the aim to develop and scale regional estimates of giant and bull kelp canopy biomass, this was challenged by several factors. Key outcomes include 1) an investigation of the regional differences in allometric relationships for canopy biomass derivation, and 2) characterizing the features of both the survey design and kelp patch that influenced our ability to reliably retrieve estimates of canopy biomass from the UAV imagery. Finally, we suggest *in situ* sample designs to improve outcomes for future approaches to deriving canopy biomass using remote sensing platforms.

METHODS

Survey locations–Six sites along the California coastline were selected for *in situ* diver and UAV surveys in July and August 2019 (**Figures 1**, **2**; **Table 1**). Three of the sites consisted of pure bull kelp, two in Mendocino County in northern California (**Figure 1** magenta box; **Figures 2A, B**) and one along the northeastern side of the Monterey Peninsula in central California (**Figure 1** green box; **Figure 2C**). The other three consisted of pure giant kelp along the northeastern side of the Monterey Peninsula (**Figure 1** green box; **Figures 2D–F**). The length of time between conducting the dive and UAV surveys for sites did not exceed 30 days. Site locations were chosen based on accessibility to kelp beds, protection from large swell, sporophyte collection and transport to shore, and ease of accessibility for UAV flight operations.

FIGURE 1 | A map of the California coastline illustrating specific areas where survey sites were located in Mendocino County (magenta box) and Monterey County (green box).

UAV data acquisition and processing–A graphical overview describing the processing scheme for UAV imagery (top panel) and *in situ* surveys (bottom panel) is described in **Figure 3**. High resolution multispectral imagery were obtained at each survey site (**Table 1**) using a DJI Matrice 100 quadcopter mounted with a MicaSense RedEdge-M pointed nadir to the water surface. The RedEdge-M simultaneously captures data in five spectral bands, the blue (475 nm), green (560 nm), red (668 nm), red-edge (717 nm), and near-infrared (NIR; 840 nm) (See **Supplementary Table S1** for

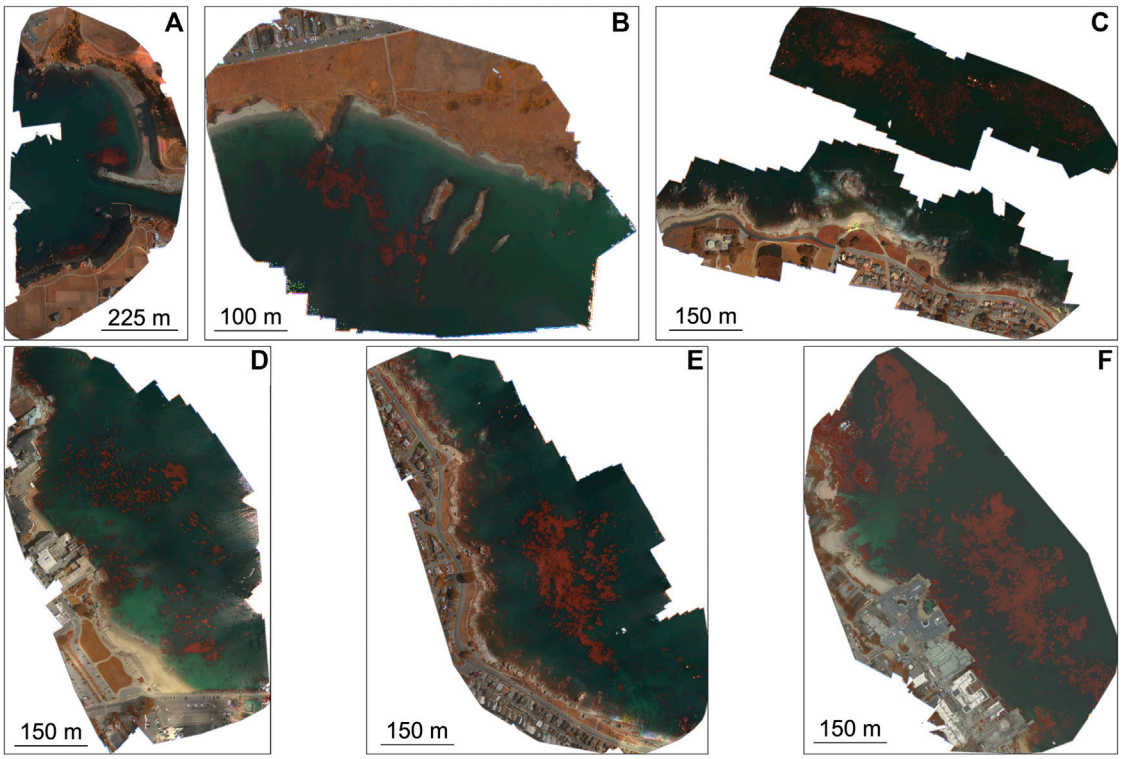

FIGURE 2 | Micasense RedEdge-M false color orthomosaics of the six survey sites. **(A)** Noyo Harbor (NH), Mendocino County; **(B)** Portuguese Beach (PB), Mendocino Peninsula; **(C)** Point Piños (PP), Monterey Peninsula; **(D)** Otter Cove (OC), Monterey Peninsula; **(E)** San Carlos Beach (SCB), Monterey Peninsula; **(F)** Hopkins Marine Station (HMS), Monterey Peninsula.

TABLE 1 | Detailed description of each survey location including region (Mendocino County or Monterey Peninsula), kelp genera, dive site coordinates, dive survey date, substrate type, UAV survey date, and mean tidal height during each UAV survey, survey site mean state (MLLW and MHHW) from Pt. Arena, CA and Monterey, CA (tidesandcurrents.noaa.gov).

Site Name	Site Location	Kelp Genera	Latitude	Longitude	Dive Survey Date	Substrate Type	UAV Survey Date	UAV Survey Tidal Height (m)	Site Tidal Range (m)
Noyo Harbor (NH)	Mendocino County	bull kelp	39.429	−123.810	7 August 2019	Sandy Rocky	8 August 2019	0.77	Pt. Arena, CA MLLW = -0.012 MHHW = +1.7
Portuguese Beach (PB)	Mendocino County	bull kelp	39.303	−123.802	8 August 2019	Sandy Rocky	8 August 2019	1.72	
Point Piños (PP)	Monterey Peninsula	bull kelp	36.630	−121.919	August 14 and 28, 2019	Rocky	12 September 2019	1.34	Monterey, CA MLLW = +0.018 MHHW = +1.4
Otter Cove (OC)	Monterey Peninsula	giant kelp	36.640	−121.928	26 July 2019	Rocky	2 July 2019	1.1	
San Carlos Beach (SCB)	Monterey Peninsula	giant kelp	36.612	−121.894	22 July 2019	Sandy Rocky	3 July 2019	0.14	
Hopkins Marine Station (HMS)	Monterey Peninsula	giant kelp	36.621	−121.901	10 July 2019	Sandy Rocky	5 July 2019	0.98	

FWHM). The RedEdge-M was equipped with a downwelling light sensor (DLS) for all flights. To calibrate reflectance for each flight, we imaged a spectral calibration panel with known reflectance during the middle of each mission when UAV batteries were swapped. Our along-track overlap between consecutive images was 80% and side-track overlap between consecutive flight lines was 75%. Sun glint can distort the reflectance of pixels when imagery is collected when the Sun is at or close to zenith (90°). To avoid glint contamination, we conducted flights at or close to optimal Sun angle conditions (~45° to zenith).

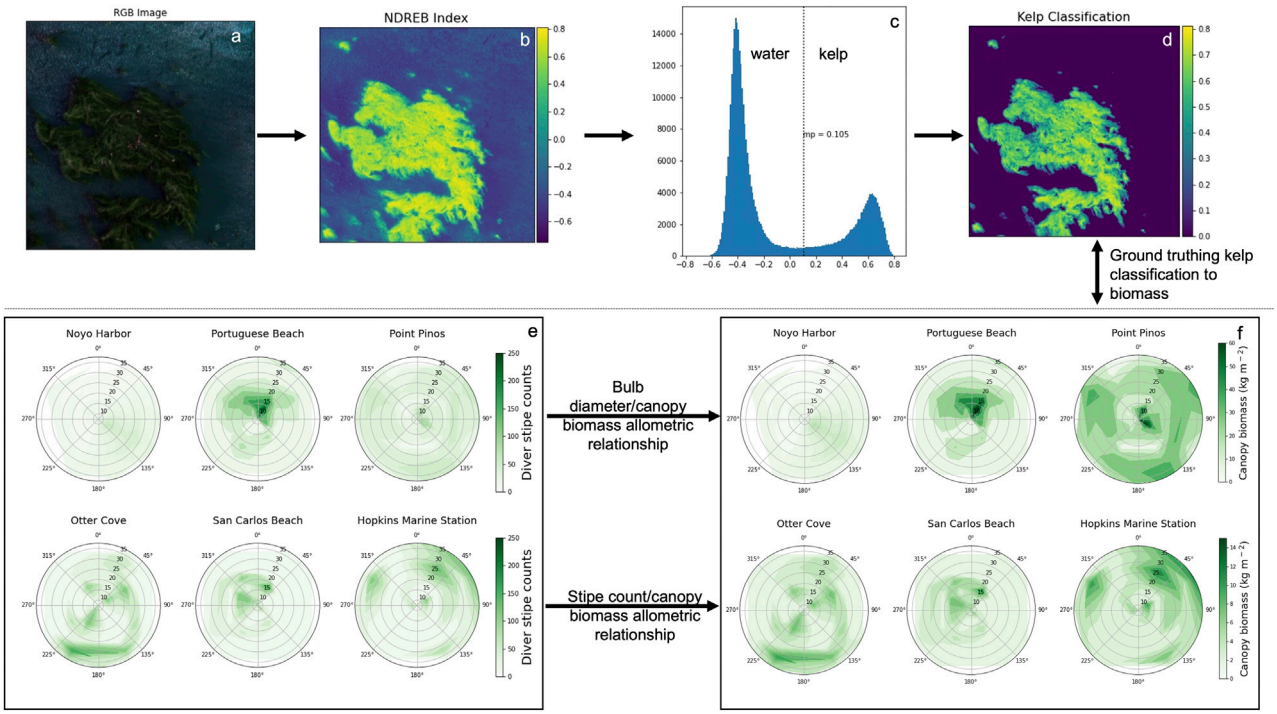

FIGURE 3 | A flow chart of the methodology used in the detection of kelp in each 10 cm pixel (top panel) and deriving *in situ* kelp canopy biomass via diver and morphometric surveys (bottom panel).

RedEdge-M imagery was processed in the photogrammetric software Pix4D Mapper (Pix4D, 1,008 Prilly, Switzerland). Raw images with pixel values in digital numbers (DN) were converted to radiance (L; W m^{-2} nm^{-1} sr^{-1}) using a standard MicaSense radiometric calibration model. Radiance values were converted to unitless reflectance (ρ) using a band constant reflectance calibration factor (F; 1/W m^{-2} nm^{-1} sr^{-1}). F was determined from the reflectance panel measurement made during survey flights by multiplying image L by F for each respective band, i, where:

$$F_i = \frac{\overline{\rho_i}}{\overline{L_i}}. \quad (1)$$

and $\overline{\rho_i}$ and $\overline{L_i}$ are the mean calibration panel reflectance and radiance values, respectively, for band i. Calibration panel reflectance values were provided by MicaSense. We assumed sky conditions were consistent throughout the duration of the flight (~20–30 min). Reflectance images were then made into orthomosaics. The stitched orthomosaics for each spectral band were exported as GeoTIFFs from Pix4D Mapper. Individual band orthomosaics were then merged and resampled to 10 cm spatial resolution using the Python 3.1 function *gdalwarp* and average interpolation as the resampling method. Finally, the five band rasters were subset to the appropriate dive site coordinates (**Table 1**; **Figure 3A**) using the Python 3.1 functions *gdal_translate* and *gdalwarp* (GDAL/OGR Contributors 2021), respectively.

Pixel based kelp detection–A vegetation index termed 'Normalized Difference Red-edge Blue' (NDREB) developed by Cavanaugh et al., 2021 was used to classify kelp pixels in UAV reflectance images (**Figures 3B–D**). Cavanaugh et al., 2021 showed that NDREB was superior at separating kelp and water compared to other multispectral indices. In brief, we calculated the NDREB $[(\rho_{\text{rededge}} - \rho_{\text{blue}})/(\rho_{\text{rededge}} + \rho_{\text{blue}})]$ for each 10 cm pixel (**Figure 3B**) and calculated histograms of the vegetation index values (**Figure 3C**). Each site image displayed a bimodal distribution of NDREB values. The midpoint between the two peaks was calculated using the Python 3.1 *findpeaks* module. Kelp was classified at each survey site by using the midpoint as the threshold value. Kelp pixels were defined as being greater than the threshold value (**Figure 3D**).

In situ surveys of kelp density and biomass–In situ surveys were used to develop spatially resolved estimates of canopy biomass for bull and giant kelp across six sites via 1) assessment of subtidal stipe (frond) density (**Figure 3E**), 2) sporophyte collection and morphometric measurement for development of genera-specific allometry and conversion of diver stipe (frond) density to canopy biomass (**Figure 3** bottom panel arrows), and the resulting derived biomass (**Figure 3F**). Results from field-based data were related to NDREB kelp classification results from UAV surveys with the aim to acquire image-based estimates of kelp canopy biomass (**Figure 3**). For both genera, sporophyte lengths were measured to the nearest mm using a diver transect tape and weights were measured to the nearest 0.01 kg using a portable electronic balance.

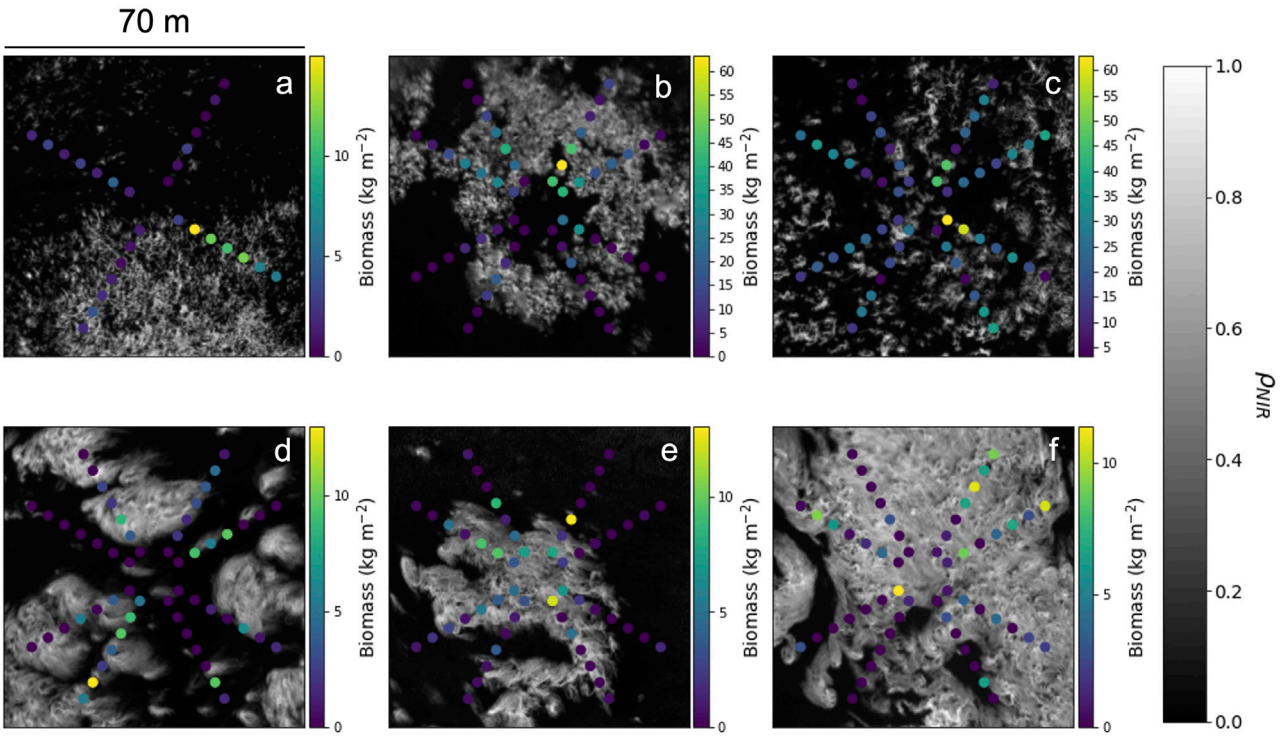

FIGURE 4 | MicaSense RedEdge-M near-infrared reflectance (ρ_{NIR}) for each dive survey site overlayed with the locations for the midpoint of each transect interval with the color of the dot corresponding to the measured *in situ* canopy biomass. **(A)** Noyo Harbor (NH), **(B)** Portuguese Beach (PB), **(C)** Point Piños (PP), **(D)** Otter Cove (OC), **(E)** San Carlos Beach (SCB), **(F)** Hopkins Marine Station (HMS).

Diver survey design - Subtidal surveys were designed to rapidly assess spatial distribution and patterns of stipe (frond) density across many kelp beds. Dive sites consisted of 3,600 m^2 square plots surveyed in a radial configuration (**Figure 4**). At five of the six sites (Portuguese Beach, Point Piños, Otter Cove, San Carlos Beach, and Hopkins Marine Station; **Figures 4B–F**), eight separate transects were conducted. At Noyo Harbor (**Figure 4A**), only four of the eight transects were conducted because ocean conditions limited dive operations. Point Piños (**Figure 4C**) was surveyed across two separate days (**Table 1**) because ocean conditions limited dive operations after the first four transects were conducted on 14 August 2019.

Survey teams consisted of two divers. One navigated each compass heading (30˚, 60˚, 120˚, 150˚, 210˚, 240˚, 300˚, and 330˚) and reeled out the transect tape to 40 m, while the other counted stipes (fronds) within a 2-m swath along the transect tape. Stipe (frond) counts were recorded for every 5-m interval (area = 10 m^2), which we have termed the 'transect interval'. Each individual transect began at the 5-m mark to avoid overlap of stipe (frond) counts at the center of the survey area. As a result, each complete dive survey consisted of a series of 4 or 8, 70 m^2 transects or a total dive survey area of 280 m^2 (Noyo Harbor) or 560 m^2 (Portuguese Beach, Point Piños, Otter Cove, San Carlos Beach, and Hopkins Marine Station). The geospatial location of each transect interval was trigonometrically determined using the GPS location (UTM) of the center buoy and the transect distance from the center buoy.

Morphology and allometry for canopy biomass - Adult sporophytes (**Figure 5**), defined as the mature stage of the bull and giant kelp diploid lifecycles, were indiscriminately collected for morphometric measurement and canopy biomass determination across multiple locations in central and northern California (**Table 2**) in 2018 and 2019, including five of the six dive sites surveyed in 2019 (Noyo Harbor, Point Piños, Otter Cove, Hopkins Marine Station, and San Carlos Beach). Specifically, we measured morphology at four sites for giant kelp (total of 11 sporophytes) in 2019 and six sites for bull kelp (total of 86 sporophytes) in 2018 and 2019 (**Table 2**). Divers removed sporophytes from the substrate manually by cutting the primary stipe just above the holdfast (**Figure 5**; **Supplementary Figure S1A**), brought them to the surface and then to shore where morphometric measurements were conducted on a clean surface (**Supplementary Figures S1B–F**). When tissue hydration could not be maintained using fresh seawater, a portable pop-up tent was used to shade samples (**Supplementary Figures 1C, D**).

Bull kelp morphometric measurements were made for stipe length and width, bulb diameter, sub-bulb diameter (15 cm below the base of the bulb), longest blade length/width, longest blade weight, number of blades, canopy weight (top 1 m of stipe including all the blade biomass), and total sporophyte weight (**Figure 5**). Central and northern California data from 2018 to 2019 (n = 86) were combined with data collected on the western

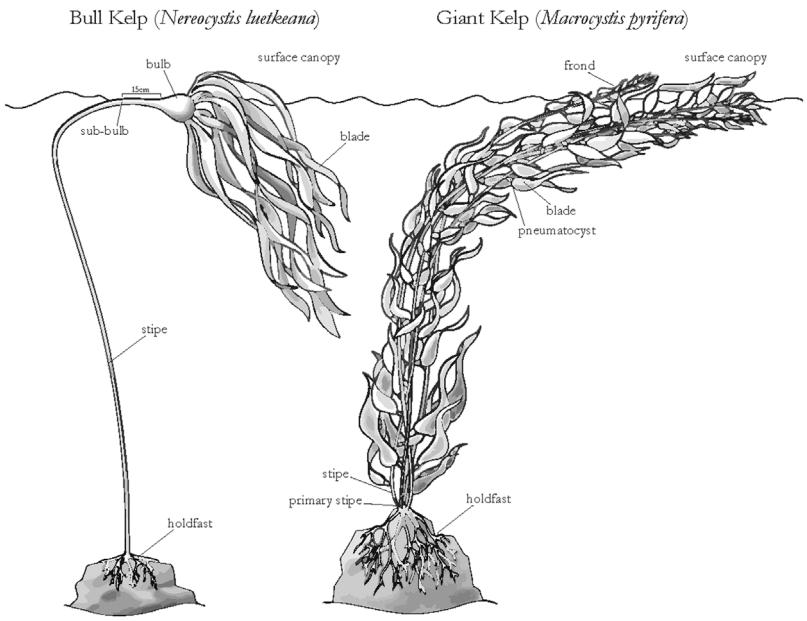

FIGURE 5 | Relevant morphometric characteristics of bull kelp (Nereocystis leutkeana) and giant kelp (Macrocystis pyrifera) adult sporophytes (image credit: Niky Taylor; UCSC).

TABLE 2 | Detailed information of site-specific sporophyte collection including site name, region, kelp genera, latitude/longitude, and collection dates.

Site Name	Site Location	Kelp Genera	Latitude	Longitude	Collection Date(s) - # of Sporophytes
Casper Cove	Mendocino County	bull kelp	39.362	−123.820	Sept. 17, 2018–10
Albion Cove	Mendocino County	bull kelp	39.228	−123.772	Sept. 18, 2018–15
Bodega Marine Lab	Sonoma County	bull kelp	38.311	−123.071	Sept. 25, 2018–17
Noyo Harbor	Mendocino County	bull kelp	39.429	−123.812	Sept. 19, 2018–12 7 Aug. 2019–22
Point Piños	Monterey Peninsula	bull kelp	36.641	−121.931	Aug. 28, 2019–10
Hopkins Marine Station	Monterey Peninsula	giant kelp	36.622	−121.902	8 July 2019–2 10 July 2019–1 17 July 2019–1
San Carlos Beach	Monterey Peninsula	giant kelp	36.613	−121.895	22 July 2019–1 31 July 2019–1
Ocean Cove	Monterey Peninsula	giant kelp	36.630	−121.919	26 July 2019–1 Aug. 8, 2019–1 Aug. 26, 2019–1
Steamer Lane	Santa Cruz	giant kelp	36.952	−121.023	Aug. 16, 2019–2

coast of Prince of Wales Island, Alaska in 2018 (Pearson and Eckert, 2019; n = 55).

Bulb diameter was randomly measured within the 3,600 m^2 dive survey plot. The site-specific mean bulb diameter was used to estimate the mean canopy biomass per sporophyte at each bull kelp site. The total wet biomass for each transect interval (10 m^2) was calculated by taking the product of the stipe counts within each transect interval and the site-specific mean canopy biomass per sporophyte derived from allometry.

Giant kelp sporophytes were divided into two sections, the sub-surface canopy and surface canopy (**Figure 5**). The surface canopy was determined by measuring the depth of the holdfast prior to collection. Within each section, morphometric measurements were made for total tissue weight, number of blades, and number of fronds. Central California giant kelp data were combined with SBC LTER measurements of canopy biomass and frond counts from 2002 to 2003 (Reed and Rassweiler, 2018; n = 36). At each giant kelp dive site, the canopy biomass per transect interval was estimated using the allometric relationship developed between the total number of stipes (fronds)/sporophyte and the canopy biomass. We counted within each transect interval to calculate the corresponding canopy biomass. An ANCOVA was run using the Python 3.1 *pingouin* statistics module (Vallat, 2018) to determine if

TABLE 3 | Linear regression statistics for the different morphometric measurements for estimates of wet weight.

Bull Kelp	**Slope (m)**	**Intercept (b)**	r^2	**F-Statistic**	**n**
Longest blade length (cm)	24.1 ± 2.4	153.4 ± 14.4	0.78	103.2	32
Sub-bulb diameter (cm)	0.2 ± 0.03	2.6 ± 0.16	0.72	76.2	32
Bulb diameter (cm)	0.2 ± 0.03	5.8 ± 0.20	0.64	53.1	32
Number of blades	3.0 ± 0.6	40.7 ± 40.7	0.48	27.7	32
Giant Kelp	**Slope (m)**	**Intercept (b)**	R^2	**F-Statistic**	**n**
Number of blades (canopy)	0.03 ± 0.01	0.2 ± 4.1	0.81	38.8	11
Mean frond length (canopy)	0.07 ± 0.02	-7.9 ± 9.6	0.57	10.6	10
Number of fronds (base)–this study	0.9 ± 0.3	-0.8 ± 8.6	0.48	8.2	11
Number of fronds (base)–SBC LTER	0.4 ± 0.1	4.2 ± 3.6	0.32	23.1	40

region (and season) had an influence on the slope and intercepts of the relationship between the dependent variable (bulb diameter or frond count) and canopy biomass.

Retrieving canopy biomass from NDREB–A spatial analysis was conducted to compare *in situ* derived canopy biomasses to mean NDREB kelp classification at four different radii around the transect interval (0.5, 1.5, 2.5, 5 m). We chose these radii because they relate to relevant spaceborn sensor's ground sampling distances - PlanetScope (3 m), Planet RapidEye (5 m), ESA Sentinel-2 (10 m) (spectral characteristics are described in **Supplementary Table S1**). All pixels that fell within the radius were averaged, resulting in a single mean NDREB value per transect interval location. A full site level comparison of mean biomass and mean NDREB was also conducted with relevance to deriving canopy biomass from the Landsat suite (30 m) and SBC LTER retrievals of canopy biomass with Landsat (Cavanaugh et al., 2011; Bell et al., 2015).

Semi-variogram analysis–A geostatistical approach was used to describe kelp patch spatial autocorrelation and patch characteristics by calculating the semi-variance of each survey site's NDREB (**Figure 3D**) and *in situ* biomass measurements (**Figure 3F**). Prior to conducting the variogram analysis, *in situ* biomass data were interpolated into a 2-D grid with the MATLAB function *griddata*, using a triangulation-based linear interpolation method. We used the Python 3.1 Variogram and DirectionalVariogram classes within the SciKit-GStat (skgstat) module to determine the semi-variance (γ), which can be described as half of the measured variance between pairs of values separated by an increasing lag distance between pixels (h):

$$\gamma(h) = \frac{1}{2N(h)} * \sum_{i=1}^{N(h)} \left(NDREB(x_i) - NDREB(x_{i+h})^2\right) \quad (2)$$

where NDREB (or *in situ* biomass) are the observations at locations x_i and $x_i + h$ and $N(h)$ is the number of point pairs at that lag. Semi-variance parameters were estimated by fitting spherical models to the empirical semivariograms:

$$\gamma = \eta + C * \left(1.5 * \frac{h}{r} - 0.5 * \frac{h^3}{\alpha}\right) \quad (3)$$

where η is the nugget, C is the sill, and α is the range. The η describes the total unresolved variability, or noise, while C describes the total resolved variability. The α describes the distance at which the semi-variance reaches a maximum and, therefore, the distance of spatial autocorrelation. Spherical models are ideal when the increase in semi-variance is steep or being estimated within a small region (such as the 60 m length scale of this study). However, because this was a descriptive analysis for patch characteristics, we do not report specific η, C, or α information from the different sites.

RESULTS

Allometric relationships for canopy biomass were developed for bull kelp and giant kelp based on morphometric measurements and their relationship to canopy biomass (**Figure 5**). Longest blade length was the strongest predictor of bull kelp canopy biomass (r^2 = 0.78; **Table 3**). Sub-bulb diameter, bulb diameter, and number of blades were also significant predictors of canopy biomass (r^2 = 0.72, 0.64, and 0.48, respectively; **Table 3**). Our results were consistent with Stekoll et al. (2006) for bull kelp in Alaska. Bulb diameter was selected to use for deriving canopy biomass in this study because bulb diameter can be quickly measured by divers or from a boat at the surface of the kelp canopy. The strongest predictor of giant kelp canopy biomass was the number of canopy blades (r^2 = 0.81; **Table 3**). Additionally, mean canopy frond length and number of fronds at the base of the sporophyte were statistically significant predictors of canopy biomass (r^2 = 0.57 and 0.48, respectively; $p < 0.05$). Our sample size of sporophytes was relatively small, collected in July and August 2019 (n = 11). However, combining our dataset with SBC LTER measurements of stipe (frond) count and canopy biomass collected monthly in 2002 and 2003 increased the sample size to n = 40, increased the F-statistic 23.1 ($p < 0.05$), but reduced the overall coefficient of determination to 0.32 (**Table 3**).

All *in situ* diver measurements of bull kelp bulb diameter displayed a Gaussian probability distribution (**Figures 6A–C**). The range of bulb diameter at Point Piños (**Figure 6C**; 7.06 ± 0.96; n = 148) was significantly different than Noyo Harbor (**Figure 6A**; 6.50 ± 0.76; n = 80; t-statistic = 4.5; $p < 0.05$) and Portuguese Beach (**Figure 6B**; 6.44 ± 0.64; n = 79; t-statistic = 5.12; $p < 0.05$). Additionally, the morphology of Monterey Peninsula bull kelp bulb diameter was significantly different from the morphology of bull kelp in Alaska and Mendocino (**Table 4**). As a result, there were significant differences between the bull kelp allometric

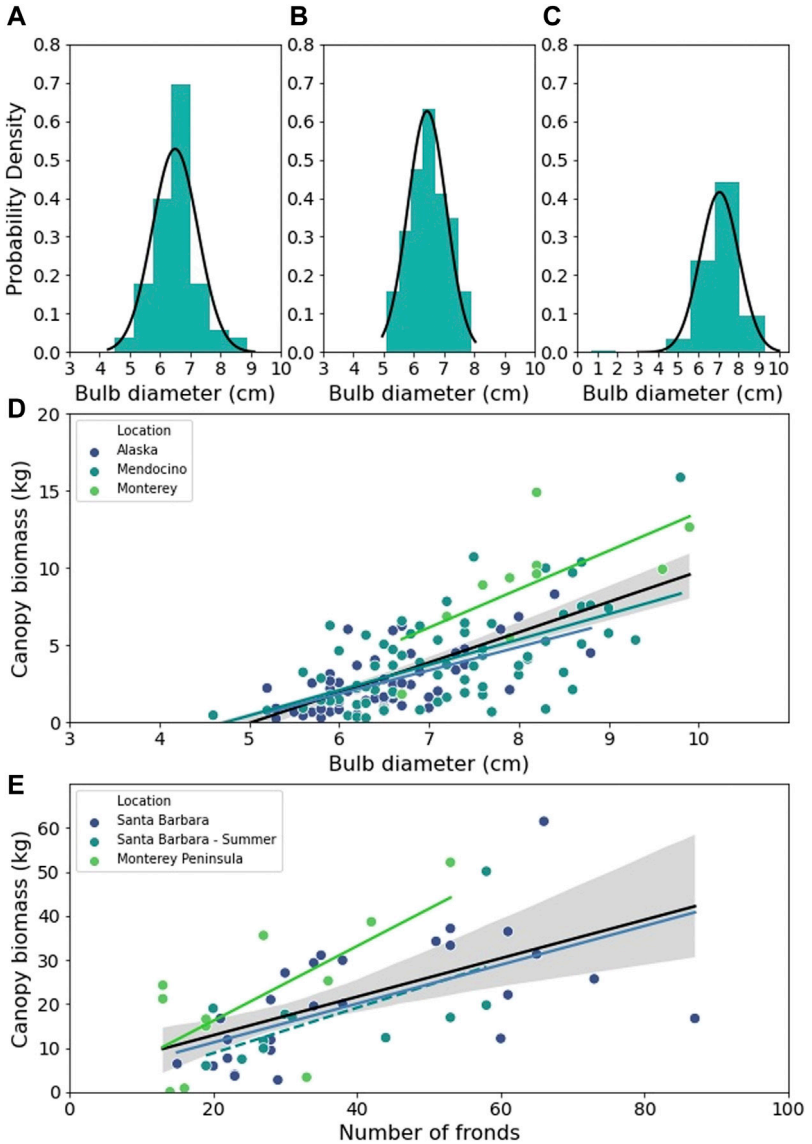

FIGURE 6 | The probability distribution of bull kelp bulb diameter for **(A)** Noyo Harbor, **(B)** Portuguese Beach, **(C)** Point Piños. **(D)** Scatter plot of wet bull kelp canopy biomass against bulb diameter fitted with OLS linear regressions for Alaska (blue line), Mendocino (teal line), Monterey (green line), and all regions combined (black line). **(E)** Scatter plot of wet giant kelp canopy biomass against frond number fitted with OLS linear regressions for all data from Santa Barbara, CA (blue line), summer data from Santa Barbara (blue dashed line), Monterey, CA (green line), and all regions combined (black line). Regression details listed in **Supplementary Table S1**. Grey shaded areas represent regression 95% CI.

TABLE 4 | Results from pairwise Tukey's HSD post-hoc test for region specific bull kelp bulb diameters. *denotes significance.

Location A	Location B	Mean (A)	Mean (B)	Std. Error	*p*-value
Alaska	Mendocino	2.6	3.9	0.47	0.012
Alaska	Monterey	2.6	9.0	0.91	*0.001
Mendocino	Monterey	3.9	9.0	0.90	*0.001

relationship by region (**Figure 6D**; **Table 5**). However, giant kelp was not influenced by region or season (**Table 5**). The per sporophyte canopy biomass measurements were generally higher for giant kelp than bull kelp and maxima were ~15 and 60 kg for bull kelp and giant kelp, respectively (**Figure 6**).

Though measured canopy biomass values ranged significantly across site and genera, NDREB values were generally within range of each other (**Figure 7**; top row = bull kelp sites; bottom row = giant kelp sites). A predictive relationship between canopy biomass and NDREB was observed at two of the study sites, Portuguese Beach (bull kelp; **Figure 7B**) and San Carlos Beach (giant kelp; **Figure 7E**) for all sampling radii (0.5, 1.5, 2.5 m; **Table 6**). Regression statistics for these two sites was characterized by high *F*-statistic and r^2 values relative to the other four sites. However, across all sites, there was no influence of averaging radii on the predictive power of the relationship between

TABLE 5 | ANCOVA results for the effect of region (and seasons for giant kelp) on the slope and intercepts of the relationship between the dependent variable (bulb diameter or frond count) and canopy biomass. Bull kelp regions are Monterey, Mendocino, and Alaska. Giant kelp regions/seasons are Santa Barbara (all), Santa Barbara (summer), and Montery. *denotes significance.

Genera	Group	Degrees of Freedom (Df)	F	*p*-value	Effect Size
Nereocystis	Region	2	11.6	$*2.3 \times 10^{-5}$	0.15
Nereocystis	Bulb Diameter (cm)	1	84.7	$*5.3 \times 10^{-16}$	0.38
Macrocystis	Region/season	2	2.6	8.5×10^{-2}	0.074
Macrocystis	Sporophyte frond	1	44.6	$*6.9 \times 10^{-9}$	0.41

canopy biomass and NDREB. Portuguese Beach (**Figure 7C**) and Point Piños exhibited the largest range in measured canopy biomass (0 to >60 kg-ww m^{-2}; **Figure 7**) that were associated with high diver recorded stipe densities (**Figures 3E, F**). Conversely, giant kelp stations had a smaller ranged in measured canopy biomass as a result of lower diver measured stipe densities (0–15 kg-ww m^{-2}; **Figures 7D–F**).

No significant relationship was observed when site level means of NDREB and *in situ* canopy biomass were compared (**Figure 8**). Portuguese Beach and Point Piños showed high mean canopy biomass relative to the mean station NDREB reflecting higher diver measured stipe densities for these two bull kelp sites (**Figures 3E, F**). The remaining four stations were characteristic of relatively low mean canopy biomass and a range of mean NDREB values from 0.18 to 0.39 reflecting sparser diver measured stipe densities at those four stations.

The descriptive variogram analysis conducted for NDREB and diver measured canopy biomass indicated differences in patch level spatial patterns between Portuguese Beach, San Carlos Beach and the other survey sites (**Figure 9**). Although we were not able to consistently develop predictions of canopy biomass from NDREB, the patterns of semi-variance across the site's spatial extents were similar between the diver surveys and NDREB, indicating that similar spatial patterns were being observed with both methods. For Portuguese Beach and San Carlos Beach (the two sites where robust relationships of canopy biomass were achieved), a dominant 'u-shaped' pattern was visible in the semi-variograms, where variability rapidly rises to the edge of the patch (the peak of the 'u-shape') and falls outside of the patch beyond approximately 30 m from the center of the survey site.

DISCUSSION

In the northeast Pacific region, bull kelp and giant kelp form the base of an ecologically and economically important temperate nearshore coastal ecosystem with extensive floating surface canopies. Remote sensing is advantageous for detecting their floating canopy and deriving large-scale estimates of surface canopy biomass, which comprises more than 90% of bull and giant kelp standing stock (Rassweiler et al., 2008). Development and validation of remotely derived kelp canopy biomass is lacking because the associated methodology is time intensive and costly, but important because biomass is necessary for determining rates of net primary productivity and quantifying carbon cycling in temperate nearshore regions. In this study, we compiled bull and giant kelp morphometric measurements from different regions in the NE Pacific to assess the validity of applying a single biomass conversion relationship across disparate regions. We also surveyed six spatially distinct sites (3 bull kelp and 3 giant kelp) with varying stipe and canopy characteristics for measurements of *in situ* canopy biomass via diver and UAV surveys with the aim to retrieve canopy biomass estimates from remote sensing imagery. The results exhibited that 1) kelp morphology differed slightly across the regions we examined but didn't strongly influence *in situ* estimates of canopy biomass, and 2) reliable, consistent remote sensing retrieval of canopy biomass was difficult using the survey approach developed here and dependent on specific kelp patch characteristics across sites.

Kelp allometry for canopy biomass measurements–Deriving and utilizing allometric relationships for canopy biomass is a key component of developing methods for canopy biomass retrieval from spaceborne and aerial platforms (Stekoll et al., 2006; Cavanaugh et al., 2010). In this study, we compared the regional differences in bull kelp bulb diameter and giant kelp stipe count as predictors of canopy biomass and found that across all regions, these metrics were robust predictors of canopy biomass. The effect of region on the slopes and intercept of the linear relationships were small for both genera (**Figure 6**; **Table 4** and **Table 5**) and indicates that it may be generally acceptable to apply a relationship derived from one region to others across the NE Pacific. It is possible that the morphological differences we observed were a result of local-scale hydrodynamics influencing tissue morphology, rather than regional-scale processes (Koehl and Alberte, 1988; Koehl, 2022).

However, the sample sizes for some of our regions were relatively low (e.g. giant kelp from the Monterey region). Sample sizes of studies collecting sporophyte morphology is influenced by the per sporophyte effort it requires to collect this information. A single giant kelp sporophyte can take up to 15 person-hours to conduct a complete morphometric survey. Bull kelp is less labor intensive, on the order of two person-hours per sporophyte. Both genera require SCUBA (from shore or boat) to collect and deliver sporophytes that can weigh up to 60 kg to the lab for processing. While the logistical challenges may be the primary reason for the lack of data, the collection of this data have not been prioritized by funding and management agencies in the past. We advocate for allocating resources into developing predictive relationships for canopy

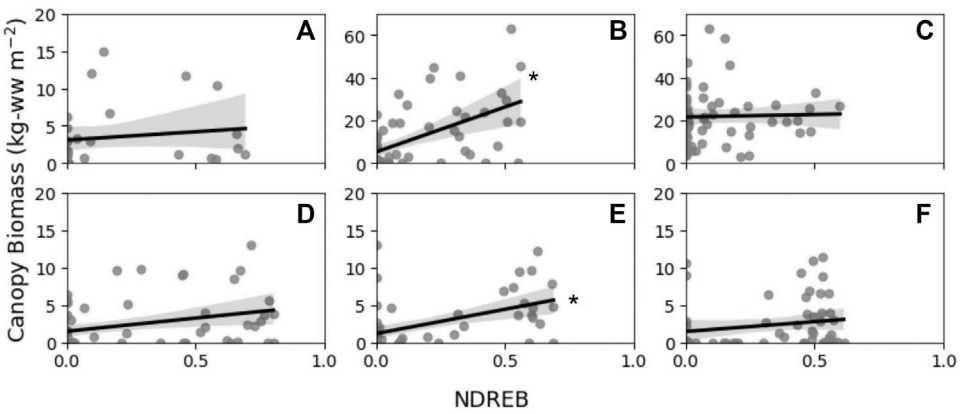

FIGURE 7 | Transect interval canopy biomass in kg wet weight (kg-ww) against average NDREB values from a 1.5 m radius around each transect interval **(A)** Noyo Harbor; **(B)** Portuguese Beach; **(C)** Point Piños; **(D)** Otter Cove; **(E)** San Carlos Beach; **(F)** Hopkins Marine Station with OLS regression (black lines) and 95% confidence intervals (grey shading). Significance of the OLS regression is indicated with an asterisk. See **Table 6** for each sampling radii and site's regression statistics.

TABLE 6 | Original Least Squared (OLS) regression statistics from **Figure 7** with slope and intercept values ± 1 standard deviation.

Station	NDREB Sampling Radii (m)	n	Slope (m)	Intercept (b)	r^2	*F*-Statistic
Noyo Harbor (NH)	0.5	28	1.1 ± 3.23	3.3 ± 0.96	0.004	0.12
	1.5	28	2.2 ± 3.06	3.1 ± 0.97	0.020	0.52
	2.5	28	2.3 ± 3.15	3.0 ± 0.98	0.025	0.68
Portuguese Beach (PB)	0.5	56	37.3 ± 7.33	5.7 ± 2.07	0.324	25.9
	1.5	56	42.1 ± 8.78	5.2 ± 2.21	0.299	23.1
	2.5	56	45.6 ± 10.0	4.7 ± 2.35	0.264	20.8
Point Piños (PP)	0.5	56	1.5 ± 7.82	21.7 ± 2.11	0.001	0.04
	1.5	56	2.4 ± 10.8	21.6 ± 2.21	0.001	0.05
	2.5	56	6.2 ± 13.5	21.2 ± 2.37	0.004	0.21
Otter Cove (OC)	0.5	56	2.7 ± 1.33	1.7 ± 0.58	0.072	4.20
	1.5	56	3.5 ± 1.42	1.5 ± 0.58	0.103	6.22
	2.5	56	3.7 ± 1.55	1.49 ± 0.59	0.097	5.79
San Carlos Beach (SCB)	0.5	56	6.5 ± 1.48	1.2 ± 0.45	0.264	19.3
	1.5	56	6.5 ± 1.49	1.2 ± 0.48	0.263	19.3
	2.5	56	6.8 ± 1.51	1.1 ± 0.48	0.273	20.3
Hopkins Marine Station (HMS)	0.5	56	2.7 ± 1.90	1.4 ± 0.78	0.036	2.00
	1.5	56	2.6 ± 1.98	1.4 ± 0.80	0.032	1.78
	2.5	56	2.4 ± 2.05	1.5 ± 0.82	0.026	1.42

biomass to further improve accuracy of kelp canopy retrieval from spaceborne sensors via long-term monitoring and targeted studies with UAVs.

The influence of kelp patch characteristics on canopy biomass retrievals–Descriptive results from the semi-variogram analysis indicated that kelp bed characteristics play a role in accurately determining canopy biomass retrievals. If a kelp patch was larger than the spatial area of the dive survey (i.e. a breakdown in autocorrelation did not occur within the survey area), we were limited in our ability to develop a robust working relationship between canopy biomass and NDREB. If the kelp patch was smaller than the spatial area of the dive survey (i.e., pixel autocorrelation broke down within the dive survey area), we were able to identify a relationship between canopy biomass and kelp fraction. This pattern in the semi-variance results described sites with a distinct kelp patch surrounded by water and biomass at these sites also had a robust correlation with NDREB. Out of the six sites, Portuguese Beach (**Figure 4B**; **Figure 7**) and San Carlos Beach (**Figure 4E**; **Figure 7**) were clear examples of this pattern, exhibiting dense, relatively homogenous stipe (frond) counts inside the kelp bed and a relatively homogenous absence of stipes (fronds) outside of the kelp bed. This indicates a potential mismatch between the scale of measurements by diver survey and remote sensing because 1) surveying large patches is quantified best by satellite remote sensing but is not feasible for *in situ* surveys, and 2) very high spatial resolution

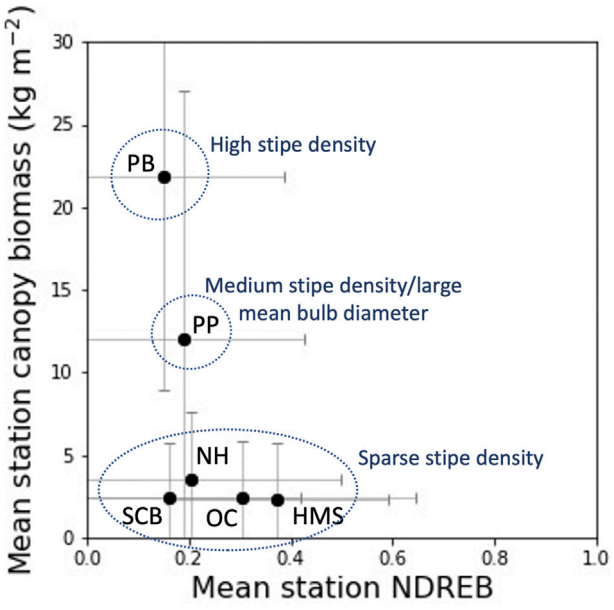

FIGURE 8 | Mean station canopy biomass plotted again mean station NDREB with ± 1SE bars in grey. Different circles represent conditions of stipe density at the different dive sites.

measurements of canopy can be observed with UAVs, but diver survey methods are limited in the coarseness of their observations.

The influence of kelp genera on canopy biomass retrievals–Bull and giant kelp have distinctly different morphologies and surface canopy characteristics which influenced accurate retrievals of canopy biomass estimates from UAV based observations. Bull kelp has a single gas-filled stipe and pneumatocyst (**Figure 5**) with long blades (length ≅ 1 m) that can number up to the hundreds concentrated at the top of the sporophyte. Unlike giant kelp blades, the blades of a bull kelp do not float on the water surface without sufficient tidal and current forcing. Because tides and current were not producing significant drag on the bull kelp canopy at our survey sites (as visible in the imagery; **Figure 4**), much of the biomass in the canopy (**Figure 5** bull kelp blades) was below the water surface at our study sites. Therefore, the spectral signature of the kelp canopy observed was emergent stipes and bulbs. This may have resulted in a heterogeneous surface comprised of kelp tissue and water and relatively low NDREB in comparison to *in situ* biomass measurements.

Diver estimates of canopy biomasses ranged significantly depending on the density of bull kelp sporophytes resulting in area normalized canopy biomasses at Portuguese Beach and Point Piños that were approximately 7 times greater than the giant kelp sites (**Figure 7**). Although bulb diameter can predict an individual sporophyte's canopy biomass with relative accuracy, using stipe counts did not translate well to area normalized canopy biomass at interval locations, either because the sporophytes fanned out and distributed at the surface or because blades were below the water surface and were not detected by the sensor on the UAV. Further consideration should be given to the deepest survey site (Point Piños; ~30 m) where it is likely that a portion of the sporophytes counted by divers didn't reach the surface, resulting in an overestimation of *in situ* canopy biomass.

Giant kelp blades grow along the entire frond from the base to the growing tip (meristem; **Figure 5**). More of the canopy biomass is floating on the water surface or just below because the base of each giant kelp blade (length ≅ 30 cm) contains a single pneumatocyst. A single giant kelp sporophyte can contain up to ~100 fronds clustered together (**Figure 5**; **Supplementary Figure S1A**). Therefore, dense floating canopies of giant kelp fronds can form, often with many

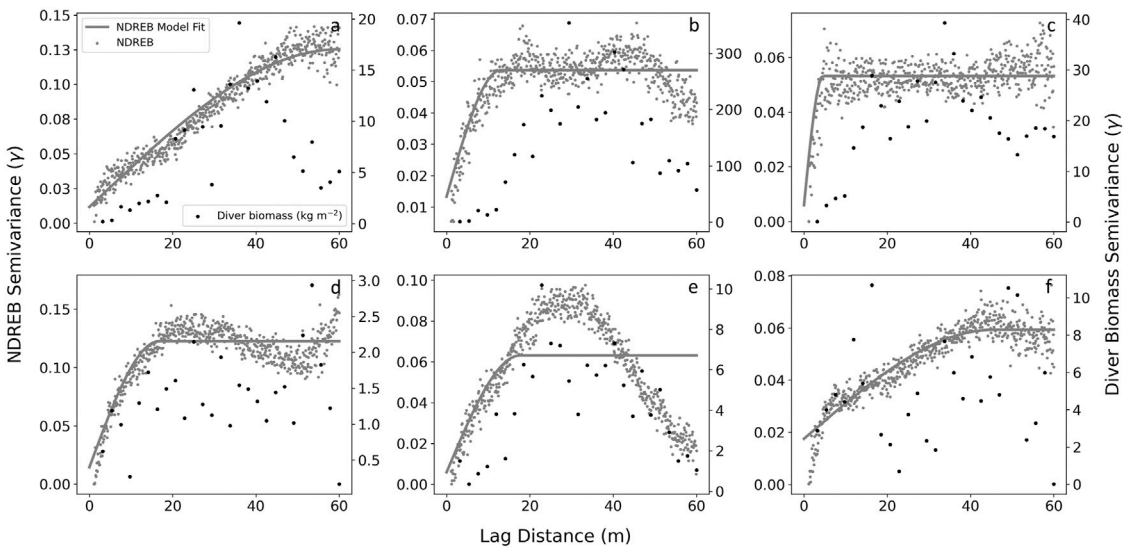

FIGURE 9 | Semi-variogram for each station NDREB (grey) and diver measured canopy biomass (black). NDREB are overlayed with a spherical model fit. **(A)** Noyo Harbor; **(B)** Portuguese Beach; **(C)** Point Piños; **(D)** Otter Cove; **(E)** San Carlos Beach; **(F)** Hopkins Marine Station.

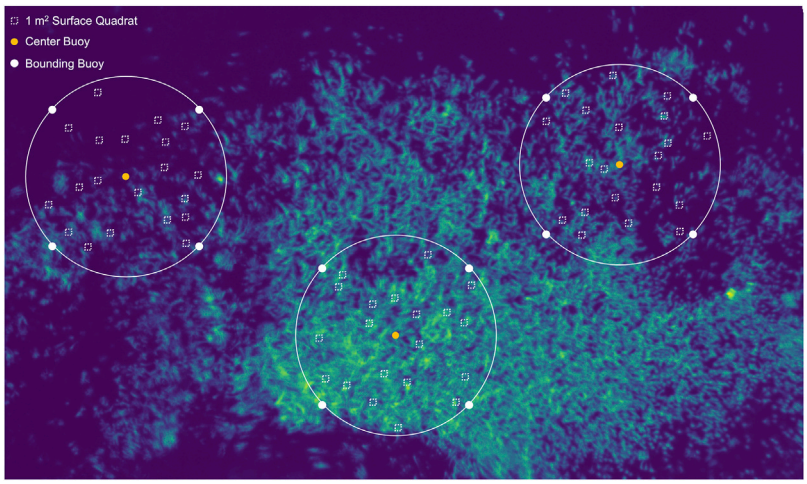

FIGURE 10 | Suggested survey design for future *in situ* validation studies of canopy biomass using a UAV platform.

fronds laying on top of each other at the surface. However, since the distribution of individual sporophytes at the substrate is often sparse and non-homogenously distributed across a kelp patch, disparities can develop between sparse diver counts of fronds and the expression of dense surface canopy, and an under-representation of *in situ* canopy biomass. It is likely that stipe count, though relatively easy for divers to conduct is an unreliable approach for remote sensing validation studies of giant kelp.

The influence of survey design on canopy biomass retrievals - The *in situ* diver survey approach developed in this study was similar to methodology for Landsat derived giant kelp canopy biomass (Rassweiler et al., 2008; Cavanaugh et al., 2011) and aerial survey derived Alaska bull kelp biomass (Stekoll et al., 2006) in that disparate kelp beds were measured to quantify canopy biomass and then associated with spectral characteristics of kelp canopy. However, the goal of our survey design was to rapidly assess as many large sites as possible by only collecting stipe (frond) counts within each 5-m section of the transect. The radial survey pattern allowed us to have eight transects of reasonable length (35 m) within each survey site. By assessing a large area, we could increase the sample size, and therefore, the number of matchup locations between *in situ* canopy biomass and UAV imagery. However, it is possible that persistent errors and offsets were introduced to the transect interval's geospatial locations via this approach. Despite SBC LTER's robust prediction of Santa Barbara giant kelp canopy biomass estimates from 30 m Landsat (Cavanaugh et al., 2011; Bell et al., 2020b), we had little success developing a similar relationship using mean site level (60 × 60 m) NDREB and canopy biomass, likely due to limitations in the number of sites that could be sampled within the given timeframe of the study.

Our findings shed light on the advantages of site-specific long-term monitoring for retrieving canopy biomass from remote sensing platforms at the kelp bed scale (~10–30 m), allows for the development of temporally and spatially robust relationships. However, this approach is not always feasible for subtidal monitoring programs (which, in itself, are lacking). We recognize there should be alternative methods to retrieving canopy biomass. UAVs provide flexibility for survey design and approach to adjust measurement temporal frequency, the spatial extent of the survey (a single bed to multiple), and postprocessing pixel spatial binning (pixel sizes from 10 cm +). If given a long enough timeseries or enough data points, UAV's can collect the required information, but as demonstrated here, it requires multiple measurements (i.e. a timeseries) to build reliable relationships.

Suggested survey design for future UAV methods–Based on the results presented here and lessons learned, we provide a recommended survey design aimed at retrieving canopy biomass estimates from remote sensing methods. Primarily, we believe measurements should focus directly on the surface canopy rather than subtidal stipe counts or biomass (**Figure 10**). This allows for direct comparison of *in situ* surface biomass measurements to pixel-based kelp classification metrics. Specifically, we recommend conducting *in situ* canopy measurements across a variety of densities (either within a single bed or multiple different beds) within a bounding box marked by buoys/markers in the center and corners (**Figure 10** white and orange dots). Buoys should remain deployed for the extent of the UAV survey for ground truthing and geospatial positioning of the *in situ* site. Quadrat sampling points for surface measurements within the bounding box can be randomized by heading/distance to remove bias associated with using underwater compass headings for calculation of GPS locations. As such GPS measurements at the center of each quadrat location can be taken. Within each 1 m^2 quadrat, measurements of the bulb diameter (bull kelp), sub-bulb diameter (bull kelp), mean canopy stipe length (giant kelp), and stipe count (bull and giant kelp) can be used to estimate canopy biomass (**Table 3**). Taking subtidal stipe counts is a good comparison to other surveys being conducted by relevant monitoring organizations (i.e. Reef Check California, CDFW, Humble State University, etc.), but as indicated by the results presented here can be unreliable for developing fine spatial scale estimates of biomass. We recommend conducting UAV surveys on the same day just before or after *in situ* canopy measurements or at a similar tidal height.

CONCLUSION

Estimation of kelp canopy area has rapidly advanced, leading to regional-scale (e.g Bell et al., 2020b) to global-scale (e.g. Mora-Soto et al., 2020) estimates, and assessments of kelp canopy area in very remote locations (Friedlander et al., 2020; Houskeeper et al., 2022). Despite these advances, it is desirable in some cases to move beyond canopy area to assess biomass, and then primary productivity, as that provides information on kelp bed health, carbon sequestration, and viability. Validation studies of kelp canopy biomass retrievals via remote sensing are lacking because the data is difficult to collect, but this data is important because accurate large-scale estimates of productivity and carbon cycling cannot be made without them. We attempted to close the data gap by developing a rapid and thorough approach to gathering the *in situ* and remote sensing data that are required to retrieve biomass from remote sensing platforms. Although, specific kelp patch configuration and survey design limited the number of sites where we successfully retrieved kelp canopy biomass, we consider our findings valuable to the kelp remote sensing community, to whom there is very little of this data available. Understanding the challenges in determining remotely derived kelp canopy biomass is important and our general conclusions can be used to extrapolate to other regions and potentially other kelp genera. To aid in future efforts, we outline an improved survey design for future *in situ* validation studies using UAVs. Finally, we strongly recommend funding/implementation of long-term monitoring programs, such as those used by the SBC LTER, across the region for both giant and bull kelp. Critically, this requires both standardization of methodology and consistent funding by management agencies for such efforts. The alternative is to rely solely on canopy area which can be a poor proxy for biomass and productivity, limiting our understanding of how kelp beds respond to short- and long-term environmental conditions.

DATA AVAILABILITY STATEMENT

The raw data supporting the conclusion of this article will be made available by the authors, without undue reservation.

AUTHOR CONTRIBUTIONS

All authors contributed to this manuscript including conceptualization, MLM and RMK; methodology, MLM and RMK; writing—original draft preparation, MLM; writing—review and editing, MLM and RMK.

FUNDING

Financial support was provided by the Dr. Earl H. Myers and Ethel M. Myers Oceanographic and Marine Biology Trust and the UCSC Department of Ocean Sciences. Vessel support and lodging was provided by Laura Rogers-Bennett's Marine Invertebrate Fisheries and Conservation Laboratory. Funding for the UAV was supported by the Ida Benson-Lynn Ocean Health endowment. The MicaSense RedEdge-M and Pix4D software was supported by the Packard Science and Technology endowment to the Institute of Marine Sciences.

ACKNOWLEDGMENTS

Many thanks to the all the people who made this work possible, including Heidi Hirsh (Stanford University), scientific divers (Logan Grady, Jeannette Peters, and Sara Hamilton), field volunteers (alphabetically: Dennis Finger, Aimee Foy, Megan Gallagher, Kyle Hughes, Kevin Hum, Josie Iselin, Quinn Letitia, John Mizell, Rich Muller, Brynn O'Hara, and Jezabel Powers), and sensitive wildlife monitors (Herrick Hanks, Teri Nicholson, Jennifer Parkin, Judi Romero, and Bill Standley). Development and testing of the MicaSense RedEdge-M was provided by Ben Erwin and Brent Roman. Helpful feedback on this manuscript was provided by Tom Bell (University of California Santa Barbara/Woods Hole Oceanographic Institute) and Niky Taylor (University of California Santa Cruz).

SUPPLEMENTARY MATERIAL

The Supplementary Material for this article can be found online at: https://www.frontiersin.org/articles/10.3389/fenvs.2022.690963/full#supplementary-material

REFERENCES

Beas-Luna, R., Micheli, F., Woodson, C. B., Carr, M., Malone, D., Torre, J., et al. (2020). Geographic Variation in Responses of Kelp Forest Communities of the California Current to Recent Climatic Changes. *Glob. Chang. Biol.* 26, 6457–6473. doi:10.1111/gcb.15273

Bell, T. W., Allen, J. G., Cavanaugh, K. C., and Siegel, D. A. (2020b). Three Decades of Variability in California's Giant Kelp Forests from the Landsat Satellites. *Remote Sens. Environ.* 238, 110811. doi:10.1016/j.rse.2018.06.039

Bell, T. W., Cavanaugh, K. C., and Siegel, D. A. (2015). Remote Monitoring of Giant Kelp Biomass and Physiological Condition: An Evaluation of the Potential for the Hyperspectral Infrared Imager (HyspIRI) Mission. *Remote Sens. Environ.* 167, 218–228. doi:10.1016/j.rse.2015.05.003

Bell, T. W., Nidzieko, N. J., Siegel, D. A., Miller, R. J., Cavanaugh, K. C., Nelson, N. B., et al. (2020a). The Utility of Satellites and Autonomous Remote Sensing Platforms for Monitoring Offshore Aquaculture Farms: A Case Study for Canopy Forming Kelps. *Front. Mar. Sci.* 7, 520223. doi:10.3389/fmars.2020.520223

Cavanaugh, K. C., Cavanaugh, K. C., Bell, T. W., and Hockridge, E. G. (2021). An Automated Method for Mapping Giant Kelp Canopy Dynamics from UAV. *Front. Environ. Sci.* 8, 587354. doi:10.3389/fenvs.2020.587354

Cavanaugh, K. C., Reed, D. C., Bell, T. W., Castorani, M. C. N., Beas-luna, R., and Barrett, N. S. (2019). Spatial Variability in the Resistance and Resilience of Giant Kelp in Southern and Baja California to a Multiyear Heatwave. *Front. Mar. Sci.* 6, 1–14. doi:10.3389/fmars.2019.00413

Cavanaugh, K., Siegel, D., Kinlan, B., and Reed, D. (2010). Scaling Giant Kelp Field Measurements to Regional Scales Using Satellite Observations. *Mar. Ecol. Prog. Ser.* 403, 13–27. doi:10.3354/meps08467

Cavanaugh, K., Siegel, D., Reed, D., and Dennison, P. (2011). Environmental Controls of Giant-Kelp Biomass in the Santa Barbara Channel, California. *Mar. Ecol. Prog. Ser.* 429, 1–17. doi:10.3354/meps09141

Dayton, P. K., Currie, V., Gerrodette, T., Keller, B. D., Rosenthal, R., and Tresca, D. V. (1984). Patch Dynamics and Stability of Some California Kelp Communities. *Ecol. Soc. Am.* 54, 253–289. doi:10.2307/1942498

Dayton, P. K., Tegner, M. J., Edwards, P. B., and Riser, K. L. (1999). Temporal and Spatial Scales of Kelp Demography: The Role of Oceanographic Climate. *Ecol. Monogr.* 69, 219–250. doi:10.1890/0012-9615(1999)069[0219:tassok]2.0.co;2

Dexter, K. F., Wernberg, T., Grace, S. P., Thormar, J., Fredriksen, S., Narvaez, C. N., et al. (2020). Marine Heatwaves and the Collapse of Marginal North Atlantic Kelp Forests. *Sci. Rep.* 10, 13388. doi:10.1038/s41598-020-70273-x

Ebeling, A. W., Laur, D. R., Rowley, R. J., and Barbara, S. (1985). Severe Storm Disturbances and Reversal of Community Structure in a Southern California Kelp Forest. *Mar. Biol.* 84, 287–294. doi:10.1007/bf00392498

Finger, D. J. I., McPherson, M. L., Houskeeper, H. F., and Kudela, R. M. (2021). Mapping Bull Kelp Canopy in Northern California Using Landsat to Enable Long-Term Monitoring. *Remote Sens. Environ.* 254, 112243. doi:10.1016/j.rse.2020.112243

Friedlander, A. M., Ballesteros, E., Bell, T. W., Caselle, J. E., Campagna, C., Goodell, W., et al. (2020). Kelp Forests at the End of the Earth: 45 Years Later. *PLoS One* 15, e0229259. doi:10.1371/journal.pone.0229259

Hamilton, S. L., Bell, T. W., Watson, J. R., Grorud-Colvert, K. A., and Menge, B. A. (2020). Remote Sensing: Generation of Long-Term Kelp Bed Data Sets for Evaluation of Impacts of Climatic Variation. *Ecology* 101 (7), e03031. doi:10.1002/ecy.3031

Hohman, R., Hutto, S., Catton, C. A., and Koe, F. (2019). *Sonoma-Mendocino Bull Kelp Recovery Plan*. San Francisco, CA: Plan for the Greater Farallones National Marine Sanctuary and the California Department of Fish and Wildlife.

Houskeeper, H. F., Rosenthal, I. S., Cavanaugh, K. C., Pawlak, C., Trouille, L., Byrnes, J. E. K., et al. (2022). Automated Satellite Remote Sensing of Giant Kelp at the Falkland Islands (Islas Malvinas). *PLoS One* 17, e0257933. doi:10.1371/journal.pone.0257933

Huovinen, P., Ramírez, J., Palacios, M., and Gómez, I. (2020). Satellite-Derived Mapping of Kelp Distribution and Water Optics in the Glacier Impacted Yendegaia Fjord (Beagle Channel, Southern Chilean Patagonia). *Sci. Total Environ.* 703, 135531. doi:10.1016/j.scitotenv.2019.135531

Koehl, M. A. R., and Alberte, R. S. (1988). Flow, Flapping, and Photosynthesis of Nereocystis Leutkeana: A Functional Comparison of Undulate and Flat Blade Morphologies. *Mar. Biol.* 99, 435–444. doi:10.1007/bf02112137

Koehl, M. A. R. (2022). Ecological Biomechanics of Marine Macrophytes. *J. Exp. Bot.* 73, 1104–1121. doi:10.1093/jxb/erab536

Ling, S. D., Johnson, C. R., Frusher, S. D., and Ridgway, K. R. (2009). Overfishing Reduces Resilience of Kelp Beds to Climate-Driven Catastrophic Phase Shift. *Proc. Natl. Acad. Sci. U. S. A.* 106, 22341. doi:10.1073/pnas.0907529106

McPherson, M. L., Finger, D. J. I., Houskeeper, H. F., Bell, T. W., Carr, M. H., Rogers-Bennett, L., et al. (2021). Large-Scale Shift in the Structure of a Kelp Forest Ecosystem Co-Occurs with an Epizootic and Marine Heatwave. *Commun. Biol.* 4, 298. doi:10.1038/s42003-021-01827-6

Mora-Soto, A., Palacios, M., Macaya, E. C., Gomez, I., Huovinen, P., Perez-Matus, A., et al. (2020). A High-Resolution Global Map of Giant Kelp (Macrocystis Pyrifera) Forests and Intertidal Green. *Remote Sens.* 12, 1–20. doi:10.3390/rs12040694

Nijland, W., Reshitnyk, L., and Rubidge, E. (2019). Satellite Remote Sensing of Canopy-Forming Kelp on a Complex Coastline: A Novel Procedure Using the Landsat Image Archive. *Remote Sens. Environ.* 220, 41–50. doi:10.1016/j.rse.2018.10.032

Oliver, E. C. J., Benthuysen, J. A., Bindoff, N. L., Hobday, A. J., Holbrook, N. J., Mundy, C. N., et al. (2017). The Unprecedented 2015/16 Tasman Sea Marine Heatwave. *Nat. Commun.* 8, 1–12. doi:10.1038/ncomms16101

Pearson, H., and Eckert, G. L. (2019). Morphometrics of Bull Kelp Forests in Southeast Alaska During Summer 2018 [Internet]. Available at: https://knb.ecoinformatics.org/view/urn%3Auuid%3A8463ff07-cc96-4853-bfca-79b3ee1d69e3.

Rasher, D. B., Steneck, R. S., Halfar, J., Kroeker, K. J., Ries, J. B., Tinker, M. T., et al. (2020). Keystone Predators Govern the Pathway and Pace of Climate Impacts in a Subarctic Marine Ecosystem. *Science* 369, 1351–1354. doi:10.1126/SCIENCE.AAV7515

Rassweiler, A., Arkema, K. K., Reed, D. C., Zimmerman, R. C., and Brzezinski, M. A. (2008). Net Primary Production, Growth, and Standing Crop Ofmacrocystis Pyriferain Southern California. *Ecology* 89, 2068. doi:10.1890/07-1109.1

Reed, D. C., and Brzezinski, M. A. (2009). "Kelp Forests," in *The Managment of Natural Coastal Carbon Sinks*. Editors D. Laffoley and G. Grimsditch (Gland, Switzerland: IUCN), 31–36.

Reed, D., and Rassweiler, A. (2018). SBC LTER: REEF: Allometric Measurements of Giant Kelp Ver 1. Environmental Data Initiative. Available at: https://doi.org/10.6073/pasta/e880e6b231af718c63f623893c678c86.

Reed, D. C., Rassweiler, A., and Arkema, K. K. (2008). Biomass Rather Than Growth Rate Determines Variation in Net Primary Production by Giant Kelp. *Ecology* 89, 2493–2505. doi:10.1890/07-1106.1

Schroeder, S. B., Dupont, C., Boyer, L., Juanes, F., and Costa, M. (2019). Passive Remote Sensing Technology for Mapping Bull Kelp (Nereocystis Luetkeana): A Review of Techniques and Regional Case Study. *Glob. Ecol. Conserv.* 19, e00683. doi:10.1016/j.gecco.2019.e00683

Stekoll, M. S., Deysher, L. E., and Hess, M. (2006). A Remote Sensing Approach to Estimating Harvestable Kelp Biomass. *J. Appl. Phycol.* 18, 323–334. doi:10.1007/s10811-006-9029-7

Steneck, R. S., Graham, M. H., Bourque, B. J., Corbett, D., Erlandson, J. M., Estes, J. A., et al. (2002). Kelp Forest Ecosystems: Biodiversity, Stability, Resilience and Future. *Envir. Conserv.* 29, 436–459. doi:10.1017/S0376892902000322

Straub, S. C., Wernberg, T., Thomsen, M. S., Moore, P. J., Burrows, M. T., Harvey, B. P., et al. (2019). Resistance, Extinction, and Everything in Between - The Diverse Responses of Seaweeds to Marine Heatwaves. *Front. Mar. Sci.* 6, 1–13. doi:10.3389/fmars.2019.00763

Teagle, H., Hawkins, S. J., Moore, P. J., and Smale, D. A. (2017). The Role of Kelp Species as Biogenic Habitat Formers in Coastal Marine Ecosystems. *J. Exp. Mar. Bio. Ecol.* 492, 81–98. doi:10.1016/j.jembe.2017.01.017

Vallat, R. (2018). Pingouin: Statistics in Python. *J. Open Sour. Soft.* 3 (31), 1026. doi:10.21105/joss.01026

Wernberg, T., Bennett, S., Babcock, R. C., de Bettignies, T., Cure, K., Depczynski, M., et al. (2016). Climate-Driven Regime Shift of a Temperate Marine Ecosystem. *Science* 353, 169–172. doi:10.1126/science.aad8745

Wernberg, T., Krumhansl, K., Filbee-dexter, K., and Pedersen, M. F. (2019). "Status and Trends for the World's Kelp Forests," in *World Seas: An Environmental Evaluation* (Elsevier), 57–78. doi:10.1016/B978-0-12-805052-1.00003-6

Young, M., Cavanaugh, K., Bell, T., Raimondi, P., Edwards, C. A., Drake, P. T., et al. (2015). Environmental Controls on Spatial Patterns in the Long-Term Persistence of Giant Kelp in Central California. *Ecology* 86, 45–60. doi:10.1890/15-0267.1

Conflict of Interest: The authors declare that the research was conducted in the absence of any commercial or financial relationships that could be construed as a potential conflict of interest.

Publisher's Note: All claims expressed in this article are solely those of the authors and do not necessarily represent those of their affiliated organizations, or those of the publisher, the editors and the reviewers. Any product that may be evaluated in this article, or claim that may be made by its manufacturer, is not guaranteed or endorsed by the publisher.

Copyright © 2022 McPherson and Kudela. This is an open-access article distributed under the terms of the Creative Commons Attribution License (CC BY). The use, distribution or reproduction in other forums is permitted, provided the original author(s) and the copyright owner(s) are credited and that the original publication in this journal is cited, in accordance with accepted academic practice. No use, distribution or reproduction is permitted which does not comply with these terms.

Advantages of publishing in Frontiers

OPEN ACCESS
Articles are free to read for greatest visibility and readership

FAST PUBLICATION
Around 90 days from submission to decision

HIGH QUALITY PEER-REVIEW
Rigorous, collaborative, and constructive peer-review

TRANSPARENT PEER-REVIEW
Editors and reviewers acknowledged by name on published articles

Frontiers
Avenue du Tribunal-Fédéral 34
1005 Lausanne | Switzerland

Visit us: www.frontiersin.org
Contact us: frontiersin.org/about/contact

REPRODUCIBILITY OF RESEARCH
Support open data and methods to enhance research reproducibility

DIGITAL PUBLISHING
Articles designed for optimal readership across devices

FOLLOW US
@frontiersin

IMPACT METRICS
Advanced article metrics track visibility across digital media

EXTENSIVE PROMOTION
Marketing and promotion of impactful research

LOOP RESEARCH NETWORK
Our network increases your article's readership